Petrological and Geochemical Constraints on the Origin and Nature of the Eagle’s Nest Intrusion, McFaulds Lake Greenstone Belt, Ontario

By

Vladislav Sheshnev

A thesis submitted in partial fulfilment of requirements for the degree of
Master of Science in Geology

2026

Department of Geology

Faculty of Science and Environmental Studies

Lakehead University
Thunder Bay, Ontario

Abstract

The Eagle's Nest intrusion is a mafic-ultramafic, blade-shaped dike that hosts the only known economically significant orthomagmatic Ni-Cu-(PGE) mineralization in the Ring of Fire region of Ontario. It is part of the Koper Lake subsuite of the more voluminous Ring of Fire Intrusive Suite (~2736–2732 Ma) and occurs within the Meso- to Neoarchean in age McFaulds Lake Greenstone Belt. The Ring of Fire Intrusive Suite is host to chromite, Fe-Ti-V, and Ni-Cu-(PGE) mineralization. Previous studies investigated the orebody and mineralization hosted by the Eagle's Nest intrusion, with limited attention to the unmineralized parts of the system. This study applied multidisciplinary petrological and geochemical techniques to evaluate the petrogenetic controls on the formation of the Eagle's Nest intrusion through the examination of the less mineralized portions of the intrusion and genetically related mafic dikes. The Eagle's Nest intrusion can be subdivided into the marginal and the inner zone. The marginal zone is composed of gabbroic rocks that exhibit the most evolved mineralogical and geochemical characteristics, with evidence of intense pseudomorphic alteration that often preserves primary magmatic textures. Contacts with the host tonalite vary, generally reflecting a prolonged high magma flux, but only rarely preserving evidence of rapid cooling and chilled margins. The marginal zone gradationally transitions into the inner zones, which consists of ultramafic ortho- to mesocumulate rocks. The inner zone is characterized by coherent linear geochemical trends that reflect olivine and chromite accumulation with variable proportions of intercumulus silicate phases and interstitial sulfides, consistent with petrographic observations. Most inner zone rocks are characterized by a strong positive correlation between MgO and Cr_2O_3, reflecting the crystallization of olivine and chromite in cotectic proportions. However, several of the mineralized peridotite samples deviate from this trend despite containing similar proportions of these minerals. Petrographic observations and intercumulus pyroxene mineral chemistry suggest that the deviation from the cotectic trend may be caused by sulfide percolation and displacement of a Cr-rich intercumulus silicate melt, rather than the presence of less than cotectic proportions of olivine and chromite. A new parental magma composition estimate was established using olivine and chromite mineral chemistry, as well as whole rock geochemistry of ultramafic cumulate rocks interpreted to reflect cotectic proportions olivine and chromite, with variable proportions of intercumulus silicate melt. The estimate yielded a parental magma composition that contained ~15 wt% MgO and ~11 wt% FeO_t, consistent with a komatiitic basalt magma. The new composition is more evolved than previous estimates, however, it is in close agreement with the composition of identified chilled margins, associated mafic dikes, and olivine. Forward thermodynamic modeling simulations of the new parental magma, reproduce the petrographically determined crystallization sequence at low pressures, suggesting that the Eagle’s Nest intrusion formed at shallow crustal levels. Whole rock geochemistry and Sm-Nd isotopes show that the Eagle’s Nest magma was derived from a depleted mantle source, above the garnet stability field, which then underwent extensive crustal contamination from multiple sources that included both the host tonalite, and older supracrustal rocks. Crustal contamination by sulfur-bearing supracrustal rocks likely contributed to attaining sulfide saturation of the magma, as evidenced by $\Delta^{33}S$ values consistent with mass-independent fractionation. The distinctive petrological and metallogenic characteristics of the Eagle’s Nest intrusion in the Esker Intrusive Complex may be a result of several distinct processes involving both emplacement dynamics and parental magma composition, resulting in unique metal endowments relative to other intrusions in the McFaulds Lake Greenstone Belt.

Acknowledgments

This research would not have been possible without the support, guidance, and generosity of many individuals and institutions. I am deeply grateful to all those who contributed their time, expertise, and encouragement throughout this project. First and foremost, I would like to thank Dr. Pete Hollings for providing me with this opportunity and for his encouragement and support over the course of this work. Your mentorship extended far beyond this research, supporting both my professional and personal growth and shaping who I am today. I am sincerely grateful for your confidence in me and your guidance. I am grateful to Wyloo for supporting this project and accommodating its technical and logistical needs. In particular, I would like to thank Matt Deller, Andrew Smith, Matt Downey, Ryan Weston, Dana Campbell, and Logan Krueger for their insightful discussions and valuable feedback. I also extend my appreciation to the staff at the Esker Site for their technical support and hospitality during field work. I would like to thank the Geology Faculty at Lakehead University for their support throughout my academic journey. Special thanks to Dr. James Tolley, Dr. Moses Angombe, and Dr. Tobias Stephan for their insightful discussions, encouragement, and organizing Thesis Therapy, your support is invaluable. Thank you to Kristi Tavener and Dr. Jonas Valiunas for their technical support in sample and thin section preparations. I would also like to extend my gratitude to Dr. James Miller, Dr. Geoff Haggie, and Dr. Wyatt Bain for their openness and thoughtful conversations that helped shape aspects of this research. This work benefited greatly from the assistance of numerous collaborators and facilities. I thank Richard Stern at the Canadian Centre for Isotopic Microanalysis for obtaining sulfur isotope data, Dr. M. Brzozowski for coordinating LA-MC-ICP-MS work, Dr. P. Yang for the guidance during EPMA work, the Western University for allowing us to use your facilities, the Isotope Geochemistry and Geochronology Research Centre at Carlton University for obtaining radiogenic isotope data, the Department of Mineral Sciences at the Smithsonian Museum for providing the secondary spinel standard mount, and Dr. M. Lesher for sharing available sulfur isotope data for the region. This research was made possible through the financial support from an NSERC Alliance Grant and Wyloo, the Bernie Schnieders Memorial Award at Lakehead University, the Estate of Ben Cowan (Ben Cowan Graduate Scholarship), and the ILSG (Eisenbrey Student Travel Award). Finally, I owe my deepest gratitude to my fellow colleagues, my family and friends, and especially to Hanna Tiitto, for their unwavering love, patience, and encouragement throughout this journey.

Table of Contents

List of Figures

List of Tables

List of Abbreviations

3BSZ	3B Shear Zone
Act	Actinolite
Amp	Amphibole
Ath	Anthophyllite
Bt	Biotite
Cb	Carbonate
CCIM	Canadian Centre for Isotopic Microanalysis
Ccp	Chalcopyrite
Cg	Coarse-grained
Chl	Chlorite
Chr	Chromite
Cpx	Clinopyroxene
En	Enstatite
EN type	Eagle's Nest type dike
Ep	Epidote
EPMA	Electron Probe Microanalysis
Fg	Fine-grained
Fo	Forsterite
Fol	Foliation
Fs	Ferrosilite
Hbl	Hornblende
HREE	Heavy Rare Earth Element
ICP-AES	Inductively Coupled Plasma Atomic Emission Spectroscopy
ICP-MS	Inductively Coupled Plasma Mass Spectrometry
IUGS	International Union of Geological Sciences
LA	Laser Ablation
LILE	Lare Ion Lithophile Element
LREE	Light Rare Earth Element
Mag	Magnetite
MC	Multi Collector
M_d	Median
MDF	Mass-Dependent Fractionation
MER	Molar Element Ratio
MFSZ	McFaulds Shear Zone

Mg	Medium-grained
MLGB	McFaulds Lake Greenstone Belt
Ol	Olivine
Opx	Orthopyroxene
PGE	Platinum Group Element
Pl	Plagioclase
Pn	Pentlandite
Po	Pyrrhotite
PPL	Plane-Polarized Light
pXRF	Portable X-Ray Fluorescence
Py	Pyrite
Pyx	Pyroxene
QFM	Quartz-Fayalite-Magnetite
Qz	Quartz
REE	Rare Earth Element
RL	Reflected Light
RoFIS	Ring of Fire Intrusive Suite
SD	Standard Deviation
SEM	Scanning Electron Microscope
Ser	Sericite
SIMS	Scanning Ion Mass Spectrometer
Srp	Serpentine
Sul	Sulfide
TIMS	Thermal Ionization Mass Spectrometer
Tlc	Talc
Tr	Tremolite
Ttn	Titanite
VCDT	Vienna Canyon Diablo Troilite
VFg	Very Fine-grained
VMS	Volcanogenic Massive Sulfide
WDS	Wavelength Dispersive Spectrometer
Wo	Wollastonite
XPL	Cross-Polarized Light

Chapter 1 Introduction

The Ring of Fire region is one of the most significant, undeveloped mineral districts in North America, hosting an extensive suite of critical metals, including chromium, nickel, copper, platinum-group elements (PGE), titanium, and vanadium, which are vital to Canada's economic and green energy transition (Government of Canada, 2022). Located approximately 530 km north of Thunder Bay, the region is underlain by the McFaulds Lake Greenstone Belt (MLGB), which has been actively explored over the past few decades. Exploration interest first began in the early 2000s with the discovery of diamond-hosting kimberlites, followed by the discovery of volcanogenic massive sulfide (VMS) base-metal mineralization, which triggered a staking rush in the region (Sage, 2000; O'Donohue and French, 2003; Metsaranta and Houlé, 2020). Exploration during the subsequent years, led to additional discoveries of VMS-style base metals, shear-zone hosted gold, and orthomagmatic Cr and Fe-Ti-V mineralization. In 2007, Noront Resources Ltd. discovered orthomagmatic Ni-Cu-(PGE) mineralization hosted within an ultramafic intrusive body, within what is now known as the Eagle's Nest intrusion (Metsaranta and Houlé, 2020). The discoveries encouraged extensive research by industry, government, and academia to better understand the geology and metal endowments within MLGB. Whereas the chromite and Fe-Ti-V hosting intrusions have been the subject of extensive research (e.g., Azar, 2010; Laarman, 2014; Kuzmich et al., 2015; Carson et al., 2015; Sappin et al., 2015; Spath, 2017), little research has been done to understand the Ni-Cu-(PGE) mineralization within the belt (i.e., Mungall et al., 2010; Zuccarelli, 2020). To address the gap, this study investigated the Eagle's Nest intrusion.

The Eagle's Nest is an example of a conduit-style orthomagmatic sulfide deposit that is hosted within a mafic-ultramafic blade-shaped dike. To date, the Eagle's Nest intrusion is host to the only economically significant orthomagmatic Ni-Cu-(PGE) mineralization within MLGB, containing 11.1 Mt of proven and probable reserves grading 1.68 % Ni, 0.87 % Cu, 0.89 g/t Pt, 3.09 g/t Pd, and 0.18 g/t Au (Burgess et al., 2012). The formation of orthomagmatic sulfide deposits, like the Eagle's Nest, are the product of a complex series of self-organizing processes, the essential elements of which are widely accepted. These processes involve the ascent of a mantle-derived magma through the crust, assimilation of sulfur from the country rock that leads to sulfide saturation and the formation of immiscible sulfide melt, which then interacts with the silicate magma and preferentially sequesters chalcophile elements, and through physical processes such as gravitational segregation and accumulation, ultimately forms a magmatic sulfide deposit (Naldrett, 2011; Barnes et al., 2016; Barnes, 2023). Magmatic sulfide deposits are subdivided into two main groups: (1) sulfide-rich deposits valued for their Ni and Cu, and (2) sulfide-poor deposits valued for their PGE contents (Naldrett, 2004).

The central point of many studies investigating magmatic igneous systems is determining the composition of the magma that is parental to a system. The parental magma composition is the composition that can explain the lithological, mineralogical, and geochemical variability within the system (Herzberg et al., 2007; Smith et al., 2024). A given parental magma is the result of magmatic differentiation processes that effected a primary mantle-derived magma during transport from the mantle. The first-order controls, although not necessarily the main ones, on the composition and the metal budget of the primary magma are mantle source processes. The degree of partial melting of a mantle source strongly controls both the composition and metal budget (Naldrett, 2011). At lower degrees of partial melting, the generated magma will tend to be less ultramafic and more enriched in Cu and PGEs (Fig. 1.1; Naldrett, 2011). In contrast, at higher degrees of partial melting, the generated melts will be more ultramafic and will be enriched in Ni relative to Cu and PGEs (Fig. 1.1; Naldrett, 2011). Through magmatic differentiation processes, the primary magma will evolve to less primitive compositions reflecting the magmatic differentiation processes that occurred during ascent. The magmatic differentiation processes will transform the primary magma into a more evolved, parental magma that reflects both the mantle source and magmatic differentiation processes (Barnes, 2023; Smith et al., 2024). As a result, the parental magma of a system is often defined as the most magnesian liquid composition that can be inferred within a system, and that can explain the variation observed within a system (Herzberg et al., 2007).

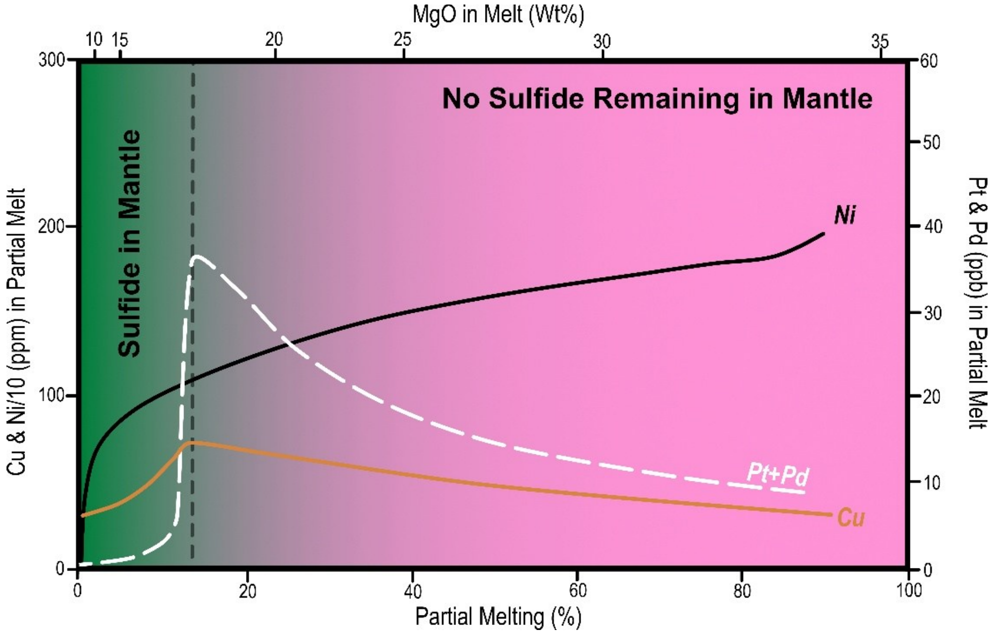

Figure 1.1: Modelled variation diagram illustrating the variability in the composition of a melt (i.e., MgO), and its metal budget as a function of the degree of partial melting. Modified after Naldrett (2010).

There are many different approaches to determine the composition of a parental magma, which include but are not limited to the identification of quenched parental liquids (e.g., Barnes et al. 2010; Godel et al., 2011), identification and/or estimation of the most primitive olivine that crystallized from the magma (e.g., Chai and Naldrett, 1992; Barnes and Fiorentini, 2012), or application of a mass-balance approach to determine the trace element compositions of liquids in equilibrium with cumulate phases (e.g., Bédard, 1994).

This study aimed to place additional constraints on the petrogenetic processes responsible for the formation of the Eagle's Nest intrusion. Specifically, it characterized the less-studied, unmineralized portions of the intrusion using drill-core observations, petrography, geochemistry, mineral chemistry, and radiogenic and stable isotope techniques. The characteristics of the Eagle's Nest intrusion were then compared to spatially associated mafic-ultramafic dikes to identify those that are genetically related. Petrographic observations, whole-rock geochemistry, and mineral chemistry of unmineralized ultramafic rocks within the Eagle's Nest intrusion were used to estimate the composition of the parental magma, which was then compared to identified chilled margins, related mafic dikes, and associated intrusions within MLGB. Using mineral chemistry, this study provided the first attempts at estimating the depth of emplacement for the Eagle's Nest intrusion. To test the validity of the estimates, forward-modelling simulations were applied using the estimated parental magma in an attempt to reproduce the mineralogical variability observed within the intrusion. Lastly, trace element and isotopic data were utilized to constrain the characteristics of the mantle source, the history of magma contamination, and the tectonic setting. Collectively, these constraints were used to enhance the understanding of the petrogenetic controls on Ni-Cu-(PGE) mineralization and provide insights that could be applied to their exploration within MLGB.

Chapter 2 Regional Geology

2.1 Superior Province

The Eagle's Nest intrusion is situated within the late-Mesoarchean to early-Neoarchean MLGB, underlain by the Oxford-Stull Domain in the northern region of the Superior Province (Fig. 2.1). The Superior Province is the largest preserved Archean craton, spanning over portions of Quebec, Ontario, Manitoba, and Minnesota, covering a total region of approximately 1,572,000 km^2 (Thurston, 1991). The Superior Province consists of a series of east-west trending volcano-plutonic and metasedimentary belts, granitic batholiths, and strongly metamorphosed high-grade gneissic terranes with distinct lithological, structural, geochemical, metamorphic, and metallogenic characteristics (Card and Ciesielski, 1986; Stott, 1997). It records the formation and modification of continental and oceanic crust between 4.3 and 2.57 Ga, with the final stage of assembly taking place during the Kenoran Orogeny, between 2.72 and 2.68 Ga (Card, 1990; Percival et al., 2006). The Superior Province has preserved its configuration since the mid-Neoarchean, when it became tectonically stable (Percival et al., 2006).

Characterization of the Superior Province has been the subject of debate, with several proposed subdivisions. The earliest subdivisions, identified the presence of geologically distinct regions, separated by major crustal structures, based on geographic and structural features (Wilson, 1939; Gill, 1949). Wilson (1949) noted that the ages of orogenic belts increased towards the central part of the Superior Province (i.e., the North Caribou Core), proposing that the Superior Province formed as results of successive accretion of orogenic belts onto its margins. As data availability increased and analytical techniques improved, a combination of lithological, geochemical, geophysical, structural, and isotopic ages, have been widely applied in an attempt to subdivide the Superior Province (Douglas, 1973; Goodwin, 1978; Stockwell, 1982).

Subsequently, Card and Ciesielski (1986) proposed a widely accepted subdivision of the Superior Province into four types of litho-tectonic subprovinces comprising volcano-plutonic, metasedimentary, plutonic, and high-grade gneiss domains.

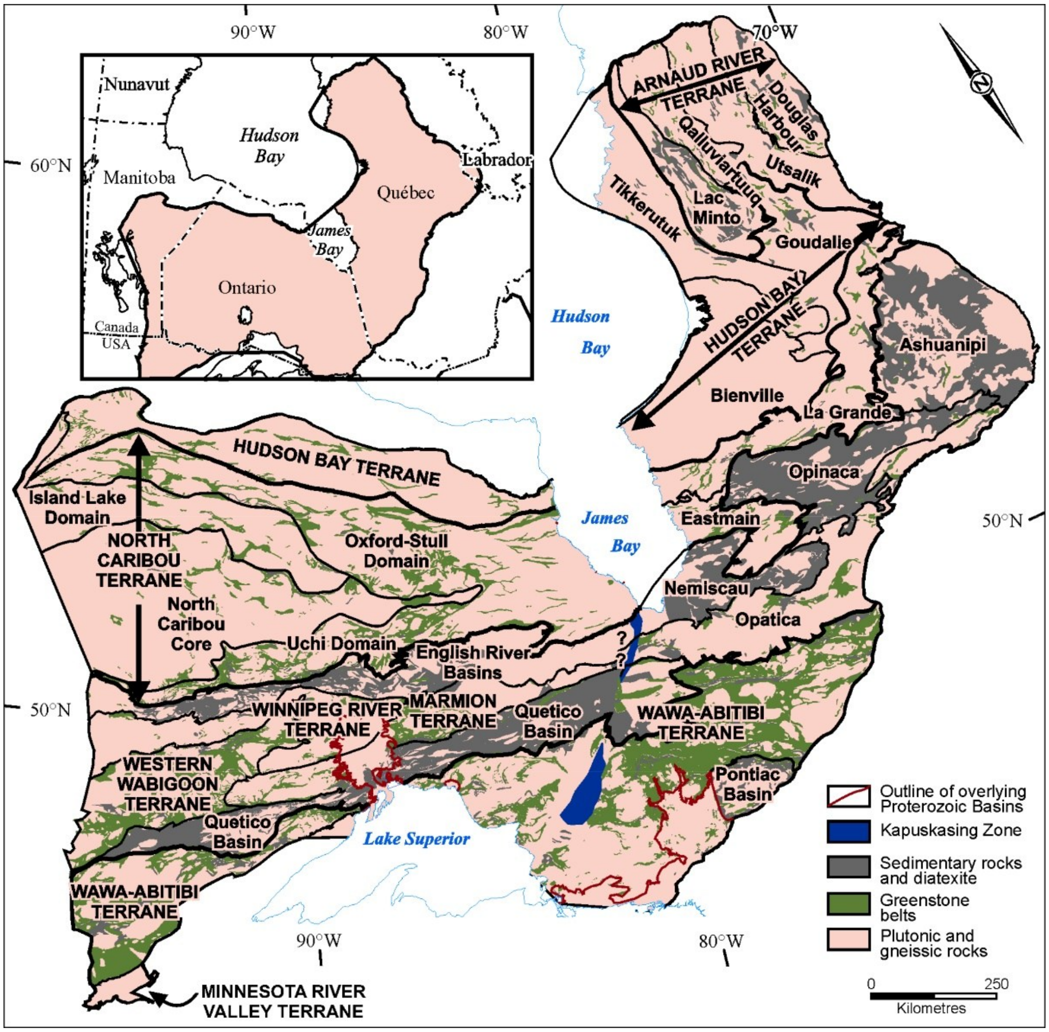

Figure 2.1: Map of the Superior Province showing its subdivision into terranes and domains (Stott et al., 2010).

Increasing understanding of bedrock geology within the Superior Province that utilized mapping, geophysics, geochronology, stable and radiogenic isotopes, and geochemistry, led to a revised subdivision approach using a hierarchical framework. By revising previous subdivisions and utilizing previous subprovince boundaries, Stott et al. (2010) proposed a terrane and domain subdivision (Fig. 2.1). Stott et al. (2010) defined a terrane as a region assembled prior to the

Neoarchean, having distinct characteristics from the surrounding regions. A terrane may consist of several, mostly younger domains that share a common basement but have distinct lithological characteristics.

The terrane and domain subdivision provides a more holistic approach in dividing the Superior Province, while still recognizing the subprovince subdivision of Card and Ciesielski (1986). Volcano-plutonic subprovinces consist of volcanic-dominant supracrustal rocks (i.e., greenstone belts) that are intruded by felsic plutonic rocks, comprising the Wawa-Abitibi and Wabigoon terranes, as well as the Uchi Domain of the North Caribou Terrane (Fig. 2.1; Card and Ciesielski, 1986). Metasedimentary subprovinces consist of sedimentary-dominant supracrustal rocks and peraluminous granitoids, comprising the English River, Quetico and Pontiac metasedimentary basins (Fig. 2.1; Card and Ciesielski, 1986; Stott et al., 2010). Plutonic subprovinces are characterized by an abundance of granitoid batholiths and lack of supracrustal rocks, comprising the Marmion and Winnipeg River terranes, as well as the North Caribou Core of the North Caribou Terrane (Fig. 2.1; Card and Ciesielski, 1986). Lastly, high-grade gneissic subprovinces consist of medium- to high-pressure upper amphibolite to granulite facies gneissic rocks of plutonic and supracrustal origin, comprising the Kapuskasing Zone (Fig. 2.1; Card and Ciesielski, 1986; Stott et al., 2010).

The amalgamation of the western part of the Superior Province, involving the accretion of terranes onto the North Caribou Core, occurred in five distinct Neoarchean orogenic events that are collectively referred to as the Kenoran Orogeny (Thurston et al., 1991; Percival et al., 2006). The initial stage of assembly is marked by the Northern Superior Orogeny (~2720 Ma), when the Hudson Bay Terrane collided with the North Caribou Terrane, trapping the previously accreted Oxford-Stull Domain along the northern margin of the North Caribou Core (Fig. 2.1; Skulski et al., 2000; Percival et al., 2006; Percival et al., 2012). Following the first orogeny, the Uchian Orogeny took place between 2720 and 2700 Ma, along the southern margin of the North Caribou Terrane. The Uchian Orogeny was marked by voluminous magmatism, the product of northward subduction of the Winnipeg River Terrane, which subsequently collided with the North Caribou Terrane, further resulting in the deposition of a turbidite sequence and the formation of the English River Basin (Stott, 1997; Percival et al., 2012). Then, the Winnipeg River and Marmion terranes were accreted onto the Wabigoon Terrane during the Central Superior Orogeny (~2700 Ma; Percival et al., 2012). Subsequently, northward subduction during the Shebandowanian Orogeny (~2690 Ma) led to the accretion of the Wawa-Abitibi Terrane (Stott, 1997; Percival et al., 2006). The final stage of the Kenoran Orogeny was marked by the Minnesotan Orogeny (~2680 Ma), during which the Minnesota River Valley Terrane collided with the Superior Province (Percival et al., 2012). Each orogeny involved collision, sedimentation, regional fabric development, regional metamorphism, felsic magmatism, and faulting marking discrete accretionary events (Percival et al., 2006).

2.2 North Caribou Terrane

The North Caribou Terrane is situated in the western portion of the Superior Province (Figs. 2.1 & 2.2). The North Caribou Terrane includes the Berens River, Sachigo, and Uchi subprovinces, which have been revised into the North Caribou Core that is now flanked by Island Lake and Oxford-Stull domains to the north, and the Uchi Domain to the south (Fig. 2.2; Stott et al., 2010). The North Caribou Terrane makes up the largest Mesoarchean subdivision of the Superior Province, the 3.0 Ga basement of which is comprised mostly of felsic intrusive rocks and subordinate greenstone belts (Thurston et al., 1991; Percival et al., 2006). The central region of the North Caribou Terrane is dominated by felsic to intermediate plutons (2.745 to 2.697 Ga) containing sporadic ca. 2.9 Ga greenstone belts, which are dominated by platformal sedimentary strata and plume-related rift sequences (Corfu and Stone, 1998; Percival et al., 2006; Stott et al., 2010).

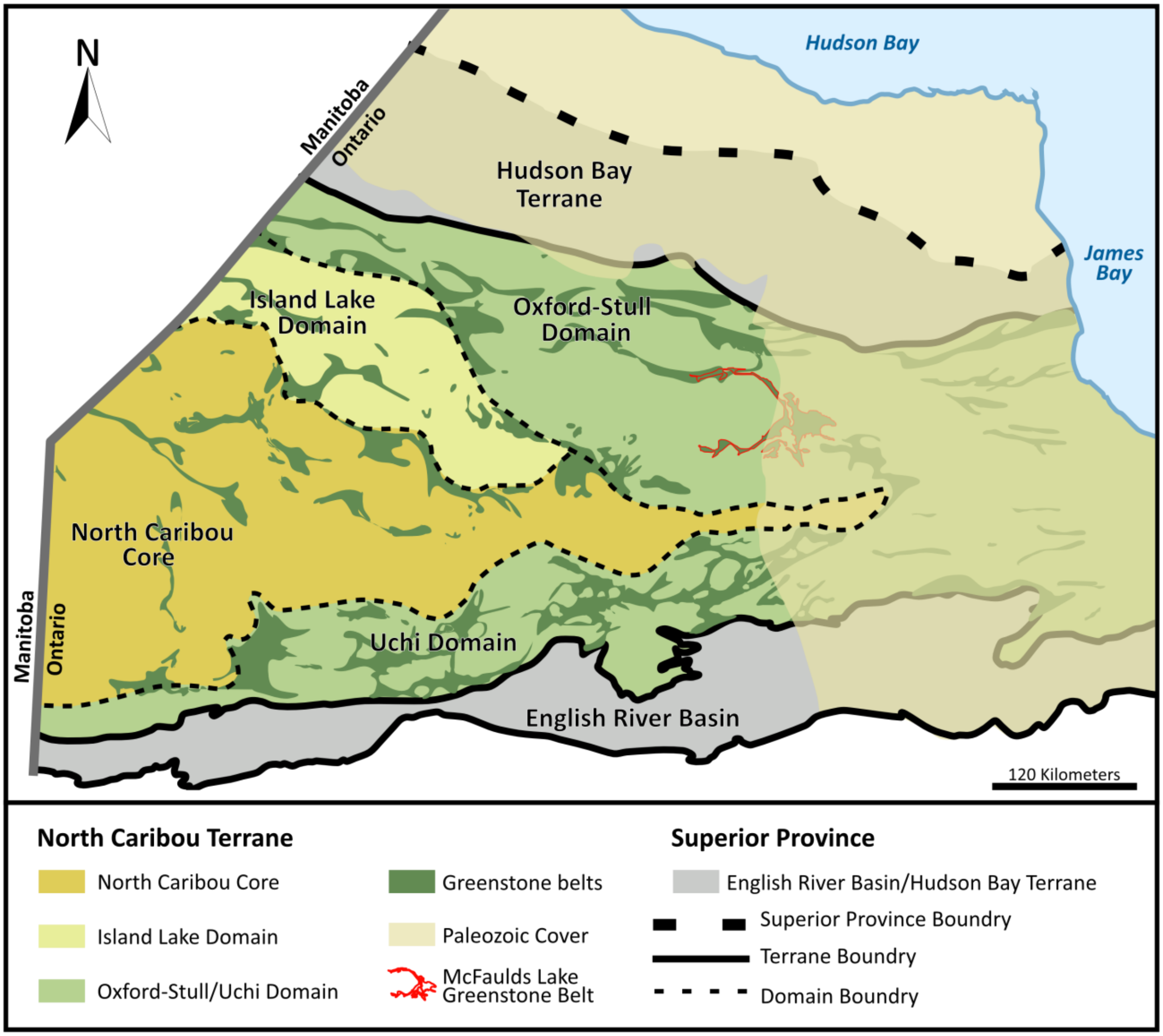

Figure 2.2: Map of western Superior Province highlighting North Caribou Terrane subdivision, location of McFaulds Lake Greenstone Belt (MLGB), and distribution of Paleozoic cover (Modified after Stott et al., 2010).

Across the North Caribou Terrane, prominent magmatic (2.89–2.895 Ga) and metamorphic (2.85–2.86 Ga) events are evident, with Neoarchean magmatism and sedimentation present within the Island Lake, Uchi, and Oxford-stull domains (Stott et al., 2010). A rift- (2.98–2.85 Ga) and arc-related (2.85–2.71 Ga) sequence were formed along the North Caribou Terrane basement, which were subsequently reworked by continental arc magmatism (2.75–2.70 Ga; Percival, 2007).

The MLGB occurs within the Oxford-Stull Domain (Fig. 2.1). The Oxford-Stull Domain represents mostly juvenile (2.88–2.73 Ga) continental northern margin of the 3.0 Ga North Caribou Terrane that was tectonically imbricated with oceanic crustal fragments prior to 2734 Ma (Skulski et al., 2000). The tectono-stratigraphy of the Oxford-Stull Domain consists of tholeiitic, calc-alkalic to alkalic volcanic rocks, and clastic metasedimentary rocks with some iron formation ranging ~2.87–2.71 Ga (Skulski et al., 2000; Stott et al., 2010). Large parts of the Oxford-Stull Domain are underlain by tonalite, granodiorite, and granite plutons ranging in age from 2.83 to 2.69 Ga (Percival, 2007). Stott et al. (2010) proposed that the Oxford-Stull Domain formed as a major intracratonic rift of the older North Caribou Terrane as it comprises juvenile Neoarchean oceanic crust with limited Mesoarchean crustal rocks at the northern and southern margins.

2.3 McFaulds Lake Greenstone Belt

The MLGB is situated at the eastern end of the Oxford-Stull Domain, where it disappears underneath Paleozoic cover (Fig. 2.2). The supracrustal rocks of the MLGB are bound by batholiths and plutons, characterized by variable strikes and arcuate contacts that can be traced over 200 km (Metsaranta and Houlé, 2020).

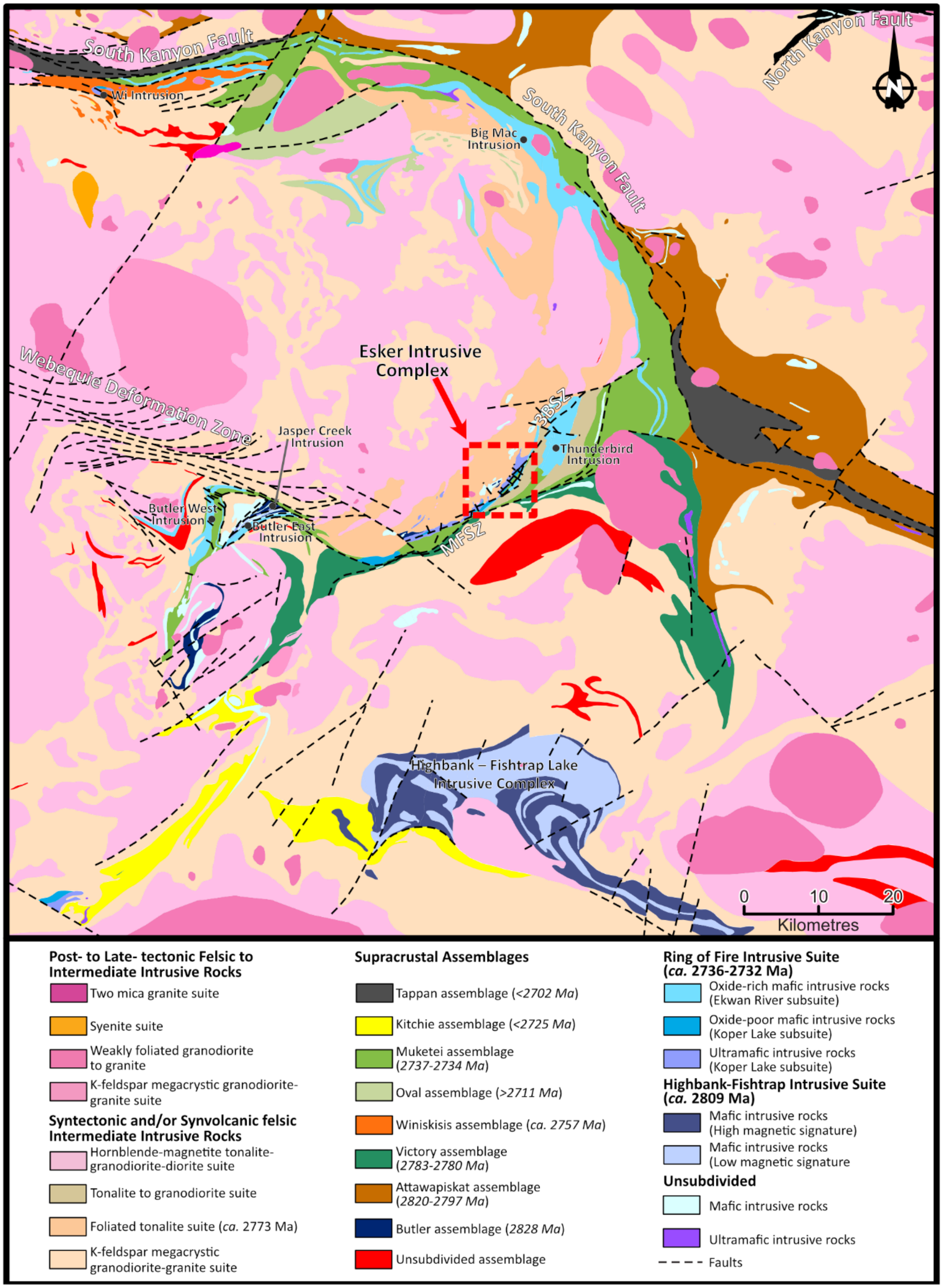

Figure 2.3: Geological map of the MLGB, illustrating the distribution of supracrustal assemblages and Ring of Fire intrusive suite magmatism (Modified from Metsaranta and Houlé, 2017d, 2017c, 2017b, 2020). Red box highlights the location of Esker intrusive complex in Figure 2.4. Abbreviations: MFSZ – McFaulds shear zone; 3BSZ – 3B shear zone.

The current understanding of stratigraphy and structures within the MLGB is incomplete, however, the belts thickness can reach up to 40 km, generally ranging from 10–20 km. The supracrustal succession has been subdivided into eight assemblages that record volcanism, sedimentation, and deformation, between 2828 and 2702 Ma (Fig. 2.3; Metsaranta and Houlé, 2020). A prominent feature of the MLGB is the well-defined, semi-continuous, positive magnetic anomaly that spans its length. This feature has been attributed to the mafic to ultramafic magmatism (2736–2732 Ma) of the Ring of Fire Intrusive Suite (RoFIS). The RoFIS is subdivided into the oxide-rich mafic intrusive rocks of the Ekwan River subsuite, and the mafic to ultramafic intrusive rocks of the Koper Lake subsuite that are host to world-class chromite deposits, economically significant Ni-Cu-(PGE), and Fe-Ti-V mineralization (Houlé et al., 2015, 2019, 2020; Metsaranta et al., 2015). Magmatism in the RoFIS is both coeval and spatially associated with the Muketei assemblage (2737–2734 Ma), which together are host to the majority of the metal endowments in the region (Houlé et al., 2020; Metsaranta and Houlé, 2020).

The following sections summarize the present-day understanding of the MLGB as described in several publications. It is important to note, that surface exposure of bedrock is highly limited with majority of the interpretations relying on geophysics in combination with, or without, drill core data, making interpretation in certain regions highly speculative (Metsaranta and Houlé, 2020).

2.3.1 Supracrustal Assemblages

Metsaranta and Houlé (2020) characterized the diverse supracrustal succession of the MLGB, comprehensively summarising the extensive work conduct through mapping and Targeted Geoscience Initiatives (Metsaranta et al., 2015; Metsaranta and Houlé, 2017a, 2017b, 2017c, 2017d). Several of the assemblages are composed of discontinuous, and geographically distinct regions. Stratigraphic correlation of these regions into their respective assemblage, are based on similarities in age, geochemistry, and lithology. Multiple areas in the northwestern, central, and southeastern regions of the MLGB lack geological data, but contain supracrustal rocks on the basis of geophysical data interpretations (Metsaranta and Houlé, 2020). The MLGB is composed of eight supracrustal assemblages comprising the late-Mesoarchean to Neoarchean Butler and Attawapiskat, the early-Neoarchean Victory and Winiskisis, and the middle-Neoarchean Muketei, Oval, Kitchie, and Tappan assemblages (Fig. 2.3; Metsaranta and Houlé, 2020).

The Butler assemblage consists of two geographically distinct regions within the MLGB. Two discontinuous, south-striking segments occur in the southwestern region, and a single segment in the central region, situated northwest of the Esker intrusive (Fig. 2.3; Metsaranta and Houlé, 2020). The Butler assemblage is composed of tholeiitic mafic volcanic rocks, with lesser komatiitic to calc-alkalic rocks, magnetite iron formation, and subordinate felsic metavolcanic rocks. The felsic metavolcanic rocks in the northern segment of the southwestern region yielded a U-Pb zircon age of 2828.7±0.9 Ma, making it the oldest supracrustal assemblage of the MLGB (Metsaranta et al., 2015; Metsaranta and Houlé, 2020). In the southwestern region, the northern segment is underlain by the Jasper Creek and Butler East intrusions (Fig. 2.3; Houlé et al., 2019). The supracrustal rocks are commonly intercalated with, or surrounded by, unsubdivided gabbroic rocks (Fig. 2.3). The northern segment of the southwestern region is separated from the Muketei assemblage to the west by a 2773.4±0.9 Ma tonalitic body, as well as subconcordant faults predating the Webequie deformation zone (Fig. 2.3). The Webequie deformation zone has been proposed to have accommodated significant dextral strike-slip displacement, which linked the southwestern and central region of the Butler assemblage before the displacement (Metsaranta and Houlé, 2020).

The Attawapiskat assemblage forms a southeast-striking segment north of the South Kanyon fault in the northern region, and a south-striking segment south of the McFaulds shear zone and South Kanyon fault in the eastern region of the MLGB (Fig. 2.3; Metsaranta and Houlé, 2020). The Attawapiskat assemblage is mostly composed of tholeiitic, and to a lesser extent, calc-alkalic mafic metavolcanic rocks, including fine- to medium-grained pillowed massive flows and gabbroic sills. Subordinate to the mafic rocks are intermediate- to felsic-metavolcanic rocks, as well as fine- to coarse-grained wacke and tuffaceous sandstone-bearing, clastic metasedimentary rocks that are locally interbedded with carbon- and sulfide-rich shales or oxide facies iron formation (Metsaranta and Houlé, 2020). In the eastern region, the Attawapiskat assemblage yielded Mesoarchean ages ranging from 2820 to 2797 Ma (Metsaranta et al., 2015; Metsaranta and Houlé, 2020). The Attawapiskat assemblage also contains localized sulfide mineralization in the mafic to intermediate metavolcanic rocks, with anomalous Cu and Zn contents found in sulfide-rich shales (Metsaranta and Houlé, 2020).

The Victory assemblage is situated in the south-central region, consisting of tholeiitic-mafic metavolcanic rocks that are intermixed with felsic to intermediate calc-alkalic metavolcanic rocks, as well as metasedimentary rocks that include iron formation and graphitic mudstone (Fig. 2.3). Dating of felsic metavolcanic rocks yielded an age range of 2783–2780 Ma, correlating the assemblage across the southern portion of the MLGB (Metsaranta and Houlé, 2020). Locally, mafic to ultramafic sills of undetermined age intrude the Victory assemblage (Metsaranta and Houlé, 2020). The Victory assemblage is structurally juxtaposed by the north-bounding McFaulds shear zone onto the Muketei assemblage (Figs. 2.3 & 2.4). To the south of the Double Eagle intrusion and McFaulds shear zone, the assemblage is strongly strained, with local C-S fabric and boudinaged quartz veining displaying dextral movement, consistent with the Webequie deformation zone, which highlights its genetic link to the McFaulds shear zone (Fig. 2.4; Buse et al., 2009; Metsaranta and Houlé, 2020). In the eastern region, the Victory and Attawapiskat assemblages form a north-south trending synform, although their contact relationships have not been constrained (Metsaranta et al., 2015; Metsaranta and Houlé, 2020). Some regions of the Victory assemblage contain disseminated through stringer pyrrhotite, locally containing elevated gold contents (Metsaranta and Houlé, 2020).

The Winiskisis assemblage forms a west-trending segment in the northwestern portion of the MLGB (Fig. 2.3). The supracrustal succession comprises predominantly schistose to gneissic, calc-alkaline felsic to intermediate metavolcanic units, with lesser clastic metasedimentary rocks, and tholeiitic to transitional mafic metavolcanic rocks (Metsaranta and Houlé, 2020). In the western part of the assemblage, a felsic metavolcanic unit yielded an age of 2757±1.0 Ma. In areas where deformation is not prominent, the supracrustal succession consists of greywacke, siltstone, shale, massive to graded felsic tuffaceous sandstone, aphyric to quartz-phyric felsic metavolcanic rocks, with subordinate mafic flows and dikes (Metsaranta and Houlé, 2020). Silicified zones containing pyrite and pyrrhotite, as well as chert-magnetite iron formation are locally present. Carbonate-rich intervals are rarely present comprising interlayered calcite and biotite horizons (Metsaranta and Houlé, 2020). The Winiskisis assemblage is intruded by the 2732.9±0.6 Ma Wi intrusion, which belongs to the Koper Lake subsuite (Fig. 2.3; Houlé et al., 2019; Metsaranta and Houlé, 2020). The Winiskisis assemblage is highly strained, with evidence of multiple phases of deformation, which include micro-folding and crenulation that overprint compositional layering and pre-existing foliation. Metsaranta and Houlé (2020) estimated that the metamorphic conditions within the Winiskisis assemblage reached upper amphibolite-facies grade.

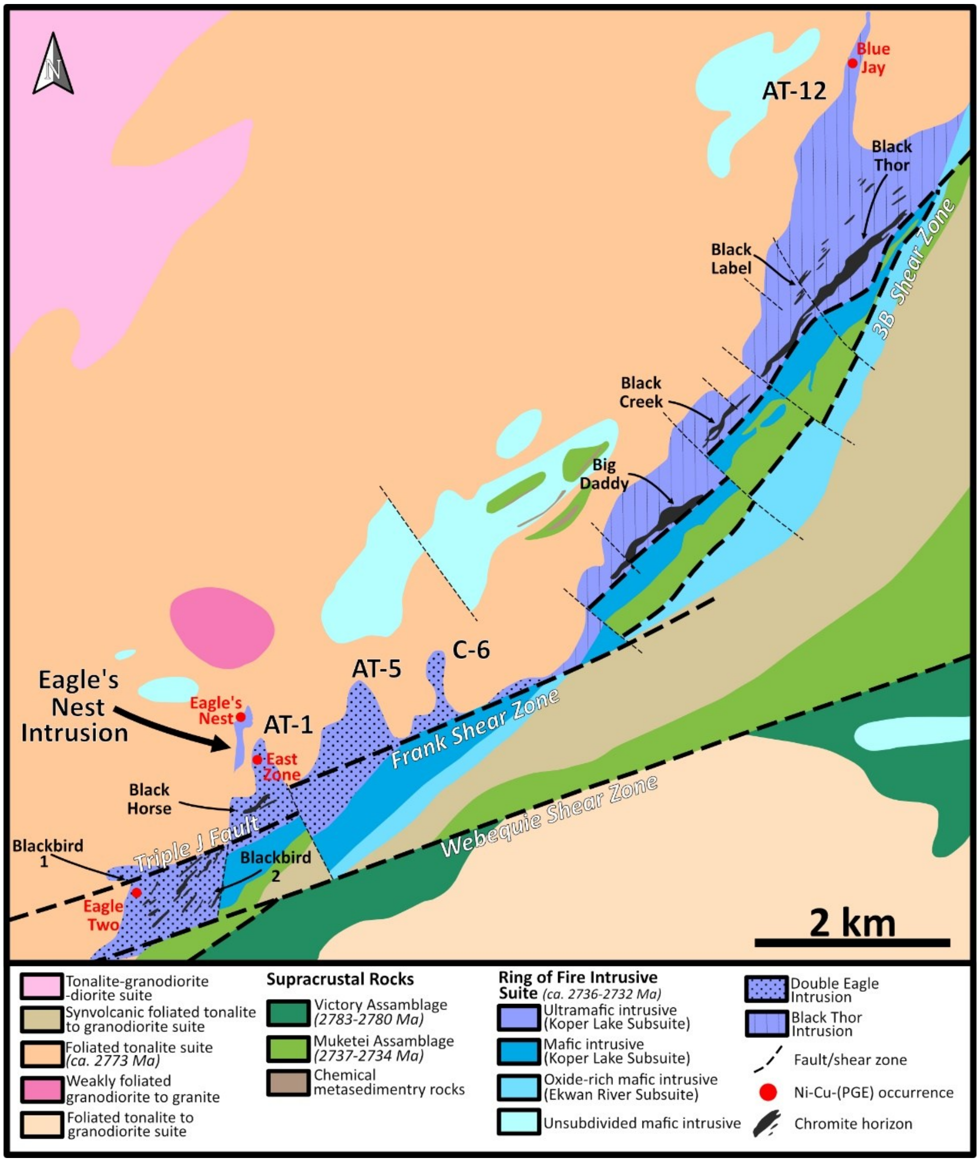

Figure 2.4: Simplified geological map of the Esker Intrusive Complex illustrating the distribution of chromite and Ni-Cu-(PGE) deposits and occurrences. Modified after Metsaranta and Houlé (2017c).

The Oval assemblage is situated in the central portion of the northern region of MLGB (Fig. 2.3). The Oval assemblage mostly consists of schistose felsic to intermediate, and to a lesser extent, mafic metavolcanic units, with localized metatexites that are either clastic metasedimentary rocks or altered metavolcanic units (Metsaranta and Houlé, 2020). The Oval assemblage is locally intruded by ferrogabbroic sills of the Ekwan River subsuite and is crosscut by a felsic–intermediate dike with an age of 2711±6.0 Ma, which is the minimum constrained age for the assemblage (Metsaranta and Houlé, 2020). Geochemically, the metavolcanic succession of the Oval assemblage is similar to that of the Muketei assemblage, although a direct correlation between two has not been made (Metsaranta and Houlé, 2020).

The Muketei assemblage is situated west of the Butler assemblage in the southwestern region, stratigraphically above the RoFIS in the central region, and south of the South Kanyon fault (Fig. 2.3). The Muketei assemblage consists predominantly of calc-alkalic, with localized transitional to tholeiitic, felsic to intermediate metavolcanic rocks, lesser alkalic, tholeiitic, and calc-alkalic mafic metavolcanic rocks, and rare ultramafic metavolcanic rocks that occur in the southwestern region, above the RoFIS (Metsaranta and Houlé, 2020). The age of the Muketei assemblage is constrained by felsic to intermediate metavolcanic rocks in the central region dated to 2737±7, 2737±3, and 2734±2 Ma, correlating the northern and southwestern regions (Metsaranta and Houlé, 2020). Mesoarchean zircons have been identified in a felsic metavolcanic unit in the central region, suggesting that it was likely emplaced into pre-existing basement. Most of the metal endowments of the MLGB are closely associated to the Muketei assemblage, and the widespread, coeval magmatism of the RoFIS (Houlé et al., 2020; Metsaranta and Houlé, 2020). The Muketei assemblage is similar in age to the magmatism of the RoFIS and to two tonalitic–granodioritic plutons (2734±1.2 Ma), near the Esker Intrusive Complex (Metsaranta and Houlé, 2020). The Muketei assemblage is host to several VMS-style mineralization occurrences in the southwestern and central regions, typically accompanied by evidence of hydrothermal alteration that preceded metamorphism (Metsaranta and Houlé, 2020).

The Muketei assemblage contains felsic to intermediate flows, tuffs, and tuff breccias, subordinate mafic metavolcanic, and rare metasedimentary rocks comprising oxide-facies iron formation and laminated chert (Metsaranta and Houlé, 2020). Intermediate intrusions are found in the central region, porphyritic dikes and sills have been observed in the southwestern part of the assemblage. The Muketei assemblage underwent several phases of deformation, that have been preserved in the central region as small-scale folds and crenulations on earlier formed foliation planes, as well as ductile shearing and faulting (Metsaranta and Houlé, 2020). Metamorphic conditions of the Muketei assemblage have been characterized as amphibolite-facies grade in the northern and southern regions, whereas the central region, proximal to the Esker Intrusive Complex, displays evidence of greenschist-facies grade (Metsaranta and Houlé, 2020).

The Kitchie assemblage is situated in the south of MLGB, proximal to the Highbank–Fishtrap Lake Intrusive Complex (Fig. 2.3). The Kitchie assemblage consists of deformed, schistose to gneissic, tholeiitic through calc-alkalic, mafic metavolcanic rocks, locally containing pillow selvages, felsic to intermediate metavolcanic rocks, and metasedimentary rocks, which rarely consist of a metagreywacke (Metsaranta and Houlé, 2020). The Kitchie assemblage is crosscut by gabbroic to pyroxenitic intrusive rocks, granitic sills and dikes, and tonalitic to granodioritic rocks, locally displaying evidence of deformation. Based on detrital zircon ages found in metasedimentary rocks within the Kitchie assemblage, which yielded ages of ca. 2790–2800 Ma, and the age of the Highbank–Fishtrap Intrusive Complex (ca. 2810 Ma), the Kitchie assemblage has been interpreted to overlie the Highbank–Fishtrap Intrusive Complex (Metsaranta and Houlé, 2020).

The Tappan assemblage occurs in two regions of the MLGB (Fig. 2.3). It occurs in the eastern part of the central region as a west-northwest-striking metasedimentary unit, and in the northwestern region, where it occurs north of the South Kanyon fault as an east-west trending segment (Fig. 2.3; Metsaranta and Houlé, 2020). The assemblage is best constrained in the central region where it consists of fine- to coarse-grained sandstone interlayered with siltstone and sulfide-bearing mudstone. The sedimentary-dominated Tappan assemblage, is interpreted to have formed from turbiditic flows, based on the occurrence of graded bedding, load structures, and cross-laminae. In the central region, detrital zircons yielded an age of <2702.5±7.2 Ma, making it the youngest supracrustal assemblage in the MLGB. In the northwestern region, the Tappan assemblage remains poorly characterized, but where it is exposed, it consists of sheared metasedimentary rocks that are similar in age (<2714±9 Ma) and rock types to the central segment, suggesting that they formed in a similar tectonic setting (Buse et al., 2009; Metsaranta and Houlé, 2020).

2.3.2 Deformation and Metamorphism

Apart from the extensive dataset available for the Esker Intrusive Complex, scarcity of outcrop and drill core has obscured the characterization of the deformation events recorded within MLGB, remaining poorly constrained. However, using the extensive available data from and around the Esker Intrusive Complex, Metsaranta and Houlé (2020) proposed five deformation events for the MLGB: (1) early-deformation prior to 2728 Ma, (2) deformation at ca. 2728 Ma, (3) deformation after 2828 Ma but before ca. 2704 Ma, (4) deformation during and after ca. 2702 Ma, and (5) late-Neoarchean deformation. The metamorphic conditions in the region are predominantly upper greenschist- to lower-amphibolite facies, with the exception of the RoFIS in parts of the Esker Intrusive Complex, where primary igneous textures are found and chlorite-biotite assemblages, suggesting lower metamorphic grade conditions.

The early-stage deformation event is evident by the presence of foliated xenoliths in the tonalite-granodiorite-diorite suite (ca. 2728–2724 Ma), structures that pre-date the suite, and covers a major portion of the region (Metsaranta and Houlé, 2020). Metsaranta and Houlé (2020) proposed that the early-stage deformation event produced the sequence stratigraphy and folding of metavolcanic rocks in the southwestern and central parts of the MLGB. Emplacement of the tonalite-granodiorite-diorite suite produced dome and synclinal keel relationship (Metsaranta and Houlé, 2020). Post-dating the emplacement of the batholiths, but prior to 2704 Ma, dextral shearing along the Webequie shear zone resulted in the formation of Frank, 3B, and McFaulds shear zones, as well as the Triple J fault zone, and other smaller shear zones in the central part of the MLGB (Metsaranta and Houlé, 2020). Synchronous with the deformation along the Webequie deformation zone, formation of the Tappan assemblage (2702 Ma), and the spatial association with the South Kanyon fault, indicated that the fault zone was active post-deposition of the sedimentary basin (Metsaranta and Houlé, 2020). Syn- to post-depositional deformation has been inferred through folding of contacts in sedimentary sequences to take place after 2702 Ma. Late, brittle Neoarchean deformation has been interpreted using geophysical lineaments (Metsaranta and Houlé, 2020).

2.3.3 Ring of Fire Intrusive Suite

The RoFIS represents a prominent mafic to ultramafic magmatic event along the strike of the MLGB, between 2735.5±0.8 and 2732.0±0.6 Ma (Fig. 2.3; Houlé et al., 2020). The RoFIS includes the oxide-rich mafic intrusive rocks of the Ekwan River subsuite and the mafic to ultramafic intrusive rocks of the Koper Lake subsuite (Houlé et al., 2019). Mungall et al. (2010)

proposed that the Thunderbird intrusion (i.e., Ekwan River subsuite) was a more evolved part of the Black Thor and Double Eagle intrusions (i.e., Koper Lake subsuite), which has been tectonically dismembered after its emplacement (Figs. 2.3 & 2.4). However, Houlé et al. (2019, 2020), define the subsuites as contemporaneous, but distinct magmatic events based on their geographic distribution, cross-cutting relationships, lithological characteristics, and geochemical signatures.

The voluminous, oxide-rich mafic intrusive rocks of the Ekwan River subsuite form several sub-continuous intrusions spanning the length of the MLGB (Fig. 2.3). The Ekwan River subsuite is host to several Fe-Ti-V occurrences in the Butler East, Butler West, Langfield, Thunderbird and Big Mac intrusions (Fig. 2.3; Mungall et al., 2010; Sappin et al., 2015; Kuzmich et al., 2015). The Ekwan River subsuite commonly forms layered intrusions comprising gabbro, melagabbro, leucogabbro, and subordinate anorthosite and pyroxenite (Kuzmich et al., 2015; Houlé et al., 2020). In contrast, the much less voluminous, mafic to ultramafic rocks of the Koper Lake subsuite, are spatially restricted to the central region of the MLGB (Fig. 2.3). The Koper Lake subsuite is composed of variably serpentinized and talc-carbonate altered dunite, peridotite, chromitite, pyroxenite, and gabbro (Houlé et al., 2020). Magmatism of the Koper Lake subsuite has been best constrained in the central regions of the MLGB, within the Esker Intrusive Complex (Figs. 2.3 & 2.4; Houlé et al., 2019, 2020).

2.3.4 Esker Intrusive Complex

The semi-continuous Esker Intrusive Complex spans ~16 km in the central region of the MLGB (Figs. 2.3 & 2.4). The complex encompasses the mafic to ultramafic Black Thor and Double Eagle intrusions, as well as several keel-like bodies (i.e., AT-12, C-6, AT-5, & AT-1) and blade-shaped dikes (i.e., Eagle's Nest intrusion) emplaced along the contact with and into the 2773 Ma tonalitic body (Fig. 2.4; Mungall et al., 2010; Houlé et al., 2020; Metsaranta and Houlé, 2020).

The keel-like bodies and the blade-shaped dike at the northwestern portion of the complex have been interpreted to be emplaced along subparallel, normal-faults in an extensional environment (Fig. 2.4; Houlé et al., 2020; Laudadio et al., 2022). Continuous magma influx through these conduits resulted in the formation of the overlying Black Thor and Double Eagle intrusions, which eventually coalesced to form the Esker Intrusive Complex (Houlé et al., 2020). Faulting along the poorly constrained 3B shear zone, and 1.5 km dextral displacement along the Frank shear zone, dismembered the complex into its present-day configuration (Houlé et al., 2020; Laudadio et al., 2022). Magmatic differentiation in the complex, from ultramafic rocks in the northwest, gradationally becoming mafic rocks towards the south-southeast, coupled with the occurrence of massive sulfide mineralization consistent with gravitational segregation at the northwestern contact of the Eagle's Nest intrusion, has been interpreted as rotation of the complex to a subvertical orientation with stratigraphic top to the south-southeast (Houlé et al., 2020; Zuccarelli et al., 2022).

The Esker Intrusive Complex comprises several, genetically linked, mafic-ultramafic intrusive bodies (Fig. 2.4). The trough-shaped Black Thor intrusion is underlain by the AT-12 conduit in the north-northwest that is host to the Blue Jay magmatic sulfide occurrence (Houlé et al., 2020). Stratigraphically overlying the AT-12 feeder conduit is the Ultramafic Series, which is host to the Black Label, Black Thor, Black Creek, and Big Daddy chromite deposits (Carson et al., 2015; Houlé et al., 2020). The Ultramafic Series is bound by the 3B shear zone to the southeast, which separates the Ultramafic Series from the Mafic Series. A Late Websterite phase (2733.6±0.7 Ma) was emplaced through the AT-12 feeder conduit, cross-cutting the Basal Series and lower zones of the Ultramafic Series (Carson et al., 2015; Spath, 2017; Houlé et al., 2020). The Double Eagle intrusion is predominantly an ultramafic intrusion with a transitional dike/chonolith morphology, underlain by the AT-1 feeder-keel and Double Eagle intrusion, and has been dismembered by the dextral movement of the Frank shear zone (i.e., Triple J fault; Laudadio et al., 2022). The Double Eagle intrusion is host to the East Zone and Eagle Two Ni-Cu-(PGE) occurrences, as well as the Black Horse, Blackbird 1, and Blackbird 2 chromite deposits. To the north, the Double Eagle intrusion is underlain by the Eagle's Nest intrusion (Fig. 2.4).

The Eagle's Nest intrusion was emplaced along a subhorizontal conduit at the base of the Double Eagle intrusion, forming a blade-shaped dike within a tonalitic body (Fig. 2.4; Mungall et al., 2010; Zuccarelli et al., 2022). A post-emplacement, regional deformation event, rotated the intrusion into its present-day, steeply west-dipping, subvertical orientation. The Eagle's Nest intrusion predominantly consists of variably altered ultramafic ortho- to mesocumulate rocks flanked by variably biotite-chlorite altered pyroxenitic and gabbroic rocks (Mungall et al., 2010; Zuccarelli et al., 2022). At the northwestern extant of the intrusion, the Eagle's Nest intrusion is host to orthomagmatic Ni-Cu-(PGE) mineralization, comprising pyrrhotite-pentlandite-chalcopyrite ± chromite, that grade from massive through net-textured and disseminated towards the southeast. The deposit varies between 50–200 m in strike length, several 10's of meters in thickness and continuous down dip for over 1300 m, parallel to the basal contact of the host intrusion (Downey, 2021).

Chapter 3 Methods

3.1 Sample Acquisition

Due to lack of exposure at surface, the Eagle’s Nest and associated dikes across the MLGB were examined using drill core. Sample collection and drill core examination were conducted at Esker site over two sampling campaigns during the Fall of 2023 and 2024. Three main objectives guided the selection of examined drill core intervals: (1) to investigate the intrusive rocks of the Eagle’s Nest intrusion at the contacts between the intrusion and the wall rock tonalite in an effort to identify chilled margins, (2) to examine lithological, mineralogical, and textural variability in ultramafic cumulate rocks throughout the intrusion, with emphasis on unmineralized intervals, and (3) to examine mafic intrusive dikes that were hypothesized to be related to magmatism of the Eagle’s Nest intrusion.

Key drill core intervals were selected for examination with the assistance of Wyloo geologists. These selected intervals were carefully examined and quick-logged, characterizing the lithologies and contacts. Collectively, a total of 191 drill core samples were collected. Of these, 118 samples were from Eagle’s Nest intrusion, including 17 samples that captured the contact between intrusive rocks and the wall rock tonalite. Additionally, 67 samples were collected from mafic and intermediate dikes predominantly across the Esker Intrusive Complex with some proximal locations to the Eagle’s Nest intrusions, as well as Blue Jay, AT7, and Winisk River targets. Of the dike samples, 13 captured the contacts with their host. Lastly, six samples were collected from the host tonalite. Sample information is summarized in Appendix A.

3.2 Petrography

A total of 55 polished thin sections and two polished resin pucks were prepared in two separate batches. Thirty of the thin sections were prepared at Precision Petrographics in British Columbia, with the remaining 25 thin sections and the two resin pucks prepared at the Lakehead University lapidary facility. Thirty-eight thin sections and the two resin pucks were prepared from rocks of the Eagle's Nest intrusion. Of these, 16 were collected close to the contact between the intrusion and the tonalite. The other 22 thin sections and the two resin pucks consist of both mineralized and unmineralized ultramafic cumulate rocks from the Eagle's Nest intrusion. Additionally, 17 thin sections of dikes were prepared.

Thin section analysis was conducted using an Olympus BX51 microscope at the microanalytical facility at Lakehead University. The photomicrographs were taken using an Olympus SC180 microscope mounted camera. Additionally, all prepared thin sections were fully scanned in plane- and cross-polarized transmitted light, and plane-polarized reflected light, using a Zeiss Axioscope 7 microscope with a mounted Axiocam 305 color camera.

3.3 Whole Rock Geochemistry

Whole rock geochemical analysis of 154 samples was conducted at ALS Canada Ltd. using a complete characterization package (ALS code CCP-PKG01). Samples underwent fine crushing until 70 % of the sample passed through a 2 mm mesh and then split using a riffle splitter. Each crushed and split sample, weighing up to 250 g, was pulverised until 85 % of sample material could pass through a 75 μm mesh. Whole rock major oxide elements were obtained using fusion decomposition with Inductively Coupled Plasma Atomic Emission Spectroscopy (ICP–AES). To determine the base metal contents of the samples, a four-acid digestion was paired with ICP–AES. Samples in which concentrations of base metals were above the upper detection limit, Cu and Ni ore grades were determined individually using aqua regia digestion and ICP–AES finish. Trace elements were determined using Inductively Coupled Mass Spectrometry (ICP–MS) following a lithium borate fusion and aqua regia digestion. Loss on ignition was obtained by heating a 1g sample to a temperature of 1000°C and measuring the weight loss. Total carbon and sulfur were obtained on 0.1 g sample using infrared spectroscopy. Sample duplicates, analytical laboratory standards and blanks were also analyzed to assure analyses integrity.

3.3.1 Sulfide-Free Normalization

The sulfide-free renormalization method was applied to mineralized, sulfide-rich rocks (>1 wt% sulfur), with Ni assumed to be predominantly hosted in sulfides (Barnes, 2023; Naldrett, 2004). The Ni component within the silicate phases ($Ni_{(Sil)}$) of a given mineralized sample was estimated using an established equation, developed based on the natural, strong correlation between Ni and MgO contents of ultramafic rocks (Barnes, 2023):

$$Ni_{(Sil)} = \left(\left\{\left[MgO * \frac{100}{Sil_{(total)}}\right] > 10\right\} * \left\{\left[MgO * \frac{100}{Sil_{total}}\right] - 10\right\} * 90\right) * \left(\frac{Sil_{(total)}}{100}\right)$$

Where $Sil_{(total)}$ is the volatile-free total of non-sulfide, non-volatile components in raw whole rock geochemical analysis of SiO_2, TiO_2, Al_2O_3, Cr_2O_3, FeO (as total Fe), MnO, MgO, CaO, Na_2O, K_2O, and P_2O_5.

The estimated $Ni_{(Sil)}$ was subtracted from whole rock Ni to determine the remaining Ni concentration associated with sulfide phases. The Fe associated with sulfide minerals was then calculated, assuming that all remaining Ni, Cu, and S are present in sulfides. This calculation was based on the average sulfide mineral compositions for the Eagle's Nest intrusion (Zuccarelli, 2020), with the assumption that chalcopyrite contains 34.43 % Cu, 30.55 % Fe, and 34.96 % S, pentlandite contains 34.16 % Ni, 31.07 % Fe, and 33.73 % S, and pyrrhotite contains 60.55 % Fe and 39.30 % S. Although the examination of sulfide mineralogy and composition was not the primary focus of the study, utilizing the mineral chemistry of sulfide phases from the intrusion provides a more representative approach to estimating the Fe content in sulfides of the Eagle's Nest intrusion, than a user-defined S to Fe, Ni, Cu ratios.

3.4 Electron Probe Microanalysis

The compositions of olivine, pyroxene, amphibole, and oxides from the Eagle's Nest intrusion were collected at two different facilities during two separate analytical periods. The first session was conducted remotely in the summer of 2024 at the Earth and Planetary Materials Analysis Laboratory of Western University, Ontario. This session focused on obtaining olivine mineral chemistry from four polished thin sections. The second session was conducted in person in spring of 2025 at the Microbeam Laboratory of University of Manitoba, Winnipeg. This session focused on obtaining mineral chemistry of olivine, pyroxene, hornblende, and oxides across nine polished thin sections. Detailed analytical methods for each session are described below.

3.4.1 Western University

Compositional analyses of olivine were completed using a JEOL JXA-8530F electron microprobe analyzer equipped with a Wavelength Dispersive Spectrometer (WDS). Beam conditions were set to an accelerating voltage of 15 kV, a beam current of 20 nA, and a 2 µm spot size (beam diameter). Standards of natural and synthetic materials were used for calibration consisting of the following: Diopside (Mg, Si, Ca), Rhodonite (Mn), Hematite (Fe), Nickel (Ni), Rutile (Ti), and Chromite (Cr).

3.4.2 University of Manitoba

Compositional analyses of olivine, pyroxene, amphibole, and oxides, were determined using a Cameca SX-100 equipped with five WDS's. Accelerating voltage, beam current, and spot size were set to 15 kV, 20 nA and 2 μm diameter for analyses of olivine and pyroxene, 15 kV, 40 nA, and 1μm diameter for analyses of oxides, and 15 kV, 20 nA, and 5 μm diameter for analyses of amphibole. In-house primary standards were used for calibration: albite (standard #105) for Na, fayalite (#114) for Si and Fe, spessartine (#220) for Mn, titanite (#221) for Ca and Ti, chromite (#227) for Cr, orthoclase (#231) for Al and K, olivine (#241) for Mg, and $NiFe_2O_4$ (#2101) for Ni. The Armstrong/Brown/Scott-Love (prZ) matrix correction (Armstrong, 1988) in combination with FFAST matrix absorption coefficient table (version 2.1, Chantler et al., 2005) were applied. A linear off-peak correction method was applied for all WDS elements. Counting times set for the analyzed phases are summarized in Table 3.1.

Table 3.1: Elements, detector crystals, count times, and primary standards used during EPMA analysis.

		Olivine		**Pyroxene**		**Chromite**		**Amphibole**		
Element	Detector Crystal	Peak time (s)	Off peak time (s)	Peak time (s)	Off peak time(s)	Peak time (s)	Off peak time (s)	Peak time (s)	Off peak time (s)	**Primary Standard**
Si Kα	TAP	20	20	20	20	20	20	30	30	Fayalite
Ti Kα	LPET	30	20	20	20	20	20	20	20	Titanite
Al Kα	LTAP	50	50	20	20	20	20	30	30	Orthoclase
Cr Kα	LLiF	20	20	20	20	20	20	30	30	Chromite
Fe Kα	LiF	20	20	20	20	20	20	30	30	Fayalite
Mn Kα	LiF	30	20	20	20	20	20	30	30	Spessartine
Mg Kα	TAP	30	20	20	20	20	20	30	30	Olivine
Ca Kα	LPET	20	20	20	20	20	20	20	20	Titanite
Na Kα	LTAP			20	20	20	20	30	30	Albite
K Kα	LPET							20	20	Orthoclase
Ni Kα	LLiF	30	20	20	20	20	20	30	30	$NiFe_2O_4$

Additionally, ten secondary Wood spinel standards were analyzed. Secondary spinel standards were analyzed in order to apply a Fe^{3+}/ΣFe ratio correction on analyzed chromite (Davis et al., 2017). The spinel standard mount (NMNH 118320) was provided by the Department of Mineral Sciences of the Smithsonian Institution. The $Fe^{3+/}$ΣFe ratios of these secondary standards have been previously determined by Mössbauer spectroscopy (see Davis et al., 2017). The secondary spinel standards were analyzed twice, with three spots per sample, once before the analysis, and once after. The $\Delta Fe^{3+}/\Sigma Fe^{\text{Möss-EPMA}}$ was calculated, and a best fit line was determined for the secondary standard measurements to determine the slope and intercept yielding the following relationship after Wood and Virgo (1989):

$$\frac{Fe^{3+}}{\sum Fe^{\text{Möss}}} - \frac{Fe^{3+}}{\sum Fe^{\text{EPMA}}} = 0.0152 \times \left[\frac{Cr}{Al + Cr}\right] - 0.0233$$

The determined slope and intercept were used to correct the $Fe^{3+/}$ΣFe ratios of the measured chromite analyses. Although the uncorrected Fe^{3+}/ΣFe ratio of the secondary spinel standards shows a good agreement with the true Fe^{3+}/ΣFe ratio determined by Mössbauer spectroscopy (R^2=0.97; Fig. 3.1A), the linear relationship improves this agreement (R^2=0.99; Fig. 3.1B). The electron probe microanalysis (EPMA) of the secondary spinel standards reported in Appendix D.

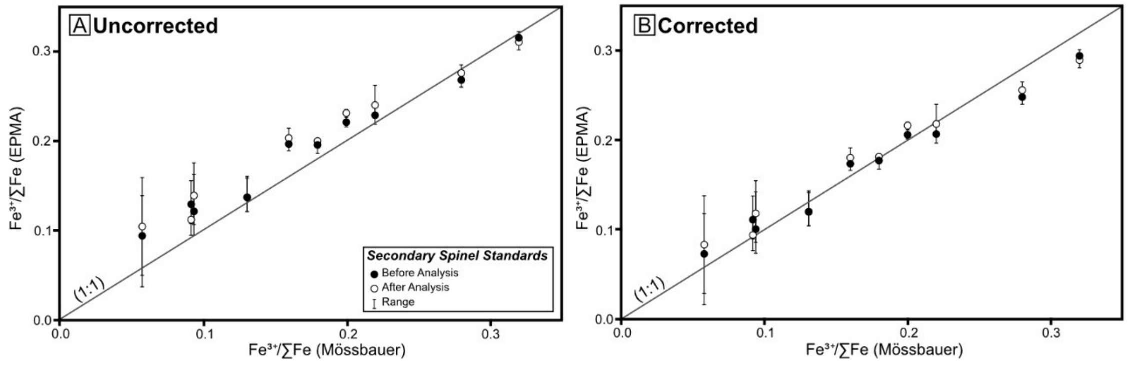

Figure 3.1: Bivariate plots comparing the true Fe^{3+}/ΣFe ratio of secondary spinel standards determined by Mössbauer spectroscopy to (A) uncorrected and (B) corrected Fe^{3+}/ΣFe ratios obtained in this study.

3.5 Radiogenic Isotopes

Samarium-neodymium isotope data was obtained for rock powders of 21 samples. These include 16 samples from rocks of the Eagle's Nest intrusion, two samples of the wall rock tonalite, and three samples of dikes. Samples were prepared and analyzed in a clean lab at the Isotope Geochronology and Geochemistry Research Centre (IGGRC) of Carleton University. Rock powders were doped with a ^{148}Nd-^{149}Sm mixed spike before being dissolved in a mixture of concentrated HF and HNO_3. Sample solutions were then dried down, and the residues were sequentially dissolved in 7 M HNO_3 and in 6 M HCl, followed by a final drying period. The sample residues were dissolved in 1.5 ml of 2.5 M HCl and were loaded onto 14 ml Bio-Rad borosilicate glass chromatography columns containing 3.0 ml of Bio-Rad AG50W-X8 cation exchange resin. The columns were washed with 3.5 ml of 6 M HCl before Rare Earth Elements (REE) were eluted using 9 ml of 6 M HCl. The REE fractions were dissolved in 0.26 M HCl and were loaded onto 2 ml prepacked Ln resin columns (Eichrom Technologies, LLC, USA). The Nd was eluted using 0.26 M HCl, followed by Sm elution using 0.5 M HCl. The Nd isotope ratios were measured using IGGRC's Thermo-Finnigan Neptune multi-collector ICP-MS. The acquired ratios were normalized against ^{146}Nd/^{144}Nd=0.7219. The ^{143}Nd/^{144}Nd ratios were normalized for offsets using bracketing JNdi-1 average values against an average JNdi-1 value 0.512100 of IGGRC's Thermo-Finnigan Triton Thermal Ionization Mass Spectrometer (TIMS).

The average values of bracketing standard reference materials for a period of six months covering this analysis session are NBS987 ^{87}Sr/^{86}Sr = 0.710236±0.000017 (2σ, n=36) and JNdi-1 ^{143}Nd/^{144}Nd = 0.512087 ± 0.000008 (2σ, n=53). The total procedure blanks for Nd are <50 pg.

3.6 Stable Isotopes

In-situ sulfur isotope data was obtained in two analytical sessions. In the first session, sulfur isotope ratios of pyrrhotite, pentlandite and chalcopyrite from 19 regions of interest across seven polished thin sections were obtained at the Canadian Centre for Isotopic Microanalysis (CCIM) at the University of Alberta using Scanning Ion Mass Spectrometer (SIMS). During the second session, sulfur isotope ratios for pentlandite and chalcopyrite in two resin pucks were obtained by Laser Ablation Multi-Collector (LA-MC) ICP-MS at the FocusMS Technologies Ltd., Nanjing, China. Detailed analytical methods of each session are described below.

3.6.1 Secondary Ion Mass Spectrometry

Nineteen regions of interest, 1.5 to 2.5 mm in diameter were cored out from the polished thin sections and arranged with CCIM reference materials into a single, 25 mm in diameter epoxy puck. The mount was lightly polished with 1 µm diamond paste before cleaning and coating with 20 nm of Au. To characterize the sulfide phases within the regions of interest secondary electron and backscattered electron images were obtained using a Zeiss EVO MA15 Scanning Electron Microscope (SEM) operating at 20 kV and ~3–5 nA beam current. Prior to the SIMS analysis, an additional 100 nm of Au was coated on the mount.

Sulfur isotopes (^{34}S, ^{33}S, and ^{32}S) were obtained using an IMS-1280 multi-collector ion microprobe with primary beam conditions of 20 keV $^{133}Cs^{+}$ ions focused to ~15 µm diameter at a beam current of ~1.5–2 nA. Prior to analysis, the primary beam was rastered across a 20×20 µm for 30 seconds. Negative secondary ions were extracted though a 10 kV potential to the grounded secondary column (transfer section). Transfer section conditions consisted of a 70 µm entrance slit width, 5×5 mm field aperture, and aperture to sample magnification of 100 times. Automated tuning of secondary ions in each analysis was preceded. A 50 µm energy slit was used to reject high energy ions. Secondary ions ($^{32}S^-$, $^{33}S^-$, and $^{34}S^-$) were simultaneously analyzed in Faraday cups (L'2 using $10^{10}\Omega$ amplifier, L1 with 10^{12} Ω amplifier, and H1 with 10^{11} Ω amplifier) at a mass resolution of ~4000, to resolve potential isobaric interference. Mean count rates for $^{32}S^-$, $^{33}S^-$, and $^{34}S^-$ were 1×10^9, 1×10^7, and 5×10^7 counts per second, respectively, determined over a 60 second counting interval. Faraday cup baselines were measured at the start of the session.

The analytical protocol involved interspersing analyses of unknowns with CCIM primary reference materials for chalcopyrite (S0321, $\delta^{34}S_{VCDT}$ = +0.2 ±0.2 ‰), pentlandite (S0571B, $\delta^{34}S_{VCDT}$ = -0.52 ±0.3 ‰), and pyrrhotite (S0322, $\delta^{34}S_{VCDT}$ = +1.15 ±0.1 ‰). Primary reference materials have no known mass-independent isotopic anomalies for the purpose of this study (i.e., $\Delta^{33}S = 0$, where $\Delta^{33}S = [(\delta^{33}S/1000 + 1) - (\delta^{34}S/1000 + 1)^{0.515}] \times 1000$ ‰). The exponential mass fractionation constant is of Farquhar et al. (2010), and the Vienna Canyon Diablo Troilite (VCDT) values for $^{33}S/^{32}S = 0.00787725$ and $^{34}S/^{32}S = 0.0441626$ (Ding et al., 2001). Instrumental mass fractionation for $^{33}S^-/^{32}S^-$ and $^{34}S^-/^{32}S^-$ was determined for the analytical sessions by utilizing the replicate analyses of the primary reference materials interspersed with the unknowns. For the primary reference materials, the standard deviation of $^{33}S^-/^{32}S^-$and $^{34}S^-/^{32}S^-$ replicates ranged from ±0.04 to ±0.14 ‰, and $\Delta^{33}S$ from ±0.04 to ±0.06 ‰. Final uncertainties in $\delta^{33}S_{VCDT}$, $\delta^{34}S_{VCDT}$, and $\Delta^{33}S$ are reported at 95% confidence level (2σ) and have typical values of ±0.15–0.25 ‰.

3.6.2 Laser Ablation Multi-Collector ICP-MS

Analysis locations of pentlandite and chalcopyrite were selected and documented using reflected light microscopy. Sulfur isotopes (^{32}S and ^{34}S) were determined using a RESOlution-LR S-155 laser-ablation system combined with a Nu Plasma II multi-collector ICP-MS. A medium-resolution source slit of Nu Plasma II was applied to achieve resolving power greater than 8000. A 193 nm ArF excimer laser (homogenised by a set of beam delivery systems) was focused on a selected analysis location with energy fluence of 2.5 J/cm^2. Each analysis incorporated a 30 second background measurement (gas blank), followed by a spot diameter of 40 µm at 5 Hz repetition rate for 35 seconds. Integration time for Nu Plasma II was set to 0.3 seconds. To transport aerosol out of the ablation cell, He was applied (400ml/minute) as a carrier gas and was mixed with Ar (~950 ml/minute) through a T-connector prior to entering the ICP torch.

A natural pyrite (in-house standard Wenshan, $\delta^{34/32}S = +1.2$ ‰ VCDT) was used as a primary standard, and pyrrhotite (Po-H, $\delta^{34/32}S = +6.0$ ‰ VCDT) was used as a secondary standard for pentlandite. A chalcopyrite standard (GBW07268, $\delta^{34/32}S = +0.2$ ‰ VCDT) was used as an external standard for every fourth chalcopyrite analysis, and natural chalcopyrite (TC1725, $\delta^{34/32}S = +12.8$ ‰ VCDT) was used as a quality control. The long-term reproducibility of $\delta^{34/32}S$ was better than 0.5 ‰ (1σ).

Chapter 4 Results

4.1 Overview of the Eagle's Nest Intrusion

The Eagle's Nest intrusion is a subvertically oriented, blade-shaped dike, approximately 500 m wide and extends vertically for over 1600 m (Fig. 4.1A). In plan view, the intrusion's thickness varies from approximately 150 m at its northern, stratigraphically lowermost part, to about 65 m at its southern part (Fig. 4.1B). However, with increasing depth, the northernmost portion narrows, becoming similar in thickness to the southernmost portion. The mineralized orebody is situated at the stratigraphically lowermost and thickest part of the intrusion, specifically at its northern portion in plan view, extending vertically along the basal contact (Fig. 4.1B). The hanging wall contact is situated at the eastern edge of the intrusion and displays a distinct curved morphology in plan view near surface (Fig. 4.1B). Brecciation along the hanging wall contact is common and is most intense below the bend, where it forms a magmatic breccia (Fig. 4.1C). Although the intrusion's orientation is subvertical, at depth, below the topographic high, it exhibits a change to a slight westward plunge.

Previous workers (Zuccarelli, 2020; Zuccarelli et al., 2022) subdivided the intrusion's mineralized zone into the Upper Embayment, which is proximal to surface, and the deeper Lower Embayment. These two embayments are separated by a topographic high at the basal contact of the intrusion, defined by absence of sulfide mineralization (Fig. 4.1C). Since this study is predominantly focused on unmineralized portions of the intrusion, the terms Upper and Lower embayments will refer to both the mineralized and unmineralized portions of the intrusion proximal to surface and at depth rather than strictly the mineralized zones.

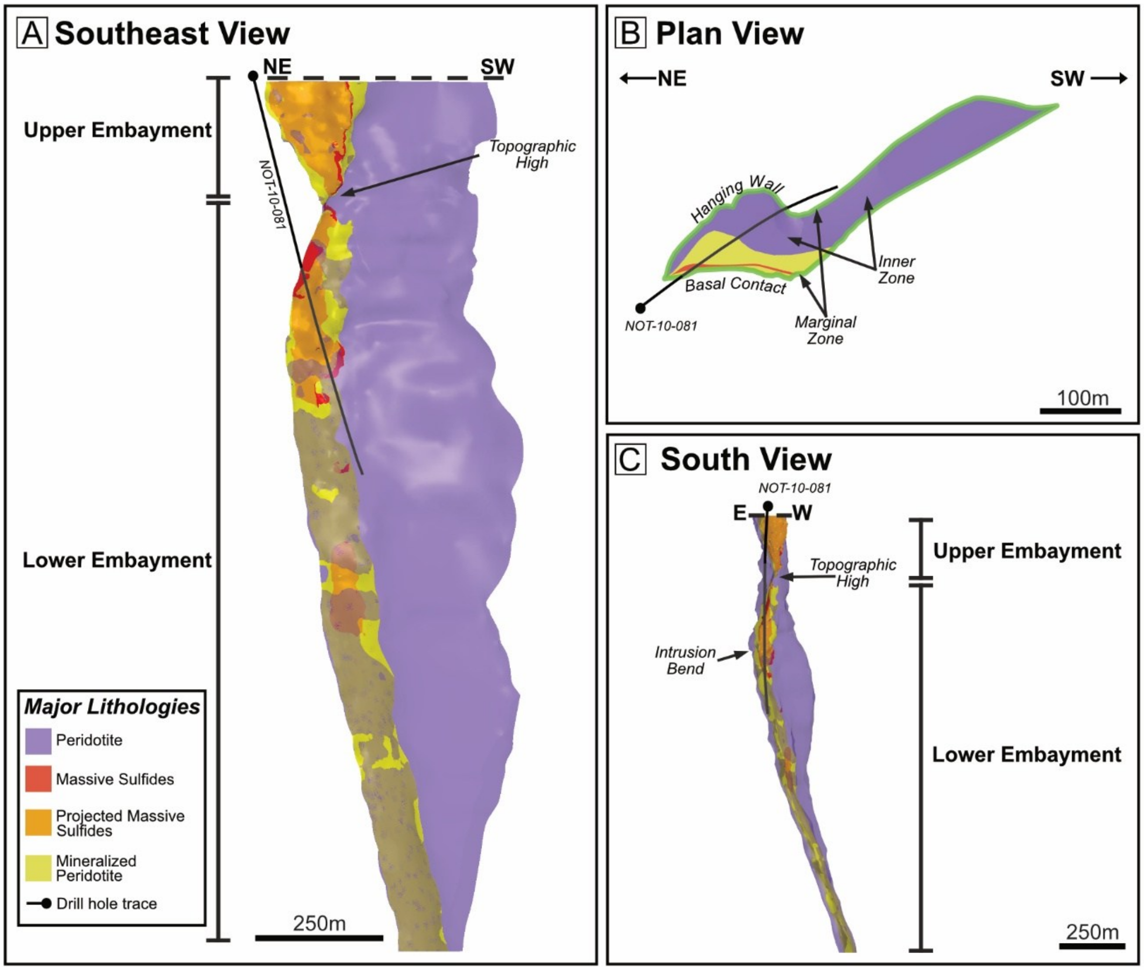

Figure 4.1: Schematic diagram of the Eagle's Nest intrusion, showing cross-section depth profile and subdivision of the main intrusion domains. The drill hole trace for NOT-10-081 is indicated by a solid black line. (A) NE–SW depth section of the Eagle's Nest intrusion illustrating the Upper and Lower embayments, separated by a paleotopographic high and abrupt lack in mineralization. (B) NE–SW plan view of the Eagle's Nest intrusion showing the subdivision of the intrusion into the marginal and inner zones as well as its basal and hanging wall contacts. (C) E-W depth section showing the change in plunge from a subvertical orientation to a westward plunge below the paleotopographic high.

Drilling at the Eagle's Nest intrusion has mostly focused on its mineralized, northernmost portions, with limited drilling at its southern extent, leaving the latter portion less well defined. Consequently, most samples for this study were collected from the northern part of the intrusion, spanning its vertical extent, with limited samples from the southern portion. The Eagle's Nest intrusion is a weakly differentiated intrusion that can be subdivided into two main zones on the basis of drill core observations (Table 4.1): (1) the marginal zone comprising mafic intrusive rocks at the contact with the wall rock tonalite, and (2) the inner zone comprising olivine-bearing ultramafic cumulate rocks that make up the bulk of the intrusion. The marginal zone is often the most intensely altered portion of the intrusion, generally pseudomorphically overprinted by greenschist facies metamorphic mineral assemblages, which were interpreted to comprise mineralogically gabbroic rocks. The inner zone is generally much less intensely altered and can be subdivided into smaller domains comprising massive sulfides, mineralized peridotite, barren peridotite, and pyroxenite. For consistency, we maintain the terminology assigned during drill core examination.

Table 4.1: Subdivision of the Eagle's Nest intrusion with primary igneous characteristics determined petrographically

Zone	Domain	Lithology	Mineralogy	Accessory	Grain Size	Texture
Marginal Zone	Chilled Margin	Microgabbro	Pyx-Pl	Chr (Trace)	Fg	Granular Variolitic
	Gabbro	Melagabbro	Pyx-Pl	Chr (Trace)	Fg to Mg	Granular
Inner Zone	Pyroxenite	Olivine – Pyroxenite	Pyx-Pl-Ol	Chr	Fg to Mg	Orthocumulate
	Barren Peridotite	Lherzolite	Ol-Opx-Cpx	Chr	Fg to Cg	Orthocumulate
	Mineralized Peridotite	Wehrlite to Harzburgite	Ol-Sul‡-Opx-Cpx	Hbl-Chr -Bt	Fg to Cg	Mesocumulate to Heteradcumulate
	Massive Sulfides	Massive Sulfides	Sul‡		Fg to Cg	Massive Granular

Abbreviations: Pyx – pyroxene, Pl – plagioclase, Ol – olivine, Opx – orthopyroxene, Cpx – clinopyroxene, Sul – sulfides, Chr – chromite, Hbl – hornblende, Bt – biotite, VFg – very fine-grained, Fg – fine-grained, Mg – medium-grained, Cg – Coarse-grained.

‡ Sulfides comprising a pyrrhotite–pentlandite–chalcopyrite assemblage.

4.1.1 Lithostratigraphy of the Eagle's Nest Intrusion

The Eagle's Nest intrusion is characterized by mafic intrusive rocks across the marginal zone, and ultramafic cumulate rocks within the inner zone. The intrusion is hosted by a massive to weakly foliated, medium- to coarse-grained tonalite composed of a plagioclase, quartz, alkali feldspar, amphibole, and biotite.

At the marginal zone, drill logs from Wyloo geologists indicated that olivine gabbro is dominant approximately 0.1–3 m from the contact. During drill core examination, the marginal zone rocks were noted to locally have a gradational transition from fine-grained microgabbro to medium-grained gabbro, further into olivine-bearing gabbro, pyroxenite, and peridotite as the distance from the contact increases moving from the marginal to the inner zone. These transitions were observed over 0.1 to 3 m intervals but can span tens of meters within intervals of magmatic breccia. Within the magmatic breccia, intrusive rocks are intercalated with tonalite xenoliths. The transition from microgabbro to gabbro was often confined to a few centimeters along the contacts with tonalite xenoliths, whereas the shift to olivine-bearing rocks is more gradual, and was observed up to several tens of meters away from the hanging wall contact. Further lithological and textural transitions within the inner zone were observed in several intervals, however, most of the examined intervals were limited to the length of several drill core boxes (3–15 m). Lithostratigraphic variations across the inner zones of the intrusion were evaluated through examination of drill hole NOT-10-081 as it captures lithological variations across the northern portion of the intrusion (Fig. 4.1).

The following section is subdivided into the marginal and inner zones. The marginal zone section addresses the variable nature of the contacts between the Eagle’s Nest and the tonalite, focusing on the lithological transitions at, and away, from the contact. The inner zone section emphasizes the major lithostratigraphic variations throughout the inner parts of the intrusion.

4.1.1.1 Marginal Zone

In an effort to identify preserved chilled margins within the intrusion, drill hole intervals intersecting the contact between the tonalite and the marginal zone were examined. From the contact with the tonalite inwards, the gabbroic rocks consist of a pyroxene and plagioclase that gradationally increases in grain size from fine- to medium-grained away from the contact. With increasing distance from the contact, plagioclase content decreases, and the unit becomes more olivine-bearing, transitioning to more ultramafic lithologies. Marginal zone rocks often exhibit a greenish to brownish appearance due to pervasive actinolite-chlorite alteration, which variably overprints the primary igneous mineral assemblage at different portions of the marginal zone. This alteration is locally accompanied by a zoned biotite alteration, the intensity of which diminishes with distance from the contacts. The marginal zone displays a range of contact morphologies that were grouped into three types: sharp, diffuse, and disrupted contacts.

Sharp contacts are characterized by a clear boundary between the marginal zone intrusive rocks and the tonalite, often preserving primary plagioclase and less often pyroxene with weak overprinting alteration (Fig. 4.2A). These contacts are planar to wavy on drill core scale, occasionally appearing irregular (Figs. 4.2B & F). Sharp contacts often display little to no foliation and tend to retain more of the primary characteristics, suggesting they were less influenced by post-magmatic processes (Figs. 4.2C–D & G–H). In a few places, where alteration intensity is higher, actinolite and chlorite tend to be pervasive, whereas biotite alteration is concentrated at the contact and decreases away from it. The tonalite adjacent to sharp contacts is mostly massive and unaltered but locally does exhibit a subtle increase in potassic alteration near the contact giving it a pinkish appearance (Figs. 4.2B & F).

Diffuse contacts are characterized by irregular boundaries, where the transition between the tonalite and marginal zone is less distinct (Fig. 4.3A). Diffuse contacts were the most common contact type observed. These often showed evidence of stronger alteration intensity and fabric development than sharp contacts (Figs. 4.3B & E).

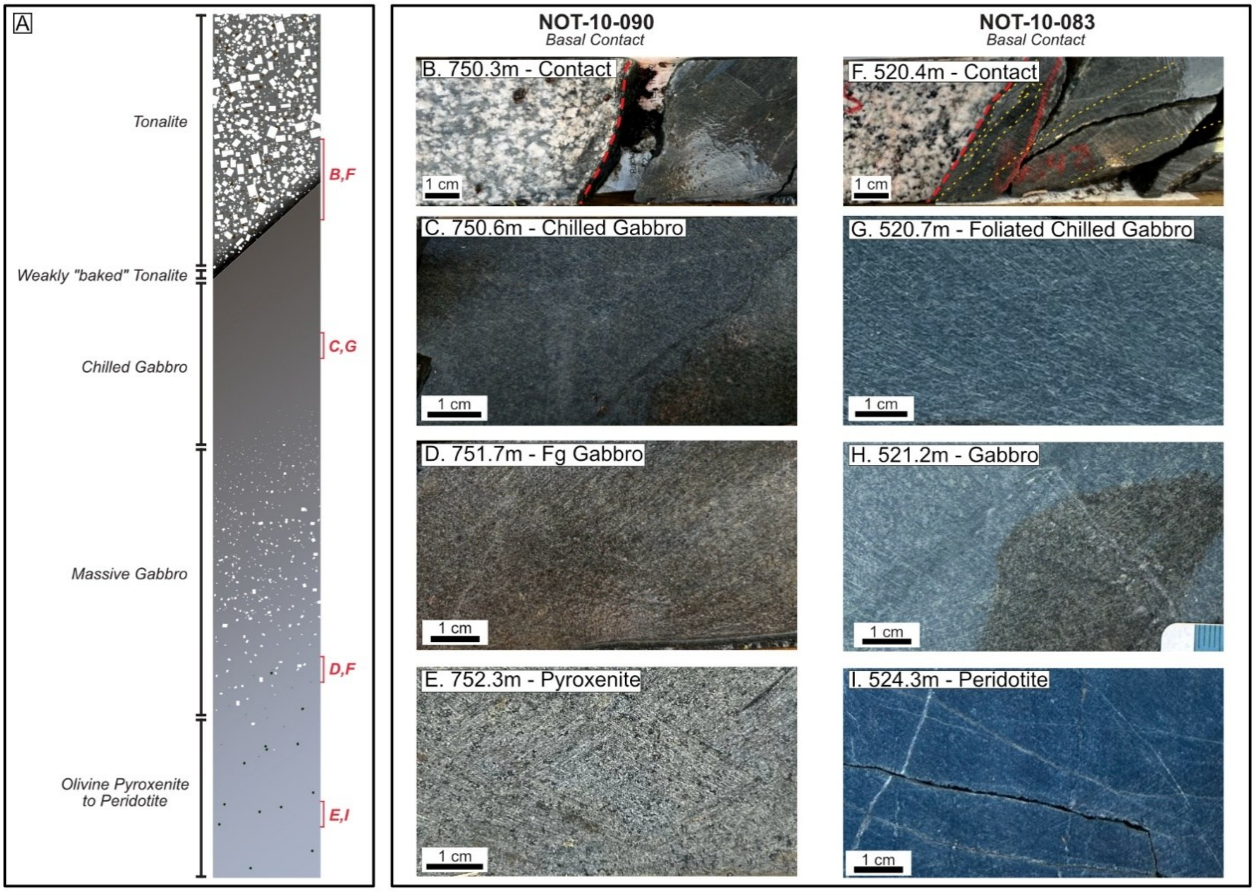

Figure 4.2: (A) Schematic illustration of a sharp contact along with representative drill core photographs of the basal contact seen in drill holes NOT-10-090 (B–E) and NOT-10-083 (F–I) illustrating the abrupt nature of the contacts and the gradational transition from mafic to ultramafic intrusive lithologies. Abbreviations: Fg – Fine-grained.

Alteration is characterized by biotite and is generally more intense than that observed at sharp contacts. A foliation was present in proximity to the contact and local massive zones of biotite-rich domains along the contact (Figs. 4.3C & F). Along some of the diffuse contacts, minor amounts of medium-grained anhedral quartz and plagioclase xenocrysts were observed within the marginal zone rocks, the abundance of which, decreases with distance away from the contact. The tonalite adjacent to diffuse contacts, was often baked, partially melted, and/or displayed a strong fabric oriented subparallel to the contact, which gradually decreased in intensity away from the contact (Figs. 4.3B–G).

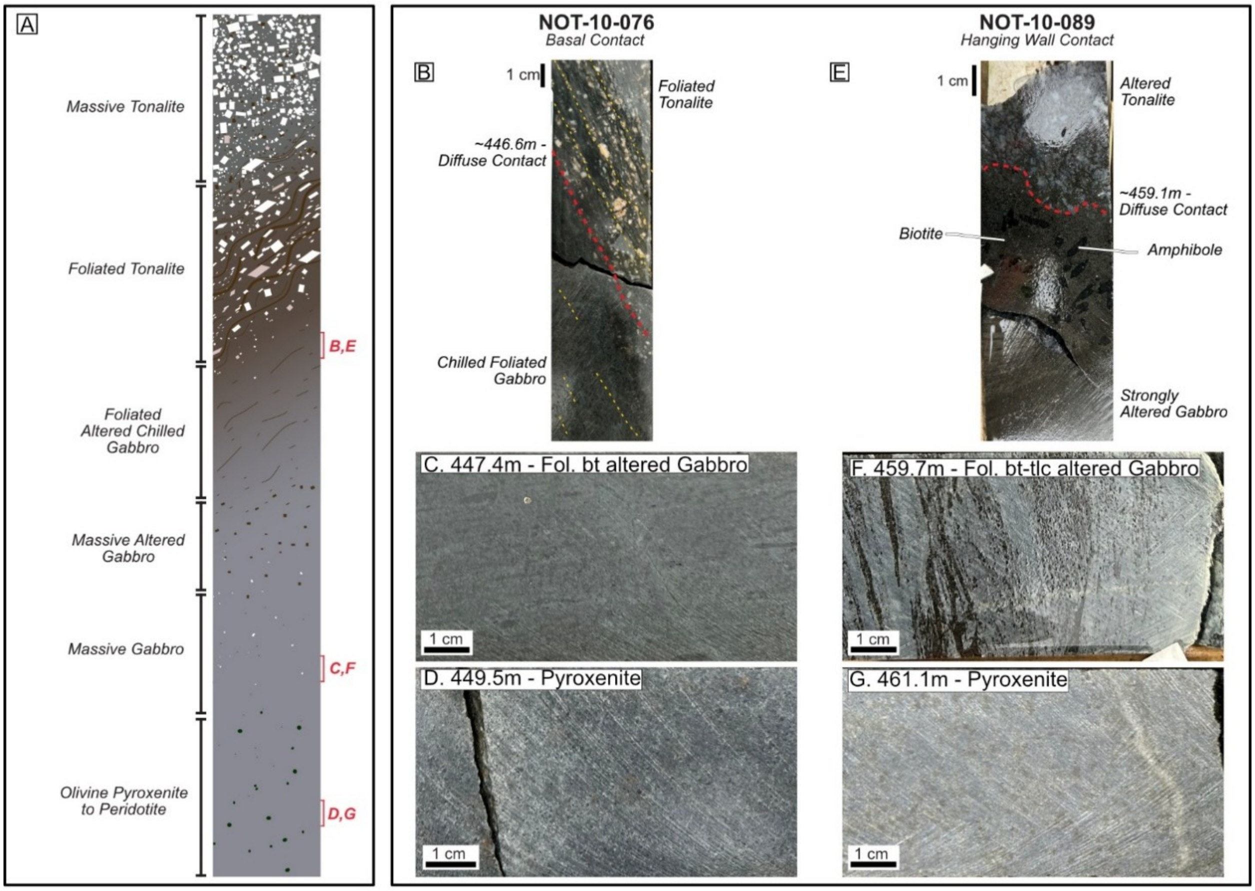

Figure 4.3: (A) Schematic illustration of a diffuse contact along with representative drill core photographs of the basal contact seen in drill hole NOT-10-076 (B–E) and the hanging wall contact seen in drill hole NOT-10-083 (F–I). At diffuse contacts, the tonalite displays higher degrees of alteration near the contact sometimes with a well-developed foliation (B) or porphyritic texture and silicification (E). Gabbroic rocks at the contact, display similar gradual transition to those in sharp contact but are overprinted by weak to moderate, biotite-chlorite-talc alteration the intensity of which decreases away from the contact (C–D, F–G). Abbreviations: Fg – Fine-grained, Fol. – foliated, bt – biotite, tlc – talc.

Disrupted contacts were the least common in the examined marginal zone intervals. Disrupted contacts occur where the contact between the tonalite and adjacent marginal zone intrusion lithologies was obscured and intruded by veins or dikelets (Figs. 4.4B, E & H). These were commonly encountered along intervals of magmatic breccia proximal to the hanging wall contact (Figs. 4.1 & 4.4A). The magmatic breccia consists of angular, generally unaltered tonalite xenoliths intercalated with gabbroic through pyroxenitic rocks. Across the magmatic breccia, the transition from fine-grained gabbro to medium-grained gabbro to pyroxenite tends to be confined to xenolith contacts, sporadically occurring throughout the examined magmatic breccia intervals. Alteration intensity varies from weak to intense, consisting of pervasive actinolite-chlorite-sericite and pervasively disseminated biotite (Figs. 4.4D & F–G).

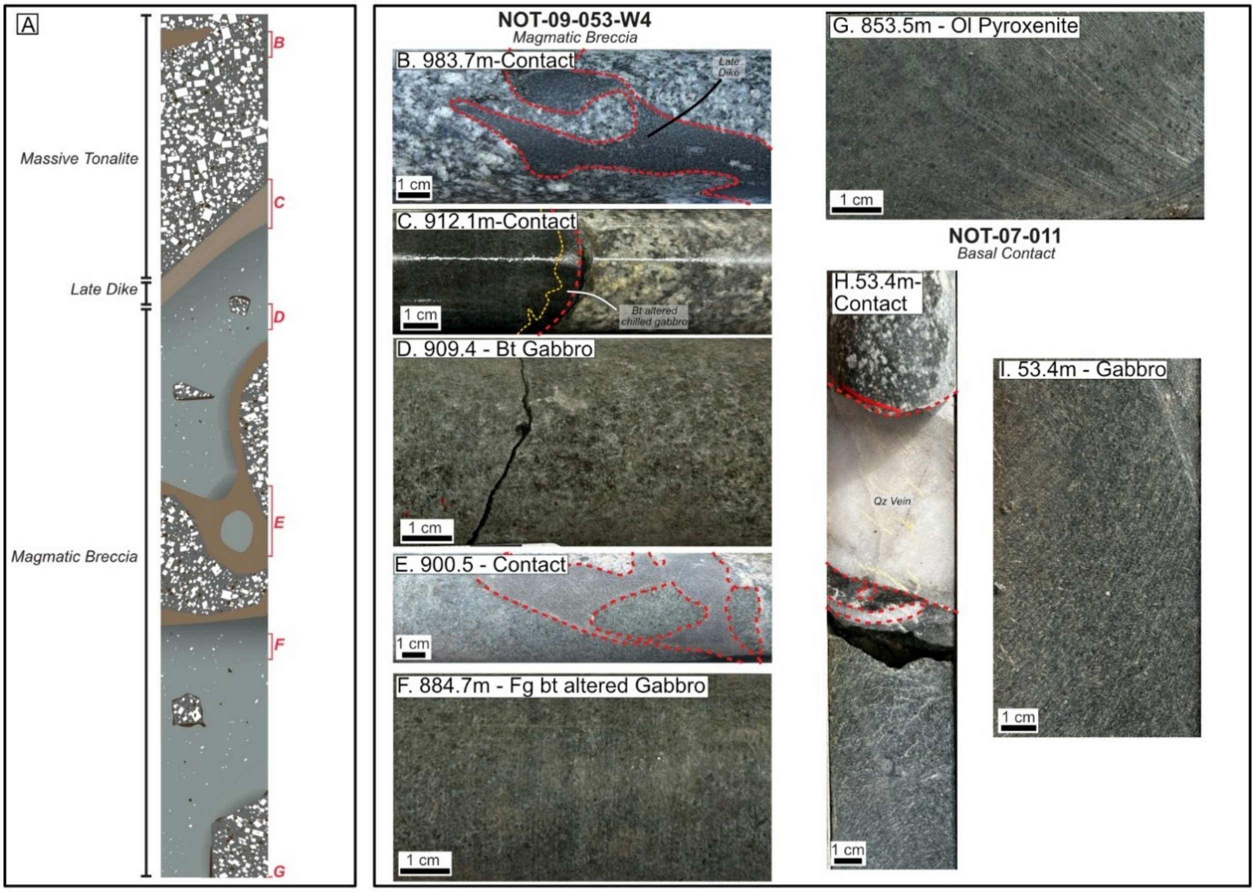

Figure 4.4: (A) Schematic illustration of a disrupted contact with representative drill core photographs of the magmatic breccia seen in NOT-09-053-W4 (B–G) and basal contact seen in NOT-07-011 (H–I). Disrupted contacts most commonly were encountered within the magmatic breccia where intermediate, aphanitic unit intrudes at the contact between tonalite xenoliths and gabbroic intrusive rocks (A, E). The gradational transition is more localized, occurring in contact with tonalite xenolith transitioning from fine- to medium-grained gabbro (C). The transition from gabbroic rocks to pyroxenites may occur at distances of up to ~60 m away from the hanging wall contact and the first appearance of intrusion rocks (E–G). Other units, such as massive quartz veins (H) and mafic to intermediate dikes are seen at contacts outside of the magmatic breccia. These often obscure the direct chilled characteristics. Abbreviations: Fg – Fine-grained, Fol. – foliated, bt – biotite, tlc – talc, ol – olivine, qz – quartz.

Where alteration is intense, acicular actinolite, zones of pervasive chlorite, or intensely disseminated biotite are present. Biotite alteration not only occurs as pervasive disseminations, but also as thin rinds (<1–3 cm), mantling the tonalite xenoliths (Fig. 4.4C). Late-stage, aphanitic, intermediate dikelets intrude the contacts between the xenoliths and marginal zone rocks. These late dikelets obscure the primary contact relationships, although, minor gradation towards finer-grained microgabbroic rocks was locally observed (Fig. 4.4C). Outside of the magmatic breccia intervals, disrupted contacts were not as commonly observed, but occurred locally, consisting of dikelets or quartz veins (Fig. 4.4H).

4.1.1.2 Inner Zone

To evaluate the variability across the inner zone of the Eagle's Nest intrusion, drill hole NOT-10-081 was selected for detailed examination. Drilled from the northern edge of the Eagle's Nest intrusion southwards, it intersects a zone of massive sulfides, mineralized ultramafic rocks, and non-mineralized ultramafic rocks that grade towards gabbroic compositions within the magmatic breccia at the hanging wall portion of the intrusion (Figs. 4.1 & 4.5A). In addition to systematic examination of NOT-10-081, a number of samples were collected across the intrusion to evaluate the mineralogical and textural changes both along the length and stratigraphy of the intrusion. These samples complement observations of the inner zone from drill hole NOT-10-081.

The inner zone consists of olivine-bearing cumulate ultramafic rocks, primarily composed of peridotite that transitions to pyroxenite towards the hanging wall of the intrusion. Contacts between inner zone lithologies are gradational and are marked by a decrease in sulfide content between the mineralized and non-mineralized peridotite, and by decreasing olivine content between the peridotite and pyroxenite (Fig. 4.5A).

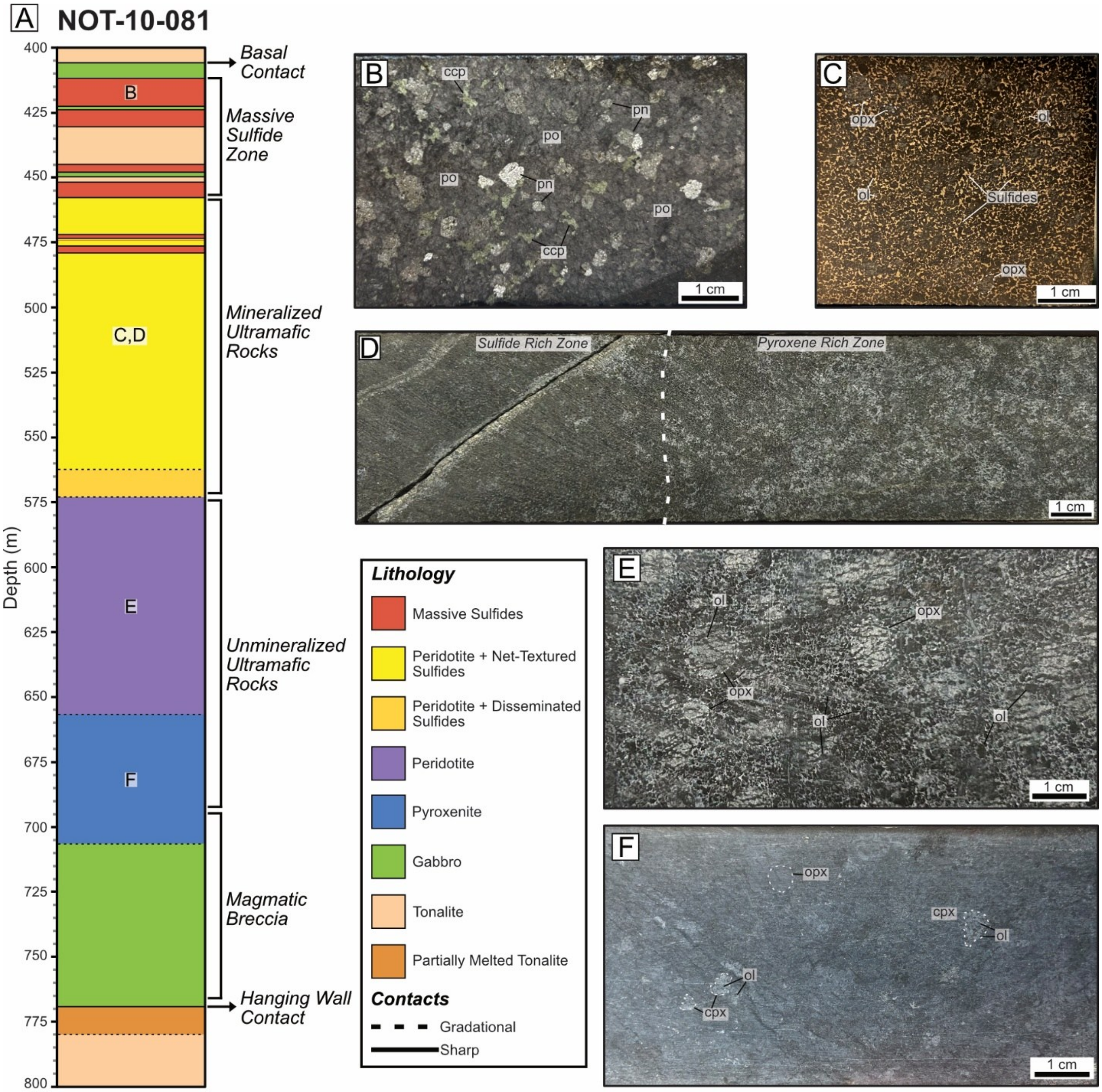

Figure 4.5: Simplified drill log column of drill hole NOT-10-081 illustrating the main zones and lithologies within the inner zone of the intrusion. (A) Drill log column across NOT-10-081, with approximate locations of corresponding drill core photos. (B) Massive sulfides comprising granular pyrrhotite and pentlandite, and intercumulus patchy chalcopyrite. (C) Peridotite, comprising fine-grained cumulate olivine, net-textured sulfides and minor amounts of orthopyroxene oikocrysts. (D) Transitional contacts between the olivine- and sulfide-rich zones and intermittent zones dominated by pyroxene. (E) Weakly altered, poikilitic barren peridotite. (F) Weakly altered pyroxenite. Note the dull luster and more subhedral morphology of orthopyroxene in comparison to the clinopyroxene. Abbreviations: po – pyrrhotite, pn – pentlandite, ccp – chalcopyrite, ol – olivine, opx – orthopyroxene, cpx – clinopyroxene.

The alteration intensity in inner zone lithologies is variable, but overall increases towards the contacts. Out of the primary silicate phases, olivine was typically the most recognizable silicate phase, occurring as black serpentinized phenocrysts. Intercumulus silicate phases were often difficult to identify and distinguish due to intense overprinting alteration by chlorite, talc, and amphibole. In less altered zones of the peridotite, the dominant intercumulus phase consisted of orthopyroxene, occurring as brownish, ellipsoidal oikocrysts (Fig. 4.5E). Clinopyroxene was generally altered in peridotite intervals, however, within the pyroxenite local unaltered grains were identified, occurring as black, anhedral, intergranular grains, distinguished from orthopyroxene by their metallic lustre (Fig. 4.5F).

The stratigraphically lowermost portion of the intrusion comprises the massive sulfide zone (Fig. 4.5A). In drill hole NOT-10-081, the massive sulfide zone consists of several intervals of massive sulfide mineralization that range from 3 to 12 m. In order of abundance, the massive sulfides consist of magnetic, bronze coloured pyrrhotite aggregates, fine- to medium-grained, granular to wispy pentlandite, and fine-grained interstitial chalcopyrite (Fig. 4.5B). The mineralized intervals are intercalated with zones of fine-grained mafic intrusive rocks and tonalite, often with abrupt contacts (Fig. 4.6A). The tonalite and mafic intrusive rocks are weakly mineralized or barren, with mineralization occurring sporadically as sulfide veins across the unit or as wispy zones proximal to contacts with massive sulfides. The transition from the massive sulfide zone to the net-textured mineralized peridotite occurs abruptly at 457.8 m (Fig. 4.6A).

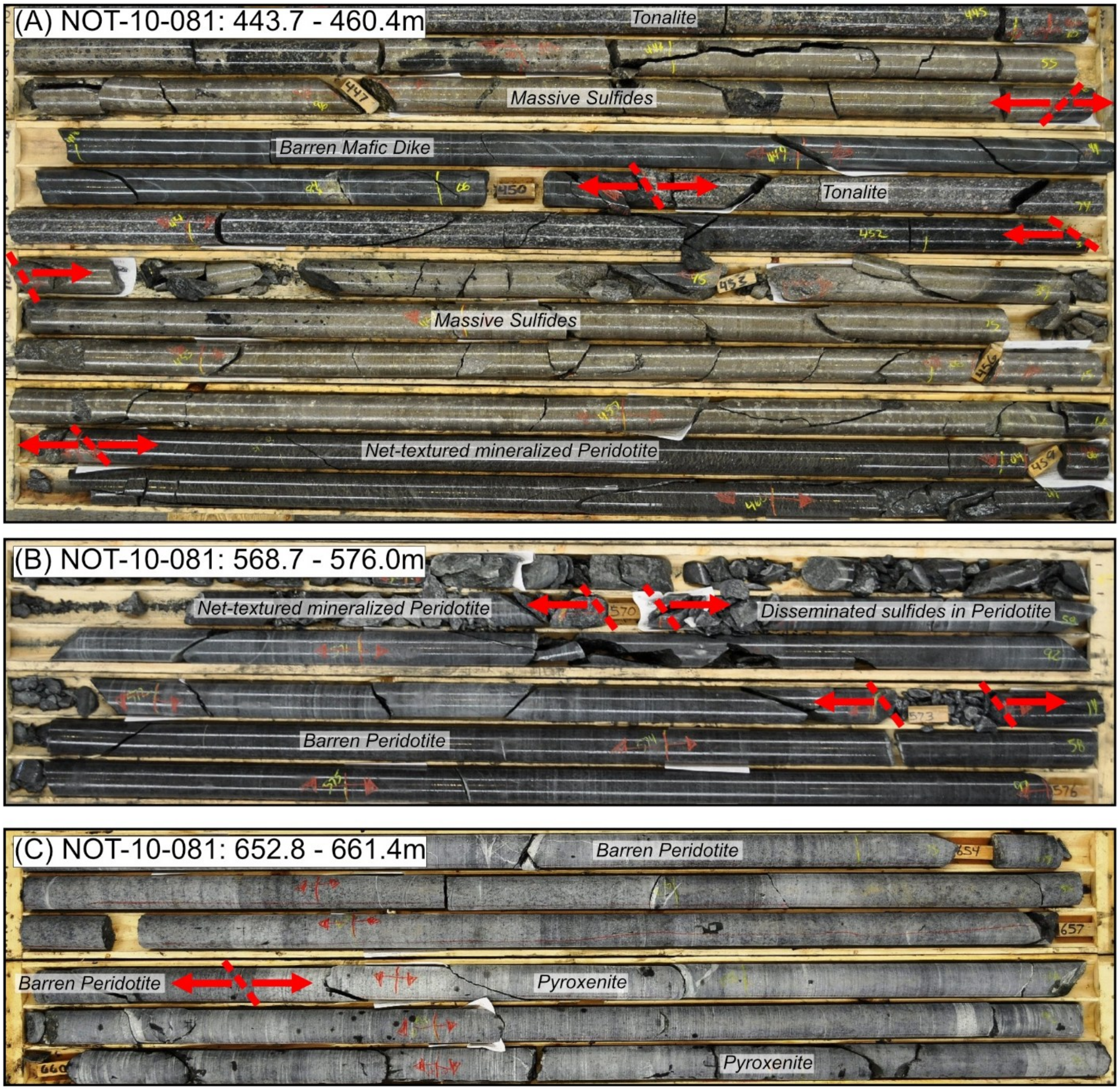

Figure 4.6: Drill core intervals illustrating the nature of the contacts seen in NOT-10-081. (A) Interval 443.7 to 460.4 m illustrating the sharp nature of the contacts between the intercalated tonalite, and mafic dikes and the massive sulfide intervals. Also seen is the transition from the massive sulfide zone into the mineralized peridotite marked by an abrupt contact at 457.8 m. (B) Intervals 568.7 to 576.0 m illustrating the gradational transition from net-textured to disseminated sulfides in mineralized peridotite into unmineralized, barren peridotite. (C) Interval 652.8 to 661.4 m illustrating the gradational transition from olivine-rich peridotite to olivine-poor pyroxenite.

In drill hole NOT-10-081, the mineralized peridotite extends from its contact with the massive sulfide zone at 457.8 to 573m (Fig. 4.5A). The mineralized peridotite consists of serpentinized, fine- to medium-grained cumulus olivine, medium-grained intercumulus to poikilitic pyroxene, and interstitial net-textured sulfides (Fig. 4.5C). Although the overall mineralogy remained consistent, modal proportions of these locally varied. The unit fluctuated between intervals dominated by olivine and net-textured sulfides with minor pyroxene, and intervals where pyroxene abundance increased, sometimes up to 40%. Pyroxene-rich intervals were patchy and light-coloured, stretching 0.1 to 1.5m in length (Fig. 4.5D). The transition into and out of these pyroxene-rich intervals was marked by a gradual increase or decrease in pyroxene abundance (Fig. 4.5D). Sulfides occur interstitial to olivine and pyroxene, and their abundance fluctuated with changing pyroxene abundance. In olivine-dominated intervals, sulfide content reached up to 35% forming continuous networks of sulfide mineralization. By contrast, in pyroxene-rich intervals, sulfide contents typically decrease to as low as 10% of the modal abundance, forming discontinuous networks (Fig. 4.5D). The transition from mineralized to unmineralized peridotite occurs gradually over a 3m interval towards the hanging wall contact, where sulfide abundance decreases from net-textured to disseminated to barren peridotite (Figs. 4.5A & 4.6B).

The barren, unmineralized peridotite extends from the mineralized peridotite contact to 657.4 m transitioning into pyroxenite (Fig. 4.5A). This unmineralized peridotite is characterized by a dark grey to greenish colour, consisting predominantly of fine-grained cumulus olivine, medium-grained orthopyroxene occurring as oikocrysts, and lesser amounts of intercumulus clinopyroxene. These minerals together sometimes formed a poikilitic texture (Fig. 4.5E). Alteration intensity varies across the unit, typically occurring in short intervals ranging from several centimetres up to 5 m. In these regions, talc-chlorite alteration was prominent, giving the unit a light green appearance. Other than serpentine pseudomorphed cumulus olivine, no other phases were identifiable in intensely altered intervals. Where overprinting alteration does not fully mask the identification of intercumulus phases, orthopyroxene was recognized by its coarser grain size and occurrence as ellipsoidal oikocrysts, whereas clinopyroxene occurred as finer grained, intercumulus, anhedral grains. The peridotite gradually transitions to pyroxenite over a 2 m interval, marked by a decrease in olivine abundance (Fig. 4.6C).

The pyroxenite extends from its gradational contact with unmineralized peridotite at 657.4 to 706 m in drill hole NOT-10-081 but was generally narrower in other intervals (Fig. 4.5A). Primary silicate phases making up the pyroxenite were best distinguished outside of the magmatic breccia interval, where the unit consists of equigranular anhedral pyroxene, and smaller amounts of serpentinized cumulus olivine (Fig. 4.5F). Outside of the magmatic breccia interval, the pyroxenite exhibits moderate alteration intensity, sometimes allowing for a distinction between orthopyroxene and clinopyroxene. Within the magmatic breccia, alteration intensity rapidly increases, completely obscuring the primary silicate phases with a chlorite, talc, amphibole, carbonate, and/or biotite alteration. In drill hole NOT-10-081, the transition from pyroxenite to gabbro occurs at approximately 706 m, extending into the marginal zone. Although the transition along the magmatic breccia is gradual, short, localized intervals of pyroxenite were observed within the magmatic breccia, away from tonalite xenoliths.

4.1.2 Eagle’s Nest Type Dikes

One of the objectives of this study was to investigate the mafic dikes of the Esker Intrusive Complex and across MLGB. Wyloo geologists, using a portable X-ray fluorescence (pXRF) analyzer, characterized dikes with ~7.8 % Fe and ~7.2 % Mg as Eagle’s Nest type dikes. These dikes are interpreted to be genetically related and contemporaneous with the formation of the Eagle’s Nest intrusion.

The Eagle's Nest type dikes range from 0.5 to 5 m in thickness and consist of variably altered, mafic intrusive rocks. They typically are greenish brown to grey in colour, are fine- to medium-grained with the primary mineralogy generally undiscernible due to intense overprinting alteration consisting of chlorite-amphibole assemblage (Fig. 4.7). These dikes often occur as intensely foliated units bound by sharp contacts with massive tonalite (Fig. 4.7C). Less commonly, they appear as fine-grained, massive intervals resembling strongly altered marginal zone gabbroic rocks within the intrusion (Fig. 4.7A). Like the intensely altered marginal gabbroic rocks, primary mineralogy was undiscernible. In addition to pervasive chlorite-amphibole alteration, these intervals are often crosscut by quartz-carbonate veinlets, and less often contain fine-grained, pervasively disseminated carbonate alteration (Fig. 4.7B).

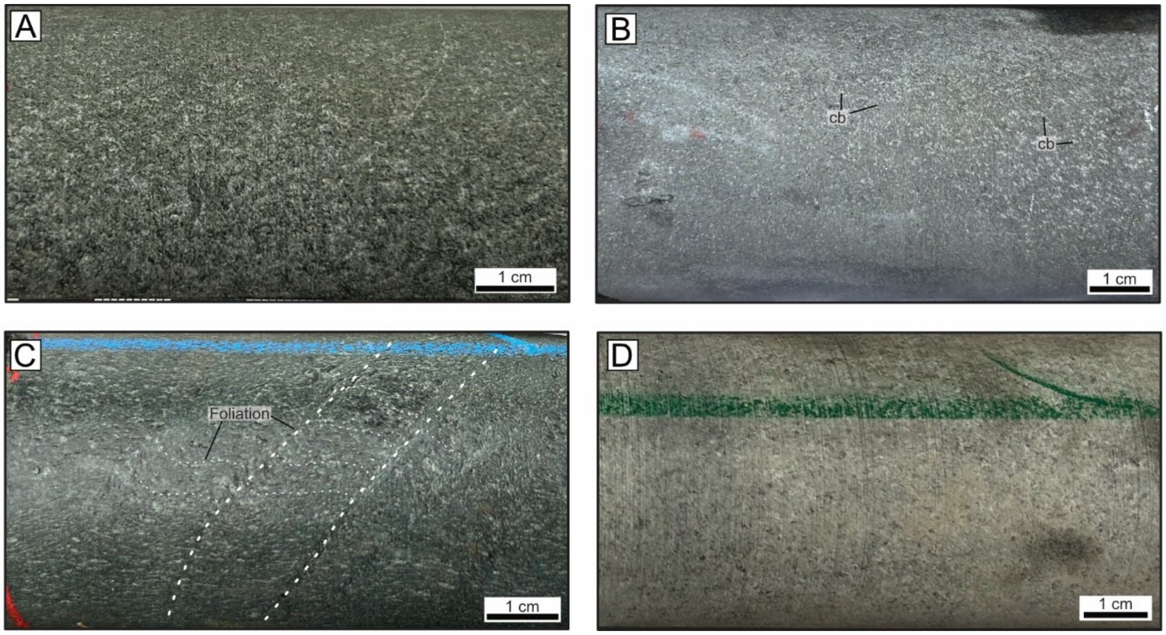

Figure 4.7: Textural and mineralogical variations in Eagle's Nest type dikes. (A) Medium-grained, gabbro, moderately overprinted by chlorite-amphibole displaying similar characteristics to marginal zone gabbroic rocks of the Eagle's Nest intrusion. (B) Fine-grained gabbro overprinted by disseminated carbonate alteration. (C) Strongly sheared gabbro overprinted by a chlorite-amphibole assemblage. Dotted lines outline foliation. (D) Strongly altered pyroxenite comprising chlorite-amphibole-talc altered pyroxene, and serpentine pseudomorphed olivine. This interval displays similar characteristics to those observed in the pyroxenitic rocks of the Eagle's Nest intrusion.

Although generally unmineralized, some dikes contain trace amounts of fine-grained euhedral pyrite. In the vicinity of the Blue Jay occurrence, a 20 m interval of an Eagle's Nest type dike was examined from drill hole NOT-23-2G02. This dike interval was significantly larger than any other examined intervals and comprises a pyroxenite. It is similar in appearance and mineralogy to pyroxenitic intervals examined within the intrusion, containing fine-grained serpentinized olivine and talc-chlorite altered pyroxene (Fig. 4.7D).

4.2 Petrography

Fifty-five polished thin sections were examined using transmitted- and reflected-light microscopy. The prepared thin sections include 16 from the marginal zone (including six of the contact between mafic intrusive rocks and the tonalite), 22 from the inner zone, and 17 from dikes across the MLGB. Additionally, two polished pucks of the mineralized peridotite were prepared for sulfur isotope analysis of sulfides. Visual interpretation was used during modal abundance estimates, mineral identification, and textural characterization. Grain sizes were determined on the microscope and are reported as very fine-grained (<0.1 mm), fine-grained (0.1–1 mm), medium-grained (1–5 mm), and coarse-grained (>5 mm). Complete thin section descriptions are provided in Appendix B.

The examined samples display variable degrees of overprinting alteration. Within the Eagle's Nest intrusion, alteration is often pseudomorphic, allowing for recognition of primary textures and typically identification of relict minerals. The marginal zone rocks are the most intensely altered within the Eagle's Nest intrusion, where the majority of the mafic igneous minerals have been pseudomorphically overprinted by alteration minerals. The inner zone rocks, specifically the mineralized peridotite, are the least altered, with nearly all of the primary silicate phases being recognizable (Fig. 4.8A). The sampled dikes are characterized by a range of alteration intensities, ranging from moderate to intense pseudomorphic alteration where the samples show characteristics of metamorphism under greenschist-facies conditions (Fig. 4.8B). Attempts were made to distinguish and estimate the proportions of the primary igneous phases. This was done based on preserved textural relationships and distinct overprinting alteration assemblages.

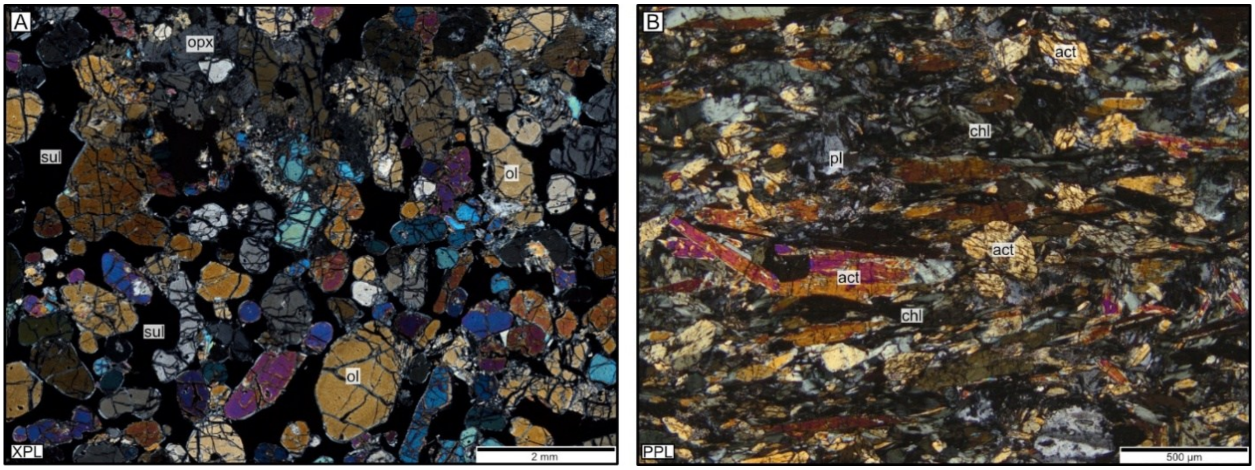

Figure 4.8: Photomicrographs showing the variability of alteration intensity across the examined samples. (A) Weakly altered mineralized peridotite. (B) Strongly altered, foliated Eagle's Nest type dike. Abbreviations: PPL – plane-polarized light, XPL – cross-polarized light, ol – olivine, opx – orthopyroxene, sul – sulfides, pl – plagioclase, act – actinolite, chl – chlorite.

4.2.1 Eagle's Nest Intrusion

4.2.1.1 Marginal Zone

All of the examined marginal zone samples come from the stratigraphically lowermost, northern portion of the intrusion (Fig. 4.1B), with the majority collected from the Lower Embayment, and four samples from the Upper Embayment. Four of the prepared thin sections were collected along the basal contact of the intrusion, with the remaining samples collected along the hanging wall, including three contact samples within the magmatic breccia.

Due to alteration, distinguishing primary mafic minerals and their proportions was challenging. As a result, none of the collected samples can be classified using the International Union of Geological Sciences (IUGS) classification scheme. Based on morphology, occurrence, and alteration assemblage, clinopyroxene is interpreted to be the most abundant phase, and plagioclase is the least altered and second most abundant mineral. Together, these phases can be interpreted to comprise gabbroic rocks. The presence of other igneous minerals (i.e. olivine and/or orthopyroxene), prior to alteration, cannot be completely ruled out, as similar alteration assemblage minerals can often overprint one another, masking the presence of other phases, in which case these rocks could be classified as olivine-bearing gabbro or gabbronorite.

General Characteristics

The majority of the marginal zone rocks have similar pre-alteration proportions of clinopyroxene to plagioclase, similar grain sizes and textural characteristics. Except for a single sample where plagioclase is more abundant than clinopyroxene, clinopyroxene is more abundant than plagioclase, therefore they can be classified as melagabbro. Most of the samples are characterized by fine to medium grain sizes, with granular texture sometimes displaying sub-ophitic textures (Fig. 4.9A). Two samples are an exception to that, displaying distinct characteristics: (1) sample EN24VS039 is characterized by a similar granular texture but a much smaller grain size (Fig. 4.9B), and (2) sample EN23VS114 is characterized by a variolitic arrangement of lath-like plagioclase with intergranular to skeletal clinopyroxene (Fig. 4.9C). These two samples can be referred to as microgabbro due to the textural evidence suggesting more rapid crystallization.

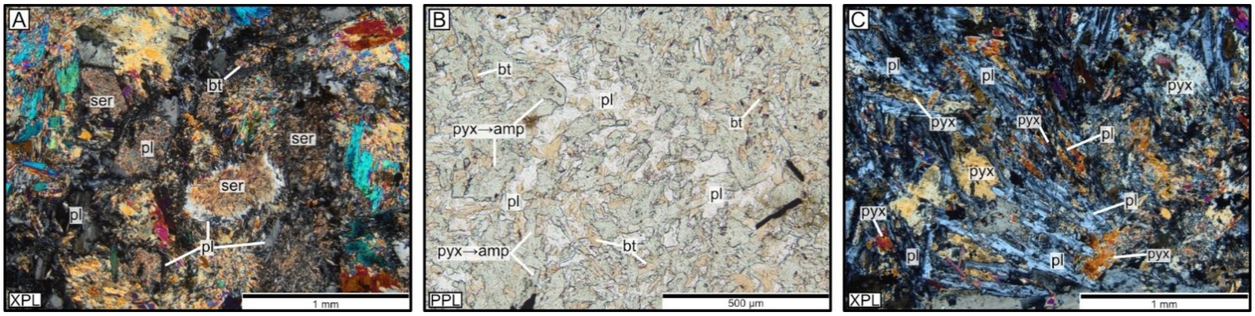

Figure 4.9: Photomicrographs showing textural variations in marginal zone rocks. (A) Medium-grained granular melagabbro consisting of equigranular plagioclase and intergranular clinopyroxene. (B) Very fine-grained granular melagabbro. (C) Medium-grained, variolitic textured melagabbro. Abbreviations: PPL – plane-polarized light, XPL – cross-polarized light, pl – plagioclase, pyx – pyroxene, ser – sericite, bt – biotite, amp – amphibole.

Mineralogy

Clinopyroxene in most samples is fine- to medium-grained, ranging 55–80 % of the modal abundance prior to alteration. It typically occurs as anhedral to subhedral grains intergranular to plagioclase and locally forming sub-ophitic textures (Figs. 4.10A & F). More rarely, it appears as euhedral grains or anhedral skeletal grains (Fig. 4.10B). Medium-grained, anhedral, granular orthopyroxene comprising 20 % of the modal abundance was observed in a single sample (EN23VS122), which is interpreted to be a gabbronorite (Fig. 4.10C).

Plagioclase is the least altered phase. Often similar in grain size to clinopyroxene, it is fine- to medium-grained and makes up 20–45 % of the modal abundance. Plagioclase more commonly occurs as euhedral to subhedral, equigranular grains (Fig. 4.10F), ranging from tabular (Figs. 4.10A & D–F) to elongate lath like morphologies (Fig. 4.10B).

Oxide minerals occur in trace amounts within the marginal zone samples. These comprise chromite, which occurs as very fine- to fine-grained, euhedral to subhedral, equant grains that are surrounded by aggregates of alteration assemblage minerals (amphibole, chlorite and biotite;

Figs. 4.11A–B). Chromite frequently displays intra-grain, gradational concentric zonation, transitioning from a blueish chromite core to a greyish magnetite rim (Fig. 4.11C).

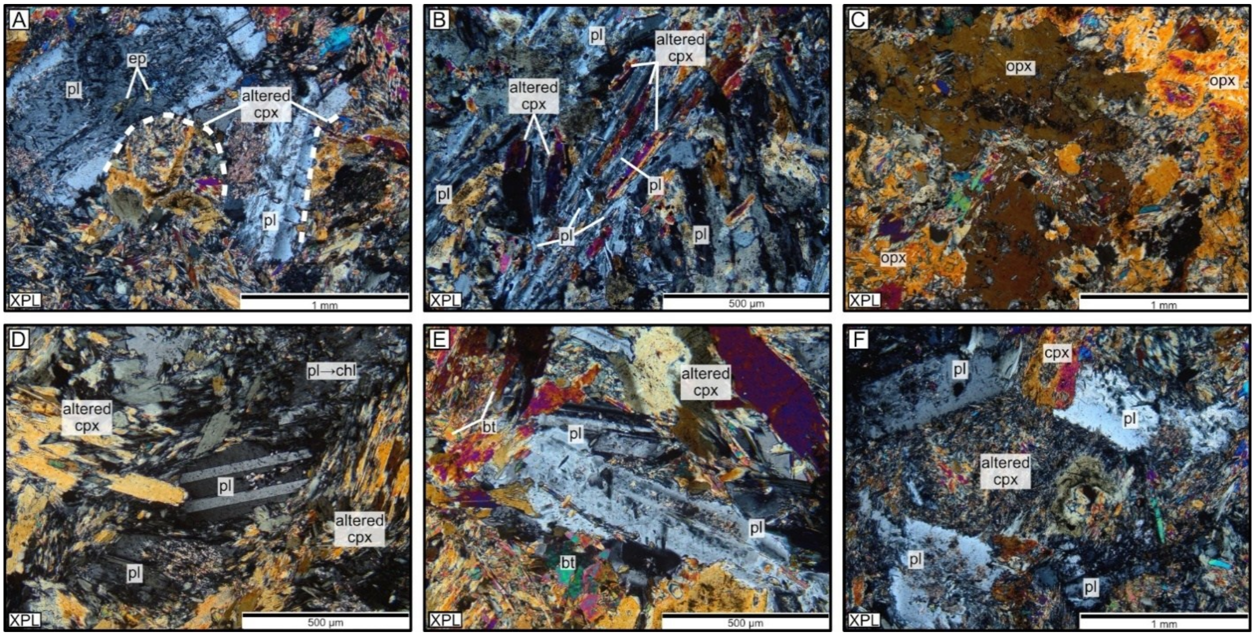

Figure 4.10: Photomicrographs showing primary silicate mineral characteristics in marginal zone rocks. (A) Equant, clinopyroxene occurring intergranular to tabular plagioclase. (B) Medium-grained, lath-like plagioclase forming a variolitic texture with intergranular to skeletal clinopyroxene. (C) Medium-grained, anhedral, orthopyroxene in the gabbronorite sample. (D) Fine-grained, tabular plagioclase with polysynthetic twinning in contact with altered pyroxene. (E) Medium-grained, twinned, subhedral, tabular plagioclase. (F) Equigranular, medium-grained plagioclase with anhedral intergranular clinopyroxene. Abbreviations: PPL – plane-polarized light, XPL – cross-polarized light, pl – plagioclase, pyx – pyroxene, opx – orthopyroxene, cpx – clinopyroxene, ep – epidote, chl – chlorite.

Mineralization

Sulfide minerals generally comprise trace amounts, rarely up to 1 % of the modal abundance. Sulfides occur as very fine- to fine-grained, disseminated, blocky and/or irregular aggregates as individual disseminated grains or in clusters interstitial to pyroxene and plagioclase (Figs. 4.11D–E). Sulfides typically comprise pyrrhotite, with lesser amounts of chalcopyrite and more rarely pentlandite (Fig. 4.11D). Rare pentlandite exsolution was observed (Fig. 4.11F).

Pyrite was identified in two samples, occurring as anhedral blocky grains. Occasionally, magnetite occurred at grain boundaries or infilled fractures within sulfide phases.

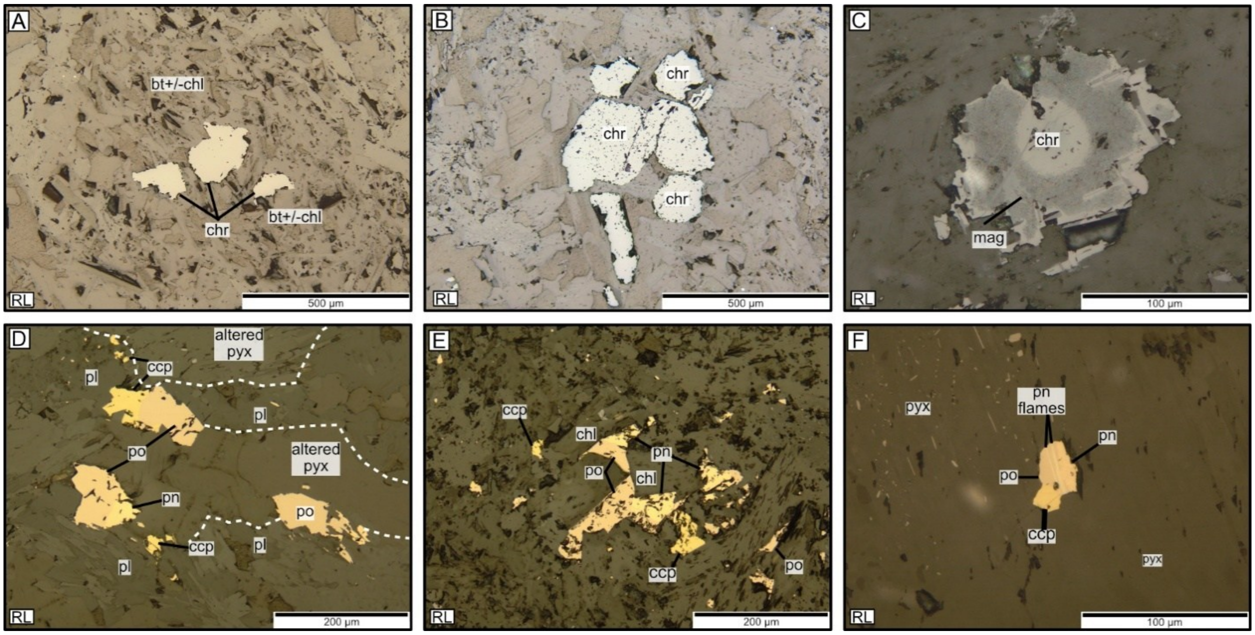

Figure 4.11: Photomicrographs showing opaque mineral characteristics in marginal zone rocks. (A) Fine-grained chromite cluster mantled by aggregates of platy biotite and chlorite. (B) Magnetite-replaced fine-grained chromite with preserved equant morphology. (C) Concentric zoning from a chromite core to a magnetite rim. (D–E) Cluster of disseminated, blocky, polysulfide aggregates interstitial to pyroxene and plagioclase. (F) Very fine-grained polysulfide grain composed of pyrrhotite, chalcopyrite, and pentlandite. Pentlandite occurs as both granular and exsolution within pyrrhotite. Abbreviations: RL – reflected light, chr – chromite, mag – magnetite, po – pyrrhotite, ccp – chalcopyrite, pn – pentlandite, bt – biotite, chl – chlorite, pl – plagioclase, pyx – pyroxene.

Alteration

Alteration assemblage minerals extensively overprint the primary silicate phases within the marginal zone. In all samples, clinopyroxene alteration is pseudomorphic, characterized by mixtures of actinolite-tremolite, hornblende, chlorite, biotite, and, more rarely, titanite (Figs. 4.12A–B). Alteration of clinopyroxene can be categorized into two styles. The first is characterized by alteration to felted or parallel, acicular aggregates of actinolite-tremolite intermingled with chlorite and biotite (Fig. 4.12A). The second is characterized by mottled to patchy, brown to greenish hornblende that contains Fe-oxide exsolution (Figs. 4.12A–C). These two alteration styles typically occur together. In the single gabbronorite sample, orthopyroxene is altered along the grain boundaries to fine- and very fine-grained aggregates of anthophyllite, talc and chlorite, giving the orthopyroxene a distinct brownish colour and grainy appearance (Figs. 4.12D–E). In comparison to clinopyroxene, alteration of plagioclase is typically minor, with a distinct alteration assemblage. Alteration of plagioclase is characterized by patchy, very fine-grained aggregates of platy sericite, often accompanied by minor amounts of epidote (Fig. 4.12F). More rarely, alteration of plagioclase is accompanied by pseudomorphic replacement by chlorite (Fig. 4.12F).

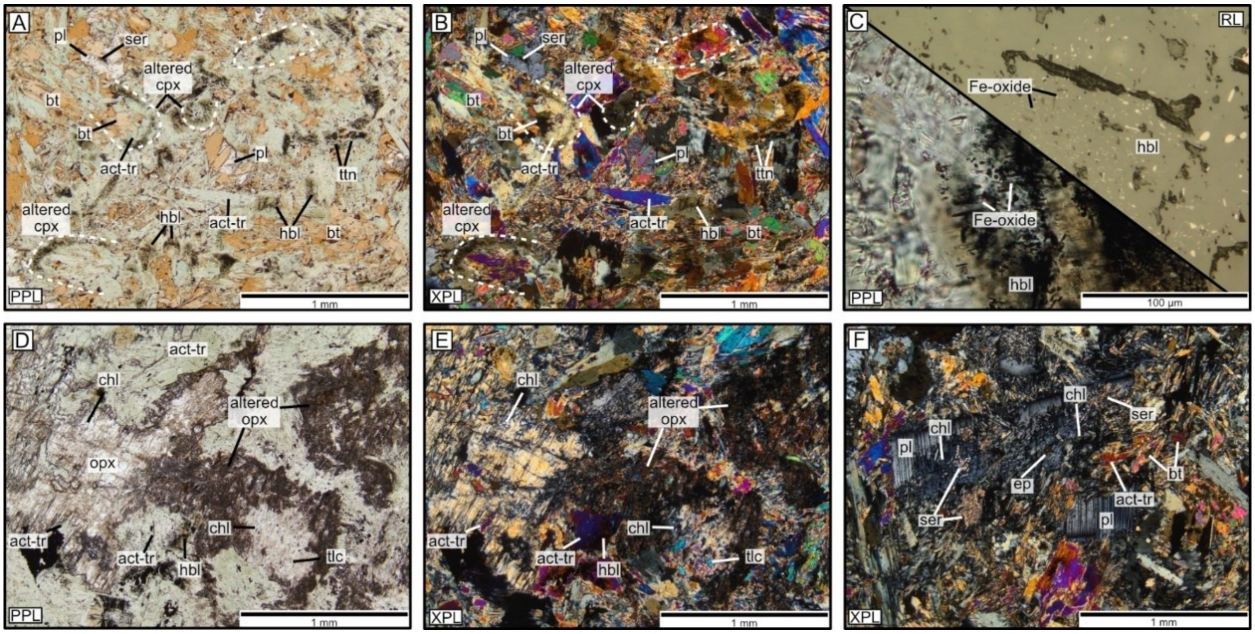

Figure 4.12: Photomicrographs showing alteration characteristics in marginal zone rocks. (A–B) Clinopyroxene alteration to felty actinolite-tremolite aggregates with patchy hornblende, accompanied by biotite and minor titanite. (C) Fine-grained, patchy hornblende alteration with very fine-grained Fe-oxide exsolution. (D-E) Orthopyroxene alteration to chlorite, anthophyllite, and talc along the grain boundaries. Note the contrasting alteration of clinopyroxene to actinolite-tremolite. (F) Plagioclase overprinted by chlorite, sericite and epidote as well as actinolite-tremolite from the surrounding clinopyroxene. Abbreviations: PPL – plane-polarized light, XPL – cross-polarized light, pl – plagioclase, cpx – clinopyroxene, opx – orthopyroxene, act-tr – actinolite-tremolite, hbl – hornblende, ser – sericite, bt – biotite, ep – epidote, chl – chlorite, ttn – titanite.

An important feature of the marginal zone samples is the presence of biotite, which makes up to 20 % of the modal abundance and is typically associated with the clinopyroxene alteration assemblage. Although most alteration assemblage minerals and their textures are tied to individual primary phases, clinopyroxene alteration often overprints grain boundaries of plagioclase (Fig. 4.12F).

4.2.1.2 Inner Zone

Twenty-two homogenous thin sections and two pucks consisting of ultramafic cumulate rocks were examined from the inner zone of the intrusion. Most of the samples were collected from the northern portion of the intrusion, with seven coming from the Upper Embayment and 12 from the Lower Embayment. Additionally, three samples were collected from the southern portion of the intrusion, within the Upper Embayment. Inner zone samples consist of seven pyroxenite and 15 peridotite samples, which include six mineralized peridotite samples containing ≥15 % sulfides modal abundance.

The inner zone rocks commonly preserve primary igneous phases and their textures better than the marginal zone rocks. The mineralogical variability across the three examined domains (Table 4.1) is controlled by variable proportions of accumulated sulfides and olivine with variable proportions of intercumulus silicate minerals that predominantly consists of orthopyroxene and clinopyroxene, with minor amounts of chromite, hornblende, biotite and plagioclase. Fourteen of the examined inner zone samples contained sufficient amounts of unaltered olivine, orthopyroxene, and clinopyroxene to be classified using the IUGS classification scheme (Fig. 4.13; Le Maitre, 2002). Excluding the presence of intercumulus sulfides, the mineralized peridotite samples range in composition from harzburgite to wehrlite, plotting near the dunite field. The modal mineral proportions of the barren peridotite domain can be classified as predominantly lherzolite, whereas the pyroxenite domain, typically much more intensely altered, ranges from websterite to olivine websterite. Although the IUGS classification provides lithogical constraints, alteration introduces subjectivity in the modal abundance estimates, potentially broadening the compositional range of the samples. For clarity, the section below will retain the domain subdivisions.

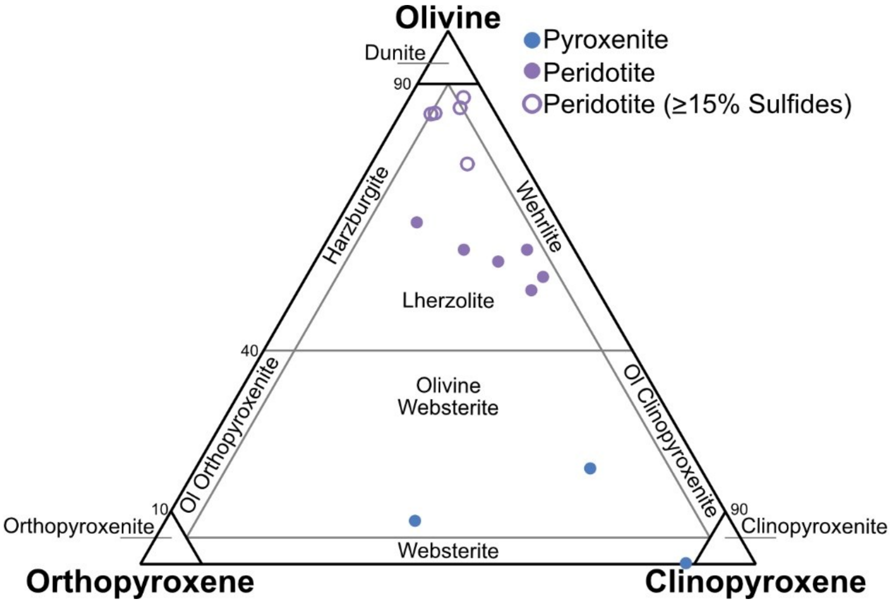

Figure 4.13: IUGS ternary classification diagram of ultramafic rocks from the inner zone of the Eagle's Nest intrusion.

General Characteristics

The pyroxenite domain can be characterized as the transitional zone between the inner zone ultramafic cumulate rocks and the marginal zone mafic intrusive rocks. The pyroxenite interval is typically narrow and is characterized by the highest alteration intensity out of the inner zone samples, making the interpretations of primary textures and igneous phases challenging. Most of the pyroxenite domain rocks consist of an intensely altered assemblage, interpreted to have comprised intercumulus pyroxene with smaller amounts of cumulus olivine (5–40 %) and minor amounts of plagioclase prior to alteration. Together, these rocks are interpreted to consist of fine- to medium-grained, orthocumulate, olivine-bearing pyroxenite (Fig. 4.14A). Recognition of olivine, outside of altered pyroxene (where it occurs as chadacrysts) was not possible. As a result, it is possible that they contained higher proportions of olivine prior to alteration, in which case some samples may be classified as feldspathic peridotite.

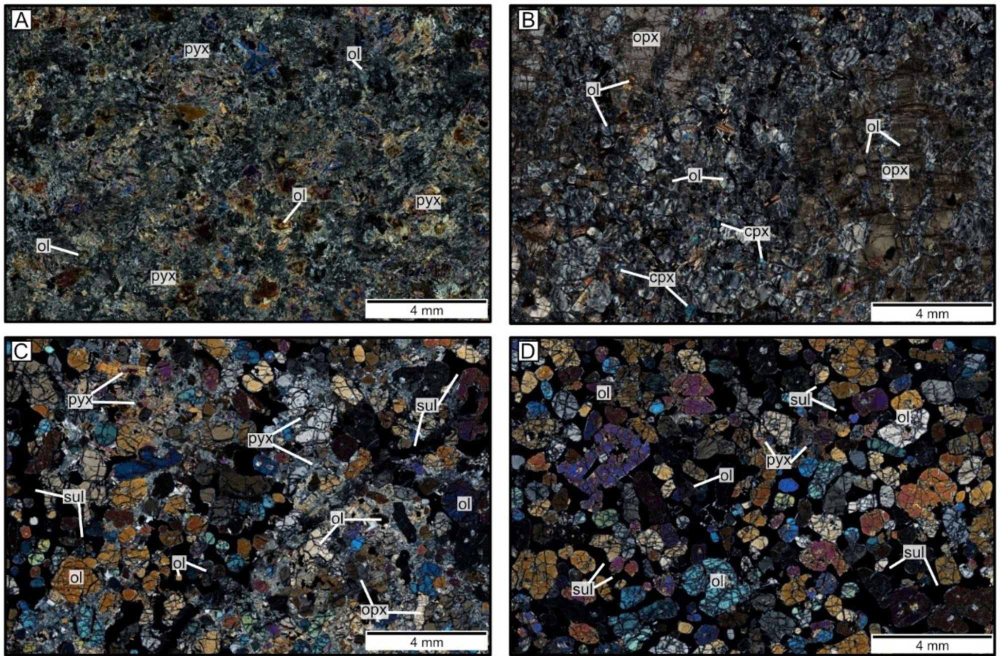

Figure 4.14: Photomicrographs in transmitted, cross-polarized light showing the lithological and textural variability within the inner zone rocks. (A) Intensely altered, orthocumulate olivine-bearing pyroxenite. (B) Orthocumulate, poikilitic barren peridotite. (C) Heteradcumulate, mineralized peridotite forming patchy to poikilitic net-textured sulfide mineralization. (D) Mesocumulate, mineralized peridotite forming continuous net-textured sulfide mineralization. Abbreviations: pyx – pyroxene, ol – olivine, cpx – clinopyroxene, opx – orthopyroxene, sul – sulfides.

The transition from the pyroxenite into the barren peridotite is characterized by less intense alteration, decreasing abundance of intercumulus silicate minerals and increasing abundance of cumulus olivine. The barren peridotite is fine- to coarse-grained, orthocumulate peridotite composed of cumulus olivine (45–70 %) and variable amounts of intercumulus minerals, consisting of poikilitic orthopyroxene and intergranular clinopyroxene, with minor amounts of hornblende (Fig. 4.14B).

The transition from the barren peridotite into the mineralized peridotite is characterized by increasing amounts of interstitial sulfides, decreasing amounts of intercumulus silicate minerals, and approximately constant amounts of cumulus olivine (60–70 %). Excluding the effects of interstitial sulfides, these rocks are fine- to coarse-grained, comprising mesocumulate peridotite that locally transitions into orthocumulate to heteradcumulate peridotite. These transitions are largely controlled by the relative abundance of interstitial sulfide to intercumulus silicate minerals. In the mesocumulate peridotite, the intercumulus silicate minerals comprise up to 10 % of the modal abundance, forming continuous net-textured sulfide mineralization (Fig. 4.14D). In contrast, in the orthocumulate to heteradcumulate peridotite intercumulus silicate minerals comprise up to 25 % of the modal abundance, which forms discontinuous, patchy to poikilitic net-textured sulfide mineralization (Fig. 4.14C). In patchy to poikilitic net-textured samples, the intercumulus silicate minerals tend to be intensely altered to amphibole, chlorite, and talc aggregates containing relict remnants of pyroxene. Since the mineralized peridotite was the least altered domain out of the examined samples, minor amounts of intercumulus hornblende and biotite were identified.

Mineralogy

Olivine is the most abundant primary silicate phase within the mineralized and barren peridotite, and the second most abundant within the pyroxenite. Olivine is typically fine- to medium-grained, rarely coarse-grained (Fig. 4.15A), occurring as subhedral to anhedral primocrysts or chadacrysts enclosed by intercumulus silicate phases. In the barren domains, the grain size of olivine primocrysts is relatively uniform within individual samples, ranging in morphology from subhedral to rounded (rarely euhedral; Fig. 4.14A–B). However, olivine that occurs as chadacrysts (in barren and mineralized rocks) enclosed by either orthopyroxene or clinopyroxene is always anhedral and typically has a smaller grain size than the primocrysts within the same sample (Fig. 4.15B). In contrast to the barren ultramafic rocks, olivine primocrysts within individual samples of the mineralized peridotite display a wide range of grain sizes (fine- to coarse-grained) and morphologies (euhedral to amoeboidal; Fig. 4.15C). In the pyroxenite samples, unaltered olivine was not identified, with the exception of a single olivine websterite sample (EN23VS100), where it was the least altered phase. In other pyroxenite samples, the occurrence of olivine was recognized by the presence of pseudomorphed chadacrysts in altered pyroxene oikocrysts. In one pyroxenite sample (EN23VS068) olivine was not identified. Minor amounts of very fine-grained chromite inclusions were observed in unaltered olivine grains.

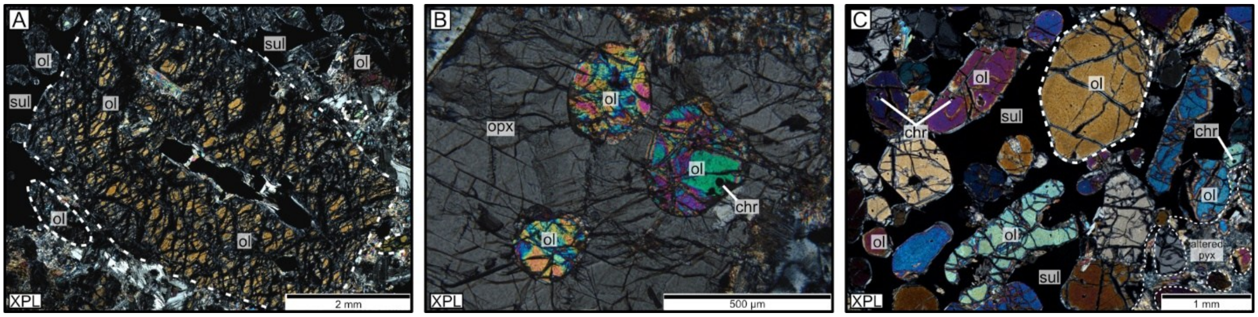

Figure 4.15: Photomicrographs showing olivine characteristics in inner zone rocks. (A) Coarse-grained, prismatic olivine, surrounded by finer in grain size olivine within a mineralized peridotite. (B) Fine-grained, anhedral olivine chadacrysts containing equant chromite inclusions mantled by an orthopyroxene oikocryst. (C) Variability of olivine grain size and morphology in a mineralized peridotite sample. Abbreviations: XPL – cross-polarized light, ol – olivine, sul – sulfides, pyx – pyroxene, opx – orthopyroxene, chr – chromite.

Pyroxene makes up the dominant intercumulus silicate phase in the inner zone lithologies. In the pyroxenite samples, pyroxene makes up 50–95 % of the modal mineralogy. In the pyroxenite samples, pyroxene is intensely altered, recognized by its locally preserved prismatic shape and an amphibole-chlorite alteration assemblage, which is interpreted to have consisted of clinopyroxene prior to alteration. Orthopyroxene was identified in three samples comprising websterite and olivine websterite occurring as relict anhedral primocrysts and ellipsoidal poikilitic oikocrysts, respectively (Fig. 4.13).

Intercumulus pyroxene in the barren and mineralized peridotite makes up 10–55 % of the modal abundance and consists of orthopyroxene and clinopyroxene. In the barren peridotite, orthopyroxene is intercumulus, occurring predominantly as medium- to coarse-grained oikocrysts with a distinct ellipsoidal shape (Fig. 4.16A).

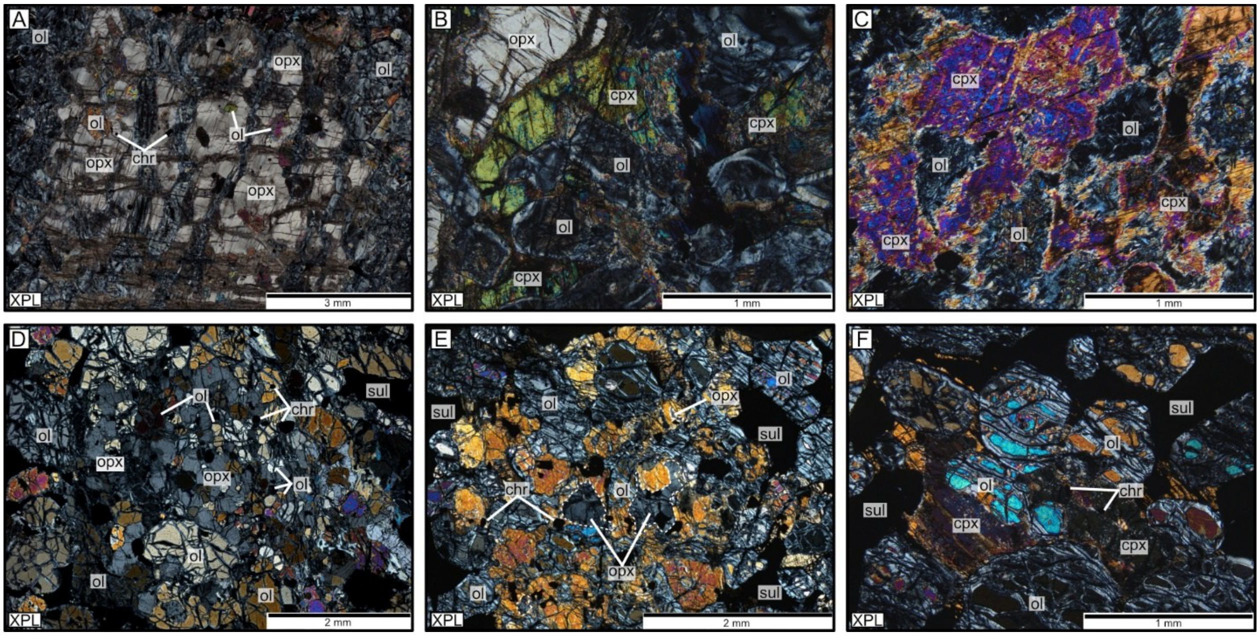

Figure 4.16: Photomicrographs showing pyroxene characteristics in inner zone rocks. (A–C) Barren peridotite. (A) Ellipsoidal orthopyroxene oikocryst enclosing olivine and chromite chadacrysts. (B) Anhedral clinopyroxene occurring intergranular to orthopyroxene and partially enclosing olivine chadacrysts. (C) Altered, anhedral clinopyroxene partially enclosing olivine chadacrysts. (D–F) Mineralized peridotite. (D) Ellipsoidal orthopyroxene oikocryst enclosing olivine and chromite chadacrysts. (E) Ellipsoidal clinopyroxene oikocryst enclosing anhedral orthopyroxene as well as olivine and chromite chadacrysts. (F) Intergranular clinopyroxene partially enclosing olivine chadacrysts. Abbreviations: XPL – cross-polarized light, opx – orthopyroxene, cpx – clinopyroxene, ol – olivine, chr – chromite, sul – sulfides.

Clinopyroxene occurs either in similar proportions or is more abundant than orthopyroxene, but it is typically smaller in grain size, ranging from fine- to medium-grained, and occurs as anhedral, intergranular grains to cumulus olivine and oikocrystic orthopyroxene (Fig. 4.16B), rarely forming poikilitic textures (Fig. 4.16C). In the mineralized peridotite, both orthopyroxene and clinopyroxene occur as either poikilitic, ellipsoidal oikocrysts (Figs. 4.16D–E) that are generally smaller in grain size than in the barren peridotite or they occur as anhedral intergranular grains (Fig. 4.16F). In the mineralized peridotite, a number of poikilitic clinopyroxene grains enclosed smaller, anhedral orthopyroxene (Fig. 4.16E). Across all examined lithologies, regardless of the domain, both clinopyroxene and orthopyroxene either partially or completely enclose olivine and chromite chadacrysts, forming poikilitic to intergranular textures.

Plagioclase (2–5 %) was identified as a minor phase in three pyroxenite samples. Plagioclase occurs as fine- to medium-grained, subhedral to euhedral tabular grains partially enclosed by altered pyroxene grains. In these samples, unaltered plagioclase was not identified. Its presence was recognized by its pseudomorphic alteration to chlorite, which preserved its primary morphology and textural relationship to pyroxene (Fig. 4.17A).

Hornblende (0.5–3 %) was identified as a minor phase in the barren and mineralized peridotite. Hornblende is fine- to medium-grained, anhedral to rarely subhedral, occurring as intergranular grains with weak brown to green pleochroism and a 56–124˚ cleavage (Fig. 4.17B). Larger hornblende grains were observed to partially mantle olivine primocrysts forming sub-poikilitic textures (Figs. 4.17B) and to mantle anhedral clinopyroxene grains (Fig. 4.17C), all of which display sharp grain contacts.

Biotite (<1 %) was identified as a minor phase in the mineralized peridotite. Biotite is very fine- to fine-grained, occurring as distinct lamellar grains interstitial to the silicate and sulfide phases (Figs. 4.17D–E). It rarely displays weak brownish pleochroism and is sometimes replaced by chlorite along cleavage planes.

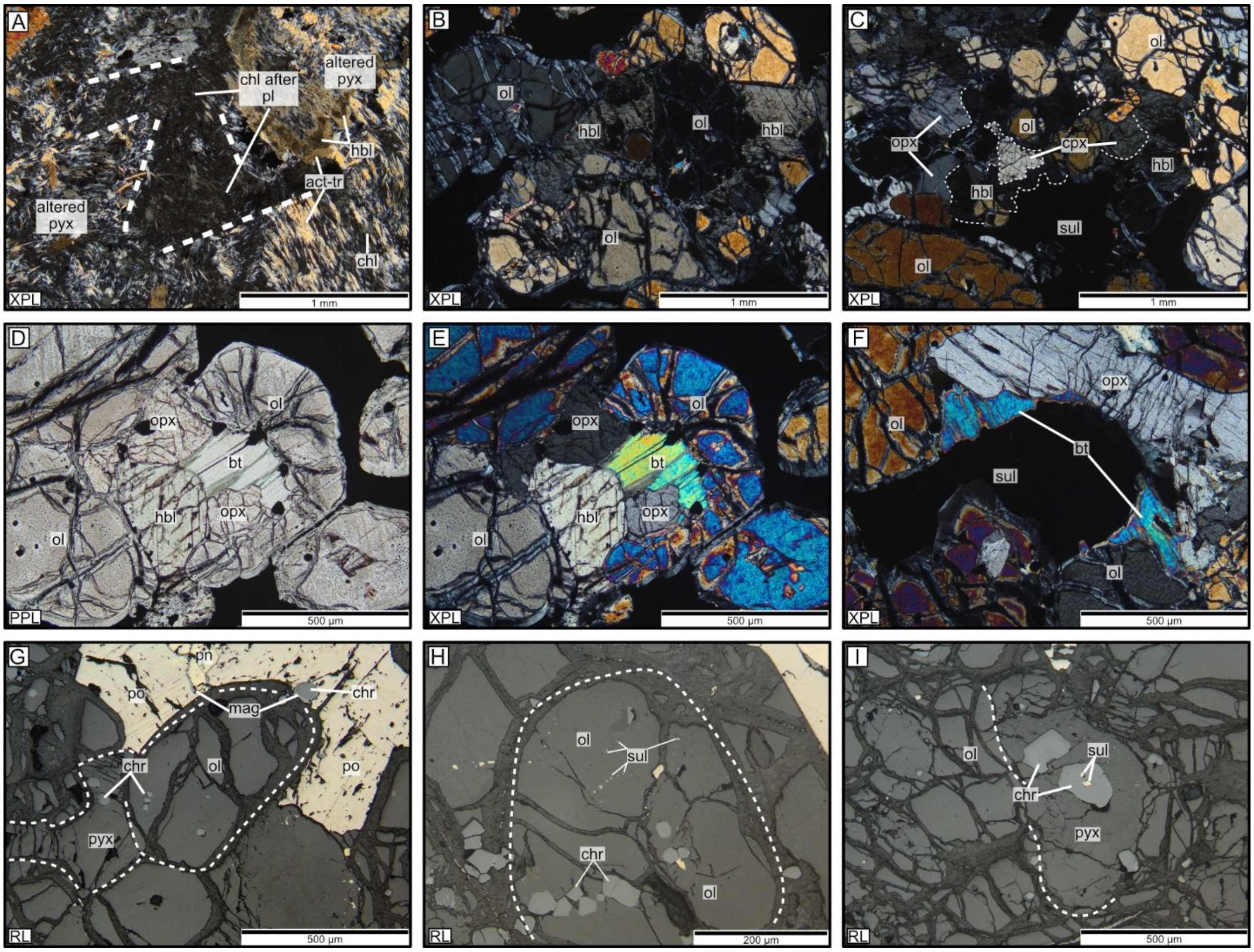

Figure 4.17: Photomicrographs showing minor phases in inner zone rocks. (A) Chlorite pseudomorphed plagioclase in an olivine pyroxenite. (B) Subhedral hornblende displaying 56–124˚ cleavage, forming sub-poikilitic texture. (C) Anhedral clinopyroxene sharply bound by hornblende, occurring intergranular to orthopyroxene. (D–E) Anhedral hornblende occurring intergranular to cumulus olivine and orthopyroxene, with platy, biotite occurring interstitial to silicate phases. (F) Platy biotite occurring interstitial to olivine, orthopyroxene and sulfide phases. (G) Equant, very fine- to fine-grained chromite occurring within olivine primocrysts, intergranular pyroxene and net textured sulfides. (H) Rounded, olivine primocryst containing equant chromite inclusions and very fine-grained, blebby, sulfide inclusion trails. (I) Equant, fine-grained chromite occurring within intercumulus pyroxene, containing very fine-grained sulfide inclusion. Abbreviations: PPL – plane-polarized light, XPL – cross-polarized light, pl – plagioclase, chl – chlorite, hbl – hornblende, bt – biotite, ol – olivine, opx – orthopyroxene, cpx – clinopyroxene, sul – sulfides.

Chromite (rarely up to 2 %) was observed across all inner zone domains, within every examined sample. Chromite is typically fine-grained, occurring as euhedral to subhedral, equant grains within intercumulus silicate phases and interstitial sulfides (Figs. 4.17G–I). Very fine-grained, equant chromite inclusions were often observed within olivine (Figs. 4.17G–H). Chromite grains were occasionally fractured, pitted, containing irregular grain boundaries, or they showed concentric zoning from a chromite core to a magnetite rim. Rarely, in the mineralized peridotite, chromite contained very fine-grained, blebby sulfide inclusions (Fig. 4.18I).

Mineralization

Sulfides were predominantly observed within the inner zone rocks, ranging from net-textured (15–25 %; Fig. 4.18A) to disseminated (1–10 %; Fig. 4.18B). Most of the mineralization was observed within the mineralized peridotite domain. In the mineralized peridotite, pyrrhotite is the dominant sulfide phase, occurring as massive anhedral grains. In contrast, pentlandite is present as fine-grained, anhedral to subhedral granular grains that are partially to completely mantled by pyrrhotite, on rare occasions occurring as exsolution within pyrrhotite. Chalcopyrite occurs as fine-grained anhedral grains within the interstitial sulfides (Fig. 4.18A). In the mineralized domain, sulfides are interstitial to silicate phases (and chromite) forming continuous interconnected networks in mesocumulate rocks (Fig. 4.18A). In mineralized samples, where the abundance of intercumulus silicate minerals increases to form heteradcumulate rocks, the abundance of sulfides decreases, forming patchy to poikilitic net-textured mineralization (Fig. 4.14C). In weakly mineralized samples, sulfides occur as disseminated, isolated polysulfide aggregates (Fig. 4.18B). Within more intensely altered samples, magnetite either surrounds the sulfide phases, or it occurs along fractures within the sulfides, sometimes accompanied by chlorite, giving the sulfides a blocky and/or irregular appearance (Figs. 4.18B–C).

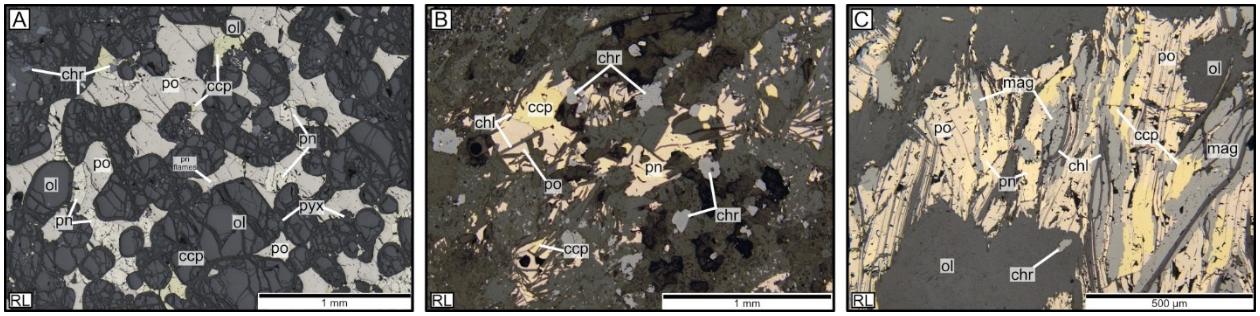

Figure 4.18: Photomicrographs showing textures of sulfide mineralization in inner zone rocks. (A) Interstitial, net-textured sulfides composed of massive, anhedral pyrrhotite, granular pentlandite, and anhedral chalcopyrite in mineralized peridotite. (B) Interstitial, blocky, disseminated sulfides composed of pyrrhotite, pentlandite and chalcopyrite, occurring interstitial to alteration phases with disseminated chromite in a pyroxenite. (C) Strongly fractured, net-textured sulfides in an intensely altered mineralized peridotite with magnetite and serpentine occurring along fractures. Abbreviations: RL – reflected light, po – pyrrhotite, pn – pentlandite, ccp – chalcopyrite, mag – magnetite, chr – chromite, ol – olivine, pyx – pyroxene.

Alteration

Alteration intensity within the inner zone is highly variable, predominantly comprising a hydrous ferromagnesian assemblage. Samples from the pyroxenite domain were the most intensely altered, only preserving minor relict textures and generally containing completely altered primary phase (Fig. 4.14A). By contrast, samples from the mineralized peridotite comprising mesocumulate rocks were the least altered, typically perfectly preserving igneous textures and nearly all primary magmatic phases (Fig. 4.14D). Across the examined samples, olivine alteration ranges from intense to weak. Typically, in completely altered olivine grains, alteration is characterized by complete pseudomorphic replacement by serpentine (Fig. 4.19A), whereas in weakly altered olivine, serpentine occurs along its fractures and grain boundaries forming alligator mesh texture (Fig. 4.19B). Rarely, olivine is altered to a greenish-yellow clay mineral along the grain boundaries, or it is pseudomorphed by talc in the pyroxenite domain. As with olivine, the alteration intensity of intercumulus silicate phases is variable. Alteration of orthopyroxene is typically composed of very fine-grained aggregates comprising mixtures of anthophyllite, talc, and chlorite. Completely altered grains have a distinct grainy appearance with a brownish colour preserving the typical ellipsoidal morphology of the grain, whereas weakly altered grains alter along grain boundaries and fractures (Figs. 4.19C–D).

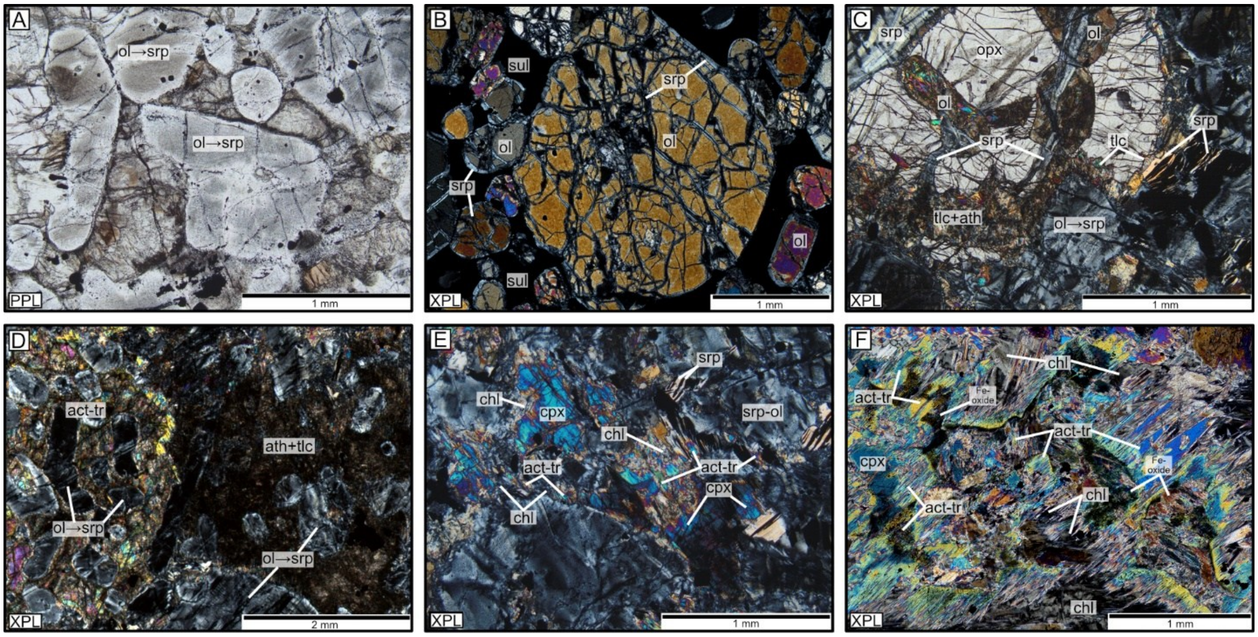

Figure 4.19: Photomicrographs showing alteration characteristics in inner zone rocks. (A) Serpentine pseudomorphed olivine. (B) Weakly altered olivine to serpentine forming alligator mesh texture. (C) Orthopyroxene oikocryst altering to talc and anthophyllite along the grain boundary. (D) Orthopyroxene oikocryst completely altered to anthophyllite and talc, and intergranular clinopyroxene altering to actinolite-tremolite. (E) Intergranular clinopyroxene altering to fine-grained aggregates of actinolite-tremolite, and chlorite. (F) Clinopyroxene outlined by Fe-oxide inclusions giving it a sponge-like appearance and is pseudomorphed by massive, felty actinolite-tremolite with minor chlorite. Abbreviations: PPL – plane-polarized light, XPL – cross-polarized light, ol – olivine, opx – orthopyroxene, cpx – clinopyroxene, act – actinolite, tr – tremolite, hbd – hornblende, ath – anthophyllite, srp – serpentine, chl – chlorite, tlc – talc, mag – magnetite.

In contrast to orthopyroxene, clinopyroxene tends to be overprinted by coarser-grained, felty to parallel aggregates of actinolite-tremolite sometimes accompanied by serpentine that either completely replace the primary grains (Figs. 4.19D–E) or partially alter along their grain boundaries (Fig. 4.19F). In a small number of samples, accessory amounts of rutile were observed, and carbonate alteration was seen in a single pyroxenite sample.

4.2.2 Dikes

Seventeen samples of dikes were examined using transmitted and reflected light microscopy. During petrographic examination, coupled with whole rock geochemistry, the sample suite was subdivided into three groups consisting of unrelated, massive Eagle's Nest type, and deformed Eagle's Nest type dikes. Six of the examined samples consist of massive, non-foliated, mafic intrusive rocks that display characteristics similar to the marginal zone of the Eagle's Nest intrusion. In contrast, the seven deformed Eagle's Nest type dikes have a well-developed metamorphic fabric with mineralogical and textural characteristics that suggest a mafic protolith metamorphosed under greenschist facies conditions.

Upon petrographic and whole rock geochemical analysis, four thin sections (EN23VS004, EN23VS008, EN23VS105, and EN23VS135) were deemed to be of rocks unrelated to the Eagle's Nest intrusion and are therefore excluded from the detailed petrographic discussion. These samples exhibit variable characteristics: EN23VS004 is a massive, fine-grained biotite-rich mafic dike (~80 % biotite, ~10 % calcite); EN23VS008 is a massive, medium-grained hornblende-rich intrusive dike; EN23VS105 is a metamorphosed mafic dike comprising coarse, variably oriented, acicular actinolite-tremolite and a biotite-carbonate groundmass; and EN23VS135 is a pyroxene-plagioclase-olivine ultramafic cumulate rock from Winisk River.

4.2.1.1 Massive Eagle's Nest Type Dikes

General Characteristics

Massive Eagle's Nest type dikes generally exhibit mineralogical, textural, and alteration characteristics similar to the gabbroic rocks along the marginal zone of the Eagle's Nest intrusion. As with the marginal zone of the Eagle's Nest intrusion, identification and characterization of the samples is based on visual interpretation of relict primary textures and mineralogy. Due to the lack of unaltered phases, none of the samples could be classified using the IUGS classification scheme. The samples contain variable proportions of clinopyroxene and plagioclase, implying a gabbroic composition. In one sample, altered olivine was identified. As with the marginal zone rocks, the presence of other phases prior to alteration cannot be completely ruled out.

Samples of massive Eagle's Nest type dikes have roughly similar proportions of clinopyroxene to plagioclase, as well as similar grain sizes and textures. In all the samples, clinopyroxene tends to be the most abundant mineral prior to alteration, whereas plagioclase is present in smaller proportions. Therefore, these rocks can be classified as melagabbro. Massive Eagle's Nest type dikes are fine- to medium-grained, generally equigranular within individual samples and rarely form sub-ophitic textures (Figs. 4.20A–B).

Mineralogy, Alteration, and Mineralization

Pyroxene is interpreted to be the most abundant silicate phase prior to alteration, comprising 50–80 % of the modal abundance. Based on its rare prismatic to equant shape, intergranular occurrence, and the alteration assemblage, it is interpreted to have been clinopyroxene. Clinopyroxene is fine- to medium-grained, occurring intergranular to plagioclase, locally partially mantling euhedral plagioclase to form sub-ophitic textures (Figs. 4.20A–C). Nearly all of the clinopyroxene is altered to felty aggregates of actinolite-tremolite, lesser amounts of chlorite (Fig. 4.20C), and rarely patchy anhedral hornblende (Figs. 4.20D–F). In the majority of the samples, accessory amounts of fine-grained titanite aggregates accompany the pyroxene alteration assemblage. Unlike the marginal zone rocks, biotite alteration is absent, except for a single sample where it makes up 10 % of the modal abundance (EN23VS054).

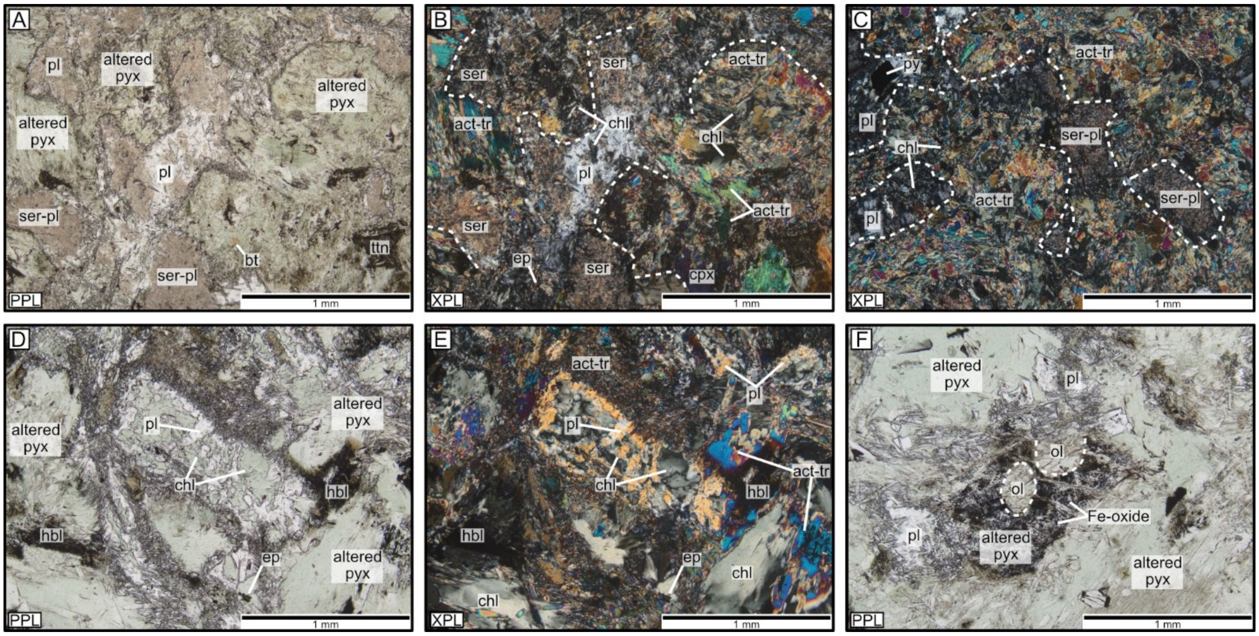

Figure 4.20: Photomicrographs showing primary and alteration characteristics of massive Eagle's Nest type dikes. (A–C) Fine-grained melagabbro, composed of equigranular plagioclase, and intergranular pyroxene prior to alteration, preserving sub-ophitic texture. Pyroxene is altered to aggregates of acicular actinolite-tremolite and chlorite. Plagioclase altering to sericite and minor epidote. (D–E) Medium-grained, olivine-bearing gabbro with tabular plagioclase, and intergranular pyroxene. Plagioclase is replaced by chlorite and pyroxene is altering to mixtures of hornblende, actinolite-tremolite, and chlorite. (F) Fine-grained, relict, rounded olivine chadacrysts in a medium-grained, altered, sponge-like textured pyroxene containing Fe-oxide inclusions in an olivine bearing gabbro. Abbreviations: PPL – plane-polarized light, XPL – cross-polarized light, pl – plagioclase, pyx – pyroxene, cpx – clinopyroxene, ol – olivine, ser – sericite, act – actinolite, tr – tremolite, hbl – hornblende, chl – chlorite, ep – epidote, py – pyrite.

Plagioclase is the least altered and second most abundant silicate phase, interpreted to make up 20–50 % of the modal abundance prior to alteration. Typically, plagioclase is similar in grain size to clinopyroxene, ranging between fine- to medium-grained, occurring as subhedral to euhedral grains with a tabular morphology (Figs. 4.20D–E). Plagioclase is generally altered by patchy, very fine-grained sericite aggregates that are accompanied by smaller amounts of epidote (Figs. 4.20B–C). More rarely, plagioclase was pseudomorphically replaced by chlorite (Figs. 4.20D–E).

Olivine was identified in a single sample (EN23VS108) where it is interpreted to make up 2–5 % of the modal abundance prior to alteration, therefore this sample can be classified as olivine-bearing melagabbro. In this sample, olivine was fine-grained, occurring as anhedral rounded grains within altered pyroxene oikocrysts (Fig. 4.20F). Similar to rocks from the pyroxenite domain in the Eagle's Nest intrusion, olivine was not identified outside the pyroxene and was only identified by its relict shape. Olivine was completely overprinted by pyroxene alteration assemblage minerals.

Oxide minerals mostly occur in trace amounts but can make up to 1 % of the modal mineralogy, consisting of very fine- to fine-grained, subhedral to anhedral chromite, typically completely replaced by magnetite. Trace amounts of very fine-grained ilmenite were observed in association with titanite.

Sulfides occur mostly in trace amounts but can reach up to 2 % of the modal abundance. In most samples, pyrite is the dominant sulfide phase, it is often cubic, with very fine- to fine-grain size, disseminated across the entirety of the sample (Fig. 4.20C). In three samples, smaller amounts of blocky chalcopyrite, pyrrhotite, and rarely pentlandite grains were identified.

4.2.1.2 Metamorphosed Eagle's Nest Type Dikes

General Characteristics

Deformed Eagle's Nest type dikes exhibit a well-developed metamorphic fabric and mineral assemblage indicative of a mafic protolith metamorphosed under greenschist facies metamorphic conditions. The dominant mineral assemblage is characterized by actinolite, sericite (after plagioclase), plagioclase, chlorite, epidote, and titanite, which are accompanied by accessory amounts of opaque minerals. Less commonly, the rocks contain small amounts of carbonate, quartz, biotite, and rutile. Due to the metamorphic nature of these samples, they could not be classified using the IUGS classification scheme.

Mineralogy, Alteration, and Mineralization

Actinolite is a major constituent, making up 30–70 % of the modal abundance, occurring as fine-grained, mostly idioblastic grains with bladed to acicular habits that are typically well-aligned, defining the metamorphic fabric (Figs. 4.21A–C). Chlorite makes up 2–40 % of the modal abundance, occurring as fine-grained, platy, subidioblastic grains that follow the foliation with actinolite. In some samples, chlorite forms more massive, lenticular lenses elongated parallel to foliation (Figs. 4.21D–E) or creates distinct compositional banding (Fig. 4.21F).

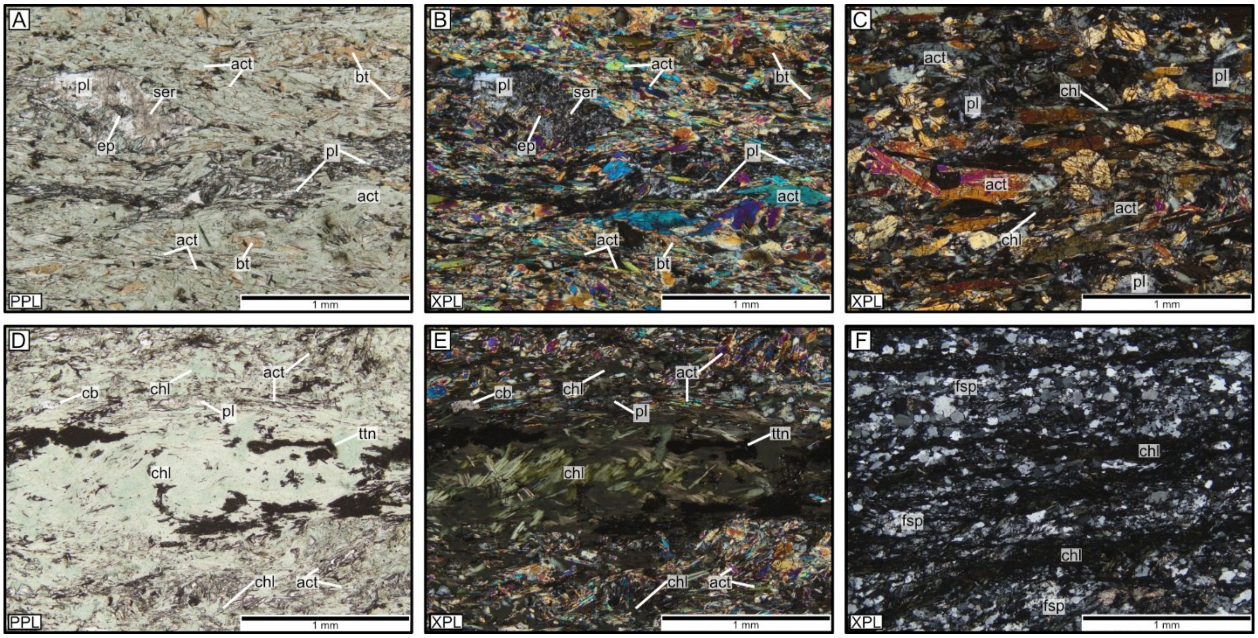

Figure 4.21: Photomicrographs showing textural and mineralogical characteristics in deformed Eagle's Nest type dikes. (A–B) Fine-grained, foliated dike composed of actinolite, plagioclase porphyroclasts, and biotite. (C) Medium-grained, foliated dike with chlorite and actinolite defining foliation and containing plagioclase porphyroclasts. (D–E) Massive lenticular chlorite lens with string-like titanite lenses, actinolite and minor plagioclase. (F) Chlorite bands separating lenses of granular feldspar and quartz. Abbreviations: PPL – plane-polarized light, XPL – cross-polarized light, pl – plagioclase, fsp – feldspar, act – actinolite, chl – chlorite, ser – sericite, bt – biotite, ep – epidote, cb – carbonate, ttn – titanite.

Plagioclase makes up 3–15 % of the modal abundance and is typically observed as strongly sericitized subidioblastic porphyroclasts (Figs. 4.21A–B). Epidote is present in smaller amounts (≤2 %) occurring as xenoblastic, very fine-grained aggregates that are often associated with alteration of plagioclase. Titanite is present as very fine-grained xenoblastic grain aggregates that form clusters or string-like lenses oriented parallel to foliation.

In addition to the main metamorphic assemblage, certain samples contain small amounts of minor minerals. These include fine-grained granoblastic quartz (~6 %, EN23VS003), fine-grained carbonate minerals partially replacing plagioclase (<5 %, EN23VS003 & EN23VS028; Fig. 4.21E), very fine- to fine-grained platy biotite (~3 %, EN23VS039 & EN23VS099), and trace amounts of very fine-grained rutile aggregates (EN23VS021).

Opaque minerals make up mostly trace amounts but can range up to 1 %. Idioblastic, equant, fine-grained chromite was identified in a single sample (EN23VS099). Sulfides occur as disseminated grains of fine-grained, idioblastic pyrite, and xenoblastic chalcopyrite.

4.3 Whole Rock Geochemistry

Whole rock geochemical data was obtained for samples from the Eagle’s Nest intrusion, the wall rock tonalite, and dikes possibly related to the intrusion. The number of samples analyzed for major and trace elements is significantly larger than the number of examined thin sections. Consequently, the geochemical characterization of these samples may overlap and not align perfectly with field-based nomenclature. As a result, the subsequent sections are organized based on similarities in intrusion lithologies and dikes determined in hand sample, modified based on petrographic examination where possible. Reporting of geochemical results is focused on characterizing the geochemical signatures of Eagle’s Nest intrusion lithologies. Which coupled with drill core and petrographic observations of sampled dikes, were used to identify genetically related, Eagle’s Nest type dikes. Raw geochemical data that was obtained during this study is reported in Appendix C.

Given the observed presence of metamorphism, alteration, and/or mineralization in most of the examined samples, whole rock geochemical data should be interpreted with caution, as it may not necessarily represent primary igneous signatures. To minimize the influence of post-magmatic processes and mineralization, all obtained geochemical data were recalculated on a volatile-free basis, and mineralized samples were additionally recalculated on a sulfide-free basis (Section 3.3.1). Due to the absence of thin sections for the majority of the analyzed samples, mineralized samples were characterized based on sulfur content. Specifically, samples containing more than 1 wt% sulfur were characterized as mineralized. In these samples, the geochemical signatures of the silicate and oxide components may be masked by the presence of sulfides. Therefore, the Fe and Ni content of the sulfide component within these samples was considered and removed from the whole rock geochemical composition (Fig. 4.22).

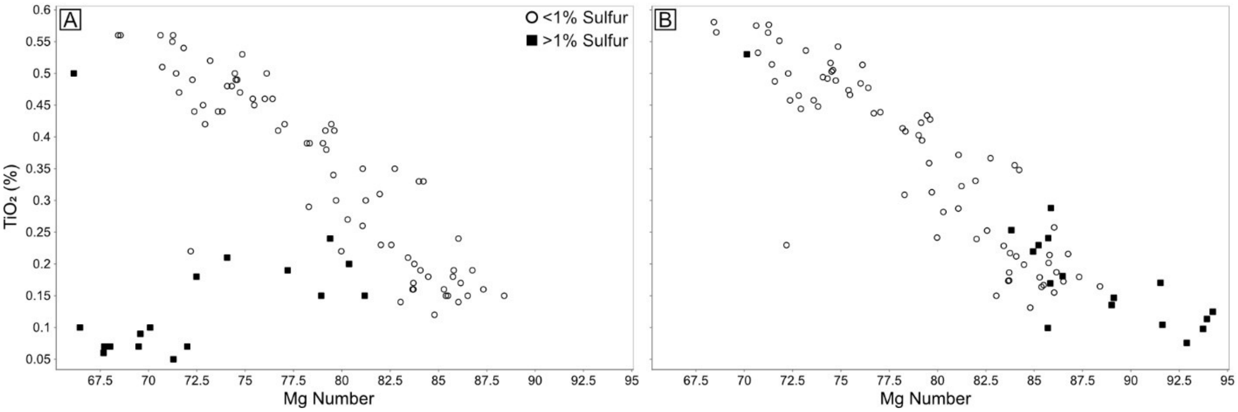

Figure 4.22: Bivariate diagrams of TiO_2 plotted against Mg number (100*Mg/(Mg+Fe)) of intrusion samples. (A) Uncorrected whole rock geochemical data. (B) Volatile-free (all samples) and sulfide-free (samples containing >1 wt% sulfur) renormalized whole rock geochemical data.

4.3.1 Eagle's Nest Intrusion

4.3.1.1 Major Elements

To evaluate the composition of rocks from the Eagle's Nest intrusion, major and minor element data were plotted on bivariate plots against MgO (Fig. 4.23). Samples from the Eagle's Nest intrusion display negative correlation for SiO_2, Al_2O_3, and CaO concentrations, while Ni and Cr have a positive correlation with increasing MgO contents. The marginal zone gabbroic rocks are characterized by overall higher median (M_d) values of SiO_2 (M_d=50.43 wt%), Al_2O_3 (M_d=10.44 wt%), CaO (M_d=7.88 wt%), and TiO_2 (M_d=0.49 wt%), and lower MgO (M_d=15.93 wt%), Ni (M_d=673 ppm) and Cr (M_d=1887 ppm; Figs. 4.23 & 4.24). In contrast, the peridotite samples from the inner zone of the intrusion are characterized by lowest concentrations of SiO_2 (M_d=44.58 wt%), Al_2O_3 (M_d=4.01 wt%), CaO (M_d=2.01 wt%), and TiO_2 (M_d=0.17 wt%), and higher concentration of MgO (M_d=37.10 wt%) and Ni (M_d=1868 ppm; Figs. 4.23 & 4.24). Samples classified as pyroxenites display compositions intermediate to the marginal zone gabbro and inner zone mineralized and barren peridotite samples.

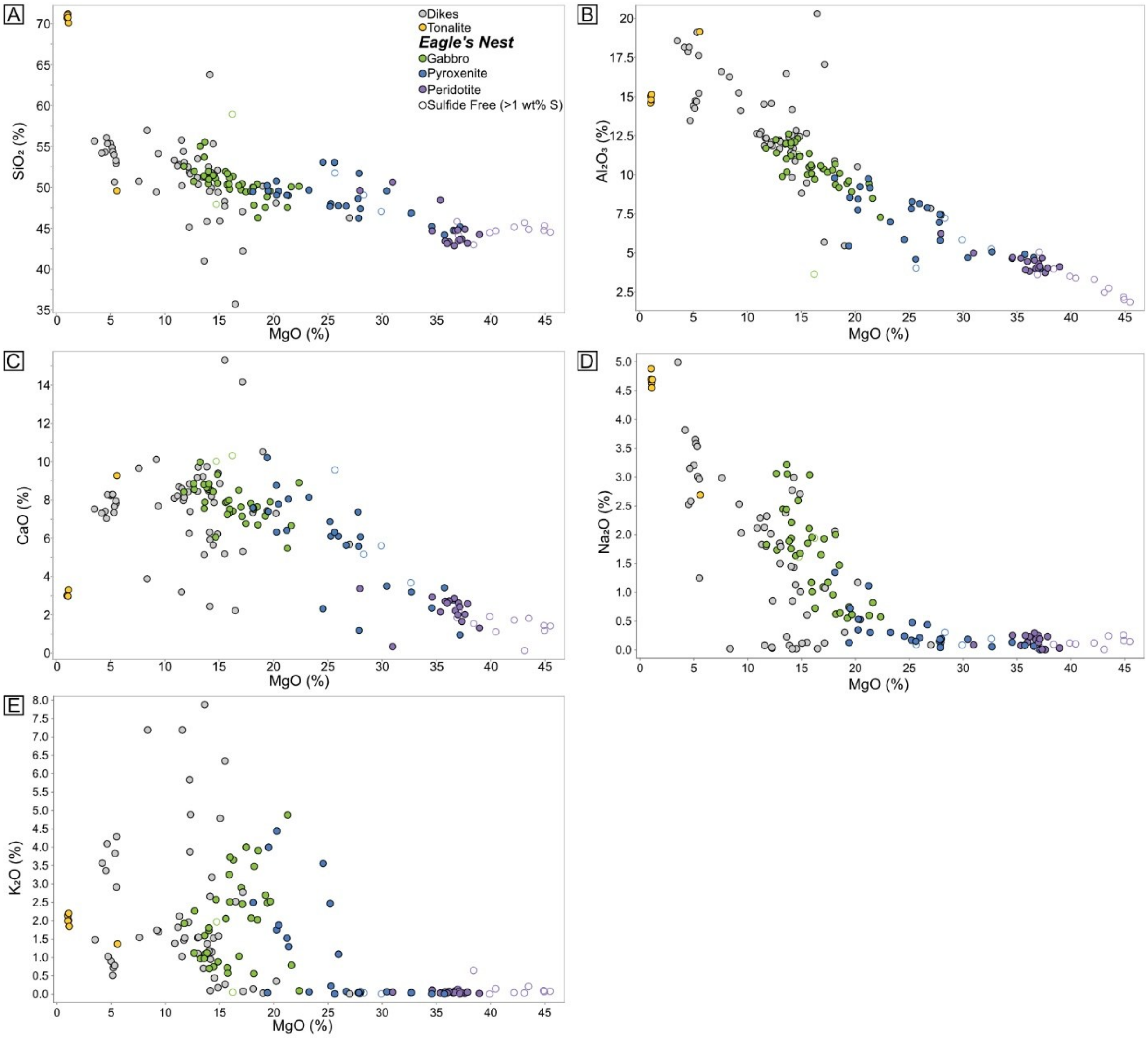

Figure 4.23: Bivariate diagrams displaying major element variations in wt% of samples from the Eagle's Nest intrusion plotted against MgO. (A) SiO_2, (B) Al_2O_3, (C) CaO, (D) Na_2O and (E) K_2O.

In Figure 4.23D–E, alkali contents display a bimodal distribution. The bimodal distribution is characterized by ultramafic cumulate rocks defining a consistent linear trend with consistently low concentrations of alkali contents, whereas the gabbro and a number of pyroxenite samples exhibit a scattered pattern with highly variable concentrations (Figs. 4.23D–E). With the exception of several pyroxenite samples, the ultramafic cumulate rocks from the inner zone are characterized by a coherent linear trend with low concentrations of Na_2O and

K_2O. In contrast, the marginal zone rocks define a rather coherent, negative sloping trend defined by increasing amounts of Na_2O with decreasing MgO. The concentration of K_2O in the marginal zone rocks is significantly more elevated, as with Na_2O, but it does not define a linear trend, rather displays a scattered distribution (Figs. 4.23D–E).

Minor elements within the Eagle's Nest intrusion define coherent linear trends with increasing contents of MgO. The Ni concentrations within the Eagle's Nest intrusion define a consistent, positively sloping, linear trend which defines increasing abundance of Ni with increasing contents of MgO (Fig. 4.24A). Similarly, Cr concentrations increase from the marginal zone gabbroic rocks, towards the ultramafic cumulate rocks of the Eagle's Nest intrusion. This is with the exception of a number of samples comprising sulfide-corrected, mineralized peridotite (Fig. 4.24B).

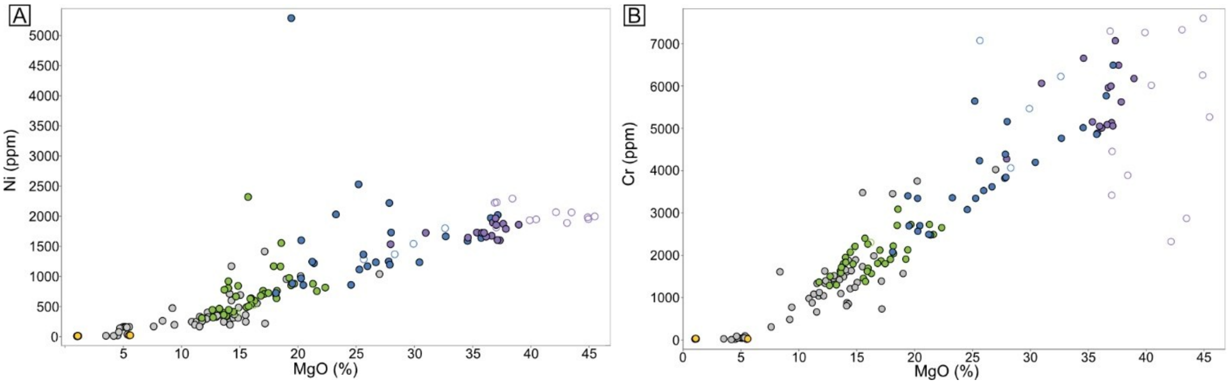

Figure 4.24: Bivariate diagrams of minor elements in ppm of samples from the Eagle's Nest intrusion plotted against MgO. (A) Ni (with Ni in sulfide component subtracted from mineralized samples containing ≥1 wt% sulfur), and (B) Cr (after sulfide correction and renormalization).

4.3.1.2 Trace Elements

Samples of the Eagle's Nest lithologies were plotted on primitive mantle normalized spider diagrams (Fig. 4.25). Trace element patterns of intrusion samples exhibit trends consistent with major element observations, with marginal zone gabbro having the highest concentrations of trace elements relative to the primitive mantle. Overall, intrusion samples are characterized by variably enriched light rare earth elements (LREE) patterns, with $La/Sm_{(n)}$ ranging from 0.84–4.39 (M_d=1.97 in the gabbro, M_d=1.65 in the pyroxenite, M_d=2.15 in the peridotite). Heavy rare earth elements (HREE) in the Eagle's Nest intrusion display more consistent, slightly fractionated patterns, with $Gd/Yb_{(n)}$ ranging from 0.66–1.76 (M_d=1.16 in the gabbro, M_d=1.19 in the pyroxenite and, M_d=1.15 in the peridotite).

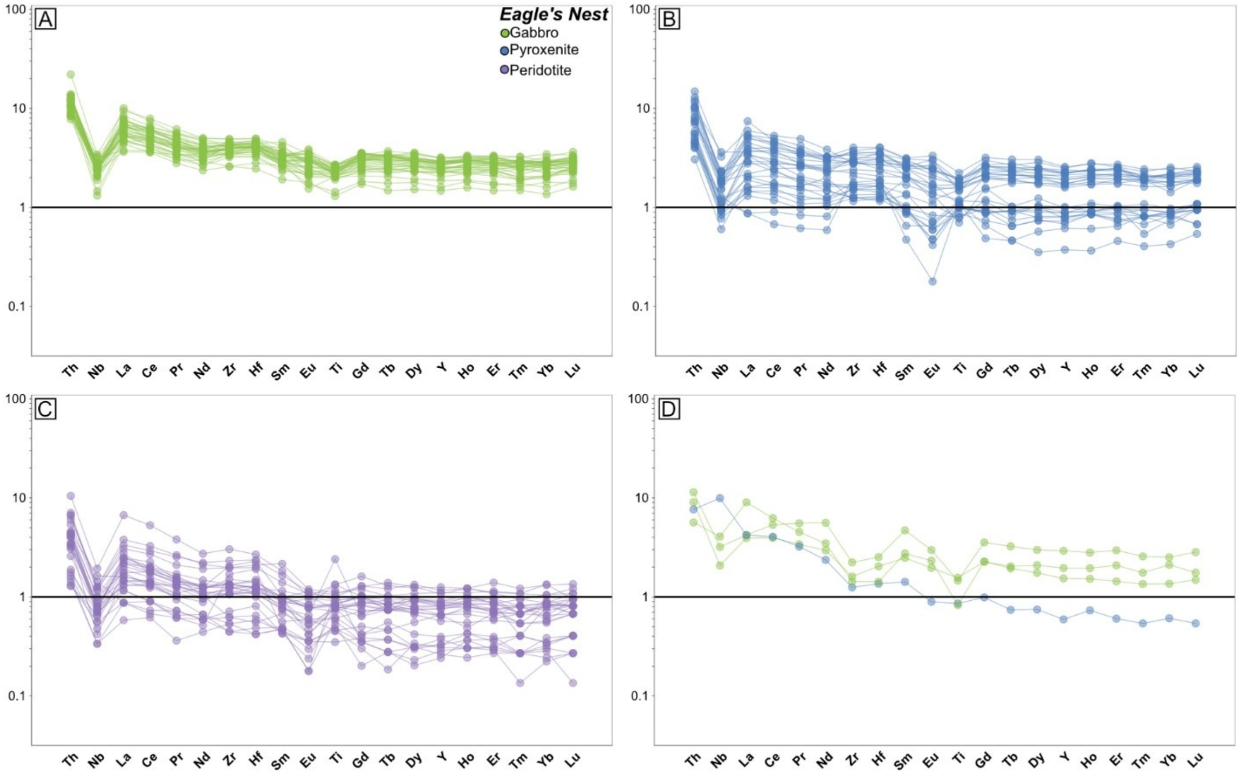

Figure 4.25: Primitive mantle normalized trace element diagrams of representative samples from the intrusion comprising (A) gabbro, (B) pyroxenite, (C) peridotite, and (D) anomalous intrusion samples. Sample values normalized to primitive mantle values of Sun and McDonough (1989).

Intrusion samples are further characterized by the enrichment of incompatible, large ion lithophile elements (LILE) relative to high field strength elements (HFSE) with pronounced negative Nb anomalies in all of the samples and variable but mostly negative Ti anomalies (Figs. 4.25A–C). The Nb/Nb* ratio, ranges from 0.20–0.64, with a median of 0.30 in the marginal zone gabbro, 0.32 in the inner zone pyroxenite and 0.30 in the inner zone peridotite. The Ti/Ti* ratio, range from 0.52–4.10, with a median of 0.80 in the gabbro, 0.81 in the pyroxenite, and 0.98 in the peridotite. More positive Ti anomalies occur in a small number of pyroxenite and peridotite samples, predominantly within the strongly mineralized samples. Most of the samples are characterized by positive Zr-Hf anomalies, with Zr/Zr* ranging from 0.59 to 3.88 and a median of 1.17 in the gabbro, 1.14 in the pyroxenite, and 1.20 in the peridotite. The samples display variable Eu anomalies, with Eu/Eu* ranging from 0.37–1.17 with a median of 0.96 in the gabbro, 0.83 in the pyroxenite, and 0.81 in the peridotite. Samples displaying positive Ti anomalies weakly correlate with samples displaying the most pronounced negative Eu anomalies.

Four of the samples (EN23VS086, EN23VS087, EN23VS047, EN23VS050), comprising three gabbro and one pyroxenite sample, are characterized by anomalous trace element patterns (Fig. 4.25D). The anomalous gabbro samples show similarities to the main sample suite in their weakly fractionated HREE patterns, with $Gd/Yb_{(n)}$ of 1.07–1.68 and negative Ti anomalies (although more pronounced), with Ti/Ti* of 0.41–0.72. Their distinction arises by the presence of pronounced negative Zr-Hf anomalies (Zr/Zr* = 0.43–0.59) and more irregular LREE patterns ($La/Sm_{(n)}$ = 0.90–3.28) in addition to deviation towards higher amounts of SiO_2. Unlike the anomalous gabbro samples, the pyroxenite sample largely falls on the same major element trends of the intrusion. However, it is characterized by enriched LREE ($La/Sm_{(n)}$ = 2.97) and pronounced positive Nb anomaly (Nb/Nb* = 1.75). Although no thin sections were prepared for these samples, they were characterized by either intense shearing and/or pervasive chlorite, talc, carbonate and/or biotite alteration in drill core.

4.3.2 Dikes

4.3.2.1 Major Elements

The Eagle's Nest type dikes are characterized by similar major element characteristics to the marginal gabbroic rocks from the Eagle's Nest intrusion, although slightly more evolved compositions. Compared to the Eagle's Nest intrusion, the Eagle's Nest type dikes show more variable major element distributions characterized by higher values of SiO_2 (M_d= 51.97 wt%), Al_2O_3 (M_d=12.11 wt%), CaO (M_d=8.20 wt%), and alkali elements (M_d=3.18 wt%) alongside lower median concentrations of MgO (M_d=13.03 wt%), Cr (M_d=1320 ppm), and Ni (M_d=328 ppm; Fig. 4.26).

In addition to the main suite of Eagle's Nest type dikes, three subgroups of mafic dikes were extracted based on trace element patterns consisting of Ti enriched, Zr-Hf depleted, and anomalous dikes. The Ti enriched, Zr-Hf depleted, and anomalous dikes have similar concentrations of MgO to gabbroic rocks from the Eagle's Nest intrusion and samples identified as Eagle's Nest type dikes, ranging from 8.37 to 17.17 wt%. However, these samples have more variable contents of SiO_2 ranging from 35.70 to 63.78 wt% and alkali elements ranging from 0.12 to 8.12 wt% (Figs. 4.26A & D). They also deviate from the main trend defined by Eagle's Nest intrusion rocks, displaying higher concentrations of Al_2O_3 (M_d=14.53 wt%) and lower concentrations of CaO (M_d=5.16 wt%; Figs. 4.26B–C).

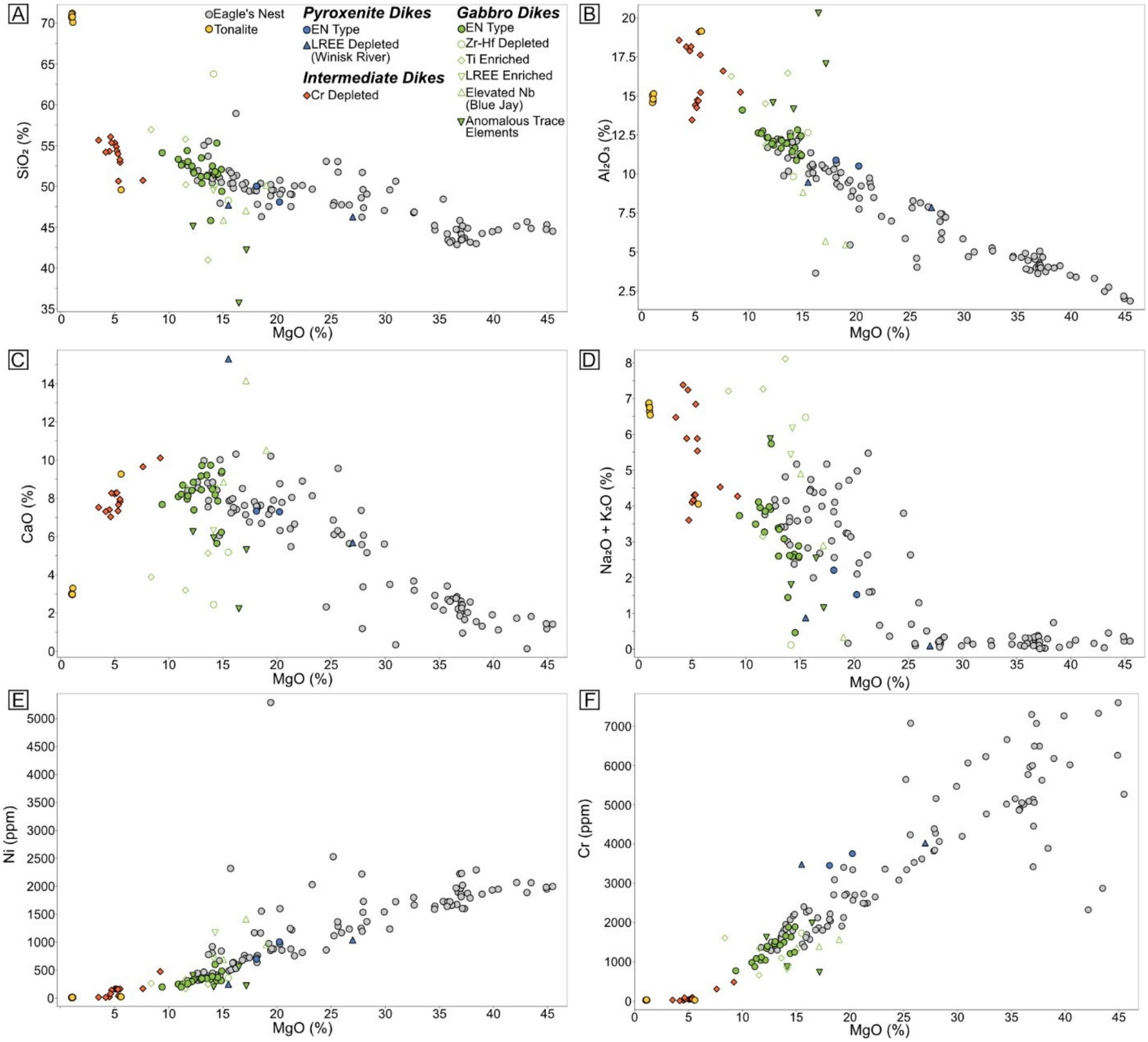

Figure 4.26: Bivariate diagrams displaying major and minor element variations of dike samples plotted against MgO. (A) SiO_2, (B) Al_2O_3, (C) CaO, (D) combined alkalis (Na_2O and K_2O), (E) Ni, and (F) Cr.

4.3.2.2 Trace Elements

The Eagle's Nest type dikes are characterized by enriched LREE with $La/Sm_{(n)}$ ranging from 1.28–4.01 and have flat to weakly fractionated HREE patterns with $Gd/Yb_{(n)}$ ranging from 0.77–1.41. Eagle's Nest type dikes are enriched in LILE relative to HFSE and are characterized by a well-defined negative Nb anomalies with Nb/Nb* between 0.23–0.82 (M_d=0.34), predominantly weak negative Ti anomalies with a median Ti/Ti* of 0.85, and slight positive Zr-

Hf anomalies with a median Zr/Zr* of 1.22. Two anomalous, more intensely altered samples largely follow similar patterns to those of rocks classified as Eagle's Nest type dikes. However, one sample displays anomalously low concentration of La, while the other lacks a pronounced Nb anomaly.

Distinct trace element patterns are displayed by gabbroic rocks that have similar concentrations of MgO to Eagle's Nest type dikes in the Ti-enriched and Zr-Hf depleted rocks (Fig. 4.27B). The Ti-enriched rocks consist of six samples, two of which display anomalous and highly irregular trace element patterns.

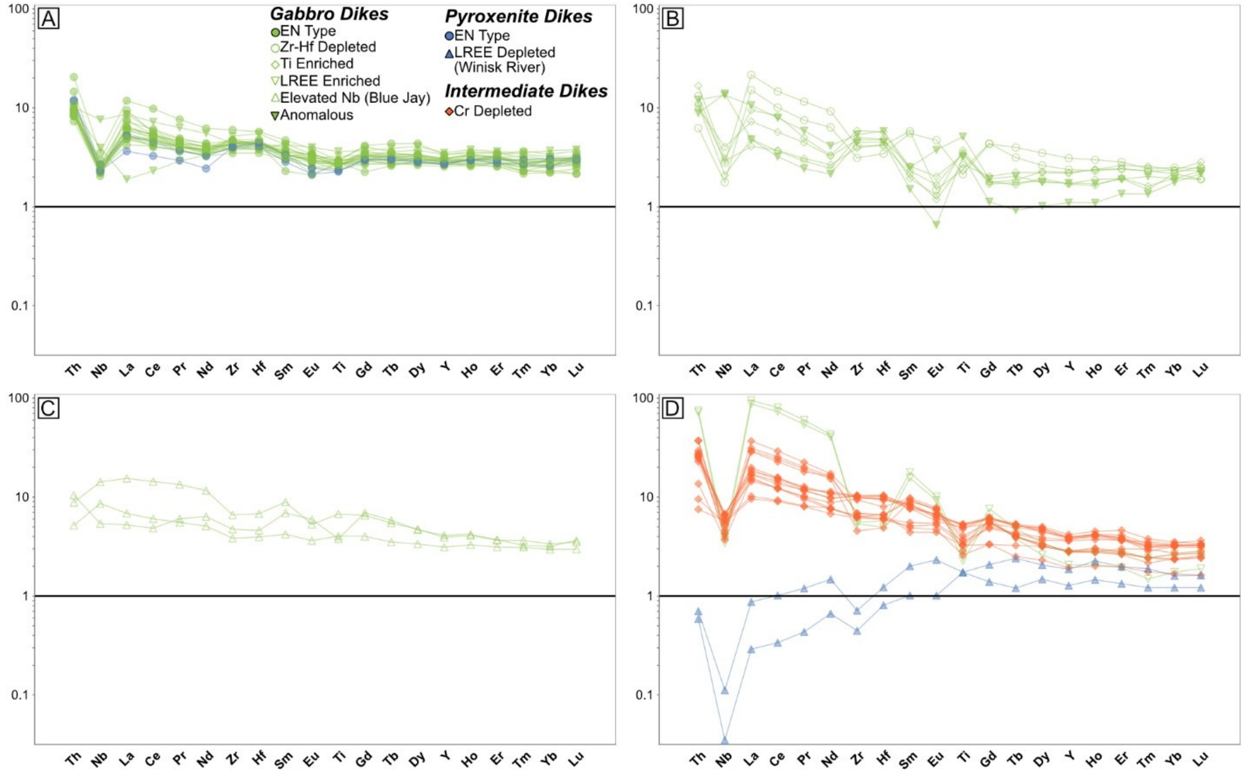

Figure 4.27: Primitive mantle normalized trace element diagrams of dikes collected in this study (A) Eagle's Nest type dikes (EN type), (B) Zr-Hf depleted and Ti enriched dikes, (C) Nb enriched (Blue Jay), and (D) unrelated LREE enriched, LREE depleted and Cr depleted dikes. Sample values normalized to primitive mantle values of Sun and McDonough (1989).

The Ti-enriched samples are characterized by pronounced positive Ti anomalies, with Ti/Ti* between 1.27–3.00, and pronounced positive Zr-Hf anomalies, with Zr/Zr* between 1.64–2.48 (Fig. 4.27B). These are characterized by enriched LREE patterns with a median La/$Sm_{(n)}$ of 3.01, and enriched HREE pattern with a median Gd/Yb_n of 0.82. The two more intensely altered samples, displaying anomalous trace element patterns are characterized by the presence of a positive Nb anomaly and irregular patterns. Two samples make up the Zr-Hf depleted sample group. The Zr-Hf depleted samples are characterized by strongly enriched LREE, with a median La/Sm_n of 3.23, and weakly fractionated HREE, with a mean Gd/Yb_n of 1.87. A pronounced negative Nb anomaly, with a mean Nb/Nb* of 0.17 is also observed. Unlike the Eagle's Nest type dikes, these samples exhibit pronounced negative Zr-Hf anomalies with a mean Zr/Zr* of 0.54 (Fig. 4.27B).

The two pyroxenitic samples collected in proximity to the Blue Jay occurrence displaying similar geochemical patterns to the Eagle's Nest intrusion, three other samples display trace element patterns that deviate from Eagle's Nest type dikes. Two of these samples are characterized by coherent trace element patterns and a positive Nb anomaly, whereas the third sample shows a weak negative Nb anomaly (Fig. 4.27C). In addition, these three samples display highly enriched contents of TiO_2 (0.82–1.46 wt%) and depleted concentrations of Al_2O_3 (5.47–8.82 wt%) at a given amount of MgO in comparison to Eagle's Nest type dikes.

While the samples discussed above generally resemble the Eagle's Nest intrusion signatures, three sample groups displaying distinct trace element signatures were deemed to be unrelated to the Eagle's Nest intrusion. These can be categorized into LREE enriched gabbro dikes, LREE depleted pyroxenite dikes, and Cr depleted intermediate dikes (Fig. 4.27D). The

LREE enriched samples were collected along the contact between Eagle's Nest intrusion and the wall rock tonalite. These are characterized by strong enrichment of LREE with a mean La/Sm$_{(n)}$ of 5.47 and strongly fractionated HREE with a mean Gd/Yb$_{(n)}$ of 3.19 (Fig. 4.27D). The LREE depleted pyroxenitic dike samples were collected in vicinity to Winisk River assemblage at the northern edge of the MLGB. These are characterized by depleted LREE with a mean La/Sm$_{(n)}$ of 0.36 and relatively flat HREE with a mean Gd/Yb$_{(n)}$ of 1.22 (Fig. 4.27D). The Cr depleted dikes were mostly collected along the contact between the Eagle's Nest intrusion and wall rock tonalite. The Cr depleted dikes are characterized by depleted amounts of Cr (8–92 ppm), high concentrations of SiO_2 (50.64–56.01 wt%), Al_2O_3 (13.46–19.01 wt%), and low MgO (3.51–5.51 wt%; Figs. 4.26A–B). The Cr depleted dikes have more enriched LREE with La/Sm$_{(n)}$ between 1.88–3.76 and more fractionated HREE with Gd/Yb$_{(n)}$ between 1.22–2.42 compared to the weakly enriched LREE and relatively unfractionated HREE of the Eagle's Nest intrusion samples (Fig. 4.27D). Distinct trace element patterns coupled with major element deviation from the Eagle's Nest intrusion trends, as well as Cr depletion in some of the samples suggest that these lithologies are unrelated to the Koper Lake magmatism and the Eagle's Nest intrusion.

4.3.3 Wall Rock Tonalite

4.3.3.1 Major Elements

The host tonalite (n=5) collected distal to the intrusion have a well-defined range, characterized by high concentrations of SiO_2 (70.10–71.21 wt%), Al_2O_3 (14.57–15.13 wt%), CaO (2.96–3.30 wt%), and combined Na_2O and K_2O (6.54–6.88 wt%), but low concentrations of MgO (1.01–1.14 wt%; Fig. 4.26). A single sample collected at the contact of the intrusion displayed evidence of partial melting and recrystallization and is characterized by lower concentrations of SiO_2 (49.57 wt%) and combined Na_2O and K_2O (4.06 wt%) and higher concentrations of Al_2O_3 (19.15 wt%), and CaO (9.27 wt%) in contrast to the unaltered tonalite samples.

4.3.3.2 Trace Elements

Trace element patterns of the unaltered tonalite samples are characterized by strongly enriched light rare earth elements (LREE) patterns with $La/Sm_{(n)}$ values ranging from 6.16–7.57 (Fig. 4.28). Heavy rare earth elements (HREE) are moderately fractionated with $Gd/Yb_{(n)}$ ranging from 1.63–2.09. The unaltered tonalite is characterized by pronounced negative Nb and Ti anomalies with Nb/Nb* ranging between 0.13–0.18 and Ti/Ti* ranging between 0.46–0.62, slight positive Zr-Hf anomalies (Zr/Zr*=1.34–1.42). The partially melted tonalite collected near the hanging wall contact of the intrusion is characterized by less enriched LREE with a $La/Sm_{(n)}$ of 2.53 and slightly more fractionated HREE with $Gd/Yb_{(n)}$ of 2.23 (Fig. 4.28). In contrast to the unaltered tonalite samples, the partially melted tonalite has a slightly positive Ti anomaly with Ti/Ti* of 1.05 and pronounced negative Zr-Hf anomalies with Zr/Zr* of 0.36.

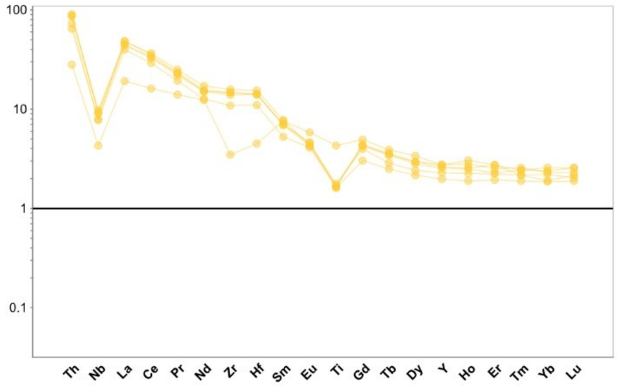

Figure 4.28: Primitive mantle normalized trace element diagram of wall rock tonalite. Sample values normalized to primitive mantle values of Sun and McDonough (1989).

4.4 Mineral Chemistry

Mineral chemistry data was obtained for major rock forming silicate and oxide minerals from the Eagle's Nest intrusion. Due to intense overprinting alteration in the majority of the examined thin sections, acquisition of mineral chemistry was limited to the least altered silicate phases in the ultramafic lithologies from the inner zone (Fig. 4.29). Unfortunately, intense alteration of the marginal zone rocks and Eagle's Nest type dikes did not allow for mineral chemistry analysis in these samples. Mineral chemistry data was obtained for olivine, pyroxene, amphibole, and oxide minerals. Complete mineral chemistry results acquired during this study are reported in Appendix D.

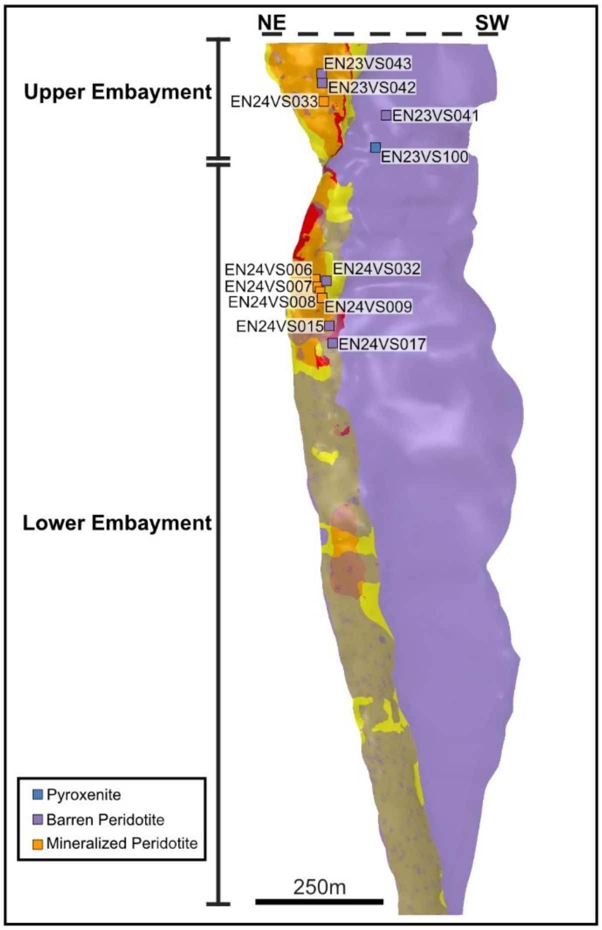

Figure 4.29: Distribution of samples in which mineral chemistry was obtained using EPMA.

4.4.1 Olivine

Five-hundred and sixteen analyses were obtained from 130 olivine grains across 12 samples were analyzed to evaluate the compositional variability across the Eagle's Nest intrusion and in an attempt to identify the most primitive olivine. In most of the examined thin sections, olivine was either strongly altered or completely absent, limiting the analysis to six samples from the barren peridotite, five from the mineralized peridotite, and one from an olivine websterite. No fresh olivine grains were identified in the examined mafic-ultramafic dikes and the marginal zone of the intrusion.

Generally, olivine composition varies from Mg_2SiO_4 to Fe_2SiO_4, with a complete solid solution between Mg^{2+} and Fe^{2+}. Classification of olivine is based on the proximity to end-member composition defined by the forsterite content (Fo=[Mg/(Mg+Fe)]*100 in mol%), which classifies the olivine as either fayalite ($Fo_{0–50}$) or forsterite ($Fo_{50–100}$).

In Figure 4.30, the mean forsterite content is plotted against the Ni content of the analyzed olivine grains. Olivine composition within the Eagle's Nest intrusion ranges from $Fo_{76.5}$ (n=5) to $Fo_{88.2}$ (n=5). The most primitive olivine ($Fo_{88.2}$) was found in a barren peridotite (EN23VS043) from the Upper Embayment, whereas the least primitive olivine ($Fo_{76.5}$) was identified in an olivine websterite (EN23VS100) from the more southern portion of the Eagle's Nest intrusion (Fig. 4.29). Across the analyzed lithologies, olivine from the barren peridotite samples displays the broadest range of forsterite contents. In barren peridotite samples from the Lower Embayment, olivine ranges between $Fo_{81.0}$ and $Fo_{87.0}$ and has a relatively narrow Ni content range between 1829 and 2529 ppm (Fig. 4.30). By contrast, olivine in barren peridotite samples from the Upper Embayment is characterized by higher Fo ($Fo_{85.3–88}$) and the highest Ni contents (2513–2890 ppm) across the sample suite.

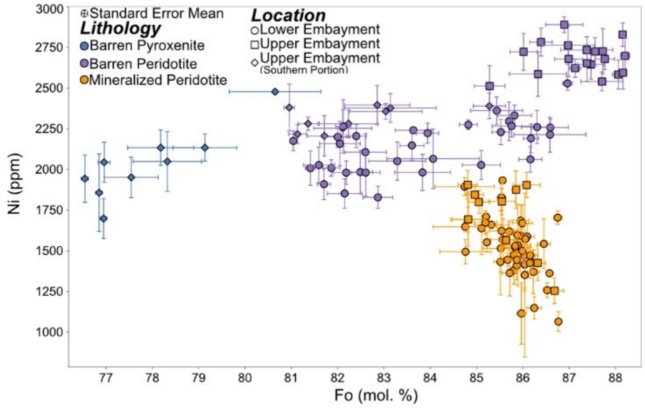

Figure 4.30: Bivariate plot of the forsterite (Fo in mol. %) content plotted against Ni content in olivine illustrating the mean compositions by analyzed grains. Error bars illustrate the standard error of the mean.

In comparison to the barren samples, which display a relatively wide range of forsterite contents, olivine from the mineralized peridotite is characterized by a narrow range of forsterite contents between $Fo_{84.7}$ and $Fo_{86.8}$ at lower Ni concentration between 1066 and 1933 ppm (Fig. 4.30). In the analyzed sample suite, the lowest forsterite contents were obtained in the olivine websterite, ranging between $Fo_{76.5}$ and $Fo_{80.6}$ and containing similar concentrations of Ni (1699 to 2478 ppm) to olivine from barren peridotite samples from the Lower Embayment (Fig. 4.30).

4.4.2 Pyroxene

Ninety-one analyses were obtained from 19 pyroxene grains across four thin sections were analyzed to evaluate the composition of pyroxene present within the Eagle's Nest intrusion. Pyroxene was analyzed in three mineralized peridotite samples (EN24VS006, EN24VS007, EN24VS008) from the Lower Embayment and one barren peridotite (EN23VS043) from the Upper Embayment (Fig. 4.29).

The pyroxene group consists of the orthorhombic (orthopyroxene) and monoclinic (clinopyroxene) minerals. Orthopyroxene is defined by a simple solid solution series between enstatite (En, $Mg_2Si_2O_6$) and ferrosilite (Fs, $Fe_2Si_2O_6$). Clinopyroxene has a more diverse range of compositions that are illustrated by the enstatite, ferrosilite, and wollastonite (Wo, $Ca_2Si_2O_6$) quadrilateral system. Pyroxene compositions are reported as the precent of end-member components Wo, En, and Fs (Fig. 4.31).

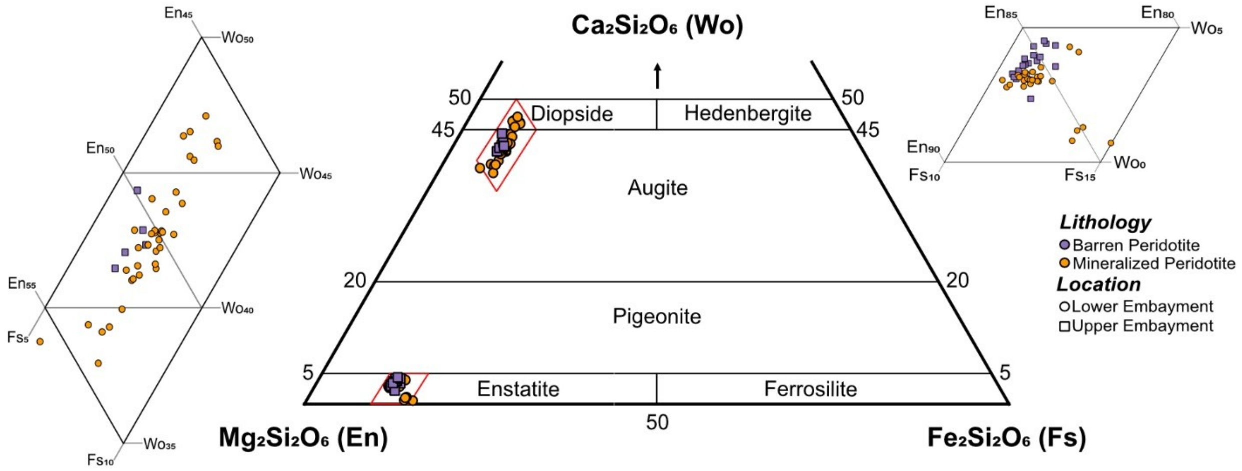

Figure 4.31: Pyroxene quadrilateral classification diagram of individual pyroxene analyses in this study. Modified after Morimoto (1988).

The pyroxene composition in the analyzed samples showed no significant variability, with overlapping compositions between the barren and mineralized peridotite samples. Pyroxene found within the Eagle's Nest intrusion consists of both orthopyroxene (enstatite) and clinopyroxene (augite-diopside; Fig. 4.31). The orthopyroxene has a Mg-rich composition ranging from $En_{83.7}$ to $En_{86.6}$. Most orthopyroxene analyses have a Mg# (Mg/(Mg+Fe)) ranging from 0.87 to 0.89. With the exception of a single grain in sample EN24VS007, which has a lower Mg# with an average of 0.86 and is also characterized by lower wollastonite content ($Wo_{0.72–1.31}$) compared to most of the analyses ($Wo_{2.37–4.18}$). The compositional difference of this grain is also highlighted by a lower Cr_2O_3 contents, with an average of 0.13 wt%, whereas the remainder of the analyses range from 0.47 to 0.82 wt% Cr_2O_3 (Fig. 4.32). The clinopyroxene composition ranges from $En_{46.3}$ to $En_{55.8}$, $Fs_{5.5}$ to $Fs_{7.8}$, and $Wo_{38.0}$ to $Wo_{47.1}$ (Fig. 4.31). Similar to orthopyroxene, clinopyroxene is characterized by a high Mg# between 0.86 and 0.91 but contains higher content of Cr_2O_3 that range from 0.78 to 1.27 wt% (Fig. 4.32).

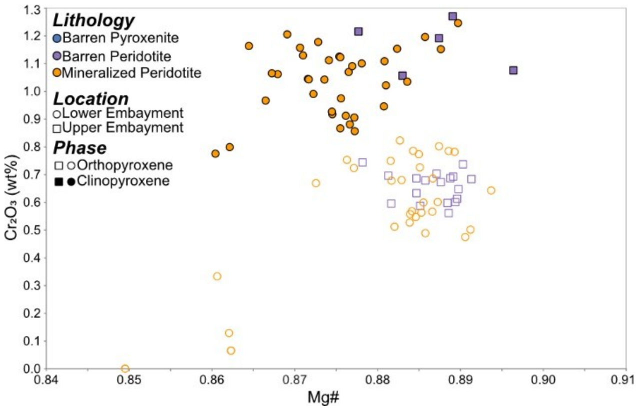

Figure 4.32: Bivariate plot of the Mg# plotted against the Cr_2O_3 content in individual pyroxene analyses.

4.4.2 Amphibole

Thirty-eight analyses were conducted on 14 amphibole grains from five thin sections, including both mineralized (EN24VS007 & EN24VS009) and barren (EN24VS015, EN24VS017, & EN24VS032) peridotite samples. The analyses of amphibole focused on the examination of minor intergranular hornblende identified in the mineralized and barren peridotite in order to evaluate the chemical composition of amphiboles that appear to have an igneous affinity.

Using the classification of Hawthorne et al. (2012), amphibole compositions were evaluated on the basis of ideal stoichiometry, using stoichiometric proportions to estimate the amount of Fe^{3+} and OH^- (Locock, 2014). The majority of the analyses belong to the calcium-subgroup, defined by $^{B}(Ca + \Sigma M^{2+})/\Sigma B \geq 0.75$ and $^{B}Ca/\Sigma B \geq {}^{B}\Sigma M^{2+}/\Sigma B$. These calcium amphiboles are primarily magnesio-hastingsite (n=17) or Ti-rich magnesio-hastingsite ($0.50 > {}^{C}Ti > 0.30$; n=18), which is the Fe^{3+} -rich ($Fe^{3+} > {}^{[6]}Al$) equivalent of paragsite (Fig. 4.33). Two other calcium amphiboles were also identified comprising one analysis of tremolite and one of edenite. A single analysis belongs to the magnesium-iron-manganese subgroup, defined by $^{B}(Ca + \Sigma M^{2+})/\Sigma B \geq 0.75$ and $^{B}\Sigma M^{2+}/\Sigma B > {}^{B}Ca/\Sigma B$, and was classified as cummingtonite.

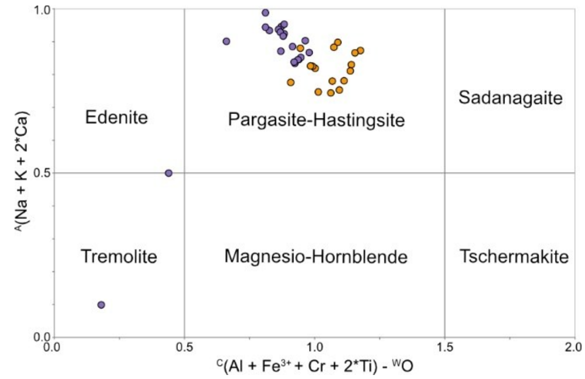

Figure 4.33: Classification diagram of the calcium subgroup amphiboles (Hawthorne et al., 2012).

4.4.4 Oxides

Seventy-nine analyses across 46 oxide mineral grains were obtained to determine the major element composition of chromite within the mineralized (EN24VS006, EN24VS007, & EN24VS008) and barren (EN23VS043) peridotite samples. A notable variability in surface texture, not observed during initial thin section examination, was noted during the EPMA analysis. These grains were divided into three groups consisting of fresh, unaltered grains (Group A), sieve-textured grains containing numerous inclusions (Group B), and gritty grains that displayed a “rough” surface (Group C; Fig. 4.34). The analyzed grains also exhibited variable degrees of alteration, illustrated by concentric zoning (Fig. 4.34A) and/or overgrowth by magnetite (Fig. 4.34B). The textural differences in Groups B and C may represent more intensely altered grains of Group A. For the most part, the analysis focused on the cores of grains belonging to Group A, and to a lesser extent, the rims and grains from Groups B and C.

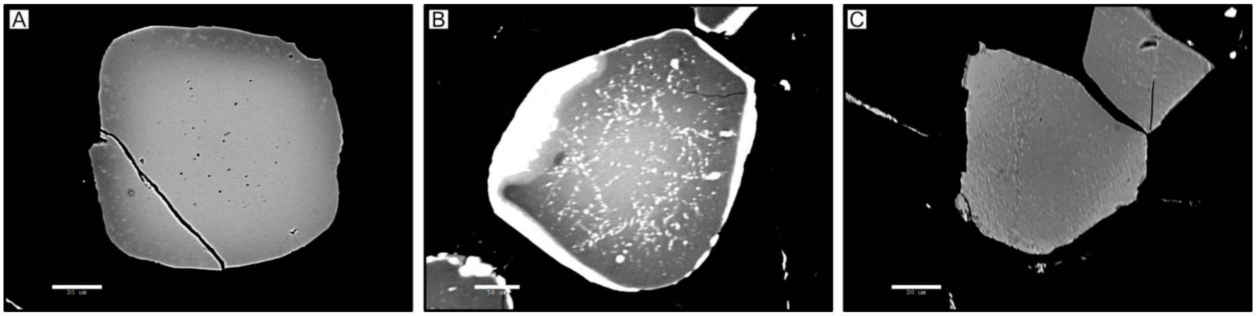

Figure 4.34: Backscatter electron images of spinel minerals illustrating surface texture variability. (A) Euhedral, unaltered grain of group A. (B) sieve textured grain illustrating the presence of inclusions in group B. (C) Subhedral grain illustrating the gritty texture of group C.

The analyzed oxide minerals belong to the spinel subgroup of the spinel supergroup. The mineral species of the spinel subgroup are determined by the dominant A- and B-cations in the general formula $A^{2+}B_2^{3+}O_4$ (Bosi et al., 2019).

During petrographic examination, all of the selected grains were characterized as chromite sometimes accompanied by magnetite along the rims. The EPMA analyses of these grains revealed that the oxides present in the samples do not strictly belong to the chromite species but rather display a range of compositions within the spinel subgroup series. The majority of the obtained analyses consist of chromite (n=56), but a smaller number of analyses were identified as magnesiochromite (n=5), hercynite (n=11), and magnetite (n=3). The compositional variability of the analyzed oxide minerals is illustrated on projection plots of the spinel prism (Fig. 4.35; Barnes and Roeder, 2001).

Distinct differences between oxide minerals analyzed in barren and mineralized peridotite are observed on the Fe^{3+}–Cr–Al ternary diagram. Oxides from the barren peridotite have a narrow compositional range, whereas those from the mineralized sample display a scattered distribution with broader compositional ranges (Fig. 4.35B). All oxide analyses from the barren peridotite belong to Group A, which consists of chromite (n=22) and a lesser amount magnesiochromite (n=4). Oxides from the barren peridotite are characterized by a narrow range in Cr# (Cr/(Cr+Al)), from 0.59 to 0.72, and $Fe^{3+}/(Fe^{3+}+Al+Cr)$ ratio, from 0.05 to 0.08 (Figs. 4.35C–D). However, they display a wide range in the Fe# ($Fe^{2+}/(Fe^{2+}+Mg)$) from 0.44 in the magnesiochromite to 0.84 in chromite.

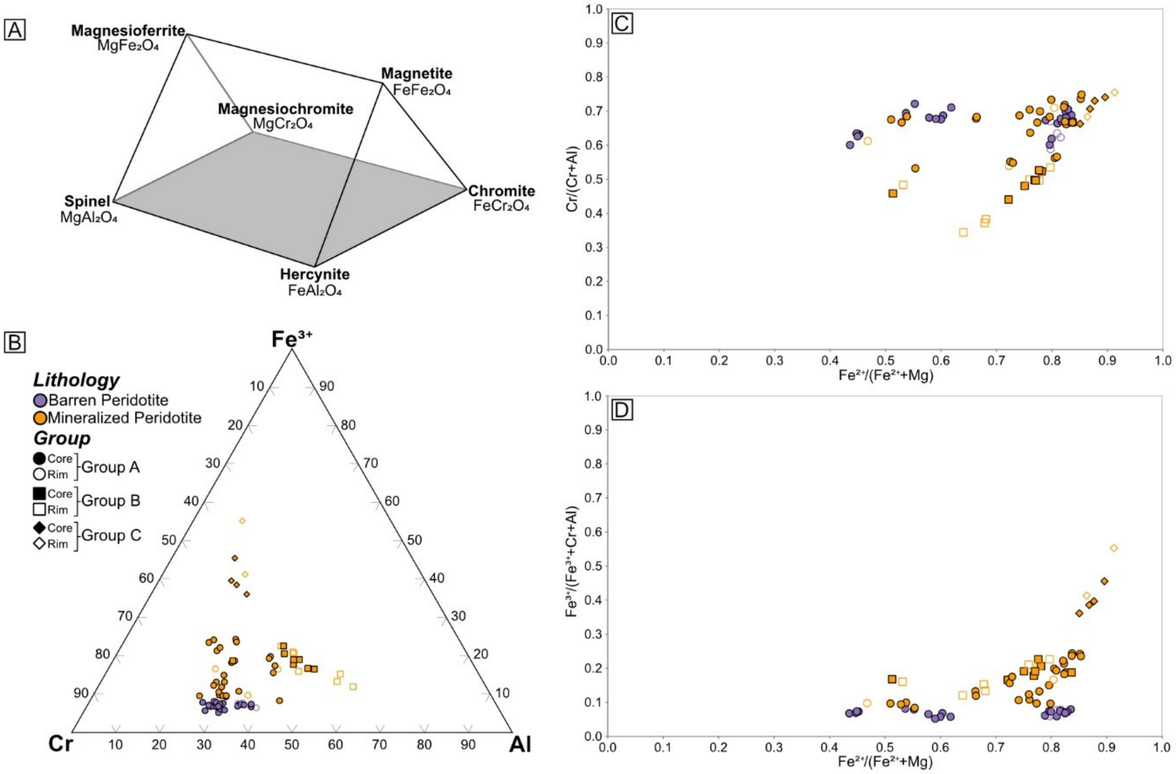

Figure 4.35: Oxide mineral compositions plotted on projections of the spinel prism. (A) Spinel prism (Haggerty, 1991). (B) Fe^{3+}–Cr–Al ternary diagram, (C) $Fe^{2+}/(Fe^{2+}+Mg)$ plotted against Cr/(Cr+Al). (D) $Fe^{2+}/(Fe^{2+}+Mg)$ plotted against $Fe^{3+}/(Fe^{3+}+Al+Cr)$.

In contrast, the oxide minerals from the mineralized peridotite display a wider compositional and textural variation. Overall, they are characterized by broader range in Cr# and $Fe^{3+}/(Fe^{3+}+Al+Cr)$ ratio but have a similar Fe# which correlates with the textural distinctions of the grains in these samples. Group A oxides consist of chromite (n=27) and magnesiochromite (n=1). These are characterized by a similar Cr# (0.53–0.74) and Fe# (0.47–0.85) to Group A oxides from the barren peridotite. However, they have an overall higher $Fe^{3+}/(Fe^{3+}+Al+Cr)$ ratio with a broader range between 0.08 and 0.24. Group B oxides consist of chromite (n=4) and hercynite (n=11). These grains are characterized by a similar Fe# (0.51–0.84) and $Fe^{3+}/(Fe^{3+}+Al+Cr)$ ratio (0.12–0.23) with a lower Cr# between 0.34 and 0.67. Group C oxides consist of chromite (n=3) and magnetite (n=3). These are characterized by an overall higher Fe# (0.85–0.91) and $Fe^{3+}/(Fe^{3+}+Al+Cr)$ ratio (0.36–0.55) at a similar Cr# between 0.66 and 0.76.

4.5 Samarium – Neodymium Isotopes

Whole rock Sm-Nd isotopic data was obtained for 21 samples. These included 15 barren samples from the Eagle's Nest intrusion, one from an Eagle's Nest type dike, and two from the wall rock tonalite (Fig. 4.36). Additionally, two Cr-depleted and one LREE-enriched sample was analyzed. The age of the Eagle's Nest intrusion has yet to be directly constrained, therefore, the εNd_T values for samples from the Eagle's Nest and Eagle's Nest type dike were calculated using the oldest date obtained for the Esker Intrusive Complex of 2735.5±0.8 Ma (Houlé et al., 2020). Based on cross-cutting relationships observed in drill-core, distinct petrographic and geochemical characteristics, the Cr-depleted and LREE-enriched units are interpreted to be younger and unrelated to the Eagle's Nest intrusion. Due to the lack of age constraints, the εNd_T values for these samples were calculated using an age of 2735.5±0.8 Ma. The εNd_T values for the tonalite samples were calculated using an age of 2773.4±0.9 Ma (Mungall et al., 2010). The obtained Sm-Nd isotopic data and calculated εNd_T values are summarized in Table 4.2.

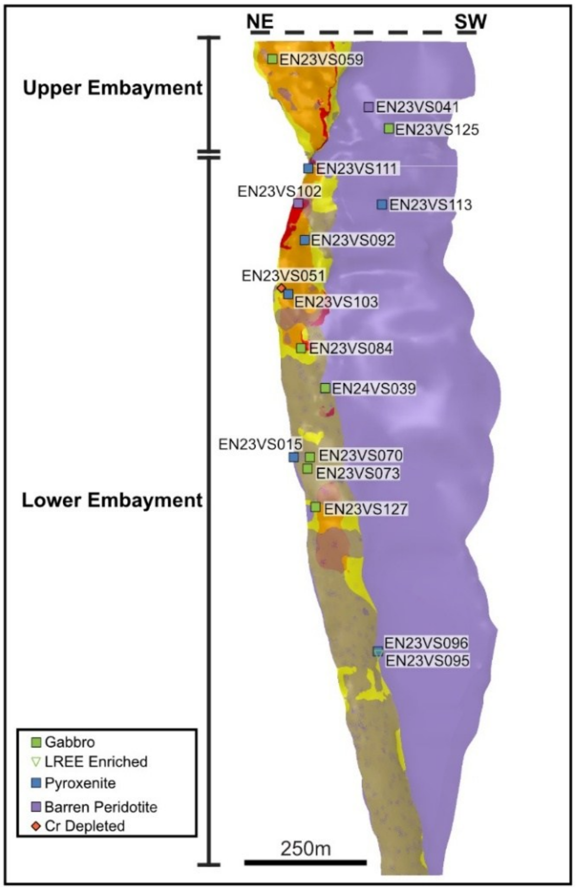

Figure 4.36: Southeast view of the Eagle's Nest intrusion showing locations of samples analyzed for whole rock Sm-Nd isotopes. Sample locations of tonalite (EN23VS129 & EN23VS132), Eagle's Nest type dike (EN23VS027), and a Cr-depleted dike (EN23VS007) are not shown.

The $\varepsilon\mathrm{Nd}_T$ values of samples from the Eagle's Nest intrusion are mostly positive but vary between -4.59 and +2.24 (Table 4.2). Both the inner zone ultramafic lithologies and the marginal zone gabbro have a wide range of overlapping $\varepsilon\mathrm{Nd}_T$ values, with the gabbroic samples inclining towards lower values ($M_d = +0.10$) than the inner zone pyroxenite ($M_d = +0.80$) and peridotite ($M_d = + 0.32$). The single sample of an Eagle's Nest type dike has an $\varepsilon\mathrm{Nd}_T$ value of -3.91. The two Cr-depleted samples have $\varepsilon\mathrm{Nd}_T$ values of -0.45 and +0.46, whereas the LREE-enriched gabbroic sample has an $\varepsilon\mathrm{Nd}_T$ of +0.87 at an age of 2735.5 Ma. The two tonalite samples have $\varepsilon\mathrm{Nd}_T$ values of -0.14 and +0.52 at an age of 2773.4 Ma.

Table 4.2: Whole rock Sm-Nd isotopic data obtained in this study

Sample	Age	Nd (ppm)	Sm (ppm)	(^{143}Nd/^{144}Nd) (Current)§	^{147}Sm/^{144}Nd‡	^{143}Nd/^{144}Nd (Initial)	^{143}Nd/^{144}Nd (2σ)	εNd$_T$
Gabbro								
EN23VS027[1]	2735.5	7.16	1.87	0.511740	0.1580	0.508888	0.000030	-3.91
EN23VS059	2735.5	4.33	1.21	0.512061	0.1696	0.508999	0.000032	-1.73
EN23VS070	2735.5	5.40	1.58	0.512245	0.1770	0.509051	0.000033	-0.72
EN23VS073	2735.5	7.57	1.81	0.511754	0.1442	0.509151	0.000028	1.25
EN23VS084	2735.5	3.97	1.26	0.512314	0.1917	0.508854	0.000036	-4.59
EN23VS125	2735.5	6.75	1.65	0.511828	0.1481	0.509154	0.000028	1.31
EN23VS127	2735.5	6.82	1.63	0.511703	0.1446	0.509093	0.000028	0.10
EN24VS039	2735.5	5.81	1.65	0.512209	0.1721	0.509102	0.000032	0.30
Pyroxenite								
EN23VS015	2735.5	3.77	1.27	0.512600	0.2037	0.508923	0.000038	-3.22
EN23VS092	2735.5	3.17	0.81	0.511978	0.1547	0.509186	0.000029	1.95
EN23VS096	2735.5	1.86	0.42	0.511585	0.1374	0.509106	0.000027	0.36
EN23VS103	2735.5	1.99	0.61	0.512488	0.1849	0.509151	0.000035	1.24
EN23VS111	2735.5	4.09	1.15	0.512125	0.1698	0.509060	0.000032	-0.54
EN23VS113	2735.5	3.33	0.90	0.512135	0.1625	0.509202	0.000031	2.24
Peridotite								
EN23VS041	2735.5	1.70	0.45	0.511946	0.1582	0.509090	0.000030	0.06
EN23VS102	2735.5	1.42	0.40	0.512179	0.1696	0.509117	0.000032	0.59
Tonalite								
EN23VS129	2773.4	17.02	2.86	0.510892	0.1017	0.509031	0.000021	-0.14
EN23VS132	2773.4	16.72	2.77	0.510895	0.1001	0.509064	0.000021	0.52
Cr-depleted [2]								
EN23VS007	2735.5	16.54	4.08	0.511754	0.1490	0.509064	0.000028	-0.45
EN23VS051	2735.5	14.21	3.55	0.511835	0.1509	0.509111	0.000029	0.46
LREE-enriched [3]								
EN23VS095	2735.5	65.75	8.40	0.510526	0.0772	0.509132	0.000017	0.87

§ Uncertainty (reproducibility of the standard) in the measured ^{143}Nd/^{144}Nd value is 0.00001.

‡ Uncertainty in ^{147}Sm/^{144}Nd value is 1%.

[1] Sample EN23VS027 is an Eagle's Nest type dike.

[2] Intermediate Cr-depleted samples. Age of emplacement is unconstrained.

[3] LREE-enriched gabbro. Age of emplacement is unconstrained.

4.6 Sulfur Isotopes

Sulfur isotope data was obtained from sulfides in nine samples from the Eagle's Nest intrusion. Acquisition of the sulfur isotope data was conducted in two stages. The first group was completed on seven poorly mineralized thin sections with emphasis put on disseminated sulfide occurrences within the marginal lithologies and utilized SIMS. The second group was completed on two pucks from the mineralized peridotite in hole NOT-10-081 and utilized LA-ICP-MS. Results summarized by sulfide type within each domain are shown in Table 4.3.

The SIMS was used to analyse five samples from the marginal zone of the intrusion, comprising gabbro (n=4), and gabbronorite (n=1). Of the marginal zone samples, three come from the hanging wall of the intrusion and two from basal contact (Fig. 4.37). In addition, two samples of inner zone pyroxenite with one distal to the main portion of the intrusion towards the southern portion (EN23VS101; Fig. 4.37). Results for SIMS analyses are reported as ratios of $^{33}S/^{32}S$ and $^{34}S/^{32}S$ as well as calculated $\delta^{33}S_{(VCDT)}$, $\delta^{34}S_{(VCDT)}$, and $\Delta^{33}S$ for individual points of analysis on chalcopyrite, pentlandite and pyrrhotite grains.

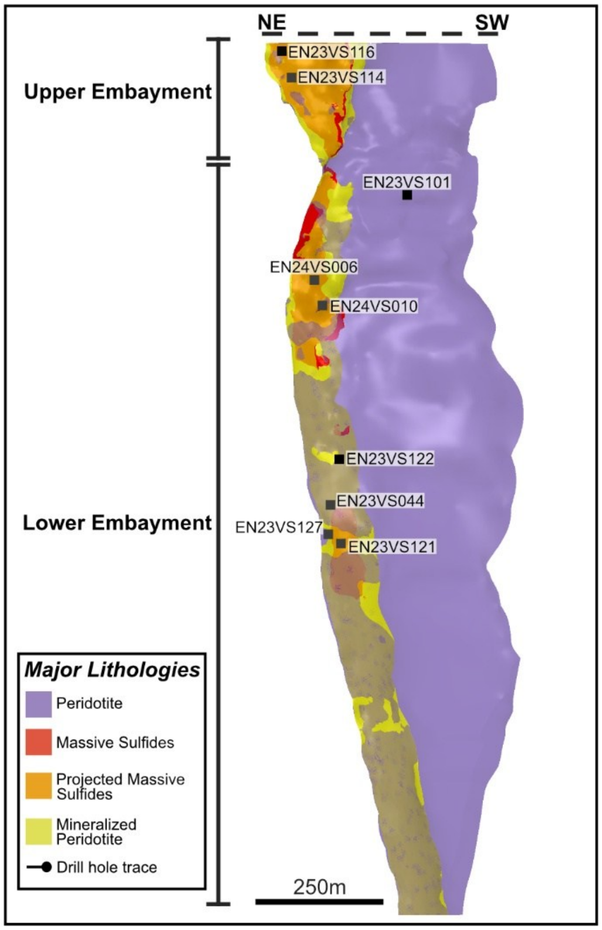

Figure 4.37: Southeast view of the Eagle's Nest intrusion showing locations of samples analyzed for sulfur isotopes.

The analyzed samples contained variable proportions and concentrations of the selected sulfide phases, which is reflected in the number of analyses conducted within each sample on a given sulfide phase. The lack of analyses for certain phases within some of the samples, does not necessarily reflect the absence of these phases, but rather that the grains were too small for analysis.

Table 4.3: Summary of sulfur isotope data from sulfides in the Eagle's Nest intrusion.

		$\delta^{34}S$ (VCDT)						$\Delta^{33}S$					
	n	Mean	Median	SD	SEM	Min	Max	Mean	Median	SD	SEM	Min	Max
Gabbro (Hanging Wall)													
Ccp	17	1.23	1.07	0.72	0.17	-0.27	2.16	0.11	0.10	0.03	0.01	0.06	0.16
Pn	27	2.16	2.48	0.97	0.19	-0.80	3.52	0.09	0.08	0.09	0.02	-0.04	0.34
Po	20	1.01	0.83	0.50	0.11	-0.07	1.67	0.07	0.08	0.04	0.01	-0.02	0.14
Gabbro (Basal Contact)													
Ccp	29	0.97	0.96	0.09	0.02	0.68	1.12	0.10	0.11	0.05	0.01	0.00	0.22
Pn	5	1.75	1.96	0.77	0.34	0.42	2.37	0.11	0.10	0.04	0.02	0.05	0.16
Po	3	1.06	1.10	0.09	0.05	0.96	1.12	0.13	0.12	0.04	0.02	0.09	0.17
Pyroxenite													
Ccp	24	0.99	1.05	0.16	0.03	0.71	1.24	-0.09	-0.09	0.04	0.01	-0.16	0.02
Pn	28	1.22	1.27	0.37	0.07	0.28	1.95	-0.11	-0.10	0.06	0.01	-0.30	-0.01
Po	12	0.31	0.33	0.12	0.03	0.07	0.45	-0.10	-0.10	0.04	0.01	-0.16	0.00
Pyroxenite (Distal)													
Pn	20	1.48	1.44	0.30	0.07	0.99	2.05	0.05	0.05	0.06	0.01	-0.08	0.15
Po	9	-1.49	-1.49	0.15	0.05	-1.72	-1.25	0.08	0.10	0.06	0.02	-0.01	0.14
Peridotite													
Ccp	39	1.03	1.08	0.37	0.06	-0.09	1.71						
Pn	39	0.01	0.01	0.34	0.06	-1.00	0.60						

Note: Summary by domain of sulfur isotope data analyzed *in-situ* from the Eagle's Nest intrusion. Gabbro (Hanging wall) include sulfides from samples EN23VS114, EN23VS121, and EN23VS127. Gabbro (Basal contact) includes sulfides analyzed from sample EN23VS116 and EN23VS122. Pyroxenite includes sulfides analyzed from sample EN23VS044. Pyroxenite (distal) includes sulfides analyzed in sample EN23VS101. Peridotite includes sulfides analyzed from samples EN24VS006 and EN24VS010. Note that the peridotite samples were analyzed via LA-ICP-MS, and values for $\Delta^{33}S$ were not obtained. Abbreviations: *SD* Standard Deviation, *SEM* Standard Error of the Mean, *Min* Minimum, *Max* Maximum.

The second group of analyzed sulfides were from the mineralized peridotite containing 25 % (EN24VS006b) and 15 % (EN24VS010) net-textured sulfides. Both samples from the Lower Embayment (Fig. 4.37). Results for LA-ICP-MS are reported as ^{32}S and ^{34}S, ratios of $^{33}S/^{32}S$ and $^{34}S/^{33}S$ as well as calculated $\delta^{34}S_{(VCDT)}$ for individual points of analysis on chalcopyrite and pentlandite with no analyses conducted on pyrrhotite and no $\Delta^{33}S$ obtained.

Sulfides from the Eagle's Nest intrusion have $\delta^{34}S$ values that range from -1.72 to +3.52 ‰ with most falling within the mantle range (0 ± 2 ‰ VCDT; Fig. 4.38; Ripley and Li, 2003). The Eagle's Nest intrusion has a mean chalcopyrite value of +1.04 ± 0.37 (SD) ‰ (n=109), pentlandite +1.10 ± 1.00 (SD) ‰ (n=119), and pyrrhotite +0.31 ± 1.03 (SD) ‰ (n=44).

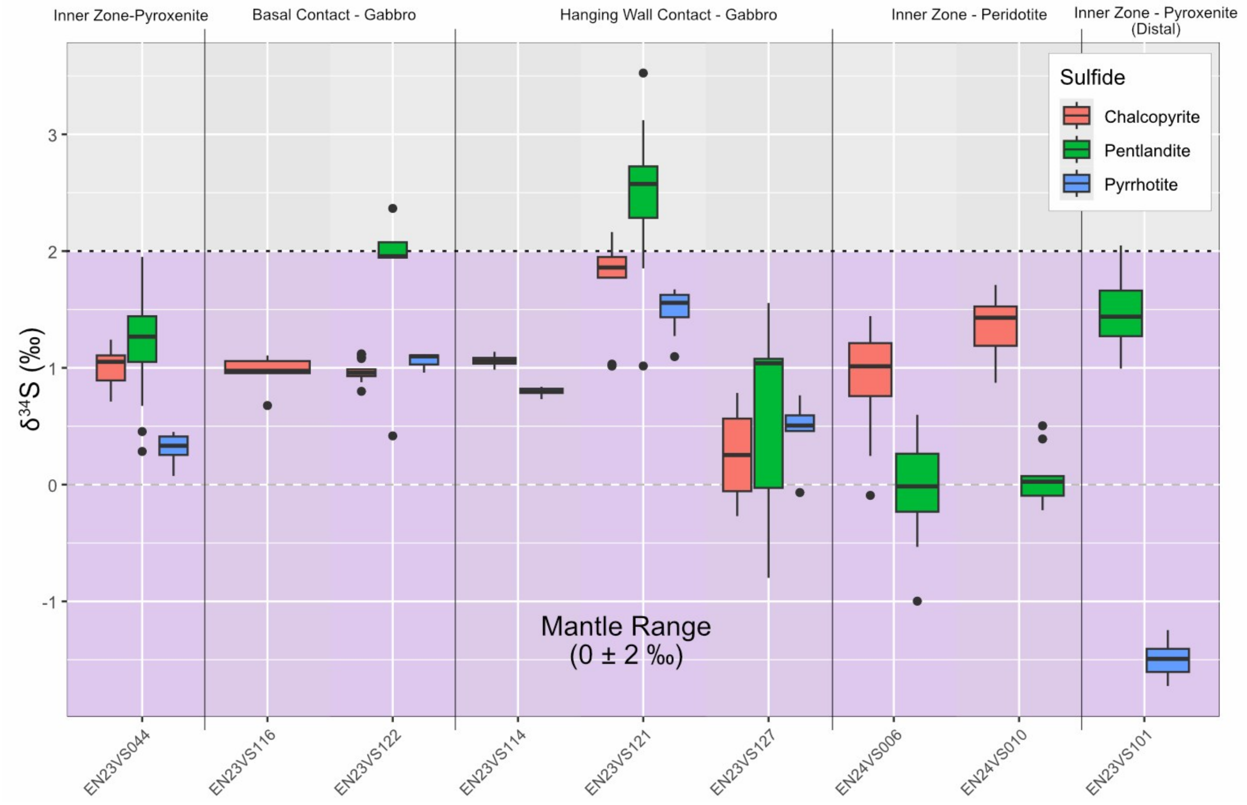

Figure 4.38: Box and whisker plot showing variations in $\delta^{34}S$ values within chalcopyrite, pentlandite and pyrrhotite within samples separated by location within the Eagle's Nest intrusion. Mantle range (0 ± 2 ‰ VCDT; Ripley and Li, 2003) is highlighted in purple.

Sulfides from the gabbro along the hanging wall contact tend to be positive but display a wide distribution, ranging from -0.07 to +3.52 ‰ (Fig. 4.38). Chalcopyrite has a mean value of +1.23 ± 0.72 (SD) ‰ (n=17), pentlandite +2.16 ± 0.97 (SD) ‰ (n=27), and pyrrhotite +1.01 ± 0.50 (SD) ‰ (n=20). Sulfides from the basal contact gabbro have a similar range (+0.42 to +2.37 ‰) to those in the hanging wall contact, with chalcopyrite averaging +0.97 ± 0.09 (SD) ‰

(n=29), pentlandite +1.06 ± 0.09 (SD) ‰ (n=5), and pyrrhotite +1.06 ± 0.09 (SD) ‰ (n=3). Chalcopyrite and pyrrhotite fall within the mantle range for $\delta^{34}S$, whereas pentlandite has higher and more positive values that mostly fall outside of the mantle range with a mean of +2.52 ± 0.50 (SD) ‰ (n=22; EN23VS121), and a single grain with a mean of +2.09 ± 0.24 (SD) ‰ (n=3; EN23VS122).

Sulfides from the inner zone pyroxenite have $\delta^{34}S$ values between -1.72 to +0.99 ‰ (Fig. 4.38). Pentlandite averages +1.22 ± 0.37 (SD) ‰ (n=28) in the pyroxenite and +1.48 ± 0.30 (SD) (n=20) in the distal pyroxenite (EN23VS101), whereas chalcopyrite has a mean value of +0.99 ± 0.16 (SD) ‰ (n=24). Pyrrhotite values vary, averaging +0.31 ± 0.12 (SD) ‰ (n= 12) in the pyroxenite to -1.49 ± 0.15 (SD) ‰ (n=9) in the distal pyroxenite. In sulfides from the inner zone that comprise mineralized peridotite, $\delta^{34}S$ values range from -0.09 to +1.71 ‰, with chalcopyrite averaging +1.03 ± 0.37 (SD) ‰ (n=39) and pentlandite +0.01 ± 0.34 (SD) ‰ (n=39). Nearly all sulfides from the pyroxenite and mineralized peridotite have $\delta^{34}S$ values that fall within the mantle range, however, a pentlandite grain in sample EN23VS101 in the distal pyroxenite exceeds it, with a mean of +2.03 ± 0.03 (SD) ‰ (n=2). In contrast to sulfides from the marginal zone and pyroxenite, the pentlandite tends to have lower values than chalcopyrite within the mineralized peridotite.

Sulfides from the Eagle's Nest intrusion have $\Delta^{33}S$ values that range from -0.30 to +0.34 ‰ which on average fall within $\Delta^{33}S$ values of both mass-dependent fractionation and the mantle range (0 ± 0.1 ‰, Farquhar and Wing, 2003; Ripley and Li, 2017). The Eagle's Nest intrusion has a mean chalcopyrite value of +0.04 ± 0.10 (SD) ‰ (n=70), pentlandite +0.01 ± 0.11 (SD) ‰ (n=80), and pyrrhotite +0.03 ± 0.09 (SD) ‰ (n=44).

Sulfides from the gabbro along the hanging wall contact have $\Delta^{33}S$ values that range from -0.04 to +0.34 ‰ (Fig. 4.39). Chalcopyrite has a mean value of +0.11 ± 0.03 (SD) ‰ (n=17), pentlandite +0.09 ± 0.09 (SD) ‰ (n=27), and pyrrhotite +0.07 ± 0.04 (SD) ‰ (n=20). Sulfides from the basal contact have a similar range (0.00 to +0.22 ‰), with chalcopyrite averaging +0.10 ± 0.05 (SD) ‰ (n=29), pentlandite +0.11 ± 0.04 (SD) ‰ (n=5), and pyrrhotite +0.13 ± 0.04 (SD) ‰ (n=3). The $\Delta^{33}S$ values in the marginal zone sulfides are mostly positive but often fall outside of mass-dependent fractionation and the mantle range upper limit.

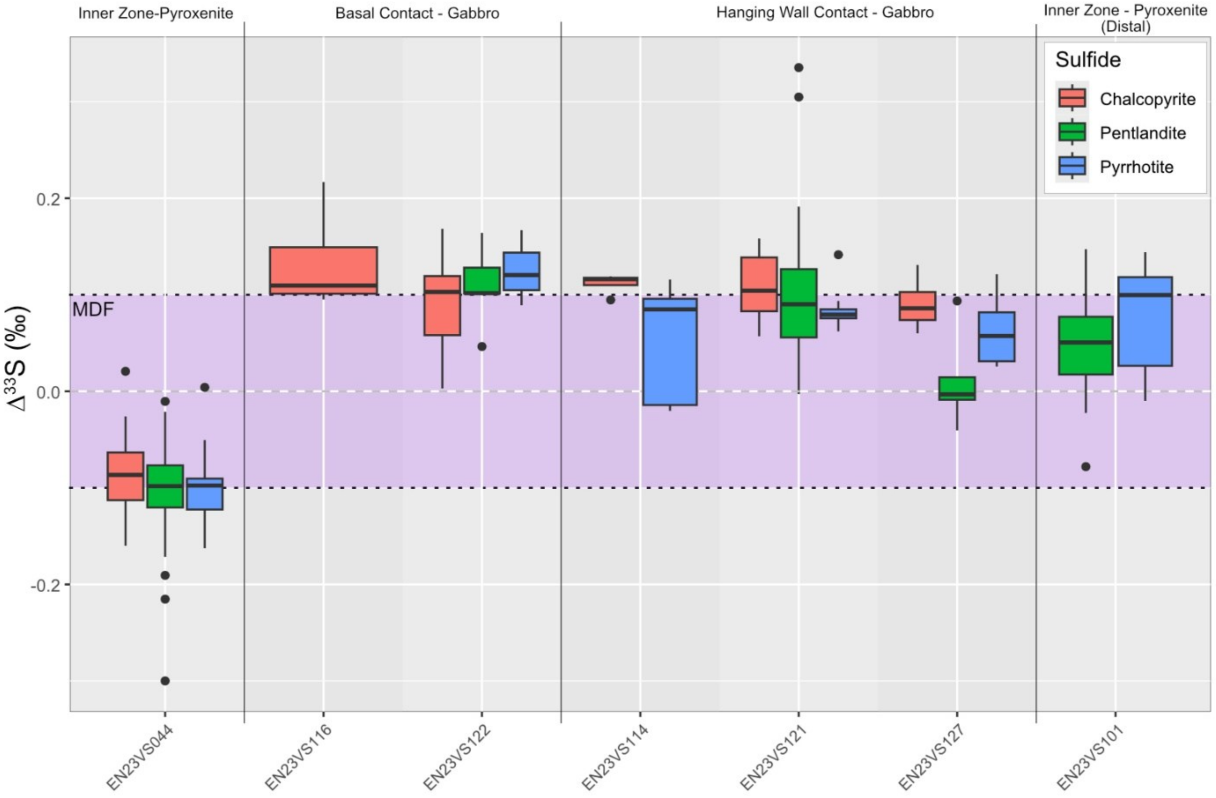

Figure 4.39: Box and whisker plot showing variations in $\Delta^{33}S$ values within chalcopyrite, pentlandite and pyrrhotite within samples separated by the location in which they occur within the Eagle's Nest intrusion. Mass-dependent fractionation (MDF) of 0 ± 0.1 ‰ (Farquhar and Wing, 2003) is highlighted in purple.

Mean $\Delta^{33}S$ values outside the mantle range are observed in chalcopyrite (EN23VS114 (n=4): +0.11 ± 0.01 ‰, EN23VS116 (n=8): +0.13 ± 0.04 ‰, EN23VS121 (n=9): +0.11 ± 0.04 ‰), pentlandite (EN23VS121 (n=22): +0.11 ± 0.09 ‰, EN23VS122 (n=5): +0.11 ± 0.04 ‰), and pyrrhotite (EN23VS122 (n=3): +0.13 ± 0.04 ‰).

Sulfides from the inner zone pyroxenite have $\Delta^{33}S$ values between -0.30 to +0.15 ‰ (Fig. 4.2). On average, pentlandite has a lower mean of -0.11 ± 0.06 (SD) ‰ (n=28) in the pyroxenite in comparison to +0.05 ± 0.06 (SD) ‰ (n=20) in the distal pyroxenite (EN23VS101). A similar trend is observed in pyrrhotite with a mean value of -0.10 ± 0.04 (SD) ‰ (n= 12) in the pyroxenite and +0.08 ± 0.06 (SD) ‰ (n=9) within the distal pyroxenite (EN23VS101). Chalcopyrite has a mean $\Delta^{33}S$ value of -0.09 ± 0.04 (SD) ‰ (n=24), similar to the range of values observed in pentlandite and pyrrhotite within the pyroxenite. Except for pentlandite in EN23VS044 (n=28; -0.11 ± 0.06 ‰), all sulfide phases fall within the mantle range. Sample EN23VS044 shows more negative values compared to the marginal zone and distal pyroxenite stretching towards the lower limit of the mantle range (Fig. 4.39).

Chapter 5 Discussion

5.1 Overview

To provide constraints on the formation of the Eagle's Nest intrusion and the genetically related dikes, the discussion incorporates only those samples that exhibit mineralogical, textural, and geochemical characteristics consistent with the Eagle's Nest intrusion. These include the marginal and inner zone samples from the Eagle's Nest intrusion and identified as Eagle's Nest type dikes based on their geochemical and petrographic similarity to the samples from the intrusion. The other groups distinguishable based on anomalous trace element patterns are excluded from the interpretation below as they either represent samples unrelated to the Eagle's Nest, samples that are related to the Eagle's Nest but have been affected by additional and/or different secondary processes, or samples that reflect potential analytical or sampling errors (e.g., instrumental error and/or contamination).

In addition to the data obtained in this study, the discussion incorporates available data for the Eagle's Nest intrusion (Wyloo Databases; Zuccarelli, 2020) as well as other portions of the Esker Intrusive Complex (Azar, 2010; Laarman, 2014; Carson, unpublished data; Farhangi, unpublished data). Samples that had a complete whole-rock geochemical suite were processed following the procedures outlined in this study. Data from the Wyloo database only included unmineralized samples (<1 wt% S and <200 ppm Cu) to mitigate the effects of mineralization.

5.2 Eagle's Nest Intrusion – Lithostratigraphy

The Eagle's Nest intrusion consists of varying proportions of olivine, pyroxene, plagioclase, chromite, and sulfides, which form a range of rock types, including gabbro, olivine pyroxenite, peridotite, and mineralized peridotite. The Eagle's Nest intrusion can be subdivided into the marginal and inner zones (Fig. 5.1A). These zones can be further subdivided into smaller domains based on mineralogical and textural characteristics.

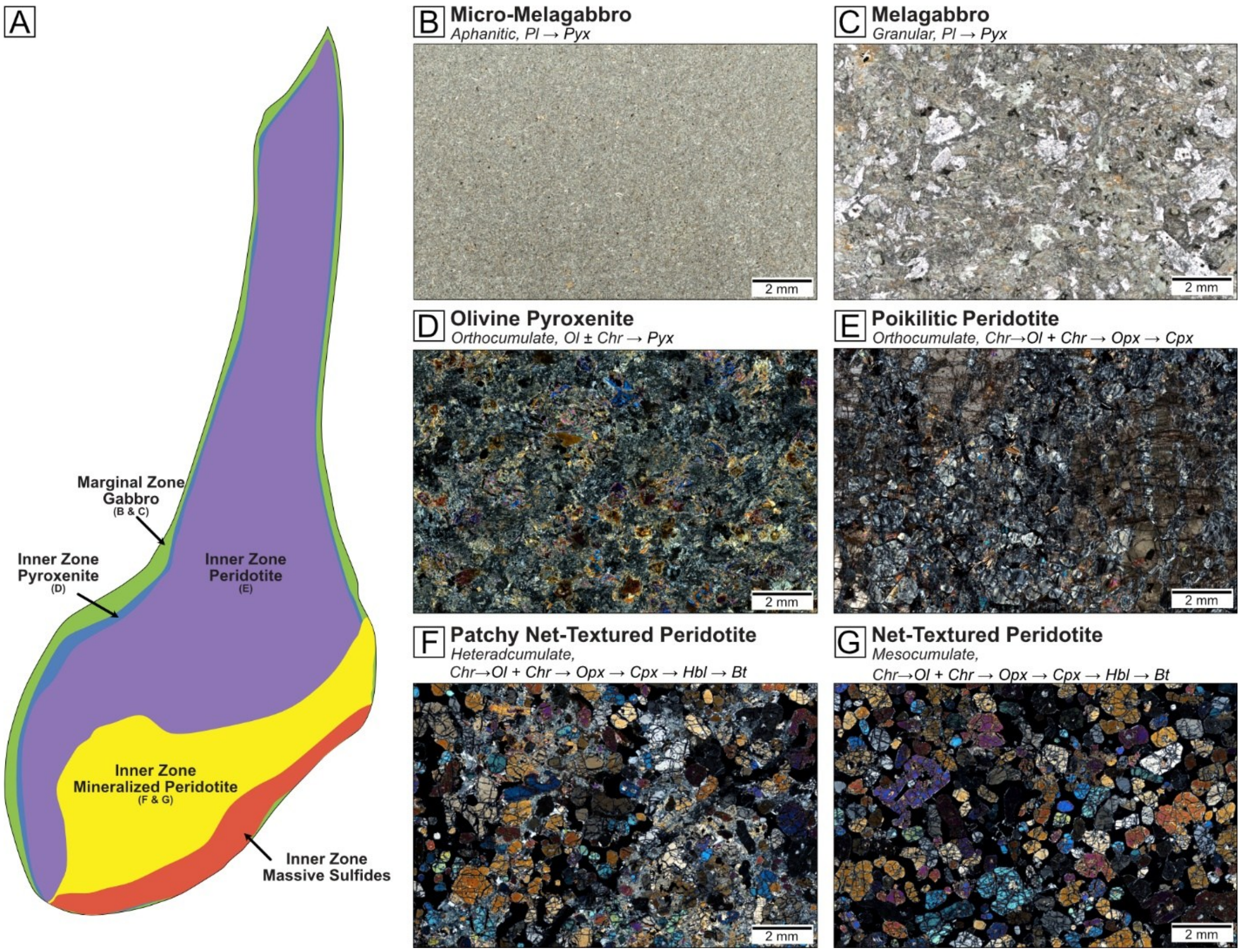

Figure 5.1: Schematic of the Eagle's Nest intrusion, illustrating its internal differentiation with thin section examples of the textural and mineralogical characteristics. (A) Schematic illustration of the internal differentiation of the Eagle's Nest. (B) micro-melagabbro, (C) medium-grained melagabbro, (D) olivine bearing pyroxenite, (E) poikilitic peridotite, (F) mineralized peridotite with patchy net-textured sulfides, and (G) mineralized peridotite with net-textured sulfides. Abbreviations: Pl – plagioclase, Pyx – pyroxene, Ol – olivine, Chr – chromite, Opx – orthopyroxene, Cpx – clinopyroxene, Hbl – hornblende, Bt – biotite.

5.2.1 Marginal Zone

The marginal zone represents the outermost portion of the Eagle's Nest intrusion and is in contact with the host tonalite. The marginal zone consists of fine- to medium-grained, granular to rarely sub-ophitic melagabbro (Figs. 5.1B–C). The major element variations of marginal zone rocks are generally more complicated than those of the inner zone. Coherent trends of increasing Si, Al, Ca, and Ti (not shown) and decreasing Ni and Cr with decreasing amounts of Mg reflect the most evolved compositions, consistent with the absence of olivine (Figs. 4.23 & 4.24). The more mobile, alkali elements (Na and K) show a much larger variation than in the inner zone rocks. The amount of Na increases with decreasing contents of Mg in the marginal zone rocks and a few pyroxenite samples that are more proximal to the contact (Fig. 4.23D). The coherent trend suggests that Na reflects a magmatic differentiation process, specifically the fractionation of plagioclase along the marginal zone which is found in abundance in the gabbroic rocks. On the other hand, the concentration of K is scattered and does not define any apparent trends, implying that it was mobile during alteration (Fig. 4.23E). The variable distribution of K correlates with the increasing abundance of biotite in proximity to the contact. Biotite in the marginal zone rocks generally accompanied the alteration assemblage after pyroxene. Together this implies that the formation of biotite is product of alteration, rather than having a magmatic igneous origin.

5.2.1.1 Chilled Margins

Examination of marginal zone rocks was conducted to identify chilled margins that may represent the parental magma composition of the Eagle’s Nest intrusion. It has been shown that when a hot magma is initially emplaced into cold country rock, the contrasting heat flux between the wall rock and the magma results in rapid crystallization of the melt and the formation of fine-grained rocks that are representative of the initial, parental magma composition (Huppert and Sparks, 1989). During solidification, the grain size of a chilled margin is expected to gradually increase away from the cooling contact. The marginal zone of the Eagle’s Nest intrusion displays highly variable contact relationships with the wall rock tonalite, as well as variations in grain size and alteration intensity, all of which reflect a complex history of igneous and metamorphic processes. Based on the morphology of the intrusion at the time of emplacement, the marginal zone can be subdivided into two parts that broadly correspond to the observed variability (Fig. 4.1B): one along the stratigraphically higher hanging wall contact, and the other along the stratigraphically lower basal contact. Along the hanging wall contact, the boundary with the intrusive mafic rocks is commonly diffuse, and lengthy intervals of magmatic breccia were observed (Figs. 4.3 & 4.4). The tonalite along the hanging wall displayed evidence of contact metamorphism, including the occurrence of baked margins and localized zones of partial melting and recrystallization. In contrast, evidence of intense contact metamorphism is rare along the basal contact, where the boundary is typically sharp and the tonalite is more commonly unaltered (Fig. 4.2).

It has been shown that over time, after the initial emplacement of magma, the conductive heat flux of the wall rock decreases whereas the heat flux of the magma increases to the point of remelting of the initially formed chilled margins (Huppert and Sparks, 1989). The highly variable characteristics suggest that the hanging wall was exposed to a higher temperature than the basal contact, to such an extent that temperatures exceeded the solidus. The localized evidence of partial melting along the hanging wall contact makes it highly unlikely that the original chilled margins were preserved compared to the basal contact, where evidence of such intense heat flux is generally absent. Over time, the heat flux of the magma decreases to less than the conductive heat flux in the wall rock, at which stage a second generation of marginal rocks will begin to form, which will not be representative of the original magma composition (Latypov et al., 2007). Most of the collected marginal zone samples, regardless of the proximal contact type (Figs. 4.2, 4.3 & 4.24), have a medium grain size and were generally sampled slightly away from the contact to avoid the intense alteration, however, they were often characterized by a granular texture suggestive of in-situ crystallization. Due to the susceptibility of marginal rocks to remelting, it is difficult to say whether all the gabbroic rocks along sharp contacts represent original or secondary marginal rocks. It can be said, however, that in areas where evidence of partial melting of the tonalite is present, the gabbroic rocks are most likely secondary marginal rocks, and the preservation of chilled margins is highly unlikely.

Despite the limitations associated with the preservation of original chilled margins, this study identified two samples that provide evidence in support of rapid crystallization. These samples were collected along sharp contacts that displayed minimal wall rock alteration, with one sample coming from the hanging wall (EN23VS114) and one from the basal contact (EN24VS039). Sample EN23VS114 is characterized by branching, fibre-like plagioclase arranged in an axiolitic-like (variolitic) form with intergranular to skeletal clinopyroxene (Figs. 4.9C & 4.10B). Several mechanisms have been proposed to explain the origin of variolitic textures. For instance, liquid immiscibility has been suggested in the Abitibi Greenstone Belt (Gélinas et al., 1976) and the Troodos Ophiolite (Ballhaus et al., 2015) based on the presence of globular morphologies and fluid exsolution textures. However, such features are absent in this sample, making it an unlikely mechanism for formation. Two other mechanisms were proposed by Fowler et al. (1987; 2002): (1) magma mixing leading to the suspension of felsic magma droplets in a mafic melt, and (2) undercooling through the interaction of a hot mafic melt with cold wall rock. The first mechanism is characterized by spheroidal varioles, if magma mixing occurred at depth, they would be expected to be more abundant outside the direct contact with the tonalite. Absence of spheroidal varioles other than in this sample, makes magma mixing unlikely. The second mechanism describes the size increase of the spherulites and the transition from spheroidal to an axiolitic form as the distance from the contact increases (Arndt and Fowler, 2004). Given the proximity to the contact and the axiolitic textures' random orientation, undercooling of the melt is a plausible explanation for this sample.

The second sample, EN24VS039, is characterized by a fine grain size, aphanitic texture with plagioclase and pyroxene forming a granular texture (Fig. 5.1B). The small grain size of this sample in proximity to the contact, suggests that it formed through rapid crystallization (Huppert and Sparks, 1989). Given the limitations associated with preservation of original chilled margins, it would be expected that during the formation of secondary marginal rocks, the temperature gradient between the melt and the tonalite would be low, which would yield a slower crystallization rate and therefore a larger grain size. Given the textures in these samples that are indicative of rapid crystallization, which would have occurred at a time when the temperature gradient would have been sufficiently large to induce rapid crystallization, it is likely that these two samples represent the initial stages of the melt.

5.2.1.2 Crystallization Sequence

The crystallization sequence of the marginal zone rocks can be established based on relict textural relationships between pyroxene and plagioclase. In rare instances, prismatic pyroxene grains are mantled by plagioclase, suggesting early crystallization of pyroxene. In most cases, tabular plagioclase is partially enclosed by subhedral to anhedral pyroxene, sometimes forming sub-ophitic textures, which indicates that plagioclase crystallized first. This sequence is also supported by variolitic, lath-like plagioclase with pyroxene filling the intergranular spaces, implying that plagioclase preceded pyroxene (Figs. 4.9C & 4.10B). Trace amounts of equant chromite suggest it appeared early in the crystallization sequence, however, its timing of crystallization relative to the silicate minerals could not be determined.

5.2.2 Inner Zone

The inner zone of the Eagle's Nest intrusion occurs distal to the contact with the tonalite, where the rocks are characterized by cumulus textures and ultramafic compositions. The inner zone is characterized by coherent trends of decreasing Si, Al, Ca, Na, K, Ni and Ti (not shown) with increasing Mg (Figs. 4.23 & 4.24). These trends reflect the variable proportions of accumulated olivine and trapped silicate melt. In comparison to the marginal rocks of the intrusion, the more mobile alkali elements define linear, coherent trends, implying that the inner zone ultramafic rocks underwent isochemical alteration. To evaluate whether olivine was the sole control on the compositional variability of the Eagle's Nest, Molar Element Ratio (MER) analysis was applied (for details on theory and practice see Pearce, 1968; Stanley and Russell, 1989; Russell and Stanley, 1990; Nicholls and Russell, 2016; Stanley, 2020). The MER plots define a slightly scattered distribution, with broadly coherent linear trends along the olivine control line with a smaller number of samples falling between the olivine and orthopyroxene accumulation trends (Fig. 5.2). The distribution along the olivine control with slight deviation towards the orthopyroxene control line, provides additional evidence that the compositional variability of the inner zone can be explained by olivine fractionation, either with, but predominantly without orthopyroxene (Figs. 5.2A–B & D). The MER analysis also suggests that neither clinopyroxene nor plagioclase significantly control the composition of the inner zone rocks (Figs. 5.2B–C). Petrographic observations are consistent with these interpretations.

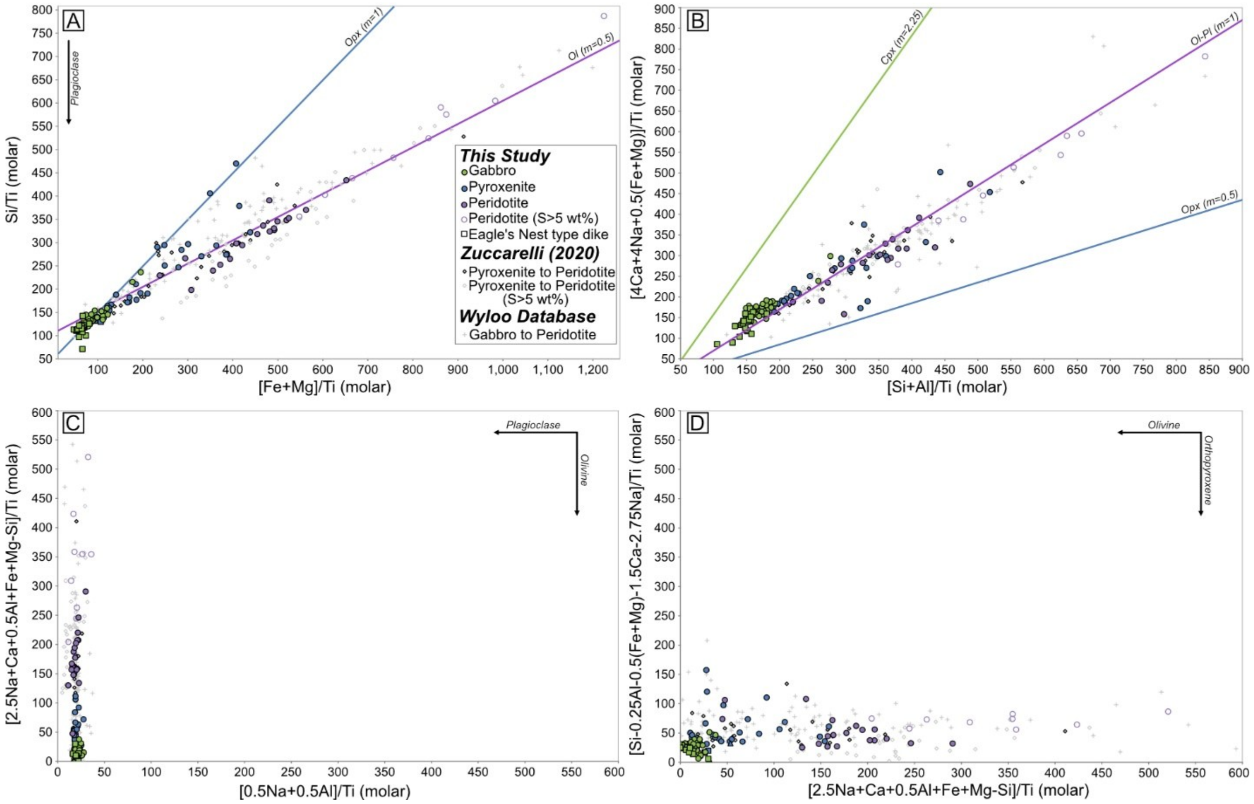

Figure 5.2: Molar element ratio diagrams testing the mineralogical controls on the composition of the Eagle's Nest (Stanley and Russell, 1989; Nicholls and Russell, 2016). Ti was selected as the common denominator, as it was recognized to be the most conserved element in the Eagle's Nest intrusion (A) MER plot testing stoichiometrically predicted trends for accumulation of stoichiometric olivine, orthopyroxene, and plagioclase. (B) MER plot testing stoichiometrically predicted trends for accumulation of stoichiometric olivine + plagioclase, orthopyroxene, and clinopyroxene. (C) MER diagram evaluating the relative impacts of plagioclase and olivine fractionation (clinopyroxene and orthopyroxene have no effects on displacement on this diagram). (D) MER diagram evaluating the relative impacts of olivine and orthopyroxene fractionation (clinopyroxene and plagioclase have no effects on displacement on this diagram).

The lithological and geochemical variations across the inner zone can be described based on the proportion of accumulated olivine, intercumulus silicate melt, and sulfides. Based on these proportions, the inner zone can be further subdivided into four domains from the stratigraphically lowermost portion upwards, comprising massive sulfides, mineralized peridotite, barren peridotite, and olivine pyroxenite. The distinction between each domain is defined by the proportion of olivine to intercumulus silicate minerals, with the mineralized peridotite having the highest modal proportion and the olivine pyroxenite having the lowest. These proportions are reflected in the geochemical trends, with the most primitive compositions containing, on average, 41.2 wt% MgO in the mesocumulate rocks (mineralized peridotite) and the least primitive containing 26.0 wt% MgO in the orthocumulate rocks (olivine pyroxenite). Although a complete section across the inner zone could not be established, the differentiation of the Eagle's Nest intrusion can be illustrated by the variability of olivine composition. In drill hole NOT-10-081, olivine composition decreases from an average of $Fo_{85.8}$ in the mineralized peridotite to $Fo_{83.5}$ in the barren peridotite and $Fo_{82.1}$ higher up in the stratigraphy. Although not from the same drill hole, the olivine pyroxenite (EN23VS100) has, on average, the most evolved composition of $Fo_{77.9}$. These trends are consistent with the differentiation of the magma within the intrusion.

5.2.2.1 Sulfide Textures and Distribution

The characterization of sulfide textures and their distribution within the Eagle's Nest intrusion have been described in detail by Mungall et al. (2010) and Zuccarelli (2020) and was largely beyond the scope of this study. However, establishing their characteristics relative to other primary phases is vital, especially within the mineralized peridotite domain. In drill hole NOT-10-081, massive sulfides occur at the stratigraphically lowermost portion of the intrusion, which abruptly transitions into net-textured mineralization, then gradationally transitions into disseminated mineralization and lastly barren peridotite. Net-textured sulfides form continuous to discontinuous networks interstitial to cumulus and intercumulus silicate minerals and chromite (Figs. 5.1F–G). The mineralized peridotite displays mineralogical and textural heterogeneity that is defined by the gradational and sporadic variability of olivine-sulfide rich domains that form continuous net-textured mineralization, which locally transitions into olivine-pyroxene rich domains forming patchy to poikilitic net-textured mineralization (Figs. 4.5D & 5.1F–G). The distribution of sulfide mineralization has been explained by a downward percolation model (Mungall et al., 2010; Zuccarelli, 2020), in which a sulfide melt migrates through a pre-existing olivine crystal mush, expelling intercumulus silicate melt upwards to form net-textured mineralization (Chung and Mungall, 2009; Barnes et al., 2017). The formation of poikilitic versus patchy net-textured mineralization provides context for the relative timing of intercumulus silicate melt crystallization. Barnes et al. (2017) described the formation of poikilitic textures in matrix ores before sulfide percolation (Figs. 4.16D–E). Conversely, the formation of patchy net-texture would occur later, from the remaining silicate melt trapped within the inter-crystalline spaces and was not completely expelled (Fig. 5.1F; Barnes et al., 2017). The formation of oikocrysts in poikilitic net-textured mineralization would then be expected to occur from a less differentiated melt, which forms intergranular textures in the patchy net-textured mineralization. However, regardless of the occurrence, pyroxene from the mineralized peridotite, have overlapping compositions and Mg#'s, implying that they formed from a similar melt (Fig. 4.32). This implies that both poikilitic and patchy net-textured mineralization formed by a similar process, most likely entrapment of intercumulus silicate melt, which is also supported by the gradational transition between net-textured, poikilitic, and patchy net-textured mineralization (Fig. 4.5D).

5.2.2.2 Chromite Cotectic Deviations

In the Eagle's Nest intrusion, chromite is a relatively minor constituent occurring across all petrographically examined rock types (Table 4.1). In Figure 4.24, the samples define a clear linear trend of increasing Cr with increasing MgO, which is interpreted to reflect the fractionation of olivine and chromite in cotectic proportions (Lesher and Stone, 1996; Barnes, 1998). Nonetheless, a few of the mineralized peridotite samples fall below the olivine-chromite cotectic trend (Fig. 4.24). A similar trend was observed by Zuccarelli (2020), with samples falling below the cotectic trend being a product of less than cotectic olivine-chromite accumulation. In the current study, available thin sections for the anomalous samples reveal that the relative abundance of olivine and chromite is similar to the abundance in samples that fall along the olivine-chromite cotectic trend, questioning the cause of the deviation. In the present understanding of the net-textured mineralization in the Eagle's Nest intrusion, sulfide melt propagated through a pre-existing olivine-crystal mush displacing intercumulus silicate melt. The small amounts of trapped silicate melt (i.e., orthopyroxene and clinopyroxene), during the mutual migration of both sulfide and silicate melt, is enriched in Cr_2O_3 containing between 0.48–0.82 wt% within orthopyroxene (excluding outliers) and 0.78–1.25 wt% within clinopyroxene, similar to the pyroxenes from the barren peridotite (Fig. 4.32). If these intercumulus phases are representative of the composition of the displaced silicate melt, then, had they crystallized prior to the migration of the sulfide melt, their compositions would be no different than the samples that fall along the olivine-chromite cotectic. As a result, the interpretation for the samples in this study that fall below the olivine-chromite cotectic, is that they were originally olivine-chromite cotectic cumulates, and the migration of sulfide melt resulted in the displacement of a Cr-rich intercumulus silicate melt, making it appear as if they are non-cotectic cumulates.

5.2.2.3 Crystallization Sequence

The mineralogy of the inner zone consists of variable proportions of olivine, orthopyroxene and clinopyroxene, with smaller amounts of hornblende, biotite, and chromite (Figs. 5.1A & D–G). The occurrence of cumulus olivine and chromite represents the earliest formed phases, occurring as cumulate grains or smaller chadacrysts enclosed by larger and later formed intercumulus silicate minerals. A small portion of chromite grains occur as fine, equant inclusions in olivine, which suggests that chromite was the first phase to crystallize, followed by olivine (Figs. 4.18D–E). The fractionation of olivine and chromite was followed by the crystallization of trapped silicate melt to form intercumulus pyroxene.

Intercumulus silicate minerals are dominated by varying proportions of orthopyroxene and clinopyroxene. The textural characteristics between orthopyroxene and clinopyroxene differs between the mineralized and barren peridotite domains. Within the mineralized peridotite, both clinopyroxene and orthopyroxene occur as ellipsoidal oikocrysts (Figs. 4.16D–E). Importantly, the occurrence of anhedral orthopyroxene patches enclosed by poikilitic clinopyroxene oikocrysts suggests a peritectic reaction where clinopyroxene forms at the expense of orthopyroxene dissolution (Fig. 4.16D), closely resembling the peritectic texture seen in the Critical Zone of the Bushveld Complex (Barnes et al., 2021). The barren peridotite lacks this peritectic relationship and instead is characterized by the presence of medium- to coarse-grained ellipsoidal orthopyroxene oikocrysts with smaller, anhedral clinopyroxene filling the intercumulus space (Fig. 4.16B). Together the textural characteristics suggest that orthopyroxene crystallized prior to the formation of clinopyroxene.

In a small number of samples, within the mineralized and barren peridotite domains, minor amounts of hornblende and biotite were identified (Fig. 4.17). Hornblende was observed in both the mineralized and barren peridotite occurring as anhedral to subhedral grains, locally displaying a lozenge shape, and occurring as intergranular to sub-poikilitic grains with sharp grain boundaries with the mutually associated olivine and pyroxene grains. The hornblende grains comprise magnesio-hastingsite and Ti-rich magnesio-hastingsite, which together with textural evidence suggest an igneous origin (Deer et al., 2013). Biotite (outside the alteration related in the marginal zone) was identified only within the mineralized peridotite occurring as lamellar grains interstitial to silicate and sulfide phases (Figs. 4.17D–F). Although the composition of biotite was not obtained, its occurrence and textural characteristics suggest a magmatic origin. Together, these phases crystallized from the remaining residual melt, after the crystallization of intercumulus pyroxene. In pyroxenitic rocks where chlorite-pseudomorphed plagioclase was identified, it appeared to have been euhedral and partially enclosed by altered pyroxene grains, indicating that it preceded the crystallization of the inferred clinopyroxene (4.17A). Based on the observed textural relationships within the inner zone rocks, the crystallization sequence can be described as follows: chromite → olivine + chromite → orthopyroxene → plagioclase → clinopyroxene → hornblende → biotite.

5.3 Nature of the Parental Magma

Identifying the composition of the parental magma has been a central point of numerous studies of magmatic systems (e.g., Godel et al., 2011; Smith et al., 2021; Bain et al., 2023). Deciphering its characteristics is key to understanding the magmatic evolution and differentiation processes, as well as depth and temperature of emplacement of the intrusion. It also provides constraints on the composition and the extent of the partial melting of the source, which is key to understanding the metal budget of ultramafic systems (Lesher and Stone, 1996; Naldrett, 2011). The following section provides new estimate on the composition of the parental magma, and thermodynamic constraints to evaluate the emplacement depth of the intrusion.

5.3.1 Composition

Determining the composition of the parental magmas in igneous systems has been central to many studies, as it provides important information about the magmatic differentiation processes, mantle source characteristics, and the identification of fertile intrusions (Barnes, 2023; Smith et al., 2024). It is important to note that there is a clear distinction between a parental and a primary magma, although they often appear to be used interchangeably (Herzberg et al., 2007; Smith et al., 2024). A primary magma is a partial melt derived from a mantle source that has not been modified by magmatic differentiation processes and therefore is representative of the mantle source composition. In contrast, a parental magma is the composition from which a range of rock types may form through magmatic differentiation processes, which can be as primitive or more evolved than the primary magma from which they were derived. The compositions of parental and primary magmas will only be the same if magmatic differentiation processes did not occur during the transport of a primary magma from the mantle source (Herzberg et al., 2007). This study attempts to estimate the parental magma composition for the Eagle's Nest intrusion, that is the magma composition from which the observed mineralogical and compositional variations were derived.

There are numerous approaches to estimating the parental magma composition which include, but are not limited to: (1) identification of quenched parental liquids such as chilled margins, associated dikes and/or sills, or equivalent extrusive rocks (e.g., Barnes et al. 2010; Godel et al., 2011), (2) using the Chai and Naldrett (1992) approach to estimate the Mg# and/or MgO–FeO based on the distribution coefficient between the olivine and melt utilizing whole rock geochemistry either in conjunction or without primitive olivine chemistry (e.g., Barnes and Fiorentini, 2012; Zuccarelli, 2020; Smith et al., 2021), or (3) applying the equilibrium distribution method of Bédard (1994), which uses a mass-balance approach to estimate the trace-element concentrations of silicate phases in cumulate rocks and of the liquids in equilibrium with them (e.g., Bédard 2001; Bain et al., 2023).

The parental magma composition of the Eagle's Nest intrusion has previously been estimated on two separate occasions. Mungall et al. (2010) estimated the major oxides and some trace elements of the parental magma by incrementally removing small amounts of the wall rock contaminant from the most magnesian chilled margin. Their modelling yielded a low-Mg komatiitic parental magma composition that contained ~11.6 wt% FeO_t and ~22.1 wt% MgO. More recently, Zuccarelli (2020) noted the presence of olivine-only cumulate rocks, inferring that the parental magma would have crystallized an olivine of Fo_{94}, which would have been in equilibrium with a high-Mg komatiitic magma that contains ~10 wt% FeO_t and ~28 wt% MgO. Although both methodologies are appropriate for estimating the parental magma they yielded drastically different compositions, with both approaches having limitations. For example, Mungall et al. (2010) used a chilled margin composition from the cogenetic Blue Jay prospect (i.e., AT12) rather than the Eagle's Nest intrusion. Although both are part of the same intrusive system, Mungall et al. (2010) approached the estimation with the assumption that the parental magma for both the Eagle's Nest intrusion and Blue Jay were the same. Zuccarelli (2020), on the other hand, used whole rock compositions from rocks of the Eagle's Nest intrusion, which were mineralized with 4 and 13 wt% S. Although the FeO_t in the mineralized samples was corrected for the presence of sulfides, neither the correction approach nor the associated uncertainty was documented.

Given the discrepancies between previously estimated parental magma compositions, the most primitive olivine composition and chilled margins, an independent estimation of the parental magma composition for the Eagle's Nest intrusion was conducted. Due to the highly altered nature of the marginal zone rocks and the Eagle's Nest type dikes, they were not used as direct representation of the parental magma. Instead, whole rock and mineral chemistry data from ultramafic cumulate rocks was used to estimate the composition of the parental magma. The resulting estimates were then compared with previous findings, as well as the compositions of chilled margins and Eagle's Nest type dikes (this study) to evaluate if they are representative of the estimated parental magma composition, despite their alteration.

The approach was adapted and modified from the methodology of several studies (i.e., Li and Ripley, 2011; Taranovic et al., 2022), which utilized whole rock compositions of ultramafic cumulate rocks and the composition of cumulus mineralogy in the samples. The concept relies on the identification of a starting composition that represents a mixture of olivine and residual silicate melt from which the olivine of a set composition (most primitive) is incrementally removed until the residual liquid is in equilibrium with the target olivine composition. The results of the estimation are reported in Table 5.1 and plotted on Figure 5.4 with the approach outlined below.

To confidently estimate the parental magma composition, a systematic approach was used to select a subset of suitable samples and to determine the composition of cumulus minerals to be removed. To increase the confidence and precision of the estimates, whole rock geochemical data was incorporated from Zuccarelli (2020). In the selection process, samples containing >5 wt% S were first excluded, because the precision of the sulfide correction progressively worsens with increasing abundance of sulfides (Barnes, 2023). After the removal of strongly mineralized samples, a subset of samples, the composition of which was predominantly controlled by olivine, were selected by calculating the residuals of each data point along the olivine-only control line (Fig. 5.2A) and selecting those falling within ±1σ of the residual distribution. The diagram was then visually inspected to account for the non-constant error along the slope.

Table 5.1: Composition of removed chromite and olivine, starting composition, estimated parental magma, median Eagle's Nest type dikes, and identified chilled margins.

Oxide (wt%)	Olivine (Fo$_{89}$)[ǂ]	Chromite[§]	Median UM (>30 wt% MgO)[¦]	Estimated Parental Magma	Median EN Type Dike[°]	Chilled Margins	
						EN23VS114	**EN24VS039**
SiO_2	40.49		44.38	52.60	52.28	51.38	50.71
TiO_2			0.19	0.54	0.58	0.56	0.58
Al_2O_3		15.52	4.53	12.09	12.17	12.00	12.24
Cr_2O_3		46.35	0.77	0.46	0.20	0.24	0.19
FeO_t	10.65	28.97	11.12	11.23	10.05	9.78	10.40
MnO	0.20		0.15	0.08	0.18	0.16	0.13
MgO	48.36	6.87	36.08	15.29	12.99	13.59	12.65
CaO			2.58	7.21	8.32	8.81	8.86
Na_2O			0.12	0.34	1.80	2.44	3.06
K_2O			0.04	0.10	1.53	0.97	1.12
P_2O_5			0.02	0.06	0.05	0.05	0.05
Equilibrium Olivine Composition				**Fo$_{89.0}$**	**Fo$_{88.5}$**	**Fo$_{89.2}$**	**Fo$_{87.8}$**

[ǂ] Model stochiometric olivine (allowing for 0.3% NiO and 0.2% MnO).
[§] Average chromite core composition in sample EN23VS043 (n=21).
[¦] Median starting composition of samples from Zuccarelli (2020) and this study (n=37).
[°] Median composition of gabbroic Eagle's Nest type dikes (n=20).

The most primitive olivine composition from the Eagle's Nest intrusion (Fo$_{88.2}$; this study) was identified, however, it is important to note that olivine composition is susceptible to modification by re-equilibration and/or reaction with immiscible sulfide melts (Li and Naldrett, 1999; Li et al., 2007). As a result, a primitive olivine composition was inferred utilizing MER's (Fig. 5.3). Considering only the subset of samples extracted above, the Mg# of the most primitive olivine is inferred to be ~Fo$_{89}$, which is broadly consistent with, but slightly more primitive than, the measured olivine (Fig. 5.3). Although the selected subset of samples represents compositions that are controlled by olivine accumulation, samples containing <30 wt% MgO are excluded from further consideration as they may contain cumulus plagioclase or pyroxene (Li and Ripley, 2011). The above outlined procedures yielded 37 suitable samples from which a median major oxide composition was taken as the starting composition (Table 5.1).

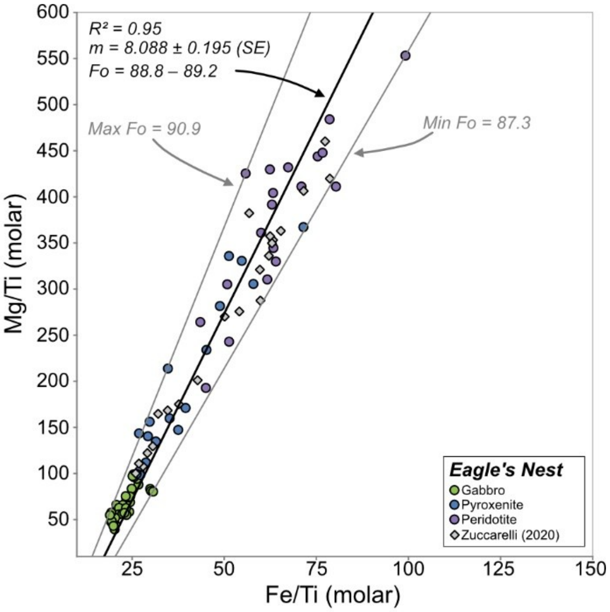

Figure 5.3: Bivariate Molar Element Ratio plot of Mg/Ti versus Fe/Ti of olivine only cumulate rocks (see text). The resulting slope is used to infer olivine composition (i.e. Mg# = [slope/(slope+1)]*100).

As mentioned above, the samples fall along the olivine-chromite cotectic cumulate trend (Fig. 4.24B), therefore, cotectic proportions (50:1; Lesher and Stone, 1996) were taken as the proportion for the removal from the starting composition. The composition of olivine was taken as the ideal stoichiometric composition of Fo_{89} with 0.3 wt% NiO and 0.2 wt% MnO, based on an average composition of olivine from barren ultramafic samples (Table 5.1). For chromite, the average core composition was taken as the representative composition from sample EN23VS043 (Table 5.1). This was done to avoid post-cumulus compositional modification recorded in the mineralized samples and chromite rims (Fig. 4.35).

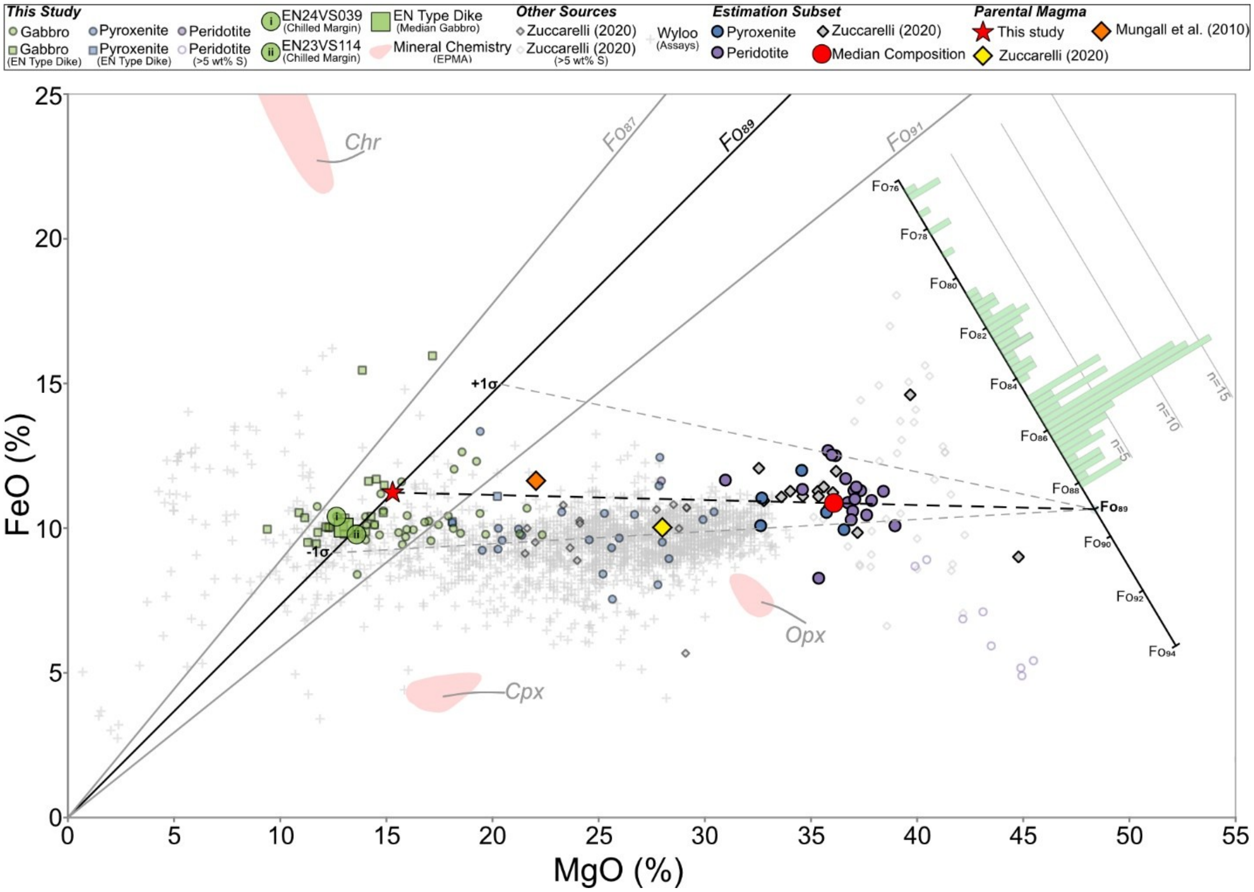

Figure 5.4: Bivariate FeO_t versus MgO plot showing whole rock geochemistry, mineral chemistry, and assay data for the Eagle's Nest intrusion and the genetically related Eagle's Nest type dikes. Also highlighted are the previously and newly estimated parental magma composition for the Eagle's Nest intrusion, as well as the compositions of chilled margins and average gabbroic Eagle's Nest type dikes (Table 5.1). Solid lines from the origin represent liquids in equilibrium with different olivine compositions (labelled by equilibrium Fo content). The olivine control line is shown together with stoichiometric olivine composition nodes (labelled by Fo content) with an overlaid histogram illustrating the olivine compositional variability (by grain average) analyzed in this study. Equilibrium liquids and olivine nodes along the control lines were calculated based on ideal stoichiometric compositions (allowing for 0.3 wt% NiO and 0.2 wt% MnO) and an Fe-Mg distribution coefficient of K_D=0.3 (Roeder and Emslie, 1970). Compositional ranges of chromite, orthopyroxene, and clinopyroxene analyzed in this study are highlighted by solid polygons. The dashed black line illustrated the modeled effect of removing the olivine-chromite mixture from the starting composition and the resulting parental magma. Grey dashed lines represent equivalent removal calculations using ±1σ of the median starting composition.

The parental magma composition was then calculated by incrementally removing a mixture of 98% Fo_{89} and 2% chromite until the residual liquid was in equilibrium with the inferred olivine composition. In all olivine-liquid calculations, iron was treated as total iron (FeO_t) and an Fe–Mg distribution coefficient between olivine and liquid of 0.3 was used (Roeder and Emslie, 1970).

The modelled parental magma composition yielded slightly higher FeO_t and MgO concentrations than the Eagle's Nest type dikes and the chilled margins (Table 5.1; Fig. 5.4). The resulting olivine compositions that would be in equilibrium with these 'liquids' fall within the range of both the observed and inferred compositions for the Eagle's Nest intrusion with $Fo_{88.5}$, $Fo_{89.2}$, and $Fo_{87.8}$ for the Eagle's Nest type dikes and chilled margins, respectively (Table 5.1). This suggests that the relative proportion of FeO_t and MgO in the chilled margins and Eagle's Nest type dikes is representative of the parental magma, despite the more intense alteration. In fact, restoration of the major oxide compositions by accounting for the addition of mobile elements (Na_2O and K_2O) in the introduced phases by alteration may result in similar compositions as the modelled parental magma. This can be achieved by accurately identifying and estimating mineral abundances, coupled with mineral chemistry, to determine the distribution of major oxides in the present samples and subsequent removal of alteration induced phases. This approach is similar in concept to 'backstripping' in the Equilibrium Distribution Method (Bédard 2001; Bain et al., 2023).

The estimated concentrations of FeO_t and MgO, as well as low TiO_2 and alkalis (Na_2O and K_2O; Table 5.1), suggest the parental magma composition was either a picritic or a komatiitic basalt in affinity, both of which contain 10–18 wt% MgO and <1 wt% TiO_2 (Lesher and Barnes, 2009). The difference between a picrite and a komatiitic basalt lies in textural distinction and association (Lesher and Barnes, 2009). The term picrite refers to olivine-porphyritic rocks that do not contain spinifex-textured olivine and/or pyroxene and are also not associated with komatiitic rocks. On the other hand, the term komatiitic basalt refers to rocks that contain spinifex texture or are directly related to a komatiitic magma (Lesher and Barnes, 2009). The cogenetic relationship of the Eagle's Nest intrusion and other intrusions hosting orthomagmatic mineralization within MLGB has been well established, they are collectively referred to as the Koper Lake subsuite (Houlé et al., 2019, 2020). In the Double Eagle intrusion, stratigraphically situated directly above the Eagle's Nest (Fig. 2.4), Azar (2010) identified an olivine with Fo_{90}. More recently, Laarman (2014) identified olivine compositions that range up to Fo_{94} in the Black Thor intrusion, the most primitive olivine compositions found to date across the Koper Lake subsuite. These primitive olivine compositions are consistent with a komatiitic magma. The well-established genetic association of the Eagle's Nest intrusion with the Double Eagle and Black Thor intrusions (i.e., Koper Lake subsuite) suggests a clear relationship between the Eagle's Nest intrusion to other intrusions that have a komatiitic affinity (Houlé et al., 2019, 2020). Therefore, the parental magma of the Eagle's Nest intrusion can be classified as a komatiitic basalt.

In addition to the major element composition of the parental magma, chromite composition can be used to evaluate the affinity of the melt from which it formed (Barnes and Roeder, 2001). The EPMA analysis of chromite grains within the Eagle's Nest intrusion revealed a wide range of compositions that reflect both primary and modified compositions (Fig. 4.35). Chromite is susceptible to hydrothermal and metamorphic alteration, which is accompanied by enrichment in Fe^{3+} and formation of magnetite or enrichment in Al, generally along the rims (Barnes, 2000; Barnes and Roeder, 2001). Taking into consideration chromite belonging to Groups B and C, found in mineralized peridotite, the textural evidence as well as the enrichment in Fe^{3+} and Al, suggests that their composition was significantly modified by metamorphic and/or hydrothermal alteration (Figs. 4.34 & 4.35; Barnes and Roeder, 2001). Taking into consideration only chromite analyses from Group A, which was characterized by the least altered appearance, the composition in both barren and mineralized samples is characterized by a relatively narrow range of Cr/(Cr+Al) ratios of 0.53–0.75 (M_d=0.68), a wider range in $Fe^{2+}/(Fe^{2+}+Mg)$ ratios of 0.44–0.85 (M_d=0.78), and mostly low $Fe^{3+}/(Fe^{3+}+Cr+Al)$ ratios of 0.05 and 0.24 (M_d=0.10; Fig. 4.35). Generally, chromite in komatiitic magmas is characterized by low Fe^{3+} contents which reflects the characteristics of a highly reduced mantle source (Roeder and Barnes, 2001). The chromite from Group A, however, deviates towards the chromite compositions in Groups B and C, which likely reflects the analysis of altered chromite rims. Overall, majority of the analyses of Group A chromite grains are consistent with derivation from a magma that has a komatiitic affinity (Roeder and Barnes, 2001). In addition, the composition of Group A chromite is similar in composition to the chromite found in the Double Eagle and Black Thor intrusions, which were similarly attributed to having a komatiitic affinity (Azar, 2010; Laarman, 2014).

The estimates from this study yielded a parental magma composition that contains 11.2 wt% FeO_t and 15.3 wt% MgO, significantly less primitive than previous estimates. The different results may be attributed to the parental magma estimation approach used (ultramafic cumulates versus chilled margins; Mungall et al., 2010) and/or to variations in sample selection (olivine-chromite cumulates versus olivine-only cumulates; Zuccarelli, 2020), and consequently previous estimates cannot be completely rejected (Fig. 5.4). The taken approach and the obtained composition in this study is not definitive, as the modelled estimates depend on both the starting composition and the removed mineral chemistry. The increase in availability of whole rock geochemical data for the Eagle's Nest intrusion, the identification of olivine more primitive than the estimated values, and changes in chromite composition will all affect the resulting estimates. However, the estimated parental magma is consistent with the identified olivine composition, chilled margins, and Eagle's Nest type dikes, suggesting it is a reasonable estimate.

5.3.2 Pressure and Temperature

To evaluate the emplacement depth and equilibration temperatures for the Eagle's Nest intrusion, the clinopyroxene-orthopyroxene pair (Equations 36 & 39 in Putrika, 2008) and clinopyroxene-only (Jorgenson et al., 2022) thermobarometers were applied. Three samples were evaluated using the pyroxene-pair thermobarometer (Fig. 5.5). During data processing, the phase within each sample that had the fewest analyses (i.e., orthopyroxene or clinopyroxene) was averaged and paired with each analysis of the phase that had the greater number of analyses. To test for equilibrium, the K_D (Fe – Mg)$_{cpx\text{-}opx}$ value for each of the pairs in a given sample was calculated ($K_D = (X_{Fe}^{cpx}/X_{Mg}^{cpx})/(X_{Fe}^{opx}/X_{Mg}^{opx})$). The majority of the calculated pairs have K_D values that range from 0.95 to 1.22, falling within the putative equilibrium value of 1.09±0.14, apart from five pairs that were excluded from further consideration as they fall outside the equilibrium value range (Putrika, 2008). Across the three samples, the resulting average pressure of equilibration ranges between ~5.5 and 6.1 kbar, equating to a depth of ~20 to 23 km (assuming a lithostatic gradient of 0.27 kbar/km; Kohlstedt et al., 1995) and equilibration temperature of ~1096 to 1122˚C (Fig. 5.5). The clinopyroxene-only thermobarometer utilizes a machine learning random forest approach of Jorgonson et al. (2022) using the algorithm implemented in Python3 tool Thermobar (Wieser et al., 2022) and was applied to each clinopyroxene analysis in each sample. Across the three samples, the resulting average pressure of equilibration ranges between ~5.3 and 6.2 kbar, equating to a depth of ~20 to 23 km (Kohlstedt et al., 1995) and equilibration temperature of ~1164 to 1176˚C (Fig. 5.5).

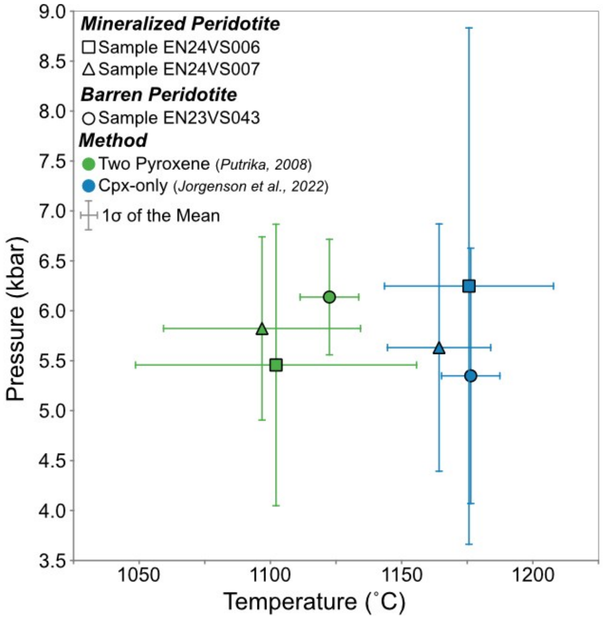

Figure 5.5: Calculated pressure and temperature estimates using pyroxene thermobarometers.

The emplacement depth for mafic to ultramafic intrusions may range from ~1 to 30 km (Hayward, 2024). The derived pressures for the Eagle's Nest are broadly consistent with several other mid- to lower-crustal intrusions, such as the Giles Complex (Ballhaus and Berry, 1989), Nova-Bollinger (Taranovic et al., 2022), and several intrusions of East Kimberley (Trudu and Hoatson, 2000). However, the estimated emplacement depth for the Eagle's Nest intrusion is inconsistent with previous interpretations, which placed it in the upper crust based on the preserved stratigraphic succession (Fig. 2.4; Mungall et al., 2010). In theory, the estimated depths could be tied with the intrusion's current position near surface and the estimated erosional level for the Oxford-Stull Domain (~10–15 km; Percival et al., 2012), assuming the current stratigraphic pile represents the remaining crust after erosion. However, it is uncertain whether ~20 km of crustal material was present at the time of emplacement. In addition, thermobarometry estimates should be interpreted with caution. Wieser et al. (2023) highlighted that clinopyroxene-based thermobarometers are highly sensitive to both analytical and experimental uncertainty. Pressure-sensitive oxides (e.g., Na_2O, Al_2O_3, Cr_2O_3) are often present in low abundance, therefore minor analytical imprecisions may propagate into a large pressure uncertainty (Wieser et al., 2023). Wieser et al. (2023) demonstrated that for a single clinopyroxene analysis, uncertainty in the calculated pressure may reach ~4 kbar (~15 km at a lithostatic gradient of 0.27 kbar/km; Kohlstedt et al., 1995) due to analytical error. Another limitation may be the limited number of analyses used and the possibility that they are not representative of the true compositions. However, in order to conclusively discard these estimates, emplacement depths for other portions of the Esker Intrusive Complex need to be obtained.

5.3.3 Forward Modelling

To test whether the estimated parental magma composition is representative of the observed crystallization sequence within the Eagle's Nest intrusion, forward modelling was conducted using the PELE (version 13.1) software developed by Boudreau (1999). The PELE software utilizes phase equilibria algorithm of the MELTS software (Ghiorso and Sack, 1995). The software interface allows for simulating a magma composition using equilibrium and fractional crystallization models at selected temperatures, pressures, and oxygen fugacities. The simulations of the parental magma composition were conducted at pressures of 0.5, 1.0, and 2.0 kbar, and oxygen fugacity between -2 and +2 log units relative to QFM (quartz-fayalite-magnetite) oxygen fugacity buffer. The modelled simulations allowed for precipitation of all petrographically observed silicate phases, excluding oxide phases. Attempts to include oxide phases (e.g., chromite) in the simulations resulted in software failure, and as a result they were excluded from the simulations.

First attempts to simulate the estimated parental magma composition failed to recreate the crystallization sequence observed within the intrusion, with orthopyroxene being the first phase to precipitate from the liquid. As a result, the estimated parental magma composition required minor adjustments. The concentrations of SiO_2, CaO, and Na_2O were adjusted to fit the liquid line of descent displayed by rocks of the Eagle's Nest intrusion (Fig. 4.23). The concentrations were adjusted to fit the liquid line of descent at 15.3 wt% MgO, with the modified composition containing 50.8 wt% SiO_2, 8.3 wt% CaO, and 1.4 wt% Na_2O. In the subsequent simulations, using the adjusted starting composition, the parental magma was assumed to be slightly hydrous based on the presence of igneous late-stage hornblende and biotite, with H_2O contents assumed to be 1.0 wt%.

Using the modified starting composition, a crystallization sequence of olivine → orthopyroxene → plagioclase → clinopyroxene (with or without → hornblende) was consistently reproduced using several different parameters. This crystallization sequence was reproduced at lower pressures of 0.5 and 1.0 kbar, across all simulated oxygen buffer conditions, using both fractional and equilibrium crystallization models (Figs. 5.6A–F). Crystallization of hornblende occurred when the simulations were modelled at oxygen buffers of QFM -2 and -1 and higher pressures (1.0 kbar; Figs. 5.6A–B). At higher oxygen fugacities of QFM +1 and +2, hornblende crystallized at lower pressures of 0.5 kbar (Figs. 5.6C–E). Simulations at 2.0 kbar, across all the selected oxygen buffers, the simulations failed to reproduce the crystallization sequence observed within the Eagle's Nest intrusion, with clinopyroxene forming after hornblende or clinopyroxene failing to crystallize (Figs. 5.6G–H). Failing to recreate the crystallization sequence of the intrusion at higher pressures, suggests that the high pressure estimates of this study are likely overestimated (Fig. 5.5). Across all the attempted simulations, the models did not form biotite. The modelled crystallization sequence of the modified parental magma composition, closely reproduces the crystallization sequence of silicate mineral phases within the

Eagle's Nest intrusion when modelled at lower pressures, consistent with emplacement into shallow crustal levels, across a range of oxygen fugacity buffers (Figs. 5.1 & 5.6A–F).

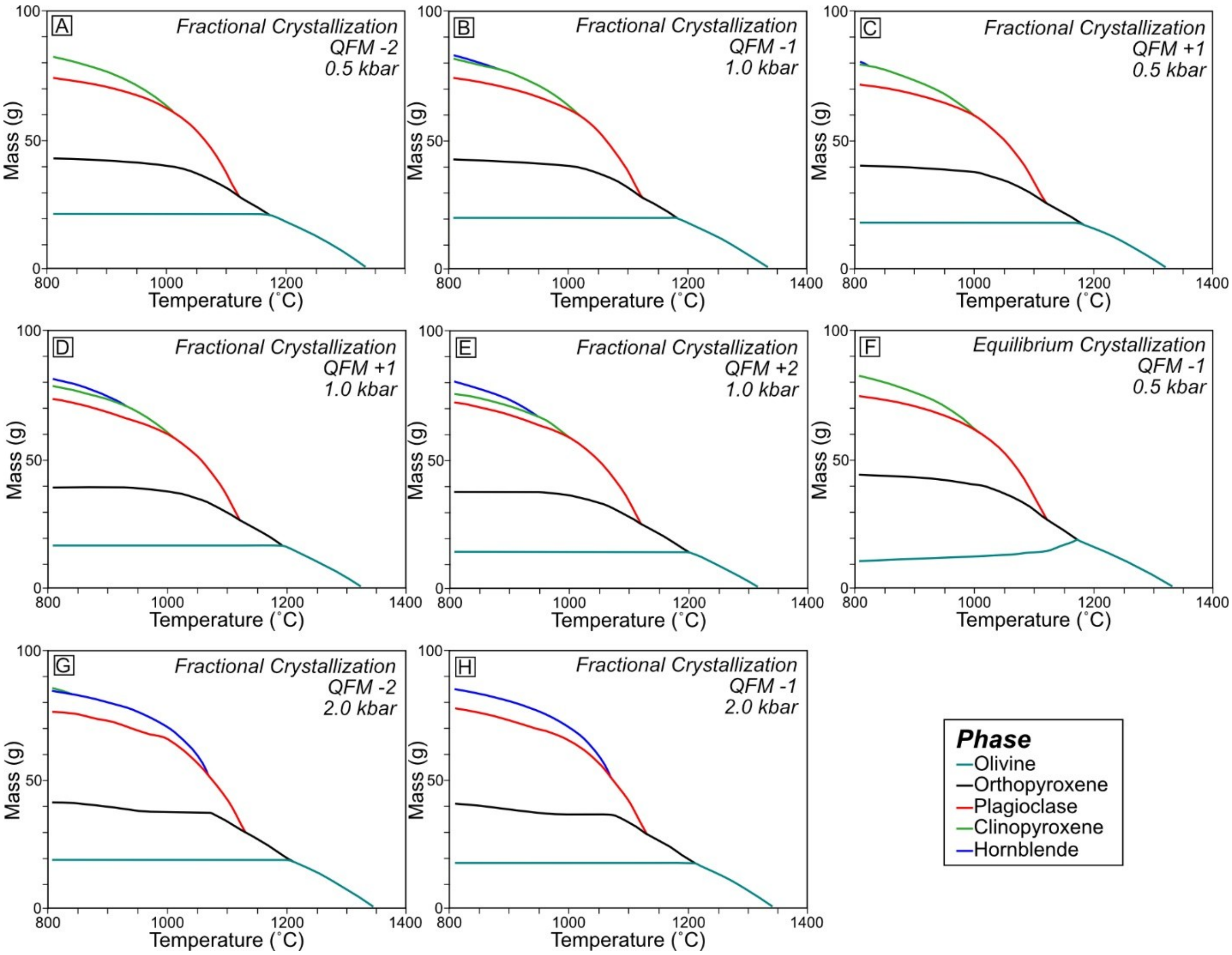

Figure 5.6: Examples of crystallization sequence simulation of the modified parental magma composition using the PELE software of Boudreau (1999). (A–B & G–H) Fractional crystallization models, and (F) Equilibrium crystallization model.

5.4 Origin of the Eagle's Nest Intrusion

5.4.1 Mantle Source and Tectonic Setting

The first stage in developing a magmatic Ni-Cu-(PGE) deposit requires the generation of a mafic to ultramafic magma through partial melting of the mantle (Naldrett, 2011). The generated melt composition and its metal budget are controlled by the degree and conditions of partial melting, as well as the mantle source composition (Lesher and Stone, 1996). Modelling by Naldrett (2011) shows that Cu and PGE concentrations in mantle-derived partial melts peak at ~13.5 % partial melting, at which stage all the mantle sulfides are incorporated into the melt. At higher degrees of partial melting, olivine progressively melts, increasing the MgO and Ni budget of the magma. The progressive melting of olivine produces increasingly MgO- and Ni-rich melts, simultaneously diluting the concentrations of Cu and PGEs. As a result, melts produced by lower degrees of partial melting would generally be more mafic and enriched in Cu and PGEs, whereas melts produced by higher degrees of partial melting would be more ultramafic and enriched in Ni.

Research has shown that the derivation of a Mg-rich komatiitic magma requires a high degree of partial melting (30–60 %) of a mantle source (Lesher and Stone, 1996; Lesher et al., 2001; Arndt et al., 2008). Because of the high degree of partial melting and the high liquidus temperatures required to generate such MgO-rich magmas, it is generally accepted that they were derived from mantle plumes (Campbell et al., 1989). Alternatively, some researchers have proposed that komatiitic magmas are a product of hydrous melting of the mantle wedge above subduction zones (Parman et al., 2001). While still debated, the most commonly accepted model is that komatiites are derived by high degrees of anhydrous partial melting associated with mantle plumes.

The geochemical signatures of komatiite and komatiite-associated magmas vary due to the composition of the mantle source, degree of partial melting, nature and degree of assimilation, fractional crystallization, processes that occur during ascent and emplacement, and the nature of post-magmatic processes (Lesher and Stone, 1996). Most komatiites are susceptible to alteration and metamorphism, which affect the distribution of highly mobile elements such as alkalis (e.g., Na, K, Rb, Ba). As a result, komatiite geochemistry and classification are often evaluated using Al, Ti, HFSE, and REE, which are typically considered the least mobile elements (Lesher and Stone, 1996). Barnes and Arndt (2019) summarized komatiite subdivision based on their distinct geochemical signatures. Aluminum-depleted (i.e., Barberton-type) and Al-undepleted (i.e., Munro-type) komatiites make up the two most common varieties, whereas the Al-enriched (i.e., Commondale-type) and Ti-enriched (i.e., Karasjok-type) are less common (Barnes and Arndt, 2019). The difference between the main types of komatiites is controlled by the depth and/or degree of partial melting (Arndt et al., 2008). Aluminum-undepleted komatiites form from high degrees of partial melting, in a source area where olivine represents the only residual mineral, generating chondritic Al_2O_3/TiO_2 and $Gd/Yb_{(n)}$ ratios. In contrast, Al-depleted komatiites form as a result of lower degrees of partial melting at greater depths, where garnet is stable. As a result, Al-depleted komatiites are characterized by lower Al_2O_3/TiO_2 and higher $Gd/Yb_{(n)}$ ratios consistent with the retention of garnet in the source. Komatiites are often spatially and temporally associated with komatiitic basalts. Two main models have been proposed to explain the relationship between komatiites and komatiitic basalts: (1) partial melting of the same mantle source, with komatiitic basalts forming as a result of lower degree of partial melting (Cambell et al., 1989; Lesher and Stone, 1996; Lesher et al., 2001), and (2) komatiitic basalts can be derived from komatiites by fractional crystallization accompanied by crustal contamination (Dostal, 2008).

The near chondritic Al_2O_3/TiO_2 ratio (~20) of the estimated parental magma (Al_2O_3/TiO_2 = 22.4) and the median ratio of the Eagle's Nest rocks (Al_2O_3/TiO_2 = 21.9) coupled with the predominantly flat HREE ($Gd/Yb_{(n)}$ = 1.16) suggest that the Eagle's Nest was derived from an Al-undepleted komatiite associated magma (Arndt et al., 2008). Generally, trace element patterns of uncontaminated Al-undepleted komatiites are characterized by a depletion in LREE and flat HREE patterns, similar to normal mid-ocean ridge basalts (N-MORB), which reflects the derivation of the magma from a previously depleted mantle source (Lesher and Stone, 1996). However, trace element patterns of the Eagle's Nest intrusion rocks are characterized by enriched LREE patterns, enrichment in LILE relative to HFSE, and they display pronounced negative Nb anomalies relative to Th (Figs. 4.25 & 5.7).

These signatures are consistent with the derivation of magmas from subduction-related settings or contamination by continental crust (Lesher et al., 2001; Murphy, 2007). Arc-like magma signatures are a product of crustal recycling during which the dehydration of a subducted slab results in the preferential enrichment of incompatible LILE in the mantle wedge, whereas HFSE are preferentially retained in oxide phases of the subducted slab (Murphy, 2007). Magmas derived from a depleted mantle sources should be systematically depleted in highly incompatible lithophile elements (e.g., Th, Nb, Ta, LREE) relative to moderately incompatible lithophile elements (e.g., Y, Zr, Hf) and highly compatible elements (e.g., Cr, Mg, Ni, Co) and as a result they are characterized by low $La/Sm_{(n)}$ values (<1; Lesher et al., 2001). On the other hand, continental crust is enriched in highly incompatible elements relative to moderately incompatible lithophile and highly compatible elements and is therefore characterized by $La/Sm_{(n)}$ values >1 and pronounced Nb anomalies. Contamination of a komatiitic melt by continental crust with an arc-like signature would result in a contaminated komatiitic magma that displays an arc-like signature, reflecting the addition of crustal material (Hollings et al., 1999). As a result, the high $La/Sm_{(n)}$ and pronounced Nb anomalies most likely reflect assimilation of continental crust (Figs. 4.25 & 5.7). The Eagle's Nest intrusion lacks a correlation between $La/Sm_{(n)}$ and $Gd/Yb_{(n)}$, which suggests that crustal contamination is not responsible for the variation in HREE (Fig. 5.7).

Consequently, Gd/Yb$_{(n)}$ ratios can be used to characterize the mantle source and petrogenetic processes, regardless of the degree of crustal contamination (Sproule et al., 2002). Thus, the Al_2O_3/TiO_2 and Gd/Yb$_{(n)}$ ratios are consistent with derivation from a relatively shallow mantle source, above the garnet stability field.

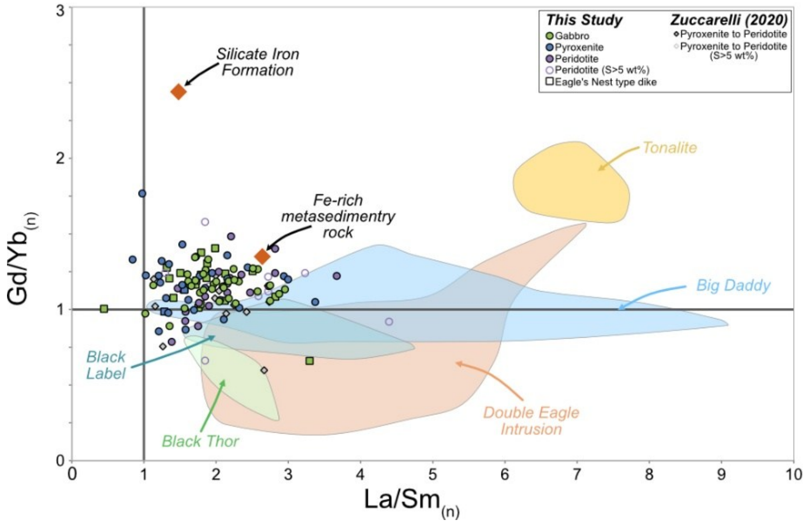

Figure 5.7: Bivariate plot of Gd/Yb$_{(n)}$ versus La/Sm$_{(n)}$ values for rocks of the Eagle's Nest intrusion, Eagle's Nest type dikes, wall rock tonalite, as well as the Double Eagle intrusion (Azar, 2010) and the Black Thor intrusion (i.e. Black Label, Big Daddy, and Black Thor; Laarman, 2014). Sample values normalized to primitive mantle values of Sun and McDonough (1989).

To evaluate the mantle source composition, Sm-Nd isotopic systematics were applied. Figure 5.8 illustrates the εNd_T values for the Eagle's Nest intrusion and the wall rock tonalite. The Eagle's Nest rocks are characterized by variable $\varepsilon Nd_{2735.5\ Ma}$ values ranging from -4.53 to +2.24, reflecting the assimilation signatures of older crustal material (see below). Two of the samples have $\varepsilon Nd_{2735.5\ Ma}$ values of +2.24 and +1.95 which are similar to the depleted mantle ($\varepsilon Nd_{2735.5\ Ma}$ = +2.16; DePaolo, 1981).

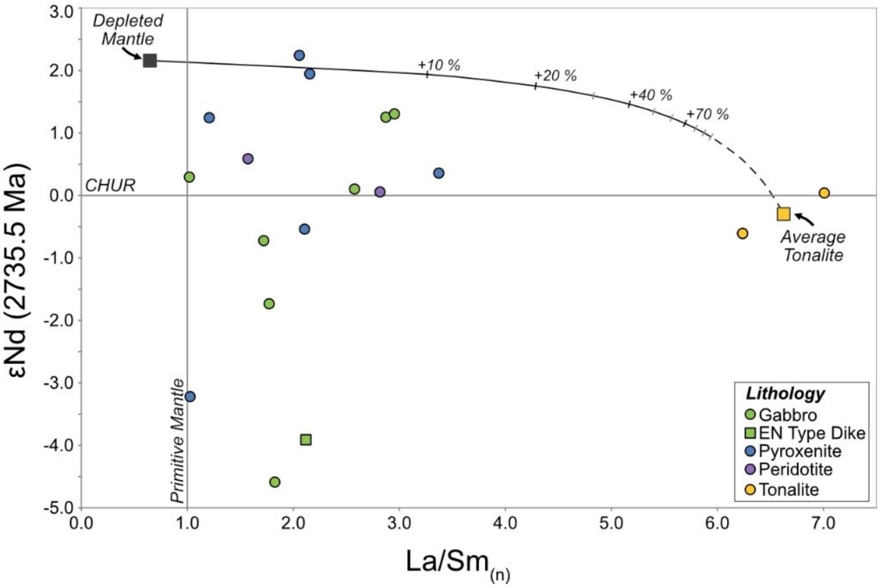

Figure 5.8: Bivariate plot of La/Sm$_{(n)}$ versus εNd$_{2735.5\ Ma}$ of the Eagle's Nest intrusion, an Eagle's Nest type dike, and wall rock tonalite. A mixing line between a depleted mantle source and the average tonalite value in samples EN23VS129 and EN23VS132. The εNd$_{2735.5\ Ma}$ of a depleted mantle (+2.16) were calculated from the DePaolo (1981) depleted mantle model. La (0.4 ppm) and Sm (0.4 ppm) of depleted upper mantle and normalizing values of primitive mantle from Sun and McDonough, 1989).

The depleted mantle εNd$_{2735.5\ Ma}$ signature in some of the Eagle's Nest rocks, the predominantly flat HREE distribution, and the near chondritic Al_2O_3/TiO_2 ratio suggest that the Eagle's Nest magma was derived from a plume-related, shallow, depleted mantle source, above the garnet stability field. Overlapping Gd/Yb$_{(n)}$ signatures of the Eagle's Nest intrusion with the Black Thor and the Double Eagle intrusions suggest they were derived from a similar mantle source (Fig. 5.7; Azar, 2010; Laarman, 2014). The majority of komatiite-associated Ni-Cu-(PGE) deposits occur in intracratonic rift zones, along rifted continental margins or in rifted arc environments (Arndt et al., 2008). Therefore, the Eagle's Nest intrusion is potentially related to rifting along the margin of the North Caribou Terrane, which was likely caused by the ascent of a mantle plume (Mungall et al., 2010; Houlé et al., 2020; Zuccarelli, 2020).

5.4.2 Crustal Contamination

To form a magmatic Ni-Cu-(PGE) deposit, a sulfur-undersaturated magma must reach sulfide saturation to be able to exsolve an immiscible sulfide liquid (Naldrett, 2011; Mungall, 2014). Sulfide saturation is reached at the point when the silicate magma is unable to dissolve sulfur at which point it forms an immiscible sulfide melt. The sulfide saturation point of a silicate melt can be triggered by an increase in pressure, a decrease in temperature, changes in magma composition, an increase in oxygen fugacity, or a decrease in sulfur fugacity (Barnes and Lightfoot, 2005). The introduction of S- and/or Si-rich crustal material through crustal contamination is often thought to be the driving factor in lowering the sulfur capacity of a melt, consequently provoking the formation of an immiscible sulfide liquid (Lesher et al., 2001; Naldrett, 2011; Barnes, 2023; Barnes and Lightfoot, 2005; Barnes et al., 2016).

Komatiites are often thought to be derived from sulfide undersaturated magmas, and incorporation of S-rich crustal rocks during ascent and/or emplacement is often thought to trigger sulfide saturation (Lesher et al., 2001; Barnes and Fiorentini, 2012). Due to the high liquidus temperatures of komatiitic magmas and their very low viscosity, komatiitic magmas can effectively transfer heat into the surrounding rocks and efficiently incorporate crustal material (Lesher and Stone, 1996). Evidence for extensive assimilation of multiple crustal sources during magma ascent and emplacement of the Eagle's Nest intrusion is abundant. The most obvious contaminant for the Eagle's Nest magma is the host tonalite. The Eagle's Nest intrusion contains an abundance of tonalite xenoliths, locally forming a magmatic breccia, as well as localized partial melting of the tonalite directly in contact with the intrusion, providing physical constraints of its incorporation during magma ascent and channelization (Figs. 4.3 & 4.4). The wall rock tonalite is highly enriched in LILE relative to HFSE, displaying pronounced negative Nb and Ti anomalies, which are indicative of its derivation from arc-magmas in a subduction zone setting (Fig. 4.28). As mentioned above, the incorporation of crustal material results in signatures that are complementary to the magmas derived from a depleted mantle source (Lesher et al., 2001). If the Eagle's Nest intrusion is a mantle-derived magma from a depleted mantle source, then the arc-like signatures suggest that the magma incorporated tonalite. Additionally, since the arc-like signatures are pervasive across all the examined portions of the intrusion, it suggests that the majority of the assimilation occurred during magma transport, rather than during emplacement, in order to distribute these signatures homogenously (Fig. 4.25).

The presence of certain mineral phases can also be used as an additional proxy to crustal contamination such as orthopyroxene (Ripley and Li, 2013; Barnes et al., 2016). The assimilation of silica-rich country rocks increases the SiO_2 activity of the melt, causing a shift in the liquidus phase from olivine to orthopyroxene (Ripley and Li, 2013). Therefore, the presence of oikocrystic orthopyroxene across the inner zone lithologies indicates that the Eagle's Nest magma assimilated enough silica-rich country rocks to make olivine unstable, and to form orthopyroxene oikocrysts (Fig. 4.16).

Crustal contamination can be further evaluated using Sm-Nd isotopes. In the Sm-Nd isotopic system, Nd is slightly more incompatible than Sm during partial melting and is therefore enriched in the partial melt (Dickin, 2005). Due to the compatibility differences between Sm and Nd, initial partial melts derived from the mantle would have lower Sm/Nd values than their mantle source (Dickin, 2005). Over time, the lower Sm/Nd values would result in negative εNd_T values in the continental crust. In contrast, the depleted mantle source magmas would have higher Sm/Nd values and evolve towards positive εNd_T values. Assimilation of older crustal material by a depleted mantle-derived magma would result in lower εNd_T relative to the mantle source.

The $\varepsilon Nd_{2735.5\ Ma}$ values for the Eagle's Nest intrusion display a range of values, some of which reflect depleted mantle signatures (Fig. 5.8). The two tonalite samples are characterized by CHUR-like $\varepsilon Nd_{2735.5\ Ma}$ values of -0.61 and +0.04 (Fig. 5.8). Eleven of the Eagle's Nest samples fall in the $\varepsilon Nd_{2735.5\ Ma}$ range of values between a depleted mantle source and the tonalite. The range of values in these 11 samples can be explained by the incorporation of the tonalite as evidenced by the deviation of the $La/Sm_{(n)}$ values and the $\varepsilon Nd_{2735.5\ Ma}$ values towards the tonalite (Fig. 5.8). A two-component mixing model between a depleted mantle source and the wall rock tonalite suggests that the $La/Sm_{(n)}$ and $\varepsilon Nd_{2735.5\ Ma}$ values of the 11 samples can be explained by the addition of up to 10–20 % of the tonalite (Fig. 5.8). However, four of the Eagle's Nest samples and the single Eagle's Nest type dike have $\varepsilon Nd_{2735.5\ Ma}$ values that range between -0.72 and -4.59, significantly lower than those of the tonalite. The more negative $\varepsilon Nd_{2735.5\ Ma}$ would require an older contaminant with significantly more negative $\varepsilon Nd_{2735.5\ Ma}$ values that cannot be explained by the assimilation of the tonalite alone. Mungall et al. (2010) noted the presence of iron formation xenoliths in the Eagle's Nest intrusion, which indicates that it was also a contaminant. Although there is no iron formation directly in contact with the Eagle's Nest intrusion, the wall-rock tonalite contains kilometer-scale enclaves of supracrustal rocks comprising iron-formation, as well as mafic intrusive and volcanic rocks, which have been interpreted to belong to the Butler assemblage (Houlé et al., 2020; Metsaranta and Houlé, 2020). The Butler assemblage has been identified as the oldest supracrustal assemblage (2828.7±0.9 Ma; Metsaranta and Houlé, 2020) within MLGB and therefore could explain the more negative $\varepsilon Nd_{2735.5\ Ma}$ values (Fig. 2.3). Additionally, the Attawapiskat, Victory, and Winiskisis supracrustal assemblages within MLGB are older than the magmatism of the Ring of Fire Intrusive Suite and may have also contributed to the crustal contamination signature of the Eagle's Nest (Fig. 2.3; Metsaranta and Houlé, 2020). Therefore, the negative $\varepsilon Nd_{2735.5\ Ma}$ values of some of the Eagle's Nest intrusion rocks could be explained by the assimilation of older supracrustal assemblages in addition to the tonalite during magma ascent and transport upstream. Unfortunately, no Sm-Nd isotope date is currently available for the older supracrustal assemblages. A comprehensive Sm-Nd isotope study of older supracrustal rocks is required to reach definitive conclusions.

5.4.2.1 Sulfur Isotopes

Incorporation of sulfur from a crustal source is often thought to be the primary driver for the formation of Ni-Cu-(PGE) deposits (Lesher and Stone, 1996; Lesher et al., 2001; Ripley and Li, 2003; Naldrett, 2011). Sulfur isotope systematics have been used to evaluate the contribution of crustal sulfur, specifically $\Delta^{33}S$, in conjunction with $\delta^{34}S$ when examining Archean-aged rocks (Ripley and Li, 2017). Sulfur isotopic systematics in magmatic systems reflect the enrichment of one of its stable isotopes relative to another (i.e., ^{32}S, ^{33}S, ^{34}S, ^{36}S). The variation across different stable sulfur isotopes is referred to as fractionation (denoted as δ or Δ notation), which can be governed by mass differences of each isotope (i.e., mass-dependent fractionation) or mass-independent processes (i.e., mass-independent fractionation; Farquhar and Wing, 2003; Seal, 2006). To evaluate the potential contribution of crustal sulfur, available S isotope data from the Black Thor and Double Eagle intrusions are incorporated (Fig. 5.9; Zuccarelli, 2020; Farhangi, unpublished data; Carson, unpublished data).

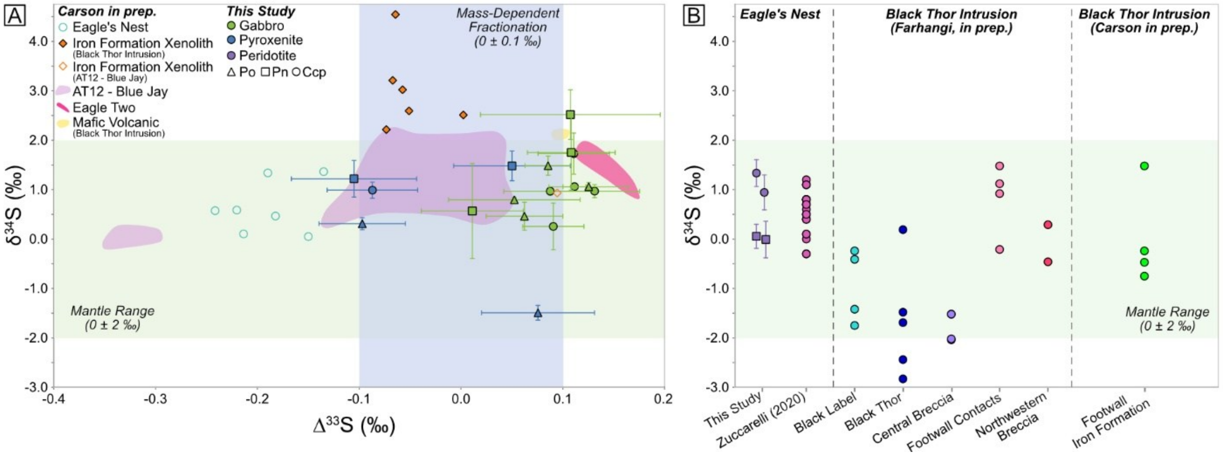

Figure 5.9: Sulfur isotopic signatures of the Eagle's Nest intrusion, and the Esker Intrusive Complex. (A) Bivariate plot of δ^{34}S versus Δ^{33}S for the Eagle's Nest intrusion (this study), Blue Jay, Eagle Two, mafic volcanic rocks from Black Thor, and iron formation xenoliths (Carson, unpublished data). (B) Bivariate plot of δ^{34}S plotted against location, for the Eagle's Nest intrusion (this study; Zuccarelli 2020), Black Thor intrusion (Farhangi, unpublished data), and Black Thor footwall iron formation (Carson, unpublished data). Data points from this study represent average sulfide phase composition in a given sample with 1σ error bars.

Except for pentlandite in two marginal gabbro samples, the variation in the δ^{34}S values across pentlandite, chalcopyrite and pyrrhotite tends to be positive and predominantly falls within the range of mantle-derived sulfur, between 0 ± 2 ‰ VCDT (Figs. 4.38 & 5.8; Ripley and Li, 2003). The observed range of δ^{34}S is slightly larger than previously obtained values for the Eagle's Nest intrusion, although it falls within the mantle range (Fig. 5.8; Zuccarelli, 2020; Carson, unpublished data). Additionally, the δ^{34}S value range of the Eagle's Nest intrusion falls in the range of Blue Jay, Eagle Two, and Black Thor, although some portions of the Black Thor intrusion tend to be more negative (Fig. 5.9; Farhangi, unpublished data; Carson, unpublished data). As mentioned above, iron formation xenoliths found within the Eagle's Nest intrusion are likely an additional contaminant and a potential source of crustal sulfur (Mungall et al., 2010; Zuccarelli, 2020). The δ^{34}S values for both the footwall iron formation in Black Thor and the iron formation xenolith from Blue Jay fall within the range of mantle-derived sulfur (Fig. 5.9; Farhangi, unpublished data; Carson, unpublished data). An exception to that is an iron formation xenolith from the Black Thor intrusion, which has $\delta^{34}S$ values that fall outside the mantle range, between +2.2 and +4.5 ‰ (Carson, unpublished data). The significant variation in the $\delta^{34}S$ values, which predominantly fall within the mantle range, cannot conclusively dictate its contribution to the Eagle's Nest intrusion. However, the deviation towards a positive $\delta^{34}S$ may suggest a sulfur contribution with a $\delta^{34}S$ signature similar to that of the iron formation xenolith from the Black Thor intrusion (Fig. 5.9). To conclusively establish whether a magma incorporated crustal sulfur, $\delta^{34}S$ values must significantly deviate from those of the mantle range (Ripley and Li, 2003). Studies have shown that $\delta^{34}S$ signatures in Archean sedimentary rocks often exhibit signatures that do not differ significantly from those of the mantle (Ripley and Li, 2017). The narrow range in $\delta^{34}S$ values of Archean sedimentary rocks is thought to be the product of low sulfate concentrations in the Archean and the inability of sulfate-reducing bacteria to generate major S isotope fractionation between sulfide and sulfate (Ripley and Li, 2017). Consequently, $\Delta^{33}S$ systematics are often used in the evaluation of a sulfur source derived from Archean sedimentary rocks (Ripley and Li, 2017).

Archean sedimentary rocks, older than ~2.45 Ga, record $\Delta^{33}S$ values that fall outside the mass-dependent fractionation range (i.e., 0 ± 0.1 ‰) recording mass-independent sulfur fractionation processes (Farquhar and Wing, 2003). These mass-independent fractionation signatures in Archean sedimentary rocks are thought to be the product of photochemical reactions in an oxygen-deprived atmosphere (Farquhar and Wing, 2003). As a result, incorporation of sulfur from Archean sedimentary rocks with a mass-independent fractionation signature, would be reflected in the incorporating magma. In comparison to $\delta^{34}S$ values of the Eagle's Nest intrusion, $\Delta^{33}S$ show a much greater range of both positive and negative values with a significant number of analyses that fall outside the mass-dependent fractionation range (Figs.

4.39 & 5.9). This deviation from the mass-dependent fractionation range suggests that the Eagle's Nest magma incorporated sulfur from Archean sedimentary rocks, which had a mass-independent fractionation signature (Fig. 5.9). The incorporation of crustal sulfur with mass-independent fractionation signatures is further supported by the strongly negative $\Delta^{33}S$ values for the Eagle's Nest intrusion obtained by Carson (unpublished data; Fig. 5.9). However, the current available $\Delta^{33}S$ data for iron formation xenoliths falls within the mass-dependent fractionation, which would be inconsistent with their incorporation into the Eagle's Nest magma (Fig. 5.9). The different $\Delta^{33}S$ values between the Eagle's Nest intrusion and the available iron formation data, suggests that the Eagle's Nest incorporated either multiple and/or different crustal sulfur sources than those that are currently available. Although no S isotope data was obtained for the host tonalite, it is unmineralized (0.01–0.04 wt% S), and it is unlikely to have been the source of crustal derived sulfur. However, its assimilation may have played a role in reaching the sulfide saturation point of the magma, by increasing the silica content and/or oxygen fugacity and consequently lowering the sulfur capacity of the melt (Barnes and Lightfoot, 2005; Ripley and Li, 2013). Nevertheless, the mass-independent $\Delta^{33}S$ signature recorded by the sulfides within the Eagle's Nest intrusion suggest incorporation of crustal derived sulfur. Further $\Delta^{33}S$ analysis of iron formation xenoliths found within the Eagle's Nest intrusion is required to establish the crustal sulfur source signature.

5.5 Regional Context

The interpretations drawn from this study are integrated with the current understanding of the mafic-ultramafic magmatism and the genetic framework responsible for the formation of orthomagmatic Ni-Cu-(PGE) and Cr deposits, to contextualize the formation of Eagle's Nest in relation to the Koper Lake subsuite. The most economically significant part of the Koper Lake subsuite occurs within a complex magmatic plumbing system, comprising the Esker Intrusive Complex (Fig. 2.4). The Esker Intrusive Complex consists of keel-like bodies (i.e., AT-12, AT-5, AT-1, C-6) and a blade-shaped dike (i.e., Eagle's Nest) at the paleostratigraphic base of the complex (i.e., northwestern extent; Fig. 2.4), which have been interpreted to be the feeder conduits to the overlaying through-shaped sill (i.e., Black Thor intrusion) and the transitional dike (i.e., Double Eagle intrusion; Houlé et al., 2020).

Previous workers have interpreted the formation of the Esker Intrusive Complex from komatiite-associated magmatism (Mungall et al., 2010; Azar, 2010; Laarman, 2014; Zuccarelli, 2020). The parental magma composition, trace element signatures, mineral chemistry, and radiogenic isotope signatures of the Eagle's Nest intrusion that were obtained in this study strongly support its derivation from a komatiite-associated magma (Table 5.1). Additionally, the results from this study suggest that magmas that formed the Eagle's Nest intrusion were derived from a depleted mantle source, with partial melting occurring above the garnet-stability field. Like other komatiitic magmas, high degrees of partial melting of a depleted mantle source are required for the generation of high-Mg magmas recorded in the Esker Intrusive Complex, fitting the commonly accepted model of its derivation from a mantle plume, which is often associated with extensional tectonic regimes (Campbell et al., 1989; Arndt et al., 2008). The current model for the RoFIS magmatism and the formation of the Esker Intrusive Complex has been interpreted to be caused by an upwelling mantle plume beneath the North Caribou Terrane, which resulted in rifting and thus the formation of guiding structures for the subsequent mantle plume-derived komatiitic melts (Fig. 2.2; Mungall et al., 2010; Houlé et al., 2020; Laudadio et al., 2022). These guiding structures have been interpreted as reactivated, subparallel, normal faults (i.e., keel-like bodies and blade-shaped dike), which allowed for continuous magma flow to the overlaying Black Thor and Double Eagle intrusions (Fig. 2.4; Houlé et al., 2020).

The feeder-conduit theory for the keel-like bodies to the overlaying Double Eagle and Black Thor intrusions is strongly supported by their physical continuity with the overlaying intrusions (Fig. 2.4). However, the connection between the Eagle's Nest and the Double Eagle intrusions is ambiguous, due to the truncation of the Eagle's Nest at depth by the Triple J fault (Fig. 2.4). Similarities in geochemical affinity, lithology, and mineralogy strongly support the genetic link of intrusions across the Esker Intrusive Complex, which implies a likely derivation from a shared primary mantle derived magma. Based on such similarities, Mungall et al. (2010) proposed that the Eagle's Nest intrusion acted as the feeder conduit to the overlaying Double Eagle intrusion. However, the Eagle's Nest hosts the only currently known economically significant magmatic Ni-Cu mineralization in the MLGB, and it lacks significant chromite mineralization as well as olivine-rich units, challenging the feeder conduit theory (Zuccarelli, 2020; Houlé et al., 2020). Such differences may arise from several interplaying factors, including magma flow dynamics, the relative timing of emplacement, and the composition of the parental magmas from which they formed.

The poorly defined internal differentiation of the Eagle's Nest intrusion, coupled with extensive evidence of thermochemical assimilation of the wall rock, implies that the Eagle's Nest intrusion accommodated a prolonged and high magma flux. High magma fluxes and prolonged flows within magma conduits are often thought to be a key factor in the formation of magmatic Ni-Cu deposits, as they provide ideal regions for extensive crustal assimilation, they facilitate a large magma to sulfide ratio (and therefore high metal tenors), and they may concentrate large volumes of dispersed sulfides (Barnes et al., 2016). These processes are often thought to play a key role in other, similar mineralized conduit systems such as the subvolcanic intrusions in the South Raglan trend (Mungall, 2007), and the Savannah deposit in the Kimberley region of Western Australia (Sproule et al., 2000). The differences in metal endowments across the Esker Intrusive Complex may lie in the varying stages or portions of the larger magmatic plumbing system that experienced different magma flow dynamics. The enclosed, blade-shaped geometry of the Eagle's Nest intrusion may imply a deeper portion of the magmatic plumbing system, which allowed for an extensive and prolonged magma flow to accumulate economically significant sulfide mineralization. In contrast, the subeconomic sulfide mineralization (e.g., Blue Jay) that occurs within the keel-like bodies and continuity with the overlaying intrusion is a potential record of the transitions of enclosed feeder conduits and the overlaying sills, where magma fluxes were less extensive and did not allow for extensive accumulation of sulfides. These keel-like bodies may be a record of the transitions of deeper or unpreserved, enclosed magma conduits, such as the Eagle's Nest intrusion.

In addition to the flow dynamics of the plumbing system, the differing characteristics may arise from the different parental magma from which they formed. The more evolved, komatiitic basalt parental magma composition of the Eagle's Nest in comparison to low-Mg komatiites in the overlaying Black Thor and Double Eagle intrusions is supported by the occurrence of less primitive olivine and absence of olivine adcumulate rocks in the Eagle's Nest (Table 4.1; Fig. 4.30). In addition, we propose that the Eagle's Nest intrusion lacks olivine-only cumulate rocks and is instead characterized by the presence of olivine and chromite in cotectic proportions, consistent with derivation from a more evolved parental magma compared to the overlaying intrusions (Fig. 4.24B). Studies have shown that mantle-derived melts with more primitive compositions (>20 wt% MgO) crystallize olivine only or less than cotectic proportions of olivine and chromite, whereas more evolved magmas would crystallize olivine and chromite in cotectic proportions (Lesher and Stone, 1996; Barnes, 1998).

Differences in parental magma compositions may arise from different degrees of partial melting of the mantle source and/or through magmatic differentiation processes operating during magma transport through the crust. Both komatiite and komatiitic basalt magmas require derivation from partial melting of a mantle source, however, komatiitic basalt magmas have been proposed to be derived from lower degrees of partial melting (~15–30 %) than komatiite magmas (~30–60 %; Lesher et al., 2001). The degree and depth of mantle partial melting have been attributed to the komatiite-picrite association in the Central Lapland Greenstone Belt (Hanski et al., 2001) and the relation of komatiites to the komatiitic basalts in the Abitibi Greenstone Belt (Sproule et al., 2002). Alternatively, the parental magma for Eagle's Nest intrusion may be more evolved as a product of the magmatic differentiation processes operating during magma transport through the crust. These may include prior olivine fractionation in a deeper staging chamber, which has been proposed to be responsible for the picritic and high-Al olivine tholeiite magmas in the Midcontinental Rift (Ripley et al., 2015), or fractional crystallization combined with crustal contamination which has been proposed as the cause for variation in the Kambalda Suite in Western Australia (Arndt and Jenner, 1986), and the Expo Intrusive Suite in the Cape Smith Greenstone Belt (Mungall, 2007).

The significant magmatic Ni-Cu mineralization of the Eagle's Nest intrusion in comparison to other parts of the Esker Intrusive Complex should not be attributed to a single process. The differing features and metal endowments across the Esker Intrusive Complex are likely a result of complex, self-organizing processes in which magma fluid dynamics, crystal fractionation and crustal contamination, mantle processes have influenced the parental magma compositions, and thus, the differing metal endowments across the complex plumbing system.

The Eagle's Nest intrusion is a unique part of the Esker Intrusive Complex as it hosts the only economically significant Ni-Cu mineralization within MLGB and that it forms a blade-shaped dike rather than a continuous keel-like structure. The differences in the metal endowments across the keel-like bodies may be a factor of each portion representing a different part of the larger magmatic plumbing system with the Eagle's Nest recording the deeper parts of the system, whereas the keel-like bodies record the shallower portion of the plumbing system and possibly what the transition may have looked like from the blade-shaped conduits into the larger overlaying sills.

Chapter 6 Conclusions

The Eagle's Nest intrusion is a mafic-ultramafic, blade-shaped dike that hosts conduit-style orthomagmatic sulfide mineralization. The intrusion can be subdivided into a marginal zone and an inner zone. The marginal zone comprises the outer most portion of the intrusion consisting of mafic intrusive rocks in contact with the host tonalite, whereas the inner zone is distal from the contact and consists of barren and mineralized ultramafic cumulate rocks.

The marginal zone exhibits the most evolved major and trace element compositions, consistent with the absence of olivine and the presence of plagioclase and represents the most intensely altered portion of the intrusion, rarely containing relict pyroxene, and often exhibiting pseudomorphic alteration. The scattered distribution of K_2O indicates that it was mobile and is caused in part by the presence of biotite. Highly variable contact relationships between the marginal zone rocks and the tonalite record a prolonged high magma flux, as evidence by partial melting, brecciation, and diffuse contacts, with rare sharp contacts indicative of a lower heat flux, which locally preserve rocks displaying evidence of rapid cooling and represent chilled margins.

The transition from the marginal zone into and within the inner zone is gradational and is marked by changes in the proportions of cumulus minerals (olivine and chromite), intercumulus minerals (orthopyroxene and clinopyroxene), and interstitial sulfides, between olivine-pyroxenite, barren peridotite, and mineralized peridotite. The coherent, linear major and trace element variations within the inner zone suggest that alteration was isochemical, and the patterns reflect magmatic differentiation processes that include olivine and chromite accumulation with variable proportions of trapped intercumulus silicate and/or sulfide melt.

Apart from a few mineralized peridotite samples, nearly all of the mafic and ultramafic rocks within the Eagle's Nest intrusion illustrate a coherent positive correlation between MgO and Cr_2O_3, which reflect the presence of olivine and chromite in cotectic proportions, consistent with petrographic observations. However, the few mineralized peridotite samples contain similar relative proportions of olivine and chromite but instead deviate from the olivine-chromite cotectic trend line. This deviation may be explained by the downward percolation model recorded by the patchy to poikilitic net-textured mineralization. The formation of patchy and poikilitic net-textured mineralization is the product the down migration of a sulfide melts through a cumulate pile, which results in the displacement of intercumulus silicate melt forming a range of sulfide mineralization textures. The displaced silicate melt composition is recorded within the intercumulus silicate phases trapped within the inter-crystalline spaces during the mutual migration of sulfide and silicate melt. The composition of the dominant intercumulus silicate phases within the mineralized samples is enriched in Cr_2O_3, with concentrations ranging up to 0.82 wt% in orthopyroxene and up to 1.25 wt% in clinopyroxene, similar to the composition in barren peridotite samples. Consequently, the presence of olivine and chromite in similar relative proportions in mineralized samples as in non-mineralized samples, the lesser abundance on Cr-rich intercumulus silicate phases, suggests that samples deviating from the olivine-chromite cotectic line are a product of a lesser abundance of Cr-rich intercumulus phases, rather than the presence of lesser amounts of chromite.

The average whole rock geochemistry of unmineralized ultramafic cumulate rocks, interpreted to contain olivine and chromite in cotectic proportions with variable intercumulus silicate minerals, was used to estimate a new parental magma composition. Through the incremental removal of cotectic proportions olivine (Fo_{89}) and chromite, the estimate yielded a parental magma composition that contains ~15 wt% MgO and ~11 wt% FeO_t, lower than previous estimates but in close agreement with the identified chilled margins, genetically related dikes, and obtained olivine composition ($Fo_{88.2}$) in this study. The low TiO_2 and alkali contents of the estimated parental magma, chromite mineral chemistry, and association to Black Thor and Double Eagle intrusions suggest that the Eagle's Nest was derived from a komatiite-associated magma and can be characterized as a komatiitic basalt.

Using forward modelling simulations in PELE, the study attempted to recreate the crystallization sequence of silicate phases within the intrusion. The concentrations of SiO_2, CaO, and Na_2O were slightly adjusted during the simulations due failure to crystallize olivine prior to orthopyroxene, suggesting that the obtained parental magma over estimated the concentration of SiO_2. The adjusted composition recreated the petrographically observed crystallization sequence of olivine → orthopyroxene → plagioclase → clinopyroxene (with or without → hornblende) at pressures of 0.5 and 1.0 kbar and oxygen buffers ranging from QFM -2 to QFM +2 using both fractional and equilibrium crystallization models. Attempts to recreate the crystallization sequence at higher pressures (i.e., 2.0 kbar) failed, which supports the suggestion that the pyroxene-only and two-pyroxene thermobarometers (~5.3 to 6.2 kbar) overestimated the crystallization pressures.

Trace element and isotope data of the Eagle's Nest, record a complex mantle source and contamination processes. Near chondritic ratio of Al_2O_3/TiO_2 and flat HREE patterns suggest that the Eagle's Nest represents an Al-undepleted komatiite-associated magma, derived from a relatively shallow mantle source, above the garnet stability region. The mantle source for the Eagle's Nest intrusion was further evaluated using Sm-Nd isotopes. Although the Eagle's Nest intrusion displays a wide range of $\varepsilon Nd_{2735.5\ Ma}$ between -4.53 and +2.24, two of the samples had positive values (+2.24 and +1.95) implying that the Eagle's Nest magma was derived from a depleted mantle source.

The presence of wall rock xenoliths and orthopyroxene, enrichment of LILE relative to HFSE, coupled with pronounced negative Nb anomalies suggest that the Eagle's Nest magma was extensively contaminated by crustal material that had an arc-like signature. In addition, the highly variable $\varepsilon Nd_{2735.5\ Ma}$ values suggest that crustal contamination not only occurred by the assimilation of the wall rock tonalite, but also by older supracrustal rocks, indicated by the more negative $\varepsilon Nd_{2735.5\ Ma}$ values (as low as -4.59) than the wall rocks tonalite (-0.61 and +0.04). Evidence of assimilation of sulfur derived from crustal material was further evaluated using S isotopes. The $\Delta^{33}S$ values of sulfides within the Eagle's Nest intrusion have highly variable signatures that fall outside the mass-dependent fractionation range. This suggests that the Eagle's Nest magma assimilated S from a crustal source that underwent mass-independent fractionation.

The Eagle's Nest intrusion is unique within the MLGB as it hosts the only known economically significant, magmatic sulfide mineralization, lacks significant chromite mineralization and olivine-only cumulate rocks. Such characteristics, in comparison to other portions of the Esker Intrusive Complex may be a product several processes that likely included magma flow dynamics, relative timing of emplacement, and the composition of the parental magma from which it formed. The more evolved parental magma composition of the Eagle's Nest intrusion, occurrence of less-primitive olivine, absence of olivine-only cumulate rocks are all consistent with the derivation of the Eagle's Nest intrusion from a more evolved magma in comparison to the Black Thor and Double Eagle intrusions.

References

Armstrong, J.T., 1988. Quantitative analysis of silicate and oxide materials: Comparison of Monte Carlo, ZAF and Phi-Rho-Z procedures. In Newbury, D.E. (Ed). *Analysis Microbeam–1988*. San Francisco: San Francisco Press, pp. 239–246.

Arndt, N.T., and Jenner, G.A., 1986. Crustally contaminated komatiites and basalts from Kambalda, Western Australia. *Chemical Geology*, vol. 56, pp. 229–255.

Arndt, N.T., and Fowler, A.D., 2004. Textures in komatiites and variolitic basalts. Eriksson, P.G., Altermann, W., Nelson, D.R., Mueller, W.U., and Catuneanu, O. (Eds.). In *The Precambrian Earth: Tempos and Events*. Elsevier, vol. 12(4) pp. 298–311.

Arndt, N.T., Lesher, C.M., and Barnes, S.J., 2008. Komatiite: Cambridge, Cambridge University Press. 467 p.

Azar, B., 2010. The Blackbird Chromite Deposit, James Bay Lowlands of Ontario, Canada: Implications for Chromitite Genesis in Ultramafic Conduits and Open Magmatic Systems. MSc Thesis, University of Toronto, Ontario, Canada, 154 p.

Bain, W.M., Hollings, P., Djon, L.M., Brzozowski, M.J., Layton-Matthews, D., Dobosz, A., and Stern, R.A., 2023. The geology, geochemistry, and magmatic evolution of the Legris Lake mafic–ultramafic complex, Ontario, Canada. *Mineralium Deposita*, vol. 59, pp. 85–108.

Ballhaus, C., and Berry, R.G., 1991. Crystallization Pressure and Cooling History of the Giles Layered Igneous Complex, Central Australia. *Journal of Petrology*, vol. 32(1), pp. 1–28.

Ballhaus, C., Fonseca, R.O., Münker, C., Kirchenbaur, M., and Zirner, A., 2015. Spheroidal textures in igneous rocks–Textural consequences of H2O saturation in basaltic melts. *Geochimica et Cosmochimica Acta*, vol. 167, pp. 241–252.

Barnes, S.J., 1998. Chromite in Komatiites, 1. Magmatic Controls on Crystallization and Composition. *Journal of Petrology*, vol. 39(10), pp. 1689–1720.

Barnes, S.J., 2000. Chromite in Komatiites, II. Modification during Greenschist to Mid-Amphibolite Facies Metamorphism. *Journal of Petrology*, vol. 41(3), pp. 387–409.

Barnes, S.J., 2023. Lithogeochemistry in exploration for intrusion-hosted magmatic Ni-Cu-Co deposits. *Geochemistry: Exploration, Environment, Analysis*, vol. 23(1), pp. geochem2022–025.

Barnes, S.J., and Roeder, P.L., 2001. The range of spinel compositions in terrestrial mafic and ultramafic rocks. *Journal of Petrology*, vol. 42(12), pp. 2279–2302.

Barnes, S.J., and Lightfoot, P.C., 2005. Formation of Magmatic Nickel Sulfide Ore Deposits and Processes Affecting Their Copper and Platinum Group Element Contents. *Economic Geology*, vol. One Hundredth Anniversary Volume, 35 p.

Barnes, S.J., and Fiorentini, M.L., 2012. Komatiite Magmas and Sulfide Nickel Deposits: A Comparison of Variably Endowed Archean Terranes. *Economic Geology*, vol. 107, pp. 755–780.

Barnes, S.J., and Arndt, N.T., 2019. Chapter 6 – Distribution and geochemistry of komatiites and basalts through the Archean. *Earth's Oldest Rocks*, pp. 103–132.

Barnes, S.J., Mair, W.D., and Curl, E.D., 2010. Composition of the Marginal Rocks and Sills of the Rustenburg Layered Suite, Bushveld Complex, South Africa: Implications for the Formation of the Platinum-Group Element Deposits. *Economic Geology*, vol. 105, pp. 1491–1511.

Barnes, S.J., Cruden, A.R., Arndt, N., and Saumur, B.M. 2016. The mineral system approach applied to magmatic Ni–Cu–PGE sulphide deposits. *Ore Geology Reviews*, vol. 76, pp. 296–316.

Barnes, S.J., Latypov, R., Chistyakova, S., Godel, B. and Schoneveld, L.E., 2021. Idiomorphic oikocrysts of clinopyroxene produced by a peritectic reaction within a solidification front of the Bushveld Complex. *Contributions to Mineralogy and Petrology*, vol. 176(5).

Barnes, S.J., Mungall, J.E., Le Vaillant, M.L., Godel, B., Lesher, C.M., Holwell, D.M., Lightfoot, P.C., Krivolutskaya, N., and Wei, B., 2017. Sulfide-silicate textures in magmatic Ni-Cu-(PGE) sulfide ore deposits: Disseminated and net-textured ores. *American Mineralogist*, vol. 102(3), pp. 473–506.

Bédard, J.H., 1994. A procedure for calculating the equilibrium distribution of trace elements among the minerals of cumulate rocks, and the concentration of trace elements in the coexisting liquids. *Chemical Geology*, vol. 118, pp. 143–153.

Bédard, J.H., 2001. Parental magmas of the Nain Plutonic Suite anorthosites and mafic cumulates: a trace element modelling approach. *Contributions to Mineralogy and Petrology*, vol. 141, pp. 747–771.

Bosi, F., Biagioni, C., and Pasero, M., 2019. Nomenclature and classification of the spinel supergroup. *European Journal of Mineralogy*, vol. 31(1), pp. 183–192.

Burgess, H., Gowans, R., Jacobs, C., Murahwi, C., and Damjanovic, B., 2012. Feasibility Study, McFaulds Lake property, Eagle's Nest project, James Bay lowlands Ontario, Canada. NI 43-101 Technical Report prepared for Noront Resources Ltd., 210 p.

Buse, S., Smar, L., Stott, G.M., and McIlraith, S.J., 2009. Precambrian geology of the Winisk Lake area. *Ontario Geological Survey*, Preliminary Map P.3607, scale 1:100 000.

Campbell, I.H., Griffiths, R.W., and Hill, R.I., 1989. Melting in an Archean mantle Plume: heads it's basalts, tails its komatiites. *Nature*, vol. 339, pp. 697–699.

Card, K.D., 1990. A review of the Superior Province of the Canadian Shield, a product of Archean accretion. *Precambrian Research*, vol. 48, pp. 99–156.

Card, K.D., and Ciesielski, A., 1986. DNAG#1. Subdivisions of the Superior Province of the Canadian Shield. *Geoscience Canada*, vol. 13(1), pp. 5–13.

Carson, H.J.E., Lesher, C.M., and Houlé, M.G., 2015. Geochemistry and petrogenesis of the Black Thor intrusive complex and associated chromite mineralization, McFaulds Lake greenstone belt, Ontario, in Ames, D.E., and Houlé, M.G. (Eds). *Targeted Geoscience Initiative 4*, Geological Survey of Canada, Open File 7856, pp. 87–102.

Carson, H.J.E., Unpublished Data. Geology, Geochemistry, and Petrogenesis of the Black Thor – Black Label Intrusion, McFaulds Greenstone Belt, Ontario. PhD Thesis, Laurentian University, Sudbury, Ontario, Canada.

Chai, G., and Naldrett, A.J., 1992. The Jinchuan ultramafic intrusion: cumulate of a high-Mg basaltic magma. *Journal of Petrology*, vol. 33(2), pp. 277–303.

Chantler, C.T., Olsen, K., Dragoset, R.A., Chang, J., Kishore, A.R., Kotochigova, S.A., and Zucker, D.S., 2005. X-Ray Form Factor, Attenuation and Scattering Tables (Version 2.1). National Institute of Standards and Technology, Gaithersburg, MD.

Chung, H., and Mungall, J.M., 2009. Physical constraints on the migration of immiscible fluids through partially molten silicates, with special reference to magmatic sulfide ores. *Earth and Planetary Science Letters*, vol. 286, pp. 14–22.

Corfu, F., and Stone, D., 1998. Age structure and orogenic significance of the Berens River composite batholiths, western Superior Province. *Canadian Journal of Earth Sciences*, vol. 35(10), pp. 1089–1109.

Davis, F.A., Cottrell, E., Birner, S.K., Warren, J.M. and Lopez, O.G., 2017. Revisiting the electron microprobe method of spinel-olivine-orthopyroxene oxybarometry applied to spinel peridotites. *American Mineralogist*, vol. 102(2), pp. 421–435.

Deer, W.A., Howie, R.A., and Zussman, J., 2013. An Introduction to the Rock-Forming Minerals–3rd Edition. The Mineralogical Society, London, 498 p.

DePaolo, D.J., 1981. Neodymium isotopes in the Colorado Front Range and crust-mantle evolution in the Proterozoic. *Nature*, vol. 291, pp. 193–196.

Dickin, A.P., 2005. Radiogenic isotope geology. Cambridge University Press, 492p.

Ding, T., Valkiers, S., Kipphardt, H., De Bièvre, P., Taylor, P.D.P., Gonfiantini, R., and Krouse, R., 2001. Calibrated sulfur isotope abundance ratios of three IAEA sulfur isotope reference materials and V-CDT with a reassessment of the atomic weight of sulfur. *Geochimica et Cosmochimica Acta*, vol. 65(15), pp. 2433–2437.

Dostal, J., 2008. Igneous Rock Associations 10. Komatiites. *Geoscience Canada*, vol. 35(1), pp. 21–31.

Douglas, R.J.W., 1973. Geological Provinces, Map 27-28, National Atlas of Canada–4th Edition. Department of Energy, Mines and Resources, Ottawa.

Downey, M., 2021. Eagle's Nest Ni-Cu-PGE deposit: 2020 Phase 1 Exploration Report. Noront Resources Limited, 174 p.

Farhangi, N., Unpublished Data. Geology, Geochemistry, and Petrogenesis of Ni-Cu-PGE Mineralization in the Black Label Intrusion, McFaulds Greenstone Belt, Ontario. MSc Thesis, Laurentian University, Sudbury, Ontario, Canada.

Farquhar, J., and Wing, B.A., 2003. Multiple sulfur isotopes and the evolution of the atmosphere. *Earth and Planetary Science Letters*, vol. 213(1–2), pp. 1–13.

Farquhar, J., Wu, N., Canfield, D., and Oduro, H., 2010. Connections between sulfur cycle evolution, sulfur isotopes, sediments, and base metal sulfide deposits. *Economic Geology*, vol. 105(3), pp. 509–533.

Fowler, A.D., Jensen, L.S., and Pelpquin, S.A., 1987. Varioles in Archean basalts; products of spherulitic crystallization. *Canadian Mineralogist*, vol. 25(2), pp. 275–289.

Fowler, A.D., Berger, B., Shore, M., Jones, M.I., and Ropchan, J., 2002. Supercooled rocks: development and significance of varioles, spherulites, dendrites and spinifex in Archaean volcanic rocks, Abitibi Greenstone belt, Canada. *Precambrian Research*, vol. 115, pp. 311–328.

Gill, J.E., 1949. Natural divisions of the Canadian Shield. Royal Society of Canada Transactions, vol. 43(4), pp. 61–69.

Gélinas, L., Brooks, C., and Trzcienski, W.E., 1976. Archaean variolites—quenched immiscible liquids. *Canadian Journal of Earth Sciences*, vol. 13(2), pp. 210–230.

Godel, B., Seat, Z., Maier, W.D., and Barnes, S.J., 2011. The Nebo-Babel Ni-Cu-PGE Sulfide Deposit (West Musgrave Block, Australia): Pt. 2. Constraints on Parental Magma and Processes, with Implications for Mineral Exploration. *Economic Geology*, vol. 106, pp. 557–584.

Goodwin, A.M., 1978. Archean crust in the Superior Geotraverse area: Geological Overview. In Proceedings of the 1978 Archean Geochemistry Conference, Department of Geology, University of Toronto, pp. 73–106.

Government of Canada, 2022. The Canadian Critical Minerals Strategy. Ottawa, Natural Resources Canada, 49 p.

Hanski, E., Huhma, H., Pastas, P., and Kamenetsky, V.S., 2001. The Palaeoproterzoic Komatiite–Picrite Association of Finnish Lapland. *Journal of Petrology*, vol. 42(5), pp. 855–876.

Haggerty, S.E. 1991. Oxide mineralogy of the upper mantle. *Reviews in Mineralogy and Geochemistry*, vol. 25(1), pp. 355–416.

Hawthorne, F.C., Oberti, R., Harlow, G.E., Maresch, W.V., Martin, R.F., Schumacher, J.C., and Welch, M.D. 2012. Nomenclature of the amphibole supergroup. *American Mineralogist*, vol. 97(11-12), pp. 2031–2048.

Hayward, N. 2024. Improving Multiscale Structural Targeting Precision for Large Ni-Cu (±PGE, Co) Sulfide Discoveries from Global Case Studies. *Economic Geology*, vol. 119(8), pp. 1745–1767.

Herzberg, C., Asimow, P.D., Arndt, N., Niu, Y., Lesher, C.M., Fitton, J.G., Cheadle, M.J., and Saunders, A.D., 2007. Temperatures in ambient mantle and plumes: Constraints from basalts, picrites, and komatiites. *Geochemistry, Geophysics, Geosystems*, vol. 8(2), pp. 1–34.

Hollings, P., Wyman, D., and Kerrich, A., 1999. Komatiite–basalt–rhyolite volcanic associations in Northern Superior Province greenstone belts: significance of plume-arc interaction in the generation of the proto continental Superior Province. *Lithos*, vol. 46(1), pp. 137–161.

Houlé, M.G., Lesher, C.M., McNicoll, V.J., Metsaranta, R.T., Sappin, A.-A., Goutier, J., Bécu, V., Gilbert, H.P., and Yang, X.M., 2015. Temporal and spatial distribution of magmatic Cr-(PGE), Ni-Cu-(PGE), and Fe-Ti-(V) deposits in the Bird River–Uchi–Oxford-Stull–La Grande Rivière–Eastmain domains: a new metallogenic province within the Superior Craton, in Ames, D.E., and Houlé, M.G. (eds). *Targeted Geoscience Initiative 4*, Geological Survey of Canada, Open File 7856, pp. 35–48.

Houlé, M.G., Lesher, C.M., Metsaranta, R.T., and Sappin, A.-A., 2019. Architecture of magmatic conduits in chromium-PGE and Ni-Cu-PGE ore systems in Superior Province: example from the 'Ring of Fire' region, Ontario, in Rogers, N. (ed). *Targeted Geoscience Initiative: 2018 Report of Activities,* Geological Survey of Canada, Open File 8549, pp. 441–448.

Houlé, M.G., Lesher, C.M., Metsaranta, R.T., Sappin, A.-A., Carson, H.J.E., Schetselaar, E.M., McNicoll, V.J., and Laudadio, A., 2020. Magmatic architecture of the Esker intrusive complex in the Ring of Fire intrusive suite, McFaulds Lake greenstone belt, Superior Province, Ontario: Implications for the genesis of Cr and Ni-Cu-(PGE) mineralization in an inflationary dyke-chonolith-sill complex, in Bleeker, W., and Houlé M.G. (eds). *Targeted Geoscience Initiative 5*, Geological Survey of Canada, Open File 8722, pp. 141–163.

Houlé, M.G., Lesher, C.M., Sappin, A.-A., Bédard, M.-P., Goutier, J., and Yang, X.M., 2020. Overview of Ni-Cu-(PGE), Cr-(PGE), and FeTi-V magmatic mineralization in the Superior Province: Insights on metallotects and metal endowment, in Bleeker, W., and Houlé M.G. (eds). *Targeted Geoscience Initiative 5*, Geological Survey of Canada, Open File 8722, pp. 117–139.

Huppert, H.E., and Sparks, R.S.J. ,1989. Chilled margins in igneous rocks. *Earth and Planetary Science Letters*, vol. 92(3-4), pp. 397–405.

Jorgenson, C., Higgins, O., Petrelli, M., Bégué, F., and Caricchi, L., 2022. A machine learning-based approach to clinopyroxene thermobarometry: Model optimization and distribution for use in Earth sciences. *Journal of Geophysical Research: Solid Earth*, 127.

Kohlstedt, D.L., Evans, B., and Mackwell, S.J., 1995. Strength of the lithosphere: constraints imposed by laboratory experiments. *Journal of Geophysical Research*, vol. 100(B9), pp. 17,587–17,602.

Kuzmich, B., Hollings, P., and Houlé, M.G., 2015. Petrogenesis of the ferrogabbroic intrusions and associated Fe-Ti-V-(P) mineralization within the McFaulds greenstone belt, Superior Province, northern Ontario, in Ames, D.E., and Houlé, M.G. (eds). *Targeted Geoscience Initiative 4*, Geological Survey of Canada, Open File 7856, pp. 115–123.

Laarman, J.E., 2014. A Detailed Metallogenic Study of the McFaulds Lake Chromite Deposits, Northern Ontario. PhD Thesis, University of Western Ontario, London, Canada, 529 p.

Laudadio, A.B., Schetselaar, E.M., Mungall, J.E., and Houlé, M.G., 2022. 3D modeling of the Esker intrusive complex, Ring of Fire intrusive suite, McFaulds Lake greenstone belt, Superior Province: Implications for mineral exploration. *Ore Geology Reviews*, vol. 145, pp. 1–23.

Le Maitre, R.W., 2002. Igneous Rocks, A Classification and Glossary of Terms – 2nd edition. Recommendations of the International Union of Geological Sciences Subcommission on the Systematics of Igneous Rocks, Cambridge University Press.

Lesher, C.M., and Stone, W.M., 1996. Exploration geochemistry of komatiites, in Wyman, D.A. (ed). Igneous Trace Element Geochemistry Applications for Massive Sulphide Exploration. *Geological Association of Canada*, Short Course Notes, vol. 12, pp. 153–204.

Lesher, C.M, and Barnes, S.J., 2009. Komatiite-associated Ni-Cu-(PGE) deposits, in Li, C. and Ripley, E.M. (eds). Magmatic Ni-Cu-PGE deposits: Genetic models and exploration. *Geological Publishing House of China*, pp. 27–101.

Lesher, C.M., Burnham, M.O., Keays, R., Barnes, S.J., and Hulbert, L., 2001. Trace-element geochemistry and petrogenesis of barren and ore-associated komatiites. *The Canadian Mineralogist*, vol. 39, pp. 673–696.

Li, C., and Naldrett, A.J., 1999. Geology and petrology of the Voisey's Bay intrusion: reaction of olivine with sulfide and silicate liquids. *Lithos*, vol. 47(1–2), pp. 1–31.

Li, C., Naldrett, A.J., and Ripley, E.M., 2007. Controls on the Fo and Ni Contents of Olivine in Sulfide-bearing Mafic/Ultramafic Intrusions: Principles, Modeling, and Examples from Voisey's Bay. *Earth Science Frontiers*, vol. 14(5), pp. 177–185.

Li, C., and Ripley, E.M., 2011. The Giant Jinchuan Ni-Cu-(PGE) Deposit: Tectonic Setting, Magma Evolution, Ore Genesis, and Exploration Implications, in Li, C., Ripley, E.M (eds). *Reviews in Economic Geology*, vol. 17, pp. 163–180.

Locock, A.J., 2014. An Excel spreadsheet to classify chemical analyses of amphiboles following the IMA 2012 recommendations. *Computers & Geosciences*, vol. 62, pp. 1–11.

Metsaranta, R.T., and Houlé, M.G., 2017a. Geochronology, mineral deposit, drill-core relogging and drill-core compilation data from the Winiskisis Channel, McFaulds Lake and Highbank Lake areas, "Ring of Fire" region, northern Ontario. Ontario Geological Survey, Miscellaneous Release – Data 343.

Metsaranta, R.T., and Houlé, M.G., 2017b. Precambrian geology of the Highbank Lake area, "Ring of Fire" region, Ontario—Southern sheet: Ontario Geological Survey, Preliminary Map P.3806. Geological Survey of Canada, Open File 8202.

Metsaranta, R.T., and Houlé, M.G., 2017c. Precambrian geology of the McFaulds Lake area, "Ring of Fire" region, Ontario—Central sheet: Ontario Geological Survey, Preliminary Map P.3805. Geological Survey of Canada, Open File 8201, scale 1:100 000.

Metsaranta, R.T., and Houlé, M.G., 2017d. Precambrian geology of the Winiskisis Channel area, "Ring of Fire" region, Ontario—Northern sheet: Ontario Geological Survey, Preliminary Map P.3804. Geological Survey of Canada, Open File 8200, scale 1:100 000.

Metsaranta, R.T., and Houlé, M.G., 2020. Precambrian geology of the McFaulds Lake "Ring of Fire" region, northern Ontario. Ontario Geological Survey, Open File Report 6359, 260 p.

Metsaranta, R.T., Houlé, M.G., McNicoll, V.J., and Kamo, S.L., 2015. Revised geological framework for the McFaulds Lake greenstone belt, Ontario, in Ames, D.E., and Houlé, M.G. (eds). *Targeted Geoscience Initiative 4*, Geological Survey of Canada, Open File 7856, pp. 61–73.

Mungall, J.E., 2007. Crustal Contamination of Picritic Magmas During Transport Through Dikes: the Expo Intrusive Suite, Cape Smith Belt, New Quebec. Journal of Petrology, vol. 15(5), pp. 1021–1039.

Mungall, J.E., 2014. Geochemistry of Magmatic Ore Deposits, *in* Treatise on Geochemistry: Elsevier, pp. 195–218.

Mungall, J.E., Harvey, J.D., Balch, S.J., Azar, B., Atkinson, J., and Hamilton, M.A., 2010. Eagle's Nest a Magmatic Ni-Sulfide Deposit in the James Bay Lowlands, Ontario, Canada, in The Challenge of Finding New Mineral Resources: Global Metallogeny, Innovative Exploration, and New Discoveries, Volume II: Zinc-Lead, Nickel-Copper-PGE, and Uranium. *Society of Economic Geologists*, Special Publication 15, pp. 539–557.

Murphy, J., 2007. Igneous Rock Associations 8. Arc Magmatism II: Geochemical and Isotopic Characteristics. *Geoscience Canada*, vol. 34, pp. 7–35.

Naldrett, A.J., 1973. Nickel sulfide deposits—their classification and genesis, with special emphasis on deposits of volcanic association. *Canadian Institute of Mining, Metallurgy and Petroleum,* CIM Bulletin, vol. 66, pp. 45–63.

Naldrett, A.J., 2004. Magmatic Sulfide Deposits: Geology, Geochemistry and Exploration. Springer-Verglag, Berlin, 727 p.

Naldrett, A.J., 2011, Fundamentals of Magmatic Sulfide Deposits. *Reviews in Economic Geology*, vol. 17, pp. 1–50.

Nicholls, J., and Russell, J.K., 2016. Igneous rock associations 20. Pearce element ratio diagrams: linking geochemical data to magmatic processes. *Geoscience Canada*, vol. 43(2), pp. 133–146.

O'Donohoe, D., and French, A., 2003. Summary of exploration work on anomalies SP3-0029 Claim P1242319 and SP3-0029 Claim P1242329, Spider-3 Joint venture. Assessment report submitted to MNDM on behalf of De Beers Canada Exploration Inc., 102 p.

Parman, S.W., Grove, T.L. and Dann, J.C., 2001. The production of Barberton komatiites in an Archean subduction zone. *Geophysical Research Letters*, vol. 28(13), pp. 2513–2516.

Pearce, T.H., 1968. A contribution to the theory of variation diagrams. *Contributions to Mineralogy and Petrology*, vol. 19, pp. 142–157.

Percival, J.A. 2007. Geology and metallogeny of the Superior Province, Canada, in Goodfellow, W.D. (Ed.). *Mineral Deposits of Canada: A Synthesis of Major Deposit-Types, District Metallogeny, the Evolution of Geological Provinces, and Exploration Methods*, Geological Association of Canada, Mineral Deposits Division, Special Publication 5, pp. 903–928.

Percival, J.A., Sanborn-Barrie, M., Skulski, T., Stott, G.M., Helmstaedt, H., and White, D.J., 2006. Tectonic evolution of the western Superior Province from NATMAP and Lithoprobe studies. *Canadian Journal of Earth Sciences*, vol. 43, pp. 1085–1117.

Percival, J.A., Skulski, T., Sanborn-Barrie, M., Stott, G., Leclair, A., Corkery, T., and Boily, M., 2012. Geology and tectonic evolution of the Superior Province, Canada, Chapter 6, in Percival, J.A., Cook, F.A., and Clowes, R.M. (eds). *Tectonic Styles in Canada: The LITHOPROBE Perspective*, Geological Association of Canada, Special Paper 49, pp. 321–378.

Putirka, K.D., 2008. Thermometers and barometers for volcanic systems. *Reviews in Mineralogy and Geochemistry*, vol. 69, pp. 61–120.

Ripley, E.M., and Li, C., 2003. Sulfur Isotope Exchange and Metal Enrichment in the Formation of Magmatic Cu-Ni-(PGE) Deposits. *Economic Geology*, vol. 98(3), pp. 635–641.

Ripley, E.M., and Li, C., 2013. Sulfide Saturation in Mafic Magmas: Is External Sulfur Required for Magmatic Ni-Cu-(PGE) Ore Genesis? *Economic Geology*, vol. 108(1), pp. 45–58.

Ripley, E.M., and Li, C., 2017. A review of the application of multiple S isotopes to magmatic Ni-Cu-PGE deposits and the significance of spatially variable Δ^{33}S values. *Economic Geology*, vol. 112(4), pp. 983–991.

Ripley, E.M., Dong, S., Li, C., and Wasylenki, L.E., 2015. Cu isotope variations between conduit and sheet-style Ni-Cu-PGE sulfide mineralization in the Midcontinent Rift System, North America. *Chemical Geology*, vol. 414, pp. 59–69.

Roeder, P.L., and Emsile, R.F., 1970. Olivine-liquid equilibrium. *Contributions to Mineralogy and Petrology*, vol. 29, pp. 275–289.

Russell, J.K. and Stanley, C.R., 1990. A theoretical basis for the development and use of chemical variation diagrams. *Geochimica et Cosmochimica Acta*, vol. 54(9), pp. 2419–2431.

Sage, R.P., 2000. Kimberlites of the Attawapiskat area, James Bay lowlands, northern Ontario. Ontario Geological Survey, Open File Report 6019, 341 p.

Sappin, A.-A., Houlé, M.G., Lesher, C.M., Metsaranta, R.T., and McNicoll, V.J., 2015. Regional characterization of mafic-ultramafic intrusions in the Oxford-Stull and Uchi domains, Superior Province, Ontario, in Ames, D.E., and Houlé, M.G. (eds). *Targeted Geoscience Initiative 4*, Geological Survey of Canada, Open File 7856, pp. 75–85.

Skulski, T., Corkery, M.T., Stone, D., Whalen, J.B., and Stern, R.A., 2000. Geological and geochronological investigations in the Stull Lake-Edmund Lake greenstone belt and granitoid rocks of the northwestern Superior Province. Report of Activities 2000, pp. 117–128.

Smith, W.D., Mair, W.D., and Bliss, I., 2021. The geology, geochemistry, and petrogenesis of the Huckleberry Cu-Ni-PGE prospect in the Labrador Trough, Canada: Perspectives for regional prospectivity. *Ore Geology Reviews*, vol. 128, 103905.

Smith, W.D., Jenkins, C.M., Augustin, C.T., Virtanen, V.J., Vukmanovic, Z., and O'Driscoll, B., 2024. Layered intrusions in the Precambrian: Observations and perspectives. *Precambrian Research*, 50th Anniversary Invited Review, vol. 415, 107615.

Spath, C.S.I., 2017. Geology and genesis of hybridized ultramafic rocks in the Black Label hybrid zone of the Black Thor intrusive complex, McFaulds Lake greenstone belt, Ontario, Canada. MSc Thesis, Laurentian University, Sudbury, Ontario, Canada, 102 p.

Sproule, R.A., Lesher, C.M., Ayer, J.A., Thurston, P.C., and Herzberg, C.T., 2002. Spatial and temporal variations in the geochemistry of komatiites and komatiitic basalts in the Abitibi greenstone belt. *Precambrian Research*, vol. 115, pp. 153–186.

Stanley, C.R., 2020. Molar element ratio analysis of lithogeochemical data: a toolbox for use in mineral exploration and mining. *Geochemistry: Exploration, Environment, Analysis*, vol. 20(2), pp. 233–256.

Stanley, C.R. and Russell, J.K., 1989. Petrologic hypothesis testing with Pearce element ratio diagrams: Derivation of diagram axes. *Contributions to Mineralogy and Petrology*, vol. 103(1), pp. 78–89.

Stockwell, C.H., 1982. Proposals for time classification and correlation of Precambrian rocks and events in Canada and adjacent areas of the Canadian Shield, Part I: A time classification of Precambrian rocks and events. Geological Survey of Canada, vol. 19.

Stott, G.M., 1997. The Superior Province, Canada, in de Wit, M.J. and Ashwal, L.D. (eds). *Greenstone Belts*, Oxford Monograph on Geology and Geophysics, vol. 35, pp. 480–507.

Stott, G.M., Corkery, M.T., Percival, J.A., Simard, M., and Goutier, J., 2010. A revised terrane subdivision of the Superior Province in Ontario. Ontario Geological Survey Summary of Field Work and Other Activities 2010, Open File Report 6260, pp. 20–1 to 20–10.

Sun, S., and McDonough, W.F., 1989. Chemical and isotopic systematics of oceanic basalts: implications for mantle composition and processes. Geological Society, London, Special Publications, vol. 42(1), pp. 313–345.

Taranovic, V., Barnes, S.J., Beresford, S., Williams, M., MacRae, C., and Schoneveld, L.E., 2022. Nova-Bollinger Ni-Cu sulfide ore deposits, Fraser zone, Western Australia: Petrogenesis of the host intrusions. *Economic Geology*, vol. 117(2), pp. 455-484.

Thurston, P.C., 1991. Archean geology of Ontario, in Thurston, P.C., Williams, H.R., Sutcliffe, R.H., and Stott, G.M. (eds), *Geology of Ontario*, Ontario Geological Survey, vol. 4, pp. 73–78.

Thurston, P.C., Osmani, I.A., and Stone, D., 1991. Northwestern Superior Province: Review and Terrane Analysis, in Thurston, P.C., Williams, H.R., Sutcliffe, R.H., and Stott, G.M. (eds). *Geology of Ontario*, Ontario Geological Survey, vol. 4, pp. 80–142.

Trudu, A.G., and Hoatson, D.M., 2000. Depths of emplacement of the mafic-ultramafic intrusion, in Hoatson, D.M., and Blake D.H. (eds), Geology and economic potential of the Palaeoproterozoic layered mafic-ultramafic intrusions in the East Kimberley, Western Australia. Canberra: Australian Geological Survey Organisation Bulletin 246, pp. 250–246.

Usselman, T.M., Hodge, D.S., Naldrett, A.J., and Campbell, I.H., 1979. Physical constraints on the characteristics of nickel-sulfide ore in ultramafic lavas. *The Canadian Mineralogist*, vol. 17, pp. 361–372.

Wieser, P., Petrelli, M., Lubbers, J., Wieser, E., Ozaydin, S., Kent, A. and Till, C., 2022. Thermobar: An open-source Python3 tool for thermobarometry and hygrometry. *Volcanica*, vol. 5(2), pp. 349–384.

Wilson, M.E., 1939. The Canadian Shield: Geology des Erde. Geology of North America 1.

Wilson, J.T., 1949. The origin of continents and Precambrian history. Royal Society of Canada, Transactions, vol. 43, pp. 157–184.

Wood, B.J., and Virgo, D., 1989. Upper mantle oxidation state: Ferric iron contents of lherzolite spinels by ^{57}Fe Mössbauer spectroscopy and resultant oxygen fugacities. *Geochimica et Cosmochimica Acta*, vol. 53(6), pp. 1277–1291.

Zuccarelli, N., 2020. Sulfide textures, geochemistry, and genesis of the Komatiite-Associated Eagle's Nest Ni-Cu-(PGE) Deposit, McFaulds Lake Greenstone Belt, Superior Province, Ontario. MSc Thesis, Laurentian University, Sudbury, Ontario, Canada, 108 p.

Zuccarelli, N., Lesher, C.M., Houlé, M.G., Weston, R., and Barnes, S.J., 2022. Diversity of Net-Textured Sulfides in Magmatic Sulfide Deposits: Insights from the Eagle's Nest Ni-Cu-(Platinum Group Element) Deposit, McFaulds Lake Greenstone Belt, Superior Province, Canada. *Economic Geology*, vol. 117, pp. 1731–1759.

Appendix A: Sample Information

Sample #	Drillhole #	From (m)	Type	Field Comment	Thin Section	Whole Rock Geochem	EPMA	S isotopes	Sm-Nd isotopes
EN23VS001	NOT-10-080	477	EN type	Foliated gabbro		●			
EN23VS002	NOT-10-080	365.42	Dike	Chlorite +/-carbonate altered mafic intrusive rock		●			
EN23VS003	NOT-10-080	376.05	EN type (?)	Foliated gabbro	●	●			
EN23VS004	NOT-10-080	276.2	Dike	Biotite-rich mafic dike	●	●			
EN23VS005	NOT-10-080	239.43	Contact dike	Intermediate dike		●			
EN23VS006	NOT-10-080	240.23	Contact dike	Intermediate dike		●			
EN23VS006b	NOT-10-080	240.23	Contact dike	Contact					
EN23VS007	NOT-09-064	673.17	Dike	Hornblende-bearing mafic dike		●			●
EN23VS008	NOT-09-064	673.66	Dike	Hornblende-bearing mafic dike		●			
EN23VS008b	NOT-09-064	674.02	Dike	Contact	●				
EN23VS009	NOT-09-064	1131.74	Eagle's Nest	Foliated gabbro		●			
EN23VS009b	NOT-09-064	1131.95	Eagle's Nest	Contact					
EN23VS010	NOT-10-090	914.82	Eagle's Nest	Gabbro		●			
EN23VS011	NOT-10-090	925.41	Eagle's Nest	Contact					
EN23VS012	NOT-10-090	949.87	EN type	Biotite-carbonate altered gabbro		●			
EN23VS013	NOT-09-064	956.58	Eagle's Nest	Microgabbro		●			
EN23VS013b	NOT-09-064	956.58	Eagle's Nest	Contact					
EN23VS014	NOT-09-064	961.48	Eagle's Nest	Microgabbro		●			
EN23VS015	NOT-09-064	968.96	Eagle's Nest	Pyroxenite		●			●
EN23VS016	NOT-09-064	967.63	Eagle's Nest	Contact	●				
EN23VS017	NOT-09-064	980.52	Eagle's Nest	Gabbro		●			
EN23VS018	NOT-09-064	980.33	Eagle's Nest	Contact					
EN23VS019	NOT-09-064	984.2	Eagle's Nest	Gabbro		●			
EN23VS020	NOT-09-064	994.64	Contact dike	Intermediate dike		●			
EN23VS020b	NOT-09-064	994.64	Contact dike	Contact					
EN23VS021	NOT-22-003	89.21	EN type	Foliated gabbro	●	●			
EN23VS022	NOT-22-003	92.49	EN type	Gabbro	●	●			
EN23VS023	NOT-22-003	104.37	EN type	Contact					
EN23VS024	NOT-22-003	105.48	EN type	Contact	●				
EN23VS025	NOT-22-003	105.67	EN type	Foliated gabbro		●			

Sample #	Drillhole #	From (m)	Type	Field Comment	Thin Section	Whole Rock Geochem	EPMA	S isotopes	Sm-Nd isotopes
EN23VS026	NOT-22-003	112.75	EN type	Foliated gabbro		●			
EN23VS027	NOT-22-003	122.46	EN type	Foliated gabbro		●			●
EN23VS028	NOT-22-003	125.71	EN type	Foliated gabbro	●	●			
EN23VS029	NOT-22-002	221.18	EN type (?)	Biotite-carbonate-quartz foliated dike		●			
EN23VS030	NOT-22-003	145.05	EN type	Altered gabbro		●			
EN23VS030b	NOT-22-003	142.5	EN type	Contact					
EN23VS031	NOT-09-064-W1	1246.4	Eagle's Nest	Gabbro		●			
EN23VS032	NOT-09-064-W1	1251	Contact dike	Foliated intermediate dike		●			
EN23VS033	NOT-10-087A	522.6	Contact dike	Hornblende-bearing mafic dike		●			
EN23VS033b	NOT-10-087A	521.98	Eagle's Nest	Contact					
EN23VS034	NOT-10-087A	532.64	Eagle's Nest	Gabbro		●			
EN23VS035	NOT-22-006	47	EN type	Gabbro		●			
EN23VS036	NOT-22-006	49.72	EN type	Contact					
EN23VS037	NOT-10-088	732.73	Eagle's Nest	Contact	●				
EN23VS038	NOT-10-088	739.87	Eagle's Nest	Microgabbro		●			
EN23VS039	NOT-08-1G075	88	EN type	Foliated gabbro	●	●			
EN23VS040	NOT-09-053-W5	570.12	EN type (?)	Biotite-carbonate-quartz foliated dike		●			
EN23VS041	NOT-11-1G243	199.7	Eagle's Nest	Lherzolite	●	●	●		●
EN23VS042	PW23-01-BR	74.2	Eagle's Nest	Lherzolite	●	●	●		
EN23VS043	PW23-01-BR	66.56	Eagle's Nest	Lherzolite	●	●	●		
EN23VS044	NOT-09-49-W3-W1	919.41	Eagle's Nest	Pyroxenite	●	●		●	
EN23VS045	NOT-20-001	143.7	Eagle's Nest	Pyroxenite	●	●			
EN23VS046	NOT-11-1G243	646.03	EN type	Gabbro	●	●			
EN23VS047	NOT-11-1G243	280.74	Eagle's Nest	Foliated gabbro		●			
EN23VS047b	NOT-11-1G243	280.74	Eagle's Nest	Contact					
EN23VS048	NOT-22-011	22.83	EN type	Altered gabbro		●			
EN23VS049	NOT-09-068-W1	885.07	Eagle's Nest	Foliated gabbro		●			
EN23VS050	NOT-09-071	902	Eagle's Nest	Gabbro		●			
EN23VS051	NOT-09-056	622.53	Contact dike	Intermediate dike		●			●

Sample #	Drillhole #	From (m)	Type	Field Comment	Thin Section	Whole Rock Geochem	EPMA	S isotopes	Sm-Nd isotopes
EN23VS052	NOT-09-062	571.66	EN type	Gabbro		●			
EN23VS053	NOT-07-011	42.1	EN type	Gabbro		●			
EN23VS054	NOT-10-093	1314.64	EN type	Gabbro	●	●			
EN23VS055	NOT-10-093	1333.05	EN type	Contact					
EN23VS056	NOT-22-001	181.45	EN type	Gabbro		●			
EN23VS057	NOT-22-003	231.84	EN type	Gabbro	●	●			
EN23VS058	NOT-22-003	289.85	EN type	Gabbro		●			
EN23VS059	NOT-08-034	63.5	Eagle's Nest	Pyroxenite		●			●
EN23VS060	NOT-08-034	70.29	EN type	Gabbro	●	●			
EN23VS061	NOT-07-008	126	Eagle's Nest	Microgabbro	●	●			
EN23VS062	NOT-10-079	797.45	Eagle's Nest	Contact	●				
EN23VS063	NOT-10-079	801.7	Eagle's Nest	Pyroxenite		●			
EN23VS064	NOT-10-079	1110.75	Eagle's Nest	Pyroxenite	●	●			
EN23VS064b	NOT-10-079	1115.61	Eagle's Nest	Contact					
EN23VS065	NOT-10-083	520.56	Eagle's Nest	Microgabbro		●			
EN23VS065b	NOT-10-083	520.46	Eagle's Nest	Contact					
EN23VS066	NOT-09-053-W4	853.5	Eagle's Nest	Peridotite		●			
EN23VS067	NOT-09-053-W4	859.68	Eagle's Nest	Pyroxenite		●			
EN23VS067b	NOT-09-053-W4	862.63	Eagle's Nest	Contact	●				
EN23VS068	NOT-09-053-W4	873.28	Eagle's Nest	Pyroxenite	●	●			
EN23VS069	NOT-09-053-W4	879.58	Contact dike	Intermediate dike		●			
EN23VS070	NOT-09-053-W4	884.75	Eagle's Nest	Gabbro		●			●
EN23VS071	NOT-09-053-W4	895.53	Eagle's Nest	Contact	●				
EN23VS072	NOT-09-053-W4	899.85	Eagle's Nest	Gabbro		●			
EN23VS072b	NOT-09-053-W4	902.87	Eagle's Nest	Contact					
EN23VS073	NOT-09-053-W4	909.54	Eagle's Nest	Gabbro		●			●
EN23VS074	NOT-09-053-W4	911.73	Eagle's Nest	Gabbro		●			
EN23VS075	NOT-09-053-W4	918.35	Contact dike	Contact					

Sample #	Drillhole #	From (m)	Type	Field Comment	Thin Section	Whole Rock Geochem	EPMA	S isotopes	Sm-Nd isotopes
EN23VS076	NOT-09-053-W4	918.35	Contact dike	Contact					
EN23VS077	NOT-09-053-W4	952.75	Contact dike	Intermediate dike		●			
EN23VS078	NOT-09-053-W4	960.3	Contact dike	Intermediate dike		●			
EN23VS078b	NOT-09-053-W4	960.3	Contact dike	Contact					
EN23VS079	NOT-09-053-W4	968.43	Contact dike	Contact					
EN23VS080	NOT-09-053-W4	974.34	Dike	Biotite-carbonate foliated dike		●			
EN23VS081	NOT-09-053-W4	977.89	Contact dike	Contact					
EN23VS082	NOT-09-053-W4	980.6	Contact dike	Contact					
EN23VS083	NOT-09-058	469.63	Eagle's Nest	Peridotite		●			
EN23VS084	NOT-09-070-W1	723.86	Eagle's Nest	Gabbro		●			●
EN23VS085	NOT-07-027	102.61	EN type	Gabbro		●			
EN23VS086	NOT-09-066	539.33	Eagle's Nest	Pyroxenite		●			
EN23VS087	NOT-09-049-W1	752.17	Eagle's Nest	Gabbro		●			
EN23VS088	NOT-09-049-W1	756.7	Eagle's Nest	Pyroxenite		●			
EN23VS089	NOT-10-089	469.48	Eagle's Nest	Peridotite		●			
EN23VS090	NOT-09-057	515.66	Eagle's Nest	Pyroxenite		●			
EN23VS091	NOT-10-076	447.12	Eagle's Nest	Gabbro		●			
EN23VS092	NOT-10-076	449.64	Eagle's Nest	Pyroxenite		●			●
EN23VS093	NOT-10-084	799.17	Eagle's Nest	Gabbro		●			
EN23VS094	NOT-10-084	804.5	Eagle's Nest	Gabbro		●			
EN23VS095	NOT-10-085-W2	1375.2	Contact dike	Foliated intermediate dike		●			●
EN23VS096	NOT-10-085-W2	1369.72	Eagle's Nest	Pyroxenite		●			●
EN23VS097	NOT-10-086	827.26	Eagle's Nest	Gabbro		●			
EN23VS097b	NOT-10-086	827.26	Eagle's Nest	Contact	●				
EN23VS098	NOT-10-096	698.8	EN type	Foliated gabbro		●			
EN23VS099	NOT-10-096	706.7	EN type	Foliated gabbro	●	●			
EN23VS100	NOT-08-037	296.7	Eagle's Nest	Olivine websterite	●	●	●		
EN23VS101	NOT-08-037	424.48	Eagle's Nest	Pyroxenite	●	●		●	
EN23VS102	NOT-09-055	467.6	Eagle's Nest	Peridotite		●			●

Sample #	Drillhole #	From (m)	Type	Field Comment	Thin Section	Whole Rock Geochem	EPMA	S isotopes	Sm-Nd isotopes
EN23VS103	NOT-09-065	635	Eagle's Nest	Pyroxenite	●	●			●
EN23VS104	NOT-22-2G01	466.24	Dike	Biotite-rich mafic intrusive rock		●			
EN23VS105	NOT-22-2G01	481.12	Dike	Amphibolite	●	●			
EN23VS106	NOT-22-2G01	499.8	Dike	Intermediate dike		●			
EN23VS107	NOT-23-2G02	43.64	EN type	Pyroxenite		●			
EN23VS108	NOT-23-2G02	60.05	EN type	Pyroxenite	●	●			
EN23VS109	NOT-23-2G02	859.6	Dike	Foliated mafic		●			
EN23VS110	NOT-10-GT04	32.25	Eagle's Nest	Gabbro	●	●			
EN23VS111	NOT-10-078	330.1	Eagle's Nest	Pyroxenite		●			●
EN23VS112	NOT-09-051	665.51	Eagle's Nest	Peridotite		●			
EN23VS113	NOT-08-038	507.09	Eagle's Nest	Pyroxenite		●			●
EN23VS114	NOT-08-030	110.4	Eagle's Nest	Microgabbro	●	●		●	
EN23VS115	NOT-07-029	83.44	Eagle's Nest	Pyroxenite		●			
EN23VS116	NOT-07-009	34.85	Eagle's Nest	Gabbro	●	●		●	
EN23VS117	NOT-07-007	72.4	Eagle's Nest	Gabbro		●			
EN23VS118	NOT-07-011	91.05	Eagle's Nest	Gabbro		●			
EN23VS119	NOT-08-039	607.15	Eagle's Nest	Pyroxenite		●			
EN23VS120	NOT-08-039	609.75	Eagle's Nest	Gabbro		●			
EN23VS121	NOT-09-053	1001.55	Eagle's Nest	Gabbro	●	●		●	
EN23VS122	NOT-09-053-W1	830.3	Eagle's Nest	Gabbronorite	●	●		●	
EN23VS123	NOT-10-GT02	416.8	Eagle's Nest	Pyroxenite		●			
EN23VS124	NOT-08-036	113.8	Eagle's Nest	Peridotite		●			
EN23VS125	NOT-08-036	255.42	Eagle's Nest	Gabbro		●			●
EN23VS126	NOT-09-053-W2	810.4	Eagle's Nest	Foliated gabbro		●		●	
EN23VS127	NOT-09-049	966.15	Eagle's Nest	Gabbro	●	●			●
EN23VS128	NOT-10-083	431.62	Wall rock	Tonalite		●			
EN23VS129	NOT-10-093	404.85	Wall rock	Tonalite		●			●
EN23VS130	NOT-10-089	350	Wall rock	Tonalite		●			
EN23VS131	NOT-12-1G005	104.95	Dike	Aphanitic intermediate dike		●			

Sample #	Drillhole #	From (m)	Type	Field Comment	Thin Section	Whole Rock Geochem	EPMA	S isotopes	Sm-Nd isotopes
EN23VS132	NOT-12-1G005	184.85	Wall rock	Tonalite		●			●
EN23VS133	NOT-09-059	495.75	EN type	Gabbro	●	●			
EN23VS134	NOT-09-059	136	Wall rock	Tonalite		●			
EN23VS135	WR-11-02	109.49	Winisk River	Pyroxenite	●	●			
EN23VS136	WR-11-02	110.81	Winisk River	Pyroxenite		●			
EN24VS001	NOT-10-081	408.6	Contact dike	Intermediate dike		●			
EN24VS002	NOT-10-081	423.1	Contact dike	Intermediate dike					
EN24VS003	NOT-10-081	448.2	Contact dike	Intermediate dike		●			
EN24VS004	NOT-10-081	475.5	Eagle's Nest	Peridotite	●	●			
EN24VS005	NOT-10-081	489.7	Eagle's Nest	Peridotite		●			
EN24VS006	NOT-10-081	504	Eagle's Nest	Lherzolite	●	●	●	●	
EN24VS007	NOT-10-081	514.55	Eagle's Nest	Lherzolite	●	●	●		
EN24VS008	NOT-10-081	524.2	Eagle's Nest	Lherzolite	●	●	●		
EN24VS009	NOT-10-081	532.9	Eagle's Nest	Wehrlite	●	●	●		
EN24VS010	NOT-10-081	555.2	Eagle's Nest	Peridotite	●	●		●	
EN24VS011	NOT-10-081	563.6	Eagle's Nest	Peridotite		●			
EN24VS012	NOT-10-081	570	Eagle's Nest	Peridotite		●			
EN24VS013	NOT-10-081	576	Eagle's Nest	Peridotite		●			
EN24VS014	NOT-10-081	589.75	Eagle's Nest	Peridotite					
EN24VS015	NOT-10-081	601.7	Eagle's Nest	Lherzolite	●	●	●		
EN24VS016	NOT-10-081	618.6	Eagle's Nest	Lherzolite		●			
EN24VS017	NOT-10-081	635.3	Eagle's Nest	Peridotite	●	●	●		
EN24VS018	NOT-10-081	645.1	Eagle's Nest	Peridotite		●			
EN24VS019	NOT-10-081	658	Eagle's Nest	Pyroxenite		●			
EN24VS020	NOT-10-081	667.7	Eagle's Nest	Contact					
EN24VS021	NOT-10-081	676.5	Eagle's Nest	Pyroxenite		●			
EN24VS022	NOT-10-081	685.45	Eagle's Nest	Pyroxenite		●			
EN24VS023	NOT-10-081	696	Eagle's Nest	Pyroxenite		●			
EN24VS024	NOT-10-081	715	Eagle's Nest	Pyroxenite		●			

Sample #	Drillhole #	From (m)	Type	Field Comment	Thin Section	Whole Rock Geochem	EPMA	S isotopes	Sm-Nd isotopes
EN24VS025	NOT-10-081	720.15	Eagle's Nest	Altered gabbro		●			
EN24VS026	NOT-10-081	730.6	Eagle's Nest	Olivine pyroxenite					
EN24VS027	NOT-10-081	761.3	Eagle's Nest	Altered gabbro					
EN24VS028	NOT-10-081	764.6	Eagle's Nest	Altered gabbro		●			
EN24VS029	NOT-10-081	766	Eagle's Nest	Pyroxenite		●			
EN24VS030	NOT-10-081	774.4	Wall rock	Partially melted tonalite		●			
EN24VS031	NOT-09-064-W1	1109.2	Eagle's Nest	Olivine websterite	●	●			
EN24VS032	NOT-09-070-W2	572	Eagle's Nest	Lherzolite	●	●	●		
EN24VS033	NOT-07-024	179.5	Eagle's Nest	Peridotite	●	●	●		
EN24VS034	NOT-07-001	113.3	Eagle's Nest	Peridotite					
EN24VS035	NOT-07-011	83.4	Eagle's Nest	Pyroxenite	●	●			
EN24VS036	NOT-07-016	54.75	Eagle's Nest	Peridotite	●	●			
EN24VS037	NOT-07-016	120.55	Eagle's Nest	Peridotite	●	●			
EN24VS038	NOT-10-095	398.7	Eagle's Nest	Contact					
EN24VS039	NOT-10-090	750.3	Eagle's Nest	Microgabbro	●	●			●
EN24VS040	NOT-10-090	779.05	Eagle's Nest	Harzburgite	●	●			
EN24VS041	NOT-10-077	291.45	Eagle's Nest	Peridotite					

Appendix B: Thin Section Descriptions

Sample # EN23VS003

Mineral	Habit	Size (mm)	Abundance (%)	Comment
Chlorite	Subidioblastic	0.1–0.5	40	Fine-grained, platy, defining foliation. Locally occurring as elongate, lenticular, foliation parallel lenses ranging from 1 to 5mm elongated in the foliation parallel direction.
Actinolite	Idioblastic	0.05–0.7	40	Very fine to fine-grained, elongate, bladed to acicular grains dominantly aligned parallel to foliation.
Carbonate	Xenoblastic	0.05–0.6	5	Fine-grained, pervasively disseminated, displaying irregular grain boundaries and equant-like morphology. Overprinting grains of plagioclase. Several elongate, discontinuous and irregular lenses (<1mm) are also observed, predominantly of massive carbonate with polygonal grain boundaries.
Quartz	Xenoblastic	0.01–0.15	6	Very fine-grained, displaying subangular equant morphologies, granoblastic, and occur throughout the sample as individual grains or as foliation parallel clusters where thin chlorite rims outline grain boundaries.
Feldspar	Xenoblastic	0.1–0.25	4	Similar in appearance to quartz, but slightly dustier and partially replaced by carbonate.
Titanite	Xenoblastic	0.05–0.25	2	Foliation parallel clusters up to 1.5mm long, consisting of very fine- to fine-grained xenoblastic aggregates. Accessory titanite sometimes occurs in association with chlorite lenses, outlining their boundaries.
Epidote	Subidioblastic	0.02–0.05	<1	Accessory amounts of very fine-grained crystals are disseminated throughout.
Pyroxene	Xenoblastic	0.5–1.3	1	Fine- to medium-grained, tail porphyroclast-like grains occur elongated in the direction of foliation. Appear to consist of segmented grains along cleavage planes and actinolite pseudomorphed grains. The core of the grains has an isotropic appearance.
Oxides	Subidioblastic	0.05–0.2	Trace	Consists of fine-grained magnetite and very fine-grained ilmenite. Magnetite occurs as several individual grains, weakly fractured, within chlorite lenses. Ilmenite appears to occur as very fine-grained, patchy exsolution within titanite grains.
Sulfides	Xenoblastic	0.01–0.08	Trace	Very fine-grained, disseminated grains of pyrite, with blebby grain morphology, occurring interstitial to actinolite and plagioclase but often surrounded by chlorite.
Comments: This sample is fine-grained, lepidoblastic, foliated, comprising actinolite, chlorite, carbonate, quartz and feldspar as well as accessory amounts of titanite, epidote, and relict pseudomorphed porphyroclasts of pyroxene. The arrangement of platy chlorite and elongate actinolite defines foliation within the sample. The sample displays the typical assemblage and texture of greenschist facies conditions.				

Sample # EN23VS004

Mineral	Habit	Size (mm)	Abundance (%)	Comment
Biotite	Euhedral to anhedral	0.05–0.3	80	Most abundant phase within the sample. Consists of fine- to very-fine grained, variably oriented platy grains. Accessory amounts of subhedral zircon occur within biotite grains. Contains very fine-grained zircon inclusions.
Carbonate	Subhedral to anhedral	0.1–0.6	10	Pervasive, fine-grained, disseminated throughout the samples and contains numerous rounded, very fine inclusions. Grains have irregular grain boundaries and prismatic to equant morphology.
Quartz	Anhedral	0.02–0.25	6	Interstitial to biotite, mostly very fine-grained, granular, displaying granoblastic polygonal grain boundaries.

Chlorite	Subhedral	0.1–0.6	3	Fine-grained, occurring as lath-like grains or as partial replacement of biotite.
Actinolite	Subhedral	0.1–0.3	1	Fine- to very fine- crystals, of elongate blade-like actinolite.
Pyrite	Anhedral	0.01–0.06	Trace	Several very fine crystals of anhedral pyrite occur as inclusions within carbonate grains.
Comments: This sample is very fine- to fine-grained, massive to very weakly foliated, mainly comprising biotite and carbonate. Small amounts of actinolite, quartz, and chlorite are present within the sample. Biotite Hornfels(?).				

Sample # EN23VS008b

Mineral	Habit	Size (mm)	Abundance (%)	Comment
Tonalite (45%)				
Plagioclase	Subhedral	2–5	70	Medium-grained, tabular grains are altered to epidote and sericite. Display irregular grain boundaries and preserve polysynthetic twinning.
Quartz	Anhedral	0.5–4	20	Fine- to medium-grained, completely recrystallized occurring in pockets of granoblastic textured grains.
Biotite	Subhedral	0.1–0.4	7	Fine-grained, platy occurs intergranular to plagioclase grains and is partially replaced by chlorite.
Amphibole	Subhedral	0.2–0.5	3	Fine-grained, anhedral to subhedral grains occur in accessory amounts, predominantly replaced by chlorite
Pyrite	Euhedral	0.2–0.5	Trace	Fine-grained, cubic grains are weakly disseminated in the tonalite.
Mafic dike (55%)				
Amphibole	Subhedral	0.2–4	70	Displays bimodal characteristics. (1) Comprises medium-grained, subhedral to euhedral grains with a sieve-like texture hosting fine-grained inclusions of plagioclase. (2) Comprises fine grains occurring as acicular grains within the groundmass to the coarser amphibole in association with plagioclase.
Plagioclase	Anhedral	0.1–0.3	30	Fine-grained, anhedral plagioclase occurring within the groundmass. Grain boundaries are poorly defined due to alteration by chlorite and overprinting finer-grained amphibole.
Comments: This sample comprises a contact between a hornblende gabbro and tonalite. Intense shearing and grain size reduction are observed in the vicinity of the moderately defined sharp contact. Pyrite concentrations appear to increase in proximity to the contact.				

Sample # EN23VS016

Mineral	Habit	Size (mm)	Abundance (%)	Comment
Pyroxenite (20%)				
Plagioclase	Subhedral	0.4–1	5–10	Moderately altered, fine-grained, subhedral, tabular grains. Grains display irregular grain boundaries and bulging with recrystallization to granular aggregates along which interstitial chlorite and biotite occur. Intensely altered grains are pseudomorphed by chlorite and biotite. Plagioclase grains appear to occur interstitial to altered pyroxene. Several grains show deformation twinning.
Pyroxene	Subhedral to anhedral	0.8–1.6	80–90	Pervasively altered, with primary characteristics very poorly preserved. Alteration consists of patchy to

				mottled, green hornblende, elongate actinolite-tremolite, chlorite and biotite. Several grains appear to preserve relic prismatic grain boundaries.
Pyrite	Subhedral to anhedral	0.03–0.5	4	Consists of fine- to very fine-grained subhedral pyrite disseminated throughout the unit and does not appear to be associated with any phase.
Oxides	Euhedral	0.1–0.4	1	Equant grains of chromite are locally occurring in clusters. The grains show slightly irregular grain boundaries and are sometimes fractured. Chromite grains are partially rimmed by magnetite, with one grain appearing skeletal and completely replaced.
Tonalite (65%)				
Plagioclase	Subhedral	0.5–3	55	Weakly altered, tabular, medium-grained plagioclase. The grains are overprinted by patchy to locally pervasive sericite, with accessory amounts of very fine-grained epidote. Grain boundaries are generally irregular, with relic rims well-preserved. Preservation of primary polysynthetic twinning is common; however, grains often exhibit undulatory extinction.
Quartz	Anhedral	1–3	35	Primary quartz grains appear to have been similar in size to plagioclase but have been completely recrystallized into polygonal, granular-textured, fine-grained aggregates.
Albite	Subhedral	0.8–1.6	2	Small amounts of medium-grained, tabular albite are observed, displaying simple albite twinning, and are similarly overprinted by sericite.
Amphibole	Subhedral to anhedral	0.2–0.7	3	Consists predominantly of hornblende that has been strongly altered to acicular actinolite-tremolite and, to a lesser extent, chlorite. Occurring interstitial to feldspar and quartz.
Sulfides	Euhedral to anhedral	0.01–0.6	3	Consists of fine- to very fine-grained disseminated Py>Po>Ccp. Pyrite occurs as discrete, cubic grains. Fine-grained, anhedral, polysulfide grains of Po and Ccp occur in trace amounts, generally as blocky, anhedral grains.
Oxides	Anhedral	0.1–1.5	1	Trace amounts of magnetite are disseminated throughout the unit, occurring as highly irregular, skeletal grains.
Intermediate Contact Dike (15%)				
Plagioclase	Euhedral	0.5–1	55	Fine-grained, lath-like grains displaying undulous extinction and polysynthetic twinning. Most of the grains appear to be recrystallized, with primary grains rarely preserved, and are overprinted by weak sericite alteration as well as biotite and chlorite.
Biotite	Subhedral	0.04–0.1	15	Subhedral, platy grains are disseminated throughout the unit. The abundance of biotite increases in proximity to the metapyroxenite.
Chlorite	Euhedral	0.03–0.2	20	Platy to fibrous, fine-grained aggregates of chlorite are disseminated throughout.
Pyrite	Euhedral to subhedral	0.01–0.08	10	Very fine-grained, cubic, equant grains are disseminated pervasively.
Oxides	Anhedral	0.01–0.04	Trace	Very fine-grained, anhedral magnetite is disseminated throughout the unit.
Comments: This sample comprises a contact between a metapyroxenite (~20%), tonalite (~65%), and an intermediate unit (~15%), which is injecting along the contact. The metapyroxenite consists of medium-grained,				

altered pyroxene and smaller amounts of interstitial plagioclase. The unit is intensely altered, with primary characteristics poorly preserved. The tonalite is moderately deformed, medium-grained, and consists of medium-grained, tabular plagioclase, recrystallized quartz, and smaller amounts of alkali feldspar and amphibole. The intermediate unit is fine-grained, consisting primarily of plagioclase, which is overprinted by biotite and chlorite. The contact between the metapyroxenite and tonalite is well-defined and sharp, with slight undulation. The concentration of biotite near the contact increases in the metapyroxenite. The contact between metapyroxenite and the intermediate unit is similar to the contact between metapyroxenite and tonalite; however, the biotite is aligned subparallel to the contact. The concentration of biotite in the intermediate unit gradationally increases towards the contact with the metapyroxenite, and at the contact abruptly stops, making a thin sliver composed of plagioclase and chlorite. The contact between the tonalite and the intermediate unit is highly irregular, where the intermediate chaotically intrudes along the grain boundaries of the tonalite.

Sample # EN23VS021

Mineral	Habit	Size (mm)	Abundance (%)	Comment
Actinolite	Idioblastic	0.01–1.5	45	Fine-grained, elongate blade-like to acicular grains locally displaying simple twinning. On the margins of dissolution-like bands, it occurs as acicular, fan-like clusters, as well as very fine-grained, elongate grains. One grain resembling the shape of a pyroxene was observed to be pseudomorphed by actinolite-tremolite. Actinolite-tremolite grains are moderately fractured and sometimes display patchy alteration to ultra-fine-grained, undiscernible aggregates.
Plagioclase	Subidioblastic to xenoblastic	0.2–0.7	15	Fine-grained, moderately sericitized grains, mostly displaying irregular grain morphologies, but locally, lath-like grains are observed. Patchy sericite alteration of plagioclase is observed in several grains. Plagioclase is characterized by its dusty appearance, with rare preservation of fresh grains and grain rims. The majority of the grains display undulous extinction, with bulging occurring more rarely, and a few grains show deformation twinning. Some grains are superimposed by fine-grained platy chlorite and actinolite-tremolite aggregates.
Sericite	Subidioblastic	0.01–0.1	20	Occurs as a very fine-grained alteration of plagioclase, ranging from pervasive to patchy in distribution.
Chlorite	Subidioblastic	0.1–0.3	15	Fine-grained, platy aggregates elongated parallel to foliation and interstitial to actinolite grains. Several chlorite lenses, elongated parallel to the foliation, are observed and are up to 0.5mm in length.
Epidote	Subidioblastic to xenoblastic	0.01–0.3	2	Very fine to fine-grained aggregates occur throughout the thin section, mostly within plagioclase grains. Often accompanies sericite in plagioclase alteration.
Titanite	Xenoblastic	0.01–0.1	2	Very fine to fine-grained aggregates of titanite occur in clusters or elongate string-like lenses parallel to foliation.
Rutile	Xenoblastic	<0.05	Accessory	Observed only within a few plagioclase grains as very fine-grained, disseminated grains with a dark red colour, closer to dissolution-like bands.
Sulfides	Anhedral	0.05–0.25	Trace	Occurs as elongate, foliation parallel, aggregate clusters of blocky pyrite aggregates that are seen to encompass sericitized plagioclase fragments.

Oxides	Subhedral	0.01–0.1	Trace	Trace amounts of magnetite mantle sulfide aggregates along fractures and grain boundaries.
Comments: This sample is foliated, lepidoblastic, consists of fine- to very fine-grained actinolite, sericitized plagioclase and chlorite with accessory amounts of epidote, titanite, rutile and relic pseudomorphed clinopyroxene. Approximately two-thirds of the sample display uniform grain size distribution and foliation intensity. In one-third of the sample, significant grain size reduction is observed, accompanied by an undiscernible black groundmass and xenocrysts of actinolite, plagioclase, and chlorite. Local fractures and faulting are seen within this zone up to 1mm wide. There are multiple, highly irregular, variably oriented veins (0.2-2.5mm, some cross-cutting foliation), plagioclase, apatite +/-carbonate veins that cut the sample and are offset by the fracturing. Plagioclase appears very dirty pervasively, and along portions of some contacts, plagioclase is fully sericitized. Acicular grains of actinolite and minor chlorite overprint the crosscutting veins, with mineral growth parallel to foliation. The mineral assemblage and texture indicate a mafic protolith that has undergone metamorphism under greenschist conditions.				

Sample # EN23VS022

Mineral	Habit	Size (mm)	Abundance (%)	Comment
Pyroxene	Subhedral	0.5–1	70–80	Pervasively overprinted by secondary alteration minerals with no primary grains preserved. Primary characteristics of the grains are difficult to discern, except for one, a subhedral, pseudomorphed grain, replaced by actinolite-tremolite, appearing to have been ~1mm and prismatic. Pyroxene grains have been completely, pervasively altered to platy chlorite (~50%) intergrown with elongated acicular to bladed aggregates of actinolite-tremolite (~30%) either pervasively or felty. Skeletal, anhedral clusters of titanite overprint several pyroxene grains.
Plagioclase	Subhedral to anhedral	0.3–1.5	20–30	Strongly overprinted by alteration assemblage minerals. Primary grain properties are more preserved than in pyroxene, with grains appearing to have been mostly subhedral, tabular to lath-like in shape. Plagioclase appears very dusty and is strongly overprinted by pervasive to selective-patchy fine-grained sericite (~15%). In patchy altered grains, relic rims are partially preserved. Along the plagioclase grain boundaries, very fine-grained aggregates of epidote were observed. 3% unaltered plagioclase observed.
Oxides	Anhedral	0.01–0.1	Trace	Trace amounts of anhedral, irregular grains of magnetite are observed locally. Minor amounts of ilmenite aggregates appear to be associated with titanite.
Sulfides	Anhedral	0.02–0.25	Trace	Consists of anhedral, fine- to very fine-grained, disseminated pyrite locally associated with trace amounts of anhedral chalcopyrite. More significant chalcopyrite concentrations are associated with a quartz vein crosscutting the sample.
Comments: Strongly altered, non-foliated, metagabbro. Plagioclase is the least altered primary phase, preserving its morphology but moderately overprinted by sericite and epidote alteration. Pyroxene in this sample is difficult to distinguish due to the high degree of its alteration by actinolite-tremolite and chlorite, as well as titanite. Several grains were observed with an equant morphology resembling that of pyroxene and were therefore inferred to have been the dominant silicate phase. The sample is cross-cut by two, 0.2mm wide, quartz-carbonate veinlets, with one containing minor chalcopyrite.				

Sample # EN23VS024

Mineral	Habit	Size (mm)	Abundance (%)	Comment
EN Type (45%)				
Chlorite	Idioblastic to subidioblastic	0.01–0.3	55	Fine-grained, platy, defining foliation and mantling lenses of quartz and plagioclase.
Quartz	Xenoblastic	0.05–0.3	40	Very fine to fine-grained quartz aggregates occurring within elongated lens-shaped clusters that display undulous extinction and granular texture
Feldspar	Xenoblastic	0.1–0.3	3	Difficult to discern from quartz within the sample, they are slightly coarser grained and sometimes display weak, patchy sericite alteration.
Epidote	Subidioblastic	0.01–0.05	1	Very fine-grained aggregates are observed within the chlorite matrix. The abundance of epidote increases towards the contact
Titanite	Xenoblastic	0.01–0.1	1	Very fine-grained patchy lenses parallel to foliation occur pervasively, comprising xenoblastic grains.
Sericite	Subidioblastic	0.01–0.05	Trace	Very fine-grained overprinting several grains of feldspar.
Tonalite (55%)				
Plagioclase	Anhedral	1–6	40	Medium- to coarse-grained, strongly deformed. Grain boundaries are highly irregular, with the development of bulging and recrystallization. Grains display undulous extinction and moderate, pervasive sericitization. Outline of original grain boundaries is observed, but grains are recrystallized into lenses with no original shape preserved.
Quartz	Anhedral	0.5–4	45	Medium-grained, anhedral, cleaner in appearance than plagioclase. Displays undulous extinction and bulging.
Chlorite	Subhedral	0.01–0.2	3	Platy to massive chlorite occurs within fractures across the unit.
Carbonate	Subhedral	0.2–0.9	2	Fine-grained, granular, anhedral aggregates occurring along fractures.
Sericite	Subhedral	0.01–0.05	15	Very fine-grained, moderately overprinting plagioclase as patchy or pervasive alteration.
Titanite	Anhedral	0.01–0.1	Trace	Occurs as fine-grained aggregates associated with chlorite and along veins.
Sulfides	Anhedral	0.01–0.05	Trace	Occurs in clusters of disseminated, blocky, chalcopyrite or as trace subhedral pyrite within fractures.

Comments: This sample comprises a contact between an EN-type dike (55%) and tonalite (40%). The mafic dike is fine-grained, lepidoblastic, strongly foliated, consisting mostly of chlorite, quartz and sericitized plagioclase with accessory amounts of epidote and titanite. Foliation is defined by the alignment of platy chlorite, which is separated by lenses of quartz and plagioclase aggregates. Towards the contact, grain size gradationally decreases, and chlorite becomes significantly more abundant than quartz-plagioclase lenses. Foliation intensity increases towards the contact, forming shear bands. Mineralogy towards the contact progressively becomes more chlorite-epidote-quartz dominant. The tonalite displays the development of a weak fabric subparallel to the contact. It consists predominantly of plagioclase and quartz, showing evidence of deformation through undulous extinction, bulging, angular shape, and grain size reduction within localised shear bands. Several carbonate veins crosscut the sample perpendicular to foliation but abruptly stop at the contact with the mafic dike.

Sample # EN23VS028

Mineral	Habit	Size (mm)	Abundance (%)	Comment
Quartz	Subidioblastic to xenoblastic	0.04–0.3	60	Localised banding/lenses of very fine-grained, clean in appearance quartz that appears to display granoblastic polygonal texture.
Plagioclase	Xenoblastic	0.02–0.5	4	Fine-grained but slightly coarser than quartz. Observed in localised bands, where it is distinguished by the presence of sericite alteration and a dirty appearance.
Sericite	Xenoblastic	0.01–0.05	8	Very fine-grained, overprints most of the plagioclase within the sample pervasively.
Titanite	Xenoblastic	0.01–0.15	1	Fine to mostly very fine-grained aggregates that occur as irregular patches or laminations parallel to foliation. Grains are skeletal in appearance.
Chlorite	Idioblastic to subidioblastic	0.05–0.25	25	Fine- to very fine-grained, platy, foliation-defining. Occurs as thinly laminated anastomosing bands of parallel aligned chlorite separated by bands and lenses of quartz +/- plagioclase.
Carbonate	Xenoblastic	0.1–0.3	1	Generally, occurs within lenses and bands of quartz-plagioclase, commonly having highly irregular grain boundaries with an equant-like morphology and appears to correlate with high degrees of alteration to sericite. Some localized carbonate grains are associated with cross-cutting fractures.
Epidote	Xenoblastic	0.01–0.1	Accessory	Discrete, very fine-grained, xenoblastic grains accompany sericite in plagioclase alteration.
Sulfides	Xenoblastic	0.01–0.25	1	Disseminated to patchy, blocky to blebby grains comprising chalcopyrite with trace very fine-grained pyrite.
Comments: This sample is highly altered, fine-grained, lepidoblastic, strongly foliated and folded, consisting predominantly of quartz, plagioclase, and chlorite, as well as accessory amounts of titanite and carbonate. The sample displays a spaced to anastomosing foliation defined by bands of foliated platy chlorite separated by bands or lenses of quartz, plagioclase +/- carbonate aggregates. The sample also displays folding of the foliation, where the thickness of chlorite bands appears to increase, and preservation of sericitized plagioclase is more abundant. The sample is crosscut by multiple fractures perpendicular to foliation, with minor chalcopyrite and carbonate occurring within them.				

Sample # EN23VS037

Mineral	Habit	Size (mm)	Abundance (%)	Comment
Mafic Intrusive (20%)				
Pyroxene	Anhedral	0.5–1.5	65	Pervasively overprinted by actinolite-tremolite and chlorite. Primary grain characteristics are not preserved.
Plagioclase	Euhedral	0.4–1.2	34	Fine-grained, weakly altered, lath-like, euhedral grains. Often shows recrystallization textures through bulging as well as undulous extinction. Weakly altered to sericite and minor epidote.
Magnetite	Anhedral	0.05–0.2	1	Anhedral, skeletal grains of magnetite occur within altered pyroxene grains.
Tonalite (80%)				
Plagioclase	Euhedral to subhedral	0.2-0.6	75	Fine-grained, predominantly lath-like, euhedral grains make up the primary constituent and the groundmass.

				Fracturing, weak sericite alteration and irregular grain boundaries are common. Often preserves polysynthetic twinning.
Alkali feldspar	Euhedral	1-3	10	Medium-grained, euhedral, tabular grains. Some grains show concentric zonation and tartan twinning. Grains are weakly fractured and have a dusty appearance.
Quartz	Anhedral	0.6-2.5	5	Occur as medium-grained pods, similar in grain size to alkali feldspar. Grains are recrystallized, with undulatory extinction and bulging textures.
Amphibole	Euhedral to subhedral	0.4-1	10	Pervasively altered to acicular actinolite-tremolite grains with minor chlorite. Occur within the groundmass, interstitial to plagioclase laths. Several grains resemble hornblende. Accessory amounts of very fine-grained rutile are seen in association with actinolite-tremolite.
Magnetite	Anhedral	0.02-0.05	Trace	Disseminated, anhedral magnetite occurs in association with actinolite-tremolite aggregates.
Comments: This sample comprises a gradational contact between a porphyritic tonalite (80%) and melagabbro (20%). The tonalite consists of medium-grained phenocrysts of alkali feldspar and recrystallized quartz that sit within a fine-grained groundmass comprising predominantly plagioclase and altered interstitial amphibole. The transition from tonalite to the melagabbro occurs gradationally. Phenocrysts of feldspar and quartz gradually become less abundant, plagioclase decreases in abundance, while actinolite-tremolite and chlorite become more abundant. The exact contact location is unclear, as the alteration assemblage of both the tonalite and the gabbro is the same. Abundance and grain size of magnetite increase within the gabbroic unit, which occurs as skeletal grains within mafic alteration minerals. The melagabbro is strongly overprinted by alteration minerals, with all mafic constituents altered to actinolite-tremolite, and likely consisted of pyroxene. Plagioclase preserves most of its primary characteristics, however, it displays evidence of recrystallization. Several veinlets filled with aligned actinolite-tremolite and chlorite crosscut the sample.				

Sample # EN23VS039

Mineral	Habit	Size (mm)	Abundance (%)	Comment
Actinolite	Idioblastic	0.05–0.5	55	Fine-grained, elongate columnar to blade-like grains sometimes displaying simple twinning. Very fine acicular grains overprint plagioclase, along grain boundaries. Several grains contain clusters of fine-grained inclusions resembling quartz; however, they are difficult to discern due to their fine-grained nature. Well-aligned defining foliation. Typical cleavage angles of 56–120 degrees are observed.
Plagioclase	Idioblastic to xenoblastic	0.1–0.6	15	Fine-grained moderately sericitized plagioclase. Sericite alters the core of the grains with relic rims preserved. Grains display bulging textures and undulous extinction. Intergranular to grains of actinolite-tremolite.
Sericite	Subidioblastic	0.01–0.05	20	Sericite occurs throughout the sample as very fine-grained, patchy clusters that overprint plagioclase partially or pervasively. In proximity to veins, sericite alteration is more intense and pervasive.
Chlorite	Subidioblastic	0.05–0.25	3	Relatively small constituent of the sample, occurring as plate-like grains that sometimes mantle actinolite and are more abundant in dissolution-like bands. One elongate, lenticular lens of chlorite aggregates is also visible within the sample, parallel to the foliation.

Epidote	Subidioblastic	0.01–0.05	1	Very fine-grained aggregates occur within plagioclase, most often concentrated along the boundaries or accompanying sericite alteration.
Titanite	Xenoblastic	0.02–0.1	3	Very fine-grained, occur in elongate, irregular, foliation-parallel lenses comprising xenoblastic, skeletal grains.
Biotite	Subidioblastic	0.01–0.03	Accessory	Very fine-grained, overprinting small amounts of some actinolite and plagioclase grains.
Sulfides	Subidioblastic	0.02–0.2	3	Consists mainly of idioblastic to subidioblastic, equant, cubic pyrite interstitial to actinolite-tremolite and is partially encompassed by chlorite. Trace amounts of very fine-grained chalcopyrite are disseminated throughout. Within a single vein, a large cluster of pyrite grains is present where the abundance of chalcopyrite appears to be slightly elevated.

Comments: This sample is fine-to very fine-grained, foliated, lepidoblastic, consisting of actinolite-tremolite, sericitized plagioclase and accessory amounts of chlorite, epidote, titanite and biotite. The sample displays a curved foliation defined by the alignment of platy chlorite and elongate actinolite-tremolite. Locally, the sample displays thin (<0.2mm) bands that resemble dissolution banding. The sample is also cut by multiple quartz-bearing veinlets (<0.1mm). The sample displays a mafic protolith assemblage that has been metamorphosed under greenschist facies conditions.

Sample # EN23VS041

Mineral	Habit	Size (mm)	Abundance (%)	Comment
Olivine	Subhedral	0.2–2	45–50	Fine- to medium-grained, cumulus, olivine. The grains display a rounded to equant morphology occurring as intensely fractured chadacrysts within a pyroxene oikocryst. Grains are pervasively altered by serpentine and magnetite along the fractures, most grains are completely replaced.
Pyroxene	Subhedral to anhedral	2–6	50–55	Medium- to coarse-grained, intercumulus, prismatic oikocrysts, enclosing olivine chadacrysts. Grains display strong, pervasive pseudomorphic to felty alteration by acicular, very fine-grained aggregates of actinolite-tremolite and chlorite. Several grains exhibit a sieve texture, characterized by very fine-grained oxide inclusions. The sample was likely dominated by clinopyroxene (40%) based on the presence of actinolite-tremolite, chlorite, and brown hornblende, which are pseudomorphic alteration intercumulus minerals. 15% comprised orthopyroxene based on anthophyllite-talc-chlorite alteration, and zones resembling equant grains
Chromite	Euhedral	0.02–0.4	1	Well-preserved chromite, disseminated through the thin section, occurs as euhedral equant grains. Grain boundaries are often well defined, and grains are sometimes weakly fractured. The chromite displays concentric zoning where primary chromite is mantled by magnetite. Chromite occurs as inclusions in both pyroxene and olivine, although in olivine, it is only observed within fractures. Chromite display bimodal grain size, with coarser grains occurring only within intercumulus silicates to olivine, while finer grains are observed in both olivine and interstitial silicates.

Sulfides	Anhedral	0.01–0.1	Trace	Very fine-grained, disseminated Po>Ccp. Mostly observed as interstitial grain along boundaries of alteration minerals. Highly irregular grains, blocky occurring in clusters of disseminated aggregates.
Comments: This sample comprises strongly altered, fine- to medium-grained, poikilitic peridotite. It consists of moderately serpentinized cumulus olivine and strongly altered to amphibole and serpentine group minerals, pyroxene, as well as small amounts of anhedral hornblende. The alteration of the sample is pervasive and pseudomorphic, with primary relationships between the clinopyroxene and olivine well defined. The preservation of relic clinopyroxene and alteration assemblage suggests that clinopyroxene was the dominant phase over orthopyroxene. Differences in alteration and relic morphology of orthopyroxene suggest it comprised 10–15% while clinopyroxene occurring as prismatic grains and altering to actinolite-tremolite and hornblende comprised 40–45%.				

Sample # EN23VS042

Mineral	Habit	Size (mm)	Abundance (%)	Comment
Olivine	Subhedral	0.15–2.2	55–60	Fine- to medium-grained, strongly altered, cumulus olivine. Grain morphologies appear to be predominantly equant and locally rounded, occurring as chadacrysts within pyroxene crystals. Most grains are completely pseudomorphed by chlorite, preserving only primary grain boundary outlines. Within the orthopyroxene oikocryst, grains tend to be more preserved; however, they are intensely fractured and weakly altered, displaying a mesh texture. Approximately 5% of primary olivine fragments are preserved.
Clinopyroxene	Anhedral	1–4	20–25	Medium-grained, intercumulus, strongly altered by alteration assemblage minerals. Primary grains are nearly absent due to alteration to amphiboles and serpentine. Grains display alteration to fine-grained felty aggregates of actinolite-tremolite and chlorite. Brown hornblende, displaying typical cleavage of 56-120°, is observed to overprint parts of relic clinopyroxene containing dendrite-like Fe-oxide inclusions. The hornblende is partially rimmed by actinolite-tremolite.
Orthopyroxene	Subhedral to Anhedral	2–6	15–20	Anhedral, medium-grained, pervasively altered orthopyroxene oikocrysts. Primary grains can be distinguished by alteration to very fine-grained aggregates of talc +/- anthophyllite. Unaltered olivine chadacrysts are preserved within pseudomorphed orthopyroxene. More equant in morphology compared to clinopyroxene, which is more prismatic.
Chromite	Euhedral to subhedral	0.01–0.3	0.5	Equant, fine- to very fine-grained, zoned chromite grains, sometimes weakly fractured and have irregular grain boundaries. Occur as inclusion in pyroxene, and sometimes in olivine along fractures. Chromite grains show zonation to magnetite along the rims. Occur as disseminated individual grains or in clusters. Bimodal grain size, with fine-grained inclusions sitting within orthopyroxene oikocrysts, and larger within interstitial clinopyroxene.

Sulfides	Anhedral	0.01–0.06	Trace	Very fine-grained, weakly disseminated grains of Po, interstitial to alteration phases and sometimes rimmed by magnetite. Grains are irregular and blocky.

Comments: This sample comprises strongly altered, fine- to medium-grained, inequigranular, poikilitic peridotite. It consists of cumulus, fine- to medium-grained olivine, and intercumulate, equant orthopyroxene and clinopyroxene, and intercumulus hornblende. Olivine in this sample is strongly pseudomorphed by serpentine, displays rounded textures, and is only preserved as intensely fractured, partially altered chadacrysts within orthopyroxene oikocrysts.

Sample # EN23VS043

Mineral	Habit	Size (mm)	Abundance (%)	Comment
Olivine	Subhedral	0.15–2.2	60–65	Fine- to medium-grained, strongly pseudomorphed, cumulus olivine. Grains are often rounded and display elliptical grain morphologies. Olivine is entirely replaced by serpentine outside of orthopyroxene oikocrysts. In the oikocrysts, grains range from fresh, rounded to partially altered, mesh-textured.
Clinopyroxene	Anhedral	0.5–3	10–15	Anhedral, medium-grained, prismatic, intercumulate clinopyroxene, strongly altered, individual primary grains are difficult to discern. Clinopyroxene occurs interstitial to orthopyroxene and olivine, where it is sometimes observed as oikocrysts. Pyroxene displays weak alteration to aggregates of actinolite-tremolite and serpentine. Magnetite and chlorite alteration occur throughout, concentrated within clinopyroxene grains. Patchy, anhedral, brown hornblende is observed to overprint clinopyroxene and contains dendrite-like inclusions of Fe-oxide.
Orthopyroxene	Anhedral	2–7	20–25	Medium- to coarse-grained, equant, weakly altered oikocrysts. Along grain boundaries and fractures, altered to talc+/-chlorite aggregates. Orthopyroxene oikocrysts preserve well, unaltered, olivine chadacrysts.
Oxides	Euhedral to subhedral	0.05–0.2	0.5	Equant, fine-grained, disseminated grains of chromite sometimes occur in clusters. Partially altered to magnetite along the rim, weakly fractured, and have irregular grain boundaries. Occurs as inclusions within pyroxene and sometimes olivine along fractures. Fine- to very fine-grained aggregates of magnetite occur within groundmass interstitial to orthopyroxene and olivine.
Sulfides	Anhedral	0.01–0.03	Trace	Very fine-grained, weakly disseminated grains of blocky Po were observed to occur in clusters.

Comments: This sample comprises medium- to coarse-grained, inequigranular, poikilitic, cumulus, peridotite. It consists of moderately serpentinized, equant to anhedral, cumulus olivine, strongly altered medium-grained intercumulate clinopyroxene oikocrysts, and coarse-grained oikocrysts of orthopyroxene preserving unaltered olivine chadacrysts. Reddish-brown hornblende is observed as a patchy anhedral overprint on clinopyroxene. Within this sample, two sets of fractures/fluids can be observed, altering within orthopyroxene oikocrysts. Serpentine group minerals infill the first set of fractures, while the second, crosscuts the first, and alters the orthopyroxene to fine-grained talc aggregates.

Sample # EN23VS044

Mineral	Habit	Size (mm)	Abundance (%)	Comment
Olivine	Subhedral	0.05–0.5	25–30	Pervasively altered, fine-grained olivine. Primary characteristics and abundance of olivine are difficult to determine, but primary grain outlines are observed within altered pyroxene oikocrysts, which appear to have been rounded equant grains. The grains are replaced by talc, with a lesser degree of serpentine.
Pyroxene	Anhedral	0.5–3	60–65	Intensely altered, medium-grained, pyroxene. The primary characteristics of the pyroxene grains are difficult to discern due to high degrees of overprinting alteration by serpentine, talc and amphibole group minerals. A few partial, remnant fragments of clinopyroxene are locally observed. Some pyroxenes exhibit a sponge-like texture, characterized by opaque inclusions. Equant morphologies, altered to talc-carbonate resembling orthopyroxene, are observed with sulfides concentrated outside these grains. The sample appears to have consisted of approximately equal amounts of clinopyroxene (~35%) and orthopyroxene (~30%).
Chromite	Euhedral to subhedral	0.04–0.4	1	Fine- to medium-grained, weakly fractured, zoned chromite grains that often display irregular grain boundaries. The grains show inner cores of chromite, which is usually rimmed/altered to magnetite. Occur in individual disseminated grains or aggregate clusters. Very fine-grained, disseminated magnetite occurs throughout, associated with serpentine.
Sulfides	Anhedral	0.05–0.6	5	Consists of polysulfide grains comprising Po (3%), Ccp (1%), and Pn (2%). The sulfides are very strongly disseminated, locally net-textured. Dominant sulfide within the sample commonly occurs as part of polysulfide grains and less commonly as finely disseminated aggregates of Po. The grains are highly irregular, blocky and are often interstitial to alteration assemblages.
Comments: This sample is intensely overprinted by alteration mineral assemblages, making the primary characteristics of minerals and their textures difficult to discern. It is fine- to medium-grained, inequigranular, poikilitic, cumulate, pyroxenite. The sample appears to have consisted of pyroxene and cumulus olivine. The olivine outlines are most well-preserved within pseudomorphed pyroxene grains, where they seem to have been rounded and now replaced by talc. Most of the sample consists of overprinting alteration minerals that occur as a fine-to very fine-grained mixture of talc, carbonate, serpentine and to a lesser extent actinolite.				

Sample # EN23VS045

Mineral	Habit	Size (mm)	Abundance (%)	Comment
Olivine	Subhedral	0.4–2.5	30–40	Completely pseudomorphed, grains of olivine that appear to have been medium-grained, subrounded strongly fractured. The grains appear to be replaced by two phases. The first phase of bastite is composed of ultra-fine-grained, fibrous serpentine and patchy talc aggregates overprinting parts of the altered olivine grains.

Pyroxene	Anhedral	0.1–5	50–60	No primary characteristics of the grains are preserved. Mineral aggregates composed of talc, carbonate and chlorite are interpreted to represent intercumulus pyroxene that has been completely altered.
Oxides	Euhedral to anhedral	0.05–0.2	2	Finely disseminated aggregates of subhedral, equant chromite often occur in clusters. Occur interstitial to altered olivine with several grains occurring as inclusions. Grains are usually rimmed or completely altered by magnetite. Small amounts of magnetite are seen to mantle sulfide phases.
Sulfides	Anhedral	0.05–0.2	7	Interstitial to olivine grains and composed of anhedral polysulfide aggregates, of disseminated to patchy Ccp (3%), Po (3%) and Pn (1%). They appear blocky and anhedral, often enclosing alteration phases. Accessory amounts of very fine-grained Po occur along fractures as disseminated anhedral grains.
Comments: This sample comprises intensely pseudomorphed, fine- to medium-grained, inequigranular, cumulate, peridotite. Olivine is completely pseudomorphed and is recognized by its equant shape and cumulus characteristics. Intercumulus material comprises chlorite-actinolite-tremolite-talc, interpreted to have been a pyroxene.				

Sample # EN23VS046

Mineral	Habit	Size (mm)	Abundance (%)	Comment
Pyroxene	Euhedral to Subhedral	0.6–1.2	65–75	Pervasively altered to alteration assemblage minerals. Alteration is pseudomorphic, preserving outlines of primary grain boundaries of pyroxene, which appears to have been equigranular, equant, and euhedral to mostly subhedral in shape. A patchy sieve texture is observed in several grains containing fine-grained inclusions of oxide minerals. Several grains display patchy to mottled brown hornblende along the primary grain boundaries. Most of the alteration is pseudomorphic, pervasively replacing primary grains to fine-grained aggregates of actinolite-tremolite and sometimes intercalated with chlorite. Subhedral to anhedral, skeletal titanite (0.5%) is seen overprinting pyroxene alteration products in several locations within the sample. Accessory amounts of fine-grained platy biotite are observed overprinting several grains.
Plagioclase	Subhedral	0.4–1.2	25–35	Plagioclase is moderately altered, with primary grain characteristics well preserved. Alteration comprises very fine-grained sericite, ranging from pervasive overprint to patchy, often preserving relic plagioclase along the rims. Very fine-grained, anhedral epidote occurs sporadically, locally accompanying sericite. Less commonly, plagioclase is observed to be overprinted by patchy chlorite. Primary grain morphologies are well-preserved, with grains ranging from mostly euhedral to subhedral in shape and exhibiting a tabular morphology. In weakly altered grains, undulous extinction and bulging occur, with polysynthetic twinning seen in the least altered grains. 5% unaltered plagioclase.

Oxides	Subhedral to anhedral	0.05–0.2	1	Consists of very fine-grained patchy aggregates of ilmenite occurring along the grain boundaries of altered pyroxenes to brown hornblende. Trace amounts of chromite grains are seen with a subhedral, equant morphology.
Sulfides	Euhedral to anhedral	0.02–1.6	1	Consists of disseminated, euhedral, cubic pyrite grains with trace amounts. Trace amounts of chalcopyrite are seen within the cross-cutting vein.
Comments: This sample comprises moderately altered, fine-grained, equigranular, non-foliated leucogabbro. Pyroxene is the dominant phase within the sample, ranging from euhedral to mostly subhedral grains. It is granular and completely overprinted by alteration assemblage minerals. Plagioclase makes up the rest of the primary mineralogy; it is the least altered phase, often preserving polysynthetic twinning and tabular-like morphology. A 3mm vein, comprising granular quartz, plagioclase, and amphibole, crosscuts the sample.				

Sample # EN23VS054

Mineral	Habit	Size (mm)	Abundance (%)	Comment
Pyroxene	Subhedral	0.5–1.5	65–75	Pervasively altered, with primary characteristics poorly preserved. Where primary grain boundaries can be recognized, grains appear to have been subhedral and equant to prismatic and intergranular. Alteration is pervasive, pseudomorphic with grains altering to fine-grained aggregates of acicular actinolite-tremolite, platy biotite, and chlorite.
Plagioclase	Euhedral to Subhedral	0.3–1.2	25–35	Fine-grained, moderately altered, lath-like to tabular plagioclase appears to be partially or completely enclosed by altered pyroxene. Least altered grains often show polysynthetic twinning. Plagioclase is overprinted by patchy to pervasive, very fine-grained sericite, which mostly overprints the core of the grains, with minor epidote. Several grains display bulging along grain boundaries, undulous extinction and deformation twinning. 10% unaltered plagioclase.
Sulfides	Anhedral	0.02–0.4	2	Fine- to very fine-grained, clusters of disseminated, blocky, Po>Ccp>Pn, with several grains of euhedral pyrite. Grains are very irregular and sometimes slightly pitted. Mostly occur as monomineralic grain clusters, but locally, polymineralic grains of Po-Ccp are observed.
Oxides	Anhedral	0.03–0.5	Trace	Oxides occur as very fine-grained disseminated clusters comprising chromite, which is rimmed by magnetite. Magnetite also occurs rimming sulfide grains.
Comments: This sample comprises moderately altered, fine- to medium-grained, inequigranular, sub-ophitic, melagabbro. Pyroxene makes up the most abundant silicate phase, which is often completely replaced by alteration minerals. Primary grains appear to partially or completely enclose plagioclase grains. Plagioclase is the least altered phase, locally showing a variolitic-like growth, intergrown with anhedral, skeletal, pervasively altered pyroxene.				

Sample # EN23VS057

Mineral	Habit	Size (mm)	Abundance (%)	Comment
Pyroxene	Subhedral	0.2–1.5	50–60	Pervasively replaced by alteration assemblage minerals. Primary characteristics are not preserved;

				however, grains appear to have been interstitial to euhedral plagioclase. Alteration consists of fine-grained aggregates comprising acicular actinolite-tremolite, platy chlorite and skeletal titanite.
Plagioclase	Euhedral to subhedral	0.5–2	40–50	Strongly altered, medium-grained, granular, euhedral, tabular grains. Pervasively replaced by very fine-grained aggregates of sericite+/-epidote, but preserves primary shape well. Alteration products of pyroxene are seen to overprint portions of the grains. <1% unaltered grains.
Magnetite	Anhedral	0.02–0.1	Trace	Trace amounts of disseminated magnetite occur interstitial to alteration phases of pyroxene.
Comments: This sample comprises intensely altered, medium-grained metagabbro. Alteration is pseudomorphic, making it difficult to discern the primary grain relationships and phases. Plagioclase appears to have been medium-grained, tabular, and pyroxene appears to have been interstitial and anhedral. Several quartz veinlets ranging from 0.05 to 0.15mm crosscut the sample.				

Sample # EN23VS060

Mineral	Habit	Size (mm)	Abundance (%)	Comment
Pyroxene	Euhedral to subhedral	0.4–1.2	70–75	Typically, pervasively altered, fine-grained, pyroxene. Alteration is pseudomorphic, preserving primary grain outlines. Primary grains appear to have been fine-grained, granular, euhedral, mostly equant to prismatic. In some areas, they appear to encompass plagioclase grains, but in others, plagioclase appears to be interstitial to pyroxene. Primary grain boundaries are often outlined by sieve-textured greenish hornblende containing inclusions of opaque minerals. Several relic grains are observed to comprise clinopyroxene, which displays simple twinning. In addition to chlorite alteration, orthopyroxene exsolution occurs. Fine-grained aggregates of actinolite-tremolite, chlorite, skeletal titanite, and accessory amounts of biotite mostly pseudomorphically alter pyroxene grains. Patchy brown hornblende often outlines the primary grain boundaries.
Plagioclase	Euhedral to anhedral	0.3–1.5	25–30	Moderately altered, mostly fine-grained, tabular, euhedral to subhedral grains. Subhedral grains appear to be interstitial to euhedral pyroxene grains. Alteration intensity is variable, with the least altered grains displaying polysynthetic twinning. Alteration consists mostly of fine-grained aggregates of sericite+/-epidote. 5% unaltered grains.
Oxides	Euhedral to anhedral	0.01–0.15	Trace	Consists of chromite and ilmenite. Chromite occurs in clusters of euhedral to subhedral, fine-grained aggregates. Grain boundaries are often irregular, and the grains are fractured. Ilmenite occurs as very fine-grained patches within titanite grains.
Sulfides	Anhedral	0.01–0.05	Trace	Consists of equal amounts of Py and Ccp. Py is generally coarser-grained, occurring as anhedral individual grains. Ccp occurs as very fine-grained, disseminated clusters.

Comments: This sample comprises moderately altered, fine-grained, sub-ophitic, melagabbro. It consists of equigranular, equant pseudomorphed pyroxene grains and smaller interstitial grains of granular plagioclase. In some areas, pyroxene appears to partially enclose grains of plagioclase, while in other locations, plagioclase appears to be interstitial to equant grains of pyroxene. The sample preserves relic fragments of clinopyroxene, which likely comprise most of the modal mineralogy.

Sample # EN23VS061

Mineral	Habit	Size (mm)	Abundance (%)	Comment
Pyroxene	Subhedral	0.4–0.9	65–75	Pervasively overprinted by alteration mineral assemblages. Primary grain characteristics are difficult to establish; however, local relic uralite alteration (brown hornblende with dendrite-like intergrowths of Fe-oxide displaying typical 56–120-degree cleavage) occurs along the margins of the primary pyroxene grains, which show subhedral shape and prismatic morphology. Uralite occurs as a patchy localised alteration or as a localised alteration along the rim. In addition, felty to parallel aggregates of fine-grained acicular actinolite-tremolite, platy biotite, chlorite, and anhedral skeletal titanite pervasively overprint pyroxene grains. Approximately 1% of primary clinopyroxene fragments are observed to be unaltered, exhibiting a dusty appearance.
Plagioclase	Euhedral to subhedral	0.4–1.2	25–35	Tabular to elongate lath-like grains, generally with irregular grain boundaries; however, the primary morphology is clear. It exhibits patchy, very fine-grained sericite+/-epidote alteration, local weak patchy replacement by chlorite, and disseminated overprinting by actinolite-tremolite and biotite. Actinolite tremolite overprinting is especially evident along plagioclase-pyroxene grain contacts. Plagioclase-plagioclase grain boundaries are often sutured, and grains are sometimes fractured, locally displaying bulging textures and development of deformation twins.
Oxides	Anhedral	0.05–0.15	Trace	Consists of magnetite-altered chromite grains, occurring as finely disseminated anhedral, blebby clusters, commonly mantled by fine-grained felty aggregates of biotite+/-chlorite. Chromite is observed as inclusions within both pyroxene and plagioclase. Pyroxene locally displays sieve texture containing inclusions of chromite. Magnetite is also observed rimming sulfide aggregates. Very fine-grained, cleavage-parallel Fe-oxide exsolutions are observed within the hornblende patches.
Sulfides	Anhedral	0.01–0.03	Trace	Few specs of very finely disseminated polymineralic grains, comprising Po>Ccp>Pn and rarely monomineralic grains of Po or Ccp. Local grains of Po display exsolution of Pn flame structures.

Comments: This sample consists of moderately altered, fine-grained, equigranular, non-foliated melagabbro. It consists of completely replaced pyroxene and weakly altered plagioclase. Determining primary proportions of orthopyroxene or clinopyroxene was not possible due to the intense degree of alteration by ferromagnesian mineral assemblages and biotite. However, the dominant alteration assemblage and the presence of unaltered clinopyroxene fragments imply that clinopyroxene was likely the dominant phase. The equigranular nature of the sample, along with the euhedral shape of the plagioclase, suggests that the sample was sub-ophitic, with pyroxene alteration products enclosing the plagioclase.

Sample # EN23VS064

Mineral	Habit	Size (mm)	Abundance (%)	Comment
Pyroxene	Subhedral	0.5–1.3	55–65	Fine-grained, poikilitic, strongly overprinted by alteration assemblages. Primary characteristics are difficult to discern, except for a few pseudomorphed, equant to subhedral grains, occasionally displaying simple twinning. Several types of alteration are observed: (1) patchy to mottled brown hornblende observed to overprint pyroxene grains, and (2) felty or parallel replacement by acicular actinolite-tremolite and chlorite, either pseudomorphic or as fine-grained aggregates. Hornblende is dusty in appearance, containing inclusions of Fe-oxide, and is overprinted along the edges by acicular actinolite-tremolite. Pyroxene grains often display irregular grain boundaries and dislocations.
Plagioclase	Euhedral to subhedral	0.5–2	25–30	Pervasively replaced by chlorite, with no unaltered fragments identified. Plagioclase is interpreted to be present based on the occurrence of tabular to lath-like shapes, which are only replaced by chlorite. These grains are often surrounded by a pyroxene alteration assemblage of minerals.
Olivine	Subhedral	0.05–0.2	5–10	Pervasively pseudomorphed, rounded, fine-grained olivine observed as anhedral chadacrysts mantled by hornblende alteration of pyroxene. These grains are overprinted by pyroxene alteration phases.
Oxides	Euhedral	0.01–0.15	Trace	Consists of chromite, magnetite, and Fe-oxide. Primary chromite grains have jagged grain boundaries and are altered to magnetite, retaining an equant primary morphology. Significantly smaller in grain size than chromite, very fine-grained anhedral inclusions of Fe-oxide are observed within the hornblende.
Sulfides	Anhedral	0.05–1.7	2	Consists of fine- to very fine-grained, polymineralic, disseminated aggregates of Po, Ccp, and Pn. Sulfides occur as blocky disseminated patches interstitial to pyroxene grains.

Comments: This sample consists of strongly altered, fine- to medium-grained, inequigranular, poikilitic, olivine melagabbro. It mainly consists of medium-grained subhedral to anhedral pyroxenes completely overprinted by variable alteration styles and assemblages. Olivine was observed as chadacrysts within altered pyroxene, where patchy hornblende alteration is present. Outside of the pyroxene oikocrysts, olivine was not identified due to the intensity of alteration. The sample likely contained more olivine than the grains observed as chadacrysts. Plagioclase is recognized within the sample by the presence of tabular to lath-like chlorite-replaced grains. The majority of the sample consists of alteration assemblage minerals, making it difficult to estimate the abundance of primary silicate phases.

Sample # EN23VS068

Mineral	Habit	Size (mm)	Abundance (%)	Comment
Clinopyroxene	Subhedral to anhedral	1.5–2.5	75–80	Medium-grained, strongly altered clinopyroxene. Primary grain characteristics are difficult to discern but appear to have been predominantly subhedral with a prismatic to equant morphology. It is overprinted by several phases of alteration comprising ferromagnesian assemblage minerals. The dominant alteration assemblage consists of actinolite-tremolite +/- chlorite overprinting clinopyroxene grains as felty, very fine-grained aggregates or as pervasive, pseudomorphic, parallel replacement by actinolite-tremolite. Brown to green, patchy hornblende is observed along pyroxene grains, locally overprinting primary clinopyroxene grains. The hornblende is often rimmed by acicular actinolite-tremolite. A large portion of the grains fragmented along cleavage planes. Biotite is observed as a myrmekite-like intergrowth with pyroxene, locally appearing as nearly complete replacement, with only very fine-grained actinolite-tremolite assemblages present.
Orthopyroxene	Subhedral	0.2–0.6	5–10	Fine-grained, weakly altered, euhedral equant commonly fractured. These grains exhibit distinct characteristics from the dominant clinopyroxene, with weak alteration along fractures characterized by iddingsite. One grain is observed to be enclosed by clinopyroxene alteration phases.
Plagioclases	Euhedral	0.2–0.8	3–5	Strongly altered, fine-grained, lath-like grains, encompassed by clinopyroxene grains. These grains are pervasively replaced by chlorite with no relic grains preserved.
Oxides	Euhedral to subhedral	0.01–0.15	Trace	Consists of chromite-magnetite and ilmenite. Chromite occurs as equant euhedral to subhedral grains, partially to completely altered to magnetite along the rim. It occurs in disseminated clusters that are often bound by platy biotite aggregates. Ilmenite is smaller in grain size and abundance than chromite or magnetite, occurring within the hornblende.
Sulfides	Anhedral	<0.1	Trace	Consists of very fine-grained, blocky to blebby, disseminated clusters of polysulfide Po and Ccp. Concentrated in the interstitial spaces of alteration phases.

Comments: This sample consists of moderately altered, medium- to fine-grained, inequigranular pyroxenite. It consists predominantly of medium-grained prismatic clinopyroxene overprinted by several alteration assemblages, and fine-grained orthopyroxene primocrysts. Unaltered plagioclase was not identified; however, it was identified through the presence of lath-like grains pseudomorphed by chlorite. In addition to the ferromagnesian minerals associated with clinopyroxene alteration, biotite makes up 30% of the sample. It is observed as the groundmass to ferromagnesian alteration minerals of pyroxene. Trace amounts of anhedral, skeletal, fine-grained titanite were observed to overprint alteration assemblages. Due to the high degree of alteration by amphibole, biotite and chlorite, it is challenging to discern accurate phase proportions.

Sample # EN23VS099

Mineral	Habit	Size (mm)	Abundance (%)	Comment
Actinolite	Idioblastic	0.1–0.5	70	Fine-grained, Idioblastic, acicular to blade-like grains, aligned parallel to foliation. Several grains appear to be more prismatic in shape, possibly a pseudomorphic replacement of primary pyroxene.
Plagioclase	Subidioblastic to xenoblastic	0.2–1	5	Fine-grained, typically tabular grains that are intensely altered to sericite and minor epidote. Where alteration is not pervasive, relic plagioclase rims are preserved, displaying undulous extinction.
Sericite	Subidioblastic	0.01–0.04	15	Very fine-grained, brown in plane-polarized light, intensely overprinting relic plagioclase grains
Chlorite	Xenoblastic	0.1–0.2	2	Fine-grained, platy, foliation-parallel aggregates are disseminated throughout the sample.
Epidote	Subidioblastic	0.01–0.06	1	Very fine to fine-grained disseminated aggregates are present throughout the sample, most commonly observed within plagioclase.
Titanite	Xenoblastic	0.01–0.08	2	Fine- to very fine-grained, string-like lenses parallel to foliation occur throughout the sample, comprising skeletal grains of titanite.
Biotite	Subidioblastic to xenoblastic	0.1–0.35	3	Platy, fine-grained, interstitial to actinolite-tremolite. Several grains are observed to be partially replaced by chlorite. Aggregates of biotite are more abundant in proximity to chromite grains.
Chromite	Subidioblastic	0.1–0.3	1	Comprises equant grains of chromite, partially altered along the rim to magnetite. Occur as individual grains or in clusters. Grains are observed to be mantled by chlorite and biotite.
Sulfides	Xenoblastic	0.03–0.4	Trace	Trace amounts of xenoblastic, angular, pyrite grains.
Comments: This sample consists of fine-grained, foliated greenschist. It consists predominantly of aligned acicular actinolite-tremolite and sericitized plagioclase as well as smaller amounts of chlorite, epidote, titanite, and biotite. Foliation is defined by the alignment of actinolite-tremolite, chlorite, and skeletal titanite lenses. Foliation intensity is zoned, with ¾ of the thin section being strongly foliated, while one-quarter is less intensely foliated, with actinolite-tremolite occurring as more prismatic variably oriented grains, possibly replacing primary pyroxene. The mineral assemblage and texture of the sample suggest a mafic protolith that has been metamorphosed under greenschist conditions.				

Sample # EN23VS100

Mineral	Habit	Size (mm)	Abundance (%)	Comment
Orthopyroxene	Subhedral	0.5–3	45–50	Pervasively overprinted by alteration assemblage minerals. Primary grain morphologies are observed and appear to have been medium-grained, strongly altered, prismatic, poikilitic grains. It is almost entirely replaced by a very fine- to fine-grained matrix comprising platy fibrous talc. Orthopyroxene contains disseminated, pervasively fine-grained opaque inclusions. Orthopyroxene is commonly rimmed by a fine-grained matrix comprising fibrous actinolite-tremolite, chlorite, and very fine-grained opaque inclusions along the grain margins. Relic remnants of orthopyroxene are preserved at the rims

				intergrown with the alteration, as anhedral, broken-up grains.
Clinopyroxene	Anhedral	0.4–1.6	35–40	Strongly overprinted by alteration assemblage minerals. Primary grains appear to have been interstitial to orthopyroxene, with 5% of primary clinopyroxene fragments preserved. The grains can be distinguished from orthopyroxene by the numerous oxide inclusions, which give it a sieve-like texture. Several grains are completely pseudomorphed by actinolite-tremolite and talc. Locally, grains contain primary olivine chadacrysts. Redish-brown hornblende occurs in association with interstitial clinopyroxene as an alteration product, locally it displays sharp grain boundaries with surrounding silicates.
Plagioclase	Anhedral	0.4–2	3–5	Completely overprinted by alteration assemblage minerals. Primary grains are difficult to discern but are interstitial and have been overprinted by chlorite and mafic minerals assemblages.
Olivine	Anhedral	0.3–1.5	5–10	Fine-grained, unaltered, anhedral olivine. Olivine is anhedral, having irregular, elongate and rounded shapes, strongly fractured and commonly rimmed by a brown clay mineral. They occur as chadacrysts in altered pyroxene grains. Within oikocrysts, olivine is rimmed by acicular actinolite and chlorite.
Oxides	Subhedral to anhedral	0.01–0.25	0.5	Consists of multiple phases, including subhedral chromite, fine-grained inclusions of ilmenite and alteration-associated magnetite. Chromite occurs as inclusions in all grains, ilmenite is ultrafine-grained, giving clinopyroxene a spongy texture, and magnetite is associated with fractures and serpentinization. Chromite is rimmed by magnetite.
Sulfides	Anhedral	0.01–0.25	Trace	Finely disseminated, polysulfide grains of Po > Ccp occur as interstitial to altered prismatic orthopyroxene grains as blocky, highly irregular aggregates, sometimes with magnetite commonly bounding their margins.
Comments: This sample is strongly overprinted by alteration assemblage minerals, making it difficult to discern the primary characteristics and model abundances. The sample is interpreted to have consisted of orthopyroxene, clinopyroxene, olivine, plagioclase and hornblende. Orthopyroxene is medium-grained, equigranular, equant, and has been completely pseudomorphed by talc aggregates, leaving the grain outline through chlorite-actinolite alteration. Clinopyroxene is anhedral, interstitial to orthopyroxene and can be distinguished by preservation of primary grain fragments, sieve texture, and actinolite-tremolite chlorite. Olivine is predominantly fine-grained and appears weakly altered. It is anhedral with irregular grain morphologies and exhibits strong fracturing. Plagioclase is completely altered, as indicated by pervasive chlorite alteration.				

Sample # EN23VS101

Mineral	Habit	Size (mm)	Abundance (%)	Comment
Pyroxene	Subhedral to anhedral	0.6–2.3	75–85	Fine- to medium-grained, moderately overprinted by alteration assemblage minerals. Alteration intensity often obscures primary characteristics. Where shapes are preserved, grains appear to have been subhedral to anhedral, prismatic to equant oikocrysts (enclosing

				altered olivine) and equigranular. Grains are moderately overprinted on the rims or completely by actinolite-tremolite, often along the rims of pyroxene grains. Felty, very fine-grained aggregates of actinolite-tremolite and chlorite were also observed after pyroxene. Some grains are characterized by the presence of sieve textured patches containing inclusions of oxide minerals. The alteration assemblage, with prismatic morphology, suggests that the dominant phase was clinopyroxene.
Olivine	Subhedral	0.1–0.5	5–10	Fine-grained, pervasively altered, chadacrysts of olivine occur within pyroxene oikocrysts. Olivine is overprinted by pyroxene alteration phases, with no unaltered fragments preserved. It is often identified by the mantling of sieve-textured pyroxene. Outside of the pyroxene oikocrysts, no olivine was observed.
Plagioclase	Euhedral	0.4–1.5	2–5	Fine-grained, pervasively pseudomorphed by chlorite. Primary grains appear to have been tabular to lath-like, partially enclosed by pyroxene.
Hornblende	Anhedral	0.1–0.3	<1	Displays moderate brown pleochroism, fine-grained, anhedral, intercumulate, mantled by actinolite-tremolite.
Oxides	Subhedral to anhedral	0.01–0.2	1	Consists of chromite, magnetite and ilmenite. Chromite is the dominant phase, often altered along the rim or pervasively by magnetite. Magnetite also occurs interstitial to chlorite laths. Within sieve-textured pyroxene, very fine-grained inclusions of magnetite and ilmenite are observed.
Sulfides	Anhedral	0.05–0.3	0.5	Consists of Pn and Po occurring as fine- to very fine-grained, blebby, polysulfide grains with local Pn flame structures within Po.
Comments: This sample consists of moderately altered, fine- to medium-grained, poikilitic, olivine pyroxenite. It consists of medium-grained, prismatic pyroxenes that are moderately overprinted by alteration assemblages. Olivine occurs as pseudomorphed chadacrysts within sieve-textured pyroxene oikocrysts. Plagioclase occurs as chlorite pseudomorphed, medium-grained laths. Fragments of relic clinopyroxene are locally preserved, therefore the sample was likely dominated by clinopyroxene. Several grains appeared to contain exsolution of orthopyroxene.				

Sample # EN23VS103

Mineral	Habit	Size (mm)	Abundance (%)	Comment
Pyroxene	Subhedral	0.5–2.5	70–80	Medium-grained strongly overprinted by alteration assemblage minerals. Primary characteristics are poorly preserved; grains appear to have been prismatic, intercumulus, and exhibit a poikilitic and ophitic texture with olivine and plagioclase chadacrysts. Pyroxene commonly displays sieve texture, containing very fine-grained chromite-magnetite inclusions. Grains are often fragmented with pseudomorphic alteration by actinolite-tremolite, to local felty replacement by aggregates of very fine-grained actinolite-tremolite and chlorite. Patchy to mottled, anhedral, fine-grained brown hornblende is locally

				observed. Several clinopyroxene fragments were observed (~1%).
Plagioclase	Euhedral	0.8–2	10–15	Pervasively pseudomorphed by chlorite. Relic grain outlines are observed, appearing to have been tabular to elongate lath-like.
Olivine	Subhedral	0.1–0.6	3–10	Fine-grained, pseudomorphed chadacrysts. Grains are observed to be mantled by sieve-textured pyroxene, with a rounded shape. These are overprinted by alteration products of the surrounding pyroxene.
Hornblende	Anhedral	0.2–0.6	<1	Fine-grained, intercumulate, anhedral, brownish grains of hornblende with dendrite-like oxide inclusions.
Oxides	Euhedral	0.05–0.3	2	Consists of chromite and magnetite. Chromite is fine-grained, commonly pitted with jagged grain boundaries. Several euhedral, equant grains are locally preserved. Chromite occurs as disseminated patches throughout the sample. It is observed to be replaced by magnetite along the rims, generally with preserved chromite cores.
Sulfides	Anhedral	0.02–0.6	2	Consists of fine- to very fine-grained, disseminated, blocky, pitted, polysulfide aggregates of Po>Ccp>Pn and, more rarely, monosulfide Po. They occur interstitial to altered pyroxenes, locally appearing remobilized along amphibole grain boundaries. Several sulfide aggregates are observed to partially encompass equant chromite grains.
Comments: This sample consists of strongly altered, fine- to medium-grained, inequigranular, poikilitic, olivine pyroxenite. It appears to have consisted of medium-grained, prismatic pyroxene, fine-grained olivine chadacrysts, and medium-grained completely pseudomorphed by chlorite, lath-like plagioclase, and accessory amounts of hornblende. This sample is strongly overprinted by alteration assemblages, with chlorite being the dominant alteration phase. Pyroxene grains are recognized through pseudomorphic alteration by variable proportions of actinolite-tremolite, and chlorite assemblage. Plagioclase is recognized by the absence of amphibole minerals, and pervasive replacement by chlorite allowing recognition of lath-like to tabular grains. One portion of the sample features a poikilophitic texture with altered pyroxene enclosing a pseudomorphed plagioclase grain, in addition to rounded olivine chadacrysts.				

Sample # EN23VS105

Mineral	Habit	Size (mm)	Abundance (%)	Comment
Actinolite	Euhedral to subhedral	0.3–5.5	65	Medium-grained, euhedral, elongate blade-like grains. There is a bimodal size distribution, but most grains are medium-grained, with smaller grains occurring within the biotite matrix. Actinolite grains contain inclusions of very fine-grained carbonate minerals, which appear as irregular to rounded, possibly a product of alteration of plagioclase within them. The second type of inclusions consists of oxides, mostly magnetite, completely enclosed by actinolite and irregularly distributed throughout the grains. Simple twinning is locally observed.
Biotite	Subhedral	0.1–0.3	25	Biotite occurs as very fine-grained aggregates interstitial to actinolite phenocrysts. Mostly, they are variably oriented, but locally, a weak foliation is defined.
Titanite	Subhedral to anhedral	0.1–0.9	1	Fine-grained, equant grains, interstitial to actinolite, are commonly observed to partially wrap the actinolite

				grains. Mostly the titanite occurs as skeletal grains containing inclusions of biotite.
Carbonate	Subhedral	0.02–0.2	5	Fine-grained aggregates are disseminated throughout the samples, locally occurring in patches within the groundmass as well as inclusions in actinolite.
Quartz	Subhedral	0.1–0.2	3	Anhedral, fine-grained aggregates locally occur within the groundmass.
Oxides	Anhedral	0.01–0.15	0.5	Very fine-grained inclusions of magnetite are disseminated throughout actinolite grains. Generally irregular to rounded in appearance
Sulfides	Subhedral to anhedral	0.05–0.25	Trace	Fine-grained, polysulfide grains consisting mostly of Ccp and Py, disseminated interstitially to actinolite grains. Pyrite is often observed to be partially or completely mantled by chalcopyrite.
Comments: This sample is porphyritic, consisting of a bimodal grain size distribution. Medium-grained actinolite, and fine-grained groundmass consisting of mostly biotite and minuscule amounts of carbonate, quartz and titanite. Although the sample does not show pronounced fabric, it mineralogically resembles a mafic protolith.				

Sample # EN23VS108

Mineral	Habit	Size (mm)	Abundance (%)	Comment
Pyroxene	Subhedral	0.5–1.5	55–65	Strongly overprinted by alteration assemblage minerals. Primary grain size and characteristics are difficult to discern, however, grains appear to have been mostly fine- to medium-grained poikilitic. Grains are overprinted by fibrous, elongate actinolite and locally replaced partially by chlorite. Primary grain outlines are locally observed, as well as mottled to patchy alteration to a brown hornblende containing very fine-grained inclusions of ilmenite. Several relic clinopyroxene fragments are observed.
Plagioclase	Euhedral to subhedral	0.5–2	35–40	Moderately overprinted by alteration assemblage minerals. Plagioclase is finer in grain size than pyroxene and mostly displays tabular morphology. It is mostly replaced by chlorite in a myrmekitic-like intergrowth. Preserved primary plagioclase fragments are often overprinted by sericite and minor epidote. Within some pseudomorphed pyroxene grains, tabular chlorite replaces plagioclase. 10% unaltered grains.
Olivine	Subhedral	0.3–0.6	2–5	Completely altered to alteration assemblages. Local outline of olivine chadacrysts is seen within altered pyroxene as rounded grains.
Oxides	Subhedral to anhedral	0.01–0.5	3	It primarily consists of magnetite, with accessory amounts of chromite. Chromite is subhedral equant grains partially altered to magnetite along the rims. Magnetite occurs in lath-like intergrowths interstitial to chlorite. Very fine-grained inclusions of ilmenite are seen within brown hornblende along altered pyroxene grain boundaries.
Sulfide	Anhedral	0.05–0.1	Trace	Trace amounts of very fine-grained, irregular, blocky grains of Ccp and Po are disseminated throughout.

Comments: This sample comprises moderately altered, fine- to medium-grained, inequigranular, olivine melagabbro. It consists of predominantly pyroxene partially enclosing plagioclase grains and completely enclosing altered olivine chadacrysts. Relic fragments of clinopyroxene were observed.

Sample # EN23VS110

Mineral	Habit	Size (mm)	Abundance (%)	Comment
Pyroxene	Euhedral to subhedral	0.5–1.2	35–40	Fine-grained, strongly overprinted by alteration assemblage minerals. Primary characteristics are difficult to discern, but locally, pyroxene appears to have been fine-grained, equant, subhedral grains, locally enclosing plagioclase. Alteration is dominated by very fine-grained felty actinolite-tremolite and chlorite aggregates, and more rarely pseudomorphic occurring as replacement by actinolite-tremolite. Actinolite-tremolite is intergrown with biotite, which in some grains is observed to completely replace the grains, preserving an equant morphology. Locally, pyroxene is overprinted by mottled to patchy, fine-grained, brown hornblende.
Plagioclase	Subhedral	0.5–4	60–65	Medium-grained, moderately altered, euhedral plagioclase with a tabular to lath-like shape. Primary grain boundaries are commonly clearly defined locally, appearing to enclose altered equant pyroxene grains. Alteration is generally selective, zonal to the core and consists of chlorite-sericite+/-epidote. Overprinting by actinolite-tremolite and biotite occurs as pervasive dissemination. Some grains preserve primary polysynthetic twinning. Grain boundaries are often jagged, with a bulging texture at plagioclase-plagioclase grain boundaries. Several grains display the development of deformation twins.
Oxides	Euhedral to subhedral	0.1–0.25	Trace	Consists of pervasively disseminated, fine-grained, euhedral to subhedral aggregates of equant chromite. Mostly have irregular grain boundaries with partial alteration to magnetite. Chromite grains are rimmed by fine-grained platy aggregates of biotite. Very fine-grained inclusions of Fe-oxide occur within patchy brown hornblende.
Sulfides	Anhedral	0.01–0.15	Trace	Consists of trace amounts of very fine-grained, blocky to blebby Po grains.
Comments: This sample comprises moderately altered, fine- to medium-grained, sub-ophitic, inequigranular, leucogabbro. It consists of medium-grained lath-like to tabular plagioclase, and small in grain size, equant to prismatic altered pyroxene. Plagioclase is the most abundant, least altered silicate phase. Pyroxene is pervasively altered to a variable proportion of actinolite-tremolite-biotite-hornblende-chlorite assemblage. Biotite comprises 20% of the sample and is mostly associated with pyroxene alteration. Aggregates of disseminated actinolite-tremolite and biotite overprint the plagioclase grains. The sample is cross-cut by an oblique 1mm vein-like shear containing aligned, elongate laths of actinolite-tremolite.				

Sample # EN23VS114

Mineral	Habit	Size (mm)	Abundance (%)	Comment
Plagioclase	Euhedral to subhedral	0.25–1	25–30	Elongate laths are tabular, weakly to moderately overprinted by patchy, very fine-grained sericite

				alteration and patchy epidote aggregates. Along plagioclase grain boundaries, it is overprinted by alteration products of pyroxene. Locally displaying simple and/or kinked deformation twinning and bulging. Grains appear to have variolitic intergrowth with skeletal pyroxene grains.
Pyroxene	Subhedral to anhedral	0.2–2	65–70	Fine- to medium-grained, lath-like to tabular grains. Lath-like grains are a skeletal texture and intergrown with spherulitic plagioclase. Strongly altered to fine-grained actinolite-tremolite-biotite-chlorite occurring as felty aggregates or pervasive replacement by actinolite-tremolite. Brown hornblende occurs as a patchy alteration within altered pyroxene grains, generally sieve-textured. Fine-grained brown biotite generally alters the cores of the grains, which are sometimes intercalated with actinolite aggregates.
Sulfide	Anhedral	0.01–0.15	Trace	Polysulfide finely disseminated aggregates consisting of Po>Cpp>Pn generally occur in dismembered clusters or individual grains, mostly interstitial but sometimes encompassed by alteration phases. Rarely associated with very fine-grained magnetite
Oxides	Euhedral to anhedral	0.01–0.25	Trace	Consists of euhedral chromite grains, generally pitted and completely replaced by magnetite. Mostly encompassed by aggregates of ferromagnesian minerals and biotite. Very fine-grained clusters of blobby magnetite are disseminated throughout.
Comments: This sample comprises moderately altered, fine-grained, inequigranular, sub-ophitic, melagabbro. It consists of variolitic plagioclase laths intergrown with skeletal grains of altered pyroxene. Some plagioclase grains are encompassed by altered pyroxene. A 0.5cm carbonate vein and a 0.1cm brown-chlorite infilled fracture crosscut the sample.				

Sample # EN23VS116

Mineral	Habit	Size (mm)	Abundance (%)	Comment
Pyroxene	Anhedral to subhedral	0.6–0.9	75–80	Strongly overprinted by alteration minerals, with original characteristics poorly preserved. Several preserved grain boundary outlines of plagioclase show subhedral shape. Alteration consists of very fine- to fine-grained acicular aggregates of actinolite-tremolite, chlorite and biotite occurring as felty or parallel aggregates. Relic clinopyroxene is rare and exhibits dislocations along its cleavage planes. Patchy, dusty in appearance, hornblende occurs along altered pyroxene grain boundaries. Several grains display sieve texture containing very fine-grained inclusions of oxides. Anhedral skeletal grains of titanite are observed to accompany pyroxene alteration products.
Plagioclase	Euhedral to subhedral	0.3–1	15–20	Tabular, commonly displaying simple or polysynthetic twinning, and sometimes exhibiting kinked/ curved morphology. Plagioclase-plagioclase boundaries are mostly sharp, rarely displaying bulging. Plagioclase is locally overprinted by weak patchy very fine-grained sericite +/- epidote alteration and weak pervasive alteration by fine-grained chlorite and actinolite aggregates. Actinolite-chlorite alteration is most

				pronounced at grain boundaries, sometimes obscuring the original crystal habit.
Oxides	Subhedral to anhedral	0.01–0.15	Trace	Consists of subhedral to anhedral chromite grains, generally with irregular grain boundaries commonly rimmed by biotite+/-chlorite aggregates. Very fine-grained Fe-oxide occurs as inclusions within titanite and brown hornblende.
Sulfides	Anhedral	0.01–0.2	Trace	Consists of anhedral blocky aggregates of chalcopyrite, sometimes containing minor amounts of Po as well as Pyrite. Generally, occur in clusters interstitial to alteration phases of pyroxenes. Very fine-grained, monomineralic Ccp is observed to be interstitial to skeletal titanite.
Comments: This sample comprises moderately altered, fine-grained, equigranular, melagabbro. It consists of fine-grained equigranular plagioclase and intergranular pyroxene. Primary textures are difficult to observe due to the high degree of pyroxene alteration.				

Sample # EN23VS121

Mineral	Habit	Size (mm)	Abundance (%)	Comment
Pyroxene	Subhedral	0.5–1.5	55–65	Fine- to medium-grained, strongly altered pyroxene. The primary characteristics of the grains are difficult to discern; however, local preserved grain boundaries display a prismatic morphology. Pyroxene is overprinted by felty and/or parallel aggregates of fine- to very fine-grained actinolite-tremolite, sometimes accompanied by chlorite and accessory amounts of biotite. Mottled to patchy, brown, fine-grained hornblende overprints pyroxene grains. Several grains comprising pyroxene alteration products appear to have elongated needle-like morphology consisting of aggregates of actinolite-tremolite-chlorite+/- biotite.
Plagioclase	Subhedral	0.7–1.2	35–45	Fine-grained, moderately altered, granular plagioclase. Strongly overprinted by alteration assemblage. Primary grains appear to have been euhedral to subhedral, predominantly lath-like to tabular in shape. Several grains preserve primary polysynthetic. Plagioclase grains display pseudomorphic alteration dominated by very fine-grained chlorite and, to a lesser degree, sericite and minor epidote. Some grains are overprinted by alteration of the pyroxene. Less intense alteration is observed where sericite is dominant, preserving relic plagioclase rims.
Oxides	Subhedral to anhedral	0.02–0.1	Trace	Consists of magnetite-altered, equant chromite grains with irregular morphologies, jagged grain boundaries and are often pitted. These are observed as inclusions within altered pyroxene grains.
Sulfides	Anhedral	0.01–0.2	Trace	Consists of very fine-grained aggregates of Po-Ccp-Pn-Py. Sulfides occur as blocky grains in disseminated clusters.
Comments: This sample comprises strongly altered, fine-grained, mela-gabbro. Alteration of this sample is intense, often preserving relic plagioclase rims. Pyroxene in this sample is completely overprinted by alteration assemblage minerals, making primary relationships and characteristics difficult to discern. Pyroxene is fine-				

grained, intergranular, overprinted by amphibole-chlorite and biotite. Plagioclase is equigranular, predominantly replaced by chlorite.

Sample # EN23VS122

Mineral	Habit	Size (mm)	Abundance (%)	Comment
Clinopyroxene	Subhedral to anhedral	0.3–1.3	60	Fine-grained, strongly overprinted by alteration assemblage minerals. Primary grain characteristics are difficult to discern, but local primary outlines appear to have been prismatic and fine-grained. The grains are locally overprinted by patchy to mottled brown hornblende containing very fine-grained inclusions of Fe oxide. Alteration is predominantly pseudomorphic, ranging from complete to strong. The grains are predominantly altered to aggregates of actinolite-tremolite and chlorite, locally intergrown with biotite (~2%).
Orthopyroxene	Anhedral	1.5–6	20	Medium- to coarse-grained, weakly altered oikocrysts. Oikocrysts are anhedral and contain chadacrysts of clinopyroxenes, some of which appear relatively unaltered. The orthopyroxene is less altered than the clinopyroxene. Along the margins of orthopyroxene, it is altered to aggregates of very fine-grained clay minerals, including chlorite and talc.
Plagioclase	Euhedral to subhedral	0.4–1.2	20	Fine-grained, moderately altered by sericite and epidote. Grains are euhedral to subhedral, tabular to lath-like in morphology. Grain boundaries are often irregular, but primary boundaries are well preserved. Plagioclase is moderately overprinted by very fine-grained sericite aggregates, often as patchy or pervasive alteration, locally accompanied by anhedral very fine-grained epidote aggregates. Primary grains often display the formation of deformation twins and undulous extinction. Several grains are observed to be partially replaced by chlorite and overprinted by disseminated actinolite-tremolite.
Oxides	Euhedral to subhedral	0.05–0.3	Trace	Consists of cumulate fine-grained, disseminated clusters of chromite aggregates that are euhedral, weakly fractured and pitted. Skeletal very fine-grained Fe-oxide exsolution occurs within patchy brown amphibole alteration of clinopyroxene.
Sulfides	Anhedral	0.05–0.4	Trace	Consists predominantly of very fine-grained, polysulfide grains of Ccp-Po-Pn. Grains have blocky shapes, occurring as interstitial disseminated clusters.
Comments: This sample comprises moderately altered, fine- to medium-grained, inequigranular, gabbronorite. Clinopyroxene is the dominant silicate phase, occurring as equant to prismatic crystals, which are strongly altered to an amphibole-chlorite +/- biotite assemblage. Plagioclase is equigranular, with a grain size similar to that of clinopyroxene. Orthopyroxene occurs as medium- to coarse-grained chadacrysts, encompassing clinopyroxene and its alteration products. Alteration assemblages locally overlap between different phases. Skeletal anhedral fine-grained titanite occurs within alteration products of clinopyroxene.				

Sample # EN23VS127

Mineral	Habit	Size (mm)	Abundance (%)	Comment
Pyroxene	Euhedral to subhedral	0.5–2.5	65–75	Fine-grained, pervasively altered pyroxene. Relative modal abundances between orthopyroxene and clinopyroxene are difficult to discern, but the grains appear to have subhedral to euhedral, and prismatic to columnar in shape. The grains are strongly overprinted by very fine-grained aggregates of actinolite, to a lesser degree chlorite and moderately by biotite. Elongated columnar grains are observed, displaying similar alteration as the prismatic grains. Biotite tends to be concentrated in the central portions of the grains intergrown with acicular actinolite-tremolite. Some of the alteration products encompass fine-grained, euhedral brown, equant amphibole.
Plagioclase	Euhedral to anhedral	0.3–1.5	25–35	Fine-grained, relatively unaltered, lath-like to tabular in shape. Grains display strong evidence of deformation, characterized by highly irregular grain boundaries, bulging, and undulous extinction. Grains are weakly overprinted by alteration products of the pyroxene as well as accessory amounts of anhedral, very fine-grained epidote aggregates.
Oxides	Subhedral to anhedral	0.05–0.2	Trace	Consists of fine-grained, equant, to anhedral grains of chromite disseminated throughout and mostly associated with grain boundaries between pyroxene and plagioclase, but sometimes enclosed by either. Small amounts of Fe-oxide are observed locally, encompassed by anhedral, fine-grained titanite.
Sulfides	Anhedral	0.01–0.3	Trace	Consists of very fine-grained disseminated Po, with several fine-grained polysulfide grains of Ccp and Po. Interstitial alteration assemblage minerals generally occur interstitially to alteration assemblage minerals, are irregular and blocky in shape and occur locally in disseminated clusters.
Comments: This sample comprises moderately altered, weakly deformed, fine- to medium-grained, inequigranular, sub-ophitic, melagabbro. It consists of fine-grained, euhedral to anhedral plagioclase that displays evidence of deformation but preserves the primary grain boundaries. Pyroxene is pervasively altered, however, equant to prismatic grain morphologies are observed to partially enclose fine-grained plagioclase laths. Alteration products of pyroxene form elongated, columnar-like grains up to 1cm in length, likely a product of alteration.				

Sample # EN23VS133

Mineral	Habit	Size (mm)	Abundance (%)	Comment
Actinolite	Idioblastic	0.03–0.4	50	Fine- to very fine-grained, elongate acicular actinolite that is aligned, defining foliation, but most are variably oriented.
Plagioclase	Subidioblastic to xenoblastic	0.1–0.4	3	Difficult to discern primary characteristics as plagioclase is nearly completely replaced by sericite. It appears to have been fine-grained. Local patches of primary plagioclase are preserved.
Sericite	Subidioblastic	0.01–0.05	35	Very fine-grained aggregates overprint plagioclase and comprise a fine-grained groundmass in the sample.

Chlorite	Subidioblastic	0.05–0.15	4	Chlorite occurs sporadically, as platy grains, mostly associated with actinolite.
Epidote	Idioblastic to subidioblastic	<0.02	1	Very fine-grained, epidote aggregates are disseminated throughout sericitized plagioclase grains.
Titanite	Xenoblastic	0.01–0.1	2	Highly irregular, mostly very fine-grained aggregates, sometimes weakly elongate parallel to foliation, are present.
Rutile	Xenoblastic	0.1–0.3	Accessory	A single patch of irregular grains is observed within a foliation-parallel quartz vein.
Sulfides	Xenoblastic	<0.02	Trace	Trace amounts of very fine-grained, irregular Py are observed within the foliation parallel quartz veins.

Comments: This sample is fine-to very fine-grained, weakly foliated, consisting of predominantly actinolite and sericitized plagioclase as well as accessory amounts of epidote, titanite and chlorite. Plagioclase is nearly completely altered to sericite. Foliation is weakly defined by the alignment of some actinolite grains. The sample is also cut by (0.05-0.25mm) quartz veinlets, with one being rutile-bearing, weakly foliated. No primary igneous characteristics are observed within the sample; however, the mineralogical assemblage and weak foliation suggest that the sample has a mafic protolith and underwent greenschist facies conditions, indicating that it is a greenschist.

Sample # EN23VS135

Mineral	Habit	Size (mm)	Abundance (%)	Comment
Clinopyroxene	Subhedral	0.4–1	55	Moderately overprinted by alteration assemblage minerals comprising acicular actinolite-tremolite and chlorite. Preserved primary poikilitic characteristics, partially enclosing pervasively altered olivine chadacrysts.
Plagioclase	Subhedral	0.1–0.3	35	Fine-grained plagioclase, pervasively replaced by chlorite, with poorly preserved primary characteristics.
Olivine	Anhedral	0.2–0.4	7	Pervasively overprinted by alteration assemblage minerals, rounded fine-grained pseudomorphed chadacrysts occur in partially altered pyroxene grains.
Oxides	Anhedral	0.01–0.2	3	Disseminated, fine-grained, anhedral magnetite altered chromite (?) disseminated throughout, displaying a bimodal grain size distribution with very fine-grained inclusions in pyroxene and coarser intergranular grains to pyroxene.
Sulfides	Anhedral	0.01–0.1	Trace	Fine-grained, disseminated, interstitial, polysulfide grains comprising Po>Ccp, displaying alteration textures and occurring interstitial to alteration assemblage minerals.

Comments: This sample is fine-grained, comprising pyroxene-plagioclase-olivine cumulate. It displays interchanging layers (~7mm) of pyroxene-olivine-rich zones and plagioclase-pyroxene-rich zones. Oxide minerals predominantly occur outside the pyroxene-dominated layers. Trace amounts of sulfides are disseminated throughout. Winisk River dike.

Sample # EN24VS004

Mineral	Habit	Size (mm)	Abundance (%)	Comment

Olivine	Euhedral to subhedral	0.2–2	60–65	Pervasively altered, bimodal in grain size, olivine. Alteration is pseudomorphic, with olivine replaced by fibrous serpentine. The primary grain shape is well preserved, occurring as euhedral, equant grains to subhedral, rounded grains. Olivine grains also host trace amounts of very fine-grained magnetite-chromite inclusions.
Pyroxene	Anhedral	0.5–2.5	10–15	Intercumulate, medium-grained, poikilitic, pervasively replaced by serpentine. Grains appear sponge textured, containing very fine-grained Fe-oxide +/-sulfide inclusions. Redish-brown, anhedral, very fine-grained, high relief rutile aggregates are observed within pseudomorphed pyroxenes.
Pyrrhotite	Anhedral	0.05–0.8	15	Anhedral, interstitial network of Po partially or completely enclosing aggregates of Ccp or Pn.
Pentlandite	Anhedral	0.02–0.25	7	Subhedral to anhedral aggregates of Pn are partially or completely enclosed by Po. Several grains are observed to be crosscut by Ccp veinlets.
Chalcopyrite	Anhedral	0.02–0.3	3	Discrete aggregates within Po sometimes occur as vein-like features within Pn.
Chromite	Euhedral to subhedral	0.06–0.4	2	Fine-grained, euhedral to subhedral equant grains occurring within silicate and sulfide phases. Chromite grains are zones with magnetite alteration along the grain boundaries, sometimes pervasive.
Comments: This sample comprises pseudomorphed, fine- to medium-grained, inequigranular, poikilitic, mineralized, peridotite. Alteration obscures intercumulate silicate minerology, but primary grain outlines and morphologies are well preserved. Olivine occurs as cumulate, equant to anhedral, fine- to medium-grained primocrysts situated within net-textured sulfides or more rarely within pseudomorphed pyroxene oikocrysts. Primary characteristics of intercumulate phases are difficult to discern. Pyroxene occurs as medium-grained oikocrysts, enclosing olivine chadacrysts. Alteration of pyroxene is more sponge-textured, containing numerous very fine-grained opaque mineral inclusions as well as accessory amounts of rutile. Mineralization in the sample comprises interstitial net-textured Po>Pn>Ccp that show high degrees of fracturing infilled by magnetite and chlorite with magnetite comprising ~5% of the sample.				

Sample # EN24VS006

Mineral	Habit	Size (mm)	Abundance (%)	Comment
Olivine	Subhedral	0.3–2	65	Weakly altered, predominantly fine-grained, cumulate olivine. Grains are strongly fractured, displaying alteration to serpentine minerals along fractures and development of mesh texture. Grains display a range of grain size from fine- to medium-grained. Most of the grains are rounded to irregular amoeboidal, however, several equant grains are observed. Minor, very fine-grained chromite inclusions are observed within the grains.
Orthopyroxene	Anhedral	0.5–2	4	Moderately altered, medium-grained, intercumulate orthopyroxene occurs as equant, poikilitic grains hosting rounded, fine-grained olivine chadacrysts and chromite inclusions. Alteration intensity ranges from subtle along fractures, to intense with complete replacement by green chlorite. Some grains display a weak replacement by talc.

Clinopyroxene	Subhedral	1-4	7	Medium-grained, intercumulate, oikocrysts of clinopyroxene. Several grains are observed to intergrow with anhedral orthopyroxene grains within the core. Grains are often rimmed by amphibole along the rims. Amphibole alteration is seen, giving clinopyroxene a dusty appearance.
Hornblende	Anhedral	0.2–0.5	2	Brown, weak- moderate pleochroism, intercumulus, partially enclosing olivine chadacrysts.
Phlogopite	Subhedral	0.2–0.5	1	Subhedral, lamellar, light brown to colourless with a bird's eye extinction, intercumulate, partially mantling olivine grains.
Pyrrhotite	anhedral	0.1–1.5	12	Strongly pitted, anhedral aggregates form a continuous network in the interstitial spaces.
Pentlandite	Subhedral to anhedral	0.05–0.6	5	Occurs predominantly as granular aggregates within pyrrhotite, moderately pitted. Small amounts of pentlandite occur as flame exsolution within pyrrhotite.
Chalcopyrite	anhedral	0.1–0.5	4	Occurs as anhedral aggregates on the edges of pyrrhotite and pentlandite grains. Less pitted than Pn and Po.
Chromite	Euhedral Subhedral	0.05–0.25	0.5	Fine-grained, equant, occurring as inclusions in olivine and pyroxene, as well as within sulfides. Grains are weakly pitted and partially to completely replaced by magnetite along the rim.

Comments: This sample consists of a mineralized peridotite with interstitial net-textured sulfide mineralization. It consists of cumulus, rounded, bimodal in grain size olivine occurring predominantly as primocrysts and to a lesser degree chadacrysts within pyroxene. Clinopyroxene is the most abundant intercumulus silicate phase occurring as equant to prismatic oikocrysts partially replaced by hornblende. Orthopyroxene is anhedral, prismatic, oikocryst. Several anhedral grains are seen to be intergrown in the cores of clinopyroxene. Subhedral to anhedral, hornblende partially encloses olivine and mantles pyroxene grains. Subhedral intercumulate phlogopite occurs interstitial to olivine and pyroxene. Sulfides are net-textured, consisting of Po>Pn>Ccp, forming a continuous network between silicate phases. Sulfides are pitted and weakly fractured, containing magnetite along the fractures. Minor fine-grained, remobilized sulfide aggregates occur as fracture fill in silicate phases. Magnetite (<1%) is observed at mantle grain boundaries and fractures of sulfide grains.

Sample # EN24VS006b

Mineral	Habit	Size (mm)	Abundance (%)	Comment
Pyrrhotite	Anhedral	0.2–1	12	Anhedral interstitial network often mantling subhedral Pn grains.
Pentlandite	Subhedral	0.1–0.6	5	Subhedral to anhedral aggregates often partially or completely mantled by Po. More fractured than Po. Trace amounts of Pn occur as flame structures within Po.
Chalcopyrite	Anhedral	0.1–0.5	3	Fine-grained anhedral grains occur at the outer edges of Po and Pn in contact with silicates.
Chromite	Euhedral	0.1–0.4	0.5	Equant grains, predominantly euhedral, altered to magnetite along the edges. Occurs as inclusions within silicates and sulfides.
Magnetite	Anhedral	0.05–0.2	0.5	Occurs predominantly on the rims of chromite grains and as fracture fill in the interstitial sulfides.

Comments: Puck of sample EN24VS006 consisting of interstitial networks of net-textured Po>Pn>Ccp. Sulfides are weakly fractured with magnetite infill along the fractures and grain boundaries. Minor remobilized Po and Ccp occur as fine-grained fracture infill in silicate phases. Sulfide inclusions are also observed within chromite grains. Oxides predominantly consist of chromite and occur as disseminated inclusions in silicate phases and interstitial sulfide masses.

Sample # EN24VS007

Mineral	Habit	Size (mm)	Abundance (%)	Comment
Olivine	subhedral	0.1–3.5	65	Mostly fine-grained, displays a range of grain sizes, and is cumulate. Most grains have rounded grain boundaries, making most grains subhedral. Some grains display an irregular amoeboidal shape. Grains are weakly fractured with chlorite and a locally trace amount of magnetite infilling the fractures and rimming most of the grains. Medium grains mostly occur within the sulfides as primocrysts, while finer grains occur as chadacrysts as well as primocrysts. Several grains contain trace amounts of subhedral to anhedral chromite inclusions. Chicken wire-textured, ultrafine-grained sulfide inclusions are observed within some grains.
Orthopyroxene	Subhedral to anhedral	0.3–4	7	Fine- to medium-grained, occurring as intercumulate subhedral grains to poikilitic grains. Grains are weakly fractured and are observed to alter to chlorite along fractures. Patches of anhedral grains occur within medium-grained clinopyroxene oikocrysts. Generally cleaner in appearance than clinopyroxene.
Clinopyroxene	Subhedral	0.1–2	4	Fine- to medium-grained, intercumulate, subhedral to anhedral grains, partially or completely enclosing olivine chadacrysts. Contain anhedral patches of orthopyroxene. Grains are rimmed by amphibole along grain boundaries, appearing dusty with disseminated amphibole-chlorite alteration.
Hornblende	Subhedral	0.2–1.5	3	Fine- to medium-grained, intercumulate, poikilitic to granular hornblende green to brown in plane polarized light. Shows typical 56-120-degree cleavage. Locally observed to enclose olivine chadacrysts and mantle pyroxene oikocrysts having distinct, sharp grain boundaries.
Phlogopite	Subhedral	0.05–0.7	0.5	Fine-grained, lamellar booklets occur interstitial to pyroxene and olivine grains. Weakly to moderately altered to chlorite along grain boundaries. Mostly colourless in plane polarized light.
Sulfides	Interstitial, net-textured	0.1–2	20	Interstitial sulfide network comprising Po (12%), Pn (5%), and Ccp (3%). The majority of the sulfides consist of Po enveloping fine-grained granular aggregates of Pn that range from subhedral to anhedral, and Ccp, which is always anhedral. Interstitial sulfides are weakly fractured, with magnetite sometimes occurring along the fractures. Small amounts of Pn occur as flame exsolution within Po. Small amounts of sulfides occur as disseminated grains with often irregular blobby shapes within fractures of silicate phases.

Chromite	Euhedral	0.02–0.4	0.5	Euhedral to subhedral, fine-grained, equant, cumulate grains occurring as disseminated grains or clusters throughout the sample, enclosed by both silicate and sulfide phases. Several grains are zoned within the sample.

Comments: This sample comprises homogeneous, fine- to medium-grained, mineralized, poikilitic peridotite. It consists of cumulate, seriate olivine, ranging from equant to rounded in shape and occurring mainly as primocrysts and chadacrysts. Orthopyroxene occurs as interstitial anhedral grains to subhedral poikilitic grains. Anhedral, fine-grained orthopyroxene is seen to be enclosed by clinopyroxene oikocrysts. Clinopyroxene is similar in grain size and characteristics to orthopyroxene, but on average is smaller in grain size. It is observed to be partially altered to hornblende along grain boundaries. Hornblende occurs as intercumulate oikocrysts, generally smaller in grain size than pyroxene. Phlogopite makes up a minor constituent of the sample, occurring interstitial to other primary magmatic phases. Sulfides make up 25% of the sample, comprising interstitial Po>Pn>Ccp.

Sample # EN24VS008

Mineral	Habit	Size (mm)	Abundance (%)	Comment
Olivine	Euhedral to subhedral	0.15–2.5	60	Mostly fine-grained but displays a range of grain sizes, cumulus. Most grains have rounded grain boundaries, making most grains subhedral. Some grains display an irregular amoeboidal shape. Grains are weakly fractured with chlorite and a trace amount of magnetite infilling the fractures and rimming most of the grains. Medium-grained olivine mostly occurs within the sulfides, while finer grains occur as chadacrysts as well as primocrysts. Locally contains trace amounts of subhedral chromite inclusions.
Orthopyroxene	Anhedral	0.4–2	5–10	Fine- to medium-grained, intercumulate, oikocrysts. Moderately fractured with chlorite infilling fractures. Cleaner in appearance than clinopyroxene and unaltered.
Clinopyroxene	Subhedral to anhedral	1–3	10–15	Medium-grained, intercumulate oikocrysts, ranging from predominantly subhedral to anhedral prismatic grains. Alteration intensity varies throughout the sample. Intensely altered grains are pervasively altered to felty aggregates of chlorite-anthophyllite +/- actinolite-tremolite, while more moderately altered grains are pseudomorphically replaced by amphibole, often containing relic fragments of clinopyroxene.
Hornblende	Subhedral to anhedral	0.1–0.4	0.5–1	Fine-grained, intercumulate, subpoikilitic hornblende. Typical cleavage is observed, with a weak pleochroism. Relatively unaltered.
Phlogopite	Subhedral	0.05–0.25	<0.5	Intercumulate, lamellar, fine-grained, moderately replaced chlorite.
Sulfides	Subhedral to anhedral	0.1–1.5	15	Consists of intercumulus, mostly continuous, net-textured sulfides comprising Po (10%), Pn (2%), and Ccp (3%). Networks are dominated by Po, often partially or completely enveloping subhedral granular grains of Pn. Zones of Ccp dominant networks are seen, with Ccp locally enveloping Pn.

				Trace amounts of magnetite occur along fractures or sulfide grain boundaries.
Chromite	Euhedral	0.02–0.25	0.5	Fine-grained, equant, cumulate grains observed as inclusions predominantly in pyroxenes and sulfides. More rarely, finer-grained chromite inclusions are enveloped by olivine.
Comments: This sample comprises weakly altered, inequigranular, fine- to medium-grained, cumulate, poikilitic, peridotite. It consists mostly of cumulate fine-grained olivine, and intercumulus medium-grained clinopyroxene, orthopyroxene, net-textured sulfides and accessory amounts of hornblende and phlogopite. Olivine is weakly altered, often rounded, occurring as primocrysts and chadacrysts within pyroxene oikocrysts. Clinopyroxene is the second most abundant intercumulate phase; it is intensely overprinted by alteration assemblage minerals, but is more abundant and larger in grain size than orthopyroxene. Orthopyroxene is smaller in grain size than clinopyroxene and is relatively unaltered. Hornblende present in this sample appears to be a replacement of clinopyroxene, which is in turn altered to aggregates of anthophyllite and chlorite. Sulfides occur interstitial to both olivine and pyroxene.				

Sample # EN24VS009

Mineral	Habit	Size (mm)	Abundance (%)	Comment
Olivine	Euhedral to subhedral	0.1–2	70	Predominantly fine-grained, cumulus, mainly occurring as primocrysts and to a lesser extent as chadacrysts. Grains often have rounded grain boundaries, with some grains exhibiting an amoeboidal shape. Grains are mostly unaltered, other than the presence of moderate fracturing with chlorite-magnetite infill. Grains contain minor amounts of subhedral, very fine-grained chromite-magnetite inclusions.
Clinopyroxene	Subhedral	0.6–2.5	7	Medium-grained, strongly altered, intercumulate, oikocrysts. Primary grains appear to have been subhedral and equant in shape. Two main types of alteration are observed. Pseudomorphic replacement by amphibole along grain boundaries or pervasively, sieve textured and containing oxide inclusions, and alteration to felty aggregates of chlorite-anthophyllite+/-actinolite-tremolite.
Orthopyroxene	Anhedral	0.3–0.6	3	Fine-grained, intercumulate grains, partially rimming olivine. Less abundant than clinopyroxene, typically cleaner in appearance and relatively unaltered.
Hornblende	Anhedral	0.1–0.4	0.5	Fine-grained, intercumulate, subpoikilitic, hornblende displaying typical cleavage, weak brown pleochroism. Relatively unaltered.
Phlogopite	Subhedral	0.02–0.6	<0.5	Intercumulate, lamellar, fine-grained, moderately replaced by chlorite.
Sulfides	Interstitial	0.1–1.2	20	Interstitial comprising Po (12%), Pn (5%), and Ccp (3%), forming disrupted networks interstitial to silicate minerals. Po is the dominant sulfide phase, forming continuous networks and partially or completely enclosing fine-grained aggregates of chalcopyrite and pentlandite. Small amounts of polysulfide aggregates or veinlets occur within fractures of silicate minerals. Sulfides are moderately pitted, and small amounts of magnetite

				are associated with fractures and grain boundaries. Minor Pn flame structures are observed in Po. A couple of olivine grains contain very fine-grained sulfide inclusions not within fractures.
Chromite	Euhedral	0.01–0.4	<0.5	Cumulate, fine to medium grained, occurs within silicate phases and sulfides. Partially altered to magnetite. Occurs as individual grains or as clusters of several grains. Anhedral magnetite often occurs as rims within equant chromite grains.
Comments: This sample consists of weakly altered, fine- to medium-grained, inequigranular, cumulate, poikilitic, wehrlite. It consists of seriate cumulate olivine, intercumulate clinopyroxene, orthopyroxene and accessory amounts of hornblende and phlogopite. Net-textured sulfides occur interstitial to silicate phases. Clinopyroxene is more abundant, coarser-grained, and intensely altered in comparison to orthopyroxene, which is fine-grained and relatively unaltered. Hornblende in this sample appears to occur as a replacement of clinopyroxene. Sulfides within the sample are interstitial to both pyroxene and olivine grains and comprise Po>Pn>Ccp. Sulfides locally enclose grains of chromite.				

Sample # EN24VS010

Mineral	**Habit**	**Size (mm)**	**Abundance (%)**	**Comment**
Pyrrhotite	Anhedral	0.1–1	8	Anhedral interstitial network often mantling subhedral Pn grains and occurring in contact with Ccp.
Pentlandite	Subhedral to anhedral	0.1–0.4	5	Subhedral to anhedral granular aggregates often mantled by Po. Trace amounts of Pn occur as flame structures within Po.
Chalcopyrite	Anhedral	0.1–0.4	4	Fine-grained anhedral grains occur at the outer edges of Po and Pn in contact with silicates.
Chromite	Euhedral	0.05–0.3	0.5	Equant grains, predominantly euhedral, altered to magnetite along the edges. Occurs as inclusions within silicates and sulfides.
Magnetite	Anhedral	0.01–0.15	0.5	Occurs predominantly on the rims of chromite grains and as fracture fill in the interstitial sulfides.
Comments: Puck of sample EN24VS010 comprising net-textured to strongly disseminated, polysulfides of Po>Pn>Ccp occurring interstitial to cumulus phases of olivine and pyroxene. Minor magnetite observed along grain sulfide phase boundaries. Ultrafine-grained disseminated aggregates of sulfides are observed along fractures of altered grains.				

Sample # EN24VS015

Mineral	**Habit**	**Size (mm)**	**Abundance (%)**	**Comment**
Olivine	Subhedral	0.1–2.2	50–55	Strongly fractured, alligator mesh textured, with a shape ranging from euhedral equant grains to anhedral rounded. Occurs both as primocrysts and chadacrysts. Fractured olivine is infilled by serpentine along the fractures, with alteration intensity ranging from weak to moderate.
Orthopyroxene	Subhedral to anhedral	1–4	5–10	Several medium-grained subhedral to anhedral, prismatic, strongly pseudomorphed orthopyroxene oikocrysts enclosing olivine chadacrysts. Alteration consists mostly of fine-grained platy talc aggregates and, to a lesser degree, local, patchy chlorite and disseminated elongate actinolite-tremolite.

Clinopyroxene	Subhedral to anhedral	1.5–4	35–40	Strongly to completely altered, anhedral, oikocrysts of clinopyroxene, enclosing chadacrysts of olivine. These grains have a similar size and shape to orthopyroxene oikocrysts but display a pseudomorphic alteration to elongate, parallel grains of actinolite-tremolite, they are dusty in appearance in plane polarized light. In other grains, alteration is felty, comprising aggregates of actinolite-tremolite and chlorite. Anhedral, dark brown hornblende is observed, appearing to partially replace clinopyroxene. The hornblende is mantled by actinolite tremolite alteration.
Chromite	Euhedral	0.05–0.25	1	Predominantly, euhedral equant grains of cumulate chromite occur mainly in the intergranular spaces enclosed by alteration products of pyroxenes and, more rarely, as very fine-grained inclusions in olivine. Grains sometimes display irregular, jagged grain boundaries and are often rimmed or completely replaced by magnetite.
Sulfides	Anhedral	0.01–0.15	Trace	Very fine-grained, disseminated patches, anhedral aggregates of Po. Grains are very blocky in shape and tend to be concentrated interstitial to alteration products and fractures.

Comments: This sample is cumulate, fine- to medium-grained, inequigranular, moderately altered lherzolite. It consists of weakly altered, cumulate, anhedral to euhedral olivine occurring as primocrysts and chadacrysts. Alteration of olivine consists of serpentine along the fractures, giving it an alligator mesh texture. The intercumulus material in this sample consists of pyroxene and hornblende, which display variable degrees and styles of alteration. Orthopyroxene oikocrysts are medium-grained and completely replaced by aggregates of fine-grained talc+/-chlorite+/-anthophyllite. Clinopyroxene is interpreted to comprise most of the sample due to the abundance of alteration assemblage minerals. Anhedral fine-grained brown hornblende sporadically occurs within the sample. It displays dendrite-like intergrowths with ilmenite inclusions often rimmed by acicular actinolite-tremolite grains. The alteration assemblage of silicate phases is similar and often overlaps, preventing an accurate estimation of mineral proportions.

Sample # EN24VS017

Mineral	Habit	Size (mm)	Abundance (%)	Comment
Olivine	Subhedral	0.2–1.5	50–55	Strongly fractured, alligator mesh textured, ranging from euhedral equant grains to anhedral rounded. Occurs both as primocrysts and chadacrysts. Alteration is localized along olivine margins and fractures comprising serpentine. Where in contact with anthophyllite altered pyroxene, olivine is rimmed by a tremolite margin.
Orthopyroxene	Subhedral	1.5–5	10–15	Medium-grained oikocrysts are completely pseudomorphed by fine-grained aggregates of predominantly talc and, to a lesser degree, chlorite and acicular amphibole. These grains occur in discrete patches and are interpreted to have consisted of orthopyroxene. These grains have abrupt and somewhat distinct boundaries with other alteration phases of clinopyroxene.
Clinopyroxene	Anhedral	1–4	25–30	Medium-grained oikocrysts, moderately altered, anhedral grains with a somewhat prismatic shape. Grains display alteration to several phases of

				amphibole. Some grains are pervasively altered and replaced by fibrous anthophyllite, some are pseudomorphed by actinolite-tremolite. Some grains display a mixture of these alteration phases. Dark brown hornblende is observed to occur in association with clinopyroxene, forming a patchy overprint.
Oxides	Euhedral to anhedral	0.01–0.2	0.5	Consists of equal proportions of chromite and magnetite. Chromite (0.5%) is fine-grained, equant, and cumulate, occurring as inclusions in olivine and intercumulus silicate phases. Chromite is locally altered to magnetite along the grain boundaries, mostly completely replaced. Magnetite occurs as fine-grained laths along fractures within silicate phases.
Sulfides	Anhedral	0.01–0.15	Trace	Anhedral grains, blocky, monosulfides consisting of Po>Pn>Ccp. Partially altered to magnetite along fractures.
Comments: This sample comprises cumulate, fine- to medium-grained, inequigranular, moderately overprinted by alteration, pyroxenite. It consists of cumulate olivine, often displaying a rounded, irregular morphology and being weakly to moderately serpentinized along fractures, exhibiting an alligator mesh texture. Pyroxenes comprise the intercumulus material of the sample, displaying variable degrees of alteration phases. Orthopyroxene is subhedral, poikilitic, and is completely pseudomorphed by very fine-grained aggregates of talc+/-chlorite+/-amphibole. Clinopyroxene is more anhedral and smaller in crystal size than orthopyroxene, and is also poikilitic, displaying more variable degrees of alteration. From pervasively pseudomorphed by actinolite-tremolite, patchy anthophyllite. Grain boundaries between altered orthopyroxene and altered clinopyroxene are discrete and well preserved. Discrimination between the two phases is attributed to different alteration products and primary morphologies.				

Sample # EN24VS031

Mineral	Habit	Size (mm)	Abundance (%)	Comment
Olivine	Subhedral	0.05–0.35	15–20	Pervasively altered, fine-grained, rounded, chadacrysts. All of the grains are altered, with primary shape characteristics only observed in pseudomorphed, sieve-textured pyroxene.
Pyroxene	Subhedral	0.5–2.5	75–80	Intensely altered, medium-grained, intercumulate, oikocrysts. Most of the primary characteristics are absent, but locally, within tremolite-actinolite pseudomorphed grains, primary characteristics are observed, with grains appearing to have a prismatic habit. Alteration varies across the thin sections and comprises predominantly of felty aggregates of chlorite, actinolite-tremolite, and talc. To a lesser degree, grains are pseudomorphed by actinolite-tremolite and exhibit sieve-textured outlines, preserving relic olivine shapes. Occurrence of somewhat equant grains altered to talc-amphibole suggests these were likely orthopyroxene (15-20), while replacement by actinolite-tremolite, hornblende and chlorite implies clinopyroxene comprises 60-65% of the sample.
Plagioclase	Euhedral to subhedral	0.5–1.5	1–5	Lath-like to tabular, medium-grained, completely replaced by chlorite. Grains are pseudomorphically

				replaced, preserving their primary morphology, which resembles plagioclase. No primary grains are observed.
Sulfides	Anhedral	0.2–3	5	Fine- to medium-grained, disseminated polysulfides comprising Po>Pn>Ccp. Disseminated aggregates are very dirty in appearance with highly irregular grain boundaries, often occurring interstitial to alteration phases. Magnetite aggregates are often observed along grain boundaries.
Oxides	Euhedral to subhedral	0.05–0.3	1	Predominantly consists of fine-grained, equant, cumulate chromite aggregates often mantled by a magnetite rim.
Comments: This sample comprises strongly altered, fine- to medium-grained, inequigranular olivine pyroxenite. Intense alteration obscures recognition of primary textures and phases. The most well-defined phase is olivine; however, it is only observed within pseudomorphed, sieve-textured pyroxene. Its occurrence within other locations cannot be discounted. Pyroxene displays variable styles and phases of alteration that often overprint one another, making the distinction of these phases difficult. Plagioclase is completely replaced by chlorite.				

Sample # EN24VS032

Mineral	Habit	Size (mm)	Abundance (%)	Comment
Olivine	Euhedral to subhedral	0.2–1.5	55–60	Mostly fine-grained, but variable in grain size, cumulate, moderately altered, olivine. Occurring as mostly rounded subhedral grains, and more rarely equant euhedral. Alteration is variable but overall moderate, occurring as serpentinization along fractures and grain boundaries.
Orthopyroxene	Subhedral	0.6–3.5	5–10	Medium-grained, pervasively altered, intercumulate oikocrysts. Pervasively altered by very fine-grained talc+/-chlorite aggregates with some grains overprinted by acicular actinolite. Relic grains are rarely preserved appearing pinkish red in plane polarized light. The primary grain shape is well-preserved, appearing to be mostly subhedral and equant.
Clinopyroxene	Subhedral	2–5.5	30–35	Medium-grained, intensely altered, intercumulate oikocrysts. Primary grain shapes are well preserved with grains occurring as prismatic, subhedral to anhedral oikocrysts. Grains are generally pervasively altered by fibrous actinolite-tremolite and patchy chlorite. Several grains are pseudomorphically altered by amphibole containing sieve-textured oxide mineral inclusions. Patchy brown hornblende appears to occur as oikocrysts containing Fe-oxide inclusions, likely an alteration product of clinopyroxene.
Oxides	Subhedral to anhedral	0.02–0.4	0.5	Consists mainly of subhedral to anhedral chromite grains, with irregular grain boundaries that are often altered to magnetite. Some grains are completely altered to magnetite. Magnetite also occurs along fractures within silicate phases.
Sulfides	Anhedral	0.03–0.15	Trace	Trace amounts of Po>Pn occurring as very finely disseminated, irregular grains at boundaries between altered pyroxene and olivine. Coarser-grained sulfides are observed to be replaced by magnetite.

Comments: This sample comprises moderately altered, fine- to medium-grained, cumulate, poikilitic, lherzolite. It consists of cumulate olivine, and intercumulate clinopyroxene and orthopyroxene, as well as minor amounts of disseminated oxides and sulfides. Olivine is relatively unaltered, preserving its primary characteristics well. Intercumulate pyroxene displays two separate alteration assemblages, allowing for the distinction of clinopyroxene and orthopyroxene. Clinopyroxene is altered to fibrous to acicular actinolite-tremolite and chlorite, while predominantly talc aggregates replace orthopyroxene.

Sample # EN24VS033

Mineral	Habit	Size (mm)	Abundance (%)	Comment
Olivine	Euhedral to subhedral	0.2–5	50–55	Predominantly fine-grained, displaying a seriate grain size distribution with one grain occurring as a euhedral coarse grain. Finer-grained olivine occurs as chadacrysts, while coarser-grained olivine occurs as primocrysts within sulfides. Grains are strongly fractured, displaying an alligator mesh texture, but most grains contain dusty, fresh fragments. Alteration along the fractures consists of chlorite and magnetite. Several relic grain fragments are overprinted by a yellow-green iddingsite.
Pyroxene	Anhedral	0.7–6.5	30–35	Predominantly medium-grained, strongly pseudomorphed, intercumulate anhedral oikocrysts. Alteration consists of fine-grained platy chlorite and aggregate mixtures of very fine-grained chlorite-talc-amphibole assemblage. Several primary fragments of orthopyroxene and clinopyroxene are observed, with clinopyroxene pseudomorphed by sieve-textured amphibole. Minor, anhedral, very fine-grained rutile occurs within alteration products.
Sulfides	Subhedral to anhedral	0.05–1.5	10	Semi-continuous to strongly disseminated sulfides comprising massive Po (6%), granular Pn (1%), and Ccp (3%). The sulfide phases are moderately fractured, with magnetite infilling fractures and grain boundaries. Very fine-grained, disseminated aggregates of sulfide are observed along fractures in silicate phases.
Chromite	Euhedral to subhedral	0.05–0.5	1	Fine-grained, predominantly euhedral, equant, cumulus grains often displaying zonation of magnetite along the boundaries and chromite cores.
Comments: This sample is moderately altered, cumulus, inequigranular, poikilitic, peridotite containing net-textured sulfide mineralization. It consists of strongly fractured, mesh-textured, cumulus olivine, altering to chlorite-magnetite along fractures and along the rims. Pyroxene is strongly pseudomorphed by chlorite-talc-amphibole, with rare fresh fragments of orthopyroxene and clinopyroxene preserved. However, a similar alteration assemblage makes the primary proportions of the pyroxenes undiscernible. Sulfides occur interstitial to pyroxene and olivine grains, forming patches of net-textured sulfides.				

Sample # EN24VS035

Mineral	Habit	Size (mm)	Abundance (%)	Comment
Olivine	Subhedral	0.1–0.3	5–15	Pervasively altered, fine-grained, subhedral to anhedral olivine. Primary olivine outlines are observed within pseudomorphed pyroxene oikocrysts.
Pyroxene	Subhedral to anhedral	0.8–1.5	80–85	Medium-grained, intensely altered, poikilitic pyroxene. Alteration obscures primary characteristics of the grains, but several relic shapes are observed, appearing to have been prismatic to equant in shape. Alteration is

				variable, from pseudomorphed grains by massive actinolite-tremolite or hornblende, to alteration to fine-grained aggregates of chlorite, actinolite-tremolite, talc, and hornblende, making up the majority of the sample.
Plagioclase	Euhedral	0.4–0.8	1–3	Lath-like to tabular, medium-grained, completely replaced by chlorite. Grains are pseudomorphically replaced, preserving their primary morphology, which resembles plagioclase. No primary grains are observed.
Sulfides	Anhedral	0.01–0.1	<1	Very fine-grained, disseminated aggregates of Po>Pn>Ccp.
Oxides	Euhedral to anhedral	0.01–0.2	1	Comprises predominantly fine-grained, euhedral chromite aggregates rimmed by magnetite.

Comments: This sample comprises intensely altered, medium-grained, inequigranular olivine pyroxenite. Alteration obscures most of the primary characteristics of the sample, except for several olivine pyroxene outlines. Plagioclase is observed as tabular grains pseudomorphed by chlorite aggregates.

Sample # EN24VS036

Mineral	Habit	Size (mm)	Abundance (%)	Comment
Olivine	Anhedral	0.15–1.5	60–65	Strongly altered, fine-grained, cumulate, euhedral equant to mostly anhedral rounded grains. Alteration is intense, with the majority of the grains pseudomorphed by serpentine. Less altered grains are observed as strongly fractured, alligator mesh textured and have a very dirty appearance.
Pyroxene	Subhedral to anhedral	0.6–4.7	35–40	Intensely altered, medium-grained, intercumulate, poikilitic grains. Alteration is in style, and mineralogy varies across the sample. Less intensely altered grains are pervasively or partially pseudomorphed by elongate actinolite-tremolite, resulting in a sieve-textured appearance, which gives the pyroxene a dusty appearance in PPL. Within these pseudomorphed grains, relic clinopyroxene fragments are observed. The majority of the intercumulate material comprises fine-grained platy aggregates of chlorite and elongate fibrous actinolite-tremolite. In chlorite-rich zones, the actinolite-tremolite outlines the olivine grains. The relative abundance of orthopyroxene to clinopyroxene is challenging to establish. However, equant grains with actinolite tremolite alteration are likely clinopyroxene (~10), while interstitial material is altered to fine aggregates of anthophyllite and chlorite, which are possibly orthopyroxene (~30)
Oxides	Subhedral to anhedral	0.02–0.3	<0.5	Consists of magnetite>chromite. Chromite is equant, completely or partially (along the rims), altered to magnetite. Magnetite is the dominant oxide phase occurring as fracture-filling laths within the silicate phases and within sulfide cross-cutting chlorite veins.
Sulfides	Anhedral	0.01–0.05	Trace	Anhedral, very fine-grained, weakly disseminated Po, often rimmed by magnetite.

Comments: This sample comprises strongly altered, fine- to medium-grained, inequigranular, cumulate, poikilitic peridotite. Alteration is pervasive, with the most recognisable phase being olivine, which is pseudomorphed mainly by serpentine, preserving primary shape and several relic fragments. Identification of igneous intercumulate phases is intensely obscured by alteration. Less altered grains are pseudomorphed,

containing relic fragments of clinopyroxene, which appear to have been equant euhedral, poikilitic grains enclosing olivine. Several grains are pseudomorphed by brown hornblende, which in turn is rimmed by actinolite tremolite. The majority of the intercumulate ground mass consists of aggregates of actinolite-tremolite, chlorite and magnetite, obscuring the recognition of phases present. Olivine grains sometimes contain less-altered, relic fragments of clinopyroxene. Several 0.1mm oblique chlorite-magnetite veins crosscut the sample.

Sample # EN24VS037

Mineral	Habit	Size (mm)	Abundance (%)	Comment
Olivine	Subhedral	0.2–2	55–60	Intensely altered, fine- to medium-grained, subhedral to anhedral, cumulate olivine. Most of the phase is pseudomorphed by serpentine, preserving the original morphology of the grains. Several relic grain fragments are observed, which have a dirty appearance. Several grains are observed to be overprinted by intercumulate alteration products outlining the relic shape of the grain.
Pyroxene	Anhedral	0.8–4	35–40	Intensely altered intercumulate phase. Due to the high degree of alteration in the intercumulate spaces, recognition of primary characteristics of the grains is impossible. Relic fragments are seen in pseudomorphed grains. The majority of the intercumulate material consists of chlorite, amphibole, magnetite, and rutile, occurring as felty aggregates with variable proportions throughout the ground mass.
Oxides	Euhedral to subhedral	0.05–0.3	0.5	Fine-grained aggregates, comprising equant chromite occurring as inclusions in silicate phases. Coarser grains occur interstitial to olivine, while the finer grains occur within olivine. Minor magnetite zoning is observed. Grains are strongly pitted and often have jagged grain boundaries.
Sulfides	Anhedral	0.01–1.2	3	Comprises interstitial, polysulfide grains, weakly disseminated throughout the sample. Sulfides are strongly pitted and fractured, with magnetite occurring along grain boundaries and sulfide edges. The sulfides comprise Po>Ccp>Pn. Ultrafine-grained sulfides are disseminated throughout altered grains.
Comments: This sample comprises intensely altered, fine- to medium-grained, inequigranular, cumulate, peridotite. The most recognizable phase within the sample is olivine, preserving its primary shape outlines and several relic fragments. Recognition of intercumulate phase minerology and textures is extremely obscured by alteration. The presence of a few relic clinopyroxene fragments, along with the alteration mineralogy, suggests that the groundmass was dominated by pyroxene. However, distinguishing between clinopyroxene and orthopyroxene, or the presence of other silicate phases, is difficult.				

Sample # EN24VS039

Mineral	Habit	Size (mm)	Abundance (%)	Comment
Pyroxene	Anhedral	0.05–0.3	65–75	Fine-grained pyroxene, completely overprinted by aggregates of amphibole, chlorite, and biotite. Relic grains are difficult to discern; however, locally, sub-ophitic relict textures are observed.
Plagioclase	Euhedral to Subhedral	0.05–0.2	25–35	Very fine-grained, occurring as euhedral tabular grains, locally mantled by pyroxene. Grains display bulging and are sometimes overprinted by alteration products of pyroxene.

<table>
<tr><td>Oxides</td><td>Subhedral</td><td>0.01–0.05</td><td>Trace</td><td>Very fine-grained, disseminated aggregates of magnetite interstitial to silicate phases, possibly after chromite.</td></tr>
<tr><td colspan="5">Comments: This sample comprises very fine- to fine-grained, strongly altered, equigranular, melagabbro. It consists of fine-grained plagioclase and intergranular pyroxene that has been completely altered to aggregates of actinolite-tremolite, chlorite and biotite. Locally, relic textures are preserved, suggesting that the samples had a very fine grain size prior to alteration.</td></tr>
</table>

Sample # EN24VS040

<table>
<tr><th>Mineral</th><th>Habit</th><th>Size (mm)</th><th>Abundance (%)</th><th>Comment</th></tr>
<tr><td>Olivine</td><td>Subhedral</td><td>0.1–1</td><td>65–70</td><td>Fine-grained, cumulus, pervasively replaced by alteration minerals. Grains preserve their primary shape, appearing rounded and mostly subhedral. All grains are completely, pervasively replaced by chlorite in grains occurring as primocrysts and sitting within sulfides. Preserved grains occur as chadacrysts; these are strongly fractured, partially altered, and occur as rounded shapes.</td></tr>
<tr><td>Pyroxene</td><td>Subhedral to anhedral</td><td>0.7–5.5</td><td>10–15</td><td>Medium-grained, subhedral to anhedral, intercumulate oikocrysts. Primary grains are pervasively pseudomorphed by brown, very fine-grained aggregates of anthophyllite-chlorite assemblage. Replaced oikocrysts are rimmed by platy chlorite. Actinolite-tremolite, talc and chlorite occur within intercumulus spaces, but the distinction of the primary phase is difficult to make. Pyroxene oikocryst alteration resembles that of orthopyroxene observed in other samples. Orthopyroxene likely makes up the majority, ~10-12%, while clinopyroxene is the minor phase, ~3%.</td></tr>
<tr><td>Sulfides</td><td>Anhedral to subhedral</td><td>0.05–1</td><td>15</td><td>Consists of interstitial sulfides comprising Po (9%), Pn (4%) and Ccp (2%). Po makes up the majority of the sulfide minerology with aggregates of Pn and Ccp enclosed by it. Minor magnetite occurs along some of the grain boundaries and fractures. Chalcopyrite veinlets are seen within Pn. Minor amounts of sulfides are remobilized and infill fractures within silicate phases</td></tr>
<tr><td>Chromite</td><td>Euhedral to subhedral</td><td>0.02–0.2</td><td>1</td><td>Fine-grained, equant, cumulate grains occurring throughout the thin section are partially or completely enclosed by either silicates or sulfide grains. Grains are zoned, with magnetite occurring along their rims.</td></tr>
<tr><td colspan="5">Comments: This sample comprises strongly altered, fine- to medium-grained, cumulus, inequigranular, poikilitic peridotite containing interstitial net-textured sulfides. It consists of subhedral, fine-grained, cumulus olivine that has been nearly completely replaced by chlorite. Only preserved grains occur within pyroxene oikocrysts, and these are strongly fractured, displaying alligator mesh texture. Pyroxene is completely replaced by anthophyllite-talc-chlorite, but primary morphology is well preserved, occurring as prismatic oikocrysts. The type of pyroxene is undeterminable, but the overall morphology resembles that of orthopyroxene.</td></tr>
</table>

Appendix C: Whole Rock Geochemistry

	Oxide	Unit	LLD	EN23VS 001	EN23VS 002	EN23VS 003	EN23VS 004	EN23VS 005	EN23VS 006	EN23VS 007	EN23VS 008	EN23VS 009	EN23VS 010	EN23VS 012	EN23VS 013
ME-ICP06	SiO_2	%	0.01	46.30	31.30	40.80	45.00	50.10	48.10	54.90	54.50	45.70	47.80	48.40	45.80
ME-ICP06	Al_2O_3	%	0.01	10.80	17.80	11.05	11.80	14.40	18.15	14.30	14.15	9.08	10.00	11.10	9.00
ME-ICP06	Fe_2O_3	%	0.01	9.93	20.50	15.30	11.30	12.15	9.97	12.65	13.05	13.15	10.95	10.45	10.95
ME-ICP06	CaO	%	0.01	7.89	1.95	8.67	4.83	7.41	7.28	8.17	8.23	6.89	7.34	6.93	6.97
ME-ICP06	MgO	%	0.01	10.95	14.45	12.35	14.45	5.21	5.08	4.97	5.11	18.50	16.35	11.55	18.20
ME-ICP06	Na_2O	%	0.01	0.03	0.02	0.07	0.12	1.18	2.86	3.18	3.63	0.53	1.05	0.80	0.70
ME-ICP06	K_2O	%	0.01	3.46	2.21	1.22	5.92	4.06	3.64	0.89	0.51	2.59	2.79	4.58	2.33
ME-ICP06	Cr_2O_3	%	0.002	0.158	0.222	0.170	0.209	0.005	0.010	0.004	0.004	0.230	0.240	0.162	0.262
ME-ICP06	TiO_2	%	0.01	0.52	0.97	0.54	0.48	1.09	0.67	1.12	1.15	0.44	0.47	0.54	0.41
ME-ICP06	MnO	%	0.01	0.15	0.27	0.37	0.20	0.16	0.12	0.22	0.21	0.24	0.17	0.19	0.17
ME-ICP06	P_2O_5	%	0.01	0.05	0.01	0.03	0.04	0.08	0.10	0.10	0.11	0.06	0.05	0.05	0.04
ME-ICP06	SrO	%	0.01	<0.01	0.01	0.01	<0.01	0.03	0.06	0.03	0.04	<0.01	0.01	0.01	<0.01
ME-ICP06	BaO	%	0.01	0.05	0.02	0.02	0.06	0.08	0.07	0.03	0.02	0.04	0.04	0.05	0.03
OA-GRA05	LOI	%	0.01	9.98	8.34	8.52	3.75	3.04	3.33	0.42	0.59	3.69	2.58	3.75	3.44
TOT-ICP06	Total	%	0.01	100.27	98.07	99.12	98.16	99.00	99.44	100.98	101.30	101.14	99.84	98.56	98.30
C-IR07	C	%	0.01	1.67	0.19	1.10	0.47	0.58	0.44	0.03	0.03	0.03	0.02	0.56	0.03
S-IR08	S	%	0.01	<0.01	<0.01	<0.01	<0.01	0.16	<0.01	0.06	0.22	0.06	0.01	0.16	0.21
ME-MS81	Ba	ppm	0.5	465.0	146.5	154.5	568.0	761.0	647.0	277.0	173.0	394.0	400.0	480.0	276.0
ME-MS81	Ce	ppm	0.1	10.0	14.0	9.4	26.0	24.1	21.5	28.1	26.9	6.4	11.4	8.2	7.0
ME-MS81	Cr	ppm	5	1195	1740	1330	1615	52	92	43	43	1835	2040	1310	1995
ME-MS81	Cs	ppm	0.01	8.31	1.54	0.36	4.87	4.97	3.14	0.51	0.22	8.70	3.17	3.30	2.84
ME-MS81	Dy	ppm	0.05	2.05	1.30	2.14	1.93	3.70	2.34	3.59	3.56	2.59	2.64	2.16	1.43
ME-MS81	Er	ppm	0.03	1.32	0.91	1.61	1.16	2.22	1.44	1.84	1.98	1.58	1.48	1.30	0.85
ME-MS81	Eu	ppm	0.02	0.36	0.63	0.35	0.25	1.13	0.74	1.10	1.03	0.65	0.45	0.42	0.38
ME-MS81	Ga	ppm	0.1	14.4	42.1	18.3	13.7	23.9	21.0	20.9	21.4	10.2	13.1	13.7	12.2
ME-MS81	Gd	ppm	0.05	1.60	1.14	1.34	2.60	3.65	1.98	3.57	3.71	2.02	2.05	1.83	1.24
ME-MS81	Ge	ppm	0.5	1.2	1.1	1.4	2.0	1.8	1.6	1.4	1.5	1.4	1.9	1.4	1.5
ME-MS81	Hf	ppm	0.05	1.26	1.80	1.32	1.29	3.23	2.07	3.16	2.88	1.30	1.54	1.30	0.99
ME-MS81	Ho	ppm	0.01	0.42	0.28	0.48	0.38	0.74	0.46	0.68	0.69	0.55	0.53	0.46	0.31
ME-MS81	La	ppm	0.1	6.5	7.3	5.2	14.8	11.6	10.8	13.6	13.0	2.5	4.7	3.8	3.3
ME-MS81	Lu	ppm	0.01	0.20	0.17	0.27	0.14	0.25	0.21	0.25	0.24	0.21	0.24	0.18	0.13
ME-MS81	Nb	ppm	0.05	2.12	9.56	1.92	1.98	4.78	3.73	4.66	4.60	1.66	2.33	1.68	1.35
ME-MS81	Nd	ppm	0.1	4.7	5.6	4.6	12.5	13.1	10.4	14.9	14.6	4.7	6.7	5.0	3.6
ME-MS81	Pr	ppm	0.02	1.24	1.62	1.14	3.19	3.26	2.78	3.39	3.52	0.94	1.56	1.09	0.91
ME-MS81	Rb	ppm	0.2	110.0	44.6	26.6	162.0	125.0	105.0	26.8	10.8	82.7	94.6	141.5	69.0
ME-MS81	Sm	ppm	0.03	1.49	1.11	1.02	2.58	3.51	1.96	3.72	3.70	1.43	1.86	1.37	1.02
ME-MS81	Sn	ppm	0.5	1.0	2.2	1.1	1.1	1.3	1.4	0.9	0.9	2.9	1.1	0.6	<0.5
ME-MS81	Sr	ppm	0.1	35.2	93.4	106.0	12.5	295.0	479.0	287.0	322.0	29.6	79.6	90.1	15.3
ME-MS81	Ta	ppm	0.1	0.1	0.7	0.1	0.1	0.3	0.2	0.4	0.3	0.2	0.2	0.1	0.1
ME-MS81	Tb	ppm	0.01	0.29	0.22	0.28	0.34	0.57	0.35	0.55	0.55	0.40	0.36	0.32	0.22
ME-MS81	Th	ppm	0.05	0.70	1.03	0.77	1.12	2.23	1.94	2.51	2.16	0.71	1.03	0.83	0.66
ME-MS81	Tm	ppm	0.01	0.19	0.15	0.27	0.17	0.28	0.22	0.21	0.25	0.21	0.20	0.17	0.12
ME-MS81	U	ppm	0.05	0.31	0.91	0.44	0.30	0.71	0.85	0.49	0.45	0.18	0.22	0.19	0.18
ME-MS81	V	ppm	5	213	249	205	192	235	177	222	230	163	173	202	151
ME-MS81	W	ppm	0.5	1.2	1.5	0.7	<0.5	0.5	0.5	0.7	0.6	0.5	0.5	0.8	0.7
ME-MS81	Y	ppm	0.1	12.6	7.9	13.8	10.8	19.0	13.0	17.6	17.9	14.1	14.4	12.0	8.5
ME-MS81	Yb	ppm	0.03	1.22	0.95	1.68	1.07	1.74	1.34	1.56	1.61	1.44	1.46	1.10	0.89
ME-MS81	Zr	ppm	1	43	60	44	46	116	70	117	112	43	55	48	36
ME-MS42	As	ppm	0.1	6.1	41.7	6.6	0.1	0.3	0.1	0.1	0.2	0.3	0.1	0.1	0.6
ME-MS42	Bi	ppm	0.01	0.03	0.07	0.07	0.01	0.08	0.03	0.03	0.03	0.08	<0.01	<0.01	0.03
ME-MS42	Hg	ppm	0.005	<0.005	<0.005	<0.005	<0.005	<0.005	<0.005	<0.005	<0.005	<0.005	<0.005	<0.005	<0.005
ME-MS42	In	ppm	0.005	0.041	0.027	0.016	0.027	0.006	0.009	0.009	0.011	0.007	0.009	<0.005	0.007
ME-MS42	Re	ppm	0.001	0.008	0.002	0.001	0.001	<0.001	0.001	<0.001	<0.001	0.007	<0.001	<0.001	0.004
ME-MS42	Sb	ppm	0.05	<0.05	0.20	0.09	<0.05	<0.05	<0.05	<0.05	<0.05	<0.05	<0.05	<0.05	<0.05
ME-MS42	Se	ppm	0.2	<0.2	<0.2	<0.2	0.2	0.2	<0.2	0.3	0.3	0.3	<0.2	<0.2	0.3
ME-MS42	Te	ppm	0.01	0.02	0.01	<0.01	0.04	0.02	<0.01	0.01	0.02	0.11	0.03	0.02	0.03
ME-MS42	Tl	ppm	0.02	0.62	0.05	0.03	0.83	0.77	0.44	0.11	0.04	1.21	0.39	0.69	0.33
ME-4ACD81	Ag	ppm	0.5	<0.5	<0.5	<0.5	<0.5	<0.5	<0.5	<0.5	<0.5	2.6	<0.5	<0.5	<0.5
ME-4ACD81	Cd	ppm	0.5	<0.5	<0.5	<0.5	<0.5	<0.5	<0.5	0.5	<0.5	1.5	<0.5	<0.5	<0.5
ME-4ACD81	Co	ppm	1	54	77	56	65	49	33	57	57	53	60	51	80
ME-4ACD81	Cu	ppm	1	5	2	1	1	64	1	40	155	300	6	4	10
ME-4ACD81	Li	ppm	10	140	90	100	180	80	70	30	20	110	90	80	40
ME-4ACD81	Mo	ppm	1	17	2	<1	<1	<1	<1	<1	<1	2	1	<1	<1
ME-4ACD81	Ni	ppm	1	323	556	337	360	163	38	164	164	976	762	325	854
ME-4ACD81	Pb	ppm	2	2	3	3	<2	6	5	7	5	<2	<2	2	<2
ME-4ACD81	Sc	ppm	1	31	15	31	34	23	16	24	25	24	25	30	25
ME-4ACD81	Zn	ppm	2	113	226	222	212	126	122	288	208	112	102	123	69
Cu-OG62	Cu	%	0.001												
Ni-OG62	Ni	%	0.001												

Oxide	Unit	EN23VS 014	EN23VS 015	EN23VS 017	EN23VS 019	EN23VS 020	EN23VS 021	EN23VS 022	EN23VS 025	EN23VS 026	EN23VS 027	EN23VS 028	EN23VS 029	EN23VS 030	EN23VS 031
SiO_2	%	46.70	48.10	51.00	49.70	53.30	51.90	49.60	45.40	37.60	45.30	51.70	40.90	59.30	49.70
Al_2O_3	%	8.40	7.34	9.83	9.39	17.55	10.20	11.85	11.30	15.20	12.50	13.45	13.20	9.14	9.78
Fe_2O_3	%	10.25	9.77	10.75	10.70	9.52	10.55	11.15	11.45	15.80	11.40	11.15	14.85	9.16	10.75
CaO	%	7.45	8.31	7.73	7.18	7.27	5.30	5.93	6.93	4.73	5.23	2.96	5.67	2.27	7.13
MgO	%	18.55	19.20	15.30	15.75	4.43	13.55	14.15	12.80	15.30	12.50	10.70	11.10	13.15	15.50
Na_2O	%	0.58	0.33	1.82	0.70	2.48	1.06	2.58	0.02	0.96	0.75	1.97	0.04	0.02	1.90
K_2O	%	2.38	1.66	2.02	3.54	3.30	1.43	0.17	0.39	0.07	0.84	0.95	5.29	0.09	2.44
Cr_2O_3	%	0.314	0.383	0.195	0.187	<0.002	0.143	0.154	0.198	0.084	0.098	0.080	0.196	0.186	0.280
TiO_2	%	0.39	0.34	0.44	0.50	0.80	0.54	0.56	0.56	0.70	0.62	0.67	0.63	0.43	0.48
MnO	%	0.18	0.20	0.18	0.18	0.13	0.15	0.16	0.15	0.19	0.12	0.12	0.21	0.08	0.17
P_2O_5	%	0.04	0.04	0.02	0.02	0.33	0.05	0.05	0.05	0.04	0.05	0.06	0.06	0.04	0.05
SrO	%	<0.01	<0.01	0.01	<0.01	0.09	<0.01	<0.01	<0.01	<0.01	<0.01	<0.01	<0.01	<0.01	0.01
BaO	%	0.03	0.02	0.03	0.04	0.09	0.01	<0.01	<0.01	<0.01	<0.01	<0.01	0.06	<0.01	0.04
LOI	%	2.88	3.39	2.33	2.01	1.42	5.07	4.45	11.00	10.50	9.52	7.02	7.43	7.58	2.25
Total	%	98.14	99.08	101.66	99.90	100.71	99.95	100.80	100.25	101.17	98.93	100.83	99.64	101.45	100.48
C	%	0.03	0.03	0.02	0.03	0.05	0.26	0.15	1.43	0.87	1.10	0.59	1.27	0.40	0.05
S	%	0.02	0.01	0.16	0.01	0.12	0.03	0.07	0.01	0.01	0.18	0.31	0.01	0.01	0.02
Ba	ppm	275.0	147.5	288.0	385.0	823.0	86.1	9.9	12.2	1.9	23.2	24.1	537.0	4.5	384.0
Ce	ppm	8.1	5.1	8.7	11.8	40.4	8.8	7.4	10.4	4.1	12.8	10.1	5.7	17.9	8.8
Cr	ppm	2570	3170	1430	1520	19	1135	1185	1440	653	776	613	1475	1500	2200
Cs	ppm	2.61	1.88	1.85	2.44	2.32	0.39	0.19	0.48	0.46	0.78	0.73	6.45	0.42	6.04
Dy	ppm	1.67	1.83	1.72	2.26	2.34	2.07	2.01	3.21	3.01	2.22	1.43	0.75	2.58	1.84
Er	ppm	1.06	1.20	1.17	1.38	1.26	1.24	1.32	1.68	1.74	1.36	0.94	0.65	1.36	1.10
Eu	ppm	0.42	0.42	0.35	0.39	1.26	0.51	0.47	0.57	0.67	0.51	0.34	0.11	0.79	0.36
Ga	ppm	10.8	10.8	11.0	11.8	19.3	12.7	15.0	16.6	29.5	18.4	20.1	28.0	15.4	11.2
Gd	ppm	1.41	1.60	1.42	2.02	3.43	1.71	1.77	2.48	2.21	1.97	1.07	0.67	2.57	1.54
Ge	ppm	1.6	1.8	1.5	1.8	1.3	1.8	1.7	1.2	1.7	1.2	1.1	1.6	2.4	1.4
Hf	ppm	1.11	0.94	1.20	1.34	2.03	1.20	1.31	1.18	1.69	1.35	1.46	1.39	1.06	1.24
Ho	ppm	0.37	0.38	0.37	0.50	0.45	0.44	0.44	0.57	0.62	0.49	0.27	0.18	0.49	0.39
La	ppm	3.6	2.0	3.9	5.8	19.7	4.1	3.3	5.9	1.3	5.9	5.0	3.3	10.4	3.9
Lu	ppm	0.16	0.18	0.19	0.22	0.19	0.16	0.20	0.21	0.28	0.23	0.14	0.16	0.18	0.19
Nb	ppm	1.48	1.64	1.52	1.99	2.80	1.56	1.59	1.46	2.82	5.42	2.87	9.91	1.26	1.72
Nd	ppm	4.4	3.6	4.6	6.5	22.0	5.0	4.6	5.9	4.5	7.5	4.4	2.9	8.6	4.8
Pr	ppm	0.95	0.73	1.05	1.50	4.98	1.13	0.99	1.32	0.80	1.74	1.23	0.67	2.07	1.15
Rb	ppm	72.7	61.7	51.9	98.0	103.5	26.9	4.6	7.7	1.6	15.8	16.6	150.0	2.5	71.4
Sm	ppm	1.31	1.26	1.16	1.62	4.05	1.48	1.37	1.92	1.88	1.80	1.14	0.67	2.45	1.36
Sn	ppm	0.5	0.6	0.8	0.6	0.8	<0.5	<0.5	0.5	2.5	0.5	0.5	1.7	<0.5	<0.5
Sr	ppm	11.6	12.3	71.3	37.2	827.0	14.6	24.8	18.0	13.3	18.4	21.8	20.8	16.0	63.7
Ta	ppm	0.1	0.1	0.1	0.1	0.2	0.1	0.1	0.1	0.1	0.1	0.1	0.6	0.1	0.1
Tb	ppm	0.27	0.30	0.27	0.35	0.43	0.30	0.29	0.47	0.42	0.34	0.18	0.10	0.43	0.26
Th	ppm	0.90	0.62	0.92	1.02	2.39	0.70	0.70	0.72	0.81	0.86	0.84	0.75	0.53	0.90
Tm	ppm	0.14	0.14	0.14	0.19	0.16	0.17	0.17	0.23	0.26	0.18	0.12	0.10	0.18	0.15
U	ppm	0.15	0.19	0.17	0.21	0.75	0.18	0.12	0.27	0.41	0.31	0.26	0.26	0.32	0.22
V	ppm	151	134	163	182	210	197	210	176	254	213	200	197	170	175
W	ppm	0.8	0.7	1.0	1.1	<0.5	0.7	<0.5	1.3	1.3	1.5	1.1	1.0	0.9	0.5
Y	ppm	10.3	10.9	10.4	13.3	12.9	12.1	12.3	15.3	16.0	12.8	7.7	5.0	14.1	10.5
Yb	ppm	1.05	1.08	0.99	1.41	1.17	1.15	1.29	1.46	1.82	1.54	0.96	0.87	1.23	1.01
Zr	ppm	40	34	41	49	77	44	47	42	58	49	53	50	35	44
As	ppm	<0.1	0.1	0.2	0.1	0.1	0.6	0.3	<0.1	<0.1	0.2	0.7	<0.1	<0.1	<0.1
Bi	ppm	0.01	0.01	0.01	0.01	0.01	0.05	0.06	0.04	0.02	0.16	0.19	0.01	0.09	0.07
Hg	ppm	<0.005	<0.005	<0.005	<0.005	<0.005	<0.005	<0.005	<0.005	<0.005	<0.005	<0.005	<0.005	<0.005	<0.005
In	ppm	0.006	0.006	0.007	0.012	0.006	0.031	0.017	0.056	0.091	0.106	0.082	0.036	0.087	<0.005
Re	ppm	0.002	0.005	<0.001	0.001	<0.001	0.001	0.001	0.001	0.001	0.001	0.001	<0.001	0.001	0.002
Sb	ppm	<0.05	<0.05	<0.05	<0.05	<0.05	<0.05	<0.05	<0.05	<0.05	<0.05	<0.05	<0.05	<0.05	<0.05
Se	ppm	<0.2	<0.2	0.3	<0.2	<0.2	<0.2	0.3	<0.2	<0.2	0.4	0.5	<0.2	0.2	<0.2
Te	ppm	0.01	0.04	0.02	0.02	<0.01	0.03	0.03	0.05	0.06	0.04	0.04	0.02	0.02	0.06
Tl	ppm	0.32	0.19	0.24	0.44	0.47	<0.02	<0.02	<0.02	<0.02	<0.02	<0.02	0.84	<0.02	0.67
Ag	ppm	<0.5	<0.5	<0.5	<0.5	<0.5	<0.5	<0.5	<0.5	<0.5	<0.5	<0.5	<0.5	<0.5	<0.5
Cd	ppm	<0.5	<0.5	<0.5	<0.5	<0.5	<0.5	<0.5	<0.5	<0.5	<0.5	<0.5	<0.5	<0.5	<0.5
Co	ppm	56	61	60	60	31	54	59	58	59	52	47	56	44	65
Cu	ppm	10	10	28	19	42	2	70	1	2	300	727	4	5	8
Li	ppm	50	70	50	80	80	100	80	100	130	110	80	200	160	80
Mo	ppm	1	<1	<1	<1	<1	<1	<1	<1	<1	<1	<1	<1	<1	<1
Ni	ppm	880	969	489	597	20	312	311	370	219	199	169	402	286	527
Pb	ppm	<2	<2	<2	<2	9	<2	<2	2	2	<2	<2	2	<2	<2
Sc	ppm	23	20	28	26	17	28	31	29	22	32	30	25	22	28
Zn	ppm	71	91	73	101	96	78	85	116	192	99	101	201	68	73
Cu	%														
Ni	%														

Oxide	Unit	EN23VS 032	EN23VS 033	EN23VS 034	EN23VS 035	EN23VS 038	EN23VS 039	EN23VS 040	EN23VS 041	EN23VS 042	EN23VS 043	EN23VS 044	EN23VS 045	EN23VS 046	EN23VS 047
SiO_2	%	47.70	55.10	45.20	52.50	48.20	51.70	37.60	40.40	39.90	40.70	39.00	38.70	51.40	54.00
Al_2O_3	%	10.85	13.40	8.85	11.90	10.05	12.25	15.10	4.27	3.57	3.67	4.84	4.35	11.20	9.70
Fe_2O_3	%	9.28	14.55	12.65	10.15	12.35	11.35	14.75	11.40	10.80	10.70	17.20	15.80	10.45	8.49
CaO	%	8.13	8.24	7.10	7.69	7.58	7.85	4.71	2.65	1.98	1.82	4.65	3.04	8.12	9.79
MgO	%	13.65	4.69	17.20	11.30	15.05	10.55	12.50	31.30	32.80	33.60	24.80	27.00	12.50	13.00
Na_2O	%	2.86	2.57	0.59	1.74	2.02	2.05	0.21	0.23	0.16	0.23	0.07	0.16	1.44	2.40
K_2O	%	3.04	1.02	3.29	1.42	0.69	1.34	7.23	0.10	0.08	0.12	0.01	0.03	1.06	0.95
Cr_2O_3	%	0.105	0.005	0.256	0.123	0.281	0.125	0.135	0.789	0.710	0.706	0.578	0.639	0.155	0.153
TiO_2	%	0.47	1.06	0.42	0.49	0.51	0.62	0.74	0.18	0.18	0.17	0.21	0.19	0.55	0.31
MnO	%	0.14	0.29	0.20	0.17	0.18	0.20	0.18	0.18	0.12	0.14	0.10	0.17	0.17	0.16
P_2O_5	%	0.26	0.10	0.04	0.05	0.05	0.05	0.05	0.02	0.01	0.02	0.02	0.01	0.05	<0.01
SrO	%	0.05	0.02	<0.01	0.02	0.01	0.01	<0.01	<0.01	<0.01	<0.01	<0.01	<0.01	0.01	0.04
BaO	%	0.06	0.02	0.05	0.02	0.01	0.03	0.07	<0.01	<0.01	<0.01	<0.01	<0.01	0.01	0.02
LOI	%	3.42	0.44	2.38	2.63	2.63	2.43	6.01	8.74	9.86	9.78	6.89	8.43	2.88	1.56
Total	%	100.02	101.51	98.23	100.20	99.61	100.56	99.29	100.26	100.17	101.66	98.37	98.52	100.00	100.57
C	%	0.54	0.04	0.03	0.02	0.03	0.07	0.93	0.05	0.04	0.03	0.60	0.11	0.03	0.04
S	%	0.30	0.02	0.01	0.08	0.84	0.26	0.05	0.06	0.05	0.05	3.86	3.22	0.18	0.24
Ba	ppm	527.0	203.0	423.0	178.5	104.0	239.0	602.0	9.1	10.6	16.6	1.3	3.3	97.2	150.5
Ce	ppm	129.0	21.9	7.4	10.8	9.3	9.0	6.5	3.6	3.4	3.2	4.3	2.1	9.4	9.5
Cr	ppm	814	46	1930	1005	2300	950	1005	6020	5320	5450	4530	5150	1365	1275
Cs	ppm	5.93	0.42	5.71	0.19	1.26	0.44	9.07	0.28	0.23	0.28	0.09	0.15	0.29	0.38
Dy	ppm	1.92	3.36	1.90	1.94	2.20	2.48	1.68	0.70	0.68	0.71	0.77	0.66	2.36	2.20
Er	ppm	0.93	1.74	1.14	1.22	1.47	1.38	1.26	0.41	0.42	0.36	0.50	0.48	1.32	1.42
Eu	ppm	1.55	0.96	0.26	0.48	0.50	0.48	0.22	0.16	0.19	0.13	0.12	0.08	0.47	0.50
Ga	ppm	14.4	23.8	10.6	13.8	12.4	13.6	20.9	5.2	4.8	4.9	6.0	5.0	13.9	11.3
Gd	ppm	3.68	3.22	1.52	1.63	1.84	1.81	1.05	0.60	0.58	0.58	0.68	0.52	1.94	2.12
Ge	ppm	1.9	1.6	1.4	1.7	1.6	1.6	1.7	1.1	1.3	1.2	1.2	1.1	1.7	2.3
Hf	ppm	1.54	3.00	1.12	1.39	1.21	1.45	1.49	0.38	0.44	0.39	0.51	0.38	1.35	0.78
Ho	ppm	0.34	0.65	0.35	0.43	0.48	0.53	0.39	0.17	0.16	0.14	0.15	0.15	0.45	0.46
La	ppm	60.1	9.9	3.1	5.0	4.2	4.1	3.3	1.7	1.6	1.5	2.3	0.9	4.5	2.9
Lu	ppm	0.14	0.23	0.18	0.16	0.20	0.23	0.17	0.05	0.07	0.06	0.07	0.07	0.25	0.21
Nb	ppm	2.44	4.36	1.45	1.87	1.68	1.74	1.49	0.62	0.55	0.58	0.72	0.55	1.79	2.28
Nd	ppm	54.9	11.9	4.2	5.9	5.1	5.1	3.3	2.0	1.7	1.7	2.2	1.4	5.4	7.6
Pr	ppm	14.95	2.81	0.98	1.36	1.23	1.17	0.80	0.47	0.41	0.43	0.48	0.27	1.21	1.53
Rb	ppm	92.2	19.2	112.5	45.8	22.4	45.0	184.5	4.5	2.7	2.7	0.6	1.3	56.8	30.2
Sm	ppm	6.92	3.41	1.25	1.52	1.29	1.51	0.86	0.39	0.44	0.45	0.61	0.38	1.55	2.09
Sn	ppm	0.7	1.3	1.4	<0.5	0.5	<0.5	1.2	<0.5	<0.5	<0.5	<0.5	<0.5	<0.5	2.0
Sr	ppm	442.0	138.5	21.4	139.5	81.2	113.0	24.8	27.1	11.4	17.6	51.8	21.9	88.8	356.0
Ta	ppm	0.1	0.3	0.1	0.1	0.1	0.1	0.1	<0.1	<0.1	<0.1	<0.1	<0.1	0.1	0.1
Tb	ppm	0.41	0.53	0.25	0.30	0.32	0.36	0.20	0.10	0.09	0.08	0.09	0.10	0.35	0.35
Th	ppm	6.08	2.05	0.86	1.24	0.91	0.74	0.90	0.28	0.29	0.26	0.39	0.36	0.84	0.97
Tm	ppm	0.11	0.23	0.15	0.16	0.17	0.20	0.19	0.05	0.03	0.04	0.06	0.04	0.20	0.19
U	ppm	0.83	0.74	0.21	0.25	0.23	0.18	0.17	<0.05	<0.05	0.05	0.23	0.21	0.28	0.30
V	ppm	160	212	145	188	190	212	291	88	83	83	113	95	215	184
W	ppm	0.5	1.4	0.5	<0.5	<0.5	<0.5	0.7	0.9	<0.5	1.2	0.8	1.1	0.8	<0.5
Y	ppm	9.4	17.1	10.7	11.6	12.0	13.3	10.1	4.2	4.1	4.0	4.6	4.0	12.9	13.3
Yb	ppm	0.86	1.55	1.02	1.09	1.33	1.48	1.16	0.40	0.39	0.41	0.44	0.37	1.23	1.24
Zr	ppm	60	108	40	52	48	49	56	15	15	15	18	14	49	25
As	ppm	<0.1	0.1	0.1	0.3	0.8	0.5	0.2	16.8	1.1	0.2	0.6	3.7	1.2	0.2
Bi	ppm	0.15	0.38	0.02	0.02	0.36	0.06	0.02	0.11	0.04	0.03	1.24	0.97	0.04	0.02
Hg	ppm	<0.005	<0.005	<0.005	<0.005	<0.005	<0.005	<0.005	<0.005	<0.005	<0.005	<0.005	<0.005	<0.005	<0.005
In	ppm	0.013	0.044	0.010	<0.005	0.020	0.007	0.056	0.007	0.012	0.011	0.036	0.032	<0.005	0.005
Re	ppm	<0.001	0.098	0.009	0.001	0.005	0.001	<0.001	<0.001	<0.001	<0.001	0.015	0.015	0.001	0.001
Sb	ppm	<0.05	<0.05	<0.05	<0.05	0.06	<0.05	<0.05	0.10	<0.05	<0.05	0.14	0.08	<0.05	<0.05
Se	ppm	0.2	<0.2	<0.2	0.2	2.7	0.7	<0.2	<0.2	<0.2	0.2	9.4	8.3	0.5	0.2
Te	ppm	0.03	0.02	0.02	0.02	0.38	0.04	0.05	0.02	<0.01	0.04	2.27	1.06	0.03	0.05
Tl	ppm	0.81	0.09	1.24	0.02	0.24	0.04	0.85	0.03	0.02	0.02	0.49	0.30	0.03	0.08
Ag	ppm	<0.5	<0.5	<0.5	<0.5	<0.5	<0.5	<0.5	<0.5	<0.5	<0.5	0.6	<0.5	<0.5	<0.5
Cd	ppm	<0.5	<0.5	<0.5	<0.5	<0.5	<0.5	<0.5	<0.5	<0.5	<0.5	<0.5	0.5	<0.5	<0.5
Co	ppm	58	36	72	58	110	55	62	120	131	127	268	240	68	42
Cu	ppm	814	8	2	54	1160	126	2	7	1	47	1975	1995	120	71
Li	ppm	70	30	100	40	30	50	230	<10	10	10	<10	<10	40	20
Mo	ppm	<1	34	2	<1	<1	<1	<1	<1	<1	<1	<1	1	<1	<1
Ni	ppm	1170	141	762	248	2320	248	247	1645	1895	1965	8550	6210	334	465
Pb	ppm	3	3	2	2	2	<2	<2	3	2	<2	5	5	<2	2
Sc	ppm	23	23	23	27	27	32	34	13	8	9	15	14	31	28
Zn	ppm	117	130	156	65	61	93	216	92	58	61	61	97	76	78
Cu	%														
Ni	%														

Oxide	Unit	EN23VS 048	EN23VS 049	EN23VS 050	EN23VS 051	EN23VS 052	EN23VS 053	EN23VS 054	EN23VS 056	EN23VS 057	EN23VS 058	EN23VS 059	EN23VS 060	EN23VS 061	EN23VS 063
SiO_2	%	51.50	48.20	54.20	53.30	52.80	50.60	50.70	50.80	51.60	49.50	47.00	50.70	51.50	47.70
Al_2O_3	%	14.70	8.78	9.93	14.45	13.75	11.40	12.25	11.55	12.00	11.55	8.78	11.05	11.30	8.89
Fe_2O_3	%	6.23	10.45	8.49	12.70	10.80	11.30	10.15	10.80	10.65	10.70	10.40	10.60	11.45	10.25
CaO	%	3.51	7.31	7.70	8.13	7.49	8.00	8.35	8.15	7.91	8.90	7.72	8.19	8.48	7.50
MgO	%	7.57	17.70	13.35	5.10	9.16	13.95	10.85	11.75	11.45	13.05	20.50	13.55	12.60	19.70
Na_2O	%	0.02	1.41	2.98	3.51	1.98	1.40	1.76	1.95	2.26	2.30	0.29	1.40	1.72	0.51
K_2O	%	6.50	1.94	1.07	0.71	1.66	1.12	2.04	1.90	1.49	0.68	1.24	1.13	2.25	1.81
Cr_2O_3	%	0.180	0.356	0.238	0.006	0.102	0.243	0.135	0.140	0.144	0.180	0.320	0.206	0.195	0.333
TiO_2	%	0.69	0.42	0.33	1.08	0.62	0.56	0.60	0.59	0.60	0.54	0.41	0.55	0.56	0.38
MnO	%	0.05	0.13	0.14	0.22	0.20	0.18	0.17	0.18	0.18	0.18	0.22	0.20	0.18	0.19
P_2O_5	%	0.07	0.03	0.01	0.11	0.07	0.04	0.05	0.04	0.05	0.05	0.04	0.04	0.05	0.03
SrO	%	<0.01	<0.01	0.02	0.03	0.02	0.01	0.02	0.01	0.01	0.01	<0.01	0.01	0.02	<0.01
BaO	%	0.02	0.02	0.03	0.02	0.03	0.02	0.03	0.03	0.04	0.02	0.02	0.02	0.04	0.02
LOI	%	8.27	2.90	2.12	0.50	2.14	3.17	1.54	1.93	2.67	3.51	4.66	2.95	1.61	4.02
Total	%	99.31	99.65	100.61	99.87	100.82	101.99	98.65	99.82	101.05	101.17	101.60	100.60	101.96	101.33
C	%	0.65	0.03	0.04	0.02	0.05	0.02	0.02	0.03	0.06	0.13	0.02	0.02	0.02	0.02
S	%	0.02	0.08	0.06	0.15	0.16	0.02	0.16	0.01	0.01	0.01	0.04	0.04	0.01	0.01
Ba	ppm	171.5	182.0	243.0	172.0	262.0	150.0	296.0	284.0	343.0	163.5	152.5	182.5	365.0	161.0
Ce	ppm	14.8	10.7	7.0	25.7	17.4	9.5	9.4	7.7	9.4	8.6	7.9	8.4	10.2	8.0
Cr	ppm	1455	2590	1675	51	753	1840	1040	1010	1090	1375	2380	1600	1490	2600
Cs	ppm	0.85	4.05	1.18	0.46	0.63	0.30	1.72	1.90	0.46	0.26	1.30	0.22	3.17	2.80
Dy	ppm	1.34	1.94	1.54	3.41	2.75	2.20	2.50	2.20	2.46	2.38	1.80	2.34	2.45	1.80
Er	ppm	0.92	1.15	1.00	1.86	1.69	1.48	1.49	1.31	1.54	1.52	1.21	1.56	1.54	1.17
Eu	ppm	0.28	0.58	0.33	1.13	0.65	0.49	0.56	0.49	0.57	0.55	0.39	0.55	0.52	0.45
Ga	ppm	16.6	12.3	11.6	20.4	14.3	13.5	13.2	12.8	13.2	12.8	10.2	12.4	14.2	10.6
Gd	ppm	1.01	1.77	1.35	3.63	2.41	2.06	1.97	1.99	2.06	1.91	1.58	1.78	2.09	1.56
Ge	ppm	1.5	2.4	1.7	1.4	1.4	1.8	1.6	1.7	1.6	2.1	1.4	1.6	1.7	1.6
Hf	ppm	1.76	1.22	0.63	3.14	1.77	1.31	1.34	1.29	1.35	1.34	1.08	1.36	1.46	1.13
Ho	ppm	0.31	0.42	0.32	0.67	0.59	0.50	0.54	0.50	0.56	0.49	0.38	0.50	0.52	0.40
La	ppm	6.5	4.3	2.7	11.7	8.1	4.3	4.3	3.3	4.3	3.6	3.7	3.5	4.4	3.4
Lu	ppm	0.19	0.17	0.13	0.24	0.24	0.22	0.20	0.19	0.22	0.23	0.16	0.21	0.24	0.16
Nb	ppm	2.20	2.03	1.48	4.25	2.52	1.68	1.68	1.70	1.62	1.70	1.42	1.64	1.86	1.24
Nd	ppm	4.5	5.0	4.0	13.4	8.4	5.5	5.5	5.2	5.4	5.1	4.2	4.7	5.3	4.4
Pr	ppm	1.37	1.30	0.94	3.17	2.11	1.27	1.21	1.11	1.27	1.13	0.95	1.12	1.30	1.06
Rb	ppm	73.8	52.8	31.0	13.4	53.4	36.2	59.9	57.0	43.9	17.5	29.3	39.9	71.7	54.6
Sm	ppm	1.03	1.47	1.10	3.38	2.09	1.49	1.62	1.62	1.61	1.72	1.35	1.46	1.56	1.13
Sn	ppm	0.6	1.5	0.9	1.0	0.7	0.5	<0.5	0.9	0.9	0.9	1.9	0.6	0.9	0.5
Sr	ppm	32.1	35.9	138.5	283.0	164.5	76.8	142.5	120.0	108.5	99.5	24.6	99.9	164.0	25.5
Ta	ppm	0.1	0.1	0.1	0.3	0.2	0.1	0.1	0.1	0.1	0.1	0.1	0.1	0.1	0.1
Tb	ppm	0.19	0.30	0.22	0.56	0.39	0.34	0.36	0.31	0.38	0.34	0.26	0.31	0.36	0.25
Th	ppm	1.42	0.99	0.77	2.32	1.74	0.94	0.80	0.75	0.82	0.80	0.98	0.75	1.07	0.90
Tm	ppm	0.11	0.19	0.13	0.23	0.25	0.20	0.21	0.19	0.22	0.21	0.15	0.19	0.21	0.15
U	ppm	0.53	0.41	0.26	0.57	0.53	0.24	0.23	0.30	0.32	0.27	0.30	0.25	0.31	0.29
V	ppm	251	175	168	222	231	230	230	219	228	220	156	224	221	168
W	ppm	0.7	<0.5	<0.5	<0.5	0.9	0.7	<0.5	<0.5	<0.5	<0.5	<0.5	0.5	1.6	<0.5
Y	ppm	7.8	11.1	8.9	17.6	15.4	13.0	14.1	13.6	13.9	13.1	10.2	12.9	13.1	10.0
Yb	ppm	1.08	1.10	1.04	1.61	1.59	1.41	1.40	1.29	1.43	1.31	1.07	1.30	1.40	1.04
Zr	ppm	66	44	18	113	67	46	53	49	51	50	41	49	50	39
As	ppm	0.3	0.6	0.3	0.3	0.1	1.0	0.4	0.1	0.1	<0.1	9.1	0.3	0.1	0.3
Bi	ppm	0.08	0.07	0.24	0.45	0.27	0.04	0.07	0.01	0.02	0.02	0.05	0.06	0.02	0.02
Hg	ppm	<0.005	<0.005	<0.005	<0.005	<0.005	<0.005	<0.005	<0.005	<0.005	0.008	0.012	<0.005	<0.005	<0.005
In	ppm	0.013	0.006	0.007	0.013	0.011	0.005	0.007	0.006	0.006	0.005	0.032	0.005	0.009	<0.005
Re	ppm	<0.001	<0.001	<0.001	<0.001	0.001	0.006	0.001	0.001	0.002	0.001	0.001	<0.001	0.001	0.001
Sb	ppm	<0.05	0.10	0.08	<0.05	<0.05	0.05	0.05	<0.05	<0.05	<0.05	<0.05	<0.05	<0.05	<0.05
Se	ppm	<0.2	0.3	0.3	<0.2	0.5	<0.2	0.4	<0.2	<0.2	<0.2	0.7	0.3	<0.2	<0.2
Te	ppm	0.05	0.11	0.28	0.01	0.03	0.02	0.08	0.01	0.01	0.03	0.18	0.03	0.01	0.04
Tl	ppm	0.03	0.55	0.32	0.08	0.11	0.03	0.19	0.14	0.02	<0.02	0.34	0.03	0.49	0.32
Ag	ppm	<0.5	<0.5	<0.5	<0.5	<0.5	<0.5	0.5	<0.5	<0.5	<0.5	<0.5	<0.5	<0.5	<0.5
Cd	ppm	<0.5	<0.5	<0.5	<0.5	<0.5	<0.5	<0.5	<0.5	<0.5	<0.5	<0.5	<0.5	<0.5	<0.5
Co	ppm	27	62	38	53	52	64	53	55	54	58	53	63	56	64
Cu	ppm	28	36	80	166	138	35	130	6	8	3	17	70	9	1
Li	ppm	330	70	40	20	40	50	50	60	60	70	90	40	60	90
Mo	ppm	<1	<1	<1	<1	<1	4	<1	1	1	<1	<1	<1	<1	1
Ni	ppm	263	1165	779	160	197	601	251	296	260	352	1220	387	319	857
Pb	ppm	2	7	2	6	4	2	49	3	<2	<2	4	2	3	<2
Sc	ppm	36	22	28	24	31	29	34	31	32	30	22	31	30	24
Zn	ppm	47	69	51	122	111	82	136	98	85	113	110	101	65	63
Cu	%														
Ni	%														

Oxide	Unit	EN23VS 064	EN23VS 065	EN23VS 066	EN23VS 067	EN23VS 068	EN23VS 069	EN23VS 070	EN23VS 072	EN23VS 073	EN23VS 074	EN23VS 077	EN23VS 078	EN23VS 080	EN23VS 083
SiO_2	%	47.60	51.70	44.90	47.00	48.00	55.60	49.10	48.70	48.30	49.10	52.60	52.40	44.90	38.00
Al_2O_3	%	6.69	11.50	5.64	9.30	8.27	18.55	10.10	10.25	10.20	10.35	17.40	17.55	10.60	3.00
Fe_2O_3	%	11.25	11.75	11.70	10.75	9.94	7.92	10.35	11.00	11.25	10.50	9.34	8.19	9.43	14.05
CaO	%	7.80	8.28	3.05	7.21	7.16	7.52	6.96	8.26	7.30	7.78	7.85	7.07	7.70	1.54
MgO	%	22.30	11.55	25.30	17.20	18.90	3.51	16.65	16.30	15.50	15.50	5.42	4.04	10.35	30.60
Na_2O	%	0.29	1.80	0.12	1.28	0.70	4.99	1.88	1.60	0.98	1.14	2.93	3.69	0.07	0.03
K_2O	%	0.06	1.90	0.02	2.37	3.87	1.48	2.39	1.00	3.62	3.17	2.88	3.45	6.43	0.05
Cr_2O_3	%	0.416	0.180	0.519	0.250	0.338	0.002	0.232	0.222	0.209	0.207	<0.002	<0.002	0.160	0.808
TiO_2	%	0.30	0.58	0.26	0.46	0.39	0.62	0.50	0.49	0.52	0.49	0.87	0.70	0.52	0.15
MnO	%	0.21	0.24	0.10	0.18	0.19	0.14	0.17	0.18	0.18	0.18	0.14	0.13	0.18	0.14
P_2O_5	%	0.02	0.04	0.03	0.05	0.04	0.37	0.05	0.05	0.05	0.05	0.24	0.30	0.04	0.01
SrO	%	<0.01	0.02	<0.01	<0.01	<0.01	0.10	0.01	<0.01	0.01	0.01	0.08	0.07	<0.01	<0.01
BaO	%	<0.01	0.05	<0.01	0.04	0.04	0.08	0.04	0.02	0.05	0.04	0.07	0.04	0.03	<0.01
LOI	%	4.90	2.16	6.38	2.93	2.50	0.90	2.71	3.02	1.92	1.89	1.59	2.63	7.64	10.05
Total	%	101.84	101.75	98.02	99.02	100.34	101.78	101.14	101.09	100.09	100.41	101.41	100.26	98.05	98.43
C	%	0.02	0.03	0.28	0.02	0.02	0.05	0.02	0.02	0.02	0.02	0.12	0.42	1.81	0.08
S	%	0.35	0.01	0.31	0.03	0.03	0.20	0.09	0.02	0.01	0.01	0.19	0.16	0.01	2.29
Ba	ppm	6.2	468.0	3.1	342.0	413.0	757.0	359.0	187.0	475.0	400.0	650.0	381.0	293.0	3.3
Ce	ppm	4.4	11.0	3.1	7.1	6.3	51.7	8.5	9.2	11.0	10.7	42.9	45.3	6.6	2.6
Cr	ppm	3220	1345	3870	1975	2610	27	1820	1755	1645	1580	16	8	1195	6050
Cs	ppm	0.81	0.67	0.04	2.35	5.30	1.20	2.77	1.00	3.18	2.74	1.92	2.97	9.22	0.23
Dy	ppm	1.87	2.31	0.73	2.24	2.10	2.36	2.23	2.20	1.98	2.11	2.45	2.51	1.63	0.68
Er	ppm	1.12	1.55	0.46	1.30	1.23	1.32	1.34	1.36	1.34	1.27	1.35	1.29	1.16	0.46
Eu	ppm	0.51	0.63	0.14	0.56	0.50	1.32	0.53	0.58	0.43	0.43	1.28	1.23	0.20	0.13
Ga	ppm	9.0	14.6	7.0	11.9	11.0	19.5	11.4	12.2	13.7	12.8	19.0	17.8	13.6	3.8
Gd	ppm	1.56	2.10	0.60	1.90	1.78	3.23	1.99	2.13	1.60	1.70	3.31	3.37	1.21	0.62
Ge	ppm	1.5	1.7	1.2	1.6	1.6	1.2	1.5	1.6	1.7	1.6	1.2	1.2	1.2	1.0
Hf	ppm	0.90	1.44	0.71	1.25	1.23	2.46	1.29	1.32	1.26	1.24	1.51	2.04	1.31	0.39
Ho	ppm	0.39	0.54	0.15	0.45	0.46	0.49	0.50	0.48	0.45	0.44	0.50	0.47	0.39	0.16
La	ppm	1.5	5.1	1.9	2.7	2.6	25.3	3.7	4.2	5.2	5.4	20.2	21.4	2.8	1.0
Lu	ppm	0.14	0.24	0.08	0.19	0.17	0.20	0.20	0.21	0.19	0.18	0.18	0.18	0.21	0.06
Nb	ppm	1.30	1.82	0.86	1.68	1.50	3.09	1.74	1.78	1.74	1.70	3.29	2.99	2.06	0.46
Nd	ppm	3.3	5.9	1.7	4.4	3.9	23.3	4.8	5.1	5.1	4.8	20.7	22.0	3.6	1.5
Pr	ppm	0.69	1.43	0.40	1.00	0.84	6.20	1.13	1.14	1.31	1.26	5.31	5.55	0.85	0.35
Rb	ppm	2.2	46.0	0.5	58.1	104.0	51.5	66.1	26.1	93.0	78.1	72.0	123.0	213.0	2.0
Sm	ppm	1.15	1.47	0.45	1.40	1.37	4.35	1.39	1.59	1.17	1.27	4.03	4.26	0.95	0.44
Sn	ppm	1.1	1.1	<0.5	1.0	0.7	0.7	0.7	0.6	1.0	0.6	1.2	0.8	0.9	0.5
Sr	ppm	22.0	145.5	24.4	40.4	19.2	893.0	71.9	47.1	50.7	66.3	693.0	635.0	34.7	7.3
Ta	ppm	0.1	0.1	<0.1	0.1	0.1	0.2	0.1	0.1	0.1	0.1	0.2	0.1	0.1	<0.1
Tb	ppm	0.27	0.36	0.09	0.33	0.29	0.44	0.31	0.36	0.27	0.29	0.43	0.42	0.24	0.11
Th	ppm	0.64	1.00	0.57	0.87	1.03	3.17	0.90	1.15	0.71	1.05	3.15	2.25	0.94	0.35
Tm	ppm	0.16	0.21	0.06	0.18	0.17	0.18	0.20	0.21	0.18	0.19	0.18	0.18	0.17	0.05
U	ppm	0.24	0.37	0.20	0.33	0.28	0.86	0.34	0.39	0.27	0.31	0.93	0.60	0.37	0.16
V	ppm	137	211	129	187	169	163	195	202	201	196	246	184	201	81
W	ppm	0.6	0.8	1.8	0.6	<0.5	0.6	0.6	0.6	<0.5	1.3	<0.5	0.8	0.6	0.7
Y	ppm	10.3	13.6	3.8	11.7	11.3	12.8	12.1	12.8	11.0	11.2	13.0	12.7	9.9	3.9
Yb	ppm	0.97	1.37	0.43	1.19	1.25	1.29	1.22	1.31	1.20	1.33	1.18	1.15	1.16	0.45
Zr	ppm	31	51	23	45	42	105	45	52	44	48	51	77	44	12
As	ppm	0.4	0.4	1.8	0.5	0.2	0.4	0.5	0.2	0.2	0.3	0.1	<0.1	<0.1	3.5
Bi	ppm	0.25	0.07	0.07	0.01	0.01	0.02	0.01	0.01	<0.01	0.01	0.01	0.02	<0.01	0.80
Hg	ppm	<0.005	<0.005	<0.005	<0.005	<0.005	<0.005	<0.005	<0.005	<0.005	<0.005	<0.005	<0.005	<0.005	<0.005
In	ppm	0.008	0.006	0.008	0.007	0.008	0.007	0.008	0.006	0.011	0.009	0.007	0.006	0.040	0.023
Re	ppm	0.003	0.002	0.001	0.006	0.002	<0.001	0.001	0.001	0.001	0.001	<0.001	<0.001	0.001	0.003
Sb	ppm	<0.05	<0.05	0.06	<0.05	<0.05	<0.05	<0.05	<0.05	<0.05	<0.05	<0.05	<0.05	<0.05	0.15
Se	ppm	1.6	<0.2	0.6	<0.2	<0.2	<0.2	0.2	<0.2	<0.2	<0.2	0.2	<0.2	<0.2	4.5
Te	ppm	0.42	0.01	0.06	0.01	0.03	<0.01	<0.01	0.01	0.02	0.02	<0.01	0.01	0.04	0.74
Tl	ppm	0.07	0.05	0.06	0.51	0.55	0.27	0.36	0.12	0.47	0.36	0.36	0.49	1.05	0.56
Ag	ppm	<0.5	<0.5	<0.5	<0.5	<0.5	<0.5	<0.5	<0.5	<0.5	<0.5	<0.5	<0.5	<0.5	0.7
Cd	ppm	<0.5	<0.5	<0.5	<0.5	<0.5	<0.5	<0.5	<0.5	<0.5	<0.5	<0.5	<0.5	<0.5	<0.5
Co	ppm	80	55	112	64	56	21	64	56	46	57	36	26	48	302
Cu	ppm	292	8	266	12	13	34	41	25	8	16	30	12	5	1460
Li	ppm	20	40	<10	80	50	30	50	50	80	70	60	70	120	<10
Mo	ppm	<1	2	<1	2	1	<1	<1	<1	<1	<1	<1	<1	<1	4
Ni	ppm	2030	310	1535	725	883	15	708	679	637	630	22	13	333	6050
Pb	ppm	2	2	2	<2	<2	9	2	2	<2	<2	5	7	<2	25
Sc	ppm	18	29	19	25	22	12	26	26	26	26	25	17	28	11
Zn	ppm	70	128	76	71	81	89	73	87	91	96	96	93	105	186
Cu	%														
Ni	%														

Oxide	Unit	EN23VS 084	EN23VS 085	EN23VS 086	EN23VS 087	EN23VS 088	EN23VS 089	EN23VS 090	EN23VS 091	EN23VS 092	EN23VS 093	EN23VS 094	EN23VS 095	EN23VS 096	EN23VS 097
SiO_2	%	47.70	49.70	38.90	55.80	46.80	39.00	45.80	44.50	44.00	50.90	49.10	48.00	39.40	49.30
Al_2O_3	%	9.80	11.85	3.43	3.45	8.06	3.25	3.56	9.70	6.90	11.00	11.55	12.15	4.16	12.15
Fe_2O_3	%	10.85	10.85	10.95	10.35	10.60	10.10	12.00	13.50	9.82	10.45	11.25	11.90	9.74	10.50
CaO	%	6.53	8.90	0.82	9.77	6.03	1.76	8.47	6.44	5.64	8.39	8.42	6.12	2.44	8.34
MgO	%	16.85	12.60	32.00	15.35	19.35	32.70	22.70	17.85	26.00	13.75	13.65	13.70	32.20	13.35
Na_2O	%	1.13	1.80	<0.01	1.84	0.51	<0.01	0.08	0.62	0.18	1.90	1.71	2.69	0.06	1.82
K_2O	%	3.86	1.49	0.01	0.05	4.24	0.02	0.01	3.76	0.06	1.70	1.76	2.58	0.03	1.08
Cr_2O_3	%	0.225	0.177	0.728	0.278	0.313	0.728	0.798	0.367	0.613	0.242	0.223	0.096	0.642	0.202
TiO_2	%	0.45	0.55	0.16	0.17	0.39	0.15	0.15	0.44	0.33	0.49	0.56	0.56	0.19	0.47
MnO	%	0.13	0.16	0.12	0.14	0.12	0.11	0.14	0.22	0.18	0.16	0.17	0.13	0.08	0.17
P_2O_5	%	0.05	0.05	0.02	0.01	0.03	0.01	0.01	0.05	0.04	0.05	0.06	0.21	0.02	0.04
SrO	%	<0.01	0.01	<0.01	0.01	<0.01	<0.01	<0.01	<0.01	<0.01	0.02	0.01	0.02	0.01	0.01
BaO	%	0.05	0.02	<0.01	<0.01	0.05	<0.01	<0.01	0.05	<0.01	0.03	0.03	0.05	<0.01	0.01
LOI	%	1.99	2.02	12.20	1.66	2.36	11.90	4.86	2.59	6.02	2.17	2.36	2.72	10.05	2.60
Total	%	99.62	100.18	99.34	98.88	98.85	99.73	98.58	100.09	99.78	101.25	100.85	100.93	99.02	100.04
C	%	0.02	0.03	1.15	0.04	0.02	0.72	0.07	0.03	0.03	0.03	0.03	0.07	0.44	0.03
S	%	0.04	0.04	0.09	1.22	0.23	0.10	2.28	0.08	0.52	0.12	0.14	0.14	0.28	0.03
Ba	ppm	417.0	196.0	3.2	29.9	498.0	3.5	2.4	456.0	13.8	232.0	281.0	448.0	4.3	119.0
Ce	ppm	7.4	8.4	7.2	11.1	6.7	2.5	3.1	9.8	9.4	9.4	10.8	142.5	5.0	8.5
Cr	ppm	1740	1415	5590	2180	2450	5640	6260	2970	4790	1910	1785	782	5080	1735
Cs	ppm	7.04	1.74	0.08	0.06	7.66	0.17	0.04	6.68	0.07	1.16	2.06	6.91	0.37	0.31
Dy	ppm	1.91	2.41	0.55	1.29	1.72	0.51	0.91	1.91	1.41	2.01	2.13	2.54	0.58	2.17
Er	ppm	1.22	1.48	0.29	0.69	1.15	0.32	0.49	1.17	0.94	1.25	1.33	1.28	0.37	1.39
Eu	ppm	0.40	0.51	0.15	0.39	0.41	0.07	0.18	0.53	0.36	0.50	0.58	1.70	0.07	0.49
Ga	ppm	11.3	13.8	4.3	4.5	10.9	4.1	5.0	11.8	8.2	13.7	13.5	16.4	5.0	13.4
Gd	ppm	1.65	2.19	0.59	1.36	1.54	0.43	0.71	1.56	1.33	1.85	1.92	4.53	0.52	1.82
Ge	ppm	1.6	1.6	1.0	2.0	2.2	1.1	1.9	1.4	1.2	2.1	1.7	2.2	1.2	1.6
Hf	ppm	1.30	1.38	0.42	0.44	1.05	0.34	0.36	1.31	0.83	1.18	1.36	1.78	0.47	1.14
Ho	ppm	0.42	0.55	0.12	0.25	0.40	0.12	0.18	0.40	0.32	0.45	0.47	0.46	0.14	0.49
La	ppm	3.7	3.4	2.9	6.2	2.5	1.1	1.1	4.6	4.1	4.6	4.5	65.1	2.4	3.7
Lu	ppm	0.19	0.21	0.04	0.11	0.16	0.05	0.08	0.17	0.14	0.21	0.23	0.20	0.08	0.22
Nb	ppm	1.70	1.72	7.09	2.90	2.58	1.16	0.87	1.80	2.32	1.83	2.00	2.88	0.67	1.78
Nd	ppm	4.0	4.9	3.2	4.7	4.4	1.3	2.0	4.3	5.2	5.1	5.7	58.0	2.4	4.7
Pr	ppm	0.94	1.13	0.89	1.25	0.95	0.34	0.41	1.15	1.36	1.19	1.39	16.55	0.57	1.10
Rb	ppm	111.0	50.4	0.5	1.3	125.0	1.4	0.4	108.0	1.0	47.1	62.3	100.5	1.2	45.0
Sm	ppm	1.31	1.46	0.63	1.22	1.20	0.33	0.59	1.31	1.23	1.32	1.48	7.91	0.46	1.17
Sn	ppm	0.5	0.8	<0.5	1.0	0.8	<0.5	0.6	1.7	0.7	0.8	0.6	3.1	<0.5	0.5
Sr	ppm	39.1	138.0	12.4	78.9	21.0	20.2	13.6	29.4	20.6	175.5	143.5	239.0	66.2	125.0
Ta	ppm	0.1	0.1	<0.1	<0.1	0.1	<0.1	<0.1	0.1	0.1	0.1	0.1	0.1	<0.1	0.1
Tb	ppm	0.29	0.35	0.08	0.21	0.28	0.08	0.11	0.28	0.25	0.30	0.36	0.52	0.10	0.35
Th	ppm	1.00	0.80	0.65	0.48	0.86	0.38	0.34	1.16	1.26	0.88	1.12	6.35	0.47	0.78
Tm	ppm	0.16	0.20	0.04	0.10	0.14	0.06	0.08	0.19	0.14	0.21	0.22	0.18	0.05	0.22
U	ppm	0.34	0.28	0.18	0.22	0.30	0.33	0.10	0.33	0.24	0.31	0.33	1.03	0.16	0.23
V	ppm	195	237	86	72	154	82	86	165	132	193	207	194	86	210
W	ppm	0.8	<0.5	<0.5	<0.5	<0.5	0.8	<0.5	<0.5	<0.5	<0.5	<0.5	<0.5	<0.5	<0.5
Y	ppm	11.5	13.8	2.7	7.0	10.0	3.0	4.5	10.8	7.9	11.0	12.6	12.4	3.6	12.2
Yb	ppm	1.21	1.46	0.30	0.67	0.98	0.32	0.48	1.24	0.81	1.28	1.36	1.32	0.41	1.43
Zr	ppm	49	50	14	16	38	12	14	46	31	38	47	62	17	38
As	ppm	0.2	0.3	4.3	1.2	0.1	2.3	1.1	0.1	0.4	<0.1	1.0	<0.1	2.9	0.2
Bi	ppm	0.02	0.04	0.24	0.74	0.13	0.21	0.39	0.17	0.13	0.11	0.08	0.03	0.46	0.03
Hg	ppm	<0.005	<0.005	<0.005	<0.005	<0.005	<0.005	<0.005	<0.005	<0.005	<0.005	<0.005	<0.005	<0.005	<0.005
In	ppm	0.005	0.005	0.011	0.035	0.007	0.010	0.009	0.013	0.030	0.006	0.008	0.023	0.015	<0.005
Re	ppm	0.001	0.001	<0.001	0.006	<0.001	<0.001	0.006	0.002	0.002	0.001	0.001	<0.001	<0.001	0.001
Sb	ppm	<0.05	<0.05	0.21	0.32	<0.05	0.09	0.11	<0.05	<0.05	<0.05	<0.05	<0.05	0.10	<0.05
Se	ppm	0.2	0.3	<0.2	2.8	0.7	0.2	4.4	0.7	1.6	0.3	0.5	0.3	0.5	0.3
Te	ppm	0.03	0.02	0.02	1.04	0.18	0.04	0.77	0.26	0.39	0.10	0.10	0.04	0.37	0.03
Tl	ppm	0.98	0.18	<0.02	0.41	1.47	0.02	0.23	1.01	0.08	0.17	0.49	0.59	0.07	0.02
Ag	ppm	<0.5	<0.5	<0.5	3.0	<0.5	<0.5	0.6	<0.5	<0.5	<0.5	1.5	<0.5	<0.5	<0.5
Cd	ppm	<0.5	<0.5	<0.5	0.7	<0.5	<0.5	<0.5	<0.5	<0.5	<0.5	0.9	<0.5	<0.5	<0.5
Co	ppm	69	57	108	109	77	96	210	80	71	50	68	55	106	57
Cu	ppm	22	63	16	8410	152	31	1550	48	477	232	319	922	111	51
Li	ppm	70	50	<10	10	110	<10	<10	100	<10	50	60	90	<10	40
Mo	ppm	<1	<1	<1	3	<1	<1	1	<1	<1	1	1	<1	<1	<1
Ni	ppm	725	330	2020	2550	1600	1875	4800	1555	1730	920	804	712	1970	346
Pb	ppm	2	3	2	6	3	3	3	<2	2	2	138	3	<2	9
Sc	ppm	26	31	12	8	22	11	11	23	19	30	29	28	13	30
Zn	ppm	72	57	94	81	75	107	175	157	104	60	142	75	53	84
Cu	%														
Ni	%														

Oxide	Unit	EN23VS 098	EN23VS 099	EN23VS 100	EN23VS 101	EN23VS 102	EN23VS 103	EN23VS 104	EN23VS 105	EN23VS 106	EN23VS 107	EN23VS 108	EN23VS 109	EN23VS 110	EN23VS 111
SiO_2	%	48.60	47.40	45.60	44.70	39.40	45.30	43.90	43.50	54.80	46.00	47.80	47.60	49.40	48.10
Al_2O_3	%	11.70	10.75	4.32	7.39	3.66	6.48	8.44	5.26	17.75	10.05	10.40	5.19	11.90	5.22
Fe_2O_3	%	11.10	12.25	10.80	10.90	9.98	8.33	15.40	12.05	6.65	11.80	10.85	13.90	10.50	14.20
CaO	%	9.38	9.03	3.22	5.28	1.17	6.87	8.48	13.10	6.88	6.98	7.01	9.99	5.86	9.78
MgO	%	12.60	14.30	28.00	25.00	34.70	25.90	14.40	15.85	4.52	19.35	17.30	18.05	14.20	18.60
Na_2O	%	1.73	0.97	0.17	0.41	0.03	0.14	0.11	0.11	3.08	1.12	1.97	0.29	2.51	0.12
K_2O	%	1.50	1.52	0.06	0.07	0.02	0.04	4.58	2.57	4.00	0.34	0.14	0.03	2.49	0.04
Cr_2O_3	%	0.177	0.221	0.483	0.425	0.722	0.476	0.161	0.162	0.010	0.451	0.412	0.173	0.215	0.394
TiO_2	%	0.56	0.50	0.16	0.31	0.16	0.24	1.40	0.81	0.55	0.47	0.48	0.78	0.45	0.22
MnO	%	0.17	0.18	0.17	0.18	0.12	0.19	0.24	0.26	0.06	0.16	0.16	0.25	0.19	0.40
P_2O_5	%	0.05	0.04	0.03	0.04	0.03	0.03	0.10	0.01	0.11	0.05	0.05	0.06	0.05	0.04
SrO	%	0.01	0.01	<0.01	<0.01	<0.01	<0.01	<0.01	0.01	0.06	<0.01	0.01	<0.01	0.01	<0.01
BaO	%	0.01	0.02	<0.01	<0.01	<0.01	<0.01	0.06	0.02	0.08	<0.01	<0.01	<0.01	0.03	<0.01
LOI	%	1.61	2.51	5.35	5.04	10.45	5.48	2.61	5.89	2.99	4.87	3.94	3.66	2.14	3.36
Total	%	99.20	99.70	98.36	99.75	100.44	99.48	99.88	99.60	101.54	101.64	100.52	99.97	99.95	100.47
C	%	0.02	0.02	0.08	0.03	0.09	0.03	0.44	1.17	0.54	0.03	0.02	0.13	0.03	0.05
S	%	0.01	0.01	0.07	0.11	0.15	0.27	0.05	0.03	0.01	<0.01	0.03	0.04	0.01	0.53
Ba	ppm	134.0	201.0	7.1	7.0	3.0	5.1	526.0	188.0	677.0	25.9	17.2	2.4	265.0	3.2
Ce	ppm	7.3	7.1	4.1	6.7	2.4	3.7	25.5	10.7	21.9	5.8	8.0	8.6	7.7	5.9
Cr	ppm	1465	1815	3860	3390	5500	3560	1300	1285	85	3590	3300	1490	1735	3260
Cs	ppm	1.43	1.18	0.25	0.16	0.22	0.15	6.16	3.96	3.15	0.57	0.06	0.57	3.64	0.20
Dy	ppm	2.25	2.26	0.60	1.26	0.60	1.32	3.50	2.48	1.70	2.08	2.14	3.43	1.71	1.55
Er	ppm	1.53	1.47	0.34	0.83	0.41	0.85	1.76	1.50	0.95	1.42	1.33	1.78	1.09	1.00
Eu	ppm	0.54	0.42	0.14	0.27	0.08	0.23	0.89	0.61	0.79	0.36	0.41	1.00	0.36	0.29
Ga	ppm	14.8	12.9	5.0	8.5	4.4	6.9	16.8	10.9	17.9	12.6	12.3	12.4	12.5	11.5
Gd	ppm	1.94	1.79	0.59	1.15	0.48	0.91	3.89	2.39	1.99	1.80	1.75	4.14	1.44	1.22
Ge	ppm	1.8	1.9	1.3	1.3	1.2	1.5	2.6	3.1	1.1	1.8	1.6	2.4	1.6	2.4
Hf	ppm	1.18	1.08	0.40	0.72	0.34	0.55	2.10	1.22	1.90	1.26	1.38	1.42	1.02	0.64
Ho	ppm	0.48	0.48	0.14	0.28	0.14	0.30	0.67	0.54	0.33	0.49	0.48	0.69	0.41	0.36
La	ppm	2.9	3.7	2.0	3.1	0.9	1.4	10.6	4.7	10.4	2.5	3.6	3.6	3.6	2.9
Lu	ppm	0.22	0.23	0.05	0.14	0.07	0.14	0.26	0.22	0.12	0.23	0.22	0.27	0.18	0.17
Nb	ppm	1.64	1.57	0.69	1.11	0.53	0.77	10.15	6.15	2.64	1.64	1.90	3.85	1.72	1.26
Nd	ppm	4.5	4.4	2.0	3.1	1.4	2.3	15.8	6.9	10.2	3.3	4.4	8.6	4.0	3.2
Pr	ppm	1.04	1.04	0.52	0.76	0.36	0.53	3.69	1.53	2.63	0.81	1.02	1.67	0.97	0.78
Rb	ppm	49.1	51.8	2.2	1.8	0.7	1.2	182.0	94.8	145.5	5.4	2.2	1.1	76.9	1.0
Sm	ppm	1.33	1.34	0.44	0.87	0.37	0.75	3.96	1.87	2.17	1.26	1.49	3.07	1.07	0.89
Sn	ppm	1.2	1.4	<0.5	<0.5	<0.5	<0.5	2.0	1.4	1.5	0.6	0.6	1.9	0.8	1.3
Sr	ppm	114.0	61.6	22.4	31.8	7.4	18.6	20.5	66.3	495.0	54.3	110.0	20.5	107.0	9.1
Ta	ppm	0.1	0.1	<0.1	0.1	<0.1	<0.1	0.6	0.3	0.1	0.1	0.1	0.2	0.1	0.1
Tb	ppm	0.33	0.35	0.08	0.21	0.08	0.19	0.59	0.38	0.27	0.32	0.33	0.63	0.24	0.23
Th	ppm	0.71	0.62	0.42	0.68	0.34	0.47	0.75	0.44	1.16	1.00	1.02	0.89	0.87	0.63
Tm	ppm	0.24	0.21	0.06	0.12	0.07	0.14	0.27	0.23	0.13	0.22	0.20	0.24	0.18	0.15
U	ppm	0.39	0.39	0.12	0.21	0.18	0.14	0.49	0.24	0.34	0.25	0.54	0.61	0.27	0.23
V	ppm	212	216	100	132	76	115	261	106	104	179	190	217	193	93
W	ppm	<0.5	<0.5	<0.5	<0.5	<0.5	<0.5	<0.5	<0.5	<0.5	0.6	0.7	2.1	<0.5	<0.5
Y	ppm	12.9	12.9	3.7	7.2	3.7	7.5	17.8	14.2	8.8	12.2	12.5	18.7	10.0	9.7
Yb	ppm	1.49	1.43	0.40	0.80	0.43	0.88	1.66	1.46	0.83	1.51	1.28	1.57	1.11	1.08
Zr	ppm	44	39	14	27	14	19	74	43	73	45	45	53	37	25
As	ppm	0.3	0.1	13.6	0.2	4.8	0.5	0.7	0.2	0.3	0.4	16.1	0.2	0.7	37.1
Bi	ppm	0.02	0.01	0.09	0.05	0.28	0.04	0.04	0.03	0.02	0.06	0.10	0.03	0.08	13.90
Hg	ppm	<0.005	<0.005	<0.005	<0.005	<0.005	<0.005	<0.005	<0.005	<0.005	<0.005	<0.005	<0.005	<0.005	0.088
In	ppm	0.006	0.005	0.007	0.010	0.016	0.010	0.035	0.016	0.007	0.006	0.010	0.012	0.011	0.008
Re	ppm	0.001	<0.001	<0.001	<0.001	<0.001	<0.001	<0.001	<0.001	<0.001	<0.001	0.001	0.007	0.001	0.007
Sb	ppm	<0.05	<0.05	0.12	<0.05	0.18	0.05	<0.05	<0.05	<0.05	<0.05	<0.05	<0.05	<0.05	1.36
Se	ppm	<0.2	<0.2	0.2	0.2	0.2	0.6	0.2	0.2	<0.2	<0.2	0.2	<0.2	<0.2	3.7
Te	ppm	0.03	0.04	0.05	0.03	0.10	0.16	0.01	0.02	<0.01	0.06	0.03	0.01	0.09	1.82
Tl	ppm	0.19	0.09	0.03	0.02	0.23	0.07	0.95	0.52	0.47	0.02	<0.02	<0.02	0.71	3.53
Ag	ppm	<0.5	<0.5	<0.5	<0.5	<0.5	<0.5	<0.5	<0.5	<0.5	<0.5	<0.5	<0.5	<0.5	15.2
Cd	ppm	<0.5	<0.5	<0.5	<0.5	<0.5	<0.5	<0.5	<0.5	<0.5	<0.5	<0.5	<0.5	<0.5	<0.5
Co	ppm	52	54	108	97	103	100	91	90	23	85	82	79	65	213
Cu	ppm	4	4	22	37	28	100	367	169	20	40	138	6	61	1235
Li	ppm	60	90	<10	<10	<10	<10	80	50	70	50	30	30	80	40
Mo	ppm	1	<1	<1	<1	<1	<1	<1	<1	<1	<1	2	<1	1	8
Ni	ppm	350	483	1235	1235	1860	1250	692	1415	77	1005	698	955	667	5290
Pb	ppm	2	2	<2	<2	6	<2	3	3	6	<2	4	3	3	37
Sc	ppm	28	29	20	19	12	24	30	19	10	22	25	21	31	13
Zn	ppm	89	82	63	68	156	63	160	120	28	94	79	119	84	409
Cu	%														
Ni	%														

Oxide	Unit	EN23VS 112	EN23VS 113	EN23VS 114	EN23VS 115	EN23VS 116	EN23VS 117	EN23VS 118	EN23VS 119	EN23VS 120	EN23VS 121	EN23VS 122	EN23VS 123	EN23VS 124	EN23VS 125
SiO_2	%	46.10	45.60	50.10	47.60	50.40	45.20	48.10	45.20	46.00	50.50	49.50	45.20	39.30	48.20
Al_2O_3	%	4.55	7.78	11.70	9.45	11.85	10.65	10.00	7.79	9.12	11.10	11.70	7.42	4.20	10.30
Fe_2O_3	%	11.80	10.25	10.60	10.75	11.00	14.10	11.25	11.00	10.55	10.25	10.90	8.87	11.30	10.70
CaO	%	0.31	5.83	8.59	6.22	8.26	9.45	7.60	5.75	5.30	7.08	8.59	6.51	1.49	7.31
MgO	%	28.20	24.80	13.25	20.60	14.15	13.90	17.40	23.80	20.60	15.40	13.65	23.90	33.60	17.50
Na_2O	%	0.08	0.20	2.38	1.08	1.60	1.52	0.93	0.45	0.58	2.97	2.15	0.16	0.01	1.93
K_2O	%	0.05	1.04	0.95	1.48	0.73	1.86	2.01	0.21	4.72	0.56	0.68	2.34	0.03	0.54
Cr_2O_3	%	0.704	0.415	0.195	0.301	0.247	0.255	0.231	0.390	0.328	0.174	0.224	0.685	0.792	0.259
TiO_2	%	0.23	0.35	0.55	0.41	0.54	0.50	0.46	0.35	0.42	0.53	0.56	0.33	0.15	0.46
MnO	%	0.08	0.15	0.16	0.16	0.17	0.34	0.21	0.23	0.12	0.15	0.16	0.18	0.09	0.16
P_2O_5	%	0.04	0.04	0.05	0.03	0.05	0.04	0.04	0.03	0.05	0.04	0.06	0.04	0.02	0.05
SrO	%	<0.01	<0.01	0.02	<0.01	0.01	0.01	<0.01	<0.01	<0.01	0.01	0.01	<0.01	<0.01	<0.01
BaO	%	<0.01	0.01	0.01	0.02	0.01	0.01	0.04	<0.01	0.03	0.01	0.01	0.01	<0.01	0.01
LOI	%	6.06	5.08	1.84	3.12	2.84	3.35	3.31	5.16	1.82	2.66	2.04	4.18	9.94	3.14
Total	%	98.20	101.55	100.40	101.22	101.86	101.19	101.58	100.36	99.64	101.43	100.23	99.83	100.92	100.56
C	%	0.02	0.03	0.05	0.02	0.03	0.72	0.03	0.03	0.03	0.02	0.03	0.03	0.07	0.05
S	%	0.24	0.13	0.08	0.10	0.03	1.25	0.02	0.11	<0.01	0.12	0.06	0.59	0.29	0.04
Ba	ppm	6.6	67.0	115.0	201.0	93.3	131.0	370.0	14.0	259.0	79.1	91.9	123.5	3.1	75.2
Ce	ppm	1.2	7.5	8.4	8.8	8.9	6.6	9.6	8.3	8.4	10.4	10.8	4.9	2.3	13.1
Cr	ppm	5520	3370	1590	2420	2030	2050	1850	3150	2640	1350	1780	5350	6360	2140
Cs	ppm	0.12	1.50	1.80	2.07	0.86	2.46	1.68	0.67	11.25	1.13	0.45	4.07	0.14	1.04
Dy	ppm	0.17	1.52	2.33	1.63	2.28	2.52	2.10	1.49	1.73	2.34	2.26	1.29	0.53	2.07
Er	ppm	0.14	1.06	1.44	1.04	1.31	1.61	1.35	1.01	1.00	1.45	1.50	0.94	0.34	1.20
Eu	ppm	0.03	0.28	0.54	0.41	0.51	0.37	0.49	0.33	0.34	0.49	0.58	0.25	0.07	0.49
Ga	ppm	7.0	9.2	13.5	10.6	12.7	13.5	12.6	9.3	10.9	11.5	12.9	9.2	5.1	12.0
Gd	ppm	0.21	1.31	1.98	1.44	1.73	1.83	1.78	1.29	1.34	2.06	2.09	1.17	0.38	1.89
Ge	ppm	1.6	1.3	1.6	1.4	1.6	1.6	1.5	1.4	1.4	1.4	1.6	1.4	1.2	1.4
Hf	ppm	0.59	0.95	1.27	1.09	1.28	1.20	1.20	0.83	1.06	1.26	1.42	0.97	0.35	1.25
Ho	ppm	0.05	0.34	0.49	0.35	0.50	0.52	0.41	0.33	0.36	0.51	0.51	0.32	0.13	0.42
La	ppm	0.6	3.5	3.6	3.7	3.7	2.6	5.4	5.1	4.9	4.8	4.8	1.9	0.9	6.9
Lu	ppm	0.03	0.15	0.21	0.17	0.22	0.25	0.22	0.13	0.17	0.23	0.23	0.14	0.06	0.22
Nb	ppm	1.02	1.34	1.90	1.62	1.91	2.27	1.90	1.32	1.54	1.84	1.76	1.33	0.57	1.88
Nd	ppm	0.7	4.1	4.6	4.4	4.9	3.6	5.0	3.9	4.3	5.8	5.6	3.0	1.3	6.3
Pr	ppm	0.17	0.93	1.14	1.16	1.16	0.85	1.19	1.03	1.06	1.31	1.40	0.74	0.30	1.54
Rb	ppm	1.5	35.3	31.4	37.1	24.2	52.3	51.7	7.8	187.5	15.5	25.4	70.9	1.3	12.4
Sm	ppm	0.21	1.10	1.44	1.11	1.53	1.24	1.27	1.10	1.23	1.81	1.55	0.94	0.42	1.51
Sn	ppm	<0.5	<0.5	0.5	0.9	<0.5	1.3	1.1	<0.5	0.6	0.6	0.5	<0.5	<0.5	0.5
Sr	ppm	5.0	17.2	152.0	40.1	123.0	52.6	36.2	38.1	20.2	82.2	138.0	20.9	8.0	56.6
Ta	ppm	<0.1	0.1	0.1	0.1	0.1	0.1	0.1	0.1	0.1	0.1	0.1	0.1	<0.1	0.1
Tb	ppm	0.03	0.23	0.35	0.25	0.35	0.36	0.33	0.23	0.25	0.36	0.34	0.20	0.08	0.31
Th	ppm	0.51	0.78	0.72	0.84	0.93	0.76	1.01	0.70	0.91	0.81	1.08	1.10	0.37	1.18
Tm	ppm	0.02	0.15	0.22	0.15	0.21	0.24	0.19	0.14	0.14	0.22	0.24	0.13	0.05	0.20
U	ppm	0.12	0.23	0.26	0.28	0.27	0.43	0.34	0.27	0.33	0.32	0.33	0.80	0.25	0.38
V	ppm	101	143	217	154	218	189	219	180	172	207	200	131	83	193
W	ppm	<0.5	<0.5	<0.5	<0.5	<0.5	<0.5	<0.5	0.5	<0.5	<0.5	<0.5	<0.5	<0.5	<0.5
Y	ppm	1.3	8.6	13.0	9.1	12.6	14.6	11.6	8.7	9.3	12.9	12.6	7.9	2.9	11.8
Yb	ppm	0.16	1.02	1.38	0.99	1.42	1.70	1.27	0.89	0.99	1.43	1.46	0.90	0.40	1.38
Zr	ppm	19	32	45	34	44	40	42	32	39	41	47	36	12	46
As	ppm	1.6	0.5	2.3	11.4	0.4	3.8	1.2	0.3	0.3	0.5	0.3	0.5	1.3	0.3
Bi	ppm	0.13	0.09	0.04	0.18	0.04	0.61	0.08	0.04	0.01	0.02	0.04	0.10	0.21	0.02
Hg	ppm	<0.005	<0.005	<0.005	<0.005	<0.005	<0.005	<0.005	<0.005	<0.005	<0.005	<0.005	<0.005	<0.005	0.006
In	ppm	<0.005	0.011	0.005	0.008	0.006	0.006	0.010	0.007	0.007	<0.005	0.009	0.009	0.012	<0.005
Re	ppm	<0.001	0.001	0.001	0.001	0.001	0.005	0.001	<0.001	0.001	<0.001	0.001	0.002	<0.001	0.001
Sb	ppm	<0.05	<0.05	<0.05	<0.05	<0.05	0.08	<0.05	<0.05	<0.05	<0.05	<0.05	<0.05	0.08	<0.05
Se	ppm	0.3	0.5	0.3	0.8	0.2	4.7	0.4	0.2	<0.2	<0.2	0.2	2.0	0.2	<0.2
Te	ppm	0.08	0.04	0.02	0.29	0.02	1.63	0.19	0.04	0.03	0.02	0.02	0.36	0.12	0.01
Tl	ppm	0.03	0.27	0.19	0.52	0.08	0.65	0.36	0.08	1.10	0.13	0.06	0.57	0.17	0.19
Ag	ppm	<0.5	<0.5	<0.5	<0.5	<0.5	0.5	<0.5	<0.5	<0.5	<0.5	<0.5	<0.5	<0.5	<0.5
Cd	ppm	<0.5	<0.5	<0.5	<0.5	<0.5	<0.5	<0.5	<0.5	<0.5	<0.5	<0.5	<0.5	<0.5	<0.5
Co	ppm	94	86	65	86	64	135	75	96	86	63	58	97	119	69
Cu	ppm	12	40	60	109	96	554	20	37	1	73	344	411	76	28
Li	ppm	10	10	30	40	50	70	100	20	140	10	30	40	<10	20
Mo	ppm	<1	<1	<1	<1	<1	<1	<1	<1	<1	<1	<1	<1	<1	<1
Ni	ppm	1725	1170	398	1245	414	4140	1170	1115	878	505	446	2530	1600	638
Pb	ppm	<2	2	4	<2	3	5	3	2	<2	2	5	<2	<2	2
Sc	ppm	13	21	32	24	28	29	26	21	25	30	31	19	9	24
Zn	ppm	93	56	80	150	80	70	99	84	69	53	70	230	106	73
Cu	%														
Ni	%														

Oxide	Unit	EN23VS 126	EN23VS 127	EN23VS 128	EN23VS 129	EN23VS 130	EN23VS 131	EN23VS 132	EN23VS 133	EN23VS 134	EN23VS 135	EN23VS 136	EN24VS 001	EN24VS 003	EN24VS 004
SiO_2	%	49.10	52.40	71.60	69.40	69.00	48.60	69.00	51.40	70.30	43.00	45.50	53.30	48.80	26.80
Al_2O_3	%	10.85	10.75	14.75	14.75	14.15	15.90	14.90	12.30	14.70	7.29	9.04	14.50	15.05	1.45
Fe_2O_3	%	11.45	9.11	3.29	3.20	3.18	10.45	3.54	11.25	3.42	12.40	10.65	14.20	11.70	25.30
CaO	%	9.07	7.37	2.98	2.94	2.93	9.25	3.25	8.03	2.96	5.28	14.60	7.25	9.99	0.08
MgO	%	14.45	13.30	1.09	1.00	1.00	7.29	1.12	10.90	1.08	25.10	14.80	5.24	9.10	25.30
Na_2O	%	1.63	3.14	4.66	4.61	4.74	2.86	4.62	2.24	4.52	0.08	0.58	3.49	2.50	<0.01
K_2O	%	0.86	1.56	2.02	2.10	1.94	1.48	1.82	1.78	2.19	0.01	0.26	0.77	1.72	0.02
Cr_2O_3	%	0.267	0.189	0.003	0.002	0.002	0.036	0.002	0.108	0.003	0.463	0.407	0.007	0.068	0.620
TiO_2	%	0.50	0.48	0.35	0.35	0.35	0.73	0.38	0.56	0.36	0.35	0.36	1.02	0.70	0.10
MnO	%	0.13	0.15	0.05	0.04	0.04	0.16	0.05	0.21	0.05	0.14	0.21	0.29	0.20	0.13
P_2O_5	%	0.05	0.03	0.08	0.08	0.08	0.09	0.10	0.05	0.10	<0.01	<0.01	0.10	0.10	0.01
SrO	%	0.01	0.06	0.04	0.04	0.04	0.03	0.04	0.02	0.04	<0.01	0.02	0.03	0.05	<0.01
BaO	%	0.02	0.03	0.06	0.05	0.05	0.02	0.05	0.06	0.05	<0.01	<0.01	0.02	0.04	<0.01
LOI	%	2.47	1.15	0.65	0.56	0.62	1.70	0.47	1.84	0.57	6.17	4.26	0.60	1.47	11.70
Total	%	100.86	99.72	101.62	99.12	98.12	98.60	99.34	100.75	100.34	100.28	100.69	100.82	101.49	91.51
C	%	0.02	0.08	0.07	0.03	0.04	0.02	0.02	0.02	0.02	0.26	0.64	0.02	0.02	0.05
S	%	0.06	0.05	0.01	0.01	0.02	1.00	0.04	0.02	0.02	0.18	0.03	0.03	0.20	10.40
Ba	ppm	207.0	308.0	529.0	465.0	484.0	218.0	475.0	577.0	491.0	2.1	48.4	145.5	409.0	2.5
Ce	ppm	9.2	14.0	51.8	58.9	58.7	16.0	62.4	8.1	65.0	0.6	1.8	27.7	16.5	1.6
Cr	ppm	2150	1545	36	22	26	294	25	858	33	3740	3320	51	478	4300
Cs	ppm	0.77	1.96	0.73	1.50	0.80	0.67	1.18	0.38	0.87	0.05	0.34	0.18	1.46	<0.01
Dy	ppm	2.22	2.15	1.59	2.17	2.06	2.71	1.78	2.39	2.19	1.09	1.52	3.22	2.88	0.23
Er	ppm	1.29	1.34	0.93	1.31	1.10	1.77	1.07	1.53	1.21	0.64	0.95	1.86	1.76	0.18
Eu	ppm	0.51	0.48	0.69	0.77	0.78	0.91	0.72	0.59	0.72	0.17	0.39	1.04	0.88	0.04
Ga	ppm	12.9	11.3	18.1	18.6	18.7	15.7	18.8	13.1	17.6	7.8	8.3	21.1	16.6	2.6
Gd	ppm	1.84	1.96	1.81	2.61	2.54	2.87	2.37	1.94	2.58	0.83	1.24	3.68	2.98	0.25
Ge	ppm	2.1	1.6	1.0	1.1	1.1	1.4	1.0	1.7	1.1	1.6	1.6	1.8	1.6	1.0
Hf	ppm	1.38	1.52	3.40	4.37	4.38	1.86	4.32	1.47	4.77	0.25	0.38	2.94	1.82	0.25
Ho	ppm	0.47	0.47	0.31	0.42	0.41	0.61	0.37	0.54	0.46	0.24	0.37	0.69	0.68	0.06
La	ppm	4.0	6.5	27.4	30.5	30.6	6.6	33.4	3.4	32.9	0.2	0.6	12.4	7.0	0.8
Lu	ppm	0.21	0.20	0.14	0.19	0.19	0.24	0.16	0.23	0.17	0.09	0.12	0.24	0.27	0.03
Nb	ppm	1.92	2.44	5.55	6.59	6.42	3.90	5.62	1.86	6.97	<0.05	0.08	4.83	4.07	0.50
Nd	ppm	5.4	6.8	17.1	20.5	20.3	9.2	21.0	5.1	23.2	0.9	2.0	15.4	10.5	0.8
Pr	ppm	1.29	1.71	5.35	6.35	6.07	2.21	6.41	1.12	6.89	0.12	0.33	3.29	2.25	0.20
Rb	ppm	27.1	44.8	48.9	65.6	55.6	45.2	56.3	51.4	64.9	0.4	10.4	15.6	55.9	0.5
Sm	ppm	1.33	1.63	2.34	3.16	3.07	2.45	3.08	1.43	3.45	0.45	0.89	3.80	2.27	0.19
Sn	ppm	1.1	0.7	1.2	1.2	1.1	0.6	1.0	0.6	1.2	<0.5	<0.5	1.0	1.5	0.8
Sr	ppm	108.0	504.0	352.0	333.0	340.0	263.0	367.0	171.5	333.0	12.0	162.0	210.0	427.0	3.2
Ta	ppm	0.2	0.2	0.6	0.7	0.7	0.2	0.4	0.1	0.6	<0.1	<0.1	0.4	0.2	<0.1
Tb	ppm	0.33	0.33	0.27	0.39	0.38	0.46	0.31	0.38	0.37	0.13	0.26	0.58	0.47	0.05
Th	ppm	1.02	1.87	5.50	7.33	7.69	0.81	6.19	0.93	7.45	0.05	0.06	2.14	0.64	0.15
Tm	ppm	0.19	0.21	0.14	0.18	0.18	0.24	0.16	0.21	0.19	0.09	0.14	0.24	0.26	0.03
U	ppm	0.42	0.54	1.80	1.76	1.62	0.20	1.39	0.32	1.84	<0.05	<0.05	0.54	0.17	0.06
V	ppm	199	192	38	41	40	214	45	227	43	189	309	224	223	63
W	ppm	<0.5	0.5	<0.5	<0.5	<0.5	<0.5	<0.5	<0.5	<0.5	<0.5	0.6	<0.5	<0.5	<0.5
Y	ppm	12.4	13.2	9.0	12.0	11.6	16.4	10.4	13.9	12.6	5.8	8.5	18.0	16.6	1.5
Yb	ppm	1.34	1.28	0.92	1.27	1.18	1.63	0.94	1.40	1.14	0.60	0.79	1.60	1.68	0.17
Zr	ppm	49	55	122	165	156	69	165	53	177	5	8	113	71	8
As	ppm	0.4	0.3	0.1	0.6	0.1	0.1	0.2	0.1	0.3	2.3	0.7	0.6	0.2	2.3
Bi	ppm	0.04	0.03	0.04	0.03	0.01	0.10	0.03	0.33	0.02	0.03	0.03	1.12	0.05	1.57
Hg	ppm	<0.005	<0.005	<0.005	<0.005	<0.005	<0.005	<0.005	<0.005	<0.005	<0.005	<0.005	<0.005	<0.005	0.010
In	ppm	<0.005	0.005	0.005	<0.005	<0.005	<0.005	0.005	0.006	<0.005	0.010	<0.005	0.028	0.029	0.045
Re	ppm	0.003	0.001	<0.001	<0.001	<0.001	0.004	<0.001	0.001	<0.001	<0.001	<0.001	<0.001	0.001	0.030
Sb	ppm	<0.05	<0.05	<0.05	<0.05	<0.05	<0.05	<0.05	<0.05	<0.05	<0.05	0.06	<0.05	<0.05	0.05
Se	ppm	0.3	<0.2	<0.2	<0.2	<0.2	1.4	<0.2	<0.2	<0.2	0.2	<0.2	<0.2	0.4	22.5
Te	ppm	0.03	0.01	<0.01	<0.01	0.01	0.06	<0.01	0.04	<0.01	0.03	0.12	0.02	0.04	2.69
Tl	ppm	0.11	0.57	0.22	0.28	0.22	0.13	0.24	0.02	0.27	<0.02	<0.02	0.05	0.25	0.80
Ag	ppm	<0.5	<0.5	<0.5	<0.5	<0.5	<0.5	<0.5	<0.5	<0.5	<0.5	<0.5	<0.5	<0.5	2.6
Cd	ppm	<0.5	<0.5	<0.5	<0.5	<0.5	<0.5	<0.5	<0.5	<0.5	<0.5	<0.5	<0.5	<0.5	<0.5
Co	ppm	55	53	7	6	7	47	7	51	6	99	54	55	46	597
Cu	ppm	60	98	10	23	4	79	15	6	9	51	6	203	794	6560
Li	ppm	50	30	30	30	30	40	30	40	30	<10	20	30	50	<10
Mo	ppm	1	<1	1	1	1	<1	1	<1	1	<1	<1	1	<1	<1
Ni	ppm	843	362	14	10	9	170	11	198	12	1040	248	156	474	>10000
Pb	ppm	3	23	8	7	5	6	6	4	6	<2	4	5	2	3
Sc	ppm	25	26	4	5	4	24	5	29	5	22	61	22	25	6
Zn	ppm	70	41	44	51	38	98	54	123	50	60	95	155	129	101
Cu	%														
Ni	%														2.090

Oxide	Unit	EN24VS 005	EN24VS 006	EN24VS 007	EN24VS 008	EN24VS 009	EN24VS 010	EN24VS 011	EN24VS 012	EN24VS 013	EN24VS 015	EN24VS 016	EN24VS 017	EN24VS 018	EN24VS 019
SiO_2	%	29.70	25.40	27.60	29.60	27.30	30.30	35.80	44.10	39.80	39.20	39.90	39.90	39.80	41.20
Al_2O_3	%	2.25	1.13	1.34	1.81	1.14	2.22	3.31	4.24	3.93	4.14	3.52	3.60	4.11	4.23
Fe_2O_3	%	23.30	23.80	25.80	22.90	26.40	21.80	16.45	8.37	11.50	11.90	12.80	12.95	12.85	12.15
CaO	%	0.74	0.66	0.89	1.20	0.87	1.16	1.29	1.96	2.40	2.61	2.51	2.49	2.41	2.15
MgO	%	26.90	25.20	27.70	28.70	27.90	28.30	32.00	32.20	33.90	33.50	33.30	32.90	33.20	31.50
Na_2O	%	0.07	0.09	0.16	0.16	0.09	0.08	0.08	0.07	0.12	0.27	0.21	0.23	0.12	0.12
K_2O	%	0.10	0.04	0.06	0.14	0.05	0.03	0.54	0.03	0.06	0.04	0.07	0.06	0.03	0.01
Cr_2O_3	%	0.541	0.591	0.553	0.267	0.452	0.215	0.449	0.639	0.645	0.628	0.625	0.607	0.639	0.628
TiO_2	%	0.09	0.07	0.07	0.05	0.06	0.07	0.24	0.15	0.15	0.12	0.20	0.21	0.16	0.17
MnO	%	0.13	0.11	0.13	0.13	0.13	0.13	0.14	0.07	0.15	0.16	0.17	0.17	0.18	0.14
P_2O_5	%	0.01	0.01	0.01	0.01	0.01	0.01	0.04	0.02	0.02	0.02	0.03	0.03	0.02	0.02
SrO	%	<0.01	<0.01	<0.01	<0.01	<0.01	<0.01	<0.01	<0.01	<0.01	<0.01	<0.01	<0.01	<0.01	<0.01
BaO	%	<0.01	<0.01	<0.01	<0.01	<0.01	<0.01	<0.01	<0.01	<0.01	<0.01	<0.01	<0.01	<0.01	<0.01
LOI	%	11.70	11.25	7.36	6.44	6.57	11.50	9.17	8.32	8.21	7.20	7.25	7.65	6.77	8.07
Total	%	95.53	88.35	91.67	91.41	90.97	95.82	99.51	100.17	100.89	99.79	100.59	100.80	100.29	100.39
C	%	0.10	0.05	0.05	0.06	0.07	0.07	0.07	0.04	0.04	0.04	0.06	0.05	0.07	0.10
S	%	8.26	11.00	11.15	9.96	11.50	8.46	3.03	0.41	0.08	0.03	0.03	0.05	0.12	0.18
Ba	ppm	19.3	10.6	17.3	35.7	20.1	3.8	25.9	2.6	7.6	5.5	10.3	8.2	3.0	3.1
Ce	ppm	2.3	1.3	1.6	1.6	1.1	2.5	9.4	2.5	3.5	2.8	4.8	5.2	3.2	2.6
Cr	ppm	4000	4260	3860	1895	3230	1560	3240	4690	4700	4650	4610	4490	4660	4570
Cs	ppm	0.42	<0.01	0.05	0.20	0.08	0.05	2.00	0.12	0.25	0.12	0.17	0.09	0.13	0.16
Dy	ppm	0.31	0.15	0.23	0.23	0.25	0.22	0.91	0.56	0.58	0.57	0.93	0.98	0.68	0.54
Er	ppm	0.17	0.14	0.13	0.15	0.15	0.19	0.67	0.33	0.43	0.29	0.52	0.53	0.40	0.41
Eu	ppm	0.09	0.03	0.05	0.06	0.06	0.06	0.17	0.09	0.17	0.10	0.18	0.19	0.13	0.10
Ga	ppm	2.9	2.2	2.2	1.8	1.9	2.1	5.3	5.9	5.0	4.9	5.2	5.5	5.3	5.6
Gd	ppm	0.25	0.21	0.12	0.23	0.18	0.21	0.96	0.50	0.52	0.43	0.76	0.77	0.53	0.44
Ge	ppm	0.8	0.9	0.8	0.8	0.6	0.8	1.3	1.5	1.3	1.2	1.2	1.1	1.1	1.1
Hf	ppm	0.17	0.13	0.13	0.20	0.18	0.15	0.83	0.39	0.38	0.33	0.61	0.73	0.43	0.44
Ho	ppm	0.07	0.06	0.04	0.05	0.05	0.07	0.20	0.14	0.15	0.11	0.20	0.20	0.14	0.14
La	ppm	1.2	0.6	0.6	0.8	0.4	1.1	4.6	1.0	1.5	1.3	2.1	2.3	1.2	1.0
Lu	ppm	0.03	0.02	0.02	0.03	0.02	0.01	0.10	0.06	0.06	0.07	0.08	0.09	0.05	0.05
Nb	ppm	0.40	0.24	0.40	0.34	0.24	0.47	1.38	0.65	0.58	0.50	0.84	0.90	0.72	0.66
Nd	ppm	1.4	0.8	0.9	0.8	0.6	0.9	3.7	1.7	1.7	1.5	2.6	3.0	1.6	1.6
Pr	ppm	0.28	0.20	0.18	0.17	0.10	0.26	1.05	0.30	0.44	0.36	0.58	0.70	0.38	0.36
Rb	ppm	2.6	0.9	1.5	4.3	1.7	1.3	30.6	1.2	3.3	1.4	2.1	1.8	0.7	0.5
Sm	ppm	0.30	0.21	0.21	0.19	0.20	0.22	0.81	0.41	0.51	0.34	0.62	0.73	0.44	0.41
Sn	ppm	0.9	1.0	1.1	1.4	0.8	0.8	0.8	<0.5	<0.5	<0.5	<0.5	<0.5	<0.5	<0.5
Sr	ppm	8.4	6.6	10.0	11.2	11.8	9.2	8.5	9.4	16.4	21.7	17.9	17.3	13.6	15.0
Ta	ppm	<0.1	<0.1	<0.1	<0.1	<0.1	<0.1	0.1	<0.1	<0.1	<0.1	0.1	0.1	<0.1	<0.1
Tb	ppm	0.06	0.03	0.03	0.04	0.02	0.04	0.14	0.08	0.10	0.08	0.15	0.13	0.09	0.07
Th	ppm	0.16	0.12	0.11	0.14	0.13	0.11	0.89	0.30	0.36	0.29	0.46	0.56	0.39	0.38
Tm	ppm	0.02	0.01	0.02	0.03	0.02	0.02	0.09	0.05	0.05	0.05	0.07	0.08	0.06	0.06
U	ppm	0.06	<0.05	0.07	0.05	0.07	0.05	0.20	0.14	0.09	0.07	0.14	0.16	0.10	0.13
V	ppm	64	56	55	34	52	34	83	101	82	79	96	99	91	92
W	ppm	<0.5	<0.5	<0.5	<0.5	0.6	<0.5	<0.5	<0.5	<0.5	<0.5	<0.5	<0.5	<0.5	<0.5
Y	ppm	1.8	1.1	1.2	1.7	1.4	1.5	5.7	3.4	3.6	3.0	4.9	5.3	3.7	3.3
Yb	ppm	0.19	0.11	0.15	0.17	0.12	0.14	0.65	0.42	0.42	0.32	0.52	0.51	0.42	0.42
Zr	ppm	7	5	6	7	6	5	34	14	15	13	22	26	17	17
As	ppm	0.8	2.0	0.9	1.2	1.1	0.7	0.7	0.7	0.4	1.1	1.1	1.5	2.3	1.8
Bi	ppm	1.17	1.70	1.51	1.35	1.70	0.74	0.59	0.13	0.10	0.05	0.04	0.06	0.06	0.13
Hg	ppm	0.017	0.016	0.007	0.019	0.012	0.021	0.013	<0.005	<0.005	<0.005	<0.005	<0.005	<0.005	<0.005
In	ppm	0.089	0.135	0.080	0.230	0.077	0.083	0.083	0.023	0.007	0.006	0.007	0.008	0.007	0.008
Re	ppm	0.019	0.022	0.027	0.021	0.023	0.020	0.003	0.001	<0.001	<0.001	0.001	0.001	0.002	0.001
Sb	ppm	<0.05	<0.05	<0.05	<0.05	<0.05	<0.05	<0.05	0.05	0.17	<0.05	<0.05	<0.05	0.12	0.12
Se	ppm	18.5	23.4	24.6	22.7	25.6	15.7	7.0	0.8	<0.2	0.2	0.2	0.3	0.3	0.3
Te	ppm	2.92	3.05	2.81	3.03	3.34	1.75	1.51	0.24	0.06	0.03	0.04	0.08	0.07	0.06
Tl	ppm	0.16	0.10	0.14	0.29	0.09	0.02	0.31	0.03	0.04	<0.02	0.02	<0.02	0.02	0.05
Ag	ppm	3.0	5.8	2.5	7.9	3.2	3.2	1.4	<0.5	<0.5	<0.5	<0.5	<0.5	<0.5	<0.5
Cd	ppm	0.7	2.4	0.9	1.9	1.1	0.8	0.5	<0.5	<0.5	<0.5	<0.5	<0.5	<0.5	<0.5
Co	ppm	432	698	681	526	719	472	200	75	126	130	128	128	108	112
Cu	ppm	3600	>10000	5490	>10000	8270	9710	3730	147	32	21	34	28	35	49
Li	ppm	<10	<10	<10	10	10	<10	10	<10	<10	<10	<10	<10	<10	<10
Mo	ppm	<1	<1	<1	<1	1	<1	<1	<1	<1	1	1	<1	<1	<1
Ni	ppm	>10000	>10000	>10000	>10000	>10000	>10000	5950	1730	1855	1675	1660	1725	1725	1590
Pb	ppm	4	11	11	6	7	3	3	<2	2	2	2	<2	<2	<2
Sc	ppm	7	5	5	6	5	7	8	15	12	11	13	13	13	14
Zn	ppm	75	130	101	83	74	70	79	60	77	91	89	89	77	77
Cu	%		1.865		2.350										
Ni	%	1.525	2.230	2.290	1.645	2.370	1.450								

Oxide	Unit	EN24VS 021	EN24VS 022	EN24VS 023	EN24VS 024	EN24VS 025	EN24VS 028	EN24VS 029	EN24VS 030	EN24VS 031	EN24VS 032	EN24VS 033	EN24VS 035	EN24VS 036	EN24VS 037
SiO_2	%	42.00	39.20	51.00	47.10	47.00	48.00	49.50	47.90	40.20	39.00	31.10	43.00	39.00	36.10
Al_2O_3	%	4.54	4.36	5.63	5.28	7.97	6.97	4.29	18.50	5.92	3.64	2.95	6.93	3.70	4.20
Fe_2O_3	%	11.00	10.40	10.25	12.60	11.15	10.40	9.67	11.95	17.45	11.00	22.70	11.85	11.35	14.90
CaO	%	2.86	3.03	2.23	1.08	6.25	8.53	5.89	8.96	4.23	2.33	1.73	5.19	2.16	1.88
MgO	%	29.30	31.70	23.60	25.40	20.30	21.40	23.90	5.40	23.20	34.20	26.10	25.90	33.20	30.80
Na_2O	%	0.05	0.07	0.23	0.04	0.77	0.55	0.14	2.60	0.25	0.21	0.16	0.17	0.17	0.06
K_2O	%	0.04	0.01	3.42	0.02	0.74	0.09	0.01	1.32	0.03	0.05	0.09	0.04	0.02	0.03
Cr_2O_3	%	0.614	0.599	0.424	0.478	0.319	0.353	0.544	0.003	0.459	0.702	0.328	0.552	0.637	0.513
TiO_2	%	0.19	0.19	0.23	0.22	0.29	0.27	0.14	0.90	0.18	0.14	0.07	0.30	0.16	0.20
MnO	%	0.12	0.14	0.10	0.08	0.16	0.21	0.14	0.13	0.11	0.12	0.15	0.19	0.11	0.11
P_2O_5	%	0.02	0.03	0.02	0.03	0.03	0.03	0.03	0.16	0.02	0.02	0.02	0.04	0.02	0.03
SrO	%	0.02	0.01	<0.01	<0.01	<0.01	0.01	<0.01	0.08	<0.01	<0.01	<0.01	<0.01	0.01	0.01
BaO	%	<0.01	<0.01	0.03	<0.01	0.01	<0.01	<0.01	0.04	<0.01	<0.01	<0.01	<0.01	<0.01	<0.01
LOI	%	8.16	9.46	3.28	6.01	4.14	3.98	4.78	2.02	6.23	8.97	10.15	6.02	9.56	9.74
Total	%	98.91	99.20	100.44	98.34	99.13	100.79	99.03	99.96	98.28	100.38	95.55	100.18	100.10	98.57
C	%	0.31	0.47	0.04	0.04	0.04	0.05	0.05	0.09	0.03	0.10	0.04	0.03	0.05	0.05
S	%	0.34	0.21	0.58	0.30	0.43	0.09	0.81	0.23	4.58	0.04	7.77	0.44	0.04	2.40
Ba	ppm	2.7	2.9	285.0	2.2	106.0	12.5	1.4	366.0	3.7	10.7	21.8	5.6	4.7	4.5
Ce	ppm	3.1	2.8	1.6	1.2	6.4	7.1	2.9	28.7	2.4	3.1	4.0	5.4	3.5	5.8
Cr	ppm	4270	4310	2960	3500	2340	2540	3950	25	3330	5080	2410	4080	4520	3700
Cs	ppm	0.15	0.11	6.55	0.08	1.14	0.09	0.06	1.84	0.04	0.04	0.40	0.04	0.21	0.22
Dy	ppm	0.55	0.75	0.42	0.26	1.32	1.12	0.74	2.50	0.69	0.54	0.41	1.48	0.66	0.80
Er	ppm	0.36	0.46	0.31	0.22	0.81	0.71	0.42	1.32	0.46	0.36	0.33	0.92	0.35	0.55
Eu	ppm	0.10	0.08	0.11	0.03	0.29	0.30	0.23	0.98	0.12	0.13	0.10	0.20	0.14	0.20
Ga	ppm	5.5	5.6	7.7	6.7	9.3	8.9	7.1	23.6	6.9	4.8	3.3	8.7	4.3	4.8
Gd	ppm	0.55	0.53	0.39	0.29	1.09	1.03	0.94	2.94	0.54	0.52	0.30	1.21	0.61	0.71
Ge	ppm	1.2	1.2	1.5	1.4	1.5	1.6	1.7	1.2	1.3	1.3	0.9	1.4	1.1	0.9
Hf	ppm	0.58	0.51	0.51	0.58	0.87	0.76	0.38	1.39	0.42	0.35	0.31	0.75	0.46	0.65
Ho	ppm	0.14	0.15	0.10	0.06	0.30	0.26	0.15	0.50	0.17	0.13	0.08	0.28	0.13	0.18
La	ppm	1.4	1.1	0.6	0.6	3.0	3.3	1.3	13.2	1.0	1.4	1.7	2.3	1.7	2.6
Lu	ppm	0.08	0.07	0.07	0.04	0.14	0.12	0.08	0.15	0.07	0.06	0.05	0.14	0.06	0.07
Nb	ppm	0.70	0.64	0.91	0.82	0.94	1.04	0.43	3.06	0.60	0.55	0.52	1.08	0.71	0.90
Nd	ppm	1.7	1.7	1.1	0.8	3.2	4.0	2.7	16.8	1.5	1.7	1.4	3.4	1.8	2.9
Pr	ppm	0.44	0.33	0.23	0.17	0.77	0.84	0.45	3.87	0.30	0.38	0.42	0.71	0.40	0.73
Rb	ppm	2.4	0.5	111.0	0.5	21.1	1.3	0.2	50.4	0.6	1.5	2.7	0.4	0.8	1.0
Sm	ppm	0.39	0.42	0.29	0.21	1.17	0.85	0.86	3.37	0.40	0.41	0.25	0.97	0.39	0.96
Sn	ppm	<0.5	<0.5	<0.5	<0.5	<0.5	<0.5	<0.5	0.9	0.6	<0.5	1.5	<0.5	<0.5	0.8
Sr	ppm	123.0	39.1	15.9	84.7	22.1	15.5	6.7	732.0	21.8	11.8	15.4	10.9	16.2	13.4
Ta	ppm	0.1	0.1	0.1	0.1	0.1	0.1	<0.1	0.2	<0.1	<0.1	<0.1	0.1	<0.1	0.1
Tb	ppm	0.07	0.10	0.05	0.05	0.19	0.16	0.11	0.42	0.10	0.09	0.05	0.21	0.08	0.11
Th	ppm	0.43	0.37	0.39	0.50	0.76	0.89	0.26	2.39	0.34	0.34	0.22	0.59	0.37	0.60
Tm	ppm	0.06	0.07	0.06	0.03	0.13	0.11	0.07	0.16	0.06	0.06	0.04	0.14	0.06	0.08
U	ppm	0.12	0.12	0.11	0.15	0.19	0.26	0.07	0.44	0.12	0.09	0.08	0.20	0.09	0.14
V	ppm	91	92	127	124	156	138	85	221	111	83	49	137	73	75
W	ppm	<0.5	<0.5	<0.5	<0.5	<0.5	1.1	<0.5	<0.5	<0.5	<0.5	<0.5	<0.5	<0.5	<0.5
Y	ppm	3.1	3.5	2.8	1.7	7.3	6.7	4.1	12.5	4.0	3.5	3.0	7.9	3.7	5.0
Yb	ppm	0.45	0.44	0.33	0.21	0.78	0.67	0.44	1.09	0.42	0.29	0.27	0.70	0.36	0.66
Zr	ppm	20	17	19	23	29	29	13	39	15	14	12	33	15	22
As	ppm	2.5	2.3	0.6	0.5	0.7	1.7	5.8	0.8	1.4	0.8	0.8	1.2	0.7	0.6
Bi	ppm	0.14	0.11	0.05	0.01	0.03	0.02	0.05	0.02	0.72	0.04	1.33	0.30	0.07	0.79
Hg	ppm	<0.005	<0.005	<0.005	<0.005	<0.005	<0.005	<0.005	<0.005	0.006	<0.005	0.016	<0.005	<0.005	<0.005
In	ppm	0.010	0.009	0.005	<0.005	0.006	<0.005	<0.005	0.015	0.027	0.008	0.328	0.020	0.008	0.069
Re	ppm	0.001	0.001	<0.001	<0.001	0.001	0.002	<0.001	0.001	0.014	0.001	0.012	0.003	<0.001	0.003
Sb	ppm	<0.05	0.10	<0.05	<0.05	<0.05	<0.05	0.09	<0.05	0.14	<0.05	<0.05	0.06	<0.05	0.06
Se	ppm	<0.2	<0.2	0.2	<0.2	0.9	<0.2	0.9	0.2	9.9	<0.2	16.6	1.2	<0.2	6.8
Te	ppm	0.07	0.03	0.01	0.05	0.02	0.03	0.09	0.01	1.92	0.02	1.88	0.20	0.02	1.80
Tl	ppm	0.06	0.02	0.74	<0.02	0.13	<0.02	0.14	0.23	0.08	0.02	0.34	0.04	<0.02	0.06
Ag	ppm	<0.5	<0.5	<0.5	<0.5	<0.5	<0.5	<0.5	<0.5	0.9	<0.5	7.0	<0.5	<0.5	1.0
Cd	ppm	<0.5	<0.5	<0.5	<0.5	<0.5	<0.5	<0.5	<0.5	<0.5	<0.5	2.9	<0.5	<0.5	<0.5
Co	ppm	119	113	75	78	110	76	106	37	267	120	344	120	126	191
Cu	ppm	82	44	5	3	257	59	234	59	2090	30	>10000	427	18	2430
Li	ppm	<10	<10	60	20	30	20	10	50	<10	<10	10	<10	<10	10
Mo	ppm	<1	<1	<1	<1	<1	<1	1	3	2	1	2	2	1	2
Ni	ppm	1665	1640	860	1195	756	816	1365	23	8310	1790	>10000	2220	1605	5830
Pb	ppm	<2	<2	2	<2	<2	<2	2	5	3	<2	10	<2	<2	3
Sc	ppm	14	14	25	20	28	25	12	22	18	11	8	19	11	9
Zn	ppm	76	88	77	79	69	102	127	113	50	67	135	108	65	89
Cu	%											2.360			
Ni	%											1.190			

Oxide	Unit	EN24VS 039	EN24VS 040
SiO_2	%	48.90	30.30
Al_2O_3	%	11.80	2.39
Fe_2O_3	%	11.15	23.00
CaO	%	8.54	1.30
MgO	%	12.20	27.20
Na_2O	%	2.95	0.08
K_2O	%	1.08	<0.01
Cr_2O_3	%	0.171	0.691
TiO_2	%	0.56	0.10
MnO	%	0.13	0.13
P_2O_5	%	0.05	0.02
SrO	%	0.02	<0.01
BaO	%	0.02	<0.01
LOI	%	1.22	10.75
Total	%	98.79	95.96
C	%	0.04	0.07
S	%	0.04	8.17
Ba	ppm	207.0	2.3
Ce	ppm	8.4	2.2
Cr	ppm	1240	4950
Cs	ppm	1.70	0.05
Dy	ppm	2.28	0.49
Er	ppm	1.53	0.28
Eu	ppm	0.58	0.11
Ga	ppm	14.5	3.0
Gd	ppm	1.87	0.39
Ge	ppm	1.9	0.6
Hf	ppm	1.38	0.39
Ho	ppm	0.48	0.09
La	ppm	3.2	1.0
Lu	ppm	0.27	0.05
Nb	ppm	1.97	0.30
Nd	ppm	5.4	1.2
Pr	ppm	1.06	0.28
Rb	ppm	29.9	0.3
Sm	ppm	2.03	0.34
Sn	ppm	1.9	<0.5
Sr	ppm	146.0	7.1
Ta	ppm	0.1	<0.1
Tb	ppm	0.38	0.09
Th	ppm	0.72	0.27
Tm	ppm	0.21	0.04
U	ppm	0.23	<0.05
V	ppm	212	65
W	ppm	<0.5	<0.5
Y	ppm	13.4	2.6
Yb	ppm	1.59	0.28
Zr	ppm	48	14
As	ppm	0.3	1.5
Bi	ppm	0.03	1.15
Hg	ppm	<0.005	0.007
In	ppm	0.011	0.059
Re	ppm	0.001	0.034
Sb	ppm	<0.05	<0.05
Se	ppm	<0.2	12.7
Te	ppm	0.03	2.01
Tl	ppm	0.26	0.04
Ag	ppm	<0.5	2.1
Cd	ppm	<0.5	<0.5
Co	ppm	49	540
Cu	ppm	92	3130
Li	ppm	40	<10
Mo	ppm	2	2
Ni	ppm	445	>10000
Pb	ppm	<2	3
Sc	ppm	32	8
Zn	ppm	50	64
Cu	%		
Ni	%		1.685

Appendix D: EPMA Mineral Chemistry

Appendix D1: Olivine Western University

Sample #EN23VS041

Oxide wt%	ol5_5	ol6_1	ol6_2	ol6_3	ol6_4	ol6_5	ol7_1	ol7_2	ol7_3	ol7_4	ol7_5	ol8_1
SiO_2	38.58	39.31	38.63	38.90	39.21	38.84	38.48	39.01	39.34	39.33	38.77	39.00
TiO_2	0.00	0.01	LOD	LOD	0.01	LOD	LOD	0.00	LOD	LOD	LOD	0.01
Cr_2O_3	0.01	0.01	LOD	0.01	0.00	0.00	0.15	0.00	LOD	0.01	LOD	LOD
FeO	18.17	14.18	17.88	15.98	16.36	16.83	18.09	16.93	15.68	15.49	17.79	15.86
MnO	0.35	0.22	0.39	0.30	0.26	0.31	0.38	0.33	0.27	0.27	0.34	0.27
MgO	42.37	45.94	42.65	44.23	44.27	43.33	42.60	43.43	44.88	44.80	42.53	44.60
NiO	0.26	0.36	0.27	0.30	0.29	0.30	0.31	0.32	0.26	0.29	0.27	0.32
CaO	LOD	LOD	LOD	LOD	LOD	LOD	LOD	LOD	0.00	LOD	LOD	0.08
Total	99.74	100.02	99.78	99.70	100.39	99.59	99.99	100.02	100.41	100.16	99.69	100.12
Cations per formula unit												
Si	0.99	0.99	0.99	0.99	0.99	0.99	0.98	0.99	0.99	0.99	0.99	0.99
Ti	0.00	0.00	0.00	0.00	0.00	0.00	0.00	0.00	0.00	0.00	0.00	0.00
Cr	0.00	0.00	0.00	0.00	0.00	0.00	0.00	0.00	0.00	0.00	0.00	0.00
Fe^{2+}	0.39	0.30	0.38	0.34	0.35	0.36	0.39	0.36	0.33	0.33	0.38	0.34
Mn	0.01	0.00	0.01	0.01	0.01	0.01	0.01	0.01	0.01	0.01	0.01	0.01
Mg	1.62	1.72	1.63	1.67	1.66	1.65	1.62	1.64	1.68	1.68	1.62	1.68
Ni	0.01	0.01	0.01	0.01	0.01	0.01	0.01	0.01	0.01	0.01	0.01	0.01
Ca	0.00	0.00	0.00	0.00	0.00	0.00	0.00	0.00	0.00	0.00	0.00	0.00
Total	3.01	3.01	3.01	3.01	3.01	3.01	3.01	3.01	3.01	3.01	3.01	3.01
Fo	80.60	85.24	80.96	83.15	82.83	82.10	80.76	82.06	83.62	83.75	80.99	83.37

Sample #EN23VS041

Oxide wt%	ol8_2	ol8_3	ol8_4	ol8_5	ol9_1	ol9_2	ol9_3	ol9_4	ol9_5	ol10_1	ol10_2	ol10_3
SiO_2	38.59	39.33	38.99	38.94	39.32	39.50	39.09	39.45	39.67	38.51	38.59	39.09
TiO_2	LOD	0.02	LOD	LOD	LOD	LOD	LOD	0.01	LOD	LOD	LOD	LOD
Cr_2O_3	LOD	LOD	0.03	0.01	0.02	LOD	0.02	0.02	0.02	LOD	0.01	0.01
FeO	17.91	13.79	16.04	16.89	14.78	13.74	14.93	13.48	13.55	18.10	17.59	15.66
MnO	0.40	0.25	0.26	0.29	0.21	0.18	0.25	0.18	0.24	0.39	0.37	0.28
MgO	42.79	46.27	44.23	43.39	45.59	46.09	44.90	46.32	46.14	42.50	42.59	44.38
NiO	0.29	0.31	0.29	0.29	0.27	0.30	0.30	0.33	0.32	0.26	0.30	0.33
CaO	LOD	0.00	0.01	LOD	LOD	LOD	0.00	0.00	0.00	LOD	LOD	0.12
Total	99.94	99.96	99.82	99.79	100.16	99.78	99.50	99.80	99.91	99.73	99.43	99.87
Cations per formula unit												
Si	0.99	0.99	0.99	0.99	0.99	0.99	0.99	0.99	0.99	0.99	0.99	0.99
Ti	0.00	0.00	0.00	0.00	0.00	0.00	0.00	0.00	0.00	0.00	0.00	0.00
Cr	0.00	0.00	0.00	0.00	0.00	0.00	0.00	0.00	0.00	0.00	0.00	0.00
Fe^{2+}	0.38	0.29	0.34	0.36	0.31	0.29	0.32	0.28	0.28	0.39	0.38	0.33
Mn	0.01	0.01	0.01	0.01	0.00	0.00	0.01	0.00	0.00	0.01	0.01	0.01
Mg	1.63	1.73	1.67	1.65	1.71	1.72	1.69	1.73	1.72	1.62	1.63	1.67
Ni	0.01	0.01	0.01	0.01	0.01	0.01	0.01	0.01	0.01	0.01	0.01	0.01
Ca	0.00	0.00	0.00	0.00	0.00	0.00	0.00	0.00	0.00	0.00	0.00	0.00
Total	3.01	3.01	3.01	3.01	3.01	3.01	3.01	3.01	3.01	3.01	3.01	3.01
Fo	80.99	85.68	83.09	82.08	84.61	85.67	84.28	85.97	85.85	80.71	81.19	83.47

Sample #EN23VS041			**Sample #EN23VS042**								
Oxide wt%	ol10_4	ol10_5	ol1_1	ol1_2	ol1_3	ol1_4	ol1_5	ol2_1	ol2_2	ol2_3	ol2_4
SiO_2	38.94	39.09	39.80	39.63	39.72	40.02	40.31	39.73	39.66	39.80	39.83
TiO_2	0.01	LOD	0.01	LOD	0.00	0.00	LOD	LOD	0.00	LOD	LOD
Cr_2O_3	0.00	0.03	0.01	LOD	0.02	0.01	0.02	0.03	0.00	0.01	0.03
FeO	17.46	15.41	12.72	12.39	12.54	12.10	12.33	12.83	11.89	11.81	11.77
MnO	0.35	0.23	0.20	0.24	0.24	0.21	0.24	0.23	0.16	0.19	0.19
MgO	42.93	44.59	46.82	47.09	46.87	47.37	47.59	46.69	47.51	47.51	47.49
NiO	0.25	0.30	0.35	0.31	0.34	0.35	0.33	0.35	0.35	0.35	0.30
CaO	LOD	LOD	0.01	0.02	0.00	0.01	0.01	0.01	0.01	0.02	0.03
Total	99.94	99.62	99.92	99.66	99.74	100.06	100.82	99.86	99.57	99.69	99.64
Cations per formula unit											
Si	0.99	0.99	0.99	0.99	0.99	0.99	0.99	0.99	0.99	0.99	0.99
Ti	0.00	0.00	0.00	0.00	0.00	0.00	0.00	0.00	0.00	0.00	0.00
Cr	0.00	0.00	0.00	0.00	0.00	0.00	0.00	0.00	0.00	0.00	0.00
Fe^{2+}	0.37	0.33	0.27	0.26	0.26	0.25	0.25	0.27	0.25	0.25	0.24
Mn	0.01	0.00	0.00	0.01	0.01	0.00	0.01	0.00	0.00	0.00	0.00
Mg	1.63	1.68	1.74	1.75	1.74	1.75	1.75	1.74	1.76	1.76	1.76
Ni	0.01	0.01	0.01	0.01	0.01	0.01	0.01	0.01	0.01	0.01	0.01
Ca	0.00	0.00	0.00	0.00	0.00	0.00	0.00	0.00	0.00	0.00	0.00
Total	3.01	3.01	3.01	3.01	3.01	3.01	3.01	3.01	3.01	3.01	3.01
Fo	81.42	83.76	86.78	87.14	86.95	87.47	87.31	86.64	87.69	87.76	87.79

Sample #EN23VS042

Oxide wt%	ol3_1	ol3_2	ol3_3	ol3_4	ol3_5	ol4_1	ol4_2	ol4_3	ol4_4	ol4_5	ol5_1	ol5_2
SiO_2	39.83	39.90	39.88	39.82	39.72	39.67	39.60	39.74	39.66	39.01	39.63	39.88
TiO_2	0.00	LOD	LOD	LOD	LOD	0.00	LOD	0.01	LOD	LOD	LOD	LOD
Cr_2O_3	0.02	0.01	0.00	0.00	0.01	0.00	0.03	0.07	0.00	0.09	0.03	0.11
FeO	11.75	12.63	11.61	11.51	11.66	11.70	12.30	12.38	11.85	14.42	11.80	12.27
MnO	0.23	0.20	0.20	0.20	0.16	0.20	0.16	0.15	0.21	0.23	0.16	0.17
MgO	47.83	47.19	47.92	47.74	47.46	47.33	47.35	47.36	47.88	44.96	47.64	47.66
NiO	0.32	0.36	0.34	0.36	0.32	0.40	0.37	0.31	0.34	0.34	0.33	0.39
CaO	LOD	0.00	0.00	0.06	0.10	0.01	0.00	0.01	0.01	0.49	0.02	0.01
Total	99.99	100.28	99.93	99.67	99.43	99.31	99.79	100.03	99.92	99.54	99.58	100.44
Cations per formula unit												
Si	0.99	0.99	0.99	0.99	0.99	0.99	0.99	0.99	0.99	0.99	0.99	0.99
Ti	0.00	0.00	0.00	0.00	0.00	0.00	0.00	0.00	0.00	0.00	0.00	0.00
Cr	0.00	0.00	0.00	0.00	0.00	0.00	0.00	0.00	0.00	0.00	0.00	0.00
Fe^{2+}	0.24	0.26	0.24	0.24	0.24	0.24	0.26	0.26	0.25	0.30	0.25	0.25
Mn	0.00	0.00	0.00	0.00	0.00	0.00	0.00	0.00	0.00	0.00	0.00	0.00
Mg	1.77	1.75	1.77	1.77	1.76	1.76	1.76	1.75	1.77	1.69	1.77	1.76
Ni	0.01	0.01	0.01	0.01	0.01	0.01	0.01	0.01	0.01	0.01	0.01	0.01
Ca	0.00	0.00	0.00	0.00	0.00	0.00	0.00	0.00	0.00	0.01	0.00	0.00
Total	3.01	3.01	3.01	3.01	3.01	3.01	3.01	3.01	3.01	3.01	3.01	3.01
Fo	87.89	86.95	88.04	88.09	87.88	87.82	87.28	87.21	87.81	84.75	87.80	87.38

Sample #EN23VS042

Oxide wt%	ol5_3	ol5_4	ol5_5	ol6_1	ol6_2	ol6_3	ol6_4	ol6_5	ol7_1	ol7_2	ol7_3	ol7_4
SiO_2	39.95	39.92	39.13	39.46	39.55	39.20	39.74	39.53	39.83	39.80	39.92	40.00
TiO_2	0.02	LOD	LOD	0.02	LOD	LOD	0.00	LOD	0.00	LOD	0.00	0.00
Cr_2O_3	0.03	0.02	0.03	0.03	0.00	0.05	0.01	0.02	0.00	LOD	0.14	0.02
FeO	11.37	11.36	13.95	13.61	12.25	14.99	11.74	13.04	11.75	11.81	11.64	11.94
MnO	0.20	0.17	0.26	0.21	0.21	0.25	0.18	0.28	0.20	0.17	0.19	0.17
MgO	47.74	47.98	45.14	45.94	47.37	45.30	47.68	46.27	47.52	47.80	45.92	47.66
NiO	0.34	0.34	0.35	0.31	0.28	0.31	0.37	0.37	0.37	0.36	0.29	0.39
CaO	LOD	LOD	0.03	0.01	0.01	0.02	0.00	0.01	0.12	0.00	1.35	LOD
Total	99.64	99.77	98.89	99.59	99.68	100.11	99.72	99.51	99.80	99.94	99.45	100.18
Cations per formula unit												
Si	0.99	0.99	0.99	0.99	0.99	0.99	0.99	0.99	0.99	0.99	1.00	0.99
Ti	0.00	0.00	0.00	0.00	0.00	0.00	0.00	0.00	0.00	0.00	0.00	0.00
Cr	0.00	0.00	0.00	0.00	0.00	0.00	0.00	0.00	0.00	0.00	0.00	0.00
Fe^{2+}	0.24	0.24	0.30	0.29	0.26	0.32	0.24	0.27	0.24	0.25	0.24	0.25
Mn	0.00	0.00	0.01	0.00	0.00	0.01	0.00	0.01	0.00	0.00	0.00	0.00
Mg	1.77	1.77	1.71	1.72	1.76	1.70	1.77	1.73	1.76	1.77	1.71	1.76
Ni	0.01	0.01	0.01	0.01	0.01	0.01	0.01	0.01	0.01	0.01	0.01	0.01
Ca	0.00	0.00	0.00	0.00	0.00	0.00	0.00	0.00	0.00	0.00	0.04	0.00
Total	3.01	3.01	3.01	3.01	3.01	3.01	3.01	3.01	3.01	3.01	3.00	3.01
Fo	88.22	88.27	85.23	85.75	87.33	84.35	87.86	86.35	87.82	87.82	87.55	87.68

Sample #EN23VS042

Oxide wt%	ol7_5	ol8_1	ol8_2	ol8_3	ol8_4	ol8_5	ol9_1	ol9_2	ol9_3	ol9_4	ol9_5	ol10_1
SiO_2	39.65	39.82	39.67	39.60	39.64	39.88	39.39	39.37	39.27	39.35	39.05	39.46
TiO_2	LOD	0.00	LOD	LOD	LOD	LOD	0.02	LOD	0.04	0.02	0.01	0.01
Cr_2O_3	0.03	0.04	0.02	0.01	0.03	LOD	0.01	0.03	0.01	0.03	0.02	0.02
FeO	11.86	12.06	12.42	13.62	12.51	12.26	13.85	13.25	14.26	13.79	15.07	12.94
MnO	0.17	0.18	0.21	0.23	0.19	0.20	0.25	0.22	0.26	0.21	0.27	0.16
MgO	47.70	47.74	47.11	46.31	47.23	47.42	45.54	46.35	45.24	46.06	45.10	46.87
NiO	0.33	0.37	0.31	0.33	0.31	0.38	0.33	0.37	0.31	0.27	0.32	0.34
CaO	0.01	0.01	LOD	0.02	0.01	0.01	0.03	0.01	0.02	0.00	0.00	0.00
Total	99.70	100.22	99.73	100.09	99.91	100.12	99.41	99.58	99.41	99.73	99.84	99.79
Cations per formula unit												
Si	0.99	0.99	0.99	0.99	0.99	0.99	0.99	0.99	0.99	0.99	0.99	0.99
Ti	0.00	0.00	0.00	0.00	0.00	0.00	0.00	0.00	0.00	0.00	0.00	0.00
Cr	0.00	0.00	0.00	0.00	0.00	0.00	0.00	0.00	0.00	0.00	0.00	0.00
Fe^{2+}	0.25	0.25	0.26	0.28	0.26	0.25	0.29	0.28	0.30	0.29	0.32	0.27
Mn	0.00	0.00	0.00	0.00	0.00	0.00	0.01	0.00	0.01	0.00	0.01	0.00
Mg	1.77	1.76	1.75	1.72	1.75	1.75	1.71	1.73	1.70	1.72	1.70	1.75
Ni	0.01	0.01	0.01	0.01	0.01	0.01	0.01	0.01	0.01	0.01	0.01	0.01
Ca	0.00	0.00	0.00	0.00	0.00	0.00	0.00	0.00	0.00	0.00	0.00	0.00
Total	3.01	3.01	3.01	3.01	3.01	3.01	3.01	3.01	3.01	3.01	3.01	3.01
Fo	87.76	87.59	87.12	85.84	87.06	87.34	85.42	86.18	84.97	85.62	84.22	86.59

Sample #EN23VS042					**Sample #EN23VS043**					
Oxide wt%	ol10_2	ol10_3	ol10_4	ol10_5	ol1_1	ol1_2	ol1_3	ol1_4	ol1_5	ol2_1
SiO_2	39.58	39.60	39.72	39.21	39.21	39.75	39.51	39.03	39.43	39.88
TiO_2	LOD	LOD	LOD	0.01	0.02	LOD	LOD	LOD	LOD	0.01
Cr_2O_3	0.01	0.01	0.01	0.02	LOD	0.02	0.02	0.04	0.03	0.04
FeO	13.01	12.60	13.05	13.86	12.96	11.86	12.10	13.83	12.09	11.37
MnO	0.21	0.20	0.18	0.24	0.17	0.19	0.18	0.23	0.17	0.17
MgO	46.60	46.92	47.01	45.76	46.53	46.87	47.42	45.71	47.25	48.22
NiO	0.34	0.40	0.35	0.34	0.36	0.36	0.38	0.35	0.38	0.37
CaO	0.00	0.00	0.00	0.01	0.05	0.24	0.04	0.01	0.08	0.00
Total	99.76	99.72	100.32	99.46	99.29	99.29	99.66	99.19	99.42	100.06
Cations per formula unit										
Si	0.99	0.99	0.99	0.99	0.99	0.99	0.99	0.99	0.99	0.99
Ti	0.00	0.00	0.00	0.00	0.00	0.00	0.00	0.00	0.00	0.00
Cr	0.00	0.00	0.00	0.00	0.00	0.00	0.00	0.00	0.00	0.00
Fe^{2+}	0.27	0.26	0.27	0.29	0.27	0.25	0.25	0.29	0.25	0.24
Mn	0.00	0.00	0.00	0.01	0.00	0.00	0.00	0.00	0.00	0.00
Mg	1.74	1.75	1.74	1.72	1.74	1.75	1.76	1.72	1.76	1.78
Ni	0.01	0.01	0.01	0.01	0.01	0.01	0.01	0.01	0.01	0.01
Ca	0.00	0.00	0.00	0.00	0.00	0.01	0.00	0.00	0.00	0.00
Total	3.01	3.01	3.01	3.01	3.01	3.01	3.01	3.01	3.01	3.01
Fo	86.46	86.90	86.53	85.48	86.49	87.57	87.48	85.49	87.45	88.31

Sample #EN23VS043

Oxide wt%	ol2_2	ol2_3	ol2_4	ol2_5	ol3_1	ol3_2	ol3_3	ol3_4	ol4_1	ol4_2	ol4_3	ol4_4
SiO_2	39.87	39.41	39.79	39.61	39.33	39.72	39.43	39.18	39.62	39.97	39.90	39.88
TiO_2	LOD	0.00	LOD	LOD	0.01	LOD	0.01	0.02	LOD	0.00	0.00	LOD
Cr_2O_3	0.03	0.04	0.04	0.04	0.11	0.03	0.16	0.02	0.02	0.09	0.00	0.02
FeO	11.51	11.67	11.43	11.94	12.12	11.62	11.95	12.24	11.39	11.37	11.49	11.27
MnO	0.18	0.19	0.17	0.19	0.17	0.18	0.27	0.21	0.18	0.19	0.18	0.17
MgO	48.31	47.50	48.11	47.53	47.67	47.68	47.23	46.73	47.85	47.34	48.08	47.90
NiO	0.34	0.30	0.33	0.31	0.34	0.38	0.34	0.33	0.33	0.38	0.37	0.37
CaO	0.03	0.03	LOD	0.00	LOD	0.01	0.18	0.01	0.01	0.36	0.00	0.00
Total	100.25	99.14	99.88	99.59	99.74	99.61	99.56	98.75	99.39	99.70	100.01	99.60
Cations per formula unit												
Si	0.99	0.99	0.99	0.99	0.98	0.99	0.98	0.99	0.99	0.99	0.99	0.99
Ti	0.00	0.00	0.00	0.00	0.00	0.00	0.00	0.00	0.00	0.00	0.00	0.00
Cr	0.00	0.00	0.00	0.00	0.00	0.00	0.00	0.00	0.00	0.00	0.00	0.00
Fe^{2+}	0.24	0.24	0.24	0.25	0.25	0.24	0.25	0.26	0.24	0.24	0.24	0.23
Mn	0.00	0.00	0.00	0.00	0.00	0.00	0.01	0.00	0.00	0.00	0.00	0.00
Mg	1.78	1.77	1.78	1.77	1.77	1.77	1.76	1.76	1.78	1.75	1.77	1.77
Ni	0.01	0.01	0.01	0.01	0.01	0.01	0.01	0.01	0.01	0.01	0.01	0.01
Ca	0.00	0.00	0.00	0.00	0.00	0.00	0.00	0.00	0.00	0.01	0.00	0.00
Total	3.01	3.01	3.01	3.01	3.02	3.01	3.01	3.01	3.01	3.01	3.01	3.01
Fo	88.21	87.89	88.24	87.65	87.51	87.97	87.57	87.19	88.22	88.13	88.18	88.35

Sample #EN23VS043

Oxide wt%	ol4_5	ol5_1	ol5_2	ol5_3	ol5_4	ol5_5	ol6_1	ol6_2	ol6_3	ol6_4	ol6_5	ol7_1
SiO_2	39.82	39.61	39.72	39.60	39.44	39.92	39.71	39.69	39.67	39.43	39.63	39.78
TiO_2	0.01	0.03	LOD	0.01	LOD	0.01	LOD	0.02	0.01	LOD	LOD	0.01
Cr_2O_3	0.02	0.01	0.02	0.04	0.03	0.01	0.03	0.03	0.03	0.01	LOD	0.03
FeO	11.73	12.03	12.02	12.10	12.29	12.25	11.54	11.28	11.54	11.00	11.57	11.51
MnO	0.18	0.19	0.20	0.22	0.22	0.20	0.20	0.15	0.19	0.17	0.20	0.17
MgO	47.80	47.28	47.35	46.69	47.24	47.24	48.00	47.63	47.65	47.75	47.80	47.46
NiO	0.35	0.37	0.30	0.31	0.35	0.36	0.34	0.38	0.37	0.33	0.30	0.30
CaO	LOD	0.00	LOD	0.15	0.01	0.00	0.08	0.03	0.03	0.00	0.00	0.08
Total	99.91	99.52	99.60	99.11	99.58	99.98	99.86	99.19	99.48	98.65	99.49	99.31
Cations per formula unit												
Si	0.99	0.99	0.99	0.99	0.99	0.99	0.99	0.99	0.99	0.99	0.99	0.99
Ti	0.00	0.00	0.00	0.00	0.00	0.00	0.00	0.00	0.00	0.00	0.00	0.00
Cr	0.00	0.00	0.00	0.00	0.00	0.00	0.00	0.00	0.00	0.00	0.00	0.00
Fe^{2+}	0.24	0.25	0.25	0.25	0.26	0.25	0.24	0.24	0.24	0.23	0.24	0.24
Mn	0.00	0.00	0.00	0.00	0.00	0.00	0.00	0.00	0.00	0.00	0.00	0.00
Mg	1.77	1.76	1.76	1.74	1.76	1.75	1.78	1.77	1.77	1.78	1.77	1.76
Ni	0.01	0.01	0.01	0.01	0.01	0.01	0.01	0.01	0.01	0.01	0.01	0.01
Ca	0.00	0.00	0.00	0.00	0.00	0.00	0.00	0.00	0.00	0.00	0.00	0.00
Total	3.01	3.01	3.01	3.01	3.01	3.01	3.01	3.01	3.01	3.01	3.01	3.01
Fo	87.90	87.51	87.54	87.31	87.26	87.30	88.12	88.28	88.04	88.56	88.04	88.02

Sample #EN23VS043

Oxide wt%	ol7_2	ol7_3	ol7_4	ol7_5	ol8_1	ol8_2	ol8_3	ol8_4	ol8_5	ol9_1	ol9_2	ol9_3
SiO_2	39.32	39.90	39.64	39.83	39.28	39.22	39.31	39.87	39.44	39.77	39.70	39.57
TiO_2	0.00	LOD	LOD	LOD	0.02	0.02	LOD	0.01	0.00	LOD	0.03	LOD
Cr_2O_3	0.04	0.02	0.02	0.05	0.10	0.00	0.01	0.02	0.00	0.03	0.12	0.02
FeO	13.39	11.41	11.44	11.38	12.80	13.49	14.12	13.26	12.69	11.32	11.09	11.55
MnO	0.20	0.22	0.18	0.18	0.18	0.18	0.21	0.24	0.17	0.16	0.18	0.17
MgO	45.77	48.10	47.65	47.89	46.18	45.50	44.99	46.18	46.15	47.41	47.55	47.66
NiO	0.33	0.33	0.34	0.33	0.34	0.34	0.38	0.38	0.30	0.37	0.34	0.31
CaO	0.01	0.00	0.02	0.05	0.04	0.01	LOD	0.08	LOD	0.00	0.04	0.01
Total	99.04	99.98	99.28	99.68	98.94	98.74	98.99	100.03	98.74	99.04	99.04	99.28
Cations per formula unit												
Si	0.99	0.99	0.99	0.99	0.99	0.99	1.00	0.99	0.99	0.99	0.99	0.99
Ti	0.00	0.00	0.00	0.00	0.00	0.00	0.00	0.00	0.00	0.00	0.00	0.00
Cr	0.00	0.00	0.00	0.00	0.00	0.00	0.00	0.00	0.00	0.00	0.00	0.00
Fe^{2+}	0.28	0.24	0.24	0.24	0.27	0.29	0.30	0.28	0.27	0.24	0.23	0.24
Mn	0.00	0.00	0.00	0.00	0.00	0.00	0.00	0.01	0.00	0.00	0.00	0.00
Mg	1.72	1.78	1.77	1.77	1.73	1.72	1.70	1.72	1.73	1.77	1.77	1.77
Ni	0.01	0.01	0.01	0.01	0.01	0.01	0.01	0.01	0.01	0.01	0.01	0.01
Ca	0.00	0.00	0.00	0.00	0.00	0.00	0.00	0.00	0.00	0.00	0.00	0.00
Total	3.01	3.01	3.01	3.01	3.01	3.01	3.00	3.00	3.01	3.01	3.01	3.01
Fo	85.90	88.25	88.13	88.24	86.54	85.74	85.03	86.13	86.64	88.19	88.43	88.03

Sample #EN23VS043			**Sample #EN23VS100**								
Oxide wt%	ol9_4	ol9_5	ol1_1	ol1_2	ol1_3	ol1_4	ol1_5	ol2_1	ol2_2	ol2_3	ol2_4
SiO_2	39.66	39.75	37.98	37.79	38.04	38.23	38.46	37.80	37.94	38.12	37.89
TiO_2	LOD	LOD	LOD	LOD	LOD	0.00	LOD	0.02	0.00	LOD	0.01
Cr_2O_3	0.02	0.02	LOD	LOD	0.07	0.01	0.02	0.01	0.01	0.01	LOD
FeO	11.63	11.33	21.49	21.24	21.35	20.12	18.90	20.97	21.36	20.95	21.45
MnO	0.23	0.17	0.38	0.43	0.36	0.36	0.34	0.34	0.40	0.34	0.39
MgO	47.77	47.35	39.31	39.28	39.64	40.14	41.43	39.21	39.24	39.72	39.81
NiO	0.30	0.35	0.28	0.19	0.27	0.26	0.25	0.25	0.22	0.28	0.23
CaO	LOD	0.05	LOD	LOD	LOD	LOD	LOD	LOD	LOD	LOD	LOD
Total	99.58	99.00	99.40	98.90	99.70	99.11	99.37	98.60	99.18	99.41	99.78
Cations per formula unit											
Si	0.99	0.99	0.99	0.99	0.99	1.00	0.99	0.99	0.99	0.99	0.99
Ti	0.00	0.00	0.00	0.00	0.00	0.00	0.00	0.00	0.00	0.00	0.00
Cr	0.00	0.00	0.00	0.00	0.00	0.00	0.00	0.00	0.00	0.00	0.00
Fe^{2+}	0.24	0.24	0.47	0.47	0.46	0.44	0.41	0.46	0.47	0.46	0.47
Mn	0.00	0.00	0.01	0.01	0.01	0.01	0.01	0.01	0.01	0.01	0.01
Mg	1.77	1.76	1.53	1.54	1.54	1.56	1.59	1.54	1.53	1.54	1.55
Ni	0.01	0.01	0.01	0.00	0.01	0.01	0.01	0.01	0.00	0.01	0.00
Ca	0.00	0.00	0.00	0.00	0.00	0.00	0.00	0.00	0.00	0.00	0.00
Total	3.01	3.01	3.01	3.01	3.01	3.00	3.01	3.01	3.01	3.01	3.01
Fo	87.99	88.17	76.53	76.72	76.79	78.05	79.62	76.93	76.60	77.16	76.79

Sample #EN23VS100

Oxide wt%	ol2_5	ol3_1	ol3_2	ol3_3	ol3_4	ol3_5	ol4_1	ol4_2	ol4_3	ol4_4	ol4_5	ol5_1
SiO_2	37.96	37.93	38.01	38.80	38.23	38.45	38.03	38.17	38.21	38.21	38.03	38.39
TiO_2	LOD	LOD	0.00	0.01	LOD	0.00	0.00	LOD	0.01	0.00	LOD	0.01
Cr_2O_3	0.01	0.06	0.03	0.02	0.01	0.02	LOD	0.01	LOD	0.01	0.01	LOD
FeO	20.83	21.50	20.38	17.76	20.55	20.19	21.32	21.07	21.14	21.08	21.36	20.58
MnO	0.33	0.37	0.37	0.25	0.29	0.31	0.44	0.32	0.35	0.37	0.34	0.37
MgO	39.81	39.41	39.91	42.09	40.16	40.26	39.39	39.50	39.65	39.45	39.33	39.86
NiO	0.31	0.24	0.25	0.29	0.27	0.31	0.14	0.32	0.25	0.28	0.20	0.32
CaO	LOD	LOD	LOD	0.09	LOD	LOD	LOD	LOD	LOD	LOD	LOD	LOD
Total	99.20	99.47	98.94	99.31	99.49	99.52	99.30	99.36	99.58	99.39	99.25	99.52
Cations per formula unit												
Si	0.99	0.99	0.99	1.00	0.99	1.00	0.99	1.00	0.99	1.00	0.99	1.00
Ti	0.00	0.00	0.00	0.00	0.00	0.00	0.00	0.00	0.00	0.00	0.00	0.00
Cr	0.00	0.00	0.00	0.00	0.00	0.00	0.00	0.00	0.00	0.00	0.00	0.00
Fe^{2+}	0.45	0.47	0.45	0.38	0.45	0.44	0.47	0.46	0.46	0.46	0.47	0.45
Mn	0.01	0.01	0.01	0.01	0.01	0.01	0.01	0.01	0.01	0.01	0.01	0.01
Mg	1.55	1.53	1.55	1.61	1.56	1.56	1.53	1.54	1.54	1.53	1.53	1.54
Ni	0.01	0.00	0.01	0.01	0.01	0.01	0.00	0.01	0.01	0.01	0.00	0.01
Ca	0.00	0.00	0.00	0.00	0.00	0.00	0.00	0.00	0.00	0.00	0.00	0.00
Total	3.01	3.01	3.01	3.00	3.01	3.00	3.01	3.00	3.01	3.00	3.01	3.00
Fo	77.31	76.57	77.73	80.86	77.70	78.04	76.71	76.97	76.98	76.94	76.65	77.54

Sample #EN23VS100

Oxide wt%	ol5_2	ol5_3	ol5_4	ol5_5	ol6_1	ol6_2	ol6_3	ol6_4	ol6_5	ol7_1	ol7_2	ol7_3
SiO_2	38.72	39.04	39.04	38.66	38.03	38.11	37.87	38.13	38.02	38.32	38.43	38.87
TiO_2	LOD	LOD	0.00	LOD	LOD	0.01	LOD	LOD	LOD	LOD	0.00	LOD
Cr_2O_3	0.01	0.00	0.00	0.00	0.02	LOD	0.02	0.01	LOD	0.02	0.00	0.01
FeO	17.92	16.61	15.99	19.05	21.11	21.24	20.80	20.96	20.89	19.63	19.44	17.92
MnO	0.31	0.23	0.25	0.35	0.37	0.39	0.39	0.42	0.38	0.33	0.40	0.25
MgO	42.21	43.50	44.00	41.48	39.28	39.34	39.15	39.41	39.42	40.44	40.63	42.03
NiO	0.32	0.32	0.31	0.31	0.21	0.16	0.22	0.23	0.26	0.32	0.26	0.31
CaO	LOD	LOD	LOD	LOD	LOD	LOD	0.04	LOD	LOD	LOD	LOD	LOD
Total	99.47	99.67	99.59	99.81	98.99	99.22	98.48	99.13	98.93	99.02	99.14	99.35
Cations per formula unit												
Si	0.99	0.99	0.99	0.99	1.00	1.00	1.00	1.00	1.00	1.00	1.00	1.00
Ti	0.00	0.00	0.00	0.00	0.00	0.00	0.00	0.00	0.00	0.00	0.00	0.00
Cr	0.00	0.00	0.00	0.00	0.00	0.00	0.00	0.00	0.00	0.00	0.00	0.00
Fe^{2+}	0.38	0.35	0.34	0.41	0.46	0.46	0.46	0.46	0.46	0.43	0.42	0.38
Mn	0.01	0.00	0.01	0.01	0.01	0.01	0.01	0.01	0.01	0.01	0.01	0.01
Mg	1.61	1.65	1.67	1.59	1.53	1.53	1.54	1.54	1.54	1.57	1.57	1.61
Ni	0.01	0.01	0.01	0.01	0.00	0.00	0.00	0.00	0.01	0.01	0.01	0.01
Ca	0.00	0.00	0.00	0.00	0.00	0.00	0.00	0.00	0.00	0.00	0.00	0.00
Total	3.01	3.01	3.01	3.01	3.00	3.00	3.00	3.00	3.00	3.00	3.00	3.00
Fo	80.77	82.36	83.07	79.51	76.83	76.75	77.04	77.02	77.09	78.60	78.84	80.70

Sample #EN23VS100

Oxide wt%	ol7_4	ol7_5	ol8_1	ol8_2	ol8_3	ol8_4	ol8_5	ol9_1	ol9_2	ol9_3	ol9_4	ol9_5
SiO_2	37.90	38.11	38.17	38.70	38.15	37.92	38.69	38.05	37.95	38.04	38.03	38.21
TiO_2	LOD	LOD	0.00	LOD	LOD	LOD	0.01	LOD	0.00	LOD	0.00	LOD
Cr_2O_3	0.00	0.01	0.01	0.01	0.04	0.01	0.02	0.01	0.01	0.03	0.03	0.01
FeO	21.15	21.37	19.74	17.98	18.63	21.25	18.31	21.24	21.20	21.43	21.62	21.39
MnO	0.38	0.43	0.32	0.29	0.28	0.31	0.30	0.35	0.36	0.38	0.41	0.41
MgO	39.32	39.37	40.06	41.85	40.53	39.63	42.08	39.27	39.10	39.22	39.00	39.05
NiO	0.22	0.20	0.27	0.27	0.29	0.24	0.30	0.29	0.26	0.28	0.23	0.19
CaO	LOD	LOD	LOD	LOD	LOD	LOD	LOD	LOD	LOD	LOD	LOD	LOD
Total	98.96	99.44	98.55	99.08	97.89	99.33	99.68	99.18	98.87	99.36	99.31	99.22
Cations per formula unit												
Si	0.99	0.99	1.00	1.00	1.00	0.99	0.99	1.00	1.00	0.99	1.00	1.00
Ti	0.00	0.00	0.00	0.00	0.00	0.00	0.00	0.00	0.00	0.00	0.00	0.00
Cr	0.00	0.00	0.00	0.00	0.00	0.00	0.00	0.00	0.00	0.00	0.00	0.00
Fe^{2+}	0.46	0.47	0.43	0.39	0.41	0.46	0.39	0.46	0.47	0.47	0.47	0.47
Mn	0.01	0.01	0.01	0.01	0.01	0.01	0.01	0.01	0.01	0.01	0.01	0.01
Mg	1.54	1.53	1.56	1.61	1.58	1.54	1.61	1.53	1.53	1.53	1.52	1.52
Ni	0.00	0.00	0.01	0.01	0.01	0.00	0.01	0.01	0.01	0.01	0.00	0.00
Ca	0.00	0.00	0.00	0.00	0.00	0.00	0.00	0.00	0.00	0.00	0.00	0.00
Total	3.01	3.01	3.00	3.00	3.00	3.01	3.01	3.00	3.00	3.01	3.00	3.00
Fo	76.82	76.66	78.34	80.58	79.50	76.87	80.38	76.72	76.68	76.54	76.28	76.49

Appendix D2: Olivine University of Manitoba

Samples #EN24VS006

Oxide wt%	ol1_2	ol1_3	ol2_2	ol3_1	ol3_2	ol3_3	ol4_1	ol4_3	ol5_1	ol6_2	ol6_3
SiO_2	40.10	39.46	39.69	39.67	39.31	39.32	39.52	39.55	39.54	40.16	39.76
TiO_2	0.00	0.00	0.01	0.00	0.01	0.00	0.01	0.01	0.00	0.01	0.00
Al_2O_3	0.01	0.01	0.02	0.01	0.01	0.01	0.01	0.01	0.01	0.01	0.02
Cr_2O_3	0.00	0.01	0.04	0.00	0.01	0.02	0.02	0.20	0.02	0.02	0.03
FeO	12.66	12.62	14.21	13.88	13.87	14.23	13.74	13.65	13.76	13.01	13.00
MnO	0.19	0.18	0.23	0.19	0.18	0.18	0.22	0.18	0.16	0.14	0.16
MgO	46.14	46.73	45.91	46.54	46.24	46.53	46.96	47.07	46.68	47.25	46.82
NiO	0.22	0.21	0.22	0.22	0.23	0.25	0.20	0.21	0.19	0.18	0.17
CaO	0.01	0.00	0.09	0.02	0.00	0.03	0.01	0.00	0.01	0.03	0.12
Total	99.33	99.23	100.42	100.54	99.86	100.58	100.69	100.89	100.37	100.80	100.09
Cations per formula unit											
Si	1.00	0.99	0.99	0.99	0.99	0.98	0.98	0.98	0.99	0.99	0.99
Ti	0.00	0.00	0.00	0.00	0.00	0.00	0.00	0.00	0.00	0.00	0.00
Al	0.00	0.00	0.00	0.00	0.00	0.00	0.00	0.00	0.00	0.00	0.00
Cr	0.00	0.00	0.00	0.00	0.00	0.00	0.00	0.00	0.00	0.00	0.00
Fe^{2+}	0.26	0.26	0.30	0.29	0.29	0.30	0.29	0.28	0.29	0.27	0.27
Mn	0.00	0.00	0.00	0.00	0.00	0.00	0.00	0.00	0.00	0.00	0.00
Mg	1.72	1.75	1.71	1.73	1.73	1.73	1.74	1.74	1.73	1.74	1.74
Ni	0.00	0.00	0.00	0.00	0.00	0.01	0.00	0.00	0.00	0.00	0.00
Ca	0.00	0.00	0.00	0.00	0.00	0.00	0.00	0.00	0.00	0.00	0.00
Total	3.00	3.01	3.01	3.01	3.01	3.02	3.02	3.02	3.01	3.01	3.01
Fo	86.66	86.85	85.21	85.67	85.60	85.35	85.90	86.01	85.81	86.62	86.53

Samples #EN24VS006

Oxide wt%	ol7_1	ol7_2	ol8_1	ol8_2	ol8_3	ol9_1	ol9_2	ol9_3	ol10_2	ol11_2	ol11_2	ol11_2
SiO_2	40.64	40.09	39.51	39.72	39.90	39.53	39.02	39.72	39.37	39.95	39.79	39.11
TiO_2	0.01	0.01	0.00	0.00	0.00	0.00	0.01	0.02	0.01	0.01	0.01	0.00
Al_2O_3	0.01	0.01	0.01	0.01	0.01	0.00	0.01	0.08	0.03	0.01	0.02	0.05
Cr_2O_3	0.00	0.02	0.02	0.01	0.00	0.05	0.01	0.02	0.02	0.01	0.01	0.03
FeO	13.68	13.86	13.05	13.26	13.82	13.69	13.54	13.59	13.55	14.06	14.24	15.78
MnO	0.23	0.19	0.19	0.22	0.20	0.19	0.18	0.16	0.20	0.21	0.25	0.23
MgO	46.93	46.49	45.96	46.06	46.65	46.09	46.64	44.73	45.03	46.47	46.25	44.69
NiO	0.19	0.16	0.20	0.20	0.14	0.14	0.19	0.19	0.25	0.23	0.25	0.25
CaO	0.01	0.02	0.02	0.02	0.03	0.06	0.02	1.21	0.11	0.03	0.04	0.17
Total	101.72	100.85	98.96	99.49	100.76	99.75	99.63	99.71	98.56	100.98	100.85	100.31
Cations per formula unit												
Si	1.00	0.99	0.99	1.00	0.99	0.99	0.98	1.00	1.00	0.99	0.99	0.99
Ti	0.00	0.00	0.00	0.00	0.00	0.00	0.00	0.00	0.00	0.00	0.00	0.00
Al	0.00	0.00	0.00	0.00	0.00	0.00	0.00	0.00	0.00	0.00	0.00	0.00
Cr	0.00	0.00	0.00	0.00	0.00	0.00	0.00	0.00	0.00	0.00	0.00	0.00
Fe^{2+}	0.28	0.29	0.27	0.28	0.29	0.29	0.28	0.29	0.29	0.29	0.30	0.33
Mn	0.00	0.00	0.00	0.00	0.00	0.00	0.00	0.00	0.00	0.00	0.01	0.00
Mg	1.72	1.72	1.73	1.72	1.73	1.72	1.75	1.67	1.70	1.72	1.71	1.68
Ni	0.00	0.00	0.00	0.00	0.00	0.00	0.00	0.00	0.01	0.00	0.00	0.00
Ca	0.00	0.00	0.00	0.00	0.00	0.00	0.00	0.03	0.00	0.00	0.00	0.00
Total	3.00	3.01	3.00	3.00	3.01	3.01	3.02	3.00	3.00	3.01	3.01	3.01
Fo	85.95	85.67	86.26	86.10	85.75	85.72	85.99	85.44	85.56	85.49	85.27	83.46

Sample #EN24VS007

Oxide wt%	ol1_1	ol1_2	ol1_3	ol2_1	ol2_2	ol2_3	ol3_1	ol3_2	ol3_3	ol4_1	ol4_2	ol4_3
SiO_2	39.78	39.27	40.75	39.78	39.71	39.44	39.79	40.96	39.84	39.98	39.71	39.94
TiO_2	0.01	0.01	0.00	0.01	0.00	0.00	0.03	0.00	0.01	0.00	0.01	0.01
Al_2O_3	0.01	0.02	0.01	0.01	0.01	0.01	0.00	0.02	0.01	0.08	0.20	0.01
Cr_2O_3	0.00	0.01	0.00	0.00	0.00	0.00	0.08	0.01	0.00	0.04	0.02	0.00
FeO	13.74	13.83	13.18	13.47	13.19	13.23	13.04	13.34	13.63	12.86	13.27	13.14
MnO	0.16	0.15	0.17	0.20	0.15	0.22	0.24	0.14	0.21	0.18	0.16	0.19
MgO	46.20	46.13	46.86	46.25	46.99	46.86	46.84	47.11	46.79	46.94	46.52	47.13
NiO	0.18	0.22	0.18	0.21	0.17	0.15	0.15	0.13	0.16	0.23	0.16	0.20
CaO	0.04	0.02	0.08	0.01	0.00	0.01	0.00	0.02	0.00	0.08	0.18	0.02
Total	100.13	99.66	101.24	99.94	100.23	99.92	100.17	101.72	100.64	100.38	100.23	100.64
Cations per formula unit												
Si	0.99	0.99	1.00	0.99	0.99	0.99	0.99	1.00	0.99	0.99	0.99	0.99
Ti	0.00	0.00	0.00	0.00	0.00	0.00	0.00	0.00	0.00	0.00	0.00	0.00
Al	0.00	0.00	0.00	0.00	0.00	0.00	0.00	0.00	0.00	0.00	0.01	0.00
Cr	0.00	0.00	0.00	0.00	0.00	0.00	0.00	0.00	0.00	0.00	0.00	0.00
Fe^{2+}	0.29	0.29	0.27	0.28	0.27	0.28	0.27	0.27	0.28	0.27	0.28	0.27
Mn	0.00	0.00	0.00	0.00	0.00	0.00	0.01	0.00	0.00	0.00	0.00	0.00
Mg	1.72	1.73	1.72	1.72	1.74	1.74	1.74	1.72	1.73	1.74	1.73	1.74
Ni	0.00	0.00	0.00	0.00	0.00	0.00	0.00	0.00	0.00	0.00	0.00	0.00
Ca	0.00	0.00	0.00	0.00	0.00	0.00	0.00	0.00	0.00	0.00	0.00	0.00
Total	3.01	3.01	3.00	3.01	3.01	3.01	3.01	3.00	3.01	3.01	3.01	3.01
Fo	85.70	85.60	86.37	85.96	86.39	86.32	86.49	86.29	85.96	86.68	86.21	86.47

Sample #EN24VS007

Oxide wt%	ol5_1	ol5_2	ol6_1	ol6_2	ol6_3	ol7_1	ol7_2	ol7_3	ol8_1	ol8_2	ol8_3	ol9_1
SiO_2	39.69	40.08	39.80	40.13	39.56	39.52	39.25	39.90	39.65	39.71	39.64	40.02
TiO_2	0.00	0.00	0.02	0.00	0.02	0.00	0.01	0.00	0.00	0.00	0.00	0.01
Al_2O_3	0.01	0.01	0.02	0.02	0.02	0.00	0.01	0.00	0.00	0.09	0.02	0.02
Cr_2O_3	0.01	0.01	0.00	0.03	0.02	0.02	0.02	0.01	0.00	0.09	0.01	0.01
FeO	13.38	13.96	13.16	14.16	13.40	13.62	13.74	13.34	13.58	14.27	13.79	13.01
MnO	0.21	0.21	0.19	0.18	0.21	0.22	0.22	0.21	0.21	0.14	0.20	0.18
MgO	46.51	46.81	46.45	47.02	47.16	46.49	45.04	47.47	46.87	45.68	46.02	46.16
NiO	0.21	0.20	0.17	0.19	0.20	0.24	0.21	0.13	0.18	0.19	0.23	0.20
CaO	0.01	0.02	0.04	0.03	0.05	0.01	0.24	0.03	0.01	0.33	0.06	0.28
Total	100.04	101.31	99.85	101.77	100.65	100.12	98.73	101.09	100.51	100.50	99.97	99.88
Cations per formula unit												
Si	0.99	0.99	0.99	0.99	0.98	0.99	0.99	0.98	0.99	0.99	0.99	1.00
Ti	0.00	0.00	0.00	0.00	0.00	0.00	0.00	0.00	0.00	0.00	0.00	0.00
Al	0.00	0.00	0.00	0.00	0.00	0.00	0.00	0.00	0.00	0.00	0.00	0.00
Cr	0.00	0.00	0.00	0.00	0.00	0.00	0.00	0.00	0.00	0.00	0.00	0.00
Fe^{2+}	0.28	0.29	0.27	0.29	0.28	0.28	0.29	0.28	0.28	0.30	0.29	0.27
Mn	0.00	0.00	0.00	0.00	0.00	0.00	0.00	0.00	0.00	0.00	0.00	0.00
Mg	1.73	1.72	1.73	1.72	1.75	1.73	1.70	1.75	1.74	1.70	1.72	1.72
Ni	0.00	0.00	0.00	0.00	0.00	0.00	0.00	0.00	0.00	0.00	0.00	0.00
Ca	0.00	0.00	0.00	0.00	0.00	0.00	0.01	0.00	0.00	0.01	0.00	0.01
Total	3.01	3.01	3.01	3.01	3.02	3.01	3.00	3.02	3.01	3.01	3.01	3.00
Fo	86.10	85.66	86.29	85.55	86.25	85.89	85.39	86.38	86.01	85.09	85.61	86.35

Sample #EN24VS007

Oxide wt%	ol9_2	ol9_3	ol10_1	ol10_2	ol10_3	ol11_1	ol11_2	ol11_3	ol12_1	ol12_2	ol12_3
SiO_2	39.56	39.99	39.41	39.71	39.61	40.14	40.12	40.64	39.92	39.96	39.31
TiO_2	0.01	0.01	0.01	0.01	0.02	0.02	0.02	0.00	0.02	0.00	0.00
Al_2O_3	0.01	0.00	0.04	0.06	0.16	0.00	0.02	0.15	0.03	0.01	0.06
Cr_2O_3	0.02	0.03	0.03	0.07	0.00	0.06	0.00	0.01	0.01	0.06	0.11
FeO	14.02	13.79	13.48	14.43	14.34	13.27	13.75	13.62	13.61	13.64	14.63
MnO	0.22	0.17	0.19	0.21	0.18	0.27	0.19	0.17	0.25	0.21	0.19
MgO	46.27	46.34	46.62	45.78	45.37	46.90	46.56	46.06	46.88	46.28	45.67
NiO	0.18	0.20	0.21	0.21	0.22	0.19	0.22	0.23	0.16	0.22	0.20
CaO	0.04	0.01	0.02	0.13	0.43	0.03	0.01	0.20	0.16	0.13	0.21
Total	100.33	100.54	100.00	100.61	100.32	100.88	100.88	101.10	101.04	100.51	100.39
Cations per formula unit											
Si	0.99	0.99	0.99	0.99	0.99	0.99	0.99	1.00	0.99	0.99	0.98
Ti	0.00	0.00	0.00	0.00	0.00	0.00	0.00	0.00	0.00	0.00	0.00
Al	0.00	0.00	0.00	0.00	0.00	0.00	0.00	0.00	0.00	0.00	0.00
Cr	0.00	0.00	0.00	0.00	0.00	0.00	0.00	0.00	0.00	0.00	0.00
Fe^{2+}	0.29	0.29	0.28	0.30	0.30	0.27	0.28	0.28	0.28	0.28	0.31
Mn	0.00	0.00	0.00	0.00	0.00	0.01	0.00	0.00	0.01	0.00	0.00
Mg	1.72	1.72	1.74	1.70	1.69	1.73	1.72	1.69	1.73	1.71	1.70
Ni	0.00	0.00	0.00	0.00	0.00	0.00	0.00	0.00	0.00	0.00	0.00
Ca	0.00	0.00	0.00	0.00	0.01	0.00	0.00	0.01	0.00	0.00	0.01
Total	3.01	3.01	3.01	3.01	3.01	3.01	3.01	3.00	3.01	3.01	3.01
Fo	85.47	85.69	86.05	84.98	84.94	86.30	85.78	85.77	85.99	85.81	84.77

Sample #EN24VS007							**Sample # EN24VS008**			
Oxide wt%	ol13_1	ol13_2	ol13_3	ol14_1	ol14_2	ol14_3	ol1_1	ol1_2	ol1_3	ol2_1
SiO_2	39.73	39.66	39.82	39.65	39.90	39.74	39.67	39.84	40.23	39.43
TiO_2	0.00	0.01	0.00	0.00	0.00	0.00	0.00	0.01	0.01	0.01
Al_2O_3	0.01	0.01	0.02	0.01	0.02	0.03	0.01	0.01	0.01	0.02
Cr_2O_3	0.01	0.03	0.02	0.00	0.00	0.00	0.02	0.02	0.00	0.01
FeO	13.75	13.22	13.49	13.33	14.03	13.97	13.50	13.11	13.50	14.06
MnO	0.18	0.19	0.16	0.17	0.20	0.22	0.21	0.18	0.18	0.20
MgO	45.84	46.91	46.57	46.34	46.49	46.21	46.55	47.11	46.40	46.36
NiO	0.22	0.18	0.23	0.21	0.22	0.19	0.19	0.19	0.18	0.22
CaO	0.11	0.01	0.04	0.01	0.01	0.02	0.03	0.05	0.03	0.06
Total	99.85	100.23	100.36	99.72	100.87	100.38	100.19	100.52	100.54	100.37
Cations per formula unit										
Si	0.99	0.99	0.99	0.99	0.99	0.99	0.99	0.99	1.00	0.98
Ti	0.00	0.00	0.00	0.00	0.00	0.00	0.00	0.00	0.00	0.00
Al	0.00	0.00	0.00	0.00	0.00	0.00	0.00	0.00	0.00	0.00
Cr	0.00	0.00	0.00	0.00	0.00	0.00	0.00	0.00	0.00	0.00
Fe^{2+}	0.29	0.28	0.28	0.28	0.29	0.29	0.28	0.27	0.28	0.29
Mn	0.00	0.00	0.00	0.00	0.00	0.00	0.00	0.00	0.00	0.00
Mg	1.71	1.74	1.73	1.73	1.72	1.72	1.73	1.74	1.72	1.73
Ni	0.00	0.00	0.00	0.00	0.00	0.00	0.00	0.00	0.00	0.00
Ca	0.00	0.00	0.00	0.00	0.00	0.00	0.00	0.00	0.00	0.00
Total	3.01	3.01	3.01	3.01	3.01	3.01	3.01	3.01	3.00	3.01
Fo	85.60	86.34	86.02	86.10	85.52	85.50	86.01	86.50	85.96	85.46

Sample # EN24VS008

Oxide wt%	ol2_2	ol2_3	ol3_1	ol3_2	ol3_3	ol4_1	ol4_2	ol4_3	ol5_1	ol5_2	ol5_3
SiO_2	39.79	39.81	39.81	39.80	39.54	40.15	40.00	39.59	39.83	39.48	39.80
TiO_2	0.02	0.01	0.00	0.01	0.00	0.01	0.00	0.00	0.00	0.01	0.02
Al_2O_3	0.02	0.01	0.00	0.00	0.01	0.00	0.00	0.02	0.01	0.00	0.01
Cr_2O_3	0.02	0.00	0.01	0.01	0.04	0.01	0.03	0.03	0.02	0.00	0.00
FeO	14.75	14.06	14.22	14.01	13.67	13.52	14.06	14.49	13.57	13.59	13.78
MnO	0.23	0.24	0.21	0.21	0.22	0.18	0.24	0.19	0.16	0.24	0.21
MgO	45.78	46.23	46.25	46.24	46.26	46.73	46.45	46.40	46.49	46.44	46.64
NiO	0.22	0.20	0.20	0.13	0.22	0.19	0.20	0.24	0.18	0.17	0.19
CaO	0.17	0.00	0.00	0.01	0.01	0.02	0.02	0.04	0.01	0.01	0.05
Total	101.00	100.54	100.70	100.41	99.96	100.82	100.99	101.00	100.29	99.95	100.69
Cations per formula unit											
Si	0.99	0.99	0.99	0.99	0.99	0.99	0.99	0.98	0.99	0.99	0.99
Ti	0.00	0.00	0.00	0.00	0.00	0.00	0.00	0.00	0.00	0.00	0.00
Al	0.00	0.00	0.00	0.00	0.00	0.00	0.00	0.00	0.00	0.00	0.00
Cr	0.00	0.00	0.00	0.00	0.00	0.00	0.00	0.00	0.00	0.00	0.00
Fe^{2+}	0.31	0.29	0.30	0.29	0.29	0.28	0.29	0.30	0.28	0.28	0.29
Mn	0.00	0.01	0.00	0.00	0.00	0.00	0.01	0.00	0.00	0.01	0.00
Mg	1.70	1.72	1.71	1.72	1.73	1.72	1.72	1.72	1.73	1.73	1.73
Ni	0.00	0.00	0.00	0.00	0.00	0.00	0.00	0.00	0.00	0.00	0.00
Ca	0.00	0.00	0.00	0.00	0.00	0.00	0.00	0.00	0.00	0.00	0.00
Total	3.01	3.01	3.01	3.01	3.01	3.01	3.01	3.02	3.01	3.01	3.01
Fo	84.69	85.43	85.29	85.47	85.78	86.04	85.49	85.10	85.93	85.89	85.78

Sample # EN24VS008

Oxide wt%	ol6_1	ol6_2	ol6_3	ol7_1	ol7_2	ol7_3	ol8_1	ol8_2	ol8_3	ol9_1	ol9_2
SiO_2	39.85	39.72	39.42	40.23	39.98	39.94	40.00	39.70	40.16	39.88	39.33
TiO_2	0.02	0.01	0.01	0.00	0.01	0.00	0.01	0.00	0.02	0.03	0.00
Al_2O_3	0.01	0.01	0.01	0.00	0.00	0.02	0.01	0.01	0.01	0.01	0.24
Cr_2O_3	0.02	0.03	0.03	0.02	0.02	0.03	0.00	0.00	0.02	0.00	0.09
FeO	13.49	13.94	14.22	13.22	12.91	13.24	12.88	12.83	12.91	14.37	15.68
MnO	0.21	0.24	0.21	0.20	0.17	0.18	0.18	0.17	0.13	0.21	0.19
MgO	46.70	46.51	46.49	47.46	47.21	47.20	47.18	47.44	47.48	45.62	43.39
NiO	0.19	0.17	0.19	0.16	0.15	0.17	0.15	0.14	0.12	0.18	0.21
CaO	0.02	0.01	0.03	0.01	0.01	0.02	0.02	0.01	0.01	0.07	0.93
Total	100.51	100.64	100.61	101.32	100.46	100.81	100.42	100.30	100.87	100.36	100.06
Cations per formula unit											
Si	0.99	0.99	0.98	0.99	0.99	0.99	0.99	0.99	0.99	1.00	0.99
Ti	0.00	0.00	0.00	0.00	0.00	0.00	0.00	0.00	0.00	0.00	0.00
Al	0.00	0.00	0.00	0.00	0.00	0.00	0.00	0.00	0.00	0.00	0.01
Cr	0.00	0.00	0.00	0.00	0.00	0.00	0.00	0.00	0.00	0.00	0.00
Fe^{2+}	0.28	0.29	0.30	0.27	0.27	0.27	0.27	0.27	0.27	0.30	0.33
Mn	0.00	0.00	0.00	0.00	0.00	0.00	0.00	0.00	0.00	0.00	0.00
Mg	1.73	1.72	1.73	1.74	1.74	1.74	1.74	1.76	1.75	1.70	1.63
Ni	0.00	0.00	0.00	0.00	0.00	0.00	0.00	0.00	0.00	0.00	0.00
Ca	0.00	0.00	0.00	0.00	0.00	0.00	0.00	0.00	0.00	0.00	0.03
Total	3.01	3.01	3.02	3.01	3.01	3.01	3.01	3.01	3.01	3.00	3.00
Fo	86.05	85.60	85.36	86.48	86.70	86.40	86.72	86.82	86.76	84.98	83.14

Sample # EN24VS008

Oxide wt%	ol9_3	ol9_4	ol10_1	ol10_2	ol10_3	ol11_1	ol11_2	ol11_3	ol12_1	ol12_2	ol12_3
SiO_2	40.04	39.47	39.80	40.24	39.50	39.46	39.65	39.76	39.91	38.67	39.68
TiO_2	0.00	0.01	0.01	0.01	0.00	0.03	0.01	0.00	0.02	0.00	0.01
Al_2O_3	0.01	0.00	0.00	0.05	0.00	0.01	0.03	0.00	0.02	0.07	0.01
Cr_2O_3	0.02	0.00	0.00	0.04	0.02	0.01	0.01	0.03	0.02	0.17	0.00
FeO	13.88	14.15	14.28	14.22	14.19	14.30	14.21	14.11	14.34	16.17	13.97
MnO	0.18	0.14	0.19	0.19	0.26	0.18	0.24	0.20	0.17	0.15	0.21
MgO	46.31	46.12	45.78	45.12	46.01	45.84	45.97	46.10	46.87	45.50	46.33
NiO	0.17	0.20	0.17	0.21	0.24	0.18	0.20	0.21	0.21	0.22	0.20
CaO	0.02	0.01	0.01	0.67	0.00	0.01	0.16	0.02	0.10	0.18	0.01
Total	100.63	100.10	100.26	100.75	100.23	100.01	100.50	100.43	101.66	101.12	100.43
Cations per formula unit											
Si	0.99	0.99	0.99	1.00	0.99	0.99	0.99	0.99	0.98	0.97	0.99
Ti	0.00	0.00	0.00	0.00	0.00	0.00	0.00	0.00	0.00	0.00	0.00
Al	0.00	0.00	0.00	0.00	0.00	0.00	0.00	0.00	0.00	0.00	0.00
Cr	0.00	0.00	0.00	0.00	0.00	0.00	0.00	0.00	0.00	0.00	0.00
Fe^{2+}	0.29	0.30	0.30	0.30	0.30	0.30	0.30	0.29	0.30	0.34	0.29
Mn	0.00	0.00	0.00	0.00	0.01	0.00	0.01	0.00	0.00	0.00	0.00
Mg	1.71	1.72	1.70	1.67	1.72	1.71	1.71	1.71	1.72	1.70	1.72
Ni	0.00	0.00	0.00	0.00	0.00	0.00	0.00	0.00	0.00	0.00	0.00
Ca	0.00	0.00	0.00	0.02	0.00	0.00	0.00	0.00	0.00	0.00	0.00
Total	3.01	3.01	3.01	3.00	3.01	3.01	3.01	3.01	3.01	3.03	3.01
Fo	85.60	85.32	85.10	84.98	85.25	85.11	85.22	85.34	85.35	83.38	85.54

Sample # EN24VS009

Oxide wt%	ol1_1	ol1_2	ol1_3	ol1_4	ol2_1	ol2_2	ol3_1	ol3_2	ol3_3	ol4_1	ol4_2
SiO_2	39.93	39.78	40.09	40.00	40.00	39.95	39.82	39.67	39.84	40.04	39.97
TiO_2	0.00	0.00	0.00	0.01	0.00	0.01	0.01	0.00	0.00	0.01	0.00
Al_2O_3	0.00	0.01	0.00	0.00	0.03	0.00	0.02	0.00	0.00	0.01	0.01
Cr_2O_3	0.02	0.07	0.00	0.02	0.02	0.04	0.03	0.02	0.01	0.02	0.01
FeO	13.92	13.59	13.51	13.44	13.67	13.42	13.63	13.51	13.42	13.25	13.61
MnO	0.23	0.23	0.13	0.26	0.13	0.18	0.23	0.20	0.21	0.16	0.20
MgO	46.74	46.75	46.99	46.72	46.87	47.20	46.71	46.75	46.94	46.76	46.68
NiO	0.10	0.18	0.18	0.10	0.21	0.19	0.20	0.20	0.20	0.13	0.19
CaO	0.01	0.00	0.02	0.01	0.14	0.05	0.03	0.02	0.01	0.03	0.01
Total	100.94	100.62	100.93	100.56	101.06	101.03	100.68	100.35	100.62	100.40	100.68
Cations per formula unit											
Si	0.99	0.99	0.99	0.99	0.99	0.99	0.99	0.99	0.99	0.99	0.99
Ti	0.00	0.00	0.00	0.00	0.00	0.00	0.00	0.00	0.00	0.00	0.00
Al	0.00	0.00	0.00	0.00	0.00	0.00	0.00	0.00	0.00	0.00	0.00
Cr	0.00	0.00	0.00	0.00	0.00	0.00	0.00	0.00	0.00	0.00	0.00
Fe^{2+}	0.29	0.28	0.28	0.28	0.28	0.28	0.28	0.28	0.28	0.28	0.28
Mn	0.00	0.00	0.00	0.01	0.00	0.00	0.00	0.00	0.00	0.00	0.00
Mg	1.73	1.73	1.73	1.73	1.73	1.74	1.73	1.73	1.74	1.73	1.73
Ni	0.00	0.00	0.00	0.00	0.00	0.00	0.00	0.00	0.00	0.00	0.00
Ca	0.00	0.00	0.00	0.00	0.00	0.00	0.00	0.00	0.00	0.00	0.00
Total	3.01	3.01	3.01	3.01	3.01	3.01	3.01	3.01	3.01	3.01	3.01
Fo	85.69	85.97	86.11	86.10	85.94	86.25	85.94	86.05	86.18	86.28	85.94

Sample # EN24VS009

Oxide wt%	ol4_3	ol4_4	ol5_1	ol5_2	ol5_3	ol6_1	ol6_2	ol6_3	ol6_4	ol7_1	ol7_2
SiO_2	39.84	39.82	40.21	40.05	39.91	39.81	39.50	39.87	40.01	39.87	39.35
TiO_2	0.01	0.00	0.01	0.00	0.00	0.01	0.01	0.00	0.00	0.00	0.02
Al_2O_3	0.03	0.00	0.00	0.00	0.00	0.00	0.00	0.00	0.00	0.01	0.03
Cr_2O_3	0.01	0.00	0.01	0.00	0.00	0.00	0.00	0.00	0.05	0.01	0.00
FeO	13.69	13.45	13.30	13.51	13.21	13.40	13.66	13.33	13.47	13.41	13.13
MnO	0.26	0.19	0.22	0.17	0.20	0.17	0.18	0.18	0.20	0.23	0.16
MgO	46.65	46.60	46.72	46.52	46.79	47.15	46.94	47.11	46.73	46.07	45.69
NiO	0.23	0.17	0.16	0.19	0.19	0.16	0.20	0.20	0.16	0.11	0.24
CaO	0.00	0.02	0.02	0.00	0.01	0.01	0.01	0.01	0.03	0.01	0.21
Total	100.73	100.25	100.65	100.45	100.32	100.73	100.49	100.71	100.64	99.72	98.83
Cations per formula unit											
Si	0.99	0.99	1.00	0.99	0.99	0.99	0.98	0.99	0.99	1.00	0.99
Ti	0.00	0.00	0.00	0.00	0.00	0.00	0.00	0.00	0.00	0.00	0.00
Al	0.00	0.00	0.00	0.00	0.00	0.00	0.00	0.00	0.00	0.00	0.00
Cr	0.00	0.00	0.00	0.00	0.00	0.00	0.00	0.00	0.00	0.00	0.00
Fe^{2+}	0.28	0.28	0.28	0.28	0.27	0.28	0.28	0.28	0.28	0.28	0.28
Mn	0.01	0.00	0.00	0.00	0.00	0.00	0.00	0.00	0.00	0.00	0.00
Mg	1.73	1.73	1.72	1.72	1.73	1.74	1.74	1.74	1.73	1.72	1.72
Ni	0.00	0.00	0.00	0.00	0.00	0.00	0.00	0.00	0.00	0.00	0.00
Ca	0.00	0.00	0.00	0.00	0.00	0.00	0.00	0.00	0.00	0.00	0.01
Total	3.01	3.01	3.00	3.01	3.01	3.01	3.02	3.01	3.01	3.00	3.01
Fo	85.86	86.07	86.23	86.00	86.33	86.25	85.97	86.30	86.08	85.97	86.12

Sample # EN24VS009

Oxide wt%	ol8_1	ol8_2	ol8_3	ol8_4	ol9_1	ol9_2	ol9_3	ol9_4	ol10_1	ol10_2	ol10_3	ol10_4
SiO_2	39.82	40.13	39.68	39.62	39.54	39.58	39.72	40.25	39.96	39.23	39.60	39.62
TiO_2	0.01	0.00	0.00	0.01	0.02	0.00	0.00	0.01	0.01	0.00	0.00	0.00
Al_2O_3	0.00	0.00	0.01	0.00	0.00	0.04	0.01	0.00	0.00	0.00	0.00	0.00
Cr_2O_3	0.00	0.05	0.00	0.07	0.00	0.02	0.01	0.01	0.02	0.00	0.01	0.00
FeO	13.33	13.81	13.84	13.87	13.67	14.00	13.56	13.72	13.65	13.65	13.69	13.26
MnO	0.20	0.18	0.24	0.20	0.23	0.17	0.18	0.22	0.23	0.23	0.21	0.22
MgO	46.81	46.97	46.47	46.77	46.83	46.41	46.54	47.00	46.63	46.79	46.36	46.97
NiO	0.21	0.19	0.19	0.14	0.20	0.19	0.21	0.19	0.19	0.19	0.22	0.16
CaO	0.01	0.00	0.02	0.00	0.02	0.12	0.14	0.00	0.00	0.01	0.07	0.01
Total	100.41	101.35	100.44	100.68	100.51	100.54	100.37	101.40	100.68	100.10	100.17	100.24
Cations per formula unit												
Si	0.99	0.99	0.99	0.98	0.98	0.99	0.99	0.99	0.99	0.98	0.99	0.99
Ti	0.00	0.00	0.00	0.00	0.00	0.00	0.00	0.00	0.00	0.00	0.00	0.00
Al	0.00	0.00	0.00	0.00	0.00	0.00	0.00	0.00	0.00	0.00	0.00	0.00
Cr	0.00	0.00	0.00	0.00	0.00	0.00	0.00	0.00	0.00	0.00	0.00	0.00
Fe^{2+}	0.28	0.28	0.29	0.29	0.28	0.29	0.28	0.28	0.28	0.29	0.29	0.28
Mn	0.00	0.00	0.00	0.00	0.00	0.00	0.00	0.00	0.00	0.00	0.00	0.00
Mg	1.73	1.73	1.73	1.73	1.74	1.72	1.73	1.73	1.72	1.74	1.73	1.74
Ni	0.00	0.00	0.00	0.00	0.00	0.00	0.00	0.00	0.00	0.00	0.00	0.00
Ca	0.00	0.00	0.00	0.00	0.00	0.00	0.00	0.00	0.00	0.00	0.00	0.00
Total	3.01	3.01	3.01	3.01	3.02	3.01	3.01	3.01	3.01	3.02	3.01	3.01
Fo	86.22	85.84	85.69	85.74	85.93	85.52	85.96	85.93	85.89	85.93	85.79	86.33

Sample # EN24VS015

Oxide wt%	ol1_1	ol1_2	ol1_3	ol2_1	ol2_2	ol2_3	ol3_1	ol3_2	ol3_3	ol3_4	ol4_1
SiO_2	39.59	39.17	39.43	39.06	38.95	38.69	39.34	39.51	39.69	39.58	39.53
TiO_2	0.03	0.00	0.01	0.00	0.02	0.01	0.00	0.00	0.01	0.00	0.02
Al_2O_3	0.22	0.00	0.00	0.00	0.08	0.00	0.00	0.00	0.00	0.00	0.00
Cr_2O_3	0.11	0.02	0.05	0.00	0.00	0.00	0.02	0.01	0.01	0.40	0.04
FeO	16.77	17.41	17.02	16.71	16.93	16.80	16.24	15.92	15.46	15.29	16.20
MnO	0.31	0.25	0.26	0.28	0.31	0.29	0.29	0.25	0.19	0.20	0.24
MgO	41.54	43.31	43.46	43.84	42.76	43.41	44.23	45.28	45.18	45.31	44.23
NiO	0.24	0.22	0.27	0.31	0.25	0.31	0.24	0.28	0.29	0.29	0.29
CaO	1.10	0.02	0.01	0.00	0.58	0.01	0.01	0.03	0.00	0.05	0.00
Total	99.91	100.42	100.51	100.20	99.89	99.50	100.37	101.27	100.84	101.12	100.55
Cations per formula unit											
Si	1.01	0.99	1.00	0.99	0.99	0.99	0.99	0.99	0.99	0.99	0.99
Ti	0.00	0.00	0.00	0.00	0.00	0.00	0.00	0.00	0.00	0.00	0.00
Al	0.01	0.00	0.00	0.00	0.00	0.00	0.00	0.00	0.00	0.00	0.00
Cr	0.00	0.00	0.00	0.00	0.00	0.00	0.00	0.00	0.00	0.01	0.00
Fe^{2+}	0.36	0.37	0.36	0.35	0.36	0.36	0.34	0.33	0.32	0.32	0.34
Mn	0.01	0.01	0.01	0.01	0.01	0.01	0.01	0.01	0.00	0.00	0.01
Mg	1.57	1.64	1.64	1.66	1.62	1.65	1.66	1.68	1.68	1.68	1.66
Ni	0.00	0.00	0.01	0.01	0.01	0.01	0.00	0.01	0.01	0.01	0.01
Ca	0.03	0.00	0.00	0.00	0.02	0.00	0.00	0.00	0.00	0.00	0.00
Total	2.99	3.01	3.00	3.01	3.01	3.01	3.01	3.01	3.01	3.01	3.01
Fo	81.53	81.60	81.99	82.38	81.83	82.16	82.92	83.53	83.89	84.08	82.95

Sample # EN24VS015

Oxide wt%	ol4_2	ol4_3	ol5_1	ol5_2	ol5_3	ol6_1	ol6_2	ol6_3	ol6_4	ol7_1	ol7_2
SiO_2	39.69	39.33	39.20	39.87	40.21	39.48	39.44	39.37	39.17	39.52	39.89
TiO_2	0.00	0.00	0.00	0.01	0.00	0.00	0.00	0.02	0.00	0.00	0.00
Al_2O_3	0.00	0.00	0.00	0.00	0.10	0.15	0.00	0.48	0.00	0.00	0.00
Cr_2O_3	0.00	0.01	0.01	0.01	0.04	0.00	0.00	0.07	0.04	0.00	0.00
FeO	15.14	15.48	16.91	14.30	14.29	16.57	14.98	14.88	17.24	15.41	13.84
MnO	0.21	0.23	0.25	0.22	0.18	0.26	0.26	0.19	0.25	0.20	0.15
MgO	45.65	44.41	43.46	46.46	44.86	43.76	45.08	45.09	44.07	45.06	46.42
NiO	0.28	0.28	0.22	0.29	0.28	0.26	0.23	0.30	0.25	0.28	0.25
CaO	0.02	0.03	0.02	0.01	0.54	0.02	0.02	0.01	0.00	0.00	0.00
Total	101.00	99.77	100.07	101.18	100.50	100.50	100.01	100.40	101.02	100.48	100.55
Cations per formula unit											
Si	0.99	0.99	0.99	0.99	1.00	0.99	0.99	0.99	0.99	0.99	0.99
Ti	0.00	0.00	0.00	0.00	0.00	0.00	0.00	0.00	0.00	0.00	0.00
Al	0.00	0.00	0.00	0.00	0.00	0.00	0.00	0.01	0.00	0.00	0.00
Cr	0.00	0.00	0.00	0.00	0.00	0.00	0.00	0.00	0.00	0.00	0.00
Fe^{2+}	0.32	0.33	0.36	0.30	0.30	0.35	0.32	0.31	0.36	0.32	0.29
Mn	0.00	0.00	0.01	0.00	0.00	0.01	0.01	0.00	0.01	0.00	0.00
Mg	1.70	1.67	1.64	1.72	1.67	1.64	1.69	1.68	1.65	1.68	1.72
Ni	0.01	0.01	0.00	0.01	0.01	0.01	0.00	0.01	0.01	0.01	0.00
Ca	0.00	0.00	0.00	0.00	0.01	0.00	0.00	0.00	0.00	0.00	0.00
Total	3.01	3.01	3.01	3.01	3.00	3.00	3.01	3.01	3.01	3.01	3.01
Fo	84.31	83.64	82.08	85.27	84.84	82.48	84.29	84.38	82.01	83.90	85.67

Sample # EN24VS015

Oxide wt%	ol7_3	ol7_4	ol8_1	ol8_2	ol8_3	ol9_1	ol9_2	ol9_3	ol9_4	ol10_1	ol10_2
SiO_2	39.89	39.52	39.41	39.24	39.37	39.47	39.52	38.86	39.51	39.08	39.10
TiO_2	0.00	0.00	0.02	0.01	0.01	0.01	0.00	0.01	0.00	0.00	0.00
Al_2O_3	0.00	0.00	0.00	0.00	0.00	0.07	0.00	0.00	0.00	0.01	0.01
Cr_2O_3	0.00	0.10	0.01	0.00	0.00	0.03	0.03	0.02	0.05	0.02	0.04
FeO	13.84	14.17	16.87	16.62	16.05	17.01	15.89	16.63	15.87	16.40	16.18
MnO	0.26	0.25	0.29	0.23	0.26	0.27	0.22	0.28	0.27	0.25	0.24
MgO	46.16	45.86	43.62	43.79	44.62	43.84	44.88	44.10	44.69	44.02	43.68
NiO	0.28	0.23	0.24	0.23	0.29	0.24	0.21	0.23	0.25	0.26	0.27
CaO	0.00	0.02	0.09	0.01	0.02	0.03	0.01	0.01	0.01	0.04	0.05
Total	100.43	100.16	100.56	100.12	100.62	100.96	100.77	100.14	100.66	100.09	99.58
Cations per formula unit											
Si	0.99	0.99	0.99	0.99	0.99	0.99	0.99	0.98	0.99	0.99	0.99
Ti	0.00	0.00	0.00	0.00	0.00	0.00	0.00	0.00	0.00	0.00	0.00
Al	0.00	0.00	0.00	0.00	0.00	0.00	0.00	0.00	0.00	0.00	0.00
Cr	0.00	0.00	0.00	0.00	0.00	0.00	0.00	0.00	0.00	0.00	0.00
Fe^{2+}	0.29	0.30	0.36	0.35	0.34	0.36	0.33	0.35	0.33	0.35	0.34
Mn	0.01	0.01	0.01	0.00	0.01	0.01	0.00	0.01	0.01	0.01	0.01
Mg	1.71	1.71	1.64	1.65	1.67	1.64	1.68	1.67	1.67	1.66	1.65
Ni	0.01	0.00	0.00	0.00	0.01	0.00	0.00	0.00	0.01	0.01	0.01
Ca	0.00	0.00	0.00	0.00	0.00	0.00	0.00	0.00	0.00	0.00	0.00
Total	3.01	3.01	3.01	3.01	3.01	3.01	3.01	3.01	3.01	3.01	3.01
Fo	85.60	85.23	82.17	82.45	83.21	82.13	83.43	82.54	83.39	82.72	82.79

Sample # EN24VS015

Oxide wt%	ol10_3	ol11_1	ol11_2	ol11_3	ol11_4	ol12_1	ol12_2	ol12_3	ol12_4
SiO_2	38.86	38.91	39.52	39.67	39.52	39.36	39.73	40.47	39.78
TiO_2	0.00	0.01	0.01	0.00	0.01	0.00	0.00	0.00	0.00
Al_2O_3	0.01	0.00	0.00	0.00	0.00	0.00	0.00	0.01	0.00
Cr_2O_3	0.03	0.03	0.00	0.00	0.00	0.06	0.05	0.02	0.13
FeO	16.91	16.94	14.74	15.01	15.36	15.11	12.39	12.44	12.25
MnO	0.28	0.28	0.18	0.20	0.22	0.19	0.19	0.19	0.20
MgO	43.11	43.50	45.99	45.67	45.46	45.35	48.10	47.69	48.00
NiO	0.22	0.21	0.28	0.25	0.27	0.29	0.30	0.30	0.24
CaO	0.08	0.01	0.01	0.00	0.00	0.02	0.02	0.19	0.01
Total	99.50	99.91	100.71	100.81	100.85	100.38	100.78	101.30	100.60
Cations per formula unit									
Si	0.99	0.99	0.99	0.99	0.99	0.99	0.98	0.99	0.98
Ti	0.00	0.00	0.00	0.00	0.00	0.00	0.00	0.00	0.00
Al	0.00	0.00	0.00	0.00	0.00	0.00	0.00	0.00	0.00
Cr	0.00	0.00	0.00	0.00	0.00	0.00	0.00	0.00	0.00
Fe^{2+}	0.36	0.36	0.31	0.31	0.32	0.32	0.26	0.26	0.25
Mn	0.01	0.01	0.00	0.00	0.00	0.00	0.00	0.00	0.00
Mg	1.64	1.65	1.71	1.70	1.69	1.70	1.77	1.74	1.77
Ni	0.00	0.00	0.01	0.01	0.01	0.01	0.01	0.01	0.00
Ca	0.00	0.00	0.00	0.00	0.00	0.00	0.00	0.00	0.00
Total	3.01	3.01	3.01	3.01	3.01	3.01	3.02	3.01	3.02
Fo	81.96	82.07	84.76	84.43	84.06	84.25	87.37	87.24	87.48

Sample #EN24VS017

Oxide wt%	ol1_1	ol1_2	ol1_3	ol1_4	ol2_1	ol2_2	ol2_3	ol2_4	ol3_1	ol3_2	ol3_3
SiO_2	38.93	38.99	38.54	39.47	38.53	39.01	38.93	39.37	39.23	38.57	39.41
TiO_2	0.00	0.00	0.02	0.00	0.01	0.00	0.01	0.01	0.01	0.01	0.00
Al_2O_3	0.00	0.00	0.00	0.00	0.00	0.00	0.00	0.00	0.02	0.00	0.00
Cr_2O_3	0.00	0.00	0.01	0.00	0.02	0.00	0.00	0.02	0.00	0.06	0.02
FeO	17.20	16.31	17.28	17.24	17.92	16.95	16.22	16.70	17.43	16.74	16.37
MnO	0.24	0.19	0.27	0.23	0.33	0.25	0.24	0.22	0.28	0.22	0.21
MgO	43.26	44.69	43.94	44.20	43.22	43.75	44.03	44.06	43.18	43.54	44.26
NiO	0.23	0.27	0.25	0.26	0.22	0.25	0.26	0.21	0.29	0.28	0.25
CaO	0.01	0.01	0.01	0.01	0.01	0.01	0.00	0.00	0.38	0.00	0.00
Total	99.88	100.46	100.32	101.40	100.26	100.23	99.70	100.59	100.83	99.43	100.53
Cations per formula unit											
Si	0.99	0.98	0.98	0.99	0.98	0.99	0.99	0.99	0.99	0.99	0.99
Ti	0.00	0.00	0.00	0.00	0.00	0.00	0.00	0.00	0.00	0.00	0.00
Al	0.00	0.00	0.00	0.00	0.00	0.00	0.00	0.00	0.00	0.00	0.00
Cr	0.00	0.00	0.00	0.00	0.00	0.00	0.00	0.00	0.00	0.00	0.00
Fe^{2+}	0.37	0.34	0.37	0.36	0.38	0.36	0.34	0.35	0.37	0.36	0.34
Mn	0.01	0.00	0.01	0.00	0.01	0.01	0.01	0.00	0.01	0.00	0.00
Mg	1.64	1.68	1.66	1.65	1.64	1.65	1.67	1.65	1.63	1.66	1.66
Ni	0.00	0.01	0.01	0.01	0.00	0.01	0.01	0.00	0.01	0.01	0.01
Ca	0.00	0.00	0.00	0.00	0.00	0.00	0.00	0.00	0.01	0.00	0.00
Total	3.01	3.02	3.02	3.01	3.02	3.01	3.01	3.01	3.01	3.01	3.01
Fo	81.76	83.01	81.92	82.05	81.13	82.14	82.87	82.46	81.53	82.25	82.82

Sample #EN24VS017

Oxide wt%	ol3_4	ol3_5	ol4_1	ol4_2	ol4_3	ol4_4	ol5_1	ol5_2	ol5_3	ol5_4	ol6_1
SiO_2	38.76	39.08	38.55	38.76	38.69	38.60	38.51	38.92	39.08	38.65	38.74
TiO_2	0.00	0.00	0.02	0.02	0.01	0.00	0.00	0.01	0.01	0.03	0.01
Al_2O_3	0.00	0.00	0.00	0.01	0.00	0.00	0.00	0.00	0.00	0.01	0.00
Cr_2O_3	0.06	0.01	0.00	0.09	0.00	0.00	0.04	0.00	0.00	0.01	0.01
FeO	17.23	17.77	17.35	16.94	16.97	17.64	17.53	17.69	17.30	17.71	17.72
MnO	0.27	0.27	0.28	0.26	0.27	0.33	0.33	0.29	0.28	0.35	0.33
MgO	44.09	43.55	43.39	43.73	43.95	43.41	42.97	43.06	43.40	43.14	42.93
NiO	0.27	0.30	0.25	0.27	0.25	0.25	0.29	0.23	0.24	0.26	0.25
CaO	0.00	0.00	0.02	0.02	0.00	0.01	0.05	0.01	0.00	0.05	0.01
Total	100.68	100.99	99.87	100.10	100.15	100.24	99.73	100.22	100.32	100.20	99.99
Cations per formula unit											
Si	0.98	0.99	0.98	0.98	0.98	0.98	0.99	0.99	0.99	0.98	0.99
Ti	0.00	0.00	0.00	0.00	0.00	0.00	0.00	0.00	0.00	0.00	0.00
Al	0.00	0.00	0.00	0.00	0.00	0.00	0.00	0.00	0.00	0.00	0.00
Cr	0.00	0.00	0.00	0.00	0.00	0.00	0.00	0.00	0.00	0.00	0.00
Fe^{2+}	0.36	0.38	0.37	0.36	0.36	0.38	0.38	0.38	0.37	0.38	0.38
Mn	0.01	0.01	0.01	0.01	0.01	0.01	0.01	0.01	0.01	0.01	0.01
Mg	1.66	1.64	1.65	1.66	1.66	1.65	1.64	1.63	1.64	1.64	1.63
Ni	0.01	0.01	0.01	0.01	0.01	0.01	0.01	0.00	0.00	0.01	0.01
Ca	0.00	0.00	0.00	0.00	0.00	0.00	0.00	0.00	0.00	0.00	0.00
Total	3.02	3.01	3.02	3.01	3.02	3.02	3.01	3.01	3.01	3.01	3.01
Fo	82.02	81.38	81.67	82.15	82.19	81.44	81.37	81.27	81.72	81.28	81.20

Sample #EN24VS017

Oxide wt%	ol6_2	ol6_3	ol6_4	ol6_5	ol7_1	ol7_2	ol7_3	ol7_4	ol8_1	ol8_2	ol8_3
SiO_2	38.19	38.46	38.78	38.96	38.82	38.87	38.78	39.09	38.44	39.11	39.13
TiO_2	0.02	0.01	0.01	0.00	0.00	0.01	0.00	0.00	0.01	0.02	0.01
Al_2O_3	0.00	0.01	0.01	0.00	0.00	0.00	0.00	0.00	0.00	0.00	0.01
Cr_2O_3	0.27	0.02	0.00	0.01	0.03	0.00	0.11	0.01	0.01	0.02	0.02
FeO	18.39	16.64	17.29	17.05	17.70	15.98	16.64	17.55	17.83	17.99	17.88
MnO	0.27	0.23	0.29	0.24	0.35	0.25	0.32	0.34	0.33	0.31	0.27
MgO	42.82	44.05	43.12	43.68	42.87	44.19	43.59	43.39	42.95	43.34	43.07
NiO	0.24	0.30	0.23	0.28	0.22	0.29	0.29	0.29	0.27	0.29	0.29
CaO	0.02	0.01	0.04	0.01	0.01	0.01	0.01	0.02	0.02	0.01	0.05
Total	100.21	99.72	99.76	100.24	100.01	99.59	99.75	100.72	99.85	101.08	100.72
Cations per formula unit											
Si	0.98	0.98	0.99	0.99	0.99	0.99	0.99	0.99	0.98	0.99	0.99
Ti	0.00	0.00	0.00	0.00	0.00	0.00	0.00	0.00	0.00	0.00	0.00
Al	0.00	0.00	0.00	0.00	0.00	0.00	0.00	0.00	0.00	0.00	0.00
Cr	0.01	0.00	0.00	0.00	0.00	0.00	0.00	0.00	0.00	0.00	0.00
Fe^{2+}	0.39	0.35	0.37	0.36	0.38	0.34	0.35	0.37	0.38	0.38	0.38
Mn	0.01	0.01	0.01	0.01	0.01	0.01	0.01	0.01	0.01	0.01	0.01
Mg	1.63	1.67	1.64	1.65	1.63	1.67	1.65	1.64	1.64	1.63	1.63
Ni	0.00	0.01	0.00	0.01	0.00	0.01	0.01	0.01	0.01	0.01	0.01
Ca	0.00	0.00	0.00	0.00	0.00	0.00	0.00	0.00	0.00	0.00	0.00
Total	3.02	3.02	3.01	3.01	3.01	3.01	3.01	3.01	3.02	3.01	3.01
Fo	80.58	82.52	81.64	82.04	81.19	83.13	82.37	81.50	81.11	81.11	81.11

Sample #EN24VS017

Oxide wt%	ol8_4	ol9_1	ol9_2	ol9_3	ol9_4	ol9_5	ol10_1	ol10_2	ol10_3	ol10_4	ol10_5
SiO_2	38.31	38.96	39.18	39.34	39.16	39.55	38.40	39.39	39.38	39.02	38.68
TiO_2	0.01	0.01	0.00	0.00	0.00	0.00	0.00	0.00	0.00	0.00	0.00
Al_2O_3	0.01	0.00	0.00	0.00	0.00	0.00	0.00	0.00	0.00	0.01	0.00
Cr_2O_3	0.01	0.05	0.01	0.03	0.01	0.00	0.01	0.00	0.00	0.00	0.01
FeO	18.09	18.12	15.93	16.23	16.33	16.52	16.14	15.09	14.96	15.34	15.21
MnO	0.34	0.28	0.22	0.25	0.35	0.25	0.23	0.28	0.24	0.27	0.18
MgO	42.82	42.90	44.67	44.89	44.72	44.28	44.31	45.34	45.39	45.01	45.07
NiO	0.26	0.23	0.26	0.26	0.28	0.32	0.27	0.28	0.27	0.28	0.31
CaO	0.04	0.02	0.00	0.02	0.01	0.01	0.03	0.03	0.00	0.01	0.02
Total	99.88	100.58	100.26	101.02	100.86	100.92	99.41	100.41	100.24	99.95	99.48
Cations per formula unit											
Si	0.98	0.99	0.99	0.99	0.98	0.99	0.98	0.99	0.99	0.99	0.98
Ti	0.00	0.00	0.00	0.00	0.00	0.00	0.00	0.00	0.00	0.00	0.00
Al	0.00	0.00	0.00	0.00	0.00	0.00	0.00	0.00	0.00	0.00	0.00
Cr	0.00	0.00	0.00	0.00	0.00	0.00	0.00	0.00	0.00	0.00	0.00
Fe^{2+}	0.39	0.38	0.34	0.34	0.34	0.35	0.34	0.32	0.31	0.32	0.32
Mn	0.01	0.01	0.00	0.01	0.01	0.01	0.00	0.01	0.01	0.01	0.00
Mg	1.64	1.62	1.68	1.68	1.68	1.66	1.68	1.70	1.70	1.69	1.70
Ni	0.01	0.00	0.01	0.01	0.01	0.01	0.01	0.01	0.01	0.01	0.01
Ca	0.00	0.00	0.00	0.00	0.00	0.00	0.00	0.00	0.00	0.00	0.00
Total	3.02	3.01	3.01	3.01	3.02	3.01	3.02	3.01	3.01	3.01	3.02
Fo	80.84	80.84	83.33	83.14	83.00	82.69	83.03	84.26	84.39	83.95	84.08

Sample #EN24VS017					**Sample #EN24VS032**					
Oxide wt%	ol11_1	ol11_2	ol11_3	ol11_4	ol1_1	ol1_2	ol1_3	ol1_4	ol1_5	ol2_1
SiO_2	38.80	38.45	39.20	39.21	39.50	39.37	40.10	39.37	39.31	39.42
TiO_2	0.00	0.01	0.00	0.01	0.01	0.01	0.02	0.00	0.01	0.01
Al_2O_3	0.00	0.01	0.00	0.00	0.01	0.00	0.00	0.00	0.00	0.00
Cr_2O_3	0.00	0.08	0.01	0.02	0.00	0.01	0.01	0.03	0.03	0.02
FeO	17.19	16.50	16.53	16.94	15.86	14.01	13.21	13.16	13.98	13.20
MnO	0.32	0.28	0.27	0.28	0.26	0.27	0.20	0.14	0.18	0.16
MgO	43.56	44.25	44.69	43.95	44.39	46.23	46.87	47.01	46.78	47.00
NiO	0.29	0.26	0.30	0.27	0.29	0.33	0.30	0.31	0.27	0.30
CaO	0.01	0.05	0.00	0.00	0.04	0.01	0.00	0.02	0.02	0.01
Total	100.19	99.90	101.01	100.68	100.36	100.25	100.73	100.05	100.58	100.14
Cations per formula unit										
Si	0.99	0.98	0.98	0.99	0.99	0.98	0.99	0.98	0.98	0.98
Ti	0.00	0.00	0.00	0.00	0.00	0.00	0.00	0.00	0.00	0.00
Al	0.00	0.00	0.00	0.00	0.00	0.00	0.00	0.00	0.00	0.00
Cr	0.00	0.00	0.00	0.00	0.00	0.00	0.00	0.00	0.00	0.00
Fe^{2+}	0.37	0.35	0.35	0.36	0.33	0.29	0.27	0.27	0.29	0.28
Mn	0.01	0.01	0.01	0.01	0.01	0.01	0.00	0.00	0.00	0.00
Mg	1.65	1.68	1.67	1.65	1.67	1.72	1.73	1.75	1.74	1.75
Ni	0.01	0.01	0.01	0.01	0.01	0.01	0.01	0.01	0.01	0.01
Ca	0.00	0.00	0.00	0.00	0.00	0.00	0.00	0.00	0.00	0.00
Total	3.01	3.02	3.02	3.01	3.01	3.01	3.01	3.02	3.02	3.02
Fo	81.87	82.70	82.82	82.22	83.31	85.47	86.34	86.42	85.64	86.39

Sample #EN24VS032											
Oxide wt%	ol2_2	ol2_3	ol2_4	ol2_5	ol3_1	ol3_2	ol3_4	ol4_1	ol4_2	ol4_3	ol4_4
SiO_2	40.04	39.14	39.61	40.10	39.41	39.02	39.63	39.37	39.20	38.99	39.51
TiO_2	0.00	0.01	0.00	0.00	0.00	0.01	0.01	0.00	0.00	0.02	0.00
Al_2O_3	0.00	0.00	0.00	0.02	0.02	0.00	0.00	0.01	0.00	0.00	0.00
Cr_2O_3	0.01	0.00	0.01	0.03	0.03	0.06	0.00	0.01	0.02	0.02	0.03
FeO	12.45	12.25	12.82	14.11	13.57	13.98	13.83	15.16	14.27	14.30	14.59
MnO	0.17	0.18	0.20	0.22	0.22	0.21	0.18	0.29	0.19	0.23	0.22
MgO	47.51	47.44	47.64	45.43	46.13	46.60	46.42	45.62	45.97	45.56	45.67
NiO	0.29	0.28	0.30	0.27	0.28	0.32	0.28	0.29	0.28	0.30	0.29
CaO	0.12	0.00	0.01	0.09	0.08	0.01	0.01	0.02	0.02	0.03	0.02
Total	100.60	99.29	100.59	100.27	99.74	100.22	100.36	100.78	99.96	99.45	100.34
Cations per formula unit											
Si	0.99	0.98	0.98	1.00	0.99	0.98	0.99	0.98	0.98	0.98	0.99
Ti	0.00	0.00	0.00	0.00	0.00	0.00	0.00	0.00	0.00	0.00	0.00
Al	0.00	0.00	0.00	0.00	0.00	0.00	0.00	0.00	0.00	0.00	0.00
Cr	0.00	0.00	0.00	0.00	0.00	0.00	0.00	0.00	0.00	0.00	0.00
Fe^{2+}	0.26	0.26	0.27	0.29	0.28	0.29	0.29	0.32	0.30	0.30	0.31
Mn	0.00	0.00	0.00	0.00	0.00	0.00	0.00	0.01	0.00	0.00	0.00
Mg	1.75	1.77	1.76	1.69	1.72	1.74	1.73	1.70	1.72	1.72	1.70
Ni	0.01	0.01	0.01	0.01	0.01	0.01	0.01	0.01	0.01	0.01	0.01
Ca	0.00	0.00	0.00	0.00	0.00	0.00	0.00	0.00	0.00	0.00	0.00
Total	3.01	3.02	3.02	3.00	3.01	3.02	3.01	3.02	3.02	3.01	3.01
Fo	87.18	87.35	86.88	85.16	85.83	85.59	85.68	84.29	85.17	85.03	84.80

Sample #EN24VS032

Oxide wt%	ol5_1	ol5_2	ol5_3	ol5_4	ol5_5	ol6_1	ol6_2	ol6_3	ol6_4	ol6_5	ol7_1
SiO_2	39.23	39.75	39.27	39.67	39.83	39.25	39.65	39.56	39.61	39.64	39.57
TiO_2	0.00	0.00	0.01	0.00	0.01	0.00	0.01	0.01	0.00	0.00	0.00
Al_2O_3	0.00	0.00	0.00	0.00	0.00	0.02	0.00	0.03	0.00	0.01	0.01
Cr_2O_3	0.02	0.00	0.02	0.01	0.00	0.00	0.00	0.00	0.02	0.00	0.03
FeO	14.30	13.89	13.85	13.54	14.45	14.33	13.36	12.57	14.61	13.23	13.62
MnO	0.23	0.22	0.19	0.21	0.23	0.20	0.15	0.17	0.22	0.19	0.19
MgO	45.85	47.05	46.38	46.70	46.15	45.97	47.09	45.86	45.63	46.59	46.08
NiO	0.28	0.27	0.29	0.27	0.32	0.28	0.30	0.31	0.27	0.32	0.25
CaO	0.01	0.01	0.04	0.02	0.01	0.06	0.02	0.85	0.00	0.10	0.24
Total	99.92	101.18	100.06	100.41	101.00	100.10	100.58	99.36	100.37	100.08	100.00
Cations per formula unit											
Si	0.99	0.98	0.98	0.99	0.99	0.98	0.98	0.99	0.99	0.99	0.99
Ti	0.00	0.00	0.00	0.00	0.00	0.00	0.00	0.00	0.00	0.00	0.00
Al	0.00	0.00	0.00	0.00	0.00	0.00	0.00	0.00	0.00	0.00	0.00
Cr	0.00	0.00	0.00	0.00	0.00	0.00	0.00	0.00	0.00	0.00	0.00
Fe^{2+}	0.30	0.29	0.29	0.28	0.30	0.30	0.28	0.26	0.31	0.28	0.28
Mn	0.00	0.00	0.00	0.00	0.00	0.00	0.00	0.00	0.00	0.00	0.00
Mg	1.72	1.74	1.73	1.73	1.71	1.72	1.74	1.72	1.70	1.73	1.72
Ni	0.01	0.01	0.01	0.01	0.01	0.01	0.01	0.01	0.01	0.01	0.01
Ca	0.00	0.00	0.00	0.00	0.00	0.00	0.00	0.02	0.00	0.00	0.01
Total	3.01	3.02	3.02	3.01	3.01	3.02	3.02	3.01	3.01	3.01	3.01
Fo	85.11	85.79	85.65	86.01	85.06	85.12	86.27	86.67	84.77	86.26	85.78

Sample #EN24VS032

Oxide wt%	ol7_2	ol7_3	ol7_4	ol8_1	ol8_2	ol8_3	ol8_4	ol8_5	ol9_1	ol9_2	ol9_3
SiO_2	39.29	40.54	39.59	39.36	40.24	39.75	39.83	39.88	39.53	39.44	39.86
TiO_2	0.00	0.01	0.01	0.01	0.02	0.00	0.00	0.02	0.01	0.00	0.00
Al_2O_3	0.00	0.03	0.00	0.00	0.00	0.00	0.03	0.00	0.00	0.00	0.01
Cr_2O_3	0.03	0.04	0.04	0.00	0.03	0.01	0.04	0.01	0.00	0.02	0.01
FeO	13.09	12.48	13.86	14.30	13.02	12.70	12.84	13.41	14.93	13.80	13.25
MnO	0.20	0.18	0.25	0.24	0.22	0.20	0.19	0.22	0.25	0.15	0.19
MgO	47.08	45.54	46.57	45.74	47.35	47.83	46.69	46.82	46.11	46.20	46.68
NiO	0.28	0.24	0.27	0.30	0.25	0.31	0.27	0.32	0.27	0.29	0.28
CaO	0.01	1.23	0.02	0.01	0.01	0.01	0.25	0.00	0.02	0.02	0.02
Total	99.98	100.28	100.62	99.96	101.15	100.82	100.14	100.68	101.12	99.92	100.30
Cations per formula unit											
Si	0.98	1.01	0.99	0.99	0.99	0.98	0.99	0.99	0.98	0.99	0.99
Ti	0.00	0.00	0.00	0.00	0.00	0.00	0.00	0.00	0.00	0.00	0.00
Al	0.00	0.00	0.00	0.00	0.00	0.00	0.00	0.00	0.00	0.00	0.00
Cr	0.00	0.00	0.00	0.00	0.00	0.00	0.00	0.00	0.00	0.00	0.00
Fe^{2+}	0.27	0.26	0.29	0.30	0.27	0.26	0.27	0.28	0.31	0.29	0.28
Mn	0.00	0.00	0.01	0.01	0.00	0.00	0.00	0.00	0.01	0.00	0.00
Mg	1.75	1.68	1.73	1.71	1.74	1.76	1.73	1.73	1.71	1.72	1.73
Ni	0.01	0.00	0.01	0.01	0.00	0.01	0.01	0.01	0.01	0.01	0.01
Ca	0.00	0.03	0.00	0.00	0.00	0.00	0.01	0.00	0.00	0.00	0.00
Total	3.02	2.99	3.01	3.01	3.01	3.02	3.01	3.01	3.02	3.01	3.01
Fo	86.50	86.68	85.69	85.08	86.63	87.03	86.64	86.15	84.63	85.65	86.26

Sample #EN24VS032

Oxide wt%	ol9_4	ol10_1	ol10_2	ol10_3	ol10_4	ol10_5	ol11_1	ol11_2	ol11_3	ol11_4	ol11_5
SiO_2	39.54	40.54	39.42	39.93	40.12	38.99	39.31	39.53	39.41	39.52	39.63
TiO_2	0.00	0.01	0.01	0.00	0.00	0.01	0.01	0.00	0.00	0.01	0.01
Al_2O_3	0.00	0.01	0.00	0.05	0.02	0.00	0.00	0.00	0.03	0.09	0.00
Cr_2O_3	0.03	0.05	0.00	0.03	0.00	0.00	0.00	0.01	0.01	0.04	0.01
FeO	12.96	12.58	12.85	12.32	12.65	12.94	13.74	12.93	13.18	13.47	13.48
MnO	0.16	0.20	0.19	0.16	0.20	0.17	0.16	0.20	0.22	0.22	0.18
MgO	46.53	48.26	47.38	46.97	47.11	47.33	46.52	47.18	46.74	45.88	47.27
NiO	0.31	0.32	0.30	0.33	0.33	0.33	0.27	0.25	0.32	0.29	0.27
CaO	0.01	0.02	0.05	0.36	0.00	0.00	0.12	0.00	0.02	0.30	0.02
Total	99.53	101.99	100.20	100.15	100.44	99.78	100.13	100.11	99.92	99.81	100.86
Cations per formula unit											
Si	0.99	0.99	0.98	0.99	0.99	0.98	0.98	0.98	0.99	0.99	0.98
Ti	0.00	0.00	0.00	0.00	0.00	0.00	0.00	0.00	0.00	0.00	0.00
Al	0.00	0.00	0.00	0.00	0.00	0.00	0.00	0.00	0.00	0.00	0.00
Cr	0.00	0.00	0.00	0.00	0.00	0.00	0.00	0.00	0.00	0.00	0.00
Fe^{2+}	0.27	0.26	0.27	0.26	0.26	0.27	0.29	0.27	0.28	0.28	0.28
Mn	0.00	0.00	0.00	0.00	0.00	0.00	0.00	0.00	0.00	0.00	0.00
Mg	1.74	1.75	1.76	1.74	1.74	1.77	1.73	1.75	1.74	1.71	1.75
Ni	0.01	0.01	0.01	0.01	0.01	0.01	0.01	0.01	0.01	0.01	0.01
Ca	0.00	0.00	0.00	0.01	0.00	0.00	0.00	0.00	0.00	0.01	0.00
Total	3.01	3.01	3.02	3.01	3.01	3.02	3.02	3.02	3.01	3.01	3.02
Fo	86.49	87.24	86.79	87.17	86.91	86.70	85.79	86.67	86.35	85.86	86.21

Sample #EN24VS033

Oxide wt%	ol1_1	ol1_2	ol1_3	ol1_4	ol2_1	ol2_2	ol2_3	ol2_4	ol2_5	ol3_1	ol3_2
SiO_2	39.23	39.49	39.59	39.89	39.18	38.92	39.61	39.23	39.49	39.05	38.76
TiO_2	0.02	0.00	0.01	0.01	0.01	0.01	0.00	0.02	0.00	0.00	0.00
Al_2O_3	0.00	0.00	0.00	0.00	0.00	0.00	0.01	0.01	0.01	0.00	0.00
Cr_2O_3	0.02	0.01	0.03	0.00	0.00	0.01	0.00	0.00	0.00	0.00	0.01
FeO	13.09	12.82	13.17	13.68	13.94	15.01	14.32	13.79	14.48	14.30	14.39
MnO	0.36	0.36	0.30	0.31	0.31	0.27	0.31	0.31	0.31	0.28	0.24
MgO	46.38	46.86	46.85	46.67	46.16	44.86	45.60	45.71	45.97	45.37	45.25
NiO	0.15	0.17	0.20	0.21	0.22	0.21	0.25	0.21	0.25	0.24	0.19
CaO	0.12	0.01	0.01	0.01	0.00	0.19	0.05	0.06	0.03	0.00	0.01
Total	99.36	99.72	100.16	100.79	99.83	99.47	100.14	99.34	100.55	99.24	98.85
Cations per formula unit											
Si	0.99	0.99	0.99	0.99	0.98	0.99	0.99	0.99	0.99	0.99	0.99
Ti	0.00	0.00	0.00	0.00	0.00	0.00	0.00	0.00	0.00	0.00	0.00
Al	0.00	0.00	0.00	0.00	0.00	0.00	0.00	0.00	0.00	0.00	0.00
Cr	0.00	0.00	0.00	0.00	0.00	0.00	0.00	0.00	0.00	0.00	0.00
Fe^{2+}	0.28	0.27	0.27	0.28	0.29	0.32	0.30	0.29	0.30	0.30	0.31
Mn	0.01	0.01	0.01	0.01	0.01	0.01	0.01	0.01	0.01	0.01	0.01
Mg	1.74	1.75	1.74	1.73	1.73	1.69	1.70	1.72	1.71	1.71	1.71
Ni	0.00	0.00	0.00	0.00	0.00	0.00	0.00	0.00	0.01	0.00	0.00
Ca	0.00	0.00	0.00	0.00	0.00	0.01	0.00	0.00	0.00	0.00	0.00
Total	3.01	3.01	3.01	3.01	3.02	3.01	3.01	3.01	3.01	3.01	3.01
Fo	86.34	86.70	86.37	85.87	85.51	84.20	85.03	85.53	84.98	84.98	84.86

Sample #EN24VS033

Oxide wt%	ol3_3	ol3_4	ol3_5	ol4_1	ol4_2	ol4_3	ol4_4	ol4_5	ol5_1	ol5_2	ol5_3	ol5_4
SiO_2	38.86	38.81	38.90	39.60	39.57	39.68	39.66	38.92	39.12	39.19	39.22	39.41
TiO_2	0.01	0.00	0.00	0.01	0.01	0.02	0.01	0.02	0.00	0.00	0.01	0.00
Al_2O_3	0.00	0.00	0.00	0.00	0.00	0.00	0.00	0.01	0.00	0.00	0.01	0.01
Cr_2O_3	0.02	0.00	0.02	0.00	0.00	0.00	0.02	0.01	0.01	0.00	0.00	0.01
FeO	14.81	15.45	13.46	12.12	12.93	13.17	12.84	12.98	13.91	14.48	14.85	14.39
MnO	0.26	0.27	0.34	0.33	0.32	0.35	0.32	0.38	0.33	0.32	0.24	0.28
MgO	44.96	45.11	46.27	47.34	46.69	46.82	46.85	46.23	46.13	45.24	45.23	45.35
NiO	0.23	0.22	0.20	0.15	0.18	0.13	0.18	0.17	0.26	0.23	0.24	0.24
CaO	0.01	0.02	0.00	0.02	0.01	0.01	0.02	0.08	0.01	0.01	0.01	0.07
Total	99.16	99.89	99.20	99.57	99.72	100.18	99.90	98.80	99.76	99.48	99.80	99.76
Cations per formula unit												
Si	0.99	0.98	0.98	0.99	0.99	0.99	0.99	0.98	0.98	0.99	0.99	0.99
Ti	0.00	0.00	0.00	0.00	0.00	0.00	0.00	0.00	0.00	0.00	0.00	0.00
Al	0.00	0.00	0.00	0.00	0.00	0.00	0.00	0.00	0.00	0.00	0.00	0.00
Cr	0.00	0.00	0.00	0.00	0.00	0.00	0.00	0.00	0.00	0.00	0.00	0.00
Fe^{2+}	0.31	0.33	0.28	0.25	0.27	0.27	0.27	0.27	0.29	0.31	0.31	0.30
Mn	0.01	0.01	0.01	0.01	0.01	0.01	0.01	0.01	0.01	0.01	0.01	0.01
Mg	1.70	1.70	1.74	1.76	1.74	1.74	1.74	1.74	1.73	1.70	1.70	1.70
Ni	0.00	0.00	0.00	0.00	0.00	0.00	0.00	0.00	0.01	0.00	0.00	0.00
Ca	0.00	0.00	0.00	0.00	0.00	0.00	0.00	0.00	0.00	0.00	0.00	0.00
Total	3.01	3.02	3.02	3.01	3.01	3.01	3.01	3.02	3.02	3.01	3.01	3.01
Fo	84.40	83.88	85.97	87.44	86.55	86.37	86.67	86.40	85.53	84.78	84.45	84.89

Sample #EN24VS033

Oxide wt%	ol5_5	ol6_1	ol6_2	ol6_3	ol6_4	ol6_5	ol7_1	ol7_2	ol7_3	ol7_4	ol7_5
SiO_2	39.51	39.42	39.47	39.20	39.56	39.46	39.41	39.04	39.33	39.18	39.59
TiO_2	0.03	0.00	0.01	0.00	0.01	0.00	0.02	0.01	0.02	0.00	0.01
Al_2O_3	0.00	0.00	0.00	0.01	0.00	0.00	0.00	0.00	0.00	0.01	0.01
Cr_2O_3	0.00	0.00	0.00	0.01	0.00	0.04	0.00	0.00	0.00	0.01	0.00
FeO	14.14	13.91	13.45	14.45	14.26	13.28	12.51	13.83	13.71	13.14	13.59
MnO	0.28	0.33	0.37	0.24	0.32	0.32	0.40	0.30	0.33	0.31	0.32
MgO	45.57	46.34	46.72	45.09	45.43	46.72	47.37	45.82	46.00	46.65	45.98
NiO	0.21	0.21	0.25	0.24	0.20	0.25	0.21	0.24	0.26	0.24	0.26
CaO	0.01	0.01	0.01	0.02	0.01	0.01	0.01	0.09	0.00	0.02	0.13
Total	99.74	100.22	100.28	99.25	99.79	100.07	99.92	99.33	99.66	99.56	99.89
Cations per formula unit											
Si	0.99	0.99	0.98	0.99	0.99	0.99	0.98	0.99	0.99	0.98	0.99
Ti	0.00	0.00	0.00	0.00	0.00	0.00	0.00	0.00	0.00	0.00	0.00
Al	0.00	0.00	0.00	0.00	0.00	0.00	0.00	0.00	0.00	0.00	0.00
Cr	0.00	0.00	0.00	0.00	0.00	0.00	0.00	0.00	0.00	0.00	0.00
Fe^{2+}	0.30	0.29	0.28	0.31	0.30	0.28	0.26	0.29	0.29	0.28	0.28
Mn	0.01	0.01	0.01	0.01	0.01	0.01	0.01	0.01	0.01	0.01	0.01
Mg	1.71	1.73	1.74	1.70	1.70	1.74	1.76	1.72	1.72	1.74	1.72
Ni	0.00	0.00	0.01	0.00	0.00	0.00	0.00	0.00	0.01	0.00	0.01
Ca	0.00	0.00	0.00	0.00	0.00	0.00	0.00	0.00	0.00	0.00	0.00
Total	3.01	3.01	3.02	3.01	3.01	3.01	3.02	3.01	3.01	3.02	3.01
Fo	85.17	85.59	86.10	84.76	85.03	86.25	87.10	85.51	85.67	86.35	85.78

Sample #EN24VS033

Oxide wt%	ol8_1	ol8_2	ol8_3	ol8_4	ol8_5	ol9_1	ol9_2	ol9_3	ol9_4	ol9_5	ol10_1
SiO_2	39.38	39.17	39.33	39.23	38.97	39.12	38.80	39.44	39.05	38.75	38.94
TiO_2	0.01	0.00	0.00	0.00	0.00	0.01	0.00	0.00	0.02	0.01	0.00
Al_2O_3	0.01	0.00	0.01	0.00	0.00	0.00	0.01	0.00	0.00	0.00	0.00
Cr_2O_3	0.02	0.02	0.03	0.00	0.02	0.02	0.00	0.00	0.02	0.01	0.02
FeO	13.85	13.65	13.39	13.83	14.30	13.67	15.34	14.12	14.16	15.31	14.08
MnO	0.32	0.28	0.26	0.22	0.29	0.28	0.25	0.30	0.32	0.25	0.37
MgO	46.43	46.13	46.56	45.88	45.87	46.21	45.06	45.96	45.52	44.84	45.64
NiO	0.19	0.18	0.20	0.23	0.20	0.16	0.27	0.22	0.25	0.18	0.25
CaO	0.01	0.11	0.01	0.00	0.02	0.02	0.01	0.01	0.01	0.01	0.01
Total	100.21	99.55	99.78	99.39	99.67	99.48	99.73	100.04	99.35	99.36	99.31
Cations per formula unit											
Si	0.98	0.99	0.99	0.99	0.98	0.98	0.98	0.99	0.99	0.98	0.98
Ti	0.00	0.00	0.00	0.00	0.00	0.00	0.00	0.00	0.00	0.00	0.00
Al	0.00	0.00	0.00	0.00	0.00	0.00	0.00	0.00	0.00	0.00	0.00
Cr	0.00	0.00	0.00	0.00	0.00	0.00	0.00	0.00	0.00	0.00	0.00
Fe^{2+}	0.29	0.29	0.28	0.29	0.30	0.29	0.32	0.30	0.30	0.33	0.30
Mn	0.01	0.01	0.01	0.00	0.01	0.01	0.01	0.01	0.01	0.01	0.01
Mg	1.73	1.73	1.74	1.72	1.72	1.73	1.70	1.72	1.71	1.70	1.72
Ni	0.00	0.00	0.00	0.00	0.00	0.00	0.01	0.00	0.01	0.00	0.01
Ca	0.00	0.00	0.00	0.00	0.00	0.00	0.00	0.00	0.00	0.00	0.00
Total	3.02	3.01	3.01	3.01	3.02	3.02	3.02	3.01	3.01	3.02	3.02
Fo	85.66	85.77	86.11	85.54	85.11	85.77	83.97	85.30	85.14	83.92	85.24

Sample #EN24VS033

Oxide wt%	ol10_2	ol10_3	ol10_4	ol11_1	ol11_2	ol11_3	ol11_4	ol11_5
SiO_2	39.14	39.15	39.26	39.09	39.14	39.05	39.45	39.42
TiO_2	0.00	0.00	0.01	0.01	0.00	0.02	0.00	0.00
Al_2O_3	0.00	0.00	0.04	0.00	0.00	0.01	0.01	0.01
Cr_2O_3	0.00	0.00	0.01	0.01	0.00	0.00	0.01	0.00
FeO	14.69	15.08	14.13	13.37	13.81	13.40	13.64	13.53
MnO	0.31	0.33	0.30	0.35	0.36	0.37	0.30	0.29
MgO	45.29	45.56	45.10	46.37	45.85	45.76	46.44	46.19
NiO	0.22	0.27	0.23	0.19	0.25	0.22	0.27	0.26
CaO	0.01	0.00	0.38	0.01	0.01	0.18	0.02	0.01
Total	99.67	100.39	99.44	99.41	99.42	98.99	100.14	99.70
Cations per formula unit								
Si	0.99	0.98	0.99	0.98	0.99	0.99	0.99	0.99
Ti	0.00	0.00	0.00	0.00	0.00	0.00	0.00	0.00
Al	0.00	0.00	0.00	0.00	0.00	0.00	0.00	0.00
Cr	0.00	0.00	0.00	0.00	0.00	0.00	0.00	0.00
Fe^{2+}	0.31	0.32	0.30	0.28	0.29	0.28	0.29	0.28
Mn	0.01	0.01	0.01	0.01	0.01	0.01	0.01	0.01
Mg	1.70	1.71	1.70	1.74	1.72	1.72	1.73	1.73
Ni	0.00	0.01	0.00	0.00	0.01	0.00	0.01	0.01
Ca	0.00	0.00	0.01	0.00	0.00	0.00	0.00	0.00
Total	3.01	3.02	3.01	3.02	3.01	3.01	3.01	3.01
Fo	84.60	84.34	85.05	86.08	85.54	85.89	85.86	85.89

Appendix D3: Pyroxene University of Manitoba

Sample #EN23VS043

Oxide wt%	pyx1_1	pyx1_2	pyx1_3	pyx1_4	pyx1_5	pyx1_6	pyx2_1	pyx2_2	pyx2_3	pyx2_4	pyx2_5	pyx2_6	pyx3_1	pyx3_2	pyx3_3
SiO_2	56.12	56.33	56.01	55.71	56.11	54.95	55.51	56.16	55.68	55.33	56.30	55.80	56.41	55.47	55.99
TiO_2	0.09	0.09	0.08	0.08	0.08	0.13	0.06	0.08	0.09	0.10	0.09	0.08	0.08	0.23	0.07
Al_2O_3	1.73	1.70	1.62	1.63	1.35	2.20	1.49	1.60	1.60	1.91	1.71	1.82	1.65	2.01	1.58
Cr_2O_3	0.67	0.59	0.69	0.65	0.60	0.74	0.56	0.68	0.74	0.63	0.69	0.70	0.60	0.60	0.61
FeO	7.29	7.46	7.25	7.18	7.31	7.88	7.34	7.08	7.21	7.36	7.47	7.26	7.19	7.78	7.18
MnO	0.16	0.17	0.16	0.13	0.14	0.18	0.17	0.18	0.17	0.18	0.17	0.15	0.17	0.22	0.20
MgO	32.31	32.25	32.49	32.52	32.96	31.88	32.86	32.57	32.83	31.68	32.15	32.03	32.11	32.51	32.45
NiO	0.07	0.09	0.10	0.11	0.11	0.11	0.09	0.10	0.08	0.07	0.09	0.09	0.11	0.10	0.10
CaO	1.94	1.99	1.73	1.80	1.65	1.87	1.94	1.73	1.68	2.30	2.06	2.08	2.27	1.24	2.03
Na_2O	0.03	0.02	0.03	0.03	0.03	0.05	0.04	0.03	0.02	0.03	0.03	0.03	0.02	0.00	0.04
Total	100.42	100.70	100.18	99.82	100.34	100.00	100.07	100.22	100.10	99.60	100.77	100.04	100.61	100.16	100.25
Cations per formula unit															
Si	1.95	1.95	1.95	1.95	1.95	1.93	1.94	1.95	1.94	1.94	1.95	1.95	1.95	1.93	1.95
Ti	0.00	0.00	0.00	0.00	0.00	0.00	0.00	0.00	0.00	0.00	0.00	0.00	0.00	0.01	0.00
Al	0.07	0.07	0.07	0.07	0.06	0.09	0.06	0.07	0.07	0.08	0.07	0.07	0.07	0.08	0.06
Cr	0.02	0.02	0.02	0.02	0.02	0.02	0.02	0.02	0.02	0.02	0.02	0.02	0.02	0.02	0.02
Fe^{2+}	0.21	0.22	0.21	0.21	0.21	0.23	0.21	0.21	0.21	0.22	0.22	0.21	0.21	0.23	0.21
Mn	0.00	0.00	0.00	0.00	0.00	0.01	0.01	0.01	0.01	0.01	0.00	0.00	0.00	0.01	0.01
Mg	1.67	1.67	1.69	1.69	1.71	1.66	1.71	1.69	1.71	1.66	1.66	1.67	1.66	1.69	1.68
Ni	0.00	0.00	0.00	0.00	0.00	0.00	0.00	0.00	0.00	0.00	0.00	0.00	0.00	0.00	0.00
Ca	0.07	0.07	0.06	0.07	0.06	0.07	0.07	0.06	0.06	0.09	0.08	0.08	0.08	0.05	0.08
Na	0.00	0.00	0.00	0.00	0.00	0.00	0.00	0.00	0.00	0.00	0.00	0.00	0.00	0.00	0.00
Total	4.01	4.00	4.01	4.01	4.01	4.02	4.02	4.01	4.02	4.01	4.00	4.01	4.00	4.01	4.01
En	85.49	85.17	85.95	85.94	86.17	84.69	85.62	86.20	86.20	84.56	85.00	85.18	85.01	86.08	85.53
Fs	10.82	11.05	10.76	10.65	10.72	11.75	10.74	10.51	10.62	11.02	11.08	10.84	10.68	11.56	10.62
Wo	3.69	3.77	3.30	3.41	3.11	3.57	3.64	3.29	3.17	4.41	3.92	3.98	4.32	2.37	3.85

Sample #EN23VS043									**Sample #EN24VS006**				
Oxide wt%	pyx3_4	pyx3_5	pyx3_6	pyx4_1	pyx4_2	pyx4_3	pyx4_4	pyx4_5	pyx1_1	pyx1_2	pyx1_3	pyx1_4	pyx1_5
SiO_2	55.65	55.81	56.00	52.51	53.21	52.07	52.81	52.82	51.43	52.45	52.57	52.37	52.57
TiO_2	0.09	0.10	0.10	0.23	0.20	0.21	0.26	0.41	0.34	0.29	0.26	0.31	0.33
Al_2O_3	1.68	1.93	1.97	3.23	2.89	3.01	3.22	3.21	4.07	3.39	3.16	3.59	3.63
Cr_2O_3	0.69	0.70	0.68	1.27	1.19	1.08	1.06	1.22	1.16	0.97	1.18	0.99	0.93
FeO	7.22	7.64	7.33	4.09	4.13	3.66	4.22	4.42	4.85	4.46	4.59	4.58	4.25
MnO	0.21	0.22	0.18	0.10	0.19	0.13	0.18	0.13	0.09	0.13	0.10	0.13	0.17
MgO	32.48	31.82	31.89	18.41	18.26	17.76	17.87	17.80	17.36	17.62	17.67	17.53	16.61
NiO	0.10	0.09	0.09	0.03	0.06	0.06	0.07	0.04	0.04	0.02	0.04	0.02	0.00
CaO	1.90	2.28	2.37	20.42	20.79	21.99	21.15	20.72	20.84	20.95	21.08	20.98	22.18
Na_2O	0.02	0.03	0.03	0.25	0.28	0.31	0.35	0.34	0.32	0.32	0.31	0.31	0.39
Total	100.04	100.61	100.63	100.55	101.19	100.27	101.18	101.09	100.50	100.60	100.94	100.81	101.05
Cations per formula unit													
Si	1.94	1.94	1.94	1.90	1.92	1.90	1.91	1.91	1.87	1.90	1.90	1.90	1.90
Ti	0.00	0.00	0.00	0.01	0.01	0.01	0.01	0.01	0.01	0.01	0.01	0.01	0.01
Al	0.07	0.08	0.08	0.14	0.12	0.13	0.14	0.14	0.17	0.15	0.13	0.15	0.15
Cr	0.02	0.02	0.02	0.04	0.03	0.03	0.03	0.03	0.03	0.03	0.03	0.03	0.03
Fe^{2+}	0.21	0.22	0.21	0.12	0.12	0.11	0.13	0.13	0.15	0.14	0.14	0.14	0.13
Mn	0.01	0.01	0.01	0.00	0.01	0.00	0.01	0.00	0.00	0.00	0.00	0.00	0.01
Mg	1.69	1.65	1.65	0.99	0.98	0.96	0.96	0.96	0.94	0.95	0.95	0.95	0.90
Ni	0.00	0.00	0.00	0.00	0.00	0.00	0.00	0.00	0.00	0.00	0.00	0.00	0.00
Ca	0.07	0.09	0.09	0.79	0.80	0.86	0.82	0.80	0.81	0.81	0.82	0.81	0.86
Na	0.00	0.00	0.00	0.02	0.02	0.02	0.02	0.02	0.02	0.02	0.02	0.02	0.03
Total	4.01	4.01	4.01	4.01	4.01	4.03	4.02	4.01	4.02	4.01	4.02	4.01	4.01
En	85.71	84.30	84.57	52.02	51.41	49.86	50.42	50.60	49.51	50.09	49.92	49.84	47.55
Fs	10.69	11.36	10.91	6.49	6.52	5.76	6.68	7.05	7.76	7.12	7.27	7.30	6.82
Wo	3.60	4.35	4.52	41.48	42.06	44.38	42.90	42.34	42.73	42.80	42.80	42.86	45.63

Sample #EN24VS006

Oxide wt%	pyx2_1	pyx2_2	pyx2_3	pyx2_4	pyx3_1	pyx3_2	pyx3_3	pyx3_4	pyx3_5	pyx3_6	pyx4_1	pyx4_2	pyx5_1	pyx5_2	pyx6_1
SiO_2	56.48	56.62	55.63	56.15	50.45	52.51	51.83	52.53	52.43	51.59	52.42	52.48	55.11	56.91	51.48
TiO_2	0.08	0.06	0.07	0.08	0.70	0.31	0.25	0.22	0.24	0.33	0.28	0.33	0.11	0.05	0.36
Al_2O_3	1.62	1.37	1.64	1.63	4.45	3.61	3.27	2.77	3.29	3.76	3.57	3.91	2.22	1.18	3.94
Cr_2O_3	0.79	0.64	0.75	0.75	0.78	1.04	1.11	0.91	1.09	1.13	1.05	0.97	0.67	0.57	1.13
FeO	7.60	6.93	7.93	7.69	4.65	3.88	4.65	4.55	4.58	4.38	4.63	4.89	8.14	7.49	4.09
MnO	0.18	0.15	0.13	0.16	0.05	0.12	0.14	0.10	0.14	0.10	0.12	0.07	0.15	0.22	0.12
MgO	32.58	32.68	31.51	32.11	16.07	16.51	18.10	18.21	18.29	16.58	17.62	17.80	31.25	32.85	16.13
NiO	0.04	0.01	0.06	0.02	0.04	0.03	0.00	0.00	0.03	0.01	0.05	0.03	0.03	0.02	0.04
CaO	1.63	1.61	2.24	1.57	22.15	22.49	20.21	20.56	20.20	22.11	21.07	20.25	2.13	1.62	22.84
Na_2O	0.03	0.03	0.02	0.03	0.40	0.35	0.50	0.36	0.35	0.44	0.31	0.31	0.03	0.02	0.35
Total	101.02	100.09	99.99	100.18	99.74	100.83	100.06	100.20	100.64	100.42	101.10	101.05	99.85	100.93	100.48
Cations per formula unit															
Si	1.95	1.96	1.95	1.95	1.86	1.90	1.89	1.91	1.90	1.88	1.90	1.89	1.93	1.96	1.88
Ti	0.00	0.00	0.00	0.00	0.02	0.01	0.01	0.01	0.01	0.01	0.01	0.01	0.00	0.00	0.01
Al	0.07	0.06	0.07	0.07	0.19	0.15	0.14	0.12	0.14	0.16	0.15	0.17	0.09	0.05	0.17
Cr	0.02	0.02	0.02	0.02	0.02	0.03	0.03	0.03	0.03	0.03	0.03	0.03	0.02	0.02	0.03
Fe^{2+}	0.22	0.20	0.23	0.22	0.14	0.12	0.14	0.14	0.14	0.13	0.14	0.15	0.24	0.22	0.13
Mn	0.01	0.00	0.00	0.00	0.00	0.00	0.00	0.00	0.00	0.00	0.00	0.00	0.00	0.01	0.00
Mg	1.68	1.69	1.64	1.67	0.88	0.89	0.99	0.99	0.99	0.90	0.95	0.96	1.63	1.69	0.88
Ni	0.00	0.00	0.00	0.00	0.00	0.00	0.00	0.00	0.00	0.00	0.00	0.00	0.00	0.00	0.00
Ca	0.06	0.06	0.08	0.06	0.87	0.87	0.79	0.80	0.78	0.87	0.82	0.78	0.08	0.06	0.89
Na	0.00	0.00	0.00	0.00	0.03	0.02	0.04	0.03	0.02	0.03	0.02	0.02	0.00	0.00	0.02
Total	4.01	4.00	4.01	4.00	4.03	4.01	4.03	4.02	4.02	4.02	4.02	4.01	4.01	4.00	4.02
En	85.71	86.64	83.87	85.50	46.45	47.37	51.37	51.25	51.71	47.47	49.84	50.72	83.68	85.96	46.29
Fs	11.21	10.30	11.84	11.49	7.54	6.24	7.40	7.18	7.26	7.03	7.34	7.82	12.22	11.00	6.59
Wo	3.08	3.06	4.29	3.01	46.02	46.39	41.23	41.57	41.03	45.50	42.82	41.46	4.10	3.05	47.13

Sample #EN24VS006										**Sample #EN24VS007**					
Oxide wt%	pyx6_2	pyx6_3	pyx6_4	pyx6_5	pyx7_1	pyx7_2	pyx7_3	pyx7_4	pyx7_5	pyx1_1	pyx1_2	pyx1_3	pyx1_4	pyx2_1	pyx3_1
SiO_2	52.96	52.71	52.97	52.81	51.55	52.38	50.96	52.96	52.76	52.28	50.73	52.53	53.24	55.86	52.18
TiO_2	0.26	0.21	0.20	0.23	0.29	0.23	0.40	0.19	0.21	0.31	0.72	0.30	0.36	0.07	0.30
Al_2O_3	3.50	3.06	2.77	3.22	3.74	3.08	5.12	2.49	2.94	3.59	4.65	3.51	3.26	1.66	3.76
Cr_2O_3	1.05	1.15	1.12	1.10	1.06	1.02	1.25	0.86	1.20	1.07	0.80	1.16	0.92	0.73	1.11
FeO	3.32	4.37	4.95	4.70	4.81	4.32	3.99	4.48	4.03	4.45	4.60	4.67	4.43	7.50	3.96
MnO	0.10	0.16	0.14	0.18	0.09	0.11	0.09	0.14	0.16	0.08	0.07	0.10	0.14	0.21	0.06
MgO	19.07	18.37	19.51	18.98	17.75	17.96	18.04	17.98	17.51	17.74	16.12	17.65	17.31	32.43	16.42
NiO	0.02	0.00	0.02	0.02	0.02	0.02	0.00	0.02	0.02	0.02	0.00	0.02	0.01	0.04	0.01
CaO	18.43	20.47	18.97	19.47	20.30	20.74	18.33	21.29	21.66	20.68	22.32	20.51	21.27	1.61	22.59
Na_2O	0.46	0.26	0.26	0.23	0.30	0.29	1.02	0.33	0.27	0.31	0.38	0.31	0.39	0.04	0.42
Total	99.18	100.76	100.91	100.94	99.92	100.15	99.20	100.75	100.74	100.52	100.39	100.74	101.31	100.15	100.83
Cations per formula unit															
Si	1.92	1.91	1.91	1.90	1.89	1.91	1.86	1.92	1.91	1.90	1.86	1.90	1.92	1.95	1.89
Ti	0.01	0.01	0.01	0.01	0.01	0.01	0.01	0.01	0.01	0.01	0.02	0.01	0.01	0.00	0.01
Al	0.15	0.13	0.12	0.14	0.16	0.13	0.22	0.11	0.13	0.15	0.20	0.15	0.14	0.07	0.16
Cr	0.03	0.03	0.03	0.03	0.03	0.03	0.04	0.02	0.03	0.03	0.02	0.03	0.03	0.02	0.03
Fe^{2+}	0.10	0.13	0.15	0.14	0.15	0.13	0.12	0.14	0.12	0.14	0.14	0.14	0.13	0.22	0.12
Mn	0.00	0.00	0.00	0.01	0.00	0.00	0.00	0.00	0.00	0.00	0.00	0.00	0.00	0.01	0.00
Mg	1.03	0.99	1.05	1.02	0.97	0.97	0.98	0.97	0.95	0.96	0.88	0.95	0.93	1.68	0.89
Ni	0.00	0.00	0.00	0.00	0.00	0.00	0.00	0.00	0.00	0.00	0.00	0.00	0.00	0.00	0.00
Ca	0.72	0.79	0.73	0.75	0.80	0.81	0.72	0.83	0.84	0.80	0.88	0.80	0.82	0.06	0.88
Na	0.03	0.02	0.02	0.02	0.02	0.02	0.07	0.02	0.02	0.02	0.03	0.02	0.03	0.00	0.03
Total	4.00	4.01	4.02	4.01	4.02	4.02	4.03	4.02	4.01	4.01	4.02	4.01	4.00	4.01	4.02
En	55.79	51.70	54.32	53.30	50.66	50.89	53.94	50.22	49.55	50.54	46.40	50.40	49.35	85.79	47.08
Fs	5.45	6.89	7.73	7.40	7.71	6.87	6.69	7.03	6.39	7.12	7.42	7.49	7.08	11.14	6.37
Wo	38.76	41.40	37.95	39.30	41.63	42.24	39.38	42.76	44.06	42.34	46.18	42.11	43.57	3.07	46.55

Sample #EN24VS007

Oxide wt%	pyx3_2	pyx3_3	pyx4_1	pyx4_2	pyx4_3	pyx4_4	pyx5_1	pyx5_2	pyx5_3	pyx5_4	pyx5_5	pyx5_6	pyx5_7
SiO_2	52.58	53.52	56.76	56.92	56.03	56.76	52.78	52.33	53.11	52.73	52.12	52.16	53.18
TiO_2	0.21	0.18	0.00	0.01	0.02	0.02	0.24	0.33	0.26	0.33	0.45	0.40	0.23
Al_2O_3	3.07	2.42	1.03	0.90	2.50	1.15	2.73	3.78	2.89	3.33	3.74	3.78	2.62
Cr_2O_3	1.15	0.95	0.00	0.07	0.33	0.13	0.88	1.21	0.91	1.04	1.04	1.07	0.87
FeO	4.03	4.61	10.30	9.18	9.18	9.26	4.62	4.72	4.51	4.65	4.41	4.65	4.78
MnO	0.11	0.13	0.21	0.19	0.22	0.21	0.15	0.13	0.14	0.14	0.10	0.06	0.10
MgO	17.87	19.12	32.63	32.23	31.81	32.47	18.42	17.56	17.89	17.73	17.10	17.04	18.84
NiO	0.03	0.03	0.10	0.04	0.03	0.09	0.01	0.07	0.02	0.02	0.02	0.02	0.02
CaO	21.04	19.40	0.39	0.42	0.68	0.63	20.39	20.57	21.33	20.96	21.66	21.38	19.92
Na_2O	0.30	0.37	0.03	0.01	0.01	0.02	0.31	0.33	0.28	0.30	0.32	0.37	0.28
Total	100.39	100.73	101.44	99.97	100.81	100.73	100.53	101.03	101.33	101.23	100.98	100.93	100.83
Cations per formula unit													
Si	1.91	1.93	1.97	1.99	1.94	1.97	1.91	1.89	1.91	1.90	1.89	1.89	1.92
Ti	0.01	0.00	0.00	0.00	0.00	0.00	0.01	0.01	0.01	0.01	0.01	0.01	0.01
Al	0.13	0.10	0.04	0.04	0.10	0.05	0.12	0.16	0.12	0.14	0.16	0.16	0.11
Cr	0.03	0.03	0.00	0.00	0.01	0.00	0.03	0.03	0.03	0.03	0.03	0.03	0.02
Fe^{2+}	0.12	0.14	0.30	0.27	0.27	0.27	0.14	0.14	0.14	0.14	0.13	0.14	0.14
Mn	0.00	0.00	0.01	0.01	0.01	0.01	0.00	0.00	0.00	0.00	0.00	0.00	0.00
Mg	0.97	1.03	1.68	1.68	1.64	1.68	1.00	0.95	0.96	0.95	0.92	0.92	1.01
Ni	0.00	0.00	0.00	0.00	0.00	0.00	0.00	0.00	0.00	0.00	0.00	0.00	0.00
Ca	0.82	0.75	0.01	0.02	0.03	0.02	0.79	0.80	0.82	0.81	0.84	0.83	0.77
Na	0.02	0.03	0.00	0.00	0.00	0.00	0.02	0.02	0.02	0.02	0.02	0.03	0.02
Total	4.01	4.01	4.01	3.99	4.00	4.00	4.02	4.01	4.01	4.01	4.02	4.02	4.02
En	50.69	53.63	84.34	85.53	84.94	85.19	51.64	50.19	50.05	50.08	48.66	48.67	52.57
Fs	6.42	7.26	14.94	13.66	13.75	13.63	7.27	7.56	7.07	7.37	7.04	7.45	7.48
Wo	42.89	39.11	0.72	0.81	1.31	1.18	41.09	42.25	42.87	42.54	44.30	43.88	39.96

Sample #EN24VS008

Oxide wt%	pyx1_1	pyx1_2	pyx1_3	pyx1_4	pyx1_5	pyx1_6	pyx2_1	pyx2_2	pyx2_3	pyx2_4	pyx3_1	pyx3_2	pyx3_3	pyx3_4	pyx3_5
SiO_2	55.84	55.64	55.56	55.15	55.26	55.67	55.27	56.00	55.82	55.63	55.86	55.68	55.86	55.61	55.49
TiO_2	0.06	0.06	0.09	0.09	0.08	0.07	0.07	0.06	0.07	0.06	0.06	0.04	0.07	0.04	0.07
Al_2O_3	1.41	1.32	1.70	1.68	1.73	1.56	1.66	1.26	1.28	1.17	1.08	1.05	1.15	1.30	1.45
Cr_2O_3	0.57	0.56	0.69	0.77	0.82	0.68	0.68	0.60	0.55	0.51	0.50	0.49	0.56	0.60	0.53
FeO	7.66	7.54	7.39	7.49	7.76	7.68	7.71	7.53	7.61	7.82	7.18	7.57	7.73	7.41	7.68
MnO	0.11	0.15	0.14	0.17	0.19	0.17	0.18	0.12	0.13	0.16	0.16	0.15	0.14	0.21	0.18
MgO	32.80	32.65	32.41	32.33	32.74	32.46	32.21	32.69	32.72	32.79	33.02	32.94	33.01	32.71	32.80
NiO	0.04	0.04	0.03	0.05	0.04	0.04	0.05	0.05	0.02	0.05	0.05	0.04	0.00	0.06	0.04
CaO	1.60	1.65	1.73	1.77	1.70	1.88	1.68	1.65	1.63	1.61	1.48	1.51	1.56	1.73	1.63
Na_2O	0.03	0.03	0.03	0.04	0.02	0.02	0.03	0.03	0.03	0.04	0.03	0.02	0.03	0.05	0.04
Total	100.13	99.64	99.76	99.54	100.33	100.22	99.54	100.00	99.85	99.83	99.41	99.49	100.12	99.72	99.90
Cations per formula unit															
Si	1.95	1.95	1.94	1.94	1.93	1.94	1.94	1.95	1.95	1.95	1.96	1.95	1.95	1.95	1.94
Ti	0.00	0.00	0.00	0.00	0.00	0.00	0.00	0.00	0.00	0.00	0.00	0.00	0.00	0.00	0.00
Al	0.06	0.05	0.07	0.07	0.07	0.06	0.07	0.05	0.05	0.05	0.04	0.04	0.05	0.05	0.06
Cr	0.02	0.02	0.02	0.02	0.02	0.02	0.02	0.02	0.02	0.01	0.01	0.01	0.02	0.02	0.01
Fe^{2+}	0.22	0.22	0.22	0.22	0.23	0.22	0.23	0.22	0.22	0.23	0.21	0.22	0.23	0.22	0.22
Mn	0.00	0.00	0.00	0.01	0.01	0.00	0.01	0.00	0.00	0.00	0.00	0.00	0.00	0.01	0.01
Mg	1.70	1.71	1.69	1.69	1.70	1.69	1.69	1.70	1.70	1.71	1.72	1.72	1.72	1.71	1.71
Ni	0.00	0.00	0.00	0.00	0.00	0.00	0.00	0.00	0.00	0.00	0.00	0.00	0.00	0.00	0.00
Ca	0.06	0.06	0.06	0.07	0.06	0.07	0.06	0.06	0.06	0.06	0.06	0.06	0.06	0.06	0.06
Na	0.00	0.00	0.00	0.00	0.00	0.00	0.00	0.00	0.00	0.00	0.00	0.00	0.00	0.00	0.00
Total	4.02	4.02	4.01	4.02	4.02	4.02	4.01	4.01	4.01	4.02	4.01	4.02	4.02	4.02	4.02
En	85.75	85.78	85.75	85.52	85.46	85.17	85.34	85.80	85.75	85.54	86.63	86.07	85.81	85.83	85.68
Fs	11.24	11.11	10.96	11.12	11.36	11.30	11.45	11.09	11.19	11.44	10.57	11.10	11.27	10.91	11.26
Wo	3.01	3.11	3.29	3.37	3.18	3.54	3.21	3.11	3.07	3.02	2.80	2.83	2.92	3.27	3.06

Sample #EN24VS008

Oxide wt%	pyx4_1	pyx4_2	pyx4_3	pyx4_4	pyx4_5
SiO_2	55.28	55.37	55.47	55.13	56.23
TiO_2	0.09	0.07	0.08	0.07	0.05
Al_2O_3	1.72	1.72	1.69	1.57	0.99
Cr_2O_3	0.80	0.78	0.79	0.72	0.48
FeO	7.37	7.23	7.28	8.09	7.29
MnO	0.15	0.15	0.21	0.15	0.16
MgO	32.58	32.56	32.58	32.40	33.29
NiO	0.02	0.05	0.04	0.04	0.05
CaO	1.77	1.71	1.67	1.60	1.55
Na_2O	0.04	0.03	0.02	0.02	0.03
Total	99.82	99.67	99.83	99.79	100.11
Cations per formula unit					
Si	1.93	1.94	1.94	1.93	1.96
Ti	0.00	0.00	0.00	0.00	0.00
Al	0.07	0.07	0.07	0.06	0.04
Cr	0.02	0.02	0.02	0.02	0.01
Fe^{2+}	0.22	0.21	0.21	0.24	0.21
Mn	0.00	0.00	0.01	0.00	0.00
Mg	1.70	1.70	1.70	1.70	1.73
Ni	0.00	0.00	0.00	0.00	0.00
Ca	0.07	0.06	0.06	0.06	0.06
Na	0.00	0.00	0.00	0.00	0.00
Total	4.02	4.01	4.01	4.02	4.02
En	85.76	86.04	86.04	85.06	86.48
Fs	10.88	10.71	10.79	11.91	10.63
Wo	3.35	3.25	3.17	3.02	2.89

Appendix D4: Amphibole University of Manitoba

Sample #EN24VS007

Oxide wt%	amp1_1	amp1_2	amp1_3	amp2_1	amp2_2	amp2_3	amp3_1	amp3_2	amp3_3
SiO_2	42.42	43.79	43.41	43.95	44.63	43.34	41.69	41.95	41.94
TiO_2	2.00	1.03	0.63	0.52	0.69	0.50	3.27	2.99	2.72
Al_2O_3	13.28	12.82	12.59	12.84	11.82	12.96	13.86	13.75	13.39
Cr_2O_3	0.48	0.91	1.04	0.68	0.60	1.05	0.23	0.26	1.00
FeO	6.97	6.86	6.55	6.83	6.53	7.13	7.21	6.94	6.82
MnO	0.09	0.07	0.09	0.08	0.06	0.10	0.10	0.06	0.05
MgO	16.37	17.33	17.02	17.24	18.04	17.55	15.85	15.87	16.10
NiO	0.08	0.09	0.06	0.08	0.06	0.06	0.08	0.05	0.06
CaO	11.90	11.79	11.76	11.88	11.70	11.03	12.20	12.18	12.21
Na_2O	2.94	2.91	2.89	2.92	2.76	3.08	2.98	3.02	2.97
K_2O	0.59	0.53	0.57	0.62	0.54	0.55	0.57	0.59	0.59
Total	97.12	98.12	96.61	97.63	97.44	97.36	98.06	97.65	97.86
Cations per formula unit									
${}^{T}Si$	6.13	6.22	6.28	6.28	6.35	6.20	6.01	6.07	6.05
${}^{T}Al$	1.87	1.78	1.73	1.72	1.65	1.80	1.99	1.93	1.95
${}^{T}Ti$									
${}^{T}Fe^{3+}$									
T Total	8.00	8.00	8.00	8.00	8.00	8.00	8.00	8.00	8.00
${}^{C}Ti$	0.22	0.11	0.07	0.06	0.07	0.05	0.36	0.33	0.30
${}^{C}Al$	0.39	0.37	0.42	0.44	0.34	0.38	0.37	0.42	0.33
${}^{C}Cr$	0.06	0.10	0.12	0.08	0.07	0.12	0.03	0.03	0.11
${}^{C}Fe^{3+}$	0.69	0.64	0.46	0.47	0.61	0.64	0.78	0.64	0.71
${}^{C}Ni$	0.01	0.01	0.01	0.01	0.01	0.01	0.01	0.01	0.01
${}^{C}Fe^{2+}$	0.11	0.10	0.26	0.27	0.08	0.06	0.05	0.16	0.08
${}^{C}Mg$	3.53	3.67	3.67	3.67	3.83	3.74	3.41	3.42	3.46
C Total	5.00	5.00	5.00	5.00	5.00	5.00	5.00	5.00	5.00
${}^{B}Mn^{2+}$	0.01	0.01	0.01	0.01	0.01	0.01	0.01	0.01	0.01
${}^{B}Fe^{2+}$	0.04	0.08	0.07	0.08	0.09	0.15	0.04	0.04	0.03
${}^{B}Mg$									
${}^{B}Ca$	1.84	1.80	1.82	1.82	1.79	1.69	1.89	1.89	1.89
${}^{B}Na$	0.10	0.12	0.10	0.10	0.11	0.15	0.06	0.06	0.08
B Total	2.00	2.00	2.00	2.00	2.00	2.00	2.00	2.00	2.00
${}^{A}Na$	0.72	0.68	0.71	0.71	0.65	0.71	0.77	0.79	0.76
${}^{A}K$	0.11	0.10	0.11	0.11	0.10	0.10	0.11	0.11	0.11
A Total	0.83	0.78	0.82	0.83	0.75	0.81	0.87	0.90	0.87
${}^{W}OH^{-}$	1.56	1.78	1.86	1.89	1.85	1.89	1.29	1.35	1.41
${}^{W}O$	0.44	0.22	0.14	0.11	0.15	0.11	0.71	0.65	0.59
W total	2.00	2.00	2.00	2.00	2.00	2.00	2.00	2.00	2.00
Total	15.83	15.78	15.82	15.83	15.75	15.81	15.87	15.90	15.87

Sample #EN24VS007					**Sample #EN24VS009**			
Oxide wt%	amp3_4	amp4_1	amp4_2	amp4_3	amp1_1	amp1_2	amp1_3	amp2_1
SiO_2	42.34	44.47	43.99	43.90	44.97	44.51	44.23	57.87
TiO_2	2.66	0.67	0.68	0.88	0.19	0.34	0.65	0.00
Al_2O_3	13.71	12.10	12.42	12.15	11.02	11.89	11.81	0.09
Cr_2O_3	0.49	0.99	1.06	0.73	0.61	0.18	0.11	0.02
FeO	6.95	6.66	6.63	7.08	6.00	7.07	6.40	10.42
MnO	0.05	0.08	0.09	0.09	0.14	0.10	0.16	0.44
MgO	15.91	17.51	17.30	17.75	19.21	18.30	18.59	27.38
NiO	0.06	0.06	0.07	0.07	0.06	0.08	0.06	0.04
CaO	12.15	11.68	11.82	11.79	10.78	10.73	10.94	0.56
Na_2O	2.99	2.82	2.82	2.82	3.05	3.37	3.44	0.06
K_2O	0.61	0.58	0.56	0.57	0.28	0.35	0.44	0.00
Total	97.92	97.61	97.44	97.82	96.31	96.91	96.84	96.88
Cations per formula unit								
^{T}Si	6.11	6.33	6.28	6.25	6.44	6.36	6.33	7.99
^{T}Al	1.89	1.67	1.72	1.75	1.56	1.64	1.67	0.01
^{T}Ti								
$^{T}Fe^{3+}$								
T Total	8.00	8.00	8.00	8.00	8.00	8.00	8.00	8.00
^{C}Ti	0.29	0.07	0.07	0.09	0.02	0.04	0.07	
^{C}Al	0.44	0.37	0.37	0.29	0.30	0.36	0.32	0.01
^{C}Cr	0.06	0.11	0.12	0.08	0.07	0.02	0.01	0.00
$^{C}Fe^{3+}$	0.58	0.59	0.60	0.70	0.55	0.60	0.61	0.01
^{C}Ni	0.01	0.01	0.01	0.01	0.01	0.01	0.01	0.00
$^{C}Fe^{2+}$	0.21	0.14	0.14	0.06		0.07	0.01	
^{C}Mg	3.42	3.72	3.68	3.77	4.06	3.90	3.97	4.98
C Total	5.00	5.00	5.00	5.00	5.00	5.00	5.00	5.00
$^{B}Mn^{2+}$	0.01	0.01	0.01	0.01	0.02	0.01	0.02	0.05
$^{B}Fe^{2+}$	0.05	0.07	0.05	0.09	0.17	0.17	0.15	1.19
^{B}Mg					0.04			0.66
^{B}Ca	1.88	1.78	1.81	1.80	1.65	1.64	1.68	0.08
^{B}Na	0.07	0.14	0.13	0.10	0.12	0.17	0.16	0.01
B Total	2.00	2.00	2.00	2.00	2.00	2.00	2.00	2.00
^{A}Na	0.77	0.64	0.65	0.68	0.73	0.76	0.80	0.00
^{A}K	0.11	0.11	0.10	0.10	0.05	0.06	0.08	0.00
A Total	0.88	0.74	0.75	0.78	0.78	0.83	0.88	0.00
$^{W}OH^{-}$	1.42	1.86	1.85	1.81	1.96	1.93	1.86	2.00
^{W}O	0.58	0.14	0.15	0.19	0.04	0.07	0.14	0.00
W total	2.00	2.00	2.00	2.00	2.00	2.00	2.00	2.00
Total	15.88	15.74	15.75	15.78	15.78	15.82	15.88	15.00

Sample #EN24VS015								**Sample #EN24VS017**		
Oxide wt%	amp1_1	amp1_2	amp2_1	amp2_2	amp2_3	amp2_4	amp3_1	amp1_1	amp1_2	amp1_3
SiO_2	43.30	43.60	43.01	43.09	45.49	43.02	51.13	43.57	43.41	43.12
TiO_2	2.26	2.33	3.63	3.35	0.68	3.61	0.06	2.15	2.48	3.01
Al_2O_3	11.56	11.22	10.65	11.02	10.41	11.21	6.22	11.28	10.92	11.61
Cr_2O_3	0.83	0.95	0.76	0.97	0.35	0.96	0.10	0.90	1.14	0.98
FeO	6.00	6.19	5.49	5.46	5.07	5.37	4.24	6.38	5.73	6.43
MnO	0.09	0.10	0.08	0.09	0.09	0.07	0.10	0.06	0.15	0.06
MgO	17.07	17.25	18.14	17.21	19.40	17.22	21.24	17.49	17.74	16.55
NiO	0.06	0.08	0.05	0.08	0.10	0.05	0.06	0.09	0.05	0.08
CaO	11.48	11.50	11.58	11.85	11.19	11.67	11.87	11.61	11.67	11.62
Na_2O	3.21	2.87	3.12	3.18	3.23	3.20	2.05	2.79	2.64	2.93
K_2O	0.84	0.80	0.83	0.73	0.51	0.77	0.18	0.90	0.80	0.83
Total	96.70	96.89	97.35	97.04	96.52	97.14	97.25	97.21	96.72	97.21
Cations per formula unit										
^{T}Si	6.29	6.32	6.24	6.27	6.53	6.26	7.15	6.30	6.30	6.27
^{T}Al	1.71	1.68	1.76	1.73	1.47	1.74	0.85	1.71	1.70	1.73
^{T}Ti										
$^{T}Fe^{3+}$										
T Total	8.00	8.00	8.00	8.00	8.00	8.00	8.00	8.00	8.00	8.00
^{C}Ti	0.25	0.25	0.40	0.37	0.07	0.40	0.01	0.23	0.27	0.33
^{C}Al	0.27	0.24	0.07	0.16	0.29	0.18	0.18	0.22	0.17	0.26
^{C}Cr	0.10	0.11	0.09	0.11	0.04	0.11	0.01	0.10	0.13	0.11
$^{C}Fe^{3+}$	0.60	0.59	0.66	0.60	0.33	0.59	0.25	0.63	0.62	0.61
^{C}Ni	0.01	0.01	0.01	0.01	0.01	0.01	0.01	0.01	0.01	0.01
$^{C}Fe^{2+}$	0.09	0.07		0.02	0.10		0.12	0.04		0.10
^{C}Mg	3.70	3.73	3.79	3.74	4.15	3.72	4.43	3.77	3.80	3.58
C Total	5.00	5.00	5.00	5.00	5.00	5.00	5.00	5.00	5.00	5.00
$^{B}Mn^{2+}$	0.01	0.01	0.01	0.01	0.01	0.01	0.01	0.01	0.02	0.01
$^{B}Fe^{2+}$	0.05	0.09	0.01	0.05	0.18	0.06	0.12	0.10	0.07	0.07
^{B}Mg			0.14			0.02			0.04	
^{B}Ca	1.79	1.79	1.80	1.85	1.72	1.82	1.78	1.80	1.82	1.81
^{B}Na	0.16	0.11	0.04	0.09	0.09	0.09	0.09	0.10	0.06	0.11
B Total	2.00	2.00	2.00	2.00	2.00	2.00	2.00	2.00	2.00	2.00
^{A}Na	0.75	0.70	0.84	0.81	0.81	0.81	0.47	0.69	0.69	0.71
^{A}K	0.16	0.15	0.15	0.14	0.09	0.14	0.03	0.17	0.15	0.15
A Total	0.90	0.85	0.99	0.95	0.90	0.95	0.50	0.85	0.83	0.87
$^{W}OH^{-}$	1.51	1.49	1.21	1.27	1.85	1.21	1.99	1.53	1.46	1.34
^{W}O	0.49	0.51	0.79	0.73	0.15	0.79	0.01	0.47	0.54	0.66
W total	2.00	2.00	2.00	2.00	2.00	2.00	2.00	2.00	2.00	2.00
Total	15.90	15.85	15.99	15.95	15.90	15.95	15.50	15.85	15.84	15.87

Sample #EN24VS032

Oxide wt%	amp1_1	amp1_2	amp1_3	amp1_3	amp2_1	amp2_2	amp2_3	amp3_1	amp3_2	amp3_3	amp4_1
SiO_2	42.93	42.76	42.81	43.23	42.87	42.67	43.56	43.91	43.21	42.96	56.41
TiO_2	4.41	4.45	4.49	4.14	4.52	4.76	3.26	2.91	3.83	3.78	0.05
Al_2O_3	11.51	11.25	11.29	10.99	11.38	11.50	11.48	10.97	11.02	11.23	1.39
Cr_2O_3	1.17	0.73	0.74	1.17	0.61	0.57	0.80	1.15	0.71	0.76	0.05
FeO	4.97	5.72	5.75	5.63	5.34	5.11	5.50	5.41	5.00	5.58	3.31
MnO	0.09	0.09	0.10	0.04	0.08	0.09	0.04	0.06	0.09	0.07	0.12
MgO	16.94	16.95	16.83	16.82	16.86	16.99	17.18	17.29	17.43	16.89	22.67
NiO	0.07	0.07	0.07	0.08	0.08	0.08	0.10	0.09	0.08	0.08	0.08
CaO	11.72	11.73	11.64	11.66	11.76	11.73	11.88	11.78	11.88	11.80	13.18
Na_2O	3.01	2.61	2.82	2.72	3.04	2.92	3.06	2.97	2.99	3.00	0.49
K_2O	0.67	0.68	0.70	0.68	0.69	0.69	0.74	0.72	0.79	0.73	0.01
Total	97.49	97.05	97.25	97.16	97.23	97.11	97.60	97.28	97.04	96.88	97.76
Cations per formula unit											
^{T}Si	6.24	6.24	6.24	6.30	6.25	6.23	6.30	6.36	6.29	6.27	7.75
^{T}Al	1.76	1.76	1.76	1.70	1.75	1.77	1.70	1.65	1.71	1.73	0.22
^{T}Ti											0.01
$^{T}Fe^{3+}$											0.02
T Total	8.00	8.00	8.00	8.00	8.00	8.00	8.00	8.00	8.00	8.00	8.00
^{C}Ti	0.48	0.49	0.49	0.45	0.50	0.52	0.36	0.32	0.42	0.42	
^{C}Al	0.21	0.17	0.18	0.18	0.21	0.21	0.26	0.23	0.18	0.21	
^{C}Cr	0.13	0.08	0.09	0.14	0.07	0.07	0.09	0.13	0.08	0.09	0.01
$^{C}Fe^{3+}$	0.54	0.68	0.65	0.60	0.58	0.59	0.47	0.51	0.55	0.58	0.19
^{C}Ni	0.01	0.01	0.01	0.01	0.01	0.01	0.01	0.01	0.01	0.01	0.01
$^{C}Fe^{2+}$							0.10	0.07		0.02	0.16
^{C}Mg	3.63	3.57	3.58	3.62	3.63	3.60	3.71	3.73	3.76	3.68	4.64
C Total	5.00	5.00	5.00	5.00	5.00	5.00	5.00	5.00	5.00	5.00	5.00
$^{B}Mn^{2+}$	0.01	0.01	0.01	0.01	0.01	0.01	0.01	0.01	0.01	0.01	0.01
$^{B}Fe^{2+}$	0.07	0.02	0.05	0.09	0.07	0.03	0.09	0.07	0.06	0.08	0.01
^{B}Mg	0.05	0.12	0.07	0.04	0.03	0.10			0.02		
^{B}Ca	1.83	1.83	1.82	1.82	1.84	1.84	1.84	1.83	1.85	1.85	1.94
^{B}Na	0.05	0.02	0.04	0.06	0.05	0.03	0.06	0.10	0.05	0.07	0.03
B Total	2.00	2.00	2.00	2.00	2.00	2.00	2.00	2.00	2.00	2.00	2.00
^{A}Na	0.80	0.72	0.76	0.71	0.81	0.80	0.80	0.74	0.80	0.78	0.10
^{A}K	0.12	0.13	0.13	0.13	0.13	0.13	0.14	0.13	0.15	0.14	0.00
A Total	0.92	0.85	0.89	0.84	0.94	0.93	0.93	0.87	0.94	0.92	0.10
$^{W}OH^{-}$	1.04	1.02	1.01	1.09	1.01	0.95	1.29	1.37	1.16	1.17	1.99
^{W}O	0.97	0.98	0.99	0.91	0.99	1.05	0.71	0.63	0.84	0.83	0.01
W total	2.00	2.00	2.00	2.00	2.00	2.00	2.00	2.00	2.00	2.00	2.00
Total	15.92	15.85	15.89	15.84	15.94	15.93	15.93	15.87	15.95	15.92	15.10

Appendix D5: Secondary Spinel Standards University of Manitoba

Analyzed at the beginning of the EPMA session

Oxide wt%	BAR8601-10	DB8803-3	IM8703	IO5657	KLB8320	MO4334-14	Vi314-5	OC231350	PS211	PS212
n	3	3	3	3	3	3	3	3	3	3
SiO_2	0.07	0.03	0.03	0.02	0.04	0.07	0.10	0.02	0.06	0.01
TiO_2	0.19	0.12	0.08	0.05	0.13	0.15	0.52	0.05	0.07	0.01
Al_2O_3	38.62	22.55	49.60	53.69	56.99	62.53	44.17	51.43	32.32	37.40
Cr_2O_3	29.25	45.18	14.53	14.43	9.48	3.96	20.65	16.36	35.41	30.60
FeO	10.48	12.78	11.13	10.71	9.36	8.69	11.70	10.58	13.73	12.78
Fe_2O_3	2.51	3.69	5.16	0.94	2.71	2.03	4.29	1.32	2.08	1.78
MnO	0.13	0.20	0.14	0.10	0.10	0.07	0.08	0.10	0.17	0.17
MgO	18.04	14.81	18.65	19.34	20.62	21.53	18.16	19.12	15.19	16.23
CaO	0.00	0.01	0.01	0.00	0.01	0.00	0.00	0.02	0.01	0.01
Na_2O	0.00	0.00	0.00	0.00	0.00	0.00	0.00	0.00	0.00	0.01
NiO	0.22	0.14	0.34	0.29	0.34	0.48	0.29	0.27	0.13	0.13
Total	99.53	99.51	99.66	99.56	99.77	99.53	99.95	99.28	99.18	99.14
Cations per formula unit										
Si	0.00	0.00	0.00	0.00	0.00	0.00	0.00	0.00	0.00	0.00
Ti	0.00	0.00	0.00	0.00	0.00	0.00	0.01	0.00	0.00	0.00
Al	1.28	0.81	1.58	1.67	1.74	1.87	1.43	1.62	1.12	1.26
Cr	0.65	1.09	0.31	0.30	0.19	0.08	0.45	0.35	0.82	0.69
Fe^{2+}	0.25	0.33	0.25	0.24	0.20	0.18	0.27	0.24	0.34	0.31
Fe^{3+}	0.05	0.08	0.10	0.02	0.05	0.04	0.09	0.03	0.05	0.04
Mn	0.00	0.01	0.00	0.00	0.00	0.00	0.00	0.00	0.00	0.00
Mg	0.76	0.67	0.75	0.76	0.80	0.81	0.74	0.76	0.67	0.69
Ca	0.00	0.00	0.00	0.00	0.00	0.00	0.00	0.00	0.00	0.00
Na	0.00	0.00	0.00	0.00	0.00	0.00	0.00	0.00	0.00	0.00
Ni	0.01	0.00	0.01	0.01	0.01	0.01	0.01	0.01	0.00	0.00
Total	3.00	3.00	3.00	3.00	3.00	3.00	3.00	3.00	3.00	3.00
$Fe^{3+}/\Sigma Fe$ (uncorrected)	0.20	0.22	0.32	0.09	0.23	0.20	0.27	0.12	0.14	0.13
[a]$Fe^{3+}/\Sigma Fe$ (Mössbauer)	0.18	0.20	0.32	0.06	0.22	0.16	0.28	0.09	0.13	0.09
$Fe^{3+}/\Sigma Fe$ (corrected)	0.18	0.21	0.29	0.07	0.21	0.17	0.25	0.10	0.12	0.11

[a] Wood and Virgo (1989), Bryndzia and Wood (1990), Ionov and Wood (1992)

Analyzed at the end of the EPMA session

Oxide wt%	BAR8601-10	DB8803-3	IM8703	IO5657	KLB8320	MO4334-14	Vi314-5	OC231350	PS211	PS212
n	3	3	3	3	3	3	3	3	3	3
SiO_2	0.07	0.04	0.04	0.01	0.06	0.06	0.10	0.04	0.03	0.01
TiO_2	0.19	0.12	0.08	0.06	0.12	0.15	0.52	0.05	0.08	0.02
Al_2O_3	38.51	22.59	49.83	53.72	56.80	62.34	44.30	51.54	32.27	37.26
Cr_2O_3	29.40	44.97	14.38	14.41	9.54	4.48	20.55	15.98	35.52	30.98
FeO	10.49	12.90	11.18	10.47	9.29	8.89	11.55	10.44	13.81	13.10
Fe_2O_3	2.59	3.96	5.07	1.06	2.88	2.18	4.42	1.55	2.09	1.51
MnO	0.14	0.20	0.13	0.11	0.08	0.07	0.11	0.13	0.18	0.17
MgO	18.06	14.80	18.66	19.49	20.68	21.55	18.29	19.20	15.11	16.06
CaO	0.01	0.01	0.00	0.00	0.01	0.00	0.00	0.02	0.01	0.01
Na_2O	0.00	0.00	0.00	0.00	0.00	0.00	0.00	0.00	0.00	0.00
NiO	0.22	0.13	0.35	0.29	0.32	0.47	0.28	0.28	0.14	0.13
Total	99.68	99.71	99.71	99.63	99.79	100.19	100.12	99.24	99.26	99.25
Cations per formula unit										
Si	0.00	0.00	0.00	0.00	0.00	0.00	0.00	0.00	0.00	0.00
Ti	0.00	0.00	0.00	0.00	0.00	0.00	0.01	0.00	0.00	0.00
Al	1.28	0.81	1.58	1.67	1.74	1.86	1.43	1.62	1.12	1.26
Cr	0.65	1.08	0.31	0.30	0.20	0.09	0.45	0.34	0.83	0.70
Fe^{2+}	0.25	0.33	0.25	0.23	0.20	0.19	0.26	0.23	0.34	0.31
Fe^{3+}	0.05	0.09	0.10	0.02	0.06	0.04	0.09	0.03	0.05	0.03
Mn	0.00	0.01	0.00	0.00	0.00	0.00	0.00	0.00	0.00	0.00
Mg	0.76	0.67	0.75	0.77	0.80	0.81	0.75	0.76	0.66	0.69
Ca	0.00	0.00	0.00	0.00	0.00	0.00	0.00	0.00	0.00	0.00
Na	0.00	0.00	0.00	0.00	0.00	0.00	0.00	0.00	0.00	0.00
Ni	0.00	0.00	0.01	0.01	0.01	0.01	0.01	0.01	0.00	0.00
Total	3.00	3.00	3.00	3.00	3.00	3.00	3.00	3.00	3.00	3.00
$Fe^{3+}/\Sigma Fe$ (uncorrected)	0.20	0.23	0.31	0.10	0.24	0.20	0.28	0.14	0.14	0.11
[a]$Fe^{3+}/\Sigma Fe$ (Mössbauer)	0.18	0.20	0.32	0.06	0.22	0.16	0.28	0.09	0.13	0.09
$Fe^{3+}/\Sigma Fe$ (corrected)	0.18	0.22	0.29	0.08	0.22	0.18	0.26	0.12	0.12	0.09

[a] Wood and Virgo (1989), Bryndzia and Wood (1990), Ionov and Wood (1992)

Appendix D6: Oxides University of Manitoba

Sample #EN23VS043

Phase	chr1_1	chr1_2	chr1_3	chr2_1	chr3_1	chr4_1	chr5_1	chr6_1	chr6_2	chr7_1	chr7_2	chr8_1	chr8_2	chr9_1	chr10_1	chr10_2
Group	A	A	A	A	A	A	A	A	A	A	A	A	A	A	A	A
Oxide wt%	core	core	rim	core	core	core	core	rim	core	core	core	core	rim	core	core	core
SiO_2	0.02	0.01	0.02	0.04	0.04	0.04	0.03	0.05	0.08	0.04	0.03	0.02	0.03	0.02	0.03	0.02
TiO_2	0.44	0.53	0.42	0.39	0.38	0.36	0.36	0.37	0.34	0.38	0.37	0.57	0.56	0.62	0.47	0.49
Al_2O_3	12.93	14.32	14.67	15.16	14.69	15.41	15.44	15.19	13.72	15.09	15.46	14.83	19.20	13.83	19.73	17.90
Cr_2O_3	49.96	48.49	47.74	48.21	48.09	47.88	48.30	46.11	50.25	46.38	45.57	44.99	40.95	45.50	44.27	45.80
FeO	25.84	25.75	25.88	25.89	26.84	25.88	25.20	32.27	26.54	32.31	32.70	34.28	33.58	34.75	21.82	22.62
MnO	0.27	0.29	0.33	0.31	0.37	0.35	0.35	0.57	0.41	0.51	0.50	0.60	0.50	0.57	0.21	0.27
MgO	9.18	9.63	9.60	8.67	8.10	8.16	8.35	4.02	7.77	4.21	3.77	3.63	4.13	3.25	12.16	11.68
CaO	0.00	0.00	0.01	0.00	0.00	0.02	0.02	0.01	0.01	0.01	0.04	0.00	0.01	0.00	0.02	0.01
Na_2O	0.00	0.01	0.00	0.01	0.00	0.00	0.00	0.00	0.00	0.00	0.00	0.00	0.01	0.00	0.01	0.00
NiO	0.10	0.12	0.11	0.13	0.10	0.10	0.11	0.11	0.13	0.10	0.06	0.11	0.08	0.13	0.07	0.07
Total	98.75	99.17	98.78	98.81	98.61	98.20	98.17	98.70	99.25	99.05	98.50	99.05	99.06	98.67	98.79	98.86
Cations per formula unit																
Si	0.00	0.00	0.00	0.00	0.00	0.00	0.00	0.00	0.00	0.00	0.00	0.00	0.00	0.00	0.00	0.00
Ti	0.01	0.01	0.01	0.01	0.01	0.01	0.01	0.01	0.01	0.01	0.01	0.01	0.01	0.02	0.01	0.01
Al	0.50	0.55	0.57	0.59	0.57	0.60	0.60	0.61	0.54	0.60	0.62	0.59	0.75	0.56	0.73	0.67
Cr	1.31	1.25	1.23	1.25	1.26	1.25	1.26	1.24	1.32	1.24	1.23	1.21	1.08	1.24	1.10	1.15
Fe^{2+}	0.55	0.53	0.53	0.57	0.60	0.59	0.58	0.79	0.61	0.78	0.80	0.81	0.79	0.83	0.43	0.45
Fe^{3+}	0.17	0.17	0.18	0.14	0.15	0.12	0.11	0.13	0.12	0.13	0.13	0.17	0.14	0.17	0.14	0.15
Mn	0.01	0.01	0.01	0.01	0.01	0.01	0.01	0.02	0.01	0.01	0.01	0.02	0.01	0.02	0.01	0.01
Mg	0.45	0.47	0.47	0.42	0.40	0.40	0.41	0.20	0.38	0.21	0.19	0.18	0.20	0.17	0.57	0.55
Ca	0.00	0.00	0.00	0.00	0.00	0.00	0.00	0.00	0.00	0.00	0.00	0.00	0.00	0.00	0.00	0.00
Na	0.00	0.00	0.00	0.00	0.00	0.00	0.00	0.00	0.00	0.00	0.00	0.00	0.00	0.00	0.00	0.00
Ni	0.00	0.00	0.00	0.00	0.00	0.00	0.00	0.00	0.00	0.00	0.00	0.00	0.00	0.00	0.00	0.00
Total	3.00	3.00	3.00	3.00	3.00	3.00	3.00	3.00	3.00	3.00	3.00	3.00	3.00	3.00	3.00	3.00
$Fe^{3+}/\Sigma Fe$ (uncorrected)	0.23	0.24	0.25	0.20	0.20	0.17	0.16	0.14	0.17	0.15	0.14	0.17	0.15	0.17	0.25	0.25
$Fe^{3+}/\Sigma Fe$ (corrected)	0.22	0.23	0.24	0.18	0.18	0.16	0.15	0.13	0.16	0.13	0.13	0.16	0.14	0.16	0.23	0.24

Sample #EN23VS043											**Sample #EN24VS006**			
Phase	chr11_1	chr11_2	chr12_1	chr12_2	chr12_3	chr13_1	chr13_2	chr14_1	chr14_2	chr14_3	chr1_1	chr1_2	chr2_1	chr2_2
Group	A	A	A	A	A	A	A	A	A	A	A	A	A	A
Oxide wt%	core	core	rim	core	core	core	core	rim	core	core	core	core	core	rim
SiO_2	0.02	0.03	0.02	0.02	0.03	0.03	0.01	0.03	0.02	0.02	0.04	0.08	0.02	0.05
TiO_2	0.46	0.49	0.69	0.58	0.66	0.65	0.67	0.66	0.52	0.56	0.64	0.74	0.59	0.48
Al_2O_3	17.90	18.32	16.93	13.47	14.42	18.32	17.40	16.51	13.18	14.34	14.36	15.29	14.95	18.15
Cr_2O_3	46.27	45.69	41.72	46.61	45.24	41.21	42.12	42.77	46.98	45.56	46.43	45.60	46.34	42.71
FeO	22.15	22.73	34.41	33.52	33.94	34.20	33.87	34.35	33.92	33.68	27.02	26.51	25.96	24.82
MnO	0.23	0.24	0.50	0.53	0.57	0.50	0.52	0.54	0.52	0.55	0.25	0.24	0.22	0.19
MgO	11.79	11.84	3.69	3.44	3.65	4.16	4.06	3.84	3.36	3.44	9.61	9.89	10.24	11.29
CaO	0.04	0.01	0.01	0.01	0.00	0.01	0.00	0.00	0.00	0.00	0.01	0.02	0.03	0.02
Na_2O	0.00	0.00	0.02	0.00	0.01	0.01	0.00	0.00	0.01	0.01	0.00	0.01	0.00	0.00
NiO	0.10	0.12	0.12	0.10	0.11	0.09	0.11	0.06	0.05	0.05	0.06	0.08	0.08	0.08
Total	98.96	99.47	98.10	98.29	98.63	99.17	98.77	98.77	98.56	98.21	98.42	98.45	98.42	97.79
Cations per formula unit														
Si	0.00	0.00	0.00	0.00	0.00	0.00	0.00	0.00	0.00	0.00	0.00	0.00	0.00	0.00
Ti	0.01	0.01	0.02	0.02	0.02	0.02	0.02	0.02	0.01	0.01	0.02	0.02	0.01	0.01
Al	0.67	0.68	0.68	0.55	0.58	0.72	0.69	0.66	0.54	0.58	0.56	0.59	0.57	0.69
Cr	1.16	1.14	1.12	1.27	1.22	1.09	1.12	1.14	1.28	1.24	1.21	1.18	1.19	1.08
Fe^{2+}	0.44	0.45	0.81	0.82	0.81	0.79	0.80	0.81	0.82	0.82	0.54	0.53	0.51	0.46
Fe^{3+}	0.15	0.15	0.17	0.15	0.16	0.16	0.16	0.16	0.16	0.15	0.21	0.19	0.20	0.20
Mn	0.01	0.01	0.01	0.02	0.02	0.01	0.01	0.02	0.02	0.02	0.01	0.01	0.01	0.01
Mg	0.56	0.56	0.19	0.18	0.19	0.21	0.20	0.19	0.17	0.18	0.47	0.48	0.50	0.54
Ca	0.00	0.00	0.00	0.00	0.00	0.00	0.00	0.00	0.00	0.00	0.00	0.00	0.00	0.00
Na	0.00	0.00	0.00	0.00	0.00	0.00	0.00	0.00	0.00	0.00	0.00	0.00	0.00	0.00
Ni	0.00	0.00	0.00	0.00	0.00	0.00	0.00	0.00	0.00	0.00	0.00	0.00	0.00	0.00
Total	3.00	3.00	3.00	3.00	3.00	3.00	3.00	3.00	3.00	3.00	3.00	3.00	3.00	3.00
$Fe^{3+}/\Sigma Fe$ (uncorrected)	0.25	0.26	0.17	0.15	0.16	0.17	0.16	0.17	0.16	0.15	0.28	0.27	0.28	0.30
$Fe^{3+}/\Sigma Fe$ (corrected)	0.23	0.24	0.16	0.14	0.15	0.15	0.15	0.16	0.15	0.14	0.26	0.26	0.27	0.29

Sample #EN24VS006

Phase	chr3_1	chr3_2	chr4_1	chr4_2	chr5_1	chr5_2	chr6_1	chr6_2	chr7_1	chr7_2	chr8_1	chr8_2	chr9_1	chr10_1	chr10_2	chr11_1
Group	A	A	B	B	B	B	C	C	B	B	B	B	B	B	B	A
Oxide wt%	core	core	core	rim	core	rim	core	rim	core	rim	core	rim	core	core	rim	core
SiO_2	0.03	0.03	0.05	0.03	0.02	0.03	0.03	0.05	0.03	0.03	0.15	0.07	0.04	0.03	0.02	0.05
TiO_2	0.30	0.32	0.34	0.42	0.38	0.23	0.40	0.36	0.41	0.40	0.28	0.29	0.30	0.86	0.30	1.65
Al_2O_3	19.06	18.77	12.93	17.54	18.68	28.08	6.30	4.78	18.00	19.54	20.53	19.81	20.41	23.68	22.95	21.77
Cr_2O_3	35.01	33.97	38.61	30.01	30.57	26.00	26.83	21.98	29.82	29.05	30.32	29.11	30.02	29.86	32.02	36.92
FeO	37.62	39.01	41.74	43.89	42.52	35.74	58.06	63.35	43.54	41.98	40.46	42.53	41.50	32.46	32.33	27.65
MnO	0.39	0.43	0.48	0.46	0.44	0.34	0.41	0.35	0.42	0.40	0.39	0.41	0.43	0.22	0.21	0.32
MgO	5.64	5.53	3.18	4.05	4.42	6.79	1.92	1.57	4.49	4.86	4.72	4.52	4.68	10.66	10.07	9.79
CaO	0.01	0.04	0.01	0.00	0.01	0.02	0.08	0.18	0.02	0.01	0.01	0.02	0.00	0.04	0.03	0.04
Na_2O	0.00	0.00	0.01	0.01	0.00	0.01	0.00	0.00	0.01	0.01	0.00	0.00	0.01	0.01	0.00	0.00
NiO	0.08	0.10	0.03	0.04	0.07	0.06	0.16	0.23	0.14	0.12	0.05	0.07	0.10	0.10	0.08	0.07
Total	98.14	98.19	97.40	96.46	97.11	97.29	94.19	92.86	96.89	96.41	96.91	96.83	97.49	97.92	98.00	98.26
Cations per formula unit																
Si	0.00	0.00	0.00	0.00	0.00	0.00	0.00	0.00	0.00	0.00	0.01	0.00	0.00	0.00	0.00	0.00
Ti	0.01	0.01	0.01	0.01	0.01	0.01	0.01	0.01	0.01	0.01	0.01	0.01	0.01	0.02	0.01	0.04
Al	0.74	0.73	0.53	0.71	0.74	1.05	0.28	0.21	0.72	0.77	0.81	0.78	0.80	0.88	0.85	0.82
Cr	0.92	0.89	1.06	0.81	0.81	0.65	0.79	0.66	0.80	0.77	0.80	0.77	0.79	0.74	0.80	0.93
Fe^{2+}	0.72	0.72	0.83	0.79	0.77	0.67	0.89	0.90	0.77	0.75	0.76	0.77	0.76	0.51	0.52	0.56
Fe^{3+}	0.32	0.36	0.39	0.46	0.42	0.28	0.91	1.11	0.46	0.43	0.37	0.43	0.39	0.34	0.33	0.17
Mn	0.01	0.01	0.01	0.01	0.01	0.01	0.01	0.01	0.01	0.01	0.01	0.01	0.01	0.01	0.01	0.01
Mg	0.28	0.27	0.17	0.21	0.22	0.32	0.11	0.09	0.23	0.24	0.24	0.23	0.23	0.50	0.47	0.46
Ca	0.00	0.00	0.00	0.00	0.00	0.00	0.00	0.01	0.00	0.00	0.00	0.00	0.00	0.00	0.00	0.00
Na	0.00	0.00	0.00	0.00	0.00	0.00	0.00	0.00	0.00	0.00	0.00	0.00	0.00	0.00	0.00	0.00
Ni	0.00	0.00	0.00	0.00	0.00	0.00	0.00	0.01	0.00	0.00	0.00	0.00	0.00	0.00	0.00	0.00
Total	3.00	3.00	3.00	3.00	3.00	3.00	3.00	3.00	3.00	3.00	3.00	3.00	3.00	3.00	3.00	3.00
$Fe^{3+}/\Sigma Fe$ (uncorrected)	0.31	0.33	0.32	0.37	0.35	0.29	0.51	0.55	0.38	0.37	0.32	0.36	0.34	0.40	0.39	0.23
$Fe^{3+}/\Sigma Fe$ (corrected)	0.30	0.32	0.31	0.35	0.34	0.28	0.50	0.54	0.36	0.35	0.31	0.34	0.33	0.38	0.37	0.22

Sample #EN24VS007													**Sample #EN24VS008**		
Phase	chr1_1	chr1_2	chr2_1	chr2_2	chr3_1	chr3_2	chr4_1	chr4_2	chr5_1	chr5_2	chr6_1	chr6_2	chr1_1	chr1_2	chr1_3
Group	A	A	A	A	B	B	A	A	B	B	A	A	A	A	A
Oxide wt%	core	core	rim	core	core	rim	core	core	core	rim	core	core	core	core	rim
SiO_2	0.02	0.03	0.05	0.03	0.03	0.04	0.04	0.16	0.04	0.05	0.04	0.05	0.03	0.06	0.02
TiO_2	0.50	0.44	0.40	0.52	0.40	0.15	0.35	0.35	0.21	0.12	0.20	0.19	0.30	0.34	0.31
Al_2O_3	13.82	13.82	19.21	12.54	21.01	30.88	16.88	16.79	23.96	28.17	13.05	12.84	13.00	11.47	11.49
Cr_2O_3	43.41	44.35	33.51	43.49	28.99	24.11	32.33	32.65	28.13	24.85	38.00	38.75	41.79	47.12	41.93
FeO	33.21	32.28	37.93	36.29	40.85	33.64	41.70	41.58	38.78	37.24	40.82	40.52	37.94	33.99	38.84
MnO	0.35	0.31	0.40	0.49	0.42	0.35	0.43	0.42	0.36	0.36	0.44	0.44	0.52	0.47	0.44
MgO	6.82	6.80	5.66	4.36	5.10	7.74	3.83	3.77	5.79	6.87	3.35	3.40	3.99	3.89	3.79
CaO	0.03	0.00	0.09	0.01	0.03	0.08	0.02	0.02	0.01	0.00	0.02	0.01	0.02	0.00	0.01
Na_2O	0.00	0.00	0.00	0.00	0.01	0.01	0.01	0.01	0.01	0.01	0.01	0.00	0.01	0.02	0.01
NiO	0.05	0.03	0.11	0.08	0.06	0.06	0.07	0.10	0.08	0.09	0.05	0.07	0.03	0.02	0.01
Total	98.21	98.05	97.36	97.82	96.89	97.06	95.66	95.86	97.36	97.77	95.98	96.26	97.63	97.40	96.85
Cations per formula unit															
Si	0.00	0.00	0.00	0.00	0.00	0.00	0.00	0.01	0.00	0.00	0.00	0.00	0.00	0.00	0.00
Ti	0.01	0.01	0.01	0.01	0.01	0.00	0.01	0.01	0.01	0.00	0.01	0.01	0.01	0.01	0.01
Al	0.55	0.55	0.75	0.51	0.82	1.14	0.69	0.68	0.92	1.05	0.54	0.53	0.53	0.47	0.48
Cr	1.15	1.18	0.88	1.19	0.76	0.60	0.88	0.89	0.72	0.62	1.06	1.08	1.14	1.30	1.16
Fe^{2+}	0.66	0.66	0.71	0.77	0.74	0.63	0.80	0.80	0.71	0.67	0.81	0.81	0.78	0.79	0.80
Fe^{3+}	0.27	0.25	0.34	0.27	0.39	0.25	0.41	0.40	0.34	0.32	0.39	0.38	0.31	0.20	0.34
Mn	0.01	0.01	0.01	0.01	0.01	0.01	0.01	0.01	0.01	0.01	0.01	0.01	0.02	0.01	0.01
Mg	0.34	0.34	0.28	0.22	0.25	0.36	0.20	0.19	0.28	0.32	0.18	0.18	0.21	0.20	0.20
Ca	0.00	0.00	0.00	0.00	0.00	0.00	0.00	0.00	0.00	0.00	0.00	0.00	0.00	0.00	0.00
Na	0.00	0.00	0.00	0.00	0.00	0.00	0.00	0.00	0.00	0.00	0.00	0.00	0.00	0.00	0.00
Ni	0.00	0.00	0.00	0.00	0.00	0.00	0.00	0.00	0.00	0.00	0.00	0.00	0.00	0.00	0.00
Total	3.00	3.00	3.00	3.00	3.00	3.00	3.00	3.00	3.00	3.00	3.00	3.00	3.00	3.00	3.00
$Fe^{3+}/\Sigma Fe$ (uncorrected)	0.29	0.27	0.32	0.26	0.35	0.29	0.34	0.33	0.33	0.32	0.32	0.32	0.28	0.20	0.30
$Fe^{3+}/\Sigma Fe$ (corrected)	0.28	0.26	0.31	0.25	0.33	0.27	0.32	0.32	0.31	0.31	0.31	0.30	0.27	0.19	0.29

Sample #EN24VS008

Phase	chr2_1	chr2_2	chr3_1	chr4_1	chr5_1	chr6_1	chr7_1	chr7_2	chr8_1	chr8_2	chr9_1	chr10_1	chr11_1	chr12_2
Group	A	A	A	A	C	C	A	A	A	A	A	A	C	C
Oxide wt%	core	core	core	core	core	core	core	core	core	core	core	core	core	rim
SiO_2	0.04	0.04	0.00	0.01	0.03	0.01	0.02	0.02	0.02	0.03	0.04	0.03	0.01	0.01
TiO_2	0.45	0.35	0.56	0.60	1.05	0.99	0.48	0.47	0.39	0.40	0.23	0.28	0.57	0.56
Al_2O_3	14.58	15.89	9.26	8.88	7.18	8.13	11.82	12.02	10.39	10.51	12.46	13.57	9.99	8.52
Cr_2O_3	43.47	41.52	38.46	39.41	28.99	29.20	35.86	35.88	39.50	38.70	44.25	44.44	29.27	27.39
FeO	33.82	34.47	44.67	44.33	54.14	54.12	45.35	44.74	42.18	42.75	34.62	33.24	52.68	55.97
MnO	0.45	0.46	0.60	0.54	0.49	0.48	0.56	0.53	0.52	0.54	0.45	0.43	0.47	0.45
MgO	4.47	4.76	2.82	2.79	2.32	2.51	3.16	3.16	3.38	3.42	4.65	5.08	2.86	2.58
CaO	0.02	0.01	0.00	0.02	0.02	0.07	0.01	0.01	0.01	0.01	0.01	0.01	0.00	0.01
Na_2O	0.02	0.01	0.01	0.01	0.01	0.01	0.01	0.01	0.01	0.01	0.02	0.00	0.03	0.02
NiO	0.04	0.06	0.03	0.02	0.12	0.09	0.06	0.06	0.06	0.03	0.04	0.02	0.13	0.13
Total	97.35	97.59	96.42	96.62	94.34	95.62	97.33	96.89	96.48	96.39	96.77	97.10	96.01	95.64
Cations per formula unit														
Si	0.00	0.00	0.00	0.00	0.00	0.00	0.00	0.00	0.00	0.00	0.00	0.00	0.00	0.00
Ti	0.01	0.01	0.02	0.02	0.03	0.03	0.01	0.01	0.01	0.01	0.01	0.01	0.02	0.02
Al	0.59	0.64	0.39	0.37	0.31	0.35	0.49	0.50	0.43	0.44	0.51	0.55	0.42	0.36
Cr	1.18	1.12	1.09	1.11	0.84	0.83	0.99	0.99	1.11	1.08	1.22	1.21	0.82	0.78
Fe^{2+}	0.77	0.75	0.84	0.85	0.88	0.87	0.83	0.83	0.81	0.81	0.75	0.73	0.84	0.86
Fe^{3+}	0.20	0.23	0.49	0.48	0.78	0.77	0.50	0.48	0.44	0.45	0.26	0.22	0.73	0.83
Mn	0.01	0.01	0.02	0.02	0.02	0.01	0.02	0.02	0.02	0.02	0.01	0.01	0.01	0.01
Mg	0.23	0.24	0.15	0.15	0.13	0.14	0.16	0.17	0.18	0.18	0.24	0.26	0.15	0.14
Ca	0.00	0.00	0.00	0.00	0.00	0.00	0.00	0.00	0.00	0.00	0.00	0.00	0.00	0.00
Na	0.00	0.00	0.00	0.00	0.00	0.00	0.00	0.00	0.00	0.00	0.00	0.00	0.00	0.00
Ni	0.00	0.00	0.00	0.00	0.00	0.00	0.00	0.00	0.00	0.00	0.00	0.00	0.00	0.00
Total	3.00	3.00	3.00	3.00	3.00	3.00	3.00	3.00	3.00	3.00	3.00	3.00	3.00	3.00
$Fe^{3+}/\Sigma Fe$ (uncorrected)	0.21	0.23	0.37	0.36	0.47	0.47	0.37	0.37	0.35	0.36	0.26	0.23	0.46	0.49
$Fe^{3+}/\Sigma Fe$ (corrected)	0.20	0.22	0.36	0.35	0.46	0.46	0.36	0.35	0.34	0.35	0.24	0.22	0.45	0.48

Appendix E: Samarium-Neodymium Isotopes

Sample	Drillhole #	Depth (m)	Age (Ma)	Nd (ppm)	Sm (ppm)	^{143}Nd/^{144}Nd (Current)^{a}	^{147}Sm/^{144}Nd^{b}	^{143}Nd/^{144}Nd (Initial)	^{143}Nd/^{144}Nd (2σ)	εNd$_{T}$
EN23VS007	NOT-09-064	673.2	2735.5	16.54	4.08	0.511754	0.1490	0.509064	0.000028	-0.45
EN23VS015	NOT-09-064	969.0	2735.5	3.77	1.27	0.512600	0.2037	0.508923	0.000038	-3.22
EN23VS027	NOT-22-003	122.5	2735.5	7.16	1.87	0.511740	0.1580	0.508888	0.000030	-3.91
EN23VS041	NOT-11-1G243	199.7	2735.5	1.70	0.45	0.511946	0.1582	0.509090	0.000030	0.06
EN23VS051	NOT-09-056	622.5	2735.5	14.21	3.55	0.511835	0.1509	0.509111	0.000029	0.46
EN23VS059	NOT-08-034	63.5	2735.5	4.33	1.21	0.512061	0.1696	0.508999	0.000032	-1.73
EN23VS070	NOT-09-053-W4	884.8	2735.5	5.40	1.58	0.512245	0.1770	0.509051	0.000033	-0.72
EN23VS073	NOT-09-053-W4	909.5	2735.5	7.57	1.81	0.511754	0.1442	0.509151	0.000028	1.25
EN23VS084	NOT-09-070-W1	723.9	2735.5	3.97	1.26	0.512314	0.1917	0.508854	0.000036	-4.59
EN23VS092	NOT-10-076	449.6	2735.5	3.17	0.81	0.511978	0.1547	0.509186	0.000029	1.95
EN23VS095	NOT-10-085-W2	1375.2	2735.5	65.75	8.40	0.510526	0.0772	0.509132	0.000017	0.87
EN23VS096	NOT-10-085-W2	1369.7	2735.5	1.86	0.42	0.511585	0.1374	0.509106	0.000027	0.36
EN23VS102	NOT-09-055	467.6	2735.5	1.42	0.40	0.512179	0.1696	0.509117	0.000032	0.59
EN23VS103	NOT-09-065	635.0	2735.5	1.99	0.61	0.512488	0.1849	0.509151	0.000035	1.24
EN23VS111	NOT-10-078	330.1	2735.5	4.09	1.15	0.512125	0.1698	0.509060	0.000032	-0.54
EN23VS113	NOT-08-038	507.1	2735.5	3.33	0.90	0.512135	0.1625	0.509202	0.000031	2.24
EN23VS125	NOT-08-036	255.4	2735.5	6.75	1.65	0.511828	0.1481	0.509154	0.000028	1.31
EN23VS127	NOT-09-049	966.2	2735.5	6.82	1.63	0.511703	0.1446	0.509093	0.000028	0.10
EN23VS129	NOT-10-093	404.9	2773.4	17.02	2.86	0.510892	0.1017	0.509031	0.000021	-0.14
EN23VS132	NOT-12-1G005	184.9	2773.4	16.72	2.77	0.510895	0.1001	0.509064	0.000021	0.52
EN24VS039	NOT-10-090	750.3	2735.5	5.81	1.65	0.512209	0.1721	0.509102	0.000032	0.30

[a] Uncertainty (reproducibility of the standard) in the measured ^{143}Nd/^{144}Nd value is 0.00001.

[b] Uncertainty in ^{147}Sm/^{144}Nd value is 1%.

Appendix F: Sulfur Isotopes

Appendix F1: SIMS – Pyrrhotite

Sample	Grain	Spot	$^{33}S/^{32}S$	$\delta^{33}S_{VCDT}$ (‰)	2σ (‰)	$^{34}S/^{32}S$	$\delta^{34}S_{VCDT}$ (‰)	2σ (‰)	$\Delta^{33}S$ (‰)	2σ (‰)
EN23VS044	1	1	0.007878	0.12	0.19	0.044181	0.42	0.20	-0.10	0.19
EN23VS044	1	2	0.007878	0.07	0.21	0.044177	0.33	0.20	-0.10	0.20
EN23VS044	2	1	0.007877	0.01	0.14	0.044174	0.26	0.20	-0.13	0.13
EN23VS044	3	1	0.007878	0.11	0.19	0.044182	0.45	0.20	-0.12	0.19
EN23VS044	3	2	0.007878	0.07	0.18	0.044177	0.33	0.20	-0.10	0.18
EN23VS044	4	1	0.007877	-0.01	0.21	0.044166	0.07	0.20	-0.05	0.20
EN23VS044	5	1	0.007878	0.08	0.17	0.044181	0.41	0.20	-0.13	0.17
EN23VS044	6	1	0.007879	0.22	0.21	0.044181	0.42	0.20	0.00	0.21
EN23VS044	7	1	0.007878	0.11	0.19	0.044179	0.38	0.20	-0.09	0.19
EN23VS044	8	1	0.007878	0.07	0.19	0.044176	0.30	0.20	-0.09	0.18
EN23VS044	8	2	0.007876	-0.10	0.18	0.044168	0.12	0.20	-0.16	0.17
EN23VS044	8	3	0.007877	0.02	0.18	0.044173	0.23	0.20	-0.09	0.18
EN23VS101	1	1	0.007872	-0.71	0.22	0.044092	-1.60	0.20	0.12	0.22
EN23VS101	1	2	0.007872	-0.62	0.19	0.044108	-1.25	0.20	0.03	0.19
EN23VS101	2	1	0.007872	-0.62	0.19	0.044100	-1.41	0.20	0.11	0.18
EN23VS101	3	1	0.007871	-0.80	0.26	0.044095	-1.54	0.20	-0.01	0.26
EN23VS101	4	1	0.007872	-0.69	0.23	0.044091	-1.61	0.20	0.14	0.23
EN23VS101	4	2	0.007872	-0.64	0.19	0.044097	-1.49	0.20	0.13	0.19
EN23VS101	5	1	0.007872	-0.68	0.21	0.044103	-1.35	0.20	0.01	0.20
EN23VS101	6	1	0.007872	-0.70	0.20	0.044098	-1.46	0.20	0.05	0.20
EN23VS101	7	1	0.007871	-0.79	0.22	0.044086	-1.72	0.20	0.10	0.22
EN23VS114	1	1	0.007881	0.49	0.14	0.044197	0.78	0.20	0.08	0.13
EN23VS114	2	1	0.007881	0.52	0.18	0.044199	0.82	0.20	0.10	0.18
EN23VS114	3	1	0.007880	0.40	0.21	0.044198	0.80	0.20	-0.01	0.20
EN23VS114	3	2	0.007880	0.41	0.21	0.044200	0.84	0.20	-0.02	0.20
EN23VS114	4	1	0.007881	0.49	0.18	0.044195	0.73	0.20	0.12	0.17
EN23VS121	1	1	0.007884	0.82	0.16	0.044226	1.43	0.20	0.08	0.16
EN23VS121	2	1	0.007883	0.75	0.14	0.044219	1.27	0.20	0.09	0.13
EN23VS121	2	2	0.007882	0.64	0.13	0.044211	1.10	0.20	0.08	0.12
EN23VS121	3	1	0.007884	0.92	0.19	0.044234	1.62	0.20	0.08	0.18
EN23VS121	3	2	0.007885	0.99	0.16	0.044236	1.65	0.20	0.14	0.15
EN23VS121	3	3	0.007885	0.92	0.19	0.044236	1.67	0.20	0.06	0.19
EN23VS121	4	1	0.007884	0.84	0.20	0.044227	1.47	0.20	0.08	0.19
EN23VS121	5	2	0.007884	0.89	0.18	0.044232	1.58	0.20	0.08	0.18
EN23VS121	6	1	0.007884	0.87	0.19	0.044231	1.56	0.20	0.07	0.18
EN23VS122	1	1	0.007883	0.73	0.20	0.044211	1.10	0.20	0.17	0.19
EN23VS122	1	2	0.007882	0.58	0.21	0.044205	0.96	0.20	0.09	0.20
EN23VS122	2	1	0.007883	0.69	0.17	0.044212	1.12	0.20	0.12	0.16
EN23VS127	1	1	0.007881	0.47	0.16	0.044196	0.76	0.20	0.07	0.15
EN23VS127	2	1	0.007880	0.33	0.20	0.044184	0.48	0.20	0.08	0.20
EN23VS127	3	1	0.007879	0.27	0.16	0.044183	0.45	0.20	0.04	0.15

Appendix F1 cont.

Sample	Grain	Spot	$^{33}S/^{32}S$	$\delta^{33}S_{VCDT}$ (‰)	2σ (‰)	$^{34}S/^{32}S$	$\delta^{34}S_{VCDT}$ (‰)	2σ (‰)	$\Delta^{33}S$ (‰)	2σ (‰)
EN23VS127	4	1	0.007880	0.34	0.23	0.044190	0.61	0.20	0.03	0.23
EN23VS127	5	1	0.007878	0.09	0.20	0.044160	-0.07	0.20	0.12	0.20
EN23VS127	5	2	0.007880	0.30	0.19	0.044186	0.53	0.20	0.03	0.19

Appendix F2: SIMS – Pentlandite

Sample	Grain	Spot	$^{33}S/^{32}S$	$\delta^{33}S_{VCDT}$ (‰)	2σ (‰)	$^{34}S/^{32}S$	$\delta^{34}S_{VCDT}$ (‰)	2σ (‰)	$\Delta^{33}S$ (‰)	2σ (‰)
EN23VS044	1	1	0.007882	0.66	0.20	0.044220	1.31	0.20	-0.01	0.22
EN23VS044	1	2	0.007883	0.67	0.20	0.044234	1.62	0.20	-0.16	0.22
EN23VS044	1	3	0.007882	0.62	0.20	0.044226	1.44	0.20	-0.12	0.22
EN23VS044	2	1	0.007878	0.09	0.20	0.044175	0.28	0.20	-0.06	0.22
EN23VS044	2	2	0.007880	0.36	0.20	0.044200	0.85	0.20	-0.07	0.22
EN23VS044	3	1	0.007881	0.44	0.20	0.044209	1.04	0.20	-0.10	0.22
EN23VS044	3	2	0.007879	0.25	0.20	0.044192	0.67	0.20	-0.10	0.22
EN23VS044	4	1	0.007881	0.44	0.20	0.044209	1.05	0.20	-0.10	0.22
EN23VS044	5	1	0.007883	0.68	0.20	0.044226	1.45	0.20	-0.06	0.22
EN23VS044	6	1	0.007880	0.35	0.20	0.044199	0.83	0.20	-0.08	0.22
EN23VS044	6	2	0.007881	0.46	0.20	0.044211	1.09	0.20	-0.10	0.22
EN23VS044	7	1	0.007884	0.80	0.20	0.044238	1.71	0.20	-0.08	0.22
EN23VS044	7	2	0.007882	0.59	0.20	0.044226	1.43	0.20	-0.14	0.22
EN23VS044	9	5	0.007882	0.61	0.20	0.044233	1.60	0.20	-0.22	0.22
EN23VS044	9	1	0.007882	0.57	0.20	0.044220	1.30	0.20	-0.11	0.22
EN23VS044	9	2	0.007881	0.44	0.20	0.044211	1.09	0.20	-0.13	0.22
EN23VS044	9	3	0.007882	0.64	0.20	0.044226	1.44	0.20	-0.10	0.22
EN23VS044	9	4	0.007882	0.59	0.20	0.044221	1.33	0.20	-0.09	0.22
EN23VS044	10	1	0.007884	0.83	0.20	0.044249	1.95	0.20	-0.17	0.22
EN23VS044	11	1	0.007881	0.45	0.20	0.044217	1.24	0.20	-0.19	0.22
EN23VS044	11	2	0.007881	0.53	0.20	0.044234	1.61	0.20	-0.30	0.22
EN23VS044	11	3	0.007882	0.56	0.20	0.044220	1.29	0.20	-0.10	0.22
EN23VS044	12	1	0.007883	0.77	0.20	0.044231	1.55	0.20	-0.03	0.22
EN23VS044	12	2	0.007881	0.50	0.20	0.044213	1.14	0.20	-0.09	0.22
EN23VS044	12	3	0.007881	0.50	0.20	0.044215	1.18	0.20	-0.11	0.22
EN23VS044	13	1	0.007882	0.57	0.20	0.044214	1.15	0.20	-0.03	0.22
EN23VS044	14	1	0.007879	0.21	0.20	0.044183	0.45	0.20	-0.02	0.22
EN23VS044	14	2	0.007881	0.46	0.20	0.044209	1.05	0.20	-0.08	0.22
EN23VS101	1	1	0.007882	0.55	0.20	0.044206	0.99	0.20	0.04	0.22
EN23VS101	1	2	0.007884	0.82	0.20	0.044226	1.44	0.20	0.08	0.22
EN23VS101	1	3	0.007884	0.82	0.20	0.044226	1.44	0.20	0.08	0.22
EN23VS101	1	4	0.007883	0.78	0.20	0.044231	1.55	0.20	-0.01	0.22
EN23VS101	1	5	0.007883	0.73	0.20	0.044221	1.32	0.20	0.05	0.22

Appendix F2 cont.

Sample	Grain	Spot	$^{33}S/^{32}S$	$\delta^{33}S_{VCDT}$ (‰)	2σ (‰)	$^{34}S/^{32}S$	$\delta^{34}S_{VCDT}$ (‰)	2σ (‰)	$\Delta^{33}S$ (‰)	2σ (‰)
EN23VS101	1	6	0.007884	0.87	0.20	0.044232	1.57	0.20	0.06	0.22
EN23VS101	1	7	0.007886	1.08	0.20	0.044249	1.95	0.20	0.07	0.22
EN23VS101	2	1	0.007882	0.64	0.20	0.044213	1.15	0.20	0.05	0.22
EN23VS101	2	2	0.007885	1.04	0.20	0.044239	1.73	0.20	0.15	0.22
EN23VS101	2	3	0.007884	0.86	0.20	0.044235	1.64	0.20	0.02	0.22
EN23VS101	2	4	0.007884	0.84	0.20	0.044241	1.78	0.20	-0.08	0.22
EN23VS101	2	5	0.007883	0.76	0.20	0.044226	1.43	0.20	0.02	0.22
EN23VS101	3	1	0.007886	1.08	0.20	0.044251	2.00	0.20	0.05	0.22
EN23VS101	3	2	0.007886	1.06	0.20	0.044253	2.05	0.20	0.00	0.22
EN23VS101	4	1	0.007883	0.74	0.20	0.044214	1.16	0.20	0.14	0.22
EN23VS101	5	1	0.007883	0.67	0.20	0.044222	1.34	0.20	-0.02	0.22
EN23VS101	6	1	0.007883	0.71	0.20	0.044222	1.35	0.20	0.02	0.22
EN23VS101	7	1	0.007883	0.76	0.20	0.044219	1.27	0.20	0.11	0.22
EN23VS101	7	2	0.007883	0.74	0.20	0.044214	1.16	0.20	0.14	0.22
EN23VS101	8	1	0.007883	0.71	0.20	0.044219	1.27	0.20	0.05	0.22
EN23VS121	1	1	0.007888	1.35	0.20	0.044263	2.28	0.20	0.18	0.22
EN23VS121	2	1	0.007887	1.30	0.20	0.044273	2.49	0.20	0.02	0.22
EN23VS121	3	1	0.007888	1.31	0.20	0.044275	2.55	0.20	0.00	0.22
EN23VS121	3	2	0.007882	0.64	0.20	0.044207	1.02	0.20	0.12	0.22
EN23VS121	4	1	0.007885	1.01	0.20	0.044244	1.85	0.20	0.05	0.22
EN23VS121	4	2	0.007887	1.25	0.20	0.044263	2.27	0.20	0.08	0.22
EN23VS121	5	1	0.007891	1.72	0.20	0.044281	2.69	0.20	0.34	0.22
EN23VS121	5	2	0.007888	1.38	0.20	0.044281	2.67	0.20	0.01	0.22
EN23VS121	5	3	0.007887	1.27	0.20	0.044262	2.26	0.20	0.11	0.22
EN23VS121	5	4	0.007889	1.52	0.20	0.044283	2.72	0.20	0.12	0.22
EN23VS121	5	5	0.007889	1.49	0.20	0.044265	2.31	0.20	0.30	0.22
EN23VS121	5	6	0.007889	1.53	0.20	0.044277	2.60	0.20	0.19	0.22
EN23VS121	6	1	0.007889	1.44	0.20	0.044283	2.73	0.20	0.03	0.22
EN23VS121	7	1	0.007889	1.45	0.20	0.044272	2.48	0.20	0.17	0.22
EN23VS121	6	2	0.007889	1.49	0.20	0.044285	2.77	0.20	0.06	0.22
EN23VS121	6	3	0.007890	1.60	0.20	0.044300	3.12	0.20	0.00	0.22
EN23VS121	6	4	0.007891	1.73	0.20	0.044300	3.11	0.20	0.13	0.22
EN23VS121	6	5	0.007892	1.90	0.20	0.044318	3.52	0.20	0.09	0.22
EN23VS121	7	2	0.007886	1.11	0.20	0.044250	1.97	0.20	0.09	0.22
EN23VS121	7	3	0.007888	1.32	0.20	0.044270	2.43	0.20	0.07	0.22
EN23VS121	7	4	0.007889	1.55	0.20	0.044288	2.84	0.20	0.08	0.22
EN23VS121	7	5	0.007889	1.52	0.20	0.044283	2.72	0.20	0.12	0.22
EN23VS122	1	1	0.007879	0.26	0.20	0.044181	0.42	0.20	0.05	0.22
EN23VS122	1	2	0.007886	1.17	0.20	0.044254	2.08	0.20	0.10	0.22
EN23VS122	2	1	0.007886	1.10	0.20	0.044248	1.94	0.20	0.10	0.22
EN23VS122	2	2	0.007886	1.17	0.20	0.044249	1.96	0.20	0.16	0.22

Appendix F2 cont.

Sample	Grain	Spot	$^{33}S/^{32}S$	$\delta^{33}S_{VCDT}$ (‰)	2σ (‰)	$^{34}S/^{32}S$	$\delta^{34}S_{VCDT}$ (‰)	2σ (‰)	$\Delta^{33}S$ (‰)	2σ (‰)
EN23VS122	2	3	0.007888	1.35	0.20	0.044267	2.37	0.20	0.13	0.22
EN23VS127	1	1	0.007881	0.53	0.20	0.044208	1.04	0.20	-0.01	0.22
EN23VS127	2	1	0.007881	0.51	0.20	0.044210	1.08	0.20	-0.04	0.22
EN23VS127	3	1	0.007874	-0.41	0.20	0.044127	-0.80	0.20	0.00	0.22
EN23VS127	3	2	0.007884	0.82	0.20	0.044231	1.56	0.20	0.01	0.22
EN23VS127	4	1	0.007878	0.08	0.20	0.044161	-0.03	0.20	0.09	0.22

Appendix F3: SIMS – Chalcopyrite

Sample	Grain	Spot	$^{33}S/^{32}S$	$\delta^{33}S_{VCDT}$ (‰)	2σ (‰)	$^{34}S/^{32}S$	$\delta^{34}S_{VCDT}$ (‰)	2σ (‰)	$\Delta^{33}S$ (‰)	2σ (‰)
EN23VS044	1	1	0.007879	0.24	0.20	0.044196	0.76	0.24	-0.15	0.22
EN23VS044	1	2	0.007880	0.32	0.20	0.044197	0.79	0.24	-0.08	0.22
EN23VS044	2	1	0.007881	0.47	0.20	0.044209	1.05	0.24	-0.07	0.22
EN23VS044	2	2	0.007881	0.49	0.20	0.044208	1.03	0.24	-0.04	0.22
EN23VS044	2	3	0.007881	0.52	0.20	0.044209	1.05	0.24	-0.03	0.22
EN23VS044	2	4	0.007881	0.47	0.20	0.044212	1.13	0.24	-0.11	0.22
EN23VS044	3	1	0.007881	0.50	0.20	0.044210	1.08	0.24	-0.05	0.22
EN23VS044	3	2	0.007881	0.48	0.20	0.044210	1.08	0.24	-0.08	0.22
EN23VS044	3	3	0.007880	0.32	0.20	0.044203	0.93	0.24	-0.16	0.22
EN23VS044	3	4	0.007881	0.49	0.20	0.044211	1.10	0.24	-0.07	0.22
EN23VS044	4	1	0.007880	0.30	0.20	0.044196	0.75	0.24	-0.09	0.22
EN23VS044	5	1	0.007881	0.53	0.20	0.044217	1.24	0.24	-0.11	0.22
EN23VS044	5	2	0.007881	0.43	0.20	0.044211	1.09	0.24	-0.13	0.22
EN23VS044	6	1	0.007881	0.50	0.20	0.044214	1.16	0.24	-0.10	0.22
EN23VS044	6	2	0.007881	0.44	0.20	0.044214	1.17	0.24	-0.16	0.22
EN23VS044	6	3	0.007881	0.45	0.20	0.044212	1.12	0.24	-0.13	0.22
EN23VS044	7	1	0.007880	0.41	0.20	0.044206	0.97	0.24	-0.09	0.22
EN23VS044	8	1	0.007880	0.39	0.20	0.044204	0.93	0.24	-0.09	0.22
EN23VS044	8	2	0.007881	0.47	0.20	0.044210	1.07	0.24	-0.08	0.22
EN23VS044	9	1	0.007881	0.47	0.20	0.044212	1.12	0.24	-0.10	0.22
EN23VS044	9	2	0.007880	0.35	0.20	0.044195	0.74	0.24	-0.03	0.22
EN23VS044	9	3	0.007879	0.25	0.20	0.044194	0.72	0.24	-0.12	0.22
EN23VS044	10	1	0.007880	0.39	0.20	0.044194	0.71	0.24	0.02	0.22
EN23VS044	10	2	0.007881	0.46	0.20	0.044205	0.95	0.24	-0.03	0.22
EN23VS114	1	1	0.007882	0.62	0.20	0.044206	0.98	0.24	0.12	0.22
EN23VS114	1	2	0.007883	0.70	0.20	0.044213	1.14	0.24	0.12	0.22
EN23VS114	2	1	0.007882	0.66	0.20	0.044210	1.07	0.24	0.12	0.22
EN23VS114	2	2	0.007882	0.64	0.20	0.044209	1.05	0.24	0.09	0.22
EN23VS116	1	1	0.007883	0.79	0.20	0.044211	1.11	0.24	0.22	0.22
EN23VS116	1	2	0.007882	0.66	0.20	0.044209	1.06	0.24	0.11	0.22

Appendix F3 cont.

Sample	Grain	Spot	$^{33}S/^{32}S$	$\delta^{33}S_{VCDT}$ (‰)	2σ (‰)	$^{34}S/^{32}S$	$\delta^{34}S_{VCDT}$ (‰)	2σ (‰)	$\Delta^{33}S$ (‰)	2σ (‰)
EN23VS116	1	3	0.007883	0.72	0.20	0.044209	1.06	0.24	0.18	0.22
EN23VS116	1	4	0.007882	0.63	0.20	0.044205	0.96	0.24	0.14	0.22
EN23VS116	1	5	0.007882	0.59	0.20	0.044205	0.95	0.24	0.10	0.22
EN23VS116	1	6	0.007882	0.60	0.20	0.044206	0.99	0.24	0.10	0.22
EN23VS116	1	7	0.007882	0.59	0.20	0.044205	0.96	0.24	0.10	0.22
EN23VS116	2	1	0.007881	0.46	0.20	0.044192	0.68	0.24	0.11	0.22
EN23VS121	1	1	0.007886	1.08	0.20	0.044249	1.95	0.24	0.08	0.22
EN23VS121	2	2	0.007882	0.66	0.20	0.044207	1.02	0.24	0.14	0.22
EN23VS121	3	1	0.007886	1.15	0.20	0.044248	1.93	0.24	0.15	0.22
EN23VS121	3	2	0.007885	1.04	0.20	0.044245	1.86	0.24	0.08	0.22
EN23VS121	3	3	0.007886	1.10	0.20	0.044243	1.83	0.24	0.16	0.22
EN23VS121	3	4	0.007885	0.97	0.20	0.044241	1.77	0.24	0.06	0.22
EN23VS121	3	5	0.007882	0.65	0.20	0.044208	1.03	0.24	0.12	0.22
EN23VS121	3	6	0.007887	1.21	0.20	0.044258	2.16	0.24	0.10	0.22
EN23VS121	3	7	0.007886	1.14	0.20	0.044251	2.01	0.24	0.10	0.22
EN23VS122	1	1	0.007882	0.55	0.20	0.044206	0.99	0.24	0.04	0.22
EN23VS122	1	2	0.007882	0.57	0.20	0.044206	0.99	0.24	0.06	0.22
EN23VS122	1	3	0.007882	0.61	0.20	0.044205	0.96	0.24	0.12	0.22
EN23VS122	1	4	0.007882	0.61	0.20	0.044205	0.96	0.24	0.12	0.22
EN23VS122	1	5	0.007883	0.70	0.20	0.044212	1.12	0.24	0.12	0.22
EN23VS122	1	6	0.007882	0.61	0.20	0.044206	0.97	0.24	0.11	0.22
EN23VS122	1	7	0.007882	0.67	0.20	0.044210	1.08	0.24	0.11	0.22
EN23VS122	1	8	0.007882	0.61	0.20	0.044205	0.95	0.24	0.12	0.22
EN23VS122	2	1	0.007882	0.65	0.20	0.044211	1.09	0.24	0.09	0.22
EN23VS122	3	1	0.007881	0.50	0.20	0.044203	0.92	0.24	0.03	0.22
EN23VS122	2	2	0.007882	0.61	0.20	0.044204	0.95	0.24	0.12	0.22
EN23VS122	2	3	0.007882	0.56	0.20	0.044205	0.97	0.24	0.07	0.22
EN23VS122	2	4	0.007883	0.68	0.20	0.044212	1.11	0.24	0.10	0.22
EN23VS122	2	5	0.007881	0.48	0.20	0.044204	0.93	0.24	0.00	0.22
EN23VS122	2	6	0.007882	0.60	0.20	0.044205	0.96	0.24	0.11	0.22
EN23VS122	2	7	0.007882	0.64	0.20	0.044203	0.91	0.24	0.17	0.22
EN23VS122	3	1	0.007882	0.66	0.20	0.044205	0.96	0.24	0.17	0.22
EN23VS122	3	2	0.007881	0.50	0.20	0.044201	0.88	0.24	0.04	0.22
EN23VS122	4	1	0.007881	0.51	0.20	0.044201	0.88	0.24	0.06	0.22
EN23VS122	5	1	0.007882	0.57	0.20	0.044206	0.97	0.24	0.06	0.22
EN23VS122	6	1	0.007881	0.43	0.20	0.044198	0.80	0.24	0.02	0.22
EN23VS127	1	1	0.007881	0.54	0.20	0.044197	0.79	0.24	0.13	0.22
EN23VS127	1	2	0.007878	0.07	0.20	0.044163	0.01	0.24	0.06	0.22
EN23VS127	2	1	0.007877	-0.06	0.20	0.044151	-0.27	0.24	0.08	0.22
EN23VS127	2	2	0.007880	0.35	0.20	0.044184	0.49	0.24	0.09	0.22

Appendix F4: LA-ICP-MS – Pentlandite

Sample	Grain	Spot	$^{33}S/^{32}S$	Error	$^{34}S/^{32}S$	Error	$\delta^{34}S_{VCDT}$ (‰)	1SE
EN24VS006	1	1	0.008264	0.000001	0.048499	0.000028	0.58	0.81
EN24VS006	1	2	0.008265	0.000001	0.048486	0.000022	0.26	0.64
EN24VS006	1	3	0.008264	0.000001	0.048500	0.000023	0.49	0.66
EN24VS006	2	1	0.008264	0.000001	0.048493	0.000026	0.32	0.77
EN24VS006	3	1	0.008264	0.000001	0.048474	0.000029	-0.04	0.85
EN24VS006	4	1	0.008266	0.000001	0.048482	0.000028	0.13	0.82
EN24VS006	4	2	0.008266	0.000001	0.048489	0.000023	0.30	0.67
EN24VS006	5	1	0.008263	0.000001	0.048496	0.000027	0.46	0.78
EN24VS006	5	2	0.008264	0.000001	0.048486	0.000026	0.27	0.76
EN24VS006	5	3	0.008266	0.000001	0.048484	0.000028	0.23	0.81
EN24VS006	6	1	0.008266	0.000001	0.048454	0.000025	-0.38	0.73
EN24VS006	6	2	0.008265	0.000001	0.048502	0.000027	0.60	0.78
EN24VS006	6	3	0.008265	0.000001	0.048489	0.000030	0.34	0.87
EN24VS006	6	4	0.008264	0.000001	0.048464	0.000027	-0.16	0.78
EN24VS006	6	5	0.008265	0.000001	0.048469	0.000029	-0.07	0.83
EN24VS006	7	1	0.008265	0.000001	0.048485	0.000023	0.14	0.67
EN24VS006	8	1	0.008266	0.000001	0.048476	0.000029	0.01	0.85
EN24VS006	8	2	0.008264	0.000001	0.048453	0.000024	-0.40	0.69
EN24VS006	9	1	0.008263	0.000002	0.048462	0.000024	-0.15	0.69
EN24VS006	10	1	0.008262	0.000001	0.048420	0.000029	-1.00	0.86
EN24VS006	10	2	0.008263	0.000001	0.048455	0.000032	-0.25	0.94
EN24VS006	10	3	0.008261	0.000001	0.048470	0.000031	0.07	0.91
EN24VS006	10	4	0.008265	0.000001	0.048453	0.000023	-0.30	0.66
EN24VS006	11	1	0.008264	0.000001	0.048447	0.000025	-0.48	0.74
EN24VS006	11	2	0.008264	0.000001	0.048464	0.000029	-0.18	0.84
EN24VS006	11	3	0.008264	0.000001	0.048450	0.000027	-0.53	0.78
EN24VS006	12	1	0.008262	0.000001	0.048454	0.000020	-0.45	0.59
EN24VS006	12	2	0.008263	0.000001	0.048471	0.000020	-0.07	0.59
EN24VS006	12	3	0.008266	0.000001	0.048466	0.000025	-0.13	0.72
EN24VS006	13	1	0.008266	0.000001	0.048478	0.000021	0.15	0.60
EN24VS010	1	1	0.008280	0.000001	0.048555	0.000028	-0.17	0.82
EN24VS010	2	1	0.008279	0.000001	0.048565	0.000029	0.07	0.85
EN24VS010	3	1	0.008279	0.000001	0.048556	0.000026	-0.05	0.76
EN24VS010	4	1	0.008279	0.000001	0.048557	0.000028	0.02	0.82
EN24VS010	5	1	0.008278	0.000001	0.048556	0.000029	0.05	0.85
EN24VS010	6	1	0.008280	0.000002	0.048569	0.000036	0.39	1.05
EN24VS010	7	1	0.008279	0.000001	0.048544	0.000026	-0.09	0.77
EN24VS010	8	1	0.008279	0.000001	0.048537	0.000033	-0.22	0.95
EN24VS010	9	1	0.008280	0.000002	0.048571	0.000036	0.50	1.05

Appendix F5: LA-ICP-MS – Chalcopyrite

Sample	Grain	Spot	$^{33}S/^{32}S$	Error	$^{34}S/^{32}S$	Error	$\delta^{34}S_{VCDT}$ (‰)	1SE
EN24VS006	1	1	0.008262	0.000001	0.048423	0.000023	0.75	0.68
EN24VS006	2	1	0.008263	0.000001	0.048425	0.000021	0.90	0.62
EN24VS006	3	1	0.008263	0.000001	0.048430	0.000019	1.08	0.55
EN24VS006	3	2	0.008259	0.000001	0.048440	0.000020	1.34	0.60
EN24VS006	4	1	0.008260	0.000001	0.048439	0.000018	1.29	0.52
EN24VS006	4	2	0.008262	0.000001	0.048425	0.000020	0.94	0.59
EN24VS006	4	3	0.008261	0.000001	0.048431	0.000022	1.02	0.65
EN24VS006	4	4	0.008259	0.000001	0.048425	0.000014	0.86	0.42
EN24VS006	4	5	0.008262	0.000001	0.048440	0.000017	1.16	0.48
EN24VS006	5	1	0.008264	0.000001	0.048442	0.000021	1.24	0.62
EN24VS006	5	2	0.008264	0.000001	0.048444	0.000023	1.32	0.68
EN24VS006	6	1	0.008264	0.000001	0.048448	0.000023	1.44	0.66
EN24VS006	6	2	0.008265	0.000001	0.048438	0.000017	1.21	0.50
EN24VS006	7	1	0.008264	0.000001	0.048437	0.000020	1.13	0.58
EN24VS006	7	2	0.008262	0.000001	0.048438	0.000024	1.08	0.69
EN24VS006	7	3	0.008267	0.000001	0.048448	0.000021	1.21	0.61
EN24VS006	7	4	0.008265	0.000001	0.048438	0.000024	0.86	0.69
EN24VS006	7	5	0.008265	0.000001	0.048441	0.000021	0.85	0.60
EN24VS006	8	1	0.008267	0.000001	0.048437	0.000021	0.69	0.61
EN24VS006	9	1	0.008264	0.000001	0.048430	0.000017	0.44	0.50
EN24VS006	9	2	0.008262	0.000003	0.048404	0.000018	-0.09	0.51
EN24VS006	10	1	0.008268	0.000002	0.048421	0.000023	0.25	0.67
EN24VS006	10	2	0.008264	0.000002	0.048435	0.000023	0.52	0.68
EN24VS006	11	1	0.008267	0.000002	0.048441	0.000017	0.71	0.50
EN24VS006	11	2	0.008262	0.000001	0.048442	0.000023	0.80	0.67
EN24VS006	11	3	0.008263	0.000001	0.048461	0.000018	1.26	0.53
EN24VS006	12	1	0.008259	0.000002	0.048427	0.000021	0.62	0.62
EN24VS006	13	1	0.008261	0.000001	0.048461	0.000017	1.33	0.51
EN24VS006	13	2	0.008261	0.000001	0.048452	0.000023	1.10	0.68
EN24VS006	13	3	0.008262	0.000001	0.048451	0.000024	1.01	0.70
EN24VS010	1	1	0.008276	0.000001	0.048552	0.000025	0.87	0.72
EN24VS010	2	1	0.008277	0.000001	0.048578	0.000017	1.43	0.50
EN24VS010	3	1	0.008278	0.000001	0.048574	0.000017	1.35	0.50
EN24VS010	4	1	0.008279	0.000001	0.048592	0.000018	1.71	0.52
EN24VS010	5	1	0.008278	0.000001	0.048568	0.000022	1.19	0.65
EN24VS010	6	1	0.008279	0.000001	0.048585	0.000016	1.53	0.48
EN24VS010	7	1	0.008278	0.000001	0.048558	0.000018	0.99	0.52
EN24VS010	8	1	0.008278	0.000001	0.048582	0.000017	1.53	0.50
EN24VS010	8	2	0.008278	0.000001	0.048575	0.000022	1.43	0.64